

**Synthesis of monolithic shape-stabilized phase
change materials by an *in situ* sol-gel process**

Dissertation

zur Erlangung des Doktorgrades der
Naturwissenschaften
(Dr. rer. nat.)

der

Naturwissenschaftlichen Fakultät II
Chemie, Physik und Mathematik

der Martin-Luther-Universität
Halle-Wittenberg

vorgelegt von

Herrn Felix Marske
geb. am 16.05.1992 in Wolfenbüttel

Die vorliegende kumulative Dissertation „*Synthesis of monolithic shape-stabilized phase change materials by an in situ sol-gel process*“ wurde an der Martin-Luther-Universität Halle-Wittenberg am Institut für Chemie der Naturwissenschaftlichen Fakultät II im Zeitraum vom 15.11.2017 bis 14.11.2021 unter der Leitung von Prof. Dr. Thomas Hahn angefertigt.

1. Gutachter: Prof. Dr. Thomas Hahn

2. Gutachter: Prof. Dr. Franziska Scheffler

Tag der Verteidigung: 17.05.2023

“Today, global emissions are still rising. And this has to change as a matter of urgency. I want this decade to be the Roaring Twenties of climate action and climate investment. Europe must lead this change. It’s our last chance to stop climate change”

Ursula von der Leyen [1], President of the European Commission (2021)

“Storing energy turns out to be surprisingly hard and expensive. So if a consumer tried to store enough electricity in this lithium-ion battery to run her house, she would be paying at least \$0.30 per kilowatt-hour for the battery. According to the EIA, the average price of electricity for consumers in the United States is around \$0.10 per kilowatt-hour. This is one of the reasons why we need new inventions that improve our ability to store energy cheaply and efficiently. Getting them will make it easier for solar and wind to be a big part of our zero-carbon future.”

Bill Gates [2], Founder of Microsoft (2016)

“Despite its immense value to the energy system, the role of thermal energy storage concepts is not always fully recognised by policymakers. For example, the ongoing discussions about the energy storage definition in the European Parliament would appear to exclude thermal energy storage and Power-to-Gas, or Power-to-Liquids. A broader energy storage definition, such as the European Commission’s initial proposal, is needed to allow all energy storage technologies to be considered.”

Patrick Clerens [3], European Association for the Storage of Energy (2017)

“I think heat storage is a ‘global’ solution to the entire energy storage problem. The record also shows that I backed up this assessment by placing an economic ‘bet’ with the chief asset I had: my time. It’s one thing to make armchair conversations about these issues, quite another to actually act on them.”

Robert B. Laughlin [4], Nobel Price Winner in Physics 1998 (2018)

Die kumulative Dissertation setzt sich aus fünf Artikeln zusammen:

- 1 **Synthesis of monolithic shape-stabilized phase change materials with high mechanical stability via a porogen-assisted *in situ* sol-gel process**
F. Marske, J. Martins de Souza e Silva, R. B. Wehrspohn, T. Hahn and D. Enke
Erschienen in *RSC Advances* 10 (2020)
<https://doi.org/10.1039/c9ra10631f>
- 2 **Size and surface effects of hexagonal boron nitrides on the physicochemical properties of monolithic phase change materials synthesized via sol-gel route**
F. Marske, T. Lindenberg, J. Martins de Souza e Silva, R. B. Wehrspohn, A. W. Maijenburg, T. Hahn and D. Enke
Erschienen in *Applied Thermal Engineering* 196 (2021)
<https://doi.org/10.1016/j.applthermaleng.2021.117325>
- 3 **Experimental data showing the influence of different boron nitride particles on the silica network, the butyl stearate and the porogens in shape-stabilized phase change materials**
F. Marske, T. Lindenberg, J. Martins de Souza e Silva, R. B. Wehrspohn, A. W. Maijenburg, T. Hahn and D. Enke
Erschienen in *Data in Brief* 38 (2021)
<https://doi.org/10.1016/j.dib.2021.107428>
- 4 **Influence of surfactants and organic polymers on monolithic shape-stabilized phase change materials synthesized via sol-gel route**
Felix Marske, Joe Dasler, Caroline Haupt, Kirsten Bacia, Thomas Hahn and Dirk Enke
Erschienen in *Journal of Energy Storage* 49 (2022)
<https://doi.org/10.1016/j.est.2022.104127>
- 5 **Shape stabilization of organic phase change materials as mechanical stable silica boards with high latent heats via sol-gel route**
Felix Marske, Caroline Haupt, Claudia Birkemeyer, Kirsten Bacia, Thomas Hahn and Dirk Enke
Erschienen in *Journal of Building Engineering* 60 (2022)
<https://doi.org/10.1016/j.jobbe.2022.105198>

Danksagung

Mit dem Zitat "*Man kann einem Menschen nichts beibringen, man kann ihm nur helfen es in sich selbst zu entdecken*" von Galileo Galilei möchte ich mich herzlich bei Prof. Dr. Thomas Hahn für die Betreuung meiner Doktorarbeit und für sein Vertrauen mir gegenüber bedanken. Zudem möchte ich mich noch für die vielen Ratschläge und die Unterstützung sowohl bei der Durchführung der Doktorarbeit als auch bei der technischen Konzipierung diverser Prototypen bedanken.

Wissenschaftliche Artikel zu schreiben und diese erfolgreich zu veröffentlichen, ist kein leichtes Unterfangen. Umso wichtiger ist fachlich fundierte Hilfe. Aus diesem Grund und für die Betreuung bei sämtlichen chemischen Fragestellungen möchte ich Prof. Dr. Dirk Enke tiefen Dank aussprechen.

Verrückte Ideen zu entwickeln und erfolgreich umzusetzen, erfordert einen kreativen Austausch, den ich ohne die Doktoranden aus dem Arbeitskreis Hahn M.Sc. Lennart Bode, Dr. Jan Herwig, M.Sc. Elisa Brade und M.Sc. Konstantin Storch nicht gehabt hätte. Vielen Dank. Zudem möchte ich mich für die angenehme Atmosphäre und Hilfe bei Messungen und bei Bestellungen bei Frau Jenny Bienias-Dragon und Frau Gitta Marx bedanken.

Im Laufe der Promotion durfte ich viele außergewöhnliche Menschen und Arbeitskreise kennenlernen. Hierzu zählen insbesondere der Arbeitskreis Wehrspohn mit Dr. Juliana Martins de Souza e Silva, die mir sowohl moderne wissenschaftliche Schreibregeln nähergebracht hatte als auch bei der Bildgebung via XRM helfen konnte, und der Arbeitskreis Bacia mit Prof. Dr. Kirsten Bacia und Dr. Caroline Haupt, die mir eine besondere Hilfe bei der Aufklärung des Bildungsmechanismus von Form-stabilisierten Phasenwechsel-materialien waren. Zudem möchte ich mich noch beim Arbeitskreis Kressler bedanken, bei dem ich DSC und TG messen durfte und bei Geräteproblemen stets Hilfe von Dr. Karsten Busse bekommen hatte, beim Arbeitskreis Majenburg mit M.Sc. Titus Lindenberg für die REM Messungen, bei Dr. Claudia Birkemeyer für die GC/MS Messungen und beim gesamten Arbeitskreis Bron für die Hilfe bei XRD Messungen, der Durchführung der Praktika und der guten Atmosphäre während des Laboralltags.

Als letztes möchte ich mich sowohl bei meinen zahlreichen Studenten für die Hilfe bei meiner Doktorarbeit als auch bei meinen Freunden, meiner Frau und meiner Familie für die mentale Unterstützung und den Glauben an mich bedanken. Ohne euch hätte ich es im Leben sicherlich nicht so weit geschafft und wäre nicht der Mensch, der ich heute bin.

Zusammenfassung

Weltweit werden über 50 % des Primärenergiebedarfs für das Heizen und Kühlen genutzt. Um den Primärenergiebedarf zu senken, kann Energie in Form von Wärme über das Schmelzen und Erstarren von organischen Phasenwechselmaterialien (PCMs) gespeichert werden. Die Probleme der niedrigen Wärmeleitfähigkeit, der moderaten Entflammbarkeit, dem Auslaufen aus Verbundmaterialien und der Unterkühlung von PCMs sind jedoch nur teilweise gelöst. Eine vielversprechende Lösung stellen hierbei formstabilisierte PCMs (*shape-stabilized phase change material*, ss-PCMs) dar, die das flüssige PCM in einer Gerüststruktur einschließen und am Auslaufen hindern. Die Nutzbarkeit von ss-PCMs ist jedoch durch ihre niedrige Wärmespeicherkapazität und mechanische Stabilität eingeschränkt.

Das Ziel dieser Doktorarbeit ist deshalb die Entwicklung einer neuen Sol-Gel Synthese auf Basis von stabilisiertem Silika Sol zur Formstabilisierung von PCMs mit unterschiedlichen Schmelzpunkten und hohen latenten Wärmen als monolithisches Verbundmaterial mit hoher Druckfestigkeit und hoher Wärmeleitfähigkeit. Im ersten Syntheseschritt werden hydrophobe PCMs wie reines Butylstearat (BS), sowie Mischungen (30:70) aus Paraffinen (Hexadecan (HD), Octadecan (OD)) und BS als Tropfen in einer wässrigen Phase emulgiert. Um die makroskopische Phasenseparation der Emulsion zu verhindern, wird die Viskosität der Emulsion über die Zugabe des strukturdirigierenden Reagenzes Polyvinylalkohol (PVA) erhöht. Zusätzlich werden durch den Einsatz des Tensids Natriumlaurylsulfat (SDS) die PCM-Tröpfchen über eine Mizellenschicht in der Emulsion eingekapselt und stabilisiert. Die mikroskopischen PCM-Tropfen, deren Oberfläche von SDS bedeckt ist, dienen während der Gelierung als Template (Schablone) für die sphärische Silikatstruktur des nassen ss-PCMs im Sol-Gel Prozess. Während der unterkritischen Trocknung schrumpft die mikroskopische Silikatstruktur des ss-PCMs um die Menge an immobilisiertem Wasser. Als Folge bilden sich über Alterungsprozesse neue kovalente Siloxan-Bindungen zwischen den Silikastrukturen aus, wodurch das ss-PCM kompakter und mechanisch stabiler wird. Die erhaltenen ss-PCMs haben Schmelzpunkte im Bereich von 20 °C und sehr hohe Massenanteile an PCM (bis 86 Gew%). Die Druckfestigkeit (1,2 MPa (10 °C); 0,7 MPa (30 °C)) und latente Wärme (~160 J/g) sind so hoch, dass eine breite Nutzung dieser ss-PCMs für unterschiedliche thermische Energiespeichersysteme erstmals möglich wird.

Die physikochemischen Eigenschaften des ss-PCMs (wie die Druckfestigkeit und Wärmeleitfähigkeit) verbessern sich über die Einkapselung von kleineren PCM-Tropfen, da während der Gelierung die Silikatstrukturen des ss-PCMs kleiner werden. Eine steigende Konzentration an SDS verringert dabei die Größe der PCM-Tropfen solange sich das SDS an

der PCM-Oberfläche anlagert. Bei sehr hohen Konzentrationen an SDS kollabiert die Silikatstruktur des ss-PCMs während des Trocknens auf Grund einer niedrigeren Viskosität der Emulsion und die Wärmeleitfähigkeit und Druckfestigkeit der ss-PCMs nimmt ab. Das PVA hingegen bildet Wasserstoffbrücken-Bindungen zum wachsenden Silikat-Gerüst aus und induziert Phasenseparationen. Die wässrige Phase entmischt sich in eine Silika/PVA-reiche und eine Wasser-reiche Phase, die als Templatstrukturen während der Gelierung dienen. Diese Templatstrukturen werden über die Zugabe von mehr PVA größer, wodurch der Makroporendurchmesser der Silikatstrukturen steigt und Brüchen des ss-PCMs durch größere Transportporen für Wasser während der Trocknung vorgebeugt wird.

Die hydrophilen PCMs Polyethylenglykol 600 (PEG600) und Acetamid (Ac) mit Schmelzpunkten von jeweils 23 °C und 73 °C können ebenfalls formstabilisiert werden. Während der Gelierung reagiert PEG600 stark über Wasserstoffbrücken-Bindungen mit dem Silikat, wodurch die Ausbildung eines mechanisch stabilen ss-PCMs verhindert wird und die latente Wärme 30 % geringer als theoretisch erwartet ausfällt. Das formstabilisierte Ac besteht fast ausschließlich aus mesoporösen Strukturen mit sehr hohen Druckfestigkeiten (9,6 MPa (5 °C)) und ist deshalb transluzent über dem Schmelzpunkt von reinem Ac. Auf Grund der basischen Bedingungen wird etwa 70 Gew% des Ac während der Synthese zu Essigsäure und Ammoniak zersetzt, weshalb die latente Wärme und Haltbarkeit dieser ss-PCMs gering ist.

Um die Wärmeleitfähigkeit maximal zu erhöhen, wird der Einfluss der Partikelgröße und der spezifischen Oberfläche von unterschiedlichen hexagonalen Bornitriden (BN) auf die physikochemischen Eigenschaften der ss-PCMs basierend auf BS untersucht. Eine höhere spezifische Oberfläche des BN führt zu einer stärkeren Agglomeration von BN-Plättchen während der Gelierung. Größere BN-Partikel (> 25 µm) stören die Bildung einer Silikatstruktur mit hoher Interkonnektivität. Kleinere BN-Partikel (~3 µm) erhöhen die Viskosität der Emulsion und somit die Druckfestigkeit der ss-PCMs. Die höhere Viskosität verhindert jedoch die homogene Verteilung der kleinen BN-Partikel in der Silikatstruktur und führt zu einer niedrigeren Wärmeleitfähigkeit der ss-PCMs. Zur Erhöhung der Wärmeleitfähigkeit sollten also große BN-Partikel mit kleinen spezifischen Oberflächen genutzt werden, wohingegen kleinere BN-Partikel mit kleinen spezifischen Oberflächen stärker die Druckfestigkeit erhöhen.

In dieser Arbeit hat sich herausgestellt, dass die ss-PCMs basierend auf Fettsäureestern und Paraffinen für die Nutzung in Gebäuden und in Warmwasser-Anlagen auf Grund ihrer hohen Druckfestigkeit und latenten Wärme am besten geeignet sind. Aufgrund der monolithischen Form ermöglichen die ss-PCMs neue Anwendungsfelder. Beispielsweise könnten die ss-PCMs zur passiven Kühlung von Photovoltaik-Systemen (PV) oder von Batteriezellhalter von Interesse sein, wodurch die Effizienz von PV-Anlagen gesteigert und das schnelle Laden von Batterien in Elektroautos in Zukunft ermöglicht werden könnte.

Abstract

Worldwide, more than 50 % of the primary energy demand is used for heating and cooling applications. To lower the primary energy demand, heat can be stored by organic phase change materials (PCMs) via melting and released via freezing processes. However, the low thermal conductivity, moderate flammability and supercooling effects of PCMs are only partially solved. Moreover, PCM must be confined in monolithic construction or polymeric materials to stop the leakage of liquid PCM, resulting in shape-stabilized PCMs (ss-PCMs) with low heat storage capacities and low mechanical stabilities.

For this purpose, this thesis focuses on the development of a novel sol-gel synthesis based on stabilized silica sol to confine PCMs with different melting points and high latent heats as monolithic ss-PCMs with high thermal conductivities and high mechanical stabilities.

The hydrophobic PCMs, such as butyl stearate (BS) or mixtures (30:70) of paraffins (hexadecane (HD), octadecane (OD)) with BS, are emulsified as droplets in an aqueous phase. To stop macroscopic phase separation of the emulsion, the surfactant sodium dodecyl sulfate (SDS) and the structure-directing agent poly(vinyl alcohol) (PVA) are added to build micellar layers around the emulsified PCM droplets and to increase the viscosity of the emulsion, respectively. The microscopic PCM droplets covered by SDS act as a template for the spherical silica structure obtained after silica sol addition. During subcritical drying, the silica structure of the ss-PCM shrinks by the amount of immobilized water and the ss-PCM structure becomes more compact and mechanical stable by the formation of novel siloxane bonds. The dried ss-PCMs have melting points (MP) in the range of 20 °C and high mass fractions of PCM (86 wt%). The compressive strength (1.2 MPa (10 °C); 0.7 MPa (30 °C)) and the latent heat (~160 J/g) of these ss-PCMs are so high that for the first time it is possible to use ss-PCMs for a broad range of different thermal energy storage systems.

In general, smaller PCM droplets decrease the size of the silica structures during gelation and, thus, improve the physicochemical properties of the ss-PCMs, such as the thermal conductivity and the compressive strength. An increasing concentration of SDS lowers the PCM droplet size until the whole PCM interface is covered by SDS. At very high SDS concentrations, the silica structure of the ss-PCMs collapses during drying due to a lower emulsion viscosity, decreasing the thermal conductivity and compressive strength. The PVA interacts by hydrogen-bonding with the silica structure and induces a phase-separation of the aqueous phase in a silica/PVA-enriched and a water-enriched. As a consequence, higher amounts of PVA increase the silica macropore widths of the ss-PCMs due to larger phase-separated

template structures during synthesis, but also enable a crack-free drying process and accelerate the sol-gel synthesis.

The hydrophilic PCMs polyethylene glycol 600 (PEG600) and acetamide (Ac) with MP of 23 °C and 73 °C, respectively, are shape-stabilized during gelation. The silica strongly interacts by hydrogen-bonding with PEG600 during gelation, inhibiting the formation of a mechanical stable ss-PCM and leading to a ~30 % lower latent heat than expected by the mass of PCM used for the synthesis. The shape-stabilized Ac consists mostly of mesoporous structures with high compressive strength (9.6 MPa (5 °C) and, thus, is transparent above the MP of pure Ac. Because Ac is partially degraded (~70 wt%) to acetic acid and ammonia during synthesis, the durability and latent heat are low for this kind of ss-PCMs.

To increase the thermal conductivity of the ss-PCMs to the highest extent, the influence of the particle size and the specific surface area of different hexagonal boron nitride (BN) particles on the physicochemical properties of shape-stabilized BS are investigated. A higher specific surface area of BN leads to a higher BN agglomeration during gelation. Large BN particles (> 25 µm) disturb the formation of an interconnected silica structure. Smaller BN particles (~3 µm) increase the viscosity of the reaction mixture and the compressive strength of the ss-PCMs. However, the higher viscosity hinders the homogenous distribution of BN in the silica structure and decreases the thermal conductivity of these ss-PCMs. Therefore, larger BN particles with lower specific surface areas increase the thermal conductivity of the ss-PCMs to the highest extent, but have a lower impact on the compressive strength increase than the ss-PCMs synthesized by smaller BN particles with lower specific surface areas.

In summary, the ss-PCMs based on fatty acid esters and paraffins are the most promising materials for future heat storage applications in buildings and in water heating systems. Moreover, they broaden the currently available PCM product portfolio because they are monolithic and combine high compressive strength with high latent heat. Especially the ss-PCMs thermally enhanced by BN can in the future increase the efficiency in PV systems during the day as well as enable fast-charging of batteries in electrical vehicles without loss of shape-stability and overheating problems through a fast passive cooling process.

Table of Contents

Zusammenfassung.....	I
Abstract.....	III
1 Introduction and Objective	1
2 Theoretical background	5
2.1 Thermal energy storage	5
2.2 Classification of PCMs	8
2.2.1 Organic PCMs.....	9
2.2.2 Inorganic PCMs.....	11
2.2.3 Eutectic PCMs	13
2.3 Confinement methods of PCMs	13
2.3.1 Core-shell confinement	15
2.3.2 Tubular confinement	16
2.3.3 Interfacial confinement	17
2.3.4 3D porous confinement	18
2.4 Shape-stabilized PCMs.....	22
2.5 Sol-Gel.....	22
2.5.1 Sol formation.....	23
2.5.2 Gelation	25
2.5.3 Aging.....	27
2.5.4 Drying	27
2.6 Porogen strategies.....	29
2.6.1 Structure-directing agents	31
2.6.2 Hard templates.....	35
2.7 References	38
3 Publications	64
3.1 Synthesis of monolithic shape-stabilized phase change materials with high mechanical stability via a porogen-assisted <i>in situ</i> sol-gel process	65
3.1.1 Abstract.....	66
3.1.2 Introduction	67

3.1.3	Experimental.....	69
3.1.4	Characterization of the ss-PCM.....	70
3.1.5	Results and discussion.....	72
3.1.6	Conclusions	84
3.1.7	CRedit authorship contribution statement.....	85
3.1.8	Conflicts of interest.....	85
3.1.9	Acknowledgements	85
3.1.10	References.....	86
3.1.11	Supporting Information	90
3.2	Influence of surfactants and organic polymers on monolithic shape-stabilized phase change materials synthesized via sol-gel route.....	104
3.2.1	Abstract.....	105
3.2.2	Keywords	105
3.2.3	Introduction	106
3.2.4	Experimental.....	108
3.2.5	Characterization.....	109
3.2.6	Results and discussion.....	111
3.2.7	Conclusions	128
3.2.8	Conflicts of interest.....	129
3.2.9	CRedit authorship contribution statement.....	129
3.2.10	Acknowledgements	129
3.2.11	References.....	130
3.2.12	Supporting Information	138
3.3	Shape stabilization of organic phase change materials as mechanical stable silica boards with high latent heats via sol-gel route	153
3.3.1	Abstract.....	154
3.3.2	Introduction	155
3.3.3	Experimental.....	157
3.3.4	Results and discussion.....	161
3.3.5	Conclusions	177

3.3.6	Conflicts of interest.....	179
3.3.7	CRedit author contribution statement.....	179
3.3.8	Acknowledgements.....	179
3.3.9	References.....	179
3.3.10	Supporting Information.....	188
3.4	Size and surface effects of hexagonal boron nitrides on the physicochemical properties of monolithic phase change materials synthesized via sol-gel route.....	206
3.4.1	Abstract.....	207
3.4.2	Keywords.....	207
3.4.3	Introduction.....	208
3.4.4	Experimental.....	210
3.4.5	Characterization of ss-PCMs.....	212
3.4.6	Results and discussion.....	214
3.4.7	Conclusions.....	229
3.4.8	CRedit authorship contribution statement.....	230
3.4.9	Declaration of Competing Interest.....	230
3.4.10	Acknowledgements.....	230
3.4.11	References.....	230
3.4.12	Supporting Information.....	238
3.5	Experimental data showing the influence of different boron nitride particles on the silica network, the butyl stearate and the porogens in shape-stabilized phase change materials.....	265
3.5.1	Abstract.....	266
3.5.2	Keywords.....	266
3.5.3	Specifications Table.....	267
3.5.4	Value of the Data.....	268
3.5.5	Data Description.....	268
3.5.6	Experimental Design, Materials and Methods.....	278
3.5.7	Ethics Statement.....	279
3.5.8	CRedit authorship contribution statement.....	279

3.5.9	Acknowledgments	279
3.5.10	Declaration of Competing Interest	280
3.5.11	References.....	280
4	Summarizing Discussion	281
4.1	Synthesis of ss-PCMs	281
4.2	Thermal conductivity enhancement of ss-PCMs.....	291
4.3	Characterization of ss-PCMs.....	296
4.4	References	301
5	Conclusions	305
6	Outlook and Perspective.....	311
7	Appendix	V
7.1	Curriculum Vitae	V
7.2	List of publications	VI
7.3	Project awards	VII
7.4	Statement of own contributions	VIII
7.5	Authorship contribution statement.....	IX

1 Introduction and Objective

The climate change is worldwide one of the biggest threats for humanity and is accelerated by human-induced emissions of greenhouse gases, such as carbon dioxide, methane and nitrous oxides [5, 6]. From 1990 to 2019 (Fig. 1), the worldwide greenhouse gas emissions that exclude those from land-use change increased by 57 % [7–9] and the global average median temperature change increased by 0.5 °C [10, 11]. Greenhouse gases have a high positive radiative forcing and, thus, absorb and reemit huge amounts of infrared radiation, hindering the infrared radiation to escape into space and warming the atmosphere on earth [12]. As feedback, more water is emitted from the earth into the atmosphere as vapor and clouds, which is responsible for approximately 60 % of the greenhouse effect at clear sky [13]. A higher temperature on earth leads to the melting of the glacier and polar ice caps, raising the sea level and increasing stress on terrestrial and maritime ecosystems and species [14, 15].

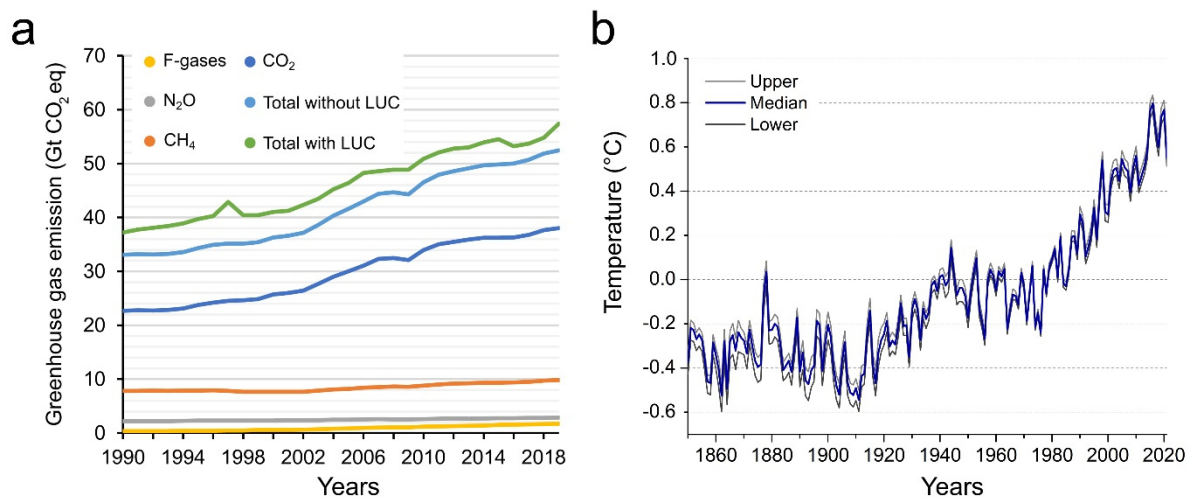


Fig. 1 a) Global greenhouse gas emission per year based on EDGAR v.5 FT2019 dataset by European Commission [7–9]. LUC: Land Use, Land Use Change and Forestry. F-gases: Fluorinated gases. b) Global average temperature anomaly per year based on HadCRUT 4.6.0.0 dataset by Hadley Centre [10, 11]. Global median temperature change represented in blue, and the upper and lower 95 % confidence intervals in light and dark grey.

To slow down the climate change, representatives of 196 state parties signed in the Paris Agreement of the United Nations Framework Convention on Climate Change (UNFCCC) in 2015 [16]. The aims of the Paris Agreement are the reduction of the greenhouse gas emission to keep the increase of the global average temperature below 2 °C above pre-industrial levels, the adaption of cities and agriculture to the impacts of climate change, and the combination of climate protection and free market economy, for example by new carbon dioxide certificates and taxes.

To achieve these aims, the German Government has passed the Federal Climate Change Act (*Bundes-Klimaschutzgesetz*) in 2019 [17]. The Federal Climate Change Act should decrease the national greenhouse gas emissions in comparison to 1990 by 55 % from 2019 to 2030 as

well as by 100 % up to 2050. However, only 13.8 % of the national primary energy demand is based on renewable energies in Germany in 2018 (Fig. 2a) [18]. Additionally, the intermittency of wind and sunlight impedes the efficient usage of wind and solar power. For these reasons, the development of new energy storage techniques is mandatory to achieve the aims of the Federal Climate Change Act.

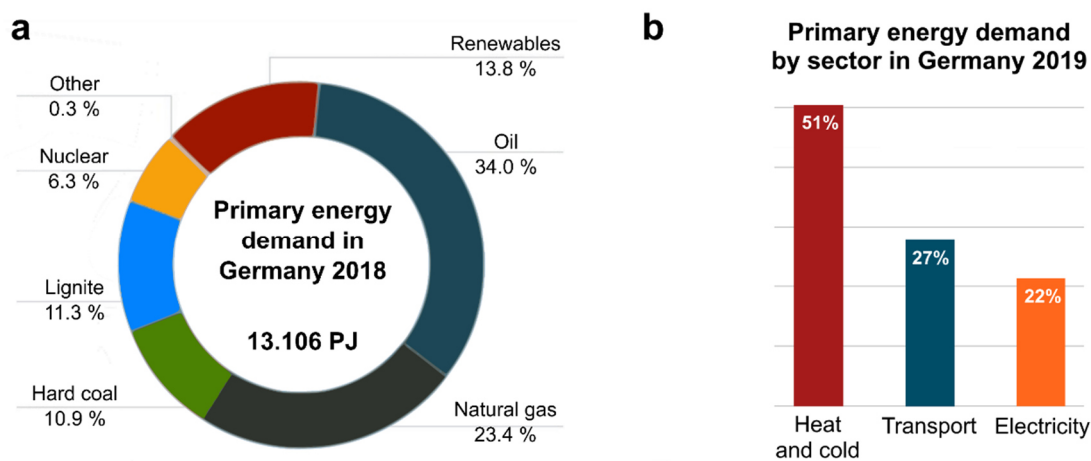


Fig. 2 a) Primary energy demand specified by energy source in Germany in 2018 [18]. b) Primary energy demand specified by sector in Germany in 2019 [19]. Energy demand for heat, cold and transport is depicted without taking electricity into account; the energy demand of the electricity sector is listed as an individual item.

According to the „Agentur für Erneuerbare Energien“ [19], over 50 % of the primary energy demand is used for heating and cooling applications in Germany in 2019 (Fig. 2b). Therefore, thermal energy storage (TES) systems play a central role in the climate-friendly transformation of the economy nowadays. For example, one of the biggest district heating systems with a volume of 50.000 m³ and a total cost of EUR 10 million was built 2018 in Halle (Saale), Germany, and can store up to 2000 MW [20–22], which is approximately 15-times larger than the storage capacity of the world’s biggest lithium-ion battery system in Hornsdale, Australia (total cost: EUR 80 million) [23].

Organic latent heat storage materials, also called phase change materials (PCMs), can store 5- to 14-times more heat per volume than sensible heat storage materials, such as bricks, concrete, and water by simply performing a phase transition from solid to liquid (Fig. 3) [24]. Therefore, organic PCMs are promising materials to store large amounts of solar energy, waste heat and off-peak electricity as thermal energy in energy-saving buildings [25–27], photovoltaics [28–30], textiles [31–33], and water-heating systems [34–36]. Generally, organic PCMs must be incorporated in suitable containers, core-shell structures, or molecular matrices in order to prevent leakage of the liquid PCM, to increase their heat transfer rate and to minimize supercooling and phase separation effects. The incorporation of liquid PCM in macroscopic plastic or steel container is called macroencapsulation and represents the simplest immobilization technique [25, 37]. However, the heat transfer and crystallization rate

of macroencapsulated PCM is nearly as low as that of the pure substance, hindering the melting process of PCM at the phase transition point and, thus, its usage in industrial applications [38]. Moreover, the size of macroencapsulated PCMs is often a limiting factor for many applications, such as for electronics, batteries, and photovoltaics.

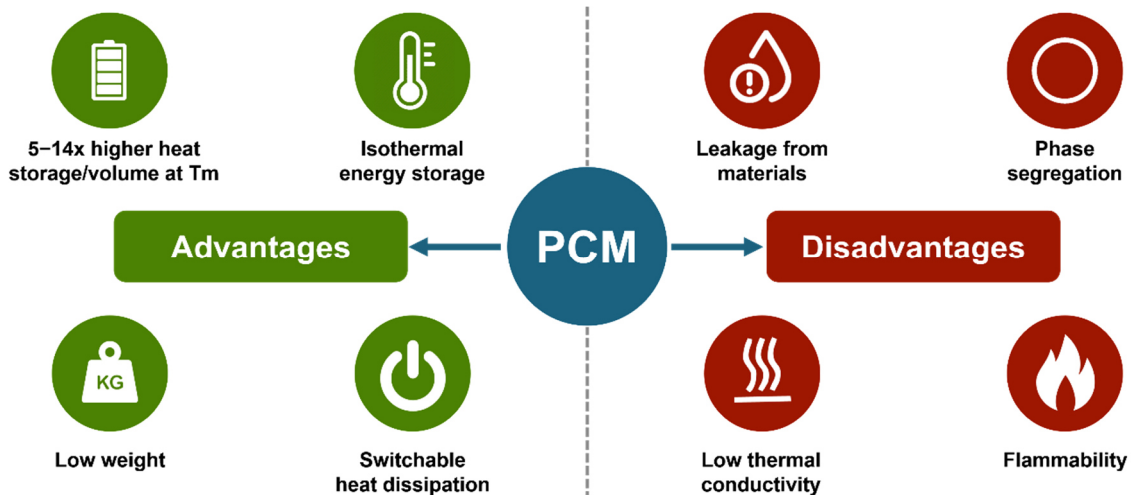


Fig. 3 Advantages and disadvantages of organic phase change materials (PCM). T_m = melting point.

The incorporation of liquid PCM in a solid carrier matrix is called shape stabilization [39–41]. The shape-stabilized PCMs (ss-PCMs) can be synthesized by applying different techniques, such as vacuum impregnation of porous monoliths, immobilization of liquid PCM during a polymerization reaction, by addition of binder molecules to produce blends, by rapid cooling processes of organic polymers below the glass transition point or its usage as additive in form of core-shell PCMs in plastics and construction materials. To test the shape stability, also known as form stabilization, the ss-PCM is placed for a long time (24 h) in an oven at high temperatures above the melting point [42]. If no leakage of liquid PCM occurs, the PCM is 100 % shape stabilized.

All methods to produce ss-PCMs as mentioned above have some big disadvantages leading to a limited usage of ss-PCM in most applications today [43]. For example, the vacuum impregnation of nanoporous containment materials is very difficult and only 20 % to 50 % of the pore volume in the monolith can be filled with liquid PCM due to high capillary forces, lowering the latent heat of the ss-PCM [44]. In case of the rapidly cooling of HDPE and PCM, the effective PCM mass fraction of the ss-PCMs is quite high (80 wt%), but the materials are flammable, have low thermal conductivities and are only shape stabilized up to 70 - 110 °C. The direct mixing of cs-PCM, PCM-impregnated particles or pure PCM with construction materials such as concrete [45–47] or gypsum [48] is only possible for low amounts of PCM (15 - 30 wt%). Moreover, the mechanical stability of these ss-PCMs is low [46, 49–53].

To overcome the current problems of ss-PCMs, it is mandatory to develop a new synthesis route for ss-PCMs with high mechanical stabilities, high form-stabilities, high thermal conductivities, high latent heats and good fire-retardant properties.

Silica is an amorphous inorganic containment material with a large specific surface area, low density, controllable pore structure, high adsorption capacity, high mechanical stability, high fire resistance, low market price and can be produced from renewable sources. All these facts point out how interesting silica can be for the containment of PCM [54–56]. There are only a few studies published about silica-based ss-PCMs. For example, the group of Li [54] synthesized a molecular silica matrix via a sol-gel process starting from tetraethyl orthosilicate (TEOS) and PEG as PCM. The ss-PCM consisted of a three-dimensional silica structure with PCM immobilized in the silica pores and was form-stable for more than 3 days when kept above the melting temperature. The silica matrix showed no chemical interactions with the immobilized PCM and the thermal conductivity was increased. However, the synthesized ss-PCM was broken and not monolithic. Mechanical stability, long-term shape stability and durability tests were missing in this study and the function of PCM as template on the interconnectivity of silica was not investigated.

Because of the promising properties of silica, a novel sol-gel synthesis of silica-based ss-PCM should be developed in this work. The synthesized ss-PCMs should have a high mechanical stability, high thermal durability, high latent heat and low flammability for building applications with a temperature range of 20 - 40 °C. Stabilized silica sol, which is a suspension of silica particles in water, should be taken as silica source because of its lower market price, lower chemical reactivity towards organic PCMs, non-flammability and non-toxicity [57, 58] compared to TEOS [59, 60].

Concomitantly, the synthesis should be analyzed by *in situ* techniques and the influence of the educts on the silica matrix and the physicochemical properties of the ss-PCM should be investigated. To broaden the application range, different PCMs should be immobilized by the sol-gel process in a silica carrier matrix to synthesize ss-PCMs with different PCM melting temperatures and thermal properties.

For an accelerated heat transfer, the ss-PCMs should be improved by addition of non-reactive additives with high thermal conductivities, such as graphite or boron nitride.

2 Theoretical background

2.1 Thermal energy storage

Due to different conservation methods for thermal energy three main groups are distinguished according to the respective underlying principle: sensible heat storage (SHS), thermochemical heat storage (THS) and latent heat storage (LHS) [61].

In SHS systems, thermal energy is stored as heat by varying the temperature of the SHS material. The amount of energy Q to be stored depends on the specific heat capacity of the material, the mass of the material, and the change in temperature according to Eq. 1 [62]:

$$Q = \int_{T_i}^{T_f} m C_p dT = m C_{ap} (T_f - T_i) \quad (\text{Eq. 1})$$

where T_i is the initial temperature of the material before heating, T_f is the final temperature of the material after heating, m is the material mass, C_p is the specific heat capacity of the material, T is the temperature of the material, and C_{ap} is the average specific heat capacity between T_i and T_f .

Typical solid SHS materials are stones, concrete, and bricks with specific heat capacities of approximately 850 - 880 J/kg·°C (Fig. 4a) [24]. They are integrated as support elements in buildings or in storage heaters as energy storage medium, which is heated electrically during night times and releases the stored heat during day times. In industrial applications, such as district heating and solar thermal systems (Fig. 4b), water is commonly used as SHS material because of its incomparable high specific heat capacity of 4190 J/kg·°C and low costs.

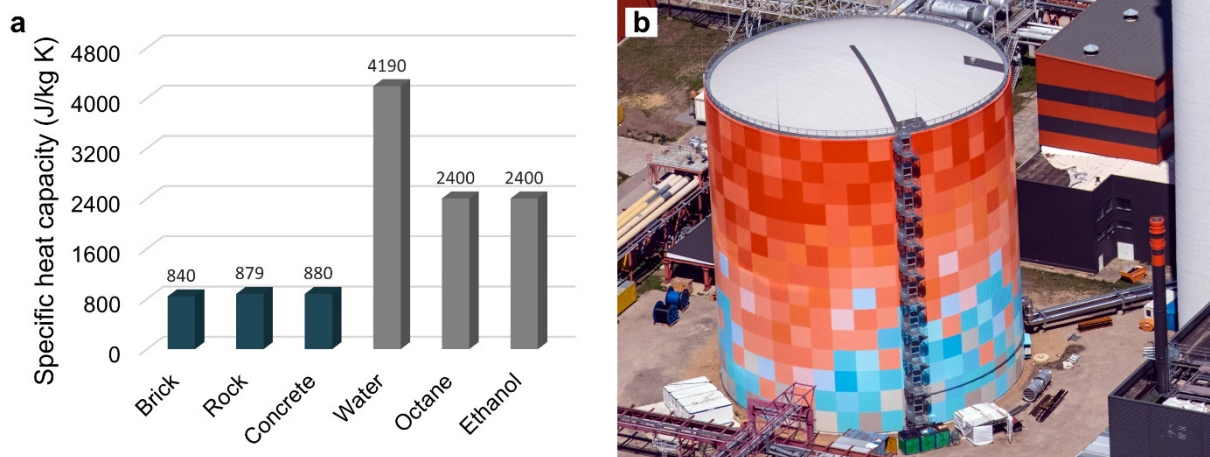


Fig. 4 a) Specific heat capacity values of solid (blue) and liquid (grey) sensible heat storage (SHS) materials [24]. b) Picture of the district heating systems of the energy park Dieselstraße in Halle (Saale), Germany (Copyright: Stadtwerke Halle (EVH GmbH)) [22]. The 50.000 m³ volume of the district heating system is filled with water as SHS material and can store up to 2000 MW [22].

Thermochemical heat storage is based on breaking and reforming of molecular bonds in a reversible chemical reaction between two different compounds at a specific temperature, such as the reaction of magnesium oxide with water to magnesium hydroxide [63]. Especially heterogenous vaporization reactions and dissociation reactions are favored in THS due to the high entropy increase by changing the phase of one reactant during the reaction. THS systems have the highest energy storage density per volume of all TES systems and enable the storage of energy in a wide temperature range over a long time. Therefore, THS materials are currently investigated for the application in critical solar power plants (CSP) and in power-to-heat-to-power systems [64]. However, the slow heat transfer from and to the storage material limits the overall storage volume and, furthermore, the low matrix permeability restricts the sorbate access [65, 66]. Additionally, these materials are built in complex, expensive reactors and, thus, are not as easy to handle as SHS materials. The heat energy stored in this process depends on the material mass, the endothermic heat of the reaction, and the extent of conversion, and is calculated as follows [24]:

$$Q = a_r m \Delta h_r \quad (\text{Eq. 2})$$

where Q is the amount of stored heat energy, m is the material mass, a_r is the material fraction reacted, and Δh_r is the endothermic heat of reaction.

The last class of TES systems are latent heat storage (LHS) systems, which can store 5- to 14-times more heat per volume than SHS materials by performing a phase transition from solid to solid, solid to liquid, solid to gas or liquid to gas and vice versa at a certain phase transition point T_p (Fig. 5). Because of the specific heat storage mechanism, LHS materials are commonly known as phase change materials (PCMs).

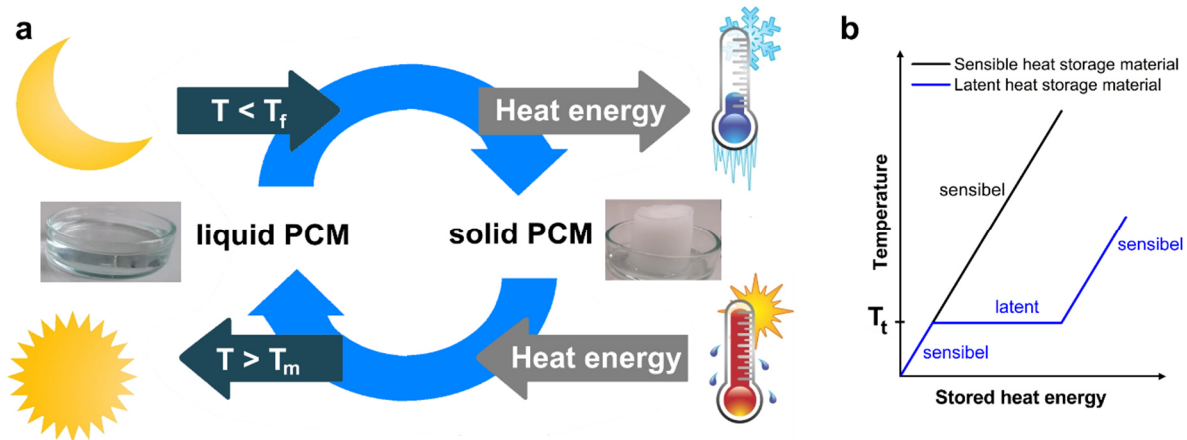


Fig. 5 a) Thermal energy storage mechanism of PCMs based on a liquid-solid phase transition. The PCM is melted during day times above the melting point T_m and stores heat energy. During night times below the freezing point T_f , the PCM is frozen and releases heat energy. b) The thermal energy storage of sensible heat storage materials and latent heat storage materials (PCMs) in dependence on the temperature and the phase transition point T_t .

The stored heat energy of SHS materials depends on the specific heat capacity of the material, the material mass, and the temperature increase, but also on the heat of fusion of the melted fraction at the phase transition point (Fig. 5b), and is calculated as follows [62]:

$$\begin{aligned}
 Q &= \int_{T_i}^{T_t} mC_p dT + ma_t \Delta h_t + \int_{T_t}^{T_f} mC_p dT \\
 &= m[C_{sp}(T_t - T_i) + a_t \Delta h_t + C_{lp}(T_f - T_t)]
 \end{aligned}
 \tag{Eq. 3}$$

where Q is the amount of stored heat energy, T_i is the initial temperature of the material before heating, T_t is the temperature of the transition point, T_f is the final temperature of the material after heating, m is the material mass, C_p is the specific heat capacity of the material, T is the temperature of the material, a_t is the material fraction undergoing a phase transition, Δh_t is the heat of fusion per unit mass, C_{sp} is the average specific heat capacity between T_i and T_t , and C_{lp} is the average specific heat capacity between T_t and T_f .

In solid-solid transitions, the heat energy is stored by a transformation of a crystalline phase. PCMs based on solid-solid phase transitions have low volume expansions at the transition point and low latent heats. If, however, the solid-gas or liquid-gas transition is used for energy storage, the PCM can store the highest amounts of heat energy of all kinds of PCMs but can easily leak out of carrier materials as gas and exhibits a high-volume expansion during phase transition. Solid-liquid transitions of PCMs constitute a good compromise for conserving thermal energy due to the low volume expansion during melting processes and the 2-times higher latent heat compared to the solid-solid transition of PCMs. For solid-liquid PCMs, the stored and released latent heat is equal to the heat of fusion as well as to the heat of crystallization.

Like THS systems, PCMs can store thermal energy over a wide temperature range for a long time. The switchable heat dissipation above and below the melting and freezing point and the isothermal heat absorption and desorption process make PCMs exhibiting melting points in the range of 15 - 40 °C perfectly suited for heat storage and temperature regulation as construction material in buildings [67]. Moreover, PCMs are used as cooling medium in batteries [68], as heat storage medium (solar salt) in critical solar power plants [69], to increase the heat storage capacity in solar water heating systems (boilers) [70], as cooling unit in photovoltaic systems [71], for temperature regulation in outdoor textiles and space suites [72], and even in solar cookers for heating of food [73].

A perfect PCM must fulfill several criteria and properties [74, 75]. Regarding the thermal properties, the PCM should have a high latent heat, a phase transition point in the desired application range, a high thermal conductivity, a high density, a high specific heat for TES as

SHS, a small volume change, a congruent melting process and no supercooling effects during phase transition. The chemical reactivity of the PCM should be low to prevent reactions with containment materials and enable a high chemical stability over a long time period. Additionally, the perfect PCM should be non-explosive, non-toxic and non-flammable. From the economical point of view, the PCM should be available in large quantities at low market prices and high qualities.

However, today PCMs are still lacking several of these characteristics [76] and the research on the synthesis of novel PCMs is still ongoing. For example, sugar alcohols have an approximately 30 % higher latent heat of fusion than paraffins but their application is currently limited due to a low nucleation rate, low chemical stability and low thermal conductivity, which have to be improved in the future [77–79].

2.2 Classification of PCMs

According to their chemical nature, solid-liquid PCMs are classified into three main groups: organic, inorganic and eutectics. The main groups are again divided into different subgroups, such as paraffinic and non-paraffinic PCMs for organic PCMs (Fig. 6). They all have different physicochemical properties and lack different criteria for the application as optimal TES material.

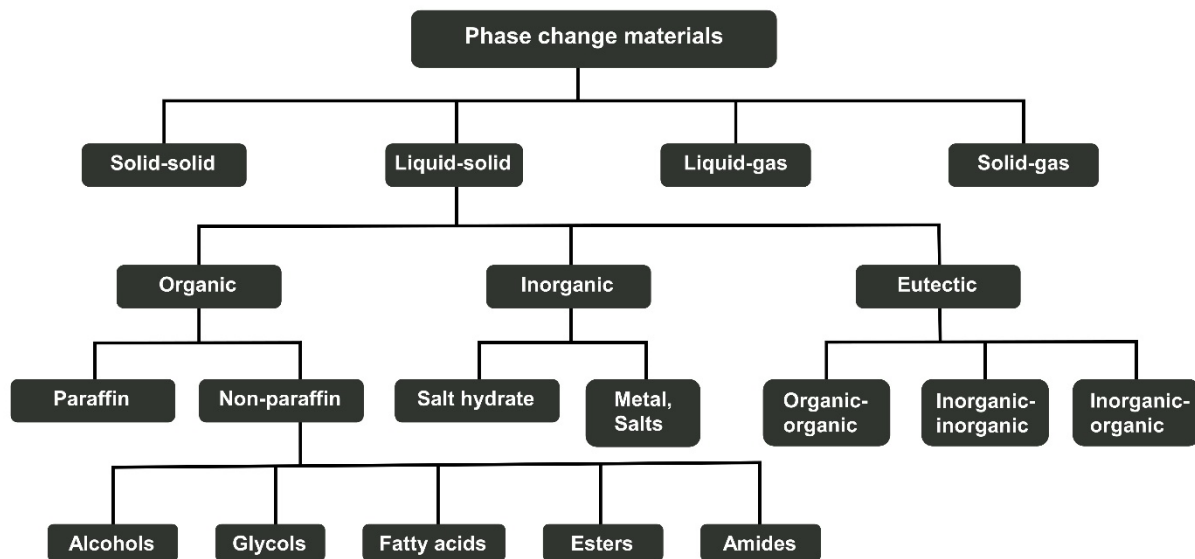


Fig. 6 Classification of PCMs is determined by the type of phase transition and the chemical nature.

2.2.1 Organic PCMs

Organic PCMs are divided into paraffins and non-paraffins [80]. Their physicochemical properties are summarized in Table 1. Both groups have high nucleation rates and, thus, crystallize and melt nearly congruently at the phase transition point. Therefore, the durability and long-term performance of organic PCMs is comparatively high, maintaining its thermal properties over long times, such as the latent heat of fusion. Their good self-nucleation properties lead to less up to even no supercooling effects. Supercooling is the difference of the melting and freezing point and should be as small as possible for PCMs. The latent heat of fusion is moderately high (125 - 280 J/g) [50, 79, 81, 82] and the energy density of these materials is in the range of 110 - 410 J/cm³ [74, 82]. Organic PCMs are all moderately flammable, have low thermal conductivities of approximately 0.25 W/mK [76] in the solid phase and are non-corrosive to containment materials. Additionally, the vapor pressure and the volume expansion at the phase transition are relative low for organic PCMs [75].

Table 1 Comparison of the physicochemical properties of the PCMs paraffins and non-paraffins [76, 79–82].

	Paraffins	Non-paraffins
Latent heat	170 - 270 J/g	125 - 280 J/g
Energy density	130 - 220 J/cm ³	110 - 410 J/cm ³
Melting points	-95 to 80 °C	-80 to 140 °C
Thermal conductivity as solid	0.2 to 0.3 W/mK	0.2 to 0.3 W/mK
Flammability	moderate	moderate to low
Supercooling	very low	very low
Incongruent melting	very low	very low
Leakage	yes	yes
Long-term performance	high	moderate to high
Corrosive	no	no

2.2.1.1 Paraffins

Paraffinic PCMs are based on linear alkanes with the formula CH₃-(CH₂)_n-CH₃. They are non-renewable and refined from petroleum with bleaching agents. The melting and freezing points of these materials are directly correlated with the chain length of the alkanes *n* (the higher the chain length the higher the melting and freezing points). This attribute makes them perfectly suited for a wide application field with different temperature ranges, such as for cooling applications at -57°C (*n*-octane) or for thermal comfort in buildings at 18 °C (*n*-hexadecane). Moreover, the exact temperature for the application can be adjusted by mixing paraffins with different melting points. Paraffins are mostly used as technical grade products with impurities (1.70 €/kg [83]) avoiding its relative high market price of approximately 3.40 €/kg for the pure

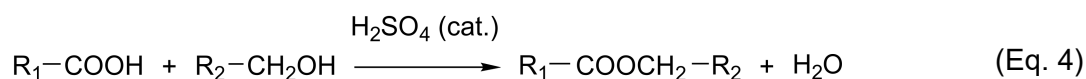
substances [84]. The technical grade paraffin is often contaminated with benzene, toluene, naphthalene, or methyl ethyl ketone, which are volatile and carcinogenic [85]. Paraffinic PCMs can be thermal stable up to 500 °C depending on their chain-length.

2.2.1.2 Non-paraffins

The group of non-paraffins is quite large and differ greatly by their physicochemical properties. For example, glycols [86, 87], fatty acids [88, 89], esters [90, 91], amides [92, 93], and alcohols [94, 95] are all classified as non-paraffinic PCMs. Most of the non-paraffins have a 2 - 2.5-times higher market price than technical grade paraffins [24]. They are mostly renewable products made from plants, vegetable oils, natural occurring triglycerides, and fermentation processes [96]. Fatty acids and polyethylene glycols (PEG) are the largest groups of non-paraffins in the current literature.

PEG is a polymer available as white powder or flakes, and is composed of dimethyl groups according to the formula $\text{HO-CH}_2\text{-(CH}_2\text{-O-CH}_2\text{)}_n\text{-CH}_2\text{-OH}$. Because of its hydroxy and dimethyl groups, PEG is soluble in water and in hydrophobic oils [97]. The different chain length of PEGs determines the thermal properties and makes them useful for a wide range of different TES applications. For example, PEG 600 (600 g/mol) with melting points of 17 - 23 °C (latent heat: 150 J/g) can be used as energy-saving construction material [98, 99] or in thermo-regulating textiles [100], whereas PEG 20000 (20.000 g/mol) with melting points of 50 - 60 °C (latent heat: 176 J/g) can be integrated in solar space heating and ventilating applications in buildings [101]. The average market price for the raw material is in the range of 1.50 €/kg [102].

Fatty acids have lower flash points and lower thermal and chemical stabilities than paraffins [103]. However, they have higher self-nucleation rates than paraffins and, thus, nearly no supercooling effects at melting and freezing. The published data of fatty acids differ slightly because of the different purity of the technical products, and the accuracy of analytical instruments [103]. They are often used as eutectic mixtures to expand their application range. The average market price for fatty acids as raw material is approximately 1.50 €/kg [83]. Fatty acids are commercially available by a wide range of companies under different trade names with higher market prices, for example by Entropy Solutions Inc. as M-27 (trade name) for 12.15 €/kg [83, 104]. For a higher thermal and chemical stability, fatty acids can be esterified by an acid catalyst (e.g., H_2SO_4) to form fatty acid esters according to the Fischer esterification (Eq. 4).



The fatty acid esters are commonly produced by extraction from plants due to a lower market price in contrast to the esterification process, which makes their market price comparable to those of fatty acids. They have lower melting points than fatty acids, and are odorless [105]. For example, stearic acid has a melting point of 69 °C, whereas the stearic acid ester, butyl stearate, has a melting point of around 22 °C. Moreover, fatty acid esters have a higher decomposition point than paraffins with the same melting points, making them useful for long-term applications with a temperature range of -70 °C to 100 °C. The latent heat of fusion of a fatty acid ester is lower if the length of the alcoholic side chain is longer. Therefore, butyl stearate has a 25 % lower latent heat of fusion (140 J/g) than methyl stearate [106].

2.2.2 Inorganic PCMs

Inorganic PCMs are divided in salt hydrates and metals [24, 107]. In previous studies and reviews [107–109], salts are also classified as inorganic PCMs and good SHS materials because of their high specific heat capacity and latent heat of fusion at higher temperatures above 200 °C. The class of inorganic PCMs has an up to 2-times higher energy density per volume than organic PCMs. They are non-flammable and non-toxic, but are corrosive to most containment materials. The different physicochemical properties of the subgroup of salt hydrates and metals and salts are summarized in Table 2.

Table 2 Comparison of the physicochemical properties of the PCMs salt hydrates, metals and salts [24, 107–114].

	Salt hydrates	Metals	Salts
Latent heat	100 - 300 J/g	11 - 80 J/g	100 - 370 J/g
Energy density	200 - 600 J/cm ³	150 - 500 J/cm ³	170 - 870 J/cm ³
Melting points	5 to 130 °C	-40 to 1000 °C	-90 to 500 °C
Thermal conductivity as solid	0.7 - 1.0 W/mK	8 - 90 W/mK	0.5 - 1.3 W/mK,
Flammability	no	no	no
Supercooling	moderate to high	moderate	moderate
Incongruent melting	high	moderate	moderate
Leakage	yes	yes	yes
Long-term performance	low	moderate to high	moderate to high
Corrosive	yes	yes	yes

2.2.2.1 Salt hydrates

Salt hydrates are crystalline solids of water and salt with the general formula $M \cdot nH_2O$ (M = metal salt, n = hydration number) [115–117] and have low market prices of approximately 0.17 €/kg ($CaCl_2 \cdot 6H_2O$) [83, 104]. Typical salt hydrates used as PCM are $MgCl_2 \cdot 6H_2O$ [82, 118], $Na_2SO_4 \cdot 10H_2O$ [119, 120], $Mg(NO_3)_2 \cdot 6H_2O$ [121, 122] or $CaCl_2 \cdot 6H_2O$ [123, 124]. In contrast to all other solid-liquid PCM classes (Fig. 6), salt hydrates perform a phase transition from solid to liquid not by melting, but by a dehydration and a dissolution step. First, the salt hydrate is dehydrated at a specific temperature to a salt or salt hydrate with less water molecules attached. Secondly, the dehydrated salt hydrate is dissolved in the free crystalline water. For a proper energy storage and release, these steps must be reversible. Salt hydrates are often classified as inorganic PCM and not as thermochemical heat storage material [125] because the dehydration and dissolution are thermodynamically similar to melting and freezing [24].

Salt hydrates can be used between 5 °C to 130 °C, which makes them a good alternative to organic PCMs in the same temperature range. They have several advantages over organic PCMs, such as a high density and high thermal conductivity between 0.7 W/mK and 1.0 W/mK in the solid phase [76]. Because of the high density, the salt hydrates have higher energy densities per volume than organic PCMs. However, the phase segregation and high supercooling effects hamper the efficient usage of inorganic PCMs today [126, 127]. Supercooling, also known as subcooling, is directly correlated with the low self-nucleating properties of most salt hydrates and can be high for salt hydrates (40 °C). Therefore, additional nucleating agents must be added to salt hydrates. Phase segregation effects take place during the dehydration and dissolution step due to incongruent melting. During incongruent melting, the salt hydrates are dehydrated either completely or to different dehydrated species with different solubilities in water, which precipitate at the bottom of the containment material of the salt hydrate due to density differences. This process is known as phase segregation or phase separation. The dehydrated salt species at the bottom cannot be dissolved again in the process, reducing the latent heat drastically up to zero after a few phase transitions. To minimize or to stop phase segregation, salt hydrates are encapsulated in different nanoscopic materials, such as core-shell structures [128, 129] or porous carrier materials [130, 131].

2.2.2.2 Metals and Salts

Metals and salts are mostly used for applications in the temperature range above 200 °C, for example as solar salt in critical solar power plants (CSP) [132, 133]. For implementations below

200 °C, only few applications are known, such as gallium as cooling medium in computer chips [134]. The melting points of this PCM class vary widely. For example, eutectic salt mixtures with water and HCl and metallic PCMs, such as Gallium, are available with melting temperatures of -86 °C [135] and 30 °C [136], respectively. In contrast, the melting point of salts and metals as pure substance can be in the range of 500 °C [135, 137, 138] and 1000 °C [139], respectively. Metals and salts have a high density, moderate (salts) to high (metals) thermal conductivities, and are corrosive to metal containers. The latent heat of fusion of metals and salts vary between 11 J/g (mercury) to 80 J/g (gallium) for metals [110] and 100 J/g (KNO₃) to 370 J/g (LiNO₃) for salts [111, 112]. Especially the high weight of metals and salts limits its application range. Additionally, most metals used as PCM are very expensive (100 - 400 €/kg for low-purity to high-purity gallium [140]).

2.2.3 Eutectic PCMs

An eutectic PCM is a composition of two or more PCMs with a minimum melting point, resulting in a broad spectrum of inorganic-organic [141, 142], organic-organic [143, 144], and inorganic-inorganic [71, 145] eutectics with different properties. In the crystallization and melting process of eutectics, both components act as a single compound and, thus, melt and freeze congruently. Today, only few data about the application of eutectic PCM are published [146].

2.3 Confinement methods of PCMs

To efficiently use PCMs that perform the solid-liquid transitions in industrial applications, the PCM must be incorporated in suitable containment materials to prevent leakage of liquid PCM and protect the PCM from irreversible chemical reactions with its environment, such as redox reactions, dehydration, corrosion, or recrystallization effects. Therefore, several different confinement methods of PCMs were developed in the last years. Problematically, the characterization of the mechanical stability, durability and thermal cycling of the confined PCMs is still missing in most studies today [39]. The different confinement strategies can be classified to macro-, micro- and nanoscopic methods according to the dimension of the confinement material (Fig. 7) [147].

In macroscopic confinement methods, also known as macroencapsulation, liquid PCM is filled in container with a diameter above 1 mm. Pipes, panels, and tanks made of plastic and metal with high corrosion resistance as well as high mechanical and thermal stabilities can be used as container for PCM. Macroencapsulation has the following advantages compared to other confinement methods: filling the container with PCM is simple to implement, inexpensive, scalable, and the geometries of the container can be adjusted for specific applications.

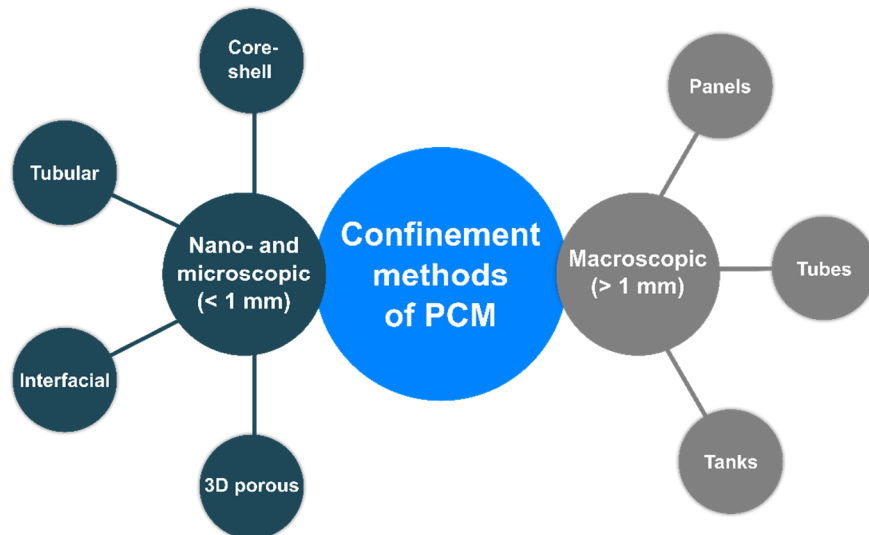


Fig. 7 Classification of PCM confinement methods by the dimension of the confinement material.

Furthermore, macroencapsulated PCM can be purchased by companies, such as Rubitherm and Axiotherm. However, macroencapsulation as confinement method only solves the leakage problem of liquid PCM but not the low thermal conductivity, the incongruent melting, or the flammability problems of PCMs [37, 38]. In contrast, micro- and nanoscopic confinement methods can also reduce the flammability of PCMs, accelerate the melting process and increase the thermal conductivity of PCMs due to the smaller dimension of the container for microscopic (1 - 1000 μm) and nanoscopic (1 - 1000 nm) materials [76]. With a lower dimension of the containment material, capillary forces, adhesions forces, surface modifications, van der Waals interactions, hydrogen bonding and geometrical effects can take place between the surface of the containment material and the PCM. These effects can influence the physicochemical properties of PCMs greatly and can improve some of the drawbacks of PCMs. The low thermal conductivity of PEG as PCM can be increased by shape-stabilization processes with graphite oxide from 0.3 W/mK to 3 W/mK due to the microscopic structure of the composite material [148]. Moreover, microscopic core-shell structures made of melamine urea-formaldehyde and thermal additives can lower the supercooling temperature of PCM by up to 90 % due to a higher heat transfer rate and a higher nucleation rate of the PCM after confinement [149]. Inflammable and flame retardant microscopic containment materials can even lower the flammability of PCMs [150].

According to the geometry of the containment material (Fig. 8), the micro- and nanoscopic confinement of PCM can be divided into the subgroups core-shell (0D), tubular (1D), interfacial (2D) and porous (3D) confinement [147].

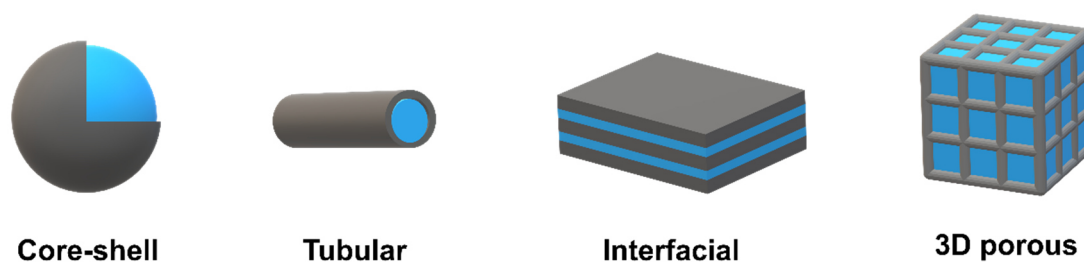


Fig. 8 Schematic representation of core-shell, tubular, interfacial and porous confinement of PCM (blue) in a nano- to microscopic containment material (grey).

Just recently, in 2018, it was postulated that nanoscopic confinement is much more efficient than microscopic confinement methods [147]. However, supercooling effects can be increased by porous structures with pore sizes smaller than 50 nm due to geometrical and chemical confinement effects. For example, the group of Zhai [151] have impregnated silica gels and controlled porous glasses (CPG) with pore sizes between 6 nm and 100 nm with tris(hydroxymethyl)-aminomethane as PCM under vacuum. The composite PCMs based on silica gel with a pore size of 100 nm had a latent heat of 250 J/g, whereas the composite PCMs based on silica gel with a pore size of 10 nm and 6 nm had only a latent heat of approximately 140 J/g and 80 J/g, respectively. The pore size effect on the PCM was not discussed and analyzed in detail but the pore size dependence on the latent heat may be based on geometrical and chemical confinement effects. If the pore size is too small in the silica gel, hydrogen bonds could be possibly formed between the silanol-groups of the silica surface and the hydroxy groups of the PCM (chemical confinement effect). The small size of the silica gel could possibly hinder the crystallization process of the PCM (geometrical confinement effect). Therefore, the ideal size and dimension of different materials for PCM containment is still unknown and cannot be predicted without further studies.

2.3.1 Core-shell confinement

PCMs encapsulated by core-shell confinement strategies are the only nano- to microscopic confined PCMs available on the market and, thus, are investigated to a large extent [152, 153]. For the synthesis, the PCM is emulsified with a surfactant as droplets in a solution and encapsulated as a core in an organic or inorganic capsule (shell), which is formed around the PCM droplet by different types of reactions, such as *in situ* polymerizations [154, 155], interfacial polymerizations [156, 157], spray-drying [158, 159] or layer-by-layer assembly [160, 161]. After filtration, separation and washing, the core-shell PCM (cs-PCM) is obtained either as slurry or wet cake, or as powder after an additional drying step. Generally, the capsule material is organic and consists mostly of polyacrylates [162], polyurethanes [163] or

polystyrenes [164]. Inorganic capsule materials enable higher heat transfer rates in the PCM phase but are brittle and, thus, need improvement in future studies [76]. The encapsulation ratio of PCM is a measure for the energy storage density of the cs-PCM at the melting point of the encapsulated PCM and depends on the shell thickness, the shell diameter and the amount of PCM encapsulated during the process. The encapsulation ratio of PCM, also described as the effective mass fraction for other confined PCMs, is mostly in the range between 50 % to 70 % [147] and can be calculated as follows [165]:

$$E_R = \frac{H_c}{H_{pure}} \quad (\text{Eq. 5})$$

where E_R is the encapsulation ratio of PCM, H_c is the latent heat of fusion of the encapsulated composite PCM (cs-PCM), and H_{pure} is the latent heat of fusion of the pure PCM before PCM immobilization.

The ratio of the hydrophobic PCM phase to the aqueous phase and the hydrophile-lipophile balance (HLB) number of the surfactant determine whether a water-in-oil (W/O) or an oil-in-water (O/W) emulsion is formed during the first step of the cs-PCM synthesis. If the hydrophobic PCM phase is larger than the aqueous phase, the aqueous phase is favored to disperse as droplets in the PCM phase and to form W/O-emulsions. To stop the formation of W/O-emulsions at high PCM amounts, surfactants with high HLB numbers must be used for the emulsification of PCM [166]. According to the Bancroft rule [167], surfactants with HLB number higher than 10 usually form O/W-emulsions. Typical surfactants for cs-PCM synthesis are cetyl trimethyl ammonium bromide (CTAB) [168], Pluronic P104 [169], Tween 80 [170], sodium dodecyl benzene sulfonic [171] and sodium dodecyl sulfate [172].

The application of cs-PCM as TES material offers many advantages such as a high thermal cycling stability, durability, mechanical stability and encapsulation ratio of PCM. However, the low thermal conductivity of the organic shell materials does not increase the low heat transfer rate in the PCM phase. Therefore, the integration of thermal conductive additives, such as graphene oxide, in shell materials is a promising technique to overcome the low thermal conductivity of cs-PCMs [173].

2.3.2 Tubular confinement

The tubular confinement is the immobilization of PCM as a liquid in nano- to microscopic tubes or fibers [87, 174, 175]. The synthesized composite PCMs can be classified as 1D core-sheath PCMs. In contrast to core-shell confinement methods, tubular confinement is quite new and

developed in the last 20 years. The sheath material consists of carbon nanotubes (CNTs) or nanofibers made of organic polymers such as polyacrylates.

Core-sheath PCMs based on CNTs have high thermal conductivities, which should increase the heat transfer in the PCM phase by considerable orders of magnitude. To synthesize core-sheath PCMs based on CNTs, the CNTs are degassed under vacuum. Afterwards, a diluted solution of PCM with lower surface tension (> 200 mN/m) is infiltrated by self-sustained diffusion at higher pressure in the porous structure of the CNT [147]. The excess PCM at the outer surface of the core-sheath PCM is removed with hot solvent and the core-sheath PCM obtained as powder after drying.

The higher thermal conductivity of core-sheath PCMs based on CNTs are offset by the substantial drawbacks of PCM leakage, low encapsulation ratios of PCM, high market price of CNTs and the phase separation tendency of PCM from CNT structures after multiple melting and freezing cycles [176, 177]. Moreover, PCM polymers such as PEG 600 cannot be infiltrated into CNT structures because of its large size.

Fibrous confined PCMs are a newer and less investigated type of 1D core-sheath PCMs than tubular PCMs based on CNTs. The synthesis method of these composite PCMs is also known as fibrous confinement and ranges from nano- to macroscale. The fibrous confined PCMs are synthesized by electrospinning and could be used in thermo-regulating textiles as competitor to nanofibers synthesized with cs-PCMs because of their higher PCM mass fraction (~50 wt%). The core of these materials is made of a PCM fiber that is covered by electrospinning with a polymeric melt (sheath), such as a melt of polyvinylpyrrolidone [178] or poly(methyl methacrylate) (PMMA) [179]. All PCM nanofiber composites show similar disadvantages to core-sheath PCMs based on CNTs, but have lower thermal conductivities and higher encapsulation ratios of PCM.

2.3.3 Interfacial confinement

To cover a 2D sheet surface with PCM, strong intermolecular hydrogen-bonding or chemical bonding between the PCM molecules and the containment surface are necessary to prevent the removal of PCM from the surface after washing or filtration steps [147]. This type of PCM confinement is named as interfacial or layered confinement technique and was developed to increase the shape-stability and mechanical strength of 2D composite PCMs, which are only hold together by weak capillary forces of PCM in porous structures. Typically, graphene oxide (GO) is used as 2D carrier molecule for the confinement of PCMs, which can form hydrogen-bonds, such as fatty acids, esters, or alcohols. The PCM is attached to the surface of GO by different self-assembly and blending methods. The group of Akhiani [180] have emulsified

palmitic acid (PA) in a solution of water and functionalized GO (0.6 %). The mixture was heated to 80 °C for 24 h to self-assemble the PCM molecules and sheets in the reaction mixture and form 3D composite PCMs after an additional drying step. The 3D composite PCMs had a high shape-stability for low GO amounts (0.6 wt%), but 10 % lower latent heats compared to the pure PCM because of strong surface interactions. At the moment, 2D and 3D layered-confined PCMs are not available on the market because of the high market price of GO, low mechanical stabilities and the strong interactions between surface and PCM, lowering the latent heat of PCM.

2.3.4 3D porous confinement

If PCM is trapped in a 3D nano- to microporous carrier structure by capillary forces or weak intermolecular interactions such as van der Waals and dipole-dipole forces, the immobilization of PCM is classified as a 3D porous confinement method [181]. The 3D porous confinement has the great advantage to obtain composite PCMs as monoliths with specific geometries. These ss-PCMs can be used for differently sized TES applications, such as walls in buildings, inner lining in solar thermal systems or heat transfer systems, or as battery cell holder. In contrast, cs-PCMs or core-sheath PCMs are available only as powder, which needs to be incorporated in additional materials, such as concrete or plastics. The mass fractions of cs-PCMs and core-sheath PCMs are limited to 15 - 30 wt% in polymeric and construction materials because of the very low shape-stabilities and mechanical strengths of these compounds [182, 183].

A perfect porous containment material for 3D porous confinement should have a large specific surface area for a high heat transfer rate, a high specific heat capacity, a high thermal conductivity, a high thermal stability, a low density, a controllable pore structure, a high mechanical stability, a high absorption capacity, a high fire resistance, a low market price and it should be produced from renewable sources. There is currently no porous material fulfilling all the requirements for an optimal containment material. However, silica, carbon and graphite as foams, aerogels, 3D polymeric structures or self-assembled intercalation compounds are among the most promising materials for the porous containment of PCM. For example, silica monoliths have a controllable pore structure, a high mechanical stability, a high adsorption capacity, a low market price and a high fire resistance, which makes them an interesting porous carrier material for building walls [184, 185]. On the other hand, graphite aerogels are more expensive than silica, but have higher thermal conductivities and lower densities and, thus, are a good candidate as battery cell holder material [108, 186, 187].

The porous confinement methods can be divided in *in situ* and *ex situ* techniques depending on whether the PCM is immobilized during (*in situ*) or after (*ex situ*) the formation of the porous structure. In contrast to core-shell, tubular or interfacial confinement, the porous confinement methods are numerous and differ greatly from each other. The most common techniques are summarized in Fig. 9.

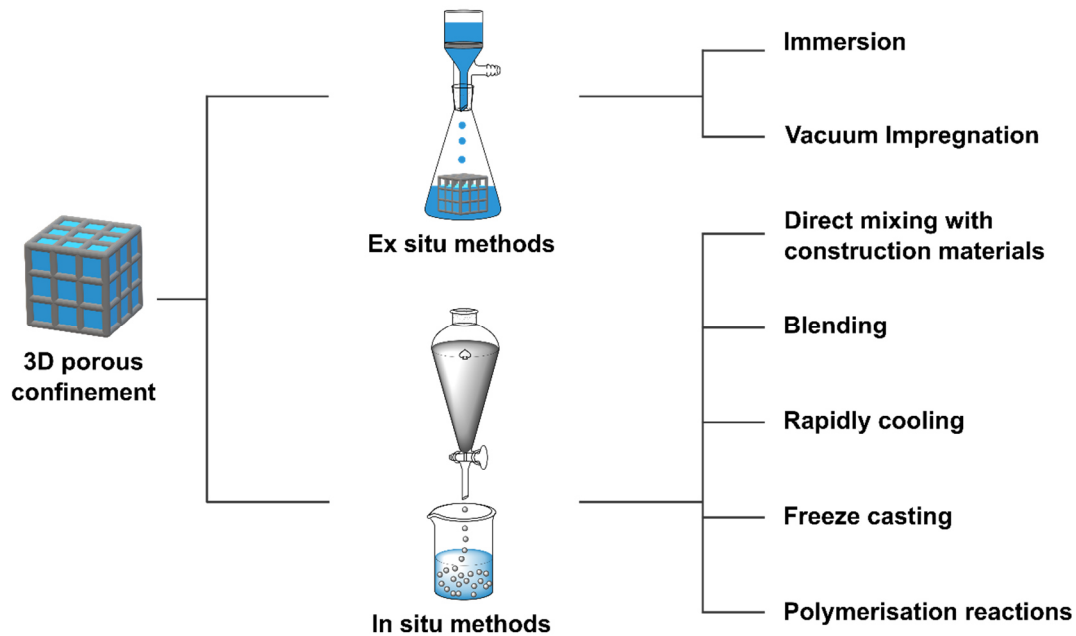


Fig. 9 Typical *ex situ* and *in situ* 3D porous confinement techniques.

The immersion and vacuum impregnation techniques are typical *ex situ* confinement methods. For the immersion methods, the porous containment material is dipped into the liquid PCM and the PCM is absorbed into the porous structure. Because the immersion process is time-consuming and only low amounts of PCM (10 to 20 wt%) are absorbed in the porous structure [188], the immersion technique is performed under vacuum nowadays. This technique is called vacuum impregnation [189–191]. The vacuum removes air from the porous containment material and accelerates the absorption of liquid PCM in the porous structure. Generally, the effective mass fraction of PCM is between 20 to 50 wt% for vacuum impregnated PCMs due to the high capillary forces in smaller nanopores [44]. If the pores in the containment material are microscopic, the capillary forces are not sufficient to immobilize PCM and PCM leaks out of the containment material. The simple experimental design, the vast amount of different available porous containment materials, the high porosity and the good mechanical properties of vacuum impregnated PCMs are big advantages for the application as TES material. However, the empty pore volume of this kind of composite PCM decreases the overall thermal

conductivity and, thus, the efficient heat transfer during melting of the PCM. Moreover, the low effective mass fraction of PCM is not sufficient for most TES applications.

To increase the effective mass fraction of PCM, the PCM can be immobilized *in situ* during the formation of the containment material, for example by direct mixing of liquid PCM with construction materials such as concrete [45–47], vermiculite [192, 193], cellulose [194], clay [195], colemanite [196] or gypsum [48]. The direct mixing was one of the first attempts to synthesize porous confined PCMs. However, PCM leakage problems occurred at higher PCM loadings of approximately 15 - 30 wt% and the mechanical stability of such ss-PCMs was low [46, 49–53].

The blending method comprises mixing of liquid PCM with the containment material followed by a self-assembly or intercalation step of the molecules in the melt, in which shape-stable blends of PCM and containment material are produced. In contrast to the direct mixing method, the containment material is not shape-stable without PCM after the synthesis. Graphite [197, 198], carbon nanotubes [199, 200] and carbon platelets [201, 202], or copper particles [203, 204] are promising containment materials for the synthesis of PCM blends due to their high thermal conductivity. These blends have high latent heats and are highly thermal conductive at low amounts of containment material, quickly to prepare and simple to shape to monolithic compounds with specific geometries. However, the particles of the containment material are generally not covalently connected but bound together by weak ionic interactions resulting in low mechanical stabilities and high phase separation tendencies after several PCM melting and freezing cycles.

The freeze casting method is divided into three or more steps [148, 205–207]. First, a slurry of a template or binder molecule with water is mixed, and low amounts of precursor molecules (e.g. GO, boron nitride, carbon, alumina) for the containment material are dispersed in the aqueous solution. In a second step, the reaction mixture is poured in a mold on top of a metal rod, which is cooled down with liquid nitrogen. The ice crystal growth of the aqueous solvent is often controlled by a freezing conductor and the ice crystals are used as templates for the 3D porous scaffold, which is formed by self-assembly of the precursor molecules around the ice crystals. In a third step, the PCM is added to the porous scaffold after freeze drying under vacuum or before freeze drying for solvent exchange. Yang *et al.* [208] have used hexagonal boron nitride sheets as precursors and GO as binder in a freeze casting method. The synthesized composite PCMs had a high thermal conductivity of 1.8 W/mK, but only a low compressive strength (5 kPa). The low compressive strength of the composite PCMs and the complicated and expensive reaction are the reason why composite PCMs synthesized by freeze casting are not available on the market.

For the confinement of PCM by rapid cooling, the liquid PCM is mixed with the organic polymers high-density-polyethylene (HDPE) [209–211] or styrene-butadiene-styrene (SBS) [212–214]. These mixtures are heated and then rapidly cooled down under the glass transition point of the organic polymer to form-stable composite PCMs. Even after multiple freezing and melting cycles, no PCM leakage is observed [215]. However, the materials are flammable, have low thermal conductivities and are only shape stabilized up to 70 - 110 °C.

In the polymerization method, the PCM is immobilized as a covalently connected polymeric structure in terms of a liquid and therefore, prevented from leakage by high capillary forces. Typical polymerization reactions for PCM immobilization are sol-gel synthesis with silica [216, 217] or graphene oxide [218, 219], radical polymerization reactions using methyl methacrylate (PMMA synthesis) [220, 221], and polyaddition reactions with isocyanates and polyols (PU synthesis) [31, 222]. To increase the thermal conductivity, the group of Ye [218] produced a paraffin/graphene gel by a hydrothermal process and additional freeze drying. The amount of graphene was low (3 wt%) and, thus, the latent heat of this composite PCM was high (more than 200 J/g). Additionally, the thermal conductivity of the pure paraffin (0.21 W/mK) was increased by approximately 33 % after immobilization.

To overcome the flammability issue of most organic polymeric structures [223–225], porous silica is a promising material due to its large specific surface area, low density, controllable pore structure, high adsorption capacity, high mechanical stability and high fire resistance. In contrast to alumina, silica is not reactive against organic PCMs. The group of Li [54] synthesized a silica-based composite PCM via a sol-gel process with high effective mass fractions of PCM of up to 80 wt%. The silica matrix of the composite PCM was interconnected and chemically inert against the PCM (PEG), as shown by infrared spectroscopy and X-ray diffraction analyses. However, the composite PCMs were not monolithic after synthesis and had 32.7 % lower latent heats (50 wt% PCM) even after 3 repetitions of melting/ freezing of the sample. He *et al.* [217] developed two different sol-gel syntheses assisted by CaCl_2 and a temperature increase for the confinement of PEG in a silica matrix. After five melting and freezing cycles, it was assumed that PCM leakage occurred only when using more than 80 wt% PEG. The broken PEG/silica gel was dried at 80 °C under ambient pressure and the product grinded to fine particles. Despite the interesting thermal properties of silica-based composite PCMs, the mechanical stability, long-term form-stability of more than 1000 cycles and durability tests of the silica-based composite PCMs are currently not characterized. Moreover, the silica matrices are not analyzed in detail, which is the reason why the analysis of pore shape, porosity and the degree of interconnectivity of the silica matrix are still missing.

Because of the promising properties of silica-based composite PCMs, this work is focused on the development of a novel sol-gel synthesis to overcome current PCM problems, such as low

cycling stability, durability and mechanical stability, and to synthesize shape-stabilized PCMs (ss-PCM) with high PCM mass fraction as a monolithic compound for different industrial applications, such as energy storage in buildings and solar-thermal boilers, and for passive cooling of photovoltaic and battery systems.

2.4 Shape-stabilized PCMs

If the PCM is confined in a containment material and is prevented from leakage above its melting point, the composite PCM is classified as shape-stabilized PCM (ss-PCM) [40, 181]. Generally, the shape-stabilization (form-stabilization) of a PCM is tested by heating the ss-PCM for multiple hours (24 h) above the melting point of the pure PCM. The PCM leakage is mostly detected by a camera set up and additional weighing before and after the shape-stabilization test [218, 226].

It is declared by general definition [40, 181] that core-shell, tubular, interfacial and 3D porous composite PCMs are all shape-stabilized PCMs (ss-PCMs) (Fig. 7, Fig. 8). Comparing different studies [54, 184, 218, 220], it becomes apparent that this definition is blurred making an unambiguous classification complicated. To avoid confusion about the different terms of composite PCMs, in the present work an ss-PCM is precisely defined as a composite PCM without PCM leakage, with a specific geometric monolithic form, a compressive strength of at least 1 kPa and with a macroscopic dimension (> 1 mm) because these properties are essential for most PCM applications today. Therefore, only composite PCMs synthesized by 3D porous confinement methods or mixtures of core-shell, tubular and interfacial confined PCMs with polymeric or construction materials are classified as ss-PCM.

2.5 Sol-Gel

The sol-gel process is a bottom-up approach to synthesize porous polymeric, glass and ceramic materials by the addition of organic or inorganic precursor molecules to an aqueous solution at lower temperatures (< 100 °C) [227, 228]. The polymeric, glass and ceramic materials synthesized by the sol-gel process have many advantages, such as high specific surface areas, high porosities, good mechanical and chemical stabilities, and adjustable pore structures. These properties make them particularly suitable for applications in catalysis, sensing, optics, thermal and sound insulation, and adsorption processes. The sol-gel process can be divided into the following reaction steps: formation of a colloidal sol (hydrolysis), gelation of the primary particles to a gel (condensation), aging and drying of the wet gel (Fig. 10).

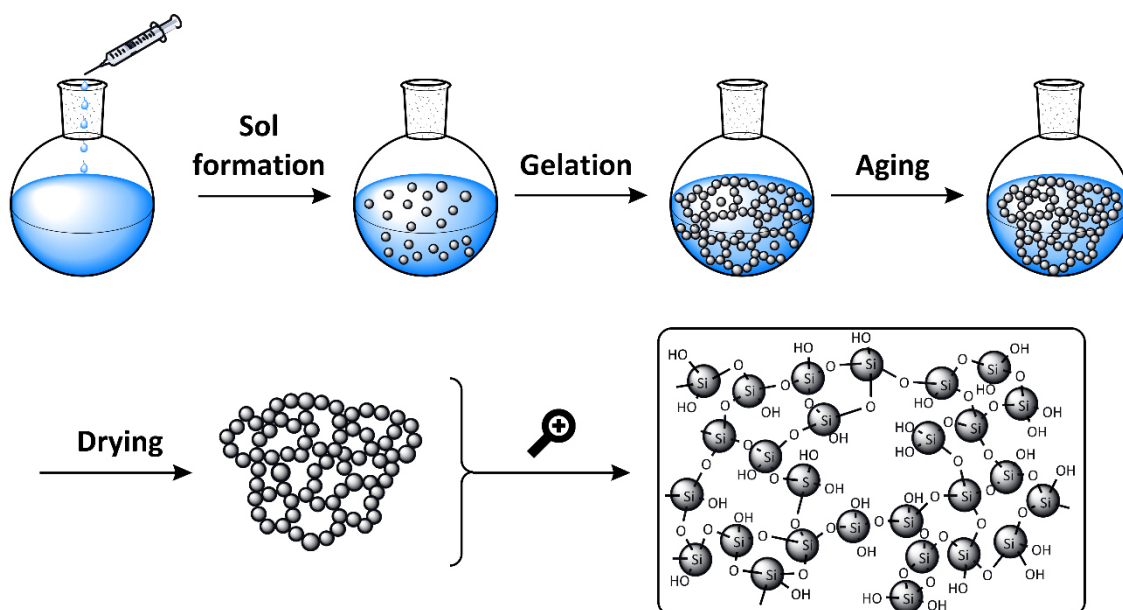


Fig. 10 Schematic illustration of the sol-gel synthesis of gels based on silica particles (grey).

2.5.1 Sol formation

The sol is formed either by a growth mechanism of precursor molecules in solution or a dissolution step of dispersed precursor particles [229, 230]. Both mechanisms are based on the simultaneous hydrolysis and condensation of precursor molecules (growth mechanism) or particles (dissolution) followed by self-assembly of these aggregates by van-der-Waals and dipole attractions. The reaction rate of the hydrolysis is higher than the condensation rate of the particles that is why the sol formation process is also named as hydrolysis [231]. The final sol particles are suspended in a solution as colloids. A colloidal solution consists of particles with diameters between 1 nm to 100 nm to prevent phase separation effects [232]. If the particle size is smaller than 1 nm, the surface tension becomes the dominant force and the particles are pushed to the surface. If, however, the particle size is larger than 100 nm, the particles settle on the bottom due to predominant gravity.

Typical precursor molecules are oxides, hydroxides, alkoxides, acrylates, amines, and salts. Amongst them, metal alkoxides, especially silicon alkoxides, have been extensively studied [233]. The reactivity of the primary particles is adjusted by the water/precursor ratio (r -value), the pH value of the solution, the temperature, the functionalization of the precursor, chemical additives, and physical parameters, such as temperature and pressure. Generally, the nucleation rate must be high and the crystallization rate as low as possible during sol formation.

For silica-based sols, metal alkoxides, such as tetraethyl orthosilicate (TEOS), can be hydrolyzed under acidic or basic conditions in an S_N2 reaction. The metal alkoxide is

nucleophilically attacked by water (acidic) or hydroxides (basic) forming a trigonal bipyramidal transition state, which reacts to the hydrolyzed metal alkoxide and the alcohol (acidic) or alcoholate (basic), respectively [227, 228]. If longer and more branched metal alkoxides are used in the sol-gel process, the alkoxide-groups shield the electrophilic metal center from nucleophilic attacks due to steric hindrance and, thus, the hydrolysis rate becomes slower.

To stop further condensation reactions, the silica-sol can be stabilized by higher pH values of around 9 and specific cations, which arrange around the negatively charged surface of the silica particles and, thus, decrease the reaction tendency between the silica particles [234–237]. These stabilized sols are commonly produced not from metal alkoxides but from water glass (sodium silicates) in industry due to a lower market price. Water glass is produced from quartz sand and alkaline salts (NaCO_3) in an alkaline melt of temperatures higher than $1000\text{ }^\circ\text{C}$ and it consists of alkali metal cations, water and silicon dioxide (SiO_2) [238]. This water glass solution is diluted from 30 wt% to 3 - 5 wt% SiO_2 due to high viscosity and then purified by ion exchangers or by electrodialysis to remove alkali metal cations and to finally obtain a polysilicic acid solution. Subsequently, the polysilicic acid solution is poured into a diluted solution of alkali metal cations, which serve as nucleation sites for the growth of primary particles. The final stabilized sol is obtained after adding specific cations (e.g. sodium, ammonia) as stabilizer and a final concentration step to 30 - 50 wt% SiO_2 . The stabilized sol is sold under specific trade names by companies like Grace, Nouryon (former AkzoNobel) or Chemiewerk Bad Köstritz (CWK) (Table 3) for the clarification of wine, beer or fruit juices, semiconductor wafer polishing, coating, color production, and as binder for ceramics [239, 240].

For example, the stabilized silica sols produced by CWK are named Köstrosol followed by the first two numbers for the average primary particle size and the last two numbers for the weight percentage of silicon dioxide.

Table 3 Physicochemical properties of stabilized silica sols from Grace [241], Nouryon [237] and CWK [242].

Company	Grace	Nouryon	CWK
Trade name	LUDOX TM-50	Levasil CB25	Köstrosol 0730
Particle size (nm)	22	11	7
Concentration SiO_2 (wt%)	50	30	30
Surface area (m^2/g)	140	250	352
Stabilizer cation	Na^+	Na^+	Na^+
pH	9.0	10	9.8
Density (g/cm^3)	1.4	1.2	1.2
Viscosity (cPs)	40	5	7

The specific average particle size and the low market price are the major advantages of stabilized silica sols compared to sols prepared by metal alkoxides [237, 243]. Moreover, stabilized silica sols are non-toxic and non-flammable [57, 58] in contrast to pure metal alkoxides, such as TEOS [59, 60]. Until recently [244, 245], silica monoliths could not be synthesized in a sol-gel process starting from stabilized silica sol under subcritical conditions, mainly due to a lack of reactivity and a low level of preorganization of silica. Preorganization describes the effect how efficiently the side groups of silica are presorted to accelerate further reaction steps in the sol-gel process. Because the silica of the stabilized sol is only attached to four small hydroxide-groups, the silica can be attacked from each direction in space with the same probability and, thus, has a low level of preorganization. As a consequence, the stabilized sol must be activated physically (temperature or pressure increase) or chemically (templates as nucleation sites, acidic or basic catalyst) to induce further condensation to a gel.

2.5.2 Gelation

The sol can react to a three-dimensional framework by polycondensation reactions of the primary particles during the gelation process. In case of silica-based sols, the primary particles form siloxane bonds under release of water (stabilized silica sol) or alcohol (metal alkoxide based sols), resulting in oligomeric structures [227, 233]. To prevent sedimentation of these bigger particles, the reaction rate of the gelation must be relatively high. Therefore, basic and acidic catalyst are often used in sol-gel processes (Fig. 11).

These catalysts can increase the reaction rate of condensation and influence the structure of the growing oligomeric particles, too (Fig. 12). For example, the formation of spherical-shaped oligomeric particles is favored under basic conditions due to the higher electrophilicity of highly condensed silica particles. In contrast, the silanol-groups of silica are protonated under acidic conditions, pushing electron density to the protonated silanol-group. As a consequence, the electrophilicity of the silicon center of lower condensed silica particles is increased, resulting in linear-branched oligomeric structures during gelation (Fig. 11).

As the oligomerization order increases with the advancing reaction, the viscosity of the reaction mixture reaches its maximum and the gelation is finished [228]. The liquid sol has turned into a solid wet gel, which prevents the liquid solvent from leakage due to a mechanically stable three-dimensional silica framework.

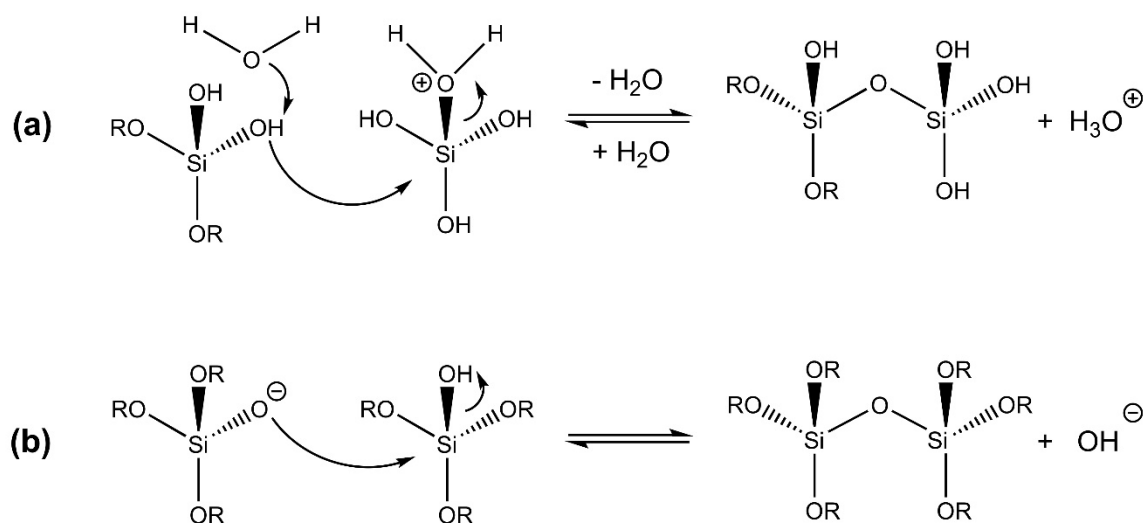


Fig. 11 Formation of oligomeric silica particles under acidic (a) and basic (b) conditions during gelation.

The gelation process is not only influenced by the pH value of the solution (Fig. 12) but also by different physical and chemical parameters, such as temperature, pressure, the molar ratio of available water to precursor (r-value), the concentrations of the educts, the ionic strength, and by additives such as templates. For example, a higher temperature increases the reaction rate of gelation. In contrast, larger porogens, such as polyethylene oxide, can interact by hydrogen-bonding or dipole-dipole interactions with the silica surface and shield the silica particles from the condensation reaction due to steric hindrance.

As a consequence, further condensation reactions between silica particles are decelerated during gelation.

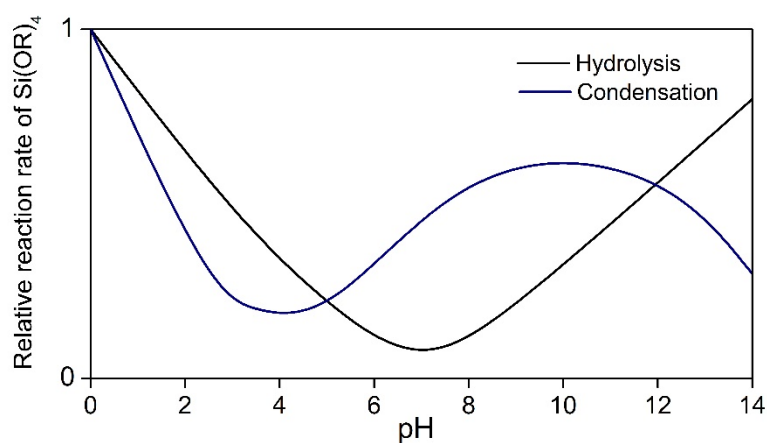


Fig. 12 Relative hydrolysis and condensation rate of Si(OR)_4 depending on the pH in the sol-gel process. The figure was adapted from Levy *et al.* [228] and slightly changed.

2.5.3 Aging

After the viscosity reaches its maximum and the gelation is finished, the liquid phase and the solid three-dimensional framework can further interact and react in the wet gel. These chemical reactions are based on polycondensation reactions, syneresis effects and Ostwald ripening and lead to more rigid and mechanically reinforced gel structures [227, 228].

For the aging of silica-gels, polycondensations are condensation reactions of silanol-groups on top of the silica surface of the framework with particles and oligomeric structures in the solution. These reactions decrease the specific surface area and porosity, and increase the mechanical stability due to a higher connectivity of the silica framework [246]. Therefore, a basic solvent increases the rate of condensation reactions compared to hydrolysis reactions and, thus, enhances aging processes (Fig. 12). The pH value can be increased by addition of bases, precursors for bases (urea) [247] or by exchange of the solvent for a basic solution during aging [248].

If two silanol-groups of the three-dimensional framework are in spatial proximity, they can react with each other by condensation reactions (oxolation) and form a siloxane group. This process is called syneresis. As a consequence, the adjacent silica structures of the siloxane group are tightened and the pore structure shrinks by the volume of water released by the condensation reaction. Syneresis effects can occur between rigid or flexible silica structures. Flexible silica structures have a higher degree of movement and connect silica structures over a larger distance whereas rigid silica structures are formed only in close proximity. Generally, syneresis effects increase the mechanical stability and reduce the flexibility of the wet gel. In some cases, however, the shrinkage of the silica gel can induce micro- to macroscopic fractures of the silica structure due to silica structures with high rigidity [249, 250].

In the process of Ostwald ripening, silica molecules are dissolved from convex surfaces with positive radii of curvature and are attached on concave surfaces with negative radii of curvature. Especially smaller silica particles have positive radii of curvature and, thus, are dissolved and attached to larger silica structures, pores, particle necks and crevices with negative radii of curvature. The silica structure becomes more compact and the mechanical stability of the gel is increased.

2.5.4 Drying

The subcritical drying is divided into the following phases, as illustrated in Fig. 13 [228, 232].

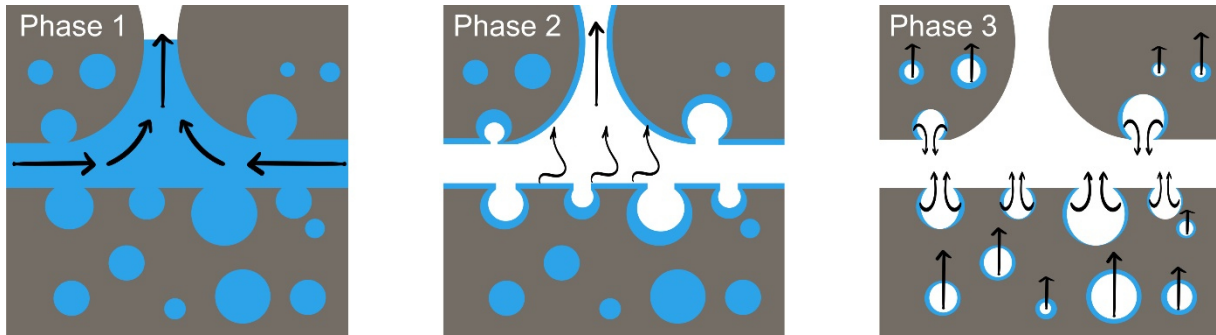


Fig. 13 Schematic illustration of the subcritical evaporation of the solvent (blue) from of a gel structure (grey).

First, the solvent diffuses from the interior of the wet gel to its surface. Then, the solvent evaporates at the surface of the wet gel and the gel shrinks by the volume of the evaporated solvent. Silanol-groups of the three-dimensional framework come closer and condense to form siloxane-bridges, stiffening the gel structure and increasing its mechanical stability.

In the second drying phase, the gel is too stiff and further shrinkage is not possible. A liquid/gas interface is formed between the pore walls and is pulled into the interior of the pores due to high capillary forces induced by the curved liquid/gas interface. The solvent diffuses as thin film to the exterior surface of the gel where it evaporates immediately. According to the Laplace-equation (Eq. 6), the solvent evaporates faster in pores with larger radii than in pores with smaller radii r_p because of the lower capillary force P_c and the surface tension of the solvent γ .

$$P_c = \frac{2\gamma \cdot \cos(\theta)}{r_p} \quad (\text{Eq. 6})$$

The high capillary forces and the different drying rates in bigger and smaller pores induce high tensions of the three-dimensional silica network, which can easily lead to cracks and fractures of the gel. To reduce the capillary forces, pressure, temperature and surface tension should be as low as possible for a crack-free drying process. The surface tension of the solvent is decreased for example by the addition of a surfactant [251] or by the exchange of aqueous solvents for alcoholic solvents with lower surface tensions [248]. After solvent exchange, an additional silylation of the hydrophilic silanol-groups can help to prevent oxolation reactions and increases the flexibility of the gel for less tensions in the silica structures [252, 253]. Furthermore, phase separation or template strategies can widen smaller pores or generate larger pores during gelation, resulting in a pore system with a larger average pore radius r_p and, thus, a lower capillary force and tension in the gel (Eq. 6) [254–256].

The final drying phase is reached, when the film evaporation of the solvent is ruptured due to less solvent remaining in the open pore structures or due to closed pores encapsulating the

solvent. The solvent is then evaporated directly by gas phase diffusion leading to a dried gel, called xerogel.

To lower the surface tension of the aqueous phase and, thus, reduce the capillary forces during drying, the wet gel can also be freeze- or supercritically-dried to produce cryogels or aerogels, respectively. In contrast to xerogels, which are dried at ambient pressure, cryogels and especially aerogels have some unique properties, such as very high porosities, large specific surface areas, very low thermal conductivities, good mechanical stabilities and very low sound velocity [257–259]. These properties sound promising for an application of these cryogels or rather aerogels in thermal insulation, sound insulation, adsorption and catalysis. However, freeze-drying and supercritical drying is a time-consuming and expensive process. Consequently, xerogels with the properties of aerogels are of great interest.

2.6 Porogen strategies

The specific pore structure, pore accessibility, porosity, shape and interconnectivity of a three-dimensional silica material determines its physicochemical properties [228, 260]. For example, a silica material with a high amount of mesopores (2 - 50 nm) has a high specific surface area and good sound and thermal insulation properties. If the silica material consists of interconnected macro- (> 50 nm) and mesopores, the mesopore accessibility increases for molecules in the gas phase, which is beneficial for catalyst carrier systems [261, 262]. A higher ratio of interconnected to fragmented silica structures increases the mechanical stability of the wet silica gel and, thus, is responsible for the form of the silica gel (powder or monolith) after drying.

The form and structure of the dried silica material depends on the solvent space between the solid network and on the type of porogen added to the reaction mixture during gelation in the sol-gel synthesis. Generally, a substance or molecule is termed as porogen, if it influences the final molecular structure of a polymer or a macromolecule during synthesis. Typical porogens are block polymers, surfactants, acids and bases, emulsion droplets, gas bubbles and solid particles. They can be distinguished in hard templates and structure-directing agents according to the type of influence (Fig. 14) [256].

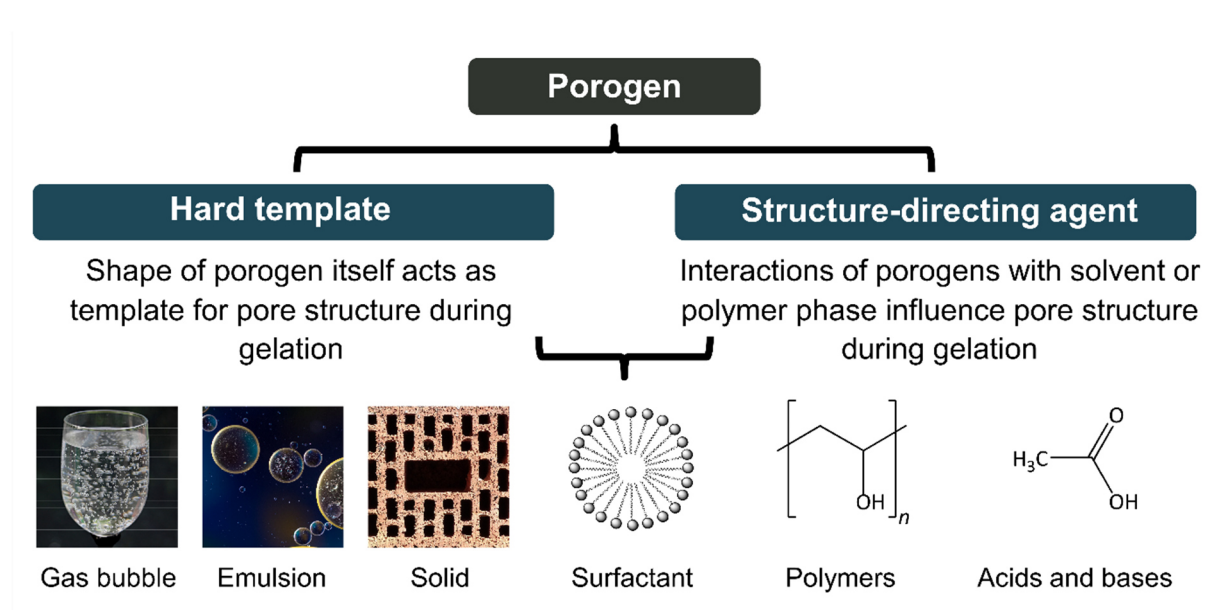


Fig. 14 Classification of porogens in hard templates and structure-directing agents. Surfactants can act as hard templates and/or as structure-directing agents.

The structure of a hard template is directly visible in the nano- to microscopic structure of a polymer or a macromolecule after synthesis. For example, the structure and size of solid particles, gas bubbles or hydrophobic droplets in an aqueous emulsion can be “frozen” during the gelation of silica precursors, which can only undergo condensation on the exterior surface of the template structures. In comparison, the influence of a structure-directing agent is not directly visible by its shape in the microscopic pore structure after gelation. The structure-directing agents can affect the pore structure by specific molecular interactions with the solvent and/or the polymer phase [255]. In a sol-gel process, organic polymers, such as poly(vinyl alcohol) (PVA) or polyethylene oxide (PEO), can interact as structure-directing agents by hydrogen-bonding to the surface of silica and decrease the solubility of the silica in the solvent phase [231]. As a consequence, the silica phase is separated from the solvent phase and the phase-separated areas are “frozen” in the structure of the silica during gelation. The combination of different porogen strategies is used to adjust different pore sizes and pore ratios of closed to open pore structures independently, control shrinkage conditions, and retain the desired product form as powder or monolith. However, silica alkoxide precursors, such as TEOS, release alcohol during the gelation reaction. The released alcohol is often disturbing the formation of supramolecular assemblies and emulsions, and, thus, is not compatible for all porogen strategies [256]. Therefore, the focus of interest is switching from silica alkoxide precursors to different functionalized or non-functionalized silicates in the last years of sol-gel science.

2.6.1 Structure-directing agents

The simplest structure-directing agent in the sol-gel process is silica itself [256]. During gelation the suspended silica particles perform polycondensation reactions and separate the suspension into a three-dimensional solid silica network and a solvent phase corresponding to a micro- to mesopore structure of the silica gel after drying.

Organic polymers, such as PVA and PEO, can as structure-directing agent also induce additional phase separations and expand the micro- to mesopore structures, for example by introducing specific macropore channels. This thermodynamic process is known as polymer-induced phase separation in sol-gel research or as polymer alloying in process engineering, and is based on a miscibility gap between an inorganic silica and an organic polymer phase in a solvent phase [263, 264]. Both phases of silica and organic polymer must have a similar miscibility in the solvent phase to enable phase separations. The miscibility gap is reached during the nucleation and growth of the silica macromolecule, if the change in the free mixing enthalpy ΔG is above zero. The influence of temperature, the change in the mixing entropy and mixing enthalpy with the change in the free mixing enthalpy is described by Gibbs-Helmholtz equation (Eq. 7).

$$\Delta G = \Delta H - T \cdot \Delta S \quad (\text{Eq. 7})$$

where ΔG is the change in the free mixing enthalpy, ΔH is the change in the mixing enthalpy, T is the temperature and ΔS is the change in the mixing entropy.

According to the Gibbs-Helmholtz equation, a phase separation is induced either by decreasing the temperature of the reaction (physical cooling), or by increasing the change in the mixing enthalpy or rather decreasing the mixing entropy, to increase the change in the free mixing enthalpy above zero (chemical cooling) [228, 263]. In case of polymer-induced phase separation, the organic polymer increases the change in the mixing enthalpy and/or decrease the change in the mixing entropy due to intermolecular interactions with the growing silica polymer in the gelation process. This thermodynamic process can be described for polymers in detail by the Flory-Huggins equation (Eq. 8) [264, 265].

$$\Delta G = RT \left[\ln_{\phi_1} \left(\frac{\Phi_1}{P_1} \right) + \ln_{\phi_2} \left(\frac{\Phi_2}{P_2} \right) + X_{12} \Phi_1 \Phi_2 \right] \quad (\text{Eq. 8})$$

with R as the universal gas constant, T as the temperature, Φ as the volume fractions of the inorganic polymer 1 and organic polymer 2, P as the polymerization degree of inorganic polymer 1 and organic polymer 2, and X as the Flory-Huggins parameter for the interaction of both polymers.

The polymer-induced phase separation is either based on enthalpic or on entropic forces. The entropic forces are described by the first two terms of the Flory-Huggins equation including the polymerization degree and the enthalpic forces by the last term including the Flory-Huggins interaction parameter. If the inorganic silica polymer grows during gelation, the polymerization degree increases and, thus, the change in the free mixing enthalpy increases slowly to positive values. Now, two cases must be distinguished. First, the organic polymer, such as poly(acrylic acid), with acidic functional groups and a high molecular weight can only interact by weak dipole-dipole and van-der-Waals interactions with the surface of the growing silica polymer [254]. Therefore, the interaction of both polymers is poor and the phases are separated into a silica-enriched and an organic polymer-enriched phase. The polymer-induced phase separation is mainly driven by entropic forces. Second, the silica and organic polymer, such as PVA or PEO, with neutral and basic functional groups highly interact by strong dipole-dipole interactions and hydrogen-bonding [254]. The organic polymer wraps around the silica polymer and reduces the solubility of the silica polymer in the solvent phase due to repulsive interactions between the hydrophobic silica/organic polymer-enriched phase and the hydrophilic solvent phase. In this case, the enthalpic forces predominate in the phase separation process. At high concentrations, the organic polymer shields silica aggregates from each other and can even stop gelation processes, resulting in non-monolithic gel structures [266]. This process is called bumper-effect (Fig. 15B). Moreover, lower amounts of the organic polymer can order different silica aggregates by sticking and pre-organizing them in the solvent phase. This sticker-effect can increase the gelation rate and the interconnectivity of the silica phase (Fig. 15A).

For an interconnected silica structure, the phase separation must be as fast as the gelation process [228]. This type of silica structure is mostly sponge-like, has a high mechanical stability, enables different pore sizes and is ordered in specific pore hierarchies. Interconnected silica pore structures are synthesized when the state of spinodal decomposition

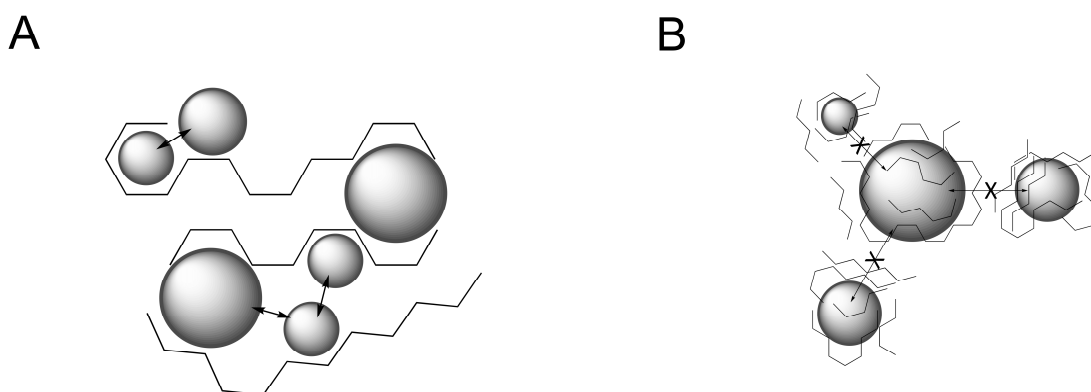


Fig. 15 Sticker- (A) and bumper-effect (B) of polymers (zigzag line) interacting by strong dipole-dipole interactions and hydrogen-bonding with silica particles (grey spheres) during gelation in the sol-gel process.

is “frozen” during gelation. The synthesis approach of interconnected silica pore structures was first described by Nakanishi *et al.* [267] and can be visualized by a two-phase diagram (Fig. 16). In this diagram, the upper region is representing the state of a homogenous phase of the miscible aqueous solvent phase and the inorganic silica phase. If the sol-gel synthesis is cooled down (physical cooling), the miscibility of the two phases will be decreased and a metastable region is reached. This metastable region is divided from the upper region by the binodal and from the lower region, the macroscopic two-phase state, by the spinodal [267]. The gelation process is described by the nucleation and growth mechanism in the metastable region and mostly particulate structures and isolated pores are formed during gelation. If the silica nucleation is only partly accelerated, e.g. by surface interactions with templates or by further physical cooling, the homogenous phase in the metastable region is spontaneously separated by spinodal decomposition. If the state of spinodal decomposition is “frozen” during gelation, silica structures with high interconnectivity are generated. Early states of spinodal decomposition are favored to decrease the size of macropores and, thus, to obtain finer and smaller pore structures due to a slightly faster gelation compared to the phase-separation process. Late states of spinodal decomposition increase the size of macropores and can even lead to spherodized silica structures [267]. After the spinodal decomposition, the two phases are phase-separated until two macroscopic phases are generated and the gelation process is decelerated or interrupted, preventing the formation of a mechanical stable wet gel. In addition to physical cooling, the state of the unstable region below the spinodal can also be reached from the single-phase state by chemical cooling via structure-directing agents (Fig. 16).

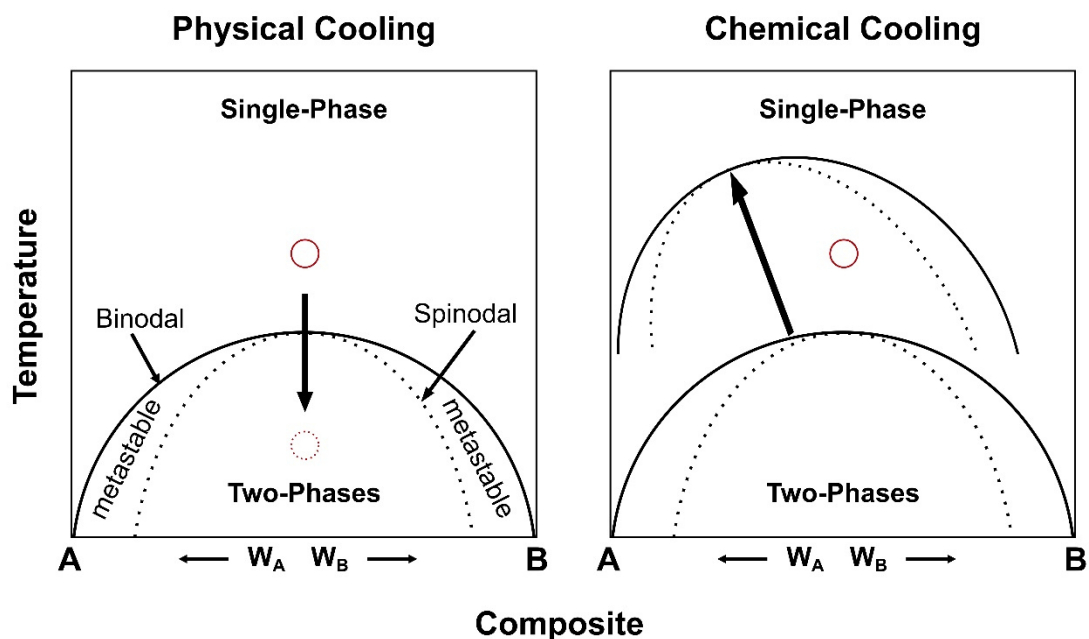


Fig. 16 Physical and chemical cooling in a two-phase diagram of phase A and phase B. The red circle represents one single-phase state (straight line) and a two-phase state after physical cooling (dashed line), respectively. This figure was adapted from Nakanishi *et al.* [267] and modified.

The structure-directing agents, such as PVA or PEO, can increase the free mixing enthalpy ΔG above zero, as described by the Flory-Huggins equation (Eq. 8). As a consequence, the whole miscibility gap is shifted to higher temperatures in Fig. 16 and the former single-phase state (red circle) becomes the new two-phase state, resulting in the spontaneous phase separation of the homogenous aqueous solvent and the inorganic silica phase.

Acids and bases are mainly used as catalyst to decrease or increase the pH value in the sol-gel process. The influence of the pH value on the hydrolysis and condensation of silica during sol-gel synthesis is well understood [227, 228]. However, only a few studies are published about the influence of the chemical nature of acids and bases on the growing silica polymer in the sol-gel synthesis. For example, Huck-Iriart *et al.* [268] compared the influence of three different acids HF, HCl and HNO₃ on the acid-catalyzed hydrolysis and condensation reactions of TEOS. The silica gels synthesized at a constant pH value of the reaction mixture were mesoporous with HF as catalyst and microporous with HCl or HNO₃ as catalyst. They concluded, that anions with high nucleophilicity (F⁻) strongly interact with the growing silica polymer and accelerate the condensation reactions by the reversible rapid formation of reactive intermediates, such as [FSi(OEt)₄]⁻. In comparison, organic acids, such as citric acid, can interact by hydrogen bonding with silanol groups of the silica network during gelation and disturb the formation of interconnected silica gel structures by cross-linking silica particles and by steric hindrance [269, 270]. In both cases, the acids affect the solubility of the silica species in solution and can increase the phase separation tendency between a silica-anion-enriched phase and a solvent-enriched phase. Therefore, acids (as well as bases) can be described as structure-directing agent, if the interaction between the corresponding anion (or cation) and the growing silica polymer is quite intense.

Surfactants are a special class of porogens because they can act as a structure-directing agent and/or as a hard (or soft) template [251, 254, 271]. Takahashi *et al.* [254] analyzed the influence of sodium dodecyl sulfate (SDS) as an anionic surfactant on the meso- and macrostructure of silica gels starting from water glass as silica source. In the sol-gel process, SDS lowered the mixing entropy between a silica-enriched and a surfactant-enriched phase by the formation of larger micelle structures and, thus, separated both phases above a certain surfactant concentration. If, however, the surfactants are cationic, such as cetyl trimethyl bromide [271], they can build attractive interactions to the growing silica polymer in solution under basic conditions and separate the reaction mixture in a silica-surfactant-enriched phase and a solvent-enriched phase, mostly by increasing the mixing enthalpy of these two phases. Therefore, anionic, non-ionic and cationic surfactants can induce as structure-directing agent different kinds of pore structures in the silica gel, such as particulate structures with uniformed pore sizes in case of anionic (SDS) and non-ionic surfactants (Pluronic P123) or platelet

structures with non-uniform pore size distributions by the addition of cationic surfactants (CTAB) to the sol-gel synthesis [254, 271]. Moreover, the surfactants can act as a hard or soft template for micro- and mesopore structures after forming specific types of micelles during gelation [272–274]. The micelles are classified as “soft” templates, when the micelle structure is slightly deformed during sol-gel synthesis. In the production of MCM-41 structures, CTAB is used at low concentrations as a structure-directing agent and at high concentrations as a template in shape of CTAB-micelles for the synthesis of silica mesopores [271].

2.6.2 Hard templates

Solid particles, foams, porous monoliths or fibers have many advantages as hard templates in sol-gel syntheses. The solids have often a specific porosity, which is generally not affected by the gelation of the silica phase during gelation. Additionally, most solids have no chemical reactivity towards silica and their size and shape varies widely, allowing to synthesize a wide range of different silica pore systems. However, solid templates are hard to remove from the silica structure and additional removal steps like calcination, template solving or chemical etching are necessary [275]. To overcome the problem of template removal, the aqueous solvent can be frozen and used as solid ice template in a freeze-casting approach in sol-gel processes. By high vacuum sublimation and freeze drying, macroporous silica materials with honeycomb pore structures could be synthesized even as stable monoliths [276, 277].

The continuous introduction of gas or the formation of gas bubbles by foaming reagents in a liquid phase is another template method to synthesize silica materials with different pore structures in sol-gel processes [278–281]. The average gas bubble size and distribution are, however, hard to control and the template stability of these bubbles is relative low. Yet, hollow silica particles in the millimeter range could have been synthesized by transferring low amounts of ammonia bubbles through a capillary tube into a silica sol [278].

The surface of droplets in an emulsion can be used as template for the preparation of interconnected and isolated macroporous silica structures in sol-gel [282–286]. This process is called emulsion templating and has several advantages compared to solid template strategies [287]. For example, liquid droplets emulsified in a continuous phase are highly deformable during the gelation process, facilitating shrinkage processes and preventing cracks during subcritical drying [256]. Moreover, the liquid droplets are easy to remove than solid templates just by extraction or drying at lower temperatures. The droplet size in an emulsion depends not only on the volume fraction of the emulsified phase but also on physical and chemical parameters, such as temperature, pressure, stirring or ultrasonic conditions (mini- or microemulsion), amount and chemical nature of surfactant, ionic strength or the pH value [288,

289]. As already discussed for the synthesis of cs-PCMs (section 2.3.1), the phase emulsified as droplets must have a lower volume fraction than the continuous phase in the emulsion or must be stabilized by surfactants with specific HLB values, such as SDS with an HLB value larger than 10 for an oil in water emulsion [166, 167]. Generally, the effect of the surfactant is higher than the one of the volume fractions. Additionally, surfactants are often required to decelerate or even prevent the separation of the emulsion in two macroscopic phases by decreasing the interfacial tension at the oil/water interface. A mathematical description of this process is given by the work W that is required to expand the droplet surface, using the interfacial tension γ between oil and water interface and the change of the droplet area ΔA (Eq. 9) [290]:

$$W = \gamma \cdot \Delta A \quad (\text{Eq. 9})$$

In an emulsion without an external energy input, the work W required to expand the droplet surface is constant. Therefore, the interfacial tension γ must be decreased in order to increase the change of the droplet area ΔA and hence, decrease the size/diameter of the droplet in an emulsion. The interfacial tension of a specific surfactant depends also on the type of counterion and the size of the hydrated counterion in the emulsion. For example, lithium dodecyl sulfate has a larger hydrated shell than sodium dodecyl sulfate in water because of its counterion and, therefore, a higher interfacial tension at the oil/ water interface, resulting in larger emulsified droplets in the continuous phase [290].

The volume fraction of the continuous phase determines the form of the droplets in the emulsion. If the volume fraction is 26 %, the spherical droplets are ordered in the most compact form in the continuous phase [256]. At lower volume fractions of the continuous phase (below 26 %), the spherical droplets are deformed or polydisperse and the emulsion is defined as high internal phase emulsion (HIPE), which can be used as templates for interconnected macroporous silica structures with a lower number of isolated pores in sol-gel processes [291].

The pH value of the solution has a great impact on the size and number of droplets covered by micellar layers. By using SDS as a surfactant in a toluene in water emulsion, a higher pH value decreases the interfacial tension and the toluene droplet size [292]. If the ionic strength of the solution is too high, the formation of stable spherical droplets in the emulsion is impaired, the average droplet size is increased and silica structures could collapse during drying in sol-gel processes [293–295].

The external physical factors temperature and pressure can increase the ion mobility, decrease the interfacial tension at the o/w interface or break stable micellar structures in emulsions. A higher temperature accelerates the formation of stable spherical toluene/SDS micelles and decreases their size [292, 296]. In comparison to temperature changes, a higher

pressure generally decreases the droplet size and is often used to synthesize different kinds of emulsions [166, 297].

Emulsions are divided in macroemulsions, miniemulsions and microemulsions according to their thermodynamical and kinetic stability. A brief summary of the different properties of these emulsions is given in Table 4.

Table 4 Physicochemical properties of macro-, mini- and microemulsions.

	Macroemulsion	Miniemulsion	Microemulsion
Droplet size (μm)	2 - 20	< 0.3	< 0.1
Color	white	opaque + translucent	translucent
Emulsion stability	seconds to days	weeks to months	years
Thermodynamical stability	unstable	unstable, but kinetically stable	stable
Emulsification conditions	low-shear forces	high-shear forces, ultrasonication	spontaneous emulsification

Macroemulsions are the simplest form of emulsions and are synthesized by low shear forces (e.g. magnetic stirring) [166]. They are milky white due to their average droplet diameter (2 - 20 μm) and easily phase separate into two macroscopic phases after seconds to hours because they are thermodynamically and kinetically unstable. In contrast, miniemulsions are translucent with an average droplet diameter below 300 nm and are stable over months due to their kinetic stability [295]. They are produced by rotor-stator systems, ultrasonication or high-pressure homogenization processes [298]. To stop Ostwald ripening effects and to stop miniemulsion demixing by droplet coalescence, low-molecular weight molecules with high hydrophobicity, such as hexadecane, are used as co-stabilizer. Miniemulsions differ from microemulsions by the formation mechanism of the emulsion [299]. Microemulsions are not synthesized by energy input but by spontaneous emulsification due to miscibility gaps. Therefore, microemulsions are thermodynamically stable in contrast to miniemulsions and have high emulsion stability over years.

In sol-gel science, the type of emulsion directly influences the size of the pore or particle template (emulsion droplet size). Miniemulsions are more stable against changes in physicochemical properties than microemulsions and have a narrow droplet size distribution. Starting from a miniemulsion with droplet sizes smaller than 100 nm stable silica nanoparticles were obtained by the sol-gel route using TEOS as silica source and hexadecane as co-stabilizer [295]. The silica nanoparticle size was thereby adjusted by varying temperature and pH. The group of Sen [300] could synthesize meso- and macroporous foams as well as macro-

cellular silica materials by a macroemulsion templating sol-gel process. To suppress the droplet coalescence of the macroemulsion during gelation, they increased the viscosity of the emulsions by varying different reaction parameters, such as educt concentrations or pH value.

2.7 References

1. Von der Leyen U (2021) Speech by President von der Leyen at the Opening of the High-Level Conference 'Investing in climate action: The Make-or-Break Decade', in cooperation with the EIB European Commission.
https://ec.europa.eu/commission/presscorner/detail/en/SPEECH_21_1361. Accessed 15 Aug 2021
2. Gates B (2016) It is surprisingly hard to store energy.
<https://www.gatesnotes.com/energy/it-is-surprisingly-hard-to-store-energy>. Accessed 20 Aug 2021
3. Colthorpe A (2017) Immense value' of thermal energy storage 'not yet recognised by Europe's policymakers. <https://www.energy-storage.news/news/immense-value-of-thermal-energy-storage-not-yet-recognised-by-europes-polic>. Accessed 18 Aug 2021
4. Laughlin R (2018), German Aerospace Center. Future heat storage technology: Interview with Nobel laureate R. Laughlin.
https://www.dlr.de/content/en/articles/news/2018/4/20181008_future-heat-storage-technology-laughlin.html. Accessed 16 Aug 2021
5. World Economic Forum (2021) The Global Risks Report 2021. Global Risks Report:1–97.
<https://www.weforum.org/reports/the-global-risks-report-2021>. Accessed 8 August 2021
6. IEA (2021) IEA Global Energy Review 2021 IEA, Paris.
<https://www.iea.org/reports/global-energy-review-2021>. Accessed 6 August 2021
7. PBL Netherlands Environmental Assessment Agency Trends in global CO₂ and total greenhouse gas emissions: 2020 Report. <https://www.pbl.nl/en/publications/trends-in-global-co2-and-total-greenhouse-gas-emissions-2020-report>. Accessed 8 August 2021
8. Global Greenhouse Gas Emissions: EDGAR v.5.0 (2020) European Commission.
https://edgar.jrc.ec.europa.eu/index.php/dataset_ghg50. Accessed 10 Aug 2021
9. Crippa M, Oreggioni G, Guizzardi D, Muntean M, Schaaf E, Lo Vullo E, Solazzo E, Monforti-Ferrario F, Olivier J, Vignati E (2019) Fossil CO₂ and GHG emissions of all world countries: 2019 report. EUR 29849. Publications Office of the European Union, Luxembourg
10. Morice CP, Kennedy JJ, Rayner NA, Jones PD (2012) Quantifying uncertainties in global and regional temperature change using an ensemble of observational estimates: The HadCRUT4 data set. *Journal of Geophysical Research*. Doi:10.1029/2011JD017187

11. HadCRUT4 Dataset (2021) Met Office Hadley Centre, England.
<https://www.metoffice.gov.uk/hadobs/hadcrut4/index.html>. Accessed 20 Aug 2021
12. Vadim A. Karatayev, Vítor V. Vasconcelos, Anne-Sophie Lafuite, Simon A. Levin, Chris T. Bauch, Madhur Anand A well-timed shift from local to global agreements accelerates climate change mitigation, *Nature Communications*. <https://doi.org/10.1038/s41467-021-23056-5>
13. Kiehl JT, Trenberth KE (1997) Earth's Annual Global Mean Energy Budget. *Bulletin of the American Meteorological Society*. Doi:10.1175/1520-0477(1997)078<0197:EAGMEB>2.0.CO;2
14. Logan CA, Dunne JP, Ryan JS, Baskett ML, Donner SD (2021) Quantifying global potential for coral evolutionary response to climate change. *Nature Climate Change*. Doi:10.1038/s41558-021-01037-2
15. Connor Nolan, Jonathan T. Overpeck, Judy R. M. Allen, Patricia M. Anderson, Julio L. Betancourt, Heather A. Binney, Simon Brewer, Mark B. Bush, Brian M. Chase, Rachid Cheddadi, Morteza Djamali, John Dodson, Mary E. Edwards, William D. Gosling, Simon Haberle, Sara C. Hotchkiss, Brian Huntley, Sarah J. Ivory, A. Peter Kershaw, Soo-Hyun Kim, Claudio Latorre, Michelle Leydet, Anne-Marie Lézine, Kam-Biu Liu, Yao Liu, A. V. Lozhkin, Matt S. McGlone, Robert A. Marchant, Arata Momohara, Patricio I. Moreno, Stefanie Müller, Bette L. Otto-Bliesner, Caiming Shen, Janelle Stevenson, Hikaru Takahara, Pavel E. Tarasov, John Tipton, Annie Vincens, Chengyu Weng, Qinghai Xu, Zhuo Zheng, Stephen T. Jackson (2018) Past and future global transformation of terrestrial ecosystems under climate change. *Science*. Doi:10.1126/science.aan5360
16. United Nations Framework Convention on Climate Change (2015) Adoption of the Paris Agreement, 21st Conference of the Parties, Paris, T.I.A.S. No. 16-1104
17. Federal Ministry for Environment, Nature Conservation and Nuclear Safety (BMU) (2019) Federal Climate Change Act (Bundes-Klimaschutzgesetz)
18. Bundesministerium für Wirtschaft und Energie (2019) Energiedaten: Gesamtausgabe. <https://www.bmwi.de/Redaktion/DE/Artikel/Energie/energiedaten-gesamtausgabe.html>. Accessed 2 August 2021
19. Agentur für Erneuerbare Energien (2019) Grafik-Dossier: Endenergieverbrauch nach Strom, Wärme und Verkehr. <https://www.unendlich-viel-energie.de/mediathek/grafiken/endenergieverbrauch-strom-waerme-verkehr>. Accessed 14 Jul 2021
20. Stadtwerke Halle (2021) Energie- und Zukunftsspeicher auf den Weg gebracht. <https://evh.de/zukunftsspeicher>. Accessed 24 Jul 2021

21. Dorothee dos Santos E (2018) Energie-Initiative nimmt in Halle Wärmespeicher in Betrieb. <https://www.euwid-energie.de/tochtergesellschaft-der-stadtwerke-halle-nimmt-waermespeicher-in-betrieb/>. Accessed 20 Jul 2021
22. a) Stadwerke Halle (2018) (Jahres- und Perspektivbericht der Stadtwerke Halle) Das Geschäftsjahr 2018 und ein Ausblick in die Zukunft. Jahres- und Perspektivbericht der Stadtwerke Halle:1–24; b) Stadtwerke Halle (EVH GmbH) (2019) Stadtwerke Halle arbeiten an der Stadt von morgen: klimafreundlich, sicher, innovativ. <https://evh.de/grosskunden/unternehmen/evh-gmbh/pressemitteilungen?id=41839>. Accessed 10 March 2021.
23. Aurecon (2019) Hornsdale Power Reserve Year 2 Technical and Market Impact Case Study. Aurecon Report:1–16. <https://www.aurecongroup.com/markets/energy/hornsdale-power-reserve-impact-study>. Accessed 20 May 2021.
24. Sharma A, Tyagi VV, Chen CR, Buddhi D (2009) Review on thermal energy storage with phase change materials and applications. *Renewable and Sustainable Energy Reviews*. Doi:10.1016/j.rser.2007.10.005
25. Rathore PKS, Shukla SK (2019) Potential of macroencapsulated PCM for thermal energy storage in buildings: A comprehensive review. *Construction and Building Materials*. Doi:10.1016/j.conbuildmat.2019.07.221
26. Wang H, Lu W, Wu Z, Zhang G (2020) Parametric analysis of applying PCM wallboards for energy saving in high-rise lightweight buildings in Shanghai. *Renewable Energy*. Doi:10.1016/j.renene.2019.05.124
27. Saffari M, Gracia A de, Fernández C, Cabeza LF (2017) Simulation-based optimization of PCM melting temperature to improve the energy performance in buildings. *Applied Energy*. Doi:10.1016/j.apenergy.2017.05.107
28. Preet S, Bhushan B, Mahajan T (2017) Experimental investigation of water based photovoltaic/thermal (PV/T) system with and without phase change material (PCM). *Solar Energy*. Doi:10.1016/j.solener.2017.07.040
29. Maatallah T, Zachariah R, Al-Amri FG (2019) Exergo-economic analysis of a serpentine flow type water based photovoltaic thermal system with phase change material (PVT-PCM/water). *Solar Energy*. Doi:10.1016/j.solener.2019.09.063
30. Akshayveer, Kumar A, Singh AP, Singh OP (2020) Effect of novel PCM encapsulation designs on electrical and thermal performance of a hybrid photovoltaic solar panel. *Solar Energy*. Doi:10.1016/j.solener.2020.05.062
31. Tariq SL, Ali HM, Akram MA, Janjua MM, Ahmadlouydarab M (2020) Nanoparticles enhanced phase change materials (NePCMs)-A recent review. *Applied Thermal Engineering*. Doi:10.1016/j.applthermaleng.2020.115305

-
32. Hu L, Li X, Ding L, Chen L, Zhu X, Mao Z, Feng X, Sui X, Wang B (2021) Flexible textiles with polypyrrole deposited phase change microcapsules for efficient photothermal energy conversion and storage. *Solar Energy Materials and Solar Cells*.
Doi:10.1016/j.solmat.2021.110985
 33. Lu Y, Xiao X, Fu J, Huan C, Qi S, Zhan Y, Zhu Y, Xu G (2019) Novel smart textile with phase change materials encapsulated core-sheath structure fabricated by coaxial electrospinning. *Chemical Engineering Journal*. Doi:10.1016/j.cej.2018.08.189
 34. Hany Abokersh M, Osman M, El-Baz O, El-Morsi M, Sharaf O (2018) Review of the phase change material (PCM) usage for solar domestic water heating systems (SDWHS). *International Journal of Energy Research*. Doi:10.1002/er.3765
 35. Wu W, Dai S, Liu Z, Dou Y, Hua J, Li M, Wang X, Wang X (2018) Experimental study on the performance of a novel solar water heating system with and without PCM. *Solar Energy*. Doi:10.1016/j.solener.2018.07.005
 36. Lu S, Zhao Y, Fang K, Li Y, Sun P (2017) Establishment and experimental verification of TRNSYS model for PCM floor coupled with solar water heating system. *Energy and Buildings*. Doi:10.1016/j.enbuild.2017.02.018
 37. Rathore PKS, Shukla SK (2020) An experimental evaluation of thermal behavior of the building envelope using macroencapsulated PCM for energy savings. *Renewable Energy*. Doi:10.1016/j.renene.2019.10.130
 38. Al-Yasiri Q, Szabó M (2021) Influential aspects on melting and solidification of PCM energy storage containers in building envelope applications. *International Journal of Green Energy*. Doi:10.1080/15435075.2021.1890082
 39. Cárdenas-Ramírez C, Jaramillo F, Gómez M (2020) Systematic review of encapsulation and shape-stabilization of phase change materials. *Journal of Energy Storage*. Doi:10.1016/j.est.2020.101495
 40. Rathore PKS, Shukla SK (2021) Enhanced thermophysical properties of organic PCM through shape stabilization for thermal energy storage in buildings: A state of the art review. *Energy and Buildings*. Doi:10.1016/j.enbuild.2021.110799
 41. Abdeali G, Bahramian AR, Abdollahi M (2020) Review on Nanostructure Supporting Material Strategies in Shape-stabilized Phase Change Materials. *Journal of Energy Storage*. Doi:10.1016/j.est.2020.101299
 42. Qu Y, Wang S, Tian Y, Zhou D (2019) Comprehensive evaluation of Paraffin-HDPE shape stabilized PCM with hybrid carbon nano-additives. *Applied Thermal Engineering*. Doi:10.1016/j.applthermaleng.2019.114404
 43. Marani A, Nehdi ML (2019) Integrating phase change materials in construction materials: Critical review. *Construction and Building Materials*.
Doi:10.1016/j.conbuildmat.2019.05.064

44. Zhou D, Zhao CY, Tian Y (2012) Review on thermal energy storage with phase change materials (PCMs) in building applications. *Applied Energy*.
Doi:10.1016/j.apenergy.2011.08.025
45. Guo R, Pan Y, Cai L, Hino S (2018) Bonding behavior of CFRP grid-concrete with PCM shotcrete. *Engineering Structures*. Doi:10.1016/j.engstruct.2018.04.059
46. Sharifi NP, Mahboub KC (2018) Application of a PCM-rich concrete overlay to control thermal induced curling stresses in concrete pavements. *Construction and Building Materials*. Doi:10.1016/j.conbuildmat.2018.06.179
47. Hawes DW, Feldman D (1992) Absorption of phase change materials in concrete. *Solar Energy Materials and Solar Cells*. Doi:10.1016/0927-0248(92)90112-3
48. Zhou G, Zhang Y, Wang X, Lin K, Xiao W (2007) An assessment of mixed type PCM-gypsum and shape-stabilized PCM plates in a building for passive solar heating. *Solar Energy*. Doi:10.1016/j.solener.2007.01.014
49. Pomianowski M, Heiselberg P, Jensen RL, Cheng R, Zhang Y (2014) A new experimental method to determine specific heat capacity of inhomogeneous concrete material with incorporated microencapsulated-PCM. *Cement and Concrete Research*.
Doi:10.1016/j.cemconres.2013.09.012
50. Singh Rathore PK, Shukla SK, Gupta NK (2020) Potential of microencapsulated PCM for energy savings in buildings: A critical review. *Sustainable Cities and Society*.
Doi:10.1016/j.scs.2019.101884
51. Errebai FB, Chikh S, Derradji L, Amara M, Younsi Z (2021) Optimum mass percentage of microencapsulated PCM mixed with gypsum for improved latent heat storage. *Journal of Energy Storage*. Doi:10.1016/j.est.2020.101910
52. Hekimoğlu G, Nas M, Ouikhalfan M, Sari A, Tyagi VV, Sharma RK, Kurbetci Ş, Saleh TA (2021) Silica fume/capric acid-stearic acid PCM included-cementitious composite for thermal controlling of buildings: Thermal energy storage and mechanical properties. *Energy*. Doi:10.1016/j.energy.2020.119588
53. Lecompte T, Le Bideau P, Glouannec P, Nortershauser D, Le Masson S (2015) Mechanical and thermo-physical behaviour of concretes and mortars containing phase change material. *Energy and Buildings*. Doi:10.1016/j.enbuild.2015.02.044
54. Li J, He L, Liu T, Cao X, Zhu H (2013) Preparation and characterization of PEG/SiO₂ composites as shape-stabilized phase change materials for thermal energy storage. *Solar Energy Materials and Solar Cells*. Doi:10.1016/j.solmat.2013.07.017
55. McLaughlin JK, Chow WH, Levy LS (1997) Amorphous silica: A review of health effects from inhalation exposure with particular reference to cancer. *Journal of toxicology and environmental health*. Doi:10.1080/15287399709532054

-
56. Rasmussen K (2013) Synthetic amorphous silicon dioxide (NM-200, NM-201, NM-202, NM-203, NM-204): Characterisation and physico-chemical properties. JRC scientific and policy reports 26046. Publications Office of the European Union, Luxembourg
 57. Ted Pella (2021) Safety Data Sheet of Colloidal Silica Suspension, 0.06 m. https://www.tedpella.com/SDS_html/815-110_sds.pdf. Accessed 10 Jul 2021
 58. Merck (2020) Sicherheitsdatenblatt von LUDOX[®] HS-40 kolloidales Silica. <https://www.sigmaaldrich.com/MSDS/MSDS/DisplayMSDSPage.do?country=DE&language=de&productNumber=420816&brand=ALDRICH&PageToGoToURL=https%3A%2F%2Fwww.sigmaaldrich.com%2Fcatalog%2Fproduct%2Faldrich%2F420816%3Flang%3Dde>. Accessed 10 Jul 2021
 59. Merck (2021) Safety Data Sheet for Tetraethylorthosilicat. https://www.merckmillipore.com/DE/de/product/msds/MDA_CHEM-800658?Origin=PDP. Accessed 20 Jul 2021
 60. Linhares T, Pessoa de Amorim MT, Durães L (2019) Silica aerogel composites with embedded fibres: a review on their preparation, properties and applications. *Journal of Materials Chemistry A*. Doi:10.1039/C9TA04811A
 61. Sarbu I, Sebarchievici C (2018) A Comprehensive Review of Thermal Energy Storage. *Sustainability*. Doi:10.3390/su10010191
 62. Lane GA (2018) Solar heat storage, latent heat materials. CRC Revivals. CRC Press, Boca Baton, Florida.
 63. Pardo P, Deydier A, Anxionnaz-Minvielle Z, Rougé S, Cabassud M, Cognet P (2014) A review on high temperature thermochemical heat energy storage. *Renewable and Sustainable Energy Reviews*. Doi:10.1016/j.rser.2013.12.014
 64. Carrillo AJ, González-Aguilar J, Romero M, Coronado JM (2019) Solar Energy on Demand: A Review on High Temperature Thermochemical Heat Storage Systems and Materials. *Chemical reviews*. Doi:10.1021/acs.chemrev.8b00315
 65. Aydin D, Casey SP, Riffat S (2015) The latest advancements on thermochemical heat storage systems. *Renewable and Sustainable Energy Reviews*. Doi:10.1016/j.rser.2014.08.054
 66. Alva G, Lin Y, Fang G (2018) An overview of thermal energy storage systems. *Energy*. Doi:10.1016/j.energy.2017.12.037
 67. Pomianowski M, Heiselberg P, Zhang Y (2013) Review of thermal energy storage technologies based on PCM application in buildings. *Energy and Buildings*. Doi:10.1016/j.enbuild.2013.08.006
 68. Jaguemont J, Omar N, van den Bossche P, Mierlo J (2018) Phase-change materials (PCM) for automotive applications: A review. *Applied Thermal Engineering*. Doi:10.1016/j.applthermaleng.2017.12.097

-
69. Zhao B, Cheng M, Liu C, Dai Z (2016) Thermal performance and cost analysis of a multi-layered solid-PCM thermocline thermal energy storage for CSP tower plants. *Applied Energy*. Doi:10.1016/j.apenergy.2016.06.034
 70. Wang Z, Qiu F, Yang W, Zhao X (2015) Applications of solar water heating system with phase change material. *Renewable and Sustainable Energy Reviews*. Doi:10.1016/j.rser.2015.07.184
 71. Pichandi R, Murugavel Kulandaivelu K, Alagar K, Dhevaguru HK, Ganesamoorthy S (2020) Performance enhancement of photovoltaic module by integrating eutectic inorganic phase change material. *Energy Sources, Part A: Recovery, Utilization, and Environmental Effects*. Doi:10.1080/15567036.2020.1817185
 72. Prajapati DG, Kandasubramanian B (2020) A Review on Polymeric-Based Phase Change Material for Thermo-Regulating Fabric Application. *Polymer Reviews*. Doi:10.1080/15583724.2019.1677709
 73. Senthil R (2021) Enhancement of productivity of parabolic dish solar cooker using integrated phase change material. *Materials Today: Proceedings*. Doi:10.1016/j.matpr.2020.02.197
 74. Abhat A (1983) Low temperature latent heat thermal energy storage: Heat storage materials. *Solar Energy*. Doi:10.1016/0038-092X(83)90186-X
 75. Magendran SS, Khan FSA, Mubarak NM, Vaka M, Walvekar R, Khalid M, Abdullah EC, Nizamuddin S, Karri RR (2019) Synthesis of organic phase change materials (PCM) for energy storage applications: A review. *Nano-Structures & Nano-Objects*. Doi:10.1016/j.nanoso.2019.100399
 76. Shchukina EM, Graham M, Zheng Z, Shchukin DG (2018) Nanoencapsulation of phase change materials for advanced thermal energy storage systems. *Chemical Society Reviews*. Doi:10.1039/c8cs00099a
 77. del Barrio EP, Godin A, Duquesne M, Daranlot J, Jolly J, Alshaer W, Kouadio T, Sommer A (2017) Characterization of different sugar alcohols as phase change materials for thermal energy storage applications. *Solar Energy Materials and Solar Cells*. Doi:10.1016/j.solmat.2016.10.009
 78. Neumann H, Burger D, Taftanazi Y, Alferez Luna MP, Hausmann T, Hagelstein G, Gschwander S (2019) Thermal stability enhancement of d-mannitol for latent heat storage applications. *Solar Energy Materials and Solar Cells*. Doi:10.1016/j.solmat.2019.109913
 79. Paul A, Shi L, Bielawski CW (2015) A eutectic mixture of galactitol and mannitol as a phase change material for latent heat storage. *Energy Conversion and Management*. Doi:10.1016/j.enconman.2015.06.013
 80. Raoux S, Wuttig M (2011) *Phase change materials: Science and applications*. Springer, New York, London

81. Rostami S, Afrand M, Shahsavari A, Sheikholeslami M, Kalbasi R, Aghakhani S, Shadloo MS, Oztop HF (2020) A review of melting and freezing processes of PCM/nano-PCM and their application in energy storage. *Energy*. Doi:10.1016/j.energy.2020.118698
82. Höhle S, König-Haagen A, Brüggemann D (2017) Thermophysical Characterization of $\text{MgCl}_2 \cdot 6\text{H}_2\text{O}$, Xylitol and Erythritol as Phase Change Materials (PCM) for Latent Heat Thermal Energy Storage (LHTES). *Materials*. Doi:10.3390/ma10040444
83. Bland A, Khzouz M, Statheros T, Gkanas E (2017) PCMs for Residential Building Applications: A Short Review Focused on Disadvantages and Proposals for Future Development. *Buildings*. Doi:10.3390/buildings7030078
84. Hassan A, Shakeel Laghari M, Rashid Y (2016) Micro-Encapsulated Phase Change Materials: A Review of Encapsulation, Safety and Thermal Characteristics. *Sustainability*. Doi:10.3390/su8101046
85. Chandel SS, Agarwal T (2017) Review of current state of research on energy storage, toxicity, health hazards and commercialization of phase changing materials. *Renewable and Sustainable Energy Reviews*. Doi:10.1016/j.rser.2016.09.070
86. Karaman S, Karaipekli A, Sarı A, Biçer A (2011) Polyethylene glycol (PEG)/diatomite composite as a novel form-stable phase change material for thermal energy storage. *Solar Energy Materials and Solar Cells*. Doi:10.1016/j.solmat.2011.01.022
87. Qian T, Zhu S, Wang H, Fan B (2019) Comparative Study of Carbon Nanoparticles and Single-Walled Carbon Nanotube for Light-Heat Conversion and Thermal Conductivity Enhancement of the Multifunctional PEG/Diatomite Composite Phase Change Material. *ACS Applied Materials & Interfaces*. Doi:10.1021/acsami.9b04349
88. Nagar S, Sharma K (2021) Modern solar systems driven by nanoparticles-based fatty acids and paraffin wax phase change materials. *Journal of Materials Science*. Doi:10.1007/s10853-020-05575-6
89. Li Q, Qiao G, Mura E, Li C, Fischer L, Ding Y (2020) Experimental and numerical studies of a fatty acid based phase change dispersion for enhancing cooling of high voltage electrical devices. *Energy*. Doi:10.1016/j.energy.2020.117280
90. Serrano S, Barreneche C, Inés Fernández A, Farid MM, Cabeza LF (2015) Composite gypsum containing fatty-ester PCM to be used as constructive system: Thermophysical characterization of two shape-stabilized formulations. *Energy and Buildings*. Doi:10.1016/j.enbuild.2014.10.015
91. Aydın AA (2013) *In situ* preparation and characterization of encapsulated high-chain fatty acid ester-based phase change material (PCM) in poly(urethane-urea) by using amino alcohol. *Chemical Engineering Journal*. Doi:10.1016/j.cej.2013.07.026

-
92. Xia L, Zhang P (2011) Thermal property measurement and heat transfer analysis of acetamide and acetamide/expanded graphite composite phase change material for solar heat storage. *Solar Energy Materials and Solar Cells*. Doi:10.1016/j.solmat.2011.03.031
 93. Sharma A, Sharma S, Buddhi D (2002) Accelerated thermal cycle test of acetamide, stearic acid and paraffin wax for solar thermal latent heat storage applications. *Energy Conversion and Management*. Doi:10.1016/S0196-8904(01)00131-5
 94. Philip N, Raam Dheep G, Sreekumar A (2020) Cold thermal energy storage with lauryl alcohol and cetyl alcohol eutectic mixture: Thermophysical studies and experimental investigation. *Journal of Energy Storage*. Doi:10.1016/j.est.2019.101060
 95. Huang X, Lin Y, Alva G, Fang G (2017) Thermal properties and thermal conductivity enhancement of composite phase change materials using myristyl alcohol/metal foam for solar thermal storage. *Solar Energy Materials and Solar Cells*. Doi:10.1016/j.solmat.2017.05.059
 96. Rozanna D, Chuah TG, Salmiah A, Choong TSY, Sa'ari M (2005) Fatty Acids as Phase Change Materials (PCMs) for Thermal Energy Storage: A Review. *International Journal of Green Energy*. Doi:10.1081/GE-200038722
 97. Sharma RK, Ganesan P, Tyagi VV, Mahlia T (2016) Accelerated thermal cycle and chemical stability testing of polyethylene glycol (PEG) 6000 for solar thermal energy storage. *Solar Energy Materials and Solar Cells*. Doi:10.1016/j.solmat.2015.12.023
 98. Omara AAM, Abuelnuor AAA, Mohammed AOA, Sirelkhatim OMA, Suleman AAM (2018) In: Yousif AF, Ahmed SYM, Elhag NAA, International Conference on Computer CEaEE (eds) 2018 International Conference on Computer, Control, Electrical, and Electronics Engineering (ICCCEEE): 12th-14th August- 2018, Corinthia Hotel, Khartoum, Sudan. IEEE, [Piscataway, NJ]
 99. Abbasi Hattan H, Madhkan M, Marani A (2021) Thermal and mechanical properties of building external walls plastered with cement mortar incorporating shape-stabilized phase change materials (SSPCMs). *Construction and Building Materials*. Doi:10.1016/j.conbuildmat.2020.121385
 100. Mondal S (2008) Phase change materials for smart textiles – An overview. *Applied Thermal Engineering*. Doi:10.1016/j.applthermaleng.2007.08.009
 101. Sari A, Alkan C, Karaipekli A, Uzun O (2009) Poly(ethylene glycol)/poly(methyl methacrylate) blends as novel form-stable phase-change materials for thermal energy storage. *Journal of Applied Polymer Science*. Doi:10.1002/app.31623
 102. Abo-Shosha MH, Nassar FA, Haggag KM, El-Sayed Z, Hassabo AG (2009) Improvement on Hydrophobicity of Synthetic Textiles by Plasma Treatment – A Review. *Textile and Apparel*. Doi:10.1108/RJTA-13-01-2009-B007

103. Yuan Y, Zhang N, Tao W, Cao X, He Y (2014) Fatty acids as phase change materials: A review. *Renewable and Sustainable Energy Reviews*.
Doi:10.1016/j.rser.2013.08.107
104. Kosny J, Shukla N, Fallahi A (2013) Cost Analysis of Simple Phase Change Material-Enhanced Building Envelopes in Southern U.S. Climates.
<https://www.osti.gov/biblio/1219890>. Accessed 15 February 2021.
105. Sarı A, Biçer A, Karaipekli A (2009) Synthesis, characterization, thermal properties of a series of stearic acid esters as novel solid–liquid phase change materials. *Materials Letters*. Doi:10.1016/j.matlet.2009.02.045
106. Feldman D, Banu D, Hawes D (1995) Low chain esters of stearic acid as phase change materials for thermal energy storage in buildings. *Solar Energy Materials and Solar Cells*. Doi:10.1016/0927-0248(94)00186-3
107. Cabeza LF, Castell A, Barreneche C, Gracia A de, Fernández AI (2011) Materials used as PCM in thermal energy storage in buildings: A review. *Renewable and Sustainable Energy Reviews*. Doi:10.1016/j.rser.2010.11.018
108. Wang G, Xu C, Wei G, Du X (2019) Numerical study of a novel dual-PCM thermal energy storage structure filled with inorganic salts and metal alloy as the PCMs. *Energy Procedia*. Doi:10.1016/j.egypro.2019.01.774
109. Milián YE, Gutiérrez A, Grágeda M, Ushak S (2017) A review on encapsulation techniques for inorganic phase change materials and the influence on their thermophysical properties. *Renewable and Sustainable Energy Reviews*.
Doi:10.1016/j.rser.2017.01.159
110. Ge H, Li H, Mei S, Liu J (2013) Low melting point liquid metal as a new class of phase change material: An emerging frontier in energy area. *Renewable and Sustainable Energy Reviews*. Doi:10.1016/j.rser.2013.01.008
111. Zhou D, Eames P (2016) Thermal characterisation of binary sodium/lithium nitrate salts for latent heat storage at medium temperatures. *Solar Energy Materials and Solar Cells*. Doi:10.1016/j.solmat.2016.08.017
112. Villada C, Jaramillo F, Castaño JG, Echeverría F, Bolívar F (2019) Design and development of nitrate-nitrite based molten salts for concentrating solar power applications. *Solar Energy*. Doi:10.1016/j.solener.2019.06.010
113. Zhao Q-G, Hu C-X, Liu S-J, Guo H, Wu Y-T (2017) The thermal conductivity of molten NaNO₃, KNO₃, and their mixtures. *Energy Procedia*. Doi:10.1016/j.egypro.2017.12.761
114. Tian H, Du L, Wei X, Deng S, Wang W, Ding J (2017) Enhanced thermal conductivity of ternary carbonate salt phase change material with Mg particles for solar thermal energy storage. *Applied Energy*. Doi:10.1016/j.apenergy.2017.07.027

115. Cabeza LF, Castell A, Barreneche C, Gracia A de, Fernández AI (2011) Materials used as PCM in thermal energy storage in buildings: A review. *Renewable and Sustainable Energy Reviews*. Doi:10.1016/j.rser.2010.11.018
116. Purohit BK, Sistla VS (2021) Inorganic salt hydrate for thermal energy storage application: A review. *Energy Storage*. Doi:10.1002/est2.212
117. Schmit H, Rathgeber C, Hooch P, Hiebler S (2020) Critical review on measured phase transition enthalpies of salt hydrates in the context of solid-liquid phase change materials. *Thermochimica Acta*. Doi:10.1016/j.tca.2019.178477
118. Zhang C, Zhang Z, Ye R, Gao X, Ling Z (2018) Characterization of $\text{MgCl}_2 \cdot 6\text{H}_2\text{O}$ -Based Eutectic/Expanded Perlite Composite Phase Change Material with Low Thermal Conductivity. *Materials*. Doi:10.3390/ma11122369
119. Zhao T, Zheng M, Munis A, Hu J, Teng H, Wei L (2019) Corrosion behaviours of typical metals in molten hydrate salt of $\text{Na}_2\text{HPO}_4 \cdot 12\text{H}_2\text{O} - \text{Na}_2\text{SO}_4 \cdot 10\text{H}_2\text{O}$ for thermal energy storage. *Corrosion Engineering, Science and Technology*. Doi:10.1080/1478422X.2019.1595296
120. Li C, Zhang B, Xie B, Zhao X, Chen J (2020) Tailored phase change behavior of $\text{Na}_2\text{SO}_4 \cdot 10\text{H}_2\text{O}$ /expanded graphite composite for thermal energy storage. *Energy Conversion and Management*. Doi:10.1016/j.enconman.2020.112586
121. Zhao BC, Li TX, He F, Gao JC, Wang RZ (2020) Demonstration of $\text{Mg}(\text{NO}_3)_2 \cdot 6\text{H}_2\text{O}$ -based composite phase change material for practical-scale medium-low temperature thermal energy storage. *Energy*. Doi:10.1016/j.energy.2020.117711
122. Ye R, Zhang C, Sun W, Fang X, Zhang Z (2018) Novel wall panels containing $\text{CaCl}_2 \cdot 6\text{H}_2\text{O}$ - $\text{Mg}(\text{NO}_3)_2 \cdot 6\text{H}_2\text{O}$ /expanded graphite composites with different phase change temperatures for building energy savings. *Energy and Buildings*. Doi:10.1016/j.enbuild.2018.07.045
123. Zou T, Liang X, Wang S, Gao X, Zhang Z, Fang Y (2020) Effect of expanded graphite size on performances of modified $\text{CaCl}_2 \cdot 6\text{H}_2\text{O}$ phase change material for cold energy storage. *Microporous and Mesoporous Materials*. Doi:10.1016/j.micromeso.2020.110403
124. Ye R, Lin W, Yuan K, Fang X, Zhang Z (2017) Experimental and numerical investigations on the thermal performance of building plane containing $\text{CaCl}_2 \cdot 6\text{H}_2\text{O}$ /expanded graphite composite phase change material. *Applied Energy*. Doi:10.1016/j.apenergy.2017.02.049
125. Trausel F, Jong A-J de, Cuypers R (2014) A Review on the Properties of Salt Hydrates for Thermochemical Storage. *Energy Procedia*. Doi:10.1016/j.egypro.2014.02.053
126. Tan P, Lindberg P, Eichler K, Löveryd P, Johansson P, Kalagasidis AS (2020) Effect of phase separation and supercooling on the storage capacity in a commercial latent heat

- thermal energy storage: Experimental cycling of a salt hydrate PCM. *Journal of Energy Storage*. Doi:10.1016/j.est.2020.101266
127. Kumar N, Hirsche J, LaClair TJ, Gluesenkamp KR, Graham S (2019) Review of stability and thermal conductivity enhancements for salt hydrates. *Journal of Energy Storage*. Doi:10.1016/j.est.2019.100794
128. Liu Z, Chen Z, Yu F (2019) Preparation and characterization of microencapsulated phase change materials containing inorganic hydrated salt with silica shell for thermal energy storage. *Solar Energy Materials and Solar Cells*. Doi:10.1016/j.solmat.2019.110004
129. Yang JM, Kim JS (2018) The microencapsulation of calcium chloride hexahydrate as a phase-change material by using the hybrid coupler of organoalkoxysilanes. *Journal of Applied Polymer Science*. Doi:10.1002/app.45821
130. Kazemi A, Naseri I, Nasiri M, Bahramian AR (2017) Effect of $MgCl_2 \cdot 6H_2O$ Phase Change Material on Thermal Insulation Performance of Carbon Aerogels. *Journal of Energy Storage*. Doi:10.1016/j.est.2016.12.002
131. Ling Z, Liu J, Wang Q, Lin W, Fang X, Zhang Z (2017) $MgCl_2 \cdot 6H_2O$ - $Mg(NO_3)_2 \cdot 6H_2O$ eutectic/ SiO_2 composite phase change material with improved thermal reliability and enhanced thermal conductivity. *Solar Energy Materials and Solar Cells*. Doi:10.1016/j.solmat.2017.07.019
132. Prieto C, Cabeza LF (2019) Thermal energy storage (TES) with phase change materials (PCM) in solar power plants (CSP). Concept and plant performance. *Applied Energy*. Doi:10.1016/j.apenergy.2019.113646
133. Wu Y, Li J, Wang M, Wang H, Zhong Y, Zhao Y, Wei M, Li Y (2018) Solar salt doped by MWCNTs as a promising high thermal conductivity material for CSP. *RSC Advances*. Doi:10.1039/C8RA03019G
134. Zhang Q, Zheng Y, Liu J (2012) Direct writing of electronics based on alloy and metal (DREAM) ink: A newly emerging area and its impact on energy, environment and health sciences. *Frontiers in Energy*. Doi:10.1007/s11708-012-0214-x
135. Oró E, Gracia A de, Castell A, Farid MM, Cabeza LF (2012) Review on phase change materials (PCMs) for cold thermal energy storage applications. *Applied Energy*. Doi:10.1016/j.apenergy.2012.03.058
136. Al Omari S-A, Ghazal AM, Elnajjar E (2018) A novel concept to enhance the applicability of solid gallium as phase change material for heat sinks by integrating within it discretely distributed chunks of un-encapsulated PCM. *International Communications in Heat and Mass Transfer*. Doi:10.1016/j.icheatmasstransfer.2017.12.014

-
137. Liu M, Sun Y, Bruno F (2020) A review of numerical modelling of high-temperature phase change material composites for solar thermal energy storage. *Journal of Energy Storage*. Doi:10.1016/j.est.2020.101378
138. Du L, Ding J, Tian H, Wang W, Wei X, Song M (2017) Thermal properties and thermal stability of the ternary eutectic salt NaCl-CaCl₂-MgCl₂ used in high-temperature thermal energy storage process. *Applied Energy*. Doi:10.1016/j.apenergy.2017.03.096
139. Fernández AI, Barreneche C, Belusko M, Segarra M, Bruno F, Cabeza LF (2017) Considerations for the use of metal alloys as phase change materials for high temperature applications. *Solar Energy Materials and Solar Cells*. Doi:10.1016/j.solmat.2017.06.054
140. 2017 Minerals Yearbook (2017) United States Geological Survey (USGS). <https://www.usgs.gov/centers/nmic/gallium-statistics-and-information>. Accessed 10 February 2021.
141. Li X, Fu Z, Qiao Y, Zhang Z, Zhou Y, Hai C, Shen Y, Sun Y, Zeng J, Ren X (2020) Preparation, Characterization, and Modification of Sodium Acetate Trihydrate-Urea Binary Eutectic Mixtures As Phase Change Material. *Energy Fuels*. Doi:10.1021/acs.energyfuels.0c00382
142. Li S, Lin S, Ling Z, Fang X, Zhang Z (2020) Growth of the Phase Change Enthalpy Induced by the Crystal Transformation of an Inorganic–Organic Eutectic Mixture of Magnesium Nitrate Hexahydrate–Glutaric Acid. *Industrial and Engineering Chemistry Research*. Doi:10.1021/acs.iecr.0c01029
143. Atinafu DG, Dong W, Huang X, Gao H, Wang G (2018) Introduction of organic-organic eutectic PCM in mesoporous N-doped carbons for enhanced thermal conductivity and energy storage capacity. *Applied Energy*. Doi:10.1016/j.apenergy.2017.12.025
144. Xie S, Sun J, Wang Z, Liu S, Han L, Ma G, Jing Y, Jia Y (2017) A thermally stable phase change material with high latent heat based on an oxalic acid dihydrate/boric acid binary eutectic system. *Solar Energy Materials and Solar Cells*. Doi:10.1016/j.solmat.2017.04.008
145. Xie N, Li Z, Gao X, Fang Y, Zhang Z (2020) Preparation and performance of modified expanded graphite/eutectic salt composite phase change cold storage material. *International Journal of Refrigeration*. Doi:10.1016/j.ijrefrig.2019.10.008
146. Rathod MK, Banerjee J (2013) Thermal stability of phase change materials used in latent heat energy storage systems: A review. *Renewable and Sustainable Energy Reviews*. Doi:10.1016/j.rser.2012.10.022
147. Aftab W, Huang X, Wu W, Liang Z, Mahmood A, Zou R (2018) Nanoconfined phase change materials for thermal energy applications. *Energy and Environmental Science*. Doi:10.1039/C7EE03587J

-
148. Yang J, Tang L-S, Bao R-Y, Bai L, Liu Z-Y, Xie B-H, Yang M-B, Yang W (2018) Hybrid network structure of boron nitride and graphene oxide in shape-stabilized composite phase change materials with enhanced thermal conductivity and light-to-electric energy conversion capability. *Solar Energy Materials and Solar Cells*. Doi:10.1016/j.solmat.2017.08.025
149. Zou D, Liu X, He R, Huang L (2019) High thermal response rate and super low supercooling degree microencapsulated phase change materials (MEPCM) developed by optimizing shell with various nanoparticles. *International Journal of Heat and Mass Transfer*. Doi:10.1016/j.ijheatmasstransfer.2019.06.057
150. Zhao P-P, Deng C, Zhao Z-Y, Huang S-C, Lu P, Wang Y-Z (2020) Nanoflake-Constructed Supramolecular Hierarchical Porous Microspheres for Fire-Safety and Highly Efficient Thermal Energy Storage. *ACS Applied Materials & Interfaces*. Doi:10.1021/acscami.0c07405
151. Zhai M, Zhang S, Sui J, Tian F, Lan XZ (2017) Solid–solid phase transition of tris(hydroxymethyl)aminomethane in nanopores of silica gel and porous glass for thermal energy storage. *Journal of Thermal Analysis and Calorimetry*. Doi:10.1007/s10973-017-6223-6
152. Giro-Paloma J, Martínez M, Cabeza LF, Fernández AI (2016) Types, methods, techniques, and applications for microencapsulated phase change materials (MPCM): A review. *Renewable and Sustainable Energy Reviews*. Doi:10.1016/j.rser.2015.09.040
153. Kosny J (2015) PCM-Enhanced Building Components: An Application of Phase Change Materials in Building Envelopes and Internal Structures. *Engineering materials and processes*. Springer International Publishing; Imprint; Springer, Cham
154. Kumar GN, Al-Aifan B, Parameshwaran R, Ram VV (2021) Facile synthesis of microencapsulated 1-dodecanol/melamine-formaldehyde phase change material using in-situ polymerization for thermal energy storage. *Colloids and Surfaces A: Physicochemical and Engineering Aspects*. Doi:10.1016/j.colsurfa.2020.125698
155. Fang G, Li H, Yang F, Liu X, Wu S (2009) Preparation and characterization of nano-encapsulated n-tetradecane as phase change material for thermal energy storage. *Chemical Engineering Journal*. Doi:10.1016/j.cej.2009.06.019
156. Cai C, Ouyang X, Zhou L, Liu G, Wang Y, Zhu G, Yao J, Militky J, Venkataraman M, Zhang G (2020) Co-solvent free interfacial polycondensation and properties of polyurea PCM microcapsules with dodecanol dodecanoate as core material. *Solar Energy*. Doi:10.1016/j.solener.2020.02.071
157. Yang X, Liu Y, Lv Z, Hua Q, Liu L, Wang B, Tang J (2021) Synthesis of high latent heat lauric acid/silica microcapsules by interfacial polymerization method for thermal energy storage. *Journal of Energy Storage*. Doi:10.1016/j.est.2020.102059

-
158. Hawlader M, Uddin MS, Khin MM (2003) Microencapsulated PCM thermal-energy storage system. *Applied Energy*. Doi:10.1016/S0306-2619(02)00146-0
 159. Methaapanon R, Kornbongkotmas S, Ataboonwongse C, Soottitantawat A (2020) Microencapsulation of n-octadecane and methyl palmitate phase change materials in silica by spray drying process. *Powder Technology*. Doi:10.1016/j.powtec.2019.10.114
 160. Seitz S, Ajiro H (2019) Self-assembling weak polyelectrolytes for the layer-by-layer encapsulation of paraffin-type phase change material icosane. *Solar Energy Materials and Solar Cells*. Doi:10.1016/j.solmat.2018.10.012
 161. Yi Q, Sukhorokov GB, Ma J, Yang X, Gu Z (2015) Encapsulation of Phase Change Materials Using Layer-by-Layer Assembled Polyelectrolytes. *International Journal of Polymer Science*. Doi:10.1155/2015/756237
 162. Chen Z-H, Yu F, Zeng X-R, Zhang Z-G (2012) Preparation, characterization and thermal properties of nanocapsules containing phase change material n-dodecanol by miniemulsion polymerization with polymerizable emulsifier. *Applied Energy*. Doi:10.1016/j.apenergy.2011.08.041
 163. Hoseini Z, Nikje MMA (2021) The Preparation of Novel Microcapsules Based on Palmitic Acid Core and Waterborne Polyurethane/Silane Shell as Phase Change Materials for Thermal Energy Storage. *Journal of Polymers and the Environment*. Doi:10.1007/s10924-020-01916-3
 164. Kazanci B, Cellat K, Paksoy H (2020) Preparation, characterization, and thermal properties of novel fire-resistant microencapsulated phase change materials based on paraffin and a polystyrene shell. *RSC Advances*. Doi:10.1039/D0RA04093B
 165. Paksoy H, Kardas G, Konuklu Y, Cellat K, Tezcan F (2017) Characterization of Concrete Mixes Containing Phase Change Materials. *IOP Conference Series: Materials Science and Engineering*. Doi:10.1088/1757-899X/251/1/012118
 166. Ruckenstein E (1996) Microemulsions, Macroemulsions, and the Bancroft Rule. *Langmuir*. Doi:10.1021/la960849m
 167. Sineva AV, Ermolat'ev DS, Pertsov AV (2007) Structural transformations in a water-n-octane + chloroform-sodium dodecyl sulfate-n-pentanol microemulsion. *Colloid Journal*. Doi:10.1134/S1061933X07010127
 168. Wan X, Chen C, Zhang H, Guo B, Zhan X (2021) Thermal enthalpy regulation of methyl hexadecanoate/silica microcapsules with CTAB as emulsifier maintaining fixed core/shell ratio. *Journal of Thermal Analysis and Calorimetry*. Doi:10.1007/s10973-021-10665-x
 169. Zhang H, Sun S, Wang X, Wu D (2011) Fabrication of microencapsulated phase change materials based on n-octadecane core and silica shell through interfacial

- polycondensation. *Colloids and Surfaces A: Physicochemical and Engineering Aspects*. Doi:10.1016/j.colsurfa.2011.08.043
170. Fang Y, Wei H, Liang X, Wang S, Liu X, Gao X, Zhang Z (2016) Preparation and Thermal Performance of Silica/ n -Tetradecane Microencapsulated Phase Change Material for Cold Energy Storage. *Energy Fuels*. Doi:10.1021/acs.energyfuels.6b01799
171. Shi J, Wu X, Sun R, Ban B, Li J, Chen J (2019) Synthesis and performance evaluation of paraffin microcapsules with calcium carbonate shell modulated by different anionic surfactants for thermal energy storage. *Colloids and Surfaces A: Physicochemical and Engineering Aspects*. Doi:10.1016/j.colsurfa.2019.03.029
172. Tahan Latibari S, Mehrali M, Mehrali M, Afifi ABM, Mahlia TMI, Akhiani AR, Metselaar HSC (2015) Facile synthesis and thermal performances of stearic acid/titania core/shell nanocapsules by sol–gel method. *Energy*. Doi:10.1016/j.energy.2015.04.008
173. Valizadeh S, Ehsani M, Torabí Angaji M (2020) Preparation, characterization and thermal properties of PCM nanocapsules with polystyrene/nano garaphen oxide shell for energy storage. *Heat Mass Transfer*. Doi:10.1007/s00231-019-02723-w
174. Zou D, Ma X, Liu X, Zheng P, Hu Y (2018) Thermal performance enhancement of composite phase change materials (PCM) using graphene and carbon nanotubes as additives for the potential application in lithium-ion power battery. *International Journal of Heat and Mass Transfer*. Doi:10.1016/j.ijheatmasstransfer.2017.12.024
175. Du X, Xu J, Deng S, Du Z, Cheng X, Wang H (2019) Amino-Functionalized Single-Walled Carbon Nanotubes-Integrated Polyurethane Phase Change Composites with Superior Photothermal Conversion Efficiency and Thermal Conductivity. *ACS Sustainable Chem. Eng.* Doi:10.1021/acssuschemeng.9b03853
176. Thayer AM (2007) Carbon nanotubes by the metric tone. *Chemical and Engineering News*. Doi:10.1021/cen-v085n046.p029
177. Kibria MA, Anisur MR, Mahfuz MH, Saidur R, Metselaar I (2015) A review on thermophysical properties of nanoparticle dispersed phase change materials. *Energy Conversion and Management*. Doi:10.1016/j.enconman.2015.02.028
178. McCann JT, Marquez M, Xia Y (2006) Melt coaxial electrospinning: a versatile method for the encapsulation of solid materials and fabrication of phase change nanofibers. *Nano Letters*. Doi:10.1021/nl0620839
179. Lu Y, Xiao X, Zhan Y, Huan C, Qi S, Cheng H, Xu G (2018) Core-Sheath Paraffin-Wax-Loaded Nanofibers by Electrospinning for Heat Storage. *ACS Applied Materials & Interfaces*. Doi:10.1021/acsami.8b02057
180. Akhiani AR, Mehrali M, Tahan Latibari S, Mehrali M, Mahlia TMI, Sadeghinezhad E, Metselaar HSC (2015) One-Step Preparation of Form-Stable Phase Change Material

- through Self-Assembly of Fatty Acid and Graphene. *The Journal of Physical Chemistry C*.
Doi:10.1021/acs.jpcc.5b06089
181. Umair MM, Zhang Y, Iqbal K, Zhang S, Tang B (2019) Novel strategies and supporting materials applied to shape-stabilize organic phase change materials for thermal energy storage—A review. *Applied Energy*. Doi:10.1016/j.apenergy.2018.11.017
182. Zhang Z, Shi G, Wang S, Fang X, Liu X (2013) Thermal energy storage cement mortar containing n-octadecane/expanded graphite composite phase change material. *Renewable Energy*. Doi:10.1016/j.renene.2012.08.024
183. Hunger M, Entrop AG, Mandilaras I, Brouwers H, Founti M (2009) The behavior of self-compacting concrete containing micro-encapsulated Phase Change Materials. *Cement and Concrete Composites*. Doi:10.1016/j.cemconcomp.2009.08.002
184. Matei C, Buhălțeanu L, Berger D, Mitran R-A (2019) Functionalized mesoporous silica as matrix for shape-stabilized phase change materials. *International Journal of Heat and Mass Transfer*. Doi:10.1016/j.ijheatmasstransfer.2019.118699
185. Li Y, Dong M, Song W, Liang X, Chen Y, Liu Y (2021) Preparation and Characterization of Paraffin/Mesoporous Silica Shape-Stabilized Phase Change Materials for Building Thermal Insulation. *Materials*. Doi:10.3390/ma14071775
186. Weng J, Ouyang D, Yang X, Chen M, Zhang G, Wang J (2019) Alleviation of thermal runaway propagation in thermal management modules using aerogel felt coupled with flame-retarded phase change material. *Energy Conversion and Management*.
Doi:10.1016/j.enconman.2019.112071
187. Mu B, Li M (2018) Fabrication and thermal properties of tetradecanol/graphene aerogel form-stable composite phase change materials. *Science Reports*.
Doi:10.1038/s41598-018-27038-4
188. Memon SA (2014) Phase change materials integrated in building walls: A state of the art review. *Renewable and Sustainable Energy Reviews*. Doi:10.1016/j.rser.2013.12.042
189. Mohseni E, Tang W, Wang S (2019) Development of thermal energy storage lightweight structural cementitious composites by means of macro-encapsulated PCM. *Construction and Building Materials*. Doi:10.1016/j.conbuildmat.2019.07.136
190. Wi S, Yang S, Park JH, Chang SJ, Kim S (2020) Climatic cycling assessment of red clay/perlite and vermiculite composite PCM for improving thermal inertia in buildings. *Building and Environment*. Doi:10.1016/j.buildenv.2019.106464
191. Nomura T, Okinaka N, Akiyama T (2009) Impregnation of porous material with phase change material for thermal energy storage. *Materials Chemistry and Physics*.
Doi:10.1016/j.matchemphys.2009.02.045
192. Costa JAC, Martinelli AE, do Nascimento RM, Mendes AM (2020) Microstructural design and thermal characterization of composite diatomite-vermiculite paraffin-based

- form-stable PCM for cementitious mortars. *Construction and Building Materials*.
Doi:10.1016/j.conbuildmat.2019.117167
193. Wei H, Xie X, Li X, Lin X (2016) Preparation and characterization of capric-myristic-stearic acid eutectic mixture/modified expanded vermiculite composite as a form-stable phase change material. *Applied Energy*. Doi:10.1016/j.apenergy.2016.06.109
194. Lee KO, Medina MA, Sun X, Jin X (2018) Thermal performance of phase change materials (PCM)-enhanced cellulose insulation in passive solar residential building walls. *Solar Energy*. Doi:10.1016/j.solener.2018.01.086
195. Boussaba L, Foufa A, Makhoul S, Lefebvre G, Royon L (2018) Elaboration and properties of a composite bio-based PCM for an application in building envelopes. *Construction and Building Materials*. Doi:10.1016/j.conbuildmat.2018.07.098
196. Horpan M, Şahan N, Paksoy H, Sivrikaya O, Günes M (2019) Direct impregnation and characterization of Colemanite/Ulexite-Mg(OH)₂ paraffin based form-stable phase change composites. *Solar Energy Materials and Solar Cells*.
Doi:10.1016/j.solmat.2019.03.018
197. Xie M, Huang J, Ling Z, Fang X, Zhang Z (2019) Improving the heat storage/release rate and photo-thermal conversion performance of an organic PCM/expanded graphite composite block. *Solar Energy Materials and Solar Cells*.
Doi:10.1016/j.solmat.2019.110081
198. Yang Y, Pang Y, Liu Y, Guo H (2018) Preparation and thermal properties of polyethylene glycol/expanded graphite as novel form-stable phase change material for indoor energy saving. *Materials Letters*. Doi:10.1016/j.matlet.2018.01.025
199. Atinafu DG, Yun BY, Wi S, Kang Y, Kim S (2021) A comparative analysis of biochar, activated carbon, expanded graphite, and multi-walled carbon nanotubes with respect to PCM loading and energy-storage capacities. *Environmental Research*.
Doi:10.1016/j.envres.2021.110853
200. Qian T, Li J, Feng W, Nian H (2017) Enhanced thermal conductivity of form-stable phase change composite with single-walled carbon nanotubes for thermal energy storage. *Science Reports*. Doi:10.1038/srep44710
201. Ramakrishnan S, Wang X, Sanjayan J (2019) Effects of various carbon additives on the thermal storage performance of form-stable PCM integrated cementitious composites. *Applied Thermal Engineering*. Doi:10.1016/j.applthermaleng.2018.11.025
202. Dong K, Sheng N, Zou D, Wang C, Shimono K, Akiyama T, Nomura T (2020) A high-thermal-conductivity, high-durability phase-change composite using a carbon fibre sheet as a supporting matrix. *Applied Energy*. Doi:10.1016/j.apenergy.2020.114685

-
203. Xie N, Niu J, Gao X, Fang Y, Zhang Z (2020) Fabrication and characterization of electrospun fatty acid form-stable phase change materials in the presence of copper nanoparticles. *International Journal of Energy Research*. Doi:10.1002/er.5543
204. Li Z, Wu Y, Zhuang B, Zhao X, Tang Y, Ding X, Chen K (2017) Preparation of novel copper-powder-sintered frame/paraffin form-stable phase change materials with extremely high thermal conductivity. *Applied Energy*. Doi:10.1016/j.apenergy.2017.10.046
205. Noël JA, White MA (2021) Freeze-cast form-stable phase change materials for thermal energy storage. *Solar Energy Materials and Solar Cells*. Doi:10.1016/j.solmat.2020.110956
206. Hu J, Huang Y, Yao Y, Pan G, Sun J, Zeng X, Sun R, Xu J-B, Song B, Wong C-P (2017) Polymer Composite with Improved Thermal Conductivity by Constructing a Hierarchically Ordered Three-Dimensional Interconnected Network of BN. *ACS Applied Materials & Interfaces*. Doi:10.1021/acsami.7b02410
207. Xue F, Jin X-Z, Wang W-Y, Qi X-D, Yang J-H, Wang Y (2020) Melamine foam and cellulose nanofiber co-mediated assembly of graphene nanoplatelets to construct three-dimensional networks towards advanced phase change materials. *Nanoscale*. Doi:10.1039/c9nr10696k
208. Yang J, Yu P, Tang L-S, Bao R-Y, Liu Z-Y, Yang M-B, Yang W (2017) Hierarchically interconnected porous scaffolds for phase change materials with improved thermal conductivity and efficient solar-to-electric energy conversion. *Nanoscale*. Doi:10.1039/c7nr05449a
209. Castellón C, Martorell I, Cabeza LF, Fernández AI, Manich AM (2011) Compatibility of plastic with phase change materials (PCM). *International Journal of Energy Research*. Doi:10.1002/er.1723
210. Sarı A (2004) Form-stable paraffin/high density polyethylene composites as solid-liquid phase change material for thermal energy storage: Preparation and thermal properties. *Energy Conversion and Management*. Doi:10.1016/j.enconman.2003.10.022
211. Yu J, Leng K, Ye H, Xu X, Luo Y, Wang J, Yang X, Yang Q, Gang W (2020) Study on thermal insulation characteristics and optimized design of pipe-embedded ventilation roof with outer-layer shape-stabilized PCM in different climate zones. *Renewable Energy*. Doi:10.1016/j.renene.2019.09.115
212. Xiao M, Feng B, Gong K (2002) Preparation and performance of shape stabilized phase change thermal storage materials with high thermal conductivity. *Energy Conversion and Management*. Doi:10.1016/S0196-8904(01)00010-3
213. Chriaa I, Trigui A, Karkri M, Jedidi I, Abdelmouleh M, Boudaya C (2020) Thermal properties of shape-stabilized phase change materials based on Low Density

- Polyethylene, Hexadecane and SEBS for thermal energy storage. Applied Thermal Engineering. Doi:10.1016/j.applthermaleng.2020.115072
214. Juárez D, Ferrand S, Fenollar O, Fombuena V, Balart R (2011) Improvement of thermal inertia of styrene–ethylene/butylene–styrene (SEBS) polymers by addition of microencapsulated phase change materials (PCMs). European Polymer Journal. Doi:10.1016/j.eurpolymj.2010.11.004
215. Fang G, Tang F, Cao L (2014) Preparation, thermal properties and applications of shape-stabilized thermal energy storage materials. Renewable and Sustainable Energy Reviews. Doi:10.1016/j.rser.2014.07.179
216. Li M, Wu Z, Tan J (2012) Properties of form-stable paraffin/silicon dioxide/expanded graphite phase change composites prepared by sol–gel method. Applied Energy. Doi:10.1016/j.apenergy.2011.11.018
217. He L, Li J, Zhou C, Zhu H, Cao X, Tang B (2014) Phase change characteristics of shape-stabilized PEG/SiO₂ composites using calcium chloride-assisted and temperature-assisted sol gel methods. Solar Energy. Doi:10.1016/j.solener.2014.02.042
218. Ye S, Zhang Q, Hu D, Feng J (2015) Core–shell-like structured graphene aerogel encapsulating paraffin: shape-stable phase change material for thermal energy storage. Journal of Materials Chemistry A. Doi:10.1039/C4TA05448B
219. Li G, Zhang X, Wang J, Fang J (2016) From anisotropic graphene aerogels to electron- and photo-driven phase change composites. Journal of Materials Chemistry A. Doi:10.1039/C6TA07587H
220. Alkan C, Sari A (2008) Fatty acid/poly(methyl methacrylate) (PMMA) blends as form-stable phase change materials for latent heat thermal energy storage. Solar Energy. Doi:10.1016/j.solener.2007.07.001
221. Zhang L, Zhu J, Zhou W, Wang J, Wang Y (2011) Characterization of polymethyl methacrylate/polyethylene glycol/aluminum nitride composite as form-stable phase change material prepared by *in situ* polymerization method. Thermochimica Acta. Doi:10.1016/j.tca.2011.07.003
222. Yang C, Fischer L, Maranda S, Worlitschek J (2015) Rigid polyurethane foams incorporated with phase change materials: A state-of-the-art review and future research pathways. Energy and Buildings. Doi:10.1016/j.enbuild.2014.10.075
223. Zeng J-L, Zhu F-R, Yu S-B, Xiao Z-L, Yan W-P, Zheng S-H, Zhang L, Sun L-X, Cao Z (2013) Myristic acid/polyaniline composites as form stable phase change materials for thermal energy storage. Solar Energy Materials and Solar Cells. Doi:10.1016/j.solmat.2013.03.006

-
224. Aydın AA (2013) *In situ* preparation and characterization of encapsulated high-chain fatty acid ester-based phase change material (PCM) in poly(urethane-urea) by using amino alcohol. *Chemical Engineering Journal*. Doi:10.1016/j.cej.2013.07.026
225. Cao R, Li X, Chen S, Yuan H, Zhang X (2017) Fabrication and characterization of novel shape-stabilized synergistic phase change materials based on PHDA/GO composites. *Energy*. Doi:10.1016/j.energy.2017.07.049
226. Tang B, Cui J, Wang Y, Jia C, Zhang S (2013) Facile synthesis and performances of PEG/SiO₂ composite form-stable phase change materials. *Solar Energy*. Doi:10.1016/j.solener.2013.08.021
227. Schubert U, Hüsing N, Laine RM (2008) *Materials syntheses: A practical guide*, 2008th edn. Springer, New York
228. Levy D, Zayat M (2015) *The sol-gel handbook: [synthesis, characterization and applications]*. Wiley-VCH Verlag & Co. KGaA, Weinheim
229. Matter F, Luna AL, Niederberger M (2020) From colloidal dispersions to aerogels: How to master nanoparticle gelation. *Nano Today*. Doi:10.1016/j.nantod.2019.100827
230. Lei Q, Guo J, Noureddine A, Wang A, Wuttke S, Brinker CJ, Zhu W (2020) Sol–Gel-Based Advanced Porous Silica Materials for Biomedical Applications. *Advanced Functional Materials*. Doi:10.1002/adfm.201909539
231. Lu X, Hasegawa G, Kanamori K, Nakanishi K (2020) Hierarchically porous monoliths prepared via sol–gel process accompanied by spinodal decomposition. *Journal of Sol-Gel Science and Technology*. Doi:10.1007/s10971-020-05370-4
232. Hench LL, West JK (1990) The sol-gel process. *Chemical Reviews*. Doi:10.1021/cr00099a003
233. Gurav JL, Jung I-K, Park H-H, Kang ES, Nadargi DY (2010) Silica Aerogel: Synthesis and Applications. *Journal of Nanomaterials*. Doi:10.1155/2010/409310
234. Lim HM, Lee J, Jeong J-H, Oh S-G, Lee S-H (2010) Comparative Study of Various Preparation Methods of Colloidal Silica. *Engineering*. Doi:10.4236/eng.2010.212126
235. Hyde EDER, Seyfaee A, Neville F, Moreno-Atanasio R (2016) Colloidal Silica Particle Synthesis and Future Industrial Manufacturing Pathways: A Review. *Industrial & Engineering Chemistry Research*. Doi:10.1021/acs.iecr.6b01839
236. Tikhonov AM (2007) Compact Layer of Alkali Ions at the Surface of Colloidal Silica. *Journal of Physical Chemistry C*. Doi:10.1021/jp065538r
237. Sögaard C, Funehag J, Abbas Z (2018) Silica sol as grouting material: a physio-chemical analysis. *Nano Convergence*. Doi:10.1186/s40580-018-0138-1
238. Shackelford JF, Doremus RH (2008) *Ceramic and glass materials: Structure, properties and processing*, 1st edn. Springer, New York

-
239. Chemiewerk Bad Köstritz (2021) Kieselisol. <https://www.cwk-bk.de/de/produkte/kieselsaeuren/kieselisol/>. Accessed 6 Jul 2021
240. Grace (2021) LUDOX Colloidal Silica. <https://grace.com/products/ludox/>. Accessed 6 Jul 2021
241. George Cernigliaro, Egon Matijevic, Yie-Shein Her, Daniel Y. Pai, Todd A. Richardson (1999) Dyed Silica Pigments and Products Made from Same, US Patent, US5885343A
242. Chemiewerk Bad Köstritz (2021) Köstrosol 0730. [https://www.cwk-bk.de/de/produkte/kieselsaeuren/kieselisol/details/?tx_datasheets_datasheetsview\[dataSheet\]=66&tx_datasheets_datasheetsview\[action\]=show&tx_datasheets_datasheetsview\[controller\]=DataSheet&cHash=0821f889e748c349fc598bd8dafcda45](https://www.cwk-bk.de/de/produkte/kieselsaeuren/kieselisol/details/?tx_datasheets_datasheetsview[dataSheet]=66&tx_datasheets_datasheetsview[action]=show&tx_datasheets_datasheetsview[controller]=DataSheet&cHash=0821f889e748c349fc598bd8dafcda45). Accessed 9 Jul 2021
243. Matos JR, Mercuri LP, Kruk M, Jaroniec M (2002) Synthesis of Large-Pore Silica with Cage-Like Structure Using Sodium Silicate and Triblock Copolymer Template. *Langmuir*. Doi:10.1021/la0155294
244. Hallak B (2016) Grundlagenuntersuchungen zur Herstellung von Silika-Xerogelen aus stabilisiertem Sol. Master Thesis, Leipzig, Germany
245. Marske F (2017) Synthese von Silika-Xerogelen als Wärmedämm- und speichermaterialien. Master Thesis, Leipzig, Germany
246. Kumar A, Yadav N, Bhatt M, Mishra NK, Singh R (2015) Sol-Gel Derived Nanomaterials and It's Applications: A Review. *Research Journal of Chemical Sciences*. https://www.researchgate.net/publication/288630167_Sol-Gel_Derived_Nanomaterials_and_It%27s_Applications_A_Review. Accessed 10 February 2021.
247. Kohns R, Haas CP, Hölzel A, Splith A, Enke D, Tallarek U (2018) Hierarchical silica monoliths with submicron macropores as continuous-flow microreactors for reaction kinetic and mechanistic studies in heterogeneous catalysis. *Reaction Chemistry & Engineering*. Doi:10.1039/C8RE00037A
248. Nakanishi K, Takahashi R, Nagakane T, Kitayama K, Koheiya N, Shikata H, Soga N (2000) Formation of Hierarchical Pore Structure in Silica Gel. *Journal of Sol-Gel Science and Technology*. Doi:10.1023/A:1008707804908
249. Sukarsono R, Rachmawati M, Susilowati SR, Husnurrofiq D, Nurwidyaningrum K, Dewi AK (2018) Effect of Sol Concentration, Aging and Drying Process on Cerium Stabilization Zirconium Gel Produced by External Gelation. *Journal of Physics: Conference Series*. Doi:10.1088/1742-6596/962/1/012056
250. Kaide A, Saeki T, Kikuchi S (2012) The Effect of Controlling the Aging Condition on the Gelling Property of Silica Sols. *Journal of the Society of Rheology, Japan*. Doi:10.1678/rheology.39.205

-
251. Matsui T, Nakanishi K, Kanamori K, Hanada T (2007) Phase Separation in Silica Sol-gel System Containing Anionic Surfactant. MRS Online Proceedings Library. Doi:10.1557/PROC-1056-HH11-60
252. Siouffi A-M (2003) Silica gel-based monoliths prepared by the sol-gel method: facts and figures. Journal of Chromatography A. Doi:10.1016/S0021-9673(03)00510-7
253. Gunji T, Ozawa M, Abe Y, West R (2001) Preparation of C 60 –Silica Hybrid Monolith by Sol-Gel Process. Journal of Sol-Gel Science and Technology. Doi:10.1023/A:1012243902181
254. Takahashi R, Sato S, Sodesawa T, Kojima Y, Mikami N (2007) Macropore Formation of Silica Gel in the Presence of Sodium Dodecyl Sulfate by Inducing Phase Separation in Alcohol-free Aqueous Solution. Journal of the Ceramic Society of Japan. Doi:10.2109/jcersj2.115.882
255. Nakanishi K, Takahashi R, Soga N (1992) Dual-porosity silica gels by polymer-incorporated sol-gel process. Journal of Non-Crystalline Solids. Doi:10.1016/S0022-3093(05)80632-5
256. Feinle A, Elsaesser MS, Hüsing N (2016) Sol-gel synthesis of monolithic materials with hierarchical porosity. Chemical Society Reviews. Doi:10.1039/c5cs00710k
257. Guo X, Zhang Q, Ding X, Shen Q, Wu C, Zhang L, Yang H (2016) Synthesis and application of several sol-gel-derived materials via sol-gel process combining with other technologies: a review. Journal of Sol-Gel Science and Technology. Doi:10.1007/s10971-015-3935-6
258. Du A, Zhou B, Zhang Z, Shen J (2013) A Special Material or a New State of Matter: A Review and Reconsideration of the Aerogel. Materials. Doi:10.3390/ma6030941
259. Pajonk GM, Repellin-Lacroix M, Abouarnadasse S, Chaouki J, Klavana D (1990) From sol-gel to aerogels and cryogels. Journal of Non-Crystalline Solids. Doi:10.1016/0022-3093(90)90106-V
260. Inayat A, Reinhardt B, Uhlig H, Einicke W-D, Enke D (2013) Silica monoliths with hierarchical porosity obtained from porous glasses. Chemical Society Reviews. Doi:10.1039/c2cs35304k
261. Enke D, Gläser R, Tallarek U (2016) Sol-Gel and Porous Glass-Based Silica Monoliths with Hierarchical Pore Structure for Solid-Liquid Catalysis. Chemie Ingenieur Technik. Doi:10.1002/cite.201600049
262. Inayat A, Reinhardt B, Herwig J, Küster C, Uhlig H, Krenkel S, Raedlein E, Enke D (2016) Recent advances in the synthesis of hierarchically porous silica materials on the basis of porous glasses. New Journal of Chemistry. Doi:10.1039/C5NJ03591K

-
263. Nakanishi K, Soga N (1991) Phase Separation in Gelling Silica-Organic Polymer Solution: Systems Containing Poly(sodium styrenesulfonate). *Journal of the American Ceramic Society*. Doi:10.1111/j.1151-2916.1991.tb06794.x
264. Nakanishi K, Komura H, Takahashi R, Soga N (1994) Phase Separation in Silica Sol-Gel System Containing Poly(ethylene oxide). I. Phase Relation and Gel Morphology. *Bulletin of the Chemical Society of Japan*. Doi:10.1246/bcsj.67.1327
265. Van Dijk MA, Wakker A (1997) Concepts of polymer thermodynamics. *Polymer thermodynamics library vol. 2*. Technomic Publ. Co, Lancaster, Pa.
266. Fleer GJ, Koopal LK, Lyklema J (1972) Polymer adsorption and its effect on the stability of hydrophobic colloids. *Kolloid-Zeitschrift und Zeitschrift für Polymere*. Doi:10.1007/BF01498559
267. Nakanishi K (1997) Pore Structure Control of Silica Gels Based on Phase Separation. *Journal of Porous Materials*. Doi:10.1023/A:1009627216939
268. Huck-Iriart C, Morales NJ, Herrera ML, Candal RJ (2021) Micro to mesoporous SiO₂xerogels: the effect of acid catalyst type in sol-gel process. *Journal of Sol-Gel Science and Technology*. DOI:10.1007/s10971-021-05601-2
269. Liu J, Huang W, Xing Y, Li R, Dai J (2011) Preparation of durable superhydrophobic surface by sol-gel method with water glass and citric acid. *Journal of Sol-Gel Science and Technology*. Doi:10.1007/s10971-010-2349-8
270. M. K. Naskar (2005) Effects of organic acids on sol-gel transition of silicic acid—Arheological study. *Journal of Materials Science*. DOI:10.1007/s10853-005-6959-4
271. Sarawade PB, Shao GN, Quang DV, Kim HT (2013) Effect of various structure directing agents on the physicochemical properties of the silica aerogels prepared at an ambient pressure. *Applied Surface Science*. Doi:10.1016/j.apsusc.2013.09.072
272. Vyshegorodtseva EV, Larichev Y, Mamontov GV (2019) The influence of CTAB/Si ratio on the textural properties of MCM-41 prepared from sodium silicate. *Journal of Sol-Gel Science and Technology*. Doi:10.1007/s10971-019-05034-y
273. Nan Z, Xue X, Hou W, Yan X, Han S (2007) Fabrication of MCM-41 mesoporous silica through the self-assembly supermolecule of β -CD and CTAB. *Journal of Solid State Chemistry*. Doi:10.1016/j.jssc.2006.11.011
274. Sunwoo Y, Karunakaran G, Cho E-B (2021) Hollow mesoporous silica nanospheres using pentablock copolymer micelle templates. *Ceramics International*. Doi:10.1016/j.ceramint.2021.01.192
275. Schneider JJ, Naumann M (2014) Template-directed synthesis and characterization of microstructured ceramic Ce/ZrO₂@SiO₂ composite tubes. *Beilstein Journal of Nanotechnology*. Doi:10.3762/bjnano.5.126

-
276. Nishihara H, Mukai SR, Yamashita D, Tamon H (2005) Ordered Macroporous Silica by Ice Templating. *Chemistry of Materials*. Doi:10.1021/cm048725f
277. Mukai SR, Onodera K, Yamada I (2011) Studies on the growth of ice crystal templates during the synthesis of a monolithic silica microhoneycomb using the ice templating method. *Adsorption*. Doi:10.1007/s10450-010-9286-2
278. Han YS, Tarutani Y, Fuji M, Takahashi M (2006) Synthesis of Hollow Silica Particle by Combination of Bubble Templating Method and Sol-Gel Transformation. *Advanced Materials Research*. Doi:10.4028/www.scientific.net/AMR.11-12.673
279. Tomita T, Kawasaki S, Okada K (2004) A Novel Preparation Method for Foamed Silica Ceramics by Sol-Gel Reaction and Mechanical Foaming. *Journal of Porous Materials*. Doi:10.1023/B:JOPO.0000027366.90408.1f
280. Song J-C, Xue F-F, Lu Z-Y, Sun Z-Y (2015) Controllable synthesis of hollow mesoporous silica particles by a facile one-pot sol-gel method. *Chemical Communications*. Doi:10.1039/C5CC03025K
281. Carn F, Colin A, Achard M-F, Deleuze H, Saadi Z, Backov R (2004) Rational Design of Macrocellular Silica Scaffolds Obtained by a Tunable Sol–Gel Foaming Process. *Advanced Materials*. Doi:10.1002/adma.200306067
282. Yu H, Wang Q, Zhao Y, Wang H (2020) A Convenient and Versatile Strategy for the Functionalization of Silica Foams Using High Internal Phase Emulsion Templates as Microreactors. *ACS Applied Materials & Interfaces*. Doi:10.1021/acsami.0c01273
283. Mahadik DB, Lee K-Y, Ghorpade RV, Park H-H (2018) Superhydrophobic and Compressible Silica-polyHIPE Covalently Bonded Porous Networks via Emulsion Templating for Oil Spill Cleanup and Recovery. *Scientific Reports*. Doi:10.1038/s41598-018-34997-1
284. Hessien M, Prouzet E (2021) Synthesis and characterization of low-cost hierarchical porous silica by nanoemulsion templating: influence of nanoemulsion volume and hydrodynamic diameter. *Journal of Sol-Gel Science and Technology*. Doi:10.1007/s10971-021-05543-9
285. Teng Z, Han Y, Li J, Yan F, Yang W (2010) Preparation of hollow mesoporous silica spheres by a sol–gel/emulsion approach. *Microporous and Mesoporous Materials*. Doi:10.1016/j.micromeso.2009.06.028
286. Imhof A, Pine DJ (1998) Uniform Macroporous Ceramics and Plastics by Emulsion Templating. *Advanced Materials*. Doi:10.1002/(SICI)1521-4095(199806)10:9<697:AID-ADMA697>3.0.CO;2-M
287. Imhof A, Pine DJ (1997) Ordered macroporous materials by emulsion templating. *Nature*. Doi:10.1038/40105

-
288. Adamson AW, Gast AP (1997) *Physical chemistry of surfaces*, 6th edn. A Wiley-Interscience publication. Wiley, New York
289. Leja J (ed) (1981) *Surface Chemistry of Froth Flotation*. Springer US, Boston, MA
290. Oh SG, Shah DO (1993) Effect of counterions on the interfacial tension and emulsion droplet size in the oil/water/dodecyl sulfate system. *The Journal of Physical Chemistry*. Doi:10.1021/j100104a003
291. Carn F, Colin A, Achard M-F, Deleuze H, Sellier E, Birot M, Backov R (2004) Inorganic monoliths hierarchically textured via concentrated direct emulsion and micellar templates Electronic supplementary information (ESI) available: XRD profiles, nitrogen physisorption data and pore size distribution calculated from density functional theory, for the xSi-HIPE0.035 series. *Journal of Materials Chemistry*. Doi:10.1039/b400984c
292. Saien J, Akbari S (2006) Interfacial Tension of Toluene + Water + Sodium Dodecyl Sulfate from (20 to 50) °C and pH between 4 and 9. *Journal of Chemical & Engineering Data*. Doi:10.1021/je060204g
293. Wright JD, Sommerdijk NA (2018) *Sol-Gel Materials*. CRC Press
294. Lins RF, Alves-Rosa MA, Pulcinelli SH, Santilli CV (2012) Formation of TiO₂ ceramic foams from the integration of the sol–gel method with surfactants assembly and emulsion. *Journal of Sol-Gel Science and Technology*. Doi:10.1007/s10971-012-2700-3
295. Pham Q-T, Yao Z-H, Wang Y-T, Wu Y-T, Chern C-S (2017) Preparation and characterization of monodisperse silica nanoparticles via miniemulsion sol–gel reaction of tetraethyl orthosilicate. *Journal of Materials Science*. Doi:10.1007/s10853-017-1402-1
296. Feng H, Verstappen NAL, Kuehne AJC, Sprakel J (2013) Well-defined temperature-sensitive surfactants for controlled emulsion coalescence. *Polymer Chemistry*. Doi:10.1039/c2py21007j
297. Floury J, Desrumaux A, Lardières J (2000) Effect of high-pressure homogenization on droplet size distributions and rheological properties of model oil-in-water emulsions. *Innovative Food Science & Emerging Technologies*. Doi:10.1016/S1466-8564(00)00012-6
298. Asua JM (2002) Miniemulsion polymerization. *Progress in Polymer Science*. Doi:10.1016/S0079-6700(02)00010-2
299. Anton N, Vandamme TF (2011) Nano-emulsions and micro-emulsions: clarifications of the critical differences. *Pharmaceutical Research*. Doi:10.1007/s11095-010-0309-1
300. Sen T, Tiddy G, Casci JL, Anderson MW (2005) Meso-cellular silica foams, macro-cellular silica foams and mesoporous solids: a study of emulsion-mediated synthesis. *Microporous and Mesoporous Materials*. Doi:10.1016/j.micromeso.2004.09.022

3 Publications

The cumulative dissertation covers five manuscripts, four of which have been published to date.

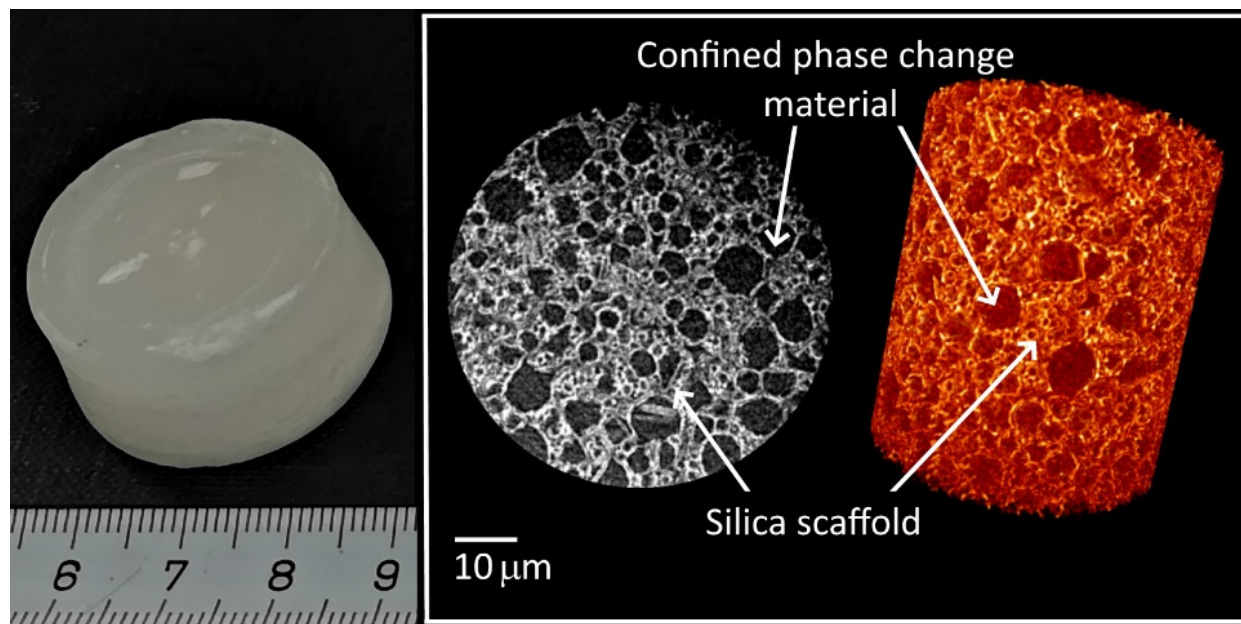
In section 3.1, the manuscript “Synthesis of monolithic shape-stabilized phase change materials with high mechanical stability via a porogen-assisted *in situ* sol-gel process” is presented. Here, a novel synthesis of monolithic shape-stabilized phase change materials (ss-PCMs) is developed by a sol-gel route starting from stabilized silica sol and butyl stearate, and the physicochemical properties of these ss-PCMs are analyzed and discussed.

In the manuscript “Influence of surfactants and organic polymers on monolithic shape-stabilized phase change materials synthesized via sol-gel route” (section 3.2), the formation process of ss-PCMs is further investigated and visualized by suitable *in situ* characterization methods (e.g. confocal microscopy) to gain mechanistical insights. Additionally, the influence of the porogens sodium dodecyl sulfate (SDS) and poly(vinyl alcohol) (PVA) is determined to tailor the dimension, shape and connectivity of the silica structure in the ss-PCMs and, thus, improve the thermal and mechanical properties of the ss-PCMs.

To increase the latent heat and the application range of the ss-PCMs, the different PCMs hexadecane, octadecane, polyethylene glycol 600 and acetamide with melting points between 20 °C and 73 °C are shape-stabilized by the sol-gel process and analyzed in detail in the manuscript “Shape stabilization of organic phase change materials as mechanical stable silica boards with high latent heats via sol-gel route” (section 3.3).

The last two manuscripts “Size and surface effects of hexagonal boron nitrides on the physicochemical properties of monolithic phase change materials synthesized via sol-gel route” (section 3.4) and “Experimental data showing the influence of different boron nitride particles on the silica network, the butyl stearate and the porogens in shape-stabilized phase change materials” (section 3.5) address the problem of the low thermal conductivity of ss-PCMs, which must be overcome to make ss-PCMs available as cooling medium in battery or photovoltaic systems. To increase the thermal conductivity of ss-PCMs to the highest extent, hexagonal boron nitride platelets with different particle sizes and specific surface areas are investigated as additive in the sol-gel process.

3.1 Synthesis of monolithic shape-stabilized phase change materials with high mechanical stability via a porogen-assisted *in situ* sol-gel process



Authors

Felix Marske,^a Juliana Martins de Souza e Silva,^b Ralf B. Wehrspohn,^b Thomas Hahn^a,
Dirk Enke^c

^a Institute of Technical Chemistry, Martin Luther University of Halle-Wittenberg, 06108 Halle (Saale), Germany

^b Institute of Physics, Martin Luther University of Halle-Wittenberg, 06108 Halle (Saale), Germany

^c Institute of Chemical Technology, Leipzig University, 04109 Leipzig, Germany

State of Publication

Accepted 27th December 2019 in *RSC Advances*

DOI: 10.1039/c9ra10631f

3.1.1 Abstract

The confinement of phase change materials (PCMs) in construction materials has recently solved leakage, supercooling and low thermal conductivity problems in the industrial use of PCMs as monolithic thermal energy storage materials. To produce shape-stabilized PCMs (ss-PCMs) as crack-free monoliths, less than 15 - 30 % v/v pure or encapsulated PCMs can be used in construction materials. Therefore, the heat storage capacity of these monolithic ss-PCM boards is comparatively low. In this study, we synthesized a novel class of monolithic ss-PCM boards with high compressive strength of 0.7 MPa at 30 °C (1.2 MPa at 10 °C), high PCM loadings of 86 wt%, and latent heats in the range of 100 J g⁻¹ via a porogen-assisted *in situ* sol-gel process. We confined butyl stearate (BS) as PCM in a core-shell-like silica matrix via stabilized silica sol as silica source, sodium dodecyl sulfate as surfactant and poly(vinyl alcohol) as co-polymer. The ss-PCMs obtained are hydrophobic, thermally stable up to 320 °C and perform 6000 state transitions from solid to liquid and vice versa, without losing melting or freezing enthalpies. We analyzed the silica structure in the ss-PCMs to understand in detail the reasons for the high mechanical stability. The silica structure in ss-PCMs consists of spherical meso- and macropores up to 10 000 nm filled with PCM, formed mostly by BS droplets in water as templates during gelation. With an increasing BS amount in the synthesis of ss-PCMs, the total nanopore volume filled with PCM in ss-PCMs increases, resulting in higher compressive strengths up to 500 % and thermal conductivities up to 60 %.

3.1.2 Introduction

The worldwide primary energy demand is one of the greatest current problems of humanity. Since 1970, energy consumption and greenhouse emissions have increased by over 100 %.¹ Fossil fuels still produce nearly 85 % of the worldwide energy, even though they are finite and have tremendous environmental impact.² Therefore, the development of renewable energy sources and energy storage materials is imperative.³

Thermal energy storage (TES) is an example of a promising energy storage concept, because it can store large amounts of energy as heat. It is typically divided into three groups: sensible heat storage (SHS), thermochemical heat storage (TCS) and latent heat storage (LHS).⁴ Most materials can store thermal energy in the form of sensible heat and the amount of stored energy depends on the specific heat capacity, mass and temperature change of the material.⁵ Sensible heat storage materials (SHS) have as major problems low energy densities and the sudden loss of energy to the environment at a temperature change. Thermochemical heat storage (TCS) materials are relatively novel and solely tested on a laboratory scale. They can store and release energy by reversible chemical reactions and show the highest energy density of all types of thermal energy storage materials.⁶ However, they present major disadvantages, such as slow heat and mass transfer from and to the storage volume, high investment costs, and complex reactor design that limits their application. In contrast, latent heat storage materials (LHS), also called phase change materials (PCMs), can store 5 - 14 times more heat per unit volume than sensible heat storage materials through a phase change at a nearly constant temperature.⁷ Moreover, they can conserve energy over a certain temperature for a long period and are used for a broad range of applications like energy-saving buildings,⁸ photovoltaics,⁹ textiles,¹⁰ and even solar cookers.¹¹ Therefore, these materials fulfil the requirements for an adequate thermal energy storage material best.¹² Their application, however, is limited by some drawbacks that are only partially under control.¹³ On one hand, inorganic PCMs, such as salts and hydrated salts, have excellent values of heat per unit volume, a suitable temperature range for the most promising applications in energy-saving buildings¹⁴ and concentrated solar power systems,¹⁵ besides good thermal conductivities. On the other hand, they suffer from supercooling and phase segregation.¹⁶ It should be mentioned that the solid–liquid phase change of salt hydrates occurs through a dehydration/hydration process, which is thermodynamically similar to the change of the aggregate state from solid to liquid. If the corresponding dehydrated salt is not completely soluble in its water of hydration, phase segregation occurs through incongruent melting. This leads to a decreased latent heat or, in the worst case, to a total loss of latent heat of the PCM after a few hydration/dehydration cycles.¹⁷ Some attempts to control supercooling by the addition of suitable nucleating agents

are described in the literature,^{18,19} but the problem of phase segregation remains unsolved, and even various encapsulation techniques have not led to a solution.²⁰

In contrast, organic PCMs, like paraffins and non-paraffins (n-alkanes, fatty acids, alcohols, polyethylene glycols), do not suffer from phase segregation or high supercooling effects, but are moderately flammable and have low thermal conductivities. Several studies attempted to address these two drawbacks of organic PCMs²¹ by the addition of 5 - 10 wt% of expanded graphite to the PCM, which results in an enhancement of the thermal conductivity of about 50 - 300 %.^{8,22} The use of 2 wt% graphite in form of nanosheets can further increase the thermal conductivity of solid paraffins in a hybrid shell structure to $1 \text{ W m}^{-1} \text{ K}^{-1}$.²³ To reduce the flammability of PCMs, melamine,²⁴ tetrabromobisphenol-A²⁵ and diethyl ethylphosphonate²⁶ can be added. These components build a physical protective barrier around the PCM during combustion and limit the transfer of flammable molecules to the gas phase. Generally, the leakage of liquid PCMs from construction materials must be prevented through the incorporation of the PCM in a suitable container, which can be a porous matrix or a core-shell structure. In recent years, the research focus shifted to micro- and nanoencapsulation of PCMs to produce core-shell PCMs (cs-PCMs), in which the core is composed by the PCM that is covered by a shell of an inorganic or organic polymer, forming particles of diameter in the micro- or nanoscale.²⁷ The encapsulation method has several advantages, such as an increased heat transfer area, high encapsulation ratios of PCMs, less supercooling effects and a convenient handling for the later incorporation in construction materials like plaster, concrete or gypsum.²⁸ The most prominent example for cs-PCMs is Micronal PCM (Microtek Laboratories, formerly by BASF). This cs-PCM consists of a paraffin core that is surrounded by a polyacrylate shell and has latent heats in the range of 100 J g^{-1} . However, the application of cs-PCMs like Micronal DS 5040 X is limited by the amount that can be later incorporated into construction materials to form monolithic shape-stabilized PCMs (ss-PCMs), which is 15% v/v for cementitious systems and 30% v/v for plaster-based systems.²⁹ Moreover, the direct mixing of cs-PCMs or pure PCMs with construction materials, like concrete, leads to a drastic loss of the overall mechanical stability. As described by Hunger *et al.*,³⁰ the compressive strength of concrete decreased from 74 MPa to 21 MPa by the addition of 5 wt% Micronal DS 5008 X. Similar results were already reported in the literature.^{31,32}

Here, we report the synthesis of a novel class of monolithic shape-stabilized PCM boards that confined organic PCMs into nanopores, thus, allowing the addition of high mass fractions of PCMs by maintaining a high mechanical stability. To the best of our knowledge, studies to synthesize monolithic ss-PCMs in the literature failed mostly because of PCM leakage, loss of form-stability, or a low compressive strength.^{33,34} We have chosen butyl stearate (BS) as prototype for organic PCMs because of its superior properties, such as congruently melting

and freezing, good thermal and chemical stabilities and non-toxicity,³⁵ and immobilized it in a silica matrix via a novel *in situ* sol-gel process, which is assisted by a surfactant and an organic copolymer. Stabilized silica sol was used as inexpensive silica source, cheaper than typically used precursors, like tetraethyl ortho-silicate.³⁶ In contrast to methods like mini-emulsion polymerization, *in situ* sol-gel is an inexpensive one-pot synthesis and can be easily up scaled in a discontinuous batch reactor.^{37,38}

3.1.3 Experimental

3.1.3.1 Materials

Köstrosol 0730 was used as stabilized silica sol (30 wt% colloidal silica particles in water, 7 nm average particle diameter) and provided by Chemiewerk Bad Köstritz, Germany. Butyl stearate (technical grade product) was obtained by Alfa Aesar. Sodium dodecyl sulfate (SDS, ≥99.0% GC, dust-free pellets) and poly(vinyl alcohol) (PVA, 88% hydrolyzed, average MW 22 000) were purchased from Sigma-Aldrich and ACROS Organics, respectively. Deionized water was used for all experiments.

3.1.3.2 Preparation of monolithic ss-PCMs

The synthesis was carried out in polypropylene beakers. First, poly(vinyl alcohol) (PVA) was dissolved in water and heated to 60 °C for 3 h. Then, sodium dodecyl sulfate (SDS) and butyl stearate (BS) were added to the PVA solution, heated to 50 °C and left at this temperature for at least 6 h. The suspension was stirred with a magnetic stirrer for 15 min at 700 rpm and 25 °C. The stabilized silica sol was added dropwise to the suspension to start the sol-gel process and stirred for another 15 min at 700 rpm and 25 °C. Afterwards, the magnetic stirrer was removed, the beaker containing the reaction mixture was closed and heated to 40 °C for 2 - 3 days. The wet composite gel was dried at ambient pressure first at 40 °C for 4 days and then at 100 °C for 20 h. The synthetic route and synthesized ss-PCM monoliths are shown in Fig. 1.1 and Movies S1.1 and S1.2.

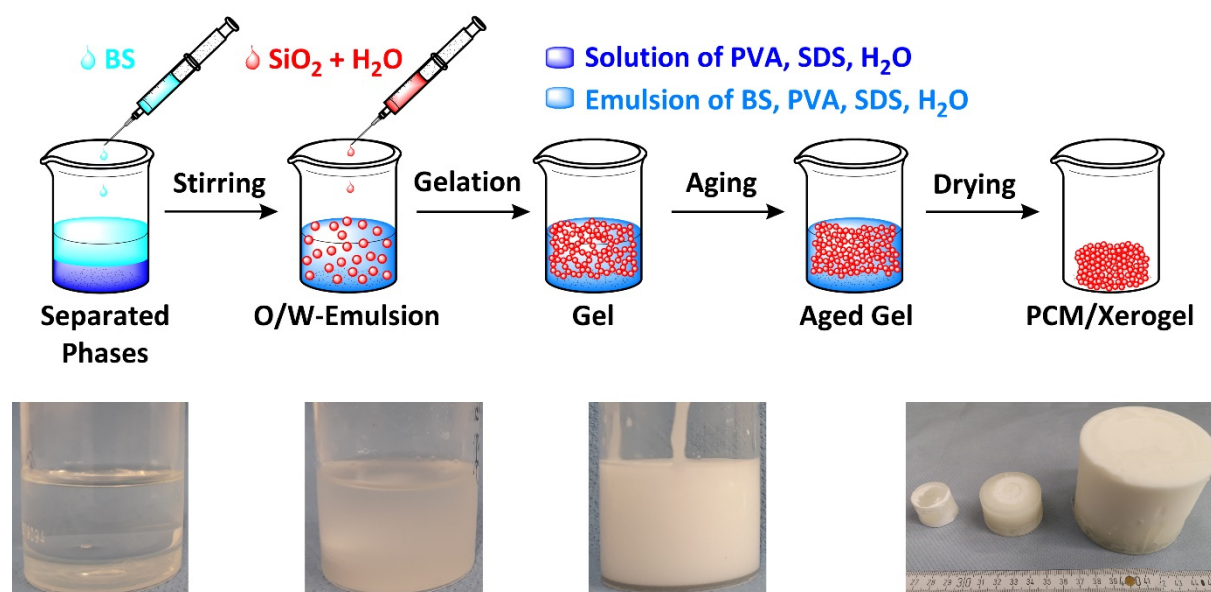


Fig. 1.1 Schematic synthesis of monolithic ss-PCM with different sizes via *in situ* sol-gel.

3.1.4 Characterization of the ss-PCM

The thermal and long-term performance of the ss-PCMs were characterized by DSC scans on an 822e calorimeter by METTLER TOLEDO with a heating rate of $1\text{ }^{\circ}\text{C min}^{-1}$ as standard and $2\text{ }^{\circ}\text{C min}^{-1}$ for the thermal cycling experiments in the DSC. The measurements were run from $-20\text{ }^{\circ}\text{C}$ to $60\text{ }^{\circ}\text{C}$ under air atmosphere. The holding times at $-20\text{ }^{\circ}\text{C}$ and $60\text{ }^{\circ}\text{C}$ were set to 10 min. Every sample was measured at least five times with the results being used to calculate the mean values for supercooling and latent heat. Differential thermal analysis and thermogravimetry (DTA/TG) were performed on a STA 409 C/CD thermal analyzer by Netzsch to evaluate the thermal stability of the ss-PCMs.

An amount of approximately 100 mg of the ss-PCMs and the pure PCM were heated-up from room temperature to $700\text{ }^{\circ}\text{C}$ with a heating rate of $10\text{ }^{\circ}\text{C min}^{-1}$ and $1\text{ }^{\circ}\text{C min}^{-1}$ under air atmosphere. The connectivity of the silica phase was analyzed via High Power Decoupling (HPDEC) Magic Angle Spinning (MAS) ^{29}Si NMR on a Bruker DRX-400 WB NMR spectrometer (Bruker Biospin, Karlsruhe, Germany) equipped with a 4 mm double resonance MAS probe maintained at $10\text{ }^{\circ}\text{C}$ by a temperature control unit. All spectra were recorded at a Larmor frequency of 79.49 MHz, acquired at a spinning speed of 12 kHz and a recycle delay of 40 s, and referenced externally to tetramethylsilane (TMS). For the measurements, the samples were scanned 256 times at a radio-frequency field strength of 42 kHz as a $\pi/2$ pulse during an acquisition time of 25 ms. To analyze the mechanical properties of the ss-PCMs, five samples were synthesized with the same chemical composition and their compressive strength was tested on a TBH355 hardness tester by ERWEKA to calculate a mean value. The five

measurements were performed at 10 °C and 30 °C for the compressive strength of the solid and liquid PCM in the solid ss-PCM. The hydrophobicity of the ss-PCMs was characterized by contact angle measurements with water on an OAC 15EC drop shape analyzer by DataPhysics. A Seven Easy pH electrode by METTLER TOLEDO was used to measure the pH value of the solution at room temperature.

The macroporosity of the ss-PCMs and silica matrix were analyzed by mercury (Hg) intrusion measurements on Pascal140 (400 kPa) and Pascal440 (400 MPa) instruments (Porotec). An amount of approximately 80 - 100 mg of the samples was used for each measurement. The micro- and mesopore structures of the silica phase in ss-PCMs were characterized by nitrogen sorption measurements at -196 °C using a Sorptomatic 1990 surface area analyzer (Porotec). An amount of approximately 100 - 150 mg of each sample was analysed before and after the calcination of the ss-PCM at 600 °C (10 h). The specific surface area of the ss-PCM was calculated via the Brunauer–Emmett–Teller (BET) method. The ss-PCMs were imaged on a Leo Gemini 1530 Zeiss scanning electron microscope. For the preparation, the samples were placed on a conductive carbon tape. The secondary electrons were accelerated to a voltage of 10 kV during the measurement. X-ray imaging experiments were performed in a Carl Zeiss Xradia 810 Ultra (Cr X-ray source, 5.4 keV). Absorption-based and phase-contrast imaging experiments were performed. For the later, a Zernike phase-ring was positioned near the back focal plane of the zone plate. In the imaging experiments, a total of 901 projections with a field-of-view (FOV) of 65 x 65 μm^2 were obtained over 180°, with an exposure time of 30 s per projection, a detector binning of 2 and the voxel size of 128 x 128 x 128 nm^3 in the final images. Image reconstruction was performed by filtered back-projection algorithm using the software integrated into the Xradia 810 Ultra. Commercial software Thermo Scientific Avizo was used for image correction segmentation, and 3D renderings presented here. Pore segmentation was done after separation of the main structure from the pores, application of the “separate objects” module using the maximum number of seeds for the watershed algorithm therefore applied. Volumes used for the small pore calculations had a minimum value of 0.14 mm^3 , corresponding approximately to a sphere with about 2.5 voxels of radius. Results presented here were obtained after performing calculations over volumes of 325 x 325 x 325 voxels.

The thermal conductivity was measured with a Hot Disk TPS 1500 thermal analyzer by Hot Disk AB in sandwich-mode. First, the monolithic sample was sawed through the middle. The thermal sensor was then covered by the two pieces (sandwich mode) and measured the thermal conductivity five times after 30 minutes. The average value was calculated.

3.1.5 Results and discussion

3.1.5.1 Development of an *in situ* synthesis for monolithic ss-PCMs

We aimed to synthesize five different ss-PCMs, named here FS1 to FS5, via *in situ* sol-gel process by varying the amounts of butyl stearate (BS), sodium dodecyl sulfate (SDS) and poly(vinyl alcohol) (PVA) (Table 1.1). SDS and PVA were used to stabilize the O/W-emulsion via creation of micelles and to increase the viscosity of the reaction mixture. The quality of the obtained ss-PCMs was characterized by form-stability and compressive strength tests. The form-stability of ss-PCMs is typically characterized by a simple PCM leakage test at higher temperatures.³⁹

Table 1.1 Chemical compositions of ss-PCMs synthesized for the development of monolithic ss-PCMs and their pH-values (pH), gelation points (GP) and compressive strengths (σ). For all compositions, 9 g of Sol and 6.75 g of water were used. The BS amount of formulations FS1 and FS2 was varied from 0 - 20 g.

Sample	PVA (g)	SDS (g)	BS (g)	pH	GP (h)	σ (MPa) at 10 °C / 30 °C
FS1	0.0	0.0	0 - 20.0	9.6	-	-
FS2	0.6	0.0	0 - 20.0	7.3	-	-
FS3	0.0	0.8	20.0	10.5	33.0	0.006 / 0.002
FS4	0.6	0.8	20.0	9.2	29.0	1.2 / 0.7
FS5	1.0	0.8	16.5	8.9	7.0	0.8 / 0.5

The PCM leakage (wt%) was calculated by the percentage mass difference of the sample before and after heat treatment for 24 h at 100 °C. For the samples FS1 and FS2, synthesized without SDS as emulsifier, the reaction mixture separates in a hydrophobic butyl stearate phase and a hydrophilic water phase after stirring. Gelation of the stabilized silica sol is initiated with the addition of at least 20 wt% BS to the reaction mixture, in contrast to what is observed for the addition of tetraethyl orthosilicate.^{38,40,41} To increase viscosity of the O/W-emulsion, we have added PVA to the reaction mixture of FS1, forming FS2 (Table 1.1). The subsequent gelation process is not only accelerated, but can start even without the addition of BS, because of a reduced pH value (9.6 to 9.0). To enable the stabilization of BS in water and prevent the phase separation observed for FS1 and FS2, we have added SDS to the synthesis of FS3 and FS4. FS3 (without PVA) is form-stable and no leakage of BS is observed at 100 °C. However, FS3 is not monolithic and has a poor compressive strength of 2 kPa at 30 °C and 6 kPa at

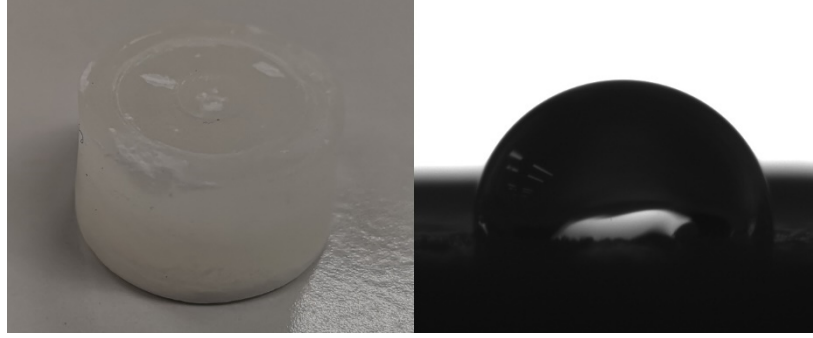


Fig. 1.2 Picture (a) and contact angle measurement of sample FS4 (b).

10 °C. In contrast, FS4 with PVA as co-polymer and SDS as surfactant, is not only form-stable, but also monolithic and shows higher values for compressive strength of ss-PCMs (0.7 MPa at 10 °C) with similar PCM mass fractions than found in the current literature (mostly in the range of 10 kPa) (Fig. 1.2(a)).⁴²

Additionally, FS4 shows no macroscopic cracks despite a high effective mass fraction $Ma(PCM)$ of 83 wt%, which was calculated by Eq. 1.1 and Eq. 1.2.

$$Ma(PCM)_{DSC} = \frac{\Delta_l^s H_m(ssPCM)}{\Delta_l^s H_m(PCM)} \cdot 100 \quad (\text{Eq. 1.1})$$

$$Ma(PCM)_{mass} = \frac{m_{ssPCM} - m_{Additives}}{m_{ssPCM}} \cdot 100 \quad (\text{Eq. 1.2})$$

where $Ma(PCM)_{DSC}$ and $Ma(PCM)_{mass}$ are, respectively, the effective mass fractions of PCM calculated via DSC and by weight (mass), $\Delta_l^s H_m(ssPCM)$ and $\Delta_l^s H_m(PCM)$ are the melting enthalpies of ss-PCM, and pure PCM and m_{ssPCM} and $m_{Additives}$ are the masses of ss-PCM and educts without water and PCM.

We are currently investigating the complex role of SDS and PVA and expect, that SDS forms micelles around BS droplets and stabilize them in gelation process, whereas PVA should induce phase separations for pore channels necessary for a break-free drying process of ss-PCM xerogels. By varying the amount of BS (70 - 94 wt%) in the synthesis of sample FS4, monolithic (FS4₇₀ - FS4₈₆) and form-stable ss-PCMs (FS4₇₀ - FS4₉₄) were synthesized (Fig. 1.3). The compressive strength increases for FS4₇₀ to FS4₇₈ and decreases for FS4₇₈ to FS4₈₆ by increasing the BS amount used for the synthesis, indicating that BS amounts lower than 78 wt% have a stabilizing function in sol-gel process. However, they were not analyzed further since compressive strength improved only marginally compared to FS4 while lowering the BS amount.

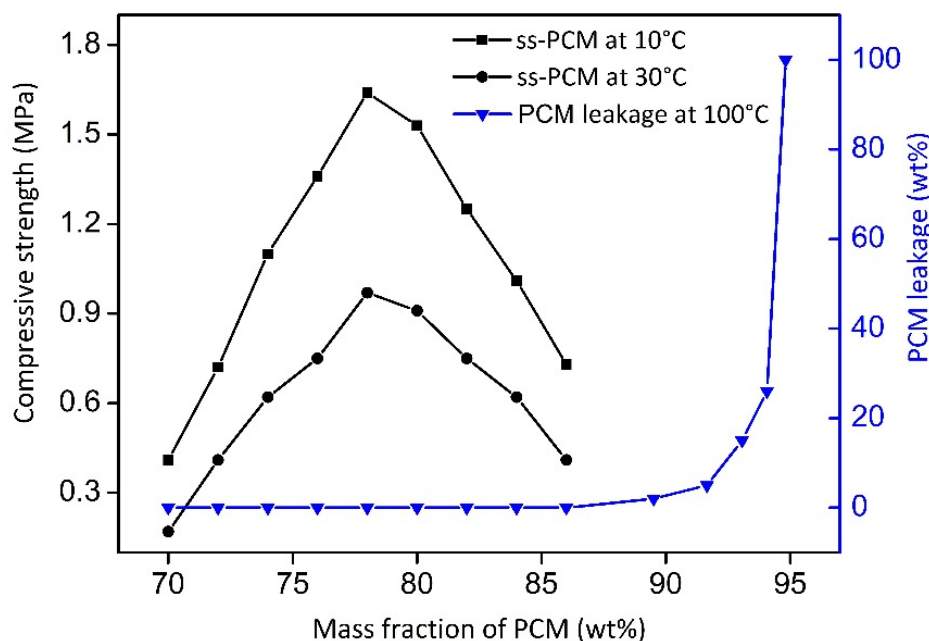


Fig. 1.3 Mechanical stabilities and PCM leakage (100 °C, 24 h) tests of ss-PCMs FS4₇₀ - FS4₉₄. The subscripts encode the amount of BS used for the synthesis. The ss-PCMs are form-stable up to 94 wt% BS and monolithic up to 86 wt% BS as PCM.

In general, a high density of ss-PCM FS4 is desirable to store more heat in a smaller volume of the silica matrix. Therefore, we calculated the density of the sample by measuring the weight and the dimensions of the cylindrical monolith FS4. The density of sample FS4 is 0.07 g cm⁻³ higher than the density of pure butyl stearate (0.86 g cm⁻³). This is due to a high shrinkage of FS4 as wet gel (approximately 35 % v/v during drying).

We analyzed the hydrophobicity of FS4 via contact angle measurement with water (Fig. 1.2(b)), as an indication of the weatherability of this ss-PCM. Weatherability is an important factor for the use of ss-PCMs in construction applications. The contact angle of 101° (>90°) indicates that FS4 is hydrophobic, pointing to a good weatherability. In ²⁹Si MAS NMR studies (Fig. 1.4), the peaks observed for the silica matrix in FS4 shows (Si-O)₂Si(O-Si)₂ species at -111 ppm (Q4) with the highest peak intensity, followed by (Si-O)₂Si(O-Si)(OH) species at -102 ppm (Q3) and (Si-O)₂Si(OH)₂ species at -92 ppm (Q2) with much lower peak intensities. Therefore, the complete silica phase is condensed without free silica particles left in the ss-PCM, which should be one reason for the high mechanical stability of FS4.

Additionally, the hydrophobicity of FS4 is based on the hydrophobic nature of butyl stearate without covalent Si-O-C- or Si-C-bonds between silica and BS, PVA or SDS. The BS has only weakly attractive interactions to the silica phase due to its ester function. Thus, BS is not able to build Si-O-C- and Si-C-bonds with the silica phase under the mild synthesis conditions in this work (Fig. 1.4).

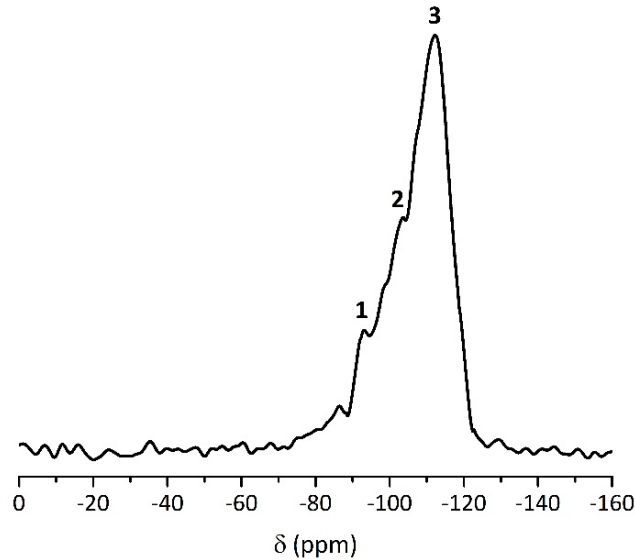


Fig. 1.4 ^{29}Si MAS NMR spectrum of ss-PCM FS4.: 1 = $(\text{Si-O})_2\text{Si}(\text{OH})_2$ (Q^2); 2 = $(\text{Si-O})_2\text{Si}(\text{O-Si})(\text{OH})$ (Q^3); 3 = $(\text{Si-O})_2\text{Si}(\text{O-Si})_2$ (Q^4).

3.1.5.2 Thermal properties of ss-PCMs

The compressive strength of 0.7 MPa (30 °C), the monolithic shape and the hydrophobic nature of FS4 makes this sample a promising thermal energy storage board that does not need to be incorporated into concrete like other cs-PCMs.^{29,30,32} However, PCMs often suffer from supercooling effects and low latent heats after confinement.⁷

For this reason, we compared the freezing and melting enthalpies of BS (technical grade) and the sample FS4 via DSC measurements (Fig. 1.5). The peaks observed for BS below 10 °C occur due to impurities of the technical product, with latent heats of approximately 20 J g⁻¹. The melting and freezing points of BS, respectively at 21.7 °C and 17.6 °C, shift to lower temperatures after its confinement in the porous silica matrix in case of sample FS4. Additionally, the freezing point of FS4 decreases by 0.7 °C more than the melting point, resulting in a slightly increased supercooling. According to literature, supercooling of confined PCMs depends on thermal conductivity, pore size of the silica matrix filled with PCM and interactions between pore surface and PCM.⁴³

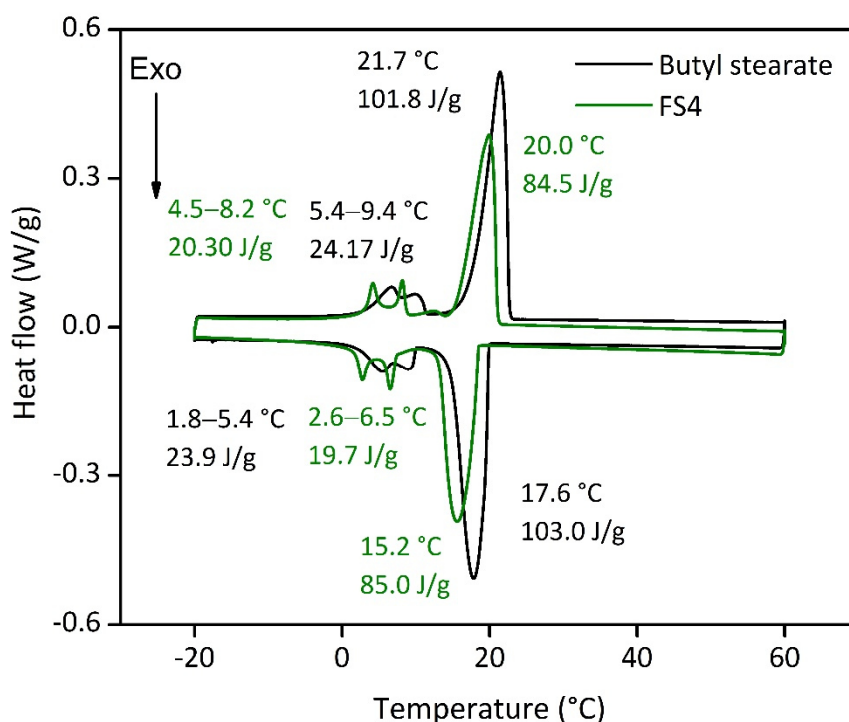


Fig. 1.5 DSC curves of butyl stearate and FS4.

Here, FS4 has a higher thermal conductivity ($0.22 \text{ W m}^{-1} \text{ K}^{-1}$, $30 \text{ }^\circ\text{C}$) than pure butyl stearate ($0.12 \text{ W m}^{-1} \text{ K}^{-1}$, $30 \text{ }^\circ\text{C}$), which should accelerate the heat transfer of the sample FS4 during state transition and shifts the melting and freezing points to lower temperatures. In contrast, the pore size effect (described via Clapeyron equation)⁴⁴ leads to an increased melting point, because of the increased pressure in the ss-PCM structure induced by capillary forces, and should occur in pore structures with smaller micro- and mesopores. Finally, the hydrophobic BS can build just weakly attractive interactions with the silica surface (Fig. 1.4), which should result in lower melting and freezing points according to the literature.^{43,45,46} In this work, the accelerated heat transfer and the weak attractive interactions between silica surface and PCM should be the dominant effects for the decreased freezing and melting points of FS4 (Fig. 1.5). Thus, we expect that the pore structure of the silica phase in FS4 mainly consists of macropores.

The effective mass fraction of PCM $Ma(PCM)$ is an important parameter to characterize the storage capacity of the silica matrix and to calculate the efficiency E of the PCM confinement. The efficiency E measures the percentage of PCM (%) immobilized in the dried xerogel after synthesis. The effective mass fractions $Ma(PCM)$ and the confinement efficiency E of FS4 were calculated by weight (mass) and DSC using Eq. 1.1 - 1.5.

$$Ma(PCM)_{max} = \frac{m_{PCM}}{m_{educts} - m_{H_2O}} \cdot 100 \quad (\text{Eq. 1.3})$$

$$E_{DSC} = \frac{Ma(PCM)_{DSC}}{Ma(PCM)_{max}} \cdot 100 \quad (\text{Eq. 1.4})$$

$$E_{mass} = \frac{Ma(PCM)_{mass}}{Ma(PCM)_{max}} \cdot 100 \quad (\text{Eq. 1.5})$$

where $Ma(PCM)_{max}$ is the highest possible value for the effective mass fraction of PCM calculated by mass, m_{educts} is the mass of the complete educts, m_{H_2O} and m_{PCM} are the masses of water and BS, and E_{DSC} and E_{mass} are the confinement efficiencies calculated by DSC and mass.

Generally, effective mass fractions are calculated by melting enthalpies of ss-PCM and pure PCM in literature (Eq. 1.1). If, however, FS4 is measured at different parts of the sample via DSC, the melting enthalpies and calculated effective mass fractions vary: parts from the middle section of the sample vary over a range of 80 - 87 wt%. From top to bottom sections, they vary by approximately 13 wt% and from the sides the variation is about 9 wt% (Fig. 1.6).

Consequently, BS must be distributed inhomogeneously in the xerogel structure and is accumulated mostly in the bottom part of the monolith FS4. For a more accurate calculation of effective mass fractions, we weighed our ss-PCMs and used the Eq. 1.2 to calculate the effective mass fraction $Ma(PCM)_{mass}$. The value of $Ma(PCM)_{mass}$ differs by only 0.5 wt% from the average $Ma(PCM)_{DSC}$ of FS4 ($\emptyset Ma(PCM)_{DSC}$) (Fig. 1.6). To validate our data, we compared the value of $Ma(PCM)_{mass}$ with $Ma(PCM)_{max}$, which corresponds to the maximal immobilized amount of PCM in ss-PCMs (Eq. 1.3). Because both values are identical, the

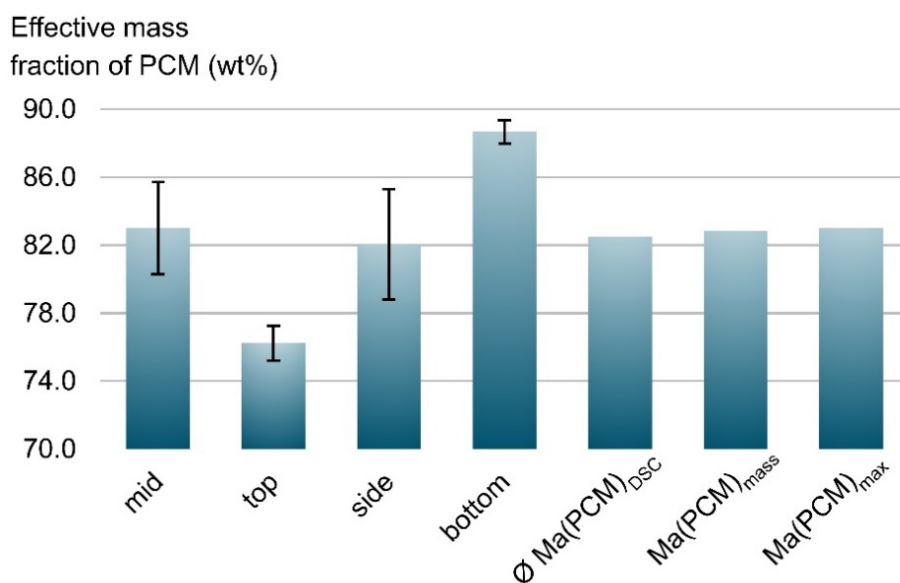


Fig. 1.6 Effective mass fractions of PCM from the mid, the side, the bottom and the top of ss-PCM FS4 and the average value from DSC $\emptyset Ma(PCM)_{DSC}$ compared to $Ma(PCM)_{mass}$ and $Ma(PCM)_{max}$ (Eq. 1.1 - 1.3).

simple weighing seems to be an appropriate method to determine the exact effective mass fraction of PCM in ss-PCMs. Moreover, the identical values of $Ma(PCM)_{mass}$, $Ma(PCM)_{DSC}$ and $Ma(PCM)_{max}$ indicate a 100% confinement of PCM in FS4 (Eq. 1.4 and 1.5). However, the ss-PCM must be fully dried to calculate $Ma(PCM)_{mass}$ (Eq. 1.2).

In summary, the high latent heats and confinement efficiencies besides a low supercooling effect enables the economically feasible use of FS4. However, the application range of FS4 is limited to its thermal stability. For this reason, we investigated the thermal stability of FS4 and pure BS by DTA/TG (Fig. 1.7). A 4 wt% weight loss is observed for FS4 between 100 - 200 °C and should be related to the decomposition of SDS and dehydration of PVA.^{47,48} The 80 wt% weight loss of FS4 at 320 °C should be related to the removal of BS. Pure BS evaporates at 330 °C, and confined BS in the sample FS4 at 320 °C, probably due to the higher thermal conductivity of FS4. At higher temperatures, PVA and high-molecular degradation products of BS completely decompose.⁴⁸ Finally, only silica (12 wt%) remains after heating FS4 up to 700 °C.

3.1.5.3 Long-term performance of ss-PCMs

Encapsulated PCMs often lose melting and freezing enthalpy after some state transitions, due to possible reactions with matrix or capsule, which can be detrimental for future low temperature applications.^{19,49} For this reason, we tested the long-term performance of our ss-PCM via DSC in a thermal cycling experiment (Fig. 1.8). Each state transition from solid to liquid and vice versa was marked as one cycle. The amount of PVA and BS of FS4 was changed slightly for this experiment to shorten the gelation time from 29 to 7 h and increase the homogeneity of the PCM distribution in the ss-PCM by the higher viscosity of the system during gelation.

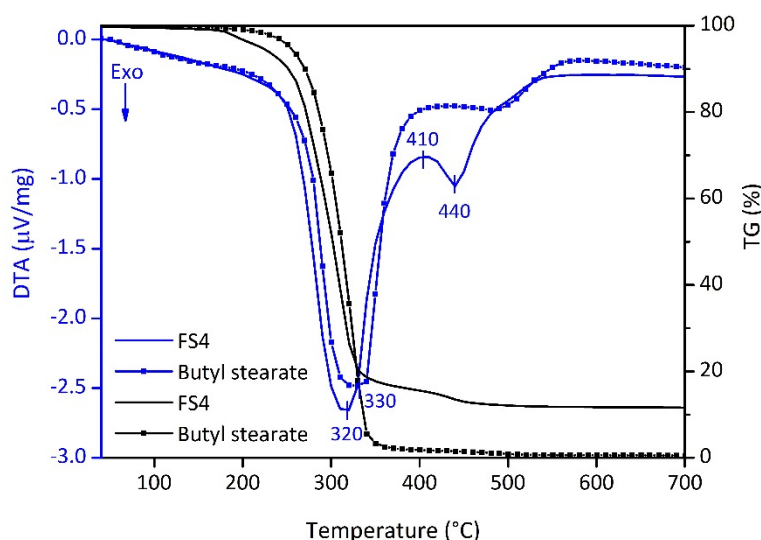


Fig. 1.7 DTA/TG curves of FS4 and pure butyl stearate (heating rate: 10 °C min⁻¹).

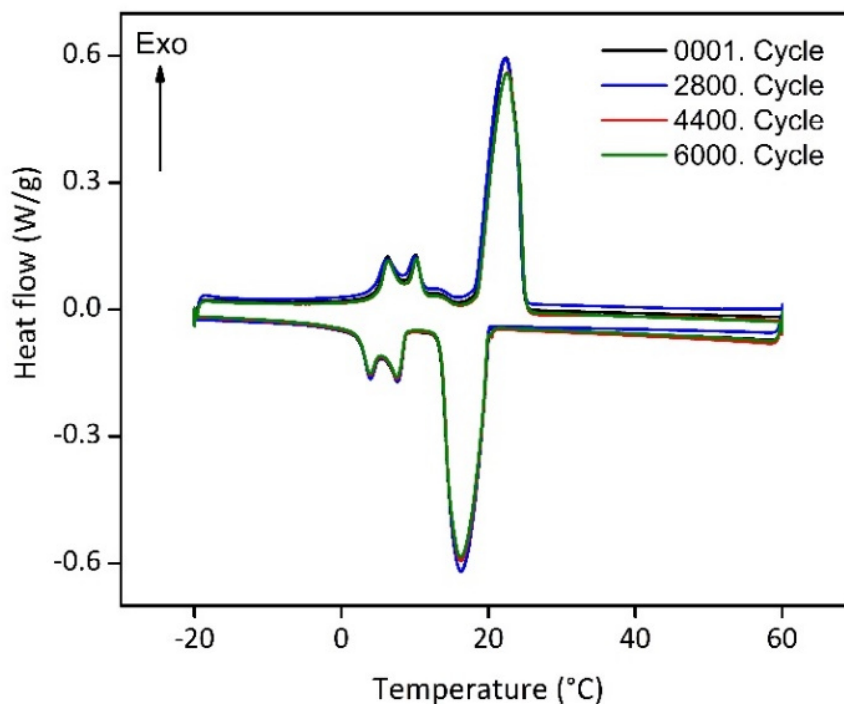


Fig. 1.8 Long-term performance tests for sample FS5. The sample was melted and frozen up to 6,000-times (6,000 cycles) via DSC measurements with a heating rate of $2\text{ }^{\circ}\text{C min}^{-1}$ to check for a possible decrease of the phase change enthalpy and, thus, the durability of the ss-PCM FS5.

The corresponding sample was named FS5 (Table 1.1) and was measured over 6000 times via DSC (Fig. 1.8). The melting enthalpies of all measurements remain similar to the value of the first cycle, with $80.4 \pm 0.67\text{ J g}^{-1}$ (standard variation of the DSC device). The sample FS5 has therefore no important decrease of melting or freezing enthalpies even after 6000 cycles. Thus, FS5 does not react irreversibly with the chemical additives, such as PVA and SDS, in the ss-PCM during state transition, which is in accordance with the results of ^{29}Si MAS NMR studies (Fig. 1.4). In the current literature, ss-PCMs and cs-PCMs are usually tested for no more than approximately 1500 cycles.^{49–51} For this reason, sample FS5 has a very high long-term performance. This result is relevant for the possible application of FS5 in building walls, because the durability of a PCM is directly related to its long-term performance.^{49,51} In the long-term performance test (Fig. 1.8), each cycle corresponds to freezing in a cold night and melting in a warm day in a composite wall. According to this definition,⁵¹ the ss-PCM FS5 is stable over 16 years in building walls. In several studies, building walls impregnated with approximately 30 wt% organic PCM and a thickness of 10 - 20 mm could lead to 2 - 3 GJ year⁻¹ energy-saving, resulting in an amortization period of 9 to 18 years.⁵² Because FS5 has 79 wt% PCM, we expect a much shorter amortization period of FS5 as energy-saving walls in buildings.

3.1.5.4 Silica structure in ss-PCMs

Our ss-PCMs FS4 and FS5 show superior characteristics for application as thermal energy storage board in buildings, such as higher mechanical stabilities (1 - 2 MPa), long-term performances (stable over 6000 thermal cycles) and higher thermal conductivities (83% higher than BS) than ss-PCMs reported in the current literature.^{49,53,54}

To understand the better performance of these samples, we first analyzed the structure of the silica phase in five ss-PCMs prepared according to the synthesis of FS5, with a BS amount of 10.0 g (FS5₁₀₀) to 20.0 g (FS5₂₀₀) (Table 1.2 and Fig. 1.9). Then, we compared the silica structures of FS5₂₀₀ with the silica structure of sample FS4 to investigate the influence of the PVA amount used for the synthesis (Table 1.1). We calcined also FS5₁₀₀ - FS5₂₀₀ and FS4 at 600 °C for 6 h (FS5_{c100} - FS5_{c200} and FS4c) to be able to distinguish the silica pores filled with air from the silica pores filled with PCM. No remaining organic substances were detected after calcination by FTIR spectroscopy (Fig. S1.1). We analysed the mesopores only with nitrogen sorption (N₂) because the high pressure of Hg intrusion (\leq 400 MPa) could decompress BS and destroy silica structures in ss-PCMs. The isotherms of FS5_{c100} - FS5_{c200} are type IV isotherms with H1/H2 hysteresis, typical for mesoporous materials (Fig. 1.9(c)). Micropores were not detected for FS5_{c100} - FS5_{c200} by N₂ sorption. The mesopore volume of FS5₁₀₀ - FS5₂₀₀ should be completely filled with PCM because N₂ sorption experiments show no N₂ sorption.

Table 1.5 Physicochemical properties¹ of samples FS4 and FS5₁₀₀ - FS5₂₀₀, corresponding to the synthesis of FS5 with BS amounts from 10.0 g (FS5₁₀₀) to 20.0 g (FS5₂₀₀), before and after calcination at 600 °C, named here FS4c and FS5_{c100} - FS5_{c200}.

Sample	Φ (%) ^{a,b}	V_{total} (cm ³ /g) ^{a,b}	V_{macro} (cm ³ /g) ^a	V_{meso} (cm ³ /g) ^b	D_{macro} (nm) ^a	D_{meso} (nm) ^b	A_{meso} (m ² /g) ^b	σ (MPa) at 10 °C / 30 °C	T_D (°C)
FS5 ₁₀₀	57	0.60	0.60	-	20036	-	-	0.3 / 0.1	200
FS5 ₁₂₅	53	0.51	0.51	-	10980	-	-	0.5 / 0.3	209
FS5 ₁₅₀	17	0.09	0.09	-	5863	-	-	1.1 / 0.6	223
FS5 ₁₇₅	10	0.05	0.05	-	14334	-	-	0.9 / 0.5	215
FS5 ₂₀₀	5	0.02	0.02	-	235	-	-	0.8 / 0.4	216
FS4	5	0.03	0.03	-	250	-	-	1.2 / 0.7	216
FS5 _{c100}	92	5.35	4.81	0.54	4031	8	211	-	-
FS5 _{c125}	93	5.67	5.10	0.57	4390	8	212	-	-
FS5 _{c150}	92	5.34	4.78	0.56	2824	8	202	-	-
FS5 _{c175}	94	6.64	6.09	0.55	1493	8	200	-	-
FS5 _{c200}	95	8.12	7.46	0.66	1460	9	213	-	-
FS4c	95	7.80	6.98	0.82	1007	8	181	-	-

¹ Porosity Φ , total pore volume V_{total} , macropore volume V_{macro} , mesopore volume V_{meso} , mean macropore diameter/50% D_{total} , mean mesopore diameter /50% D_{meso} , mesopore surface area A_{meso} , compressive strength σ and decomposition point T_D of BS in ss-PCMs (heating rate: 1 °C min⁻¹);

a: calculated via mercury intrusion; b: calculated via nitrogen sorption

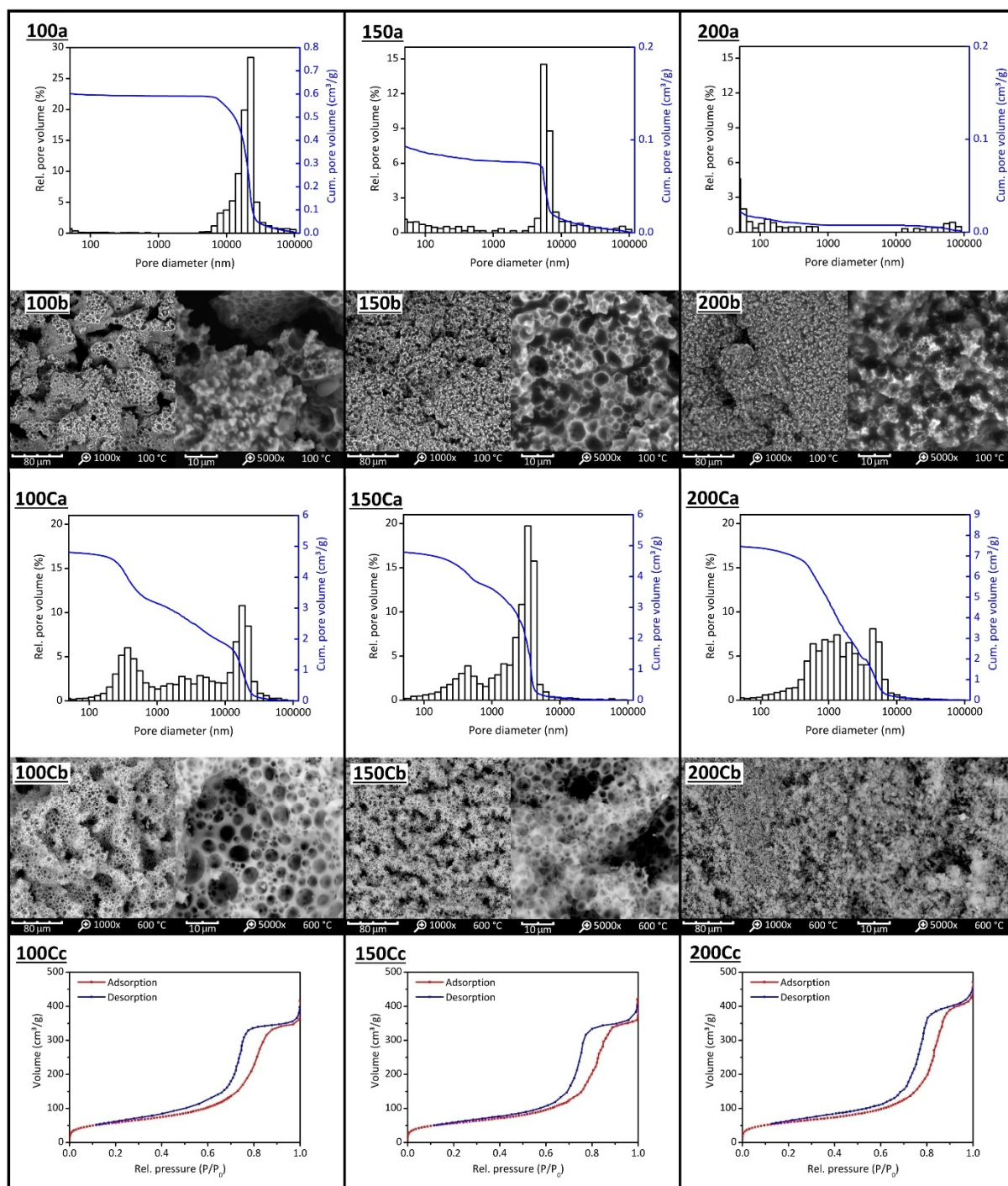


Fig. 1.9 Mercury intrusion measurements (a), SEM images (b) and nitrogen sorption isotherms (c) of FS5₁₀₀ (100) to FS5₂₀₀ (200) and FS5C₁₀₀ (100C) to FS5C₂₀₀ (200C). The amount of BS was increased from 10.0 g (FS5₁₀₀) to 20.0 g (FS5₂₀₀) and the ss-PCMs calcined (C) at 600 °C for 6 h to identify silica pores filled with air from silica pores filled with PCM.

The BS amounts above 17.5 g increase the mesopore volume slightly from 0.55 cm³ g⁻¹ for samples FS5c₁₇₅ to 0.66 cm³ g⁻¹ for FS5c₂₀₀, whereas the BS amount below 17.5 g does not affect the mesopore volume of the ss-PCMs FS5c₁₀₀ - FS5c₁₇₅. When the total pore volumes are compared (Table 1.2), two specific effects are observed. First, the total pore volumes of FS5c₁₀₀ - FS5c₁₅₀ are similar and around 5 cm³ g⁻¹, even though the BS amount used for the synthesis is increased. Second, the total pore volume increases from 5.34 cm³ g⁻¹ to 8.12 cm³ g⁻¹ for FS5c₁₅₀ - FS5c₂₀₀, indicating a change of the templates for the pore structure during gelation. Pure and emulsified BS droplets alongside water and air bubbles covered by SDS can act as templates for the silica pore structure during gelation. The total pore volume of FS5c₁₀₀ (similar to FS5c₁₂₅ and FS5c₁₅₀) must be caused by foam pores (air inclusions) with diameter above 10 000 nm (Fig. 1.9 (C)). These “wormlike” pores of FS5₁₀₀ and FS5c₁₀₀ (Fig. 1.9 (C)) have total pore volumes of 0.54 cm³ g⁻¹ and 1.8 cm³ g⁻¹.

With an increasing amount of BS, the pore volume above 10 000 nm is decreased to nearly zero for samples FS5₁₅₀ and FS5c₁₅₀ (Table 1.2). Moreover, the pore volume between 2000 - 10 000 nm of FS5c₁₅₀ increases by nearly 1.8 cm³ g⁻¹, whereas the pore volume between 2 - 2000 nm is nearly constant for FS5c₁₀₀ - FS5c₁₅₀ (2 cm³ g⁻¹). For this reason, the pores between 2 - 2000 nm and 2000 - 10 000 nm must be formed by different template types. Because the interfacial tension of SDS micelles filled with oil is quite lower than those filled with air,⁵⁵ SDS micelles filled with oil (BS) are smaller and require less work W to be formed in emulsions, according to Eq. 1.6.⁵⁶

$$W = \gamma \cdot \Delta A \quad (\text{Eq. 1.6})$$

where γ is the interfacial tension and ΔA is the increase of the interfacial area.

At a constant SDS amount, the increasing BS amount from FS5₁₀₀ to FS5₁₅₀ leads to more oil phase during gelation, that requires less work to be covered by SDS molecules than air inclusions. Simultaneously, the amount of SDS molecules in solution, which can form micelles with air (foam pores), decreases. Finally, all SDS molecules cover BS droplets in solution. This is the case for FS5₁₅₀ without foam pores above 10 000 nm (Fig. 1.9 (150b)) and results in a decrease of the mean macropore diameter from 4031 nm for FS5c₁₀₀ to 2824 nm for FS5c₁₅₀. Because the pore volume between 2000 - 10 000 nm of FS5c₁₀₀ - FS5c₁₅₀ changed by adding BS (Fig. 1.9 (100Ca and 150Ca)), the pores must be formed by BS droplets covered by SDS molecules. In SEM images, not only the pores between 2000 - 10 000 nm are spherical, but also the pores between 2 - 2000 nm, indicating spherical template arrangement (Fig. 1.9 (100Cb and 150Cb)). These spherical templates should be the reason for the increase in the total pore volume of FS5c₁₅₀ - FS5c₂₀₀ from 5.34 cm³ g⁻¹ to 8.12 cm³ g⁻¹. Because the pore volume of pores between 2000 - 10 000 nm of samples FS5c₁₅₀ - FS5c₂₀₀ (2.6 cm³ g⁻¹) is nearly

constant, the spherical templates should be pure BS droplets in water. In general, the spherical pores from 2 - 10 000 nm are located on pore bridges (Fig. 1.9 (100Cb - 200Cb)). With a BS amount above 15.0 g, the pore bridges start to fragment and loose connectivity, resulting in a decrease of the overall mechanical stability from 0.6 MPa for FS5₁₅₀ to 0.4 MPa for FS5₂₀₀ (Fig. 1.9 (150Cb and 200Cb)). Additionally, the compressive strength of FS5₁₀₀ is 0.5 MPa lower than FS5₁₅₀ due to foam pores above 10 000 nm indicating the influence of templates on the mechanical stability of ss-PCMs.

For the TGA measurements of FS5₁₀₀ to FS5₂₀₀ (Table 1.2, Fig. S1.8 and S1.9), the heating rate was reduced from 10 °C min⁻¹ to 1 °C min⁻¹ for a higher sensitivity, resulting in lower decomposition points for BS of 218 °C instead of 330 °C (Fig. 1.7 and S1.9). The decomposition point of BS in sample FS5₁₅₀ is 20 °C higher and 5 °C lower than for samples FS5₁₀₀ and FS5₂₀₀ due to the higher interconnectivity of silica particles in FS5₁₅₀ (Table 1.2 and Fig. S1.8). Thus, the interconnectivity of the silica structure directly influences the mechanical and thermal stability of the ss-PCMs. The confinement efficiencies E_{DSC} and E_{mass} (Eq. 1.4 and 1.5) for FS5₁₀₀ to FS5₂₀₀ are all nearly 100%, indicating no influence of the pore structure on the melting enthalpies (Table S1.1). The supercooling increases from 3.3 °C for FS5₁₀₀ to 5.3 °C for FS5₂₀₀ because of the increasing mass of the low thermal conductive BS (Table S1.1 and Fig. S1.10). In contrast to FS5_{C200}, sample FS4c has a higher mesopore volume of 0.82 cm³ g⁻¹ and a smaller mean macropore diameter of 1007 nm (Table 1.2 and Fig. S1.2). Moreover, FS4 and FS4c have a less fragmented spherical pore structure compared to FS5_{C200} and FS5₂₀₀ (Fig. 1.9 (200b and 200Cb) and 10(A_C)). In contrast to mercury intrusion (Table 1.2 and Fig. S1.2), the SEM images of sample FS4c show spherical macropores with pore diameters of up to 8000 nm (Fig. 1.10(B)). This contrast should result from the limitations of the mercury intrusion technique. We have analyzed the silica phase of sample FS4 via the sensitive three-dimensional (3D) high-resolution X-ray transmission microscopy (XRM) to visualize the macropores filled with PCM without calcination of the ss-PCM.

Because the SEM images of FS4c are comparable to the 3D XRM images of FS4 (Fig. 1.10 (C and D)), the calcination of FS4 at 600 °C should have only a small impact on the pore structure of the silica structure in the ss-PCM. Additionally, the 3D XRM images and movies (Fig. 1.10(D_H) and Movie S1.3 and 1.4) indicate in accordance with the results of ²⁹Si MAS NMR measurements (Fig. 1.4) a homogenous distribution of the silica phase in sample FS4 monolith without cracks or fragmented silica particles over a larger length scale in all three dimensions. The well interconnected silica particles in the ss-PCM should be the reason for the high compressive strength of FS4 (0.7 MPa, 30 °C). We expect that the lower PVA amount in FS4 affected the size and the connectivity of the micelles filled with BS and of the BS droplets through a polymer-induced phase separation during gelation. This assumption would explain

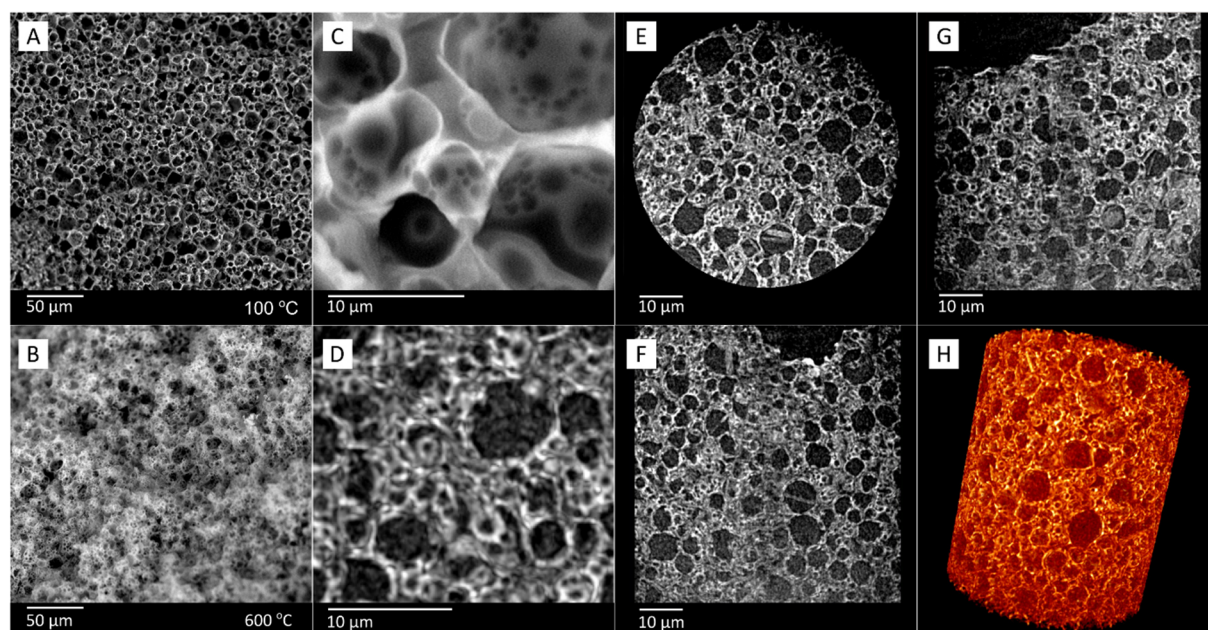


Fig. 1.10 SEM images of sample FS4, showing its morphology (A) before and (B) after calcination (FS4c). Comparison of (C) SEM and (D) corresponding X-ray images of sample FS4c, showing similar features in higher-resolution. Image (D) shows the sum of a number of XRM 2D images, to give the same impression of depth as SEM images. Images of three different planes (E - G) of sample FS4c obtained by X-ray imaging, and (H) the respective volumetric representation of the sample obtained by XRM.

the different pore structures and compressive strengths of FS4 and FS5₂₀₀. In comparison to similar ss-PCM studies, the pores of samples FS4 and FS5 filled with PCM prepared in this work are relatively small, with a more interconnected silica phase.^{41,53,57}

The compressive strength and thermal conductivity increase with a decreasing macropore diameter from FS5₁₀₀ (0.1 MPa, 0.12 W m⁻¹ K⁻¹) to FS5₁₅₀ (0.6 MPa, 0.20 W m⁻¹ K⁻¹). Higher amounts of BS (FS5₂₀₀) result in widening of the macropores and, thus, a decrease in the compressive strength (0.8 MPa) and the thermal conductivity (0.18 W m⁻¹ K⁻¹) of the sample, which is similar to recent studies about the particle size of cs-PCMs.^{17,33,58}

3.1.6 Conclusions

We used a cost-efficient *in situ* sol-gel process with different templates and phase separating agents to synthesize a novel class of monolithic ss-PCM boards with butyl stearate as PCM and stabilized silica sol as an economically friendly silica source. Our ss-PCM boards are the first reported monoliths with high compressive strengths of 1.2 MPa at 10 °C and 0.7 MPa at 30 °C despite high PCM mass percentages up to 86 wt%. Moreover, our ss-PCMs are form-stable up to 94 wt% PCM, thermally stable up to 320 °C and hydrophobic, indicating a good weatherability. Their latent heats are in the range of 85 J g⁻¹ at 20 °C and 100 J g⁻¹ at 2 - 22 °C, and are constant for at least 6000-state transitions from liquid to solid and vice versa. Consequently, the ss-PCMs are stable for 16 years in building applications.

We studied the silica structure of our ss-PCMs to understand in detail the thermal and mechanical properties of our synthesized ss-PCMs. Our results suggest that the silica particles form spherical meso- and macropores during gelation, which are mostly filled with PCM. The ss-PCMs have pores with diameters between 2 - 2000 nm, which were created by a template formed by BS in water droplets, larger pores with dimensions between 2000 - 10 000 nm created by SDS micelles filled with BS, and pores with sizes above 10 000 nm due to air inclusions (foam pores). By increasing the BS amount in the synthesis of ss-PCMs, foam pores vanish and the total pore volume of nanopores increases, resulting in a higher compressive strength (500%) and higher thermal conductivity (60%).

Our results suggest that the nanopores are the reason for the superior properties of the ss-PCMs synthesized in this work. In summary, our monolithic ss-PCMs have up to five times higher latent heats than commercially available PCM boards impregnated with PCMs or cs-PCMs and sufficient compressive strengths for most thermal energy storage applications, such as energy-saving walls – enabling new perspectives for future PCM research.

3.1.7 CRediT authorship contribution statement

Felix Marske: Conceptualization, Methodology, Validation, Formal analysis, Investigation, Data curation, Writing – original draft, Visualization. **Juliana Martins Souza e Silva:** Formal analysis, Resources, Writing – review & editing, Visualization. **Ralf B. Wehrspohn:** Resources, Writing – review & editing. **Thomas Hahn:** Supervision, Project administration, Funding acquisition, Writing – review & editing. **Dirk Enke:** Writing – review & editing, Supervision.

3.1.8 Conflicts of interest

The authors declare no conflict of interest.

3.1.9 Acknowledgements

The authors of this paper thank PhD Juliane Titus for the DTA/TG measurements of BS and FS4, M.Sc. Marianne Wenzel for ²⁹Si MAS NMR measurements, M.Sc. Jan Herwig for imaging the samples via SEM, PhD Cristine Santos de Oliveira for the visualization movie S1.4 and Ms. Jenny Bienias for the mercury intrusion and nitrogen sorption measurements. Juliana Martins de Souza e Silva and Ralf B. Wehrspohn acknowledge the DFG for the granted project WE 4051/21-1. The authors of this paper acknowledge the financial support of the Open Access Publication Fund of the Martin-Luther-University Halle-Wittenberg.

3.1.10 References

- 1 IEA, *Key World Energy Statistics 2018*, IEA, Paris, 2018.
- 2 S. Chu, Y. Cui and N. Liu, *Nat. Mater.*, 2016, **16**, 16–22.
- 3 IEA, *World Energy Outlook 2018*, IEA, Paris, 2018.
- 4 D. Lefebvre and F. H. Tezel, *Renew. Sust. Energ. Rev.*, 2017, **67**, 116–125.
- 5 G. Alva, L. Liu, X. Huang and G. Fang, *Renew. Sust. Energ. Rev.*, 2017, **68**, 693–706.
- 6 G. Alva, Y. Lin and G. Fang, *Energy*, 2018, **144**, 341–378.
- 7 A. Sharma, V. V. Tyagi, C. R. Chen and D. Buddhi, *Renew. Sust. Energ. Rev.*, 2009, **13**, 318–345.
- 8 L. Cao, Di Su, Y. Tang, G. Fang and F. Tang, *Renew. Sust. Energ. Rev.*, 2015, **48**, 500–522.
- 9 M. C. Browne, B. Norton and S. J. McCormack, *Renew. Sust. Energ. Rev.*, 2015, **47**, 762–782.
- 10 K. Pielichowska and K. Pielichowski, *Prog. Mater. Sci.*, 2014, **65**, 67–123.
- 11 A. K. Pandey, M. S. Hossain, V. V. Tyagi, N. Abd Rahim, J. A./L. Selvaraj and A. Sari, *Renew. Sust. Energ. Rev.*, 2018, **82**, 281–323.
- 12 D. Aydin, S. P. Casey and S. Riffat, *Renew. Sust. Energ. Rev.*, 2015, **41**, 356–367.
- 13 a) A. de Gracia and L. F. Cabeza, *Energy Buildings*, 2015, **103**, 414–419; b) J. Pereira da Cunha and P. Eames, *Appl. Energ.*, 2016, **177**, 227–238; c) G. G. D. Han, H. Li and J. C. Grossman, *Nat. Commun.*, 2017, **8**, 1446;
- 14 a) M. Dardir, K. Panchabikesan, F. Haghghat, M. El Mankibi and Y. Yuan, *J. Energy Storage*, 2019, **22**, 157–175; b) N. Xie, Z. Huang, Z. Luo, X. Gao, Y. Fang and Z. Zhang, *Appl. Sci.*, 2017, **7**, 1317;
- 15 a) B. Muñoz-Sánchez, I. Iparraguirre-Torres, V. Madina-Arrese, U. Izagirre-Etxeberria, A. Unzurrunzaga-Iturbe and A. García-Romero, *Energy Procedia*, 2015, **69**, 937–946; b) P. A. Galione, C. D. Pérez-Segarra, I. Rodríguez, A. Oliva and J. Rigola, *Appl. Energ.*, 2015, **142**, 337–351;
- 16 S. E. Kalnæs and B. P. Jelle, *Energy Buildings*, 2015, **94**, 150–176.
- 17 E. M. Shchukina, M. Graham, Z. Zheng and D. G. Shchukin, *Chem. Soc. Rev.*, 2018, **47**, 4156–4175.
- 18 a) H. W. Ryu, S. W. Woo, B. C. Shin and S. D. Kim, *Sol. Energ. Mat. Sol. Cells.*, 1992, **27**, 161–172; b) X. Xu, H. Cui, S. A. Memon, H. Yang and W. Tang, *Energy Buildings*, 2017, **156**, 163–172;
- 19 S. A. Mohamed, F. A. Al-Sulaiman, N. I. Ibrahim, M. H. Zahir, A. Al-Ahmed, R. Saidur, B. S. Yılbaş and A. Z. Sahin, *Renew. Sust. Energ. Rev.*, 2017, **70**, 1072–1089.

-
- 20 A. Safari, R. Saidur, F. A. Sulaiman, Y. Xu and J. Dong, *Renew. Sust. Energ. Rev.*, 2017, **70**, 905–919.
- 21 a) J. Yang, G.-Q. Qi, Y. Liu, R.-Y. Bao, Z.-Y. Liu, W. Yang, B.-H. Xie and M.-B. Yang, *Carbon*, 2016, **100**, 693–702; b) P. Bose and V. A. Amirtham, *Renew. Sust. Energ. Rev.*, 2016, **65**, 81–100; c) F. Cao and B. Yang, *Appl. Energ.*, 2014, **113**, 1512–1518; d) D. Zou, X. Ma, X. Liu, P. Zheng and Y. Hu, *Int. J. Heat Mass Transf.*, 2018, **120**, 33–41; e) A. Palacios, A. de Gracia, L. Haurie, L. F. Cabeza, A. I. Fernández and C. Barreneche, *Materials*, 2018, **11**;
- 22 a) Y. Zhang, J. Ding, X. Wang, R. Yang and K. Lin, *Sol. Energ. Mat. Sol. Cells.*, 2006, **90**, 1692–1702; b) L. Liu, Di Su, Y. Tang and G. Fang, *Renew. Sust. Energ. Rev.*, 2016, **62**, 305–317;
- 23 J.-F. Su, X.-Y. Wang, S. Han, X.-L. Zhang, Y.-D. Guo, Y.-Y. Wang, Y.-Q. Tan, N.-X. Han and W. Li, *J. Mater. Chem. A*, 2017, **5**, 23937–23951.
- 24 G. Fang, H. Li, Z. Chen and X. Liu, *Sol. Energ. Mat. Sol. Cells.*, 2011, **95**, 1875–1881.
- 25 Y. Zhang, B. Tang, L. Wang, R. Lu, D. Zhao and S. Zhang, *Energy Storage Materials*, 2017, **6**, 46–52.
- 26 X. Qiu, L. Lu and Z. Chen, *J. Appl. Polym. Sci.*, 2015, **132**, n/a-n/a.
- 27 a) C. Liu, Z. Rao, J. Zhao, Y. Huo and Y. Li, *Nano Energy*, 2015, **13**, 814–826; b) K. Tumirah, M. Z. Hussein, Z. Zulkarnain and R. Rafeadah, *Energy*, 2014, **66**, 881–890; c) A. Jamekhorshid, S. M. Sadrameli and M. Farid, *Renew. Sust. Energ. Rev.*, 2014, **31**, 531–542;
- 28 W. Su, J. Darkwa and G. Kokogiannakis, *Renew. Sust. Energ. Rev.*, 2015, **48**, 373–391.
- 29 Microtek Laboratories, *MICRONAL® DS 5040 X*, available at:
<http://microteklabs.com/pdfs/MPDS3300-0046%20Rev%201.pdf>, accessed 20 January 2019.
- 30 M. Hunger, A. G. Entrop, I. Mandilaras, H.J.H. Brouwers and M. Founti, *Cement Concrete Comp.*, 2009, **31**, 731–743.
- 31 a) T. Lecompte, P. Le Bideau, P. Glouannec, D. Nortershauser and S. Le Masson, *Energ. Buildings*, 2015, **94**, 52–60; b) A. Figueiredo, J. Lapa, R. Vicente and C. Cardoso, *Constr. Build. Mater.*, 2016, **112**, 639–647;
- 32 A. Jayalath, R. San Nicolas, M. Sofi, R. Shanks, T. Ngo, L. Aye and P. Mendis, *Constr. Build. Mater.*, 2016, **120**, 408–417.
- 33 W. Aftab, X. Huang, W. Wu, Z. Liang, A. Mahmood and R. Zou, *Energy Environ. Sci.*, 2018, **11**, 1392–1424.
- 34 L. He, J. Li, C. Zhou, H. Zhu, X. Cao and B. Tang, *Solar Energy*, 2014, **103**, 448–455.
- 35 A. Sari, A. Biçer and A. Karaipekli, *Mater. Lett.*, 2009, **63**, 1213–1216.

- 36 a) Y. Cheng, M. Xia, F. Luo, N. Li, C. Guo and C. Wei, *Colloids Surf. A*, 2016, **490**, 200–206; b) C. Sögaard, J. Funehag and Z. Abbas, *Nano Converg.*, 2018, **5**, 6;
- 37 a) J. P. Rao and K. E. Geckeler, *Prog. Polym. Sci.*, 2011, **36**, 887–913; b) D. Qi, C. Liu, Z. Chen, G. Dong and Z. Cao, *Colloid Polym. Sci.*, 2015, **293**, 463–471; c) M. G. de Cortazar and R. Rodríguez, *J. Appl. Polym. Sci.*, 2013, **127**, 5059–5064; d) H. Li, G. Fang and X. Liu, *J. Mater. Sci.*, 2010, **45**, 1672–1676;
- 38 M. Li, Z. Wu and J. Tan, *Appl. Energ.*, 2012, **92**, 456–461.
- 39 a) D. Chen, Y. Chen, X. Guo, W. Tao, J. Wang, S. Gao and J. Gao, *RSC Adv.*, 2018, **8**, 34224–34231; b) L. Niu, G. Bai and J. Song, *RSC Adv.*, 2015, **5**, 21733–21739;
- 40 L. He, J. Li, C. Zhou, H. Zhu, X. Cao and B. Tang, *Solar Energy*, 2014, **103**, 448–455.
- 41 B. Tang, J. Cui, Y. Wang, C. Jia and S. Zhang, *Solar Energy*, 2013, **97**, 484–492.
- 42 a) C. Norvell, D. J. Sailor and P. Dusicka, *J. Green Build.*, 2013, **8**, 116–124; b) Z. Zhang, G. Shi, S. Wang, X. Fang and X. Liu, *Renewable Energy*, 2013, **50**, 670–675; c) J. Yang, G.-Q. Qi, L.-S. Tang, R.-Y. Bao, L. Bai, Z.-Y. Liu, W. Yang, B.-H. Xie and M.-B. Yang, *J. Mater. Chem. A*, 2016, **4**, 9625–9634; d) S. Serrano, C. Barreneche, L. Rincón, D. Boer and L. F. Cabeza, *Constr. Build. Mater.*, 2013, **47**, 872–878;
- 43 Y. Wang, T. D. Xia, H. Zheng and H. X. Feng, *Energ. Buildings*, 2011, **43**, 2365–2370.
- 44 D. Zhang, S. Tian and D. Xiao, *Solar Energy*, 2007, **81**, 653–660.
- 45 A. Karaipekli and A. Sarı, *Solar Energy*, 2009, **83**, 323–332.
- 46 a) R. Radhakrishnan and K. E. Gubbins, *Mol. Phys.*, 1999, **96**, 1249–1267; b) R. Radhakrishnan, K. E. Gubbins, A. Watanabe and K. Kaneko, *J. Chem. Phys.*, 1999, **111**, 9058–9067;
- 47 B. Qiao, Y. Liang, T.-J. Wang and Y. Jiang, *Appl. Surf. Sci.*, 2016, **364**, 103–109.
- 48 B. Kaesche-Krischer and H. J. Heinrich, *Chem. Ing. Tech.*, 1960, **32**, 598–605.
- 49 G. Ferrer, A. Solé, C. Barreneche, I. Martorell and L. F. Cabeza, *Renewable and Sustainable Energy Reviews*, 2015, **50**, 665–685.
- 50 a) M. K. Rathod and J. Banerjee, *Renew. Sust. Energ. Rev.*, 2013, **18**, 246–258; b) A. Shukla, D. Buddhi and R. L. Sawhney, *Renewable Energy*, 2008, **33**, 2606–2614;
- 51 S. A. Mohamed, F. A. Al-Sulaiman, N. I. Ibrahim, M. H. Zahir, A. Al-Ahmed, R. Saidur, B. S. Yılbaş and A. Z. Sahin, *Renew. Sust. Energ. Rev.*, 2017, **70**, 1072–1089.
- 52 a) K. Peippo, P. Kauranen and P. D. Lund, *Energ. Buildings*, 1991, **17**, 259–270; b) P. Kauranen, K. Peippo and P. D. Lund, *Solar Energy*, 1991, **46**, 275–278; c) R. Baetens, B. P. Jelle and A. Gustavsen, *Energ. Buildings*, 2010, **42**, 1361–1368;
- 53 J. Li, L. He, T. Liu, X. Cao and H. Zhu, *Sol. Energy Mater Sol. Cells*, 2013, **118**, 48–53.
- 54 B. Tang, M. Qiu and S. Zhang, *Sol. Energ. Mat. Sol. Cells.*, 2012, **105**, 242–248.
- 55 S. G. Oh and D. O. Shah, *J. Phys. Chem.*, 1993, **97**, 284–286.
- 56 M. J. Schick, *J. Polym. Sci. B Polym. Lett. Ed.*, 1983, **21**, 680–682.

-
- 57 a) H. Yang, L. Feng, C. Wang, W. Zhao and X. Li, *Eur. Polym. J.*, 2012, **48**, 803–810; b) Y. Zhang, S. Zheng, S. Zhu, J. Ma, Z. Sun and M. Farid, *Energy Convers. Manag.*, 2018, **171**, 361–370; c) T. Qian, J. Li and Y. Deng, *Sci. Rep.*, 2016, **6**, 32392;
- 58 a) X. Wang, L. Zhang, Y.-H. Yu, L. Jia, M. Sam Mannan, Y. Chen and Z. Cheng, *Sci. Rep.*, 2015, **5**, 13357; b) Y. Zhu, Y. Qin, C. Wei, S. Liang, X. Luo, J. Wang and L. Zhang, *Energy Convers. Manag.*, 2018, **164**, 83–92.

3.1.11 Supporting Information

Additional Figures, Tables and Descriptions:

- Fig. S1.1 to S1.11
- Table S1.1
- Captions for Movie S1.1 to S1.4

Other Supplementary Materials for this manuscript include:

- Movie S1.1 to S1.4

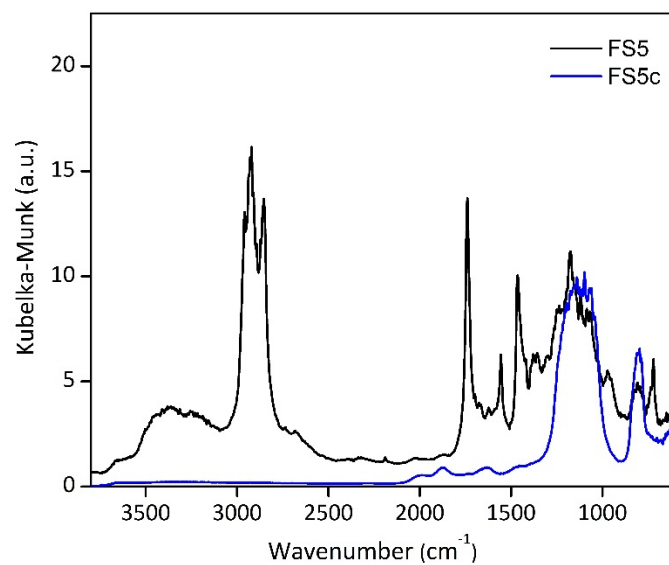


Fig. S1.1 Infrared spectrum of FS5 after drying and calcination at 600 °C (FS5c). The spectrum was measured via diffuse reflectance infrared fourier transform spectroscopy on a Vector 22 spectrometer by Bruker at 100 °C in a nitrogen atmosphere (50 scans). For preparation, 30 mg of the ss-PCM sample were mixed and grinded with approximately 100 mg potassium bromide.

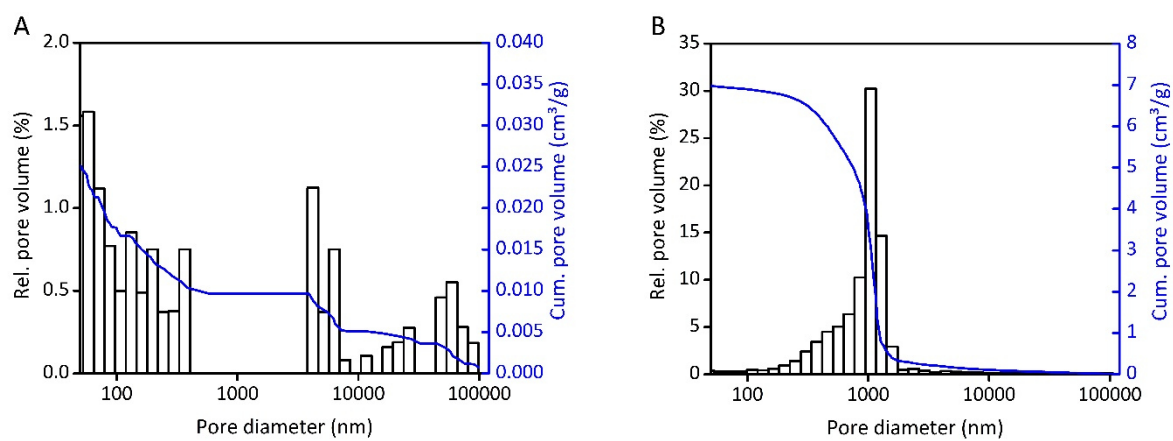


Fig. S1.2 Mercury intrusion measurements of FS4 (A) and FS4c (B).

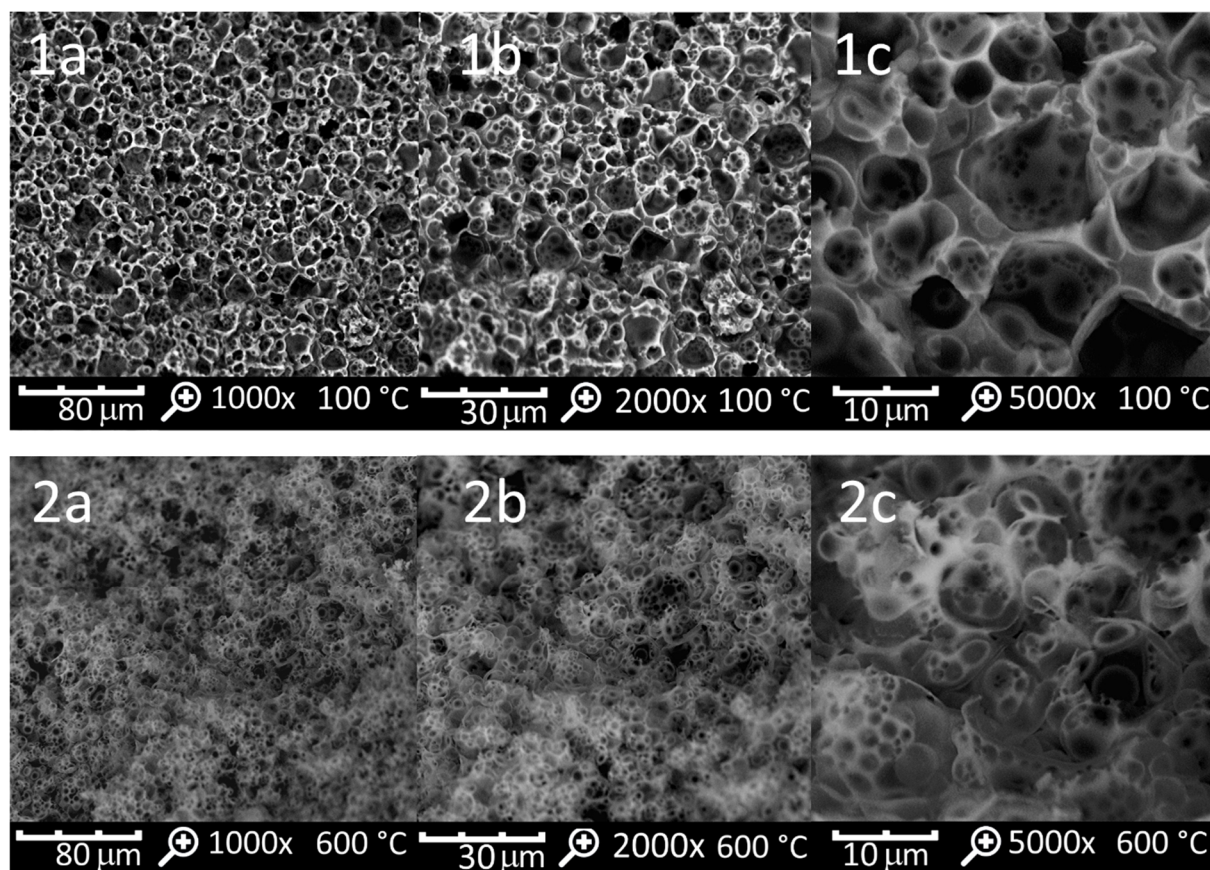


Fig. S1.3 SEM images of FS4 (1) and FS4c (2) with magnifications of 1000x (a), 2000x (b) and 5000x (c).

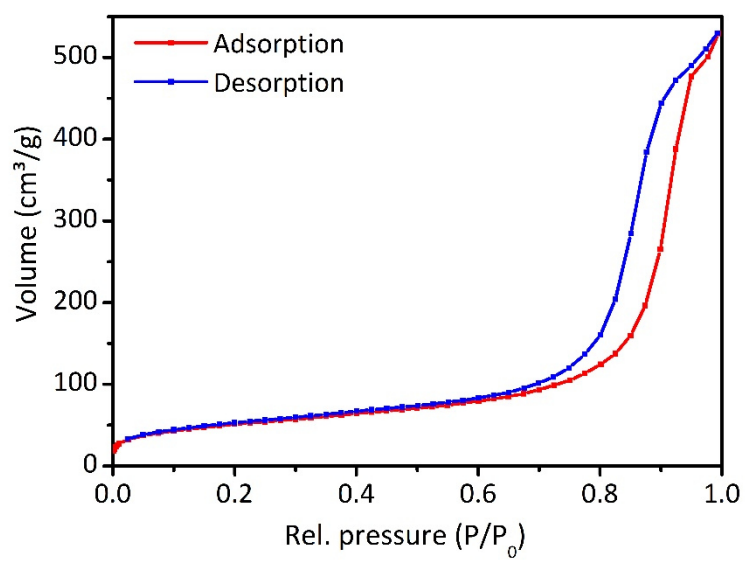


Fig. S1.4 Nitrogen adsorption isotherms of FS4c.

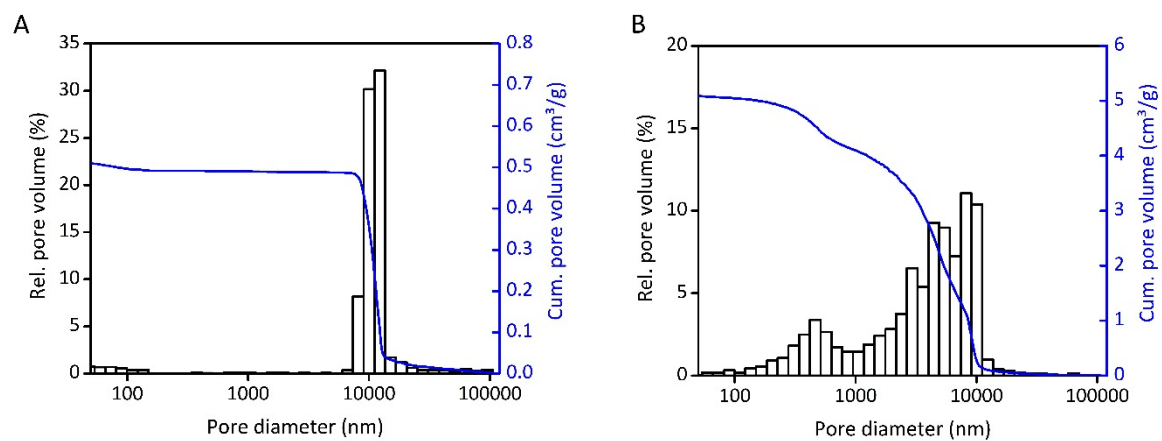


Fig. S1.5 Mercury intrusion measurements of FS5₁₂₅ (A) and FS5C₁₂₅ (B).

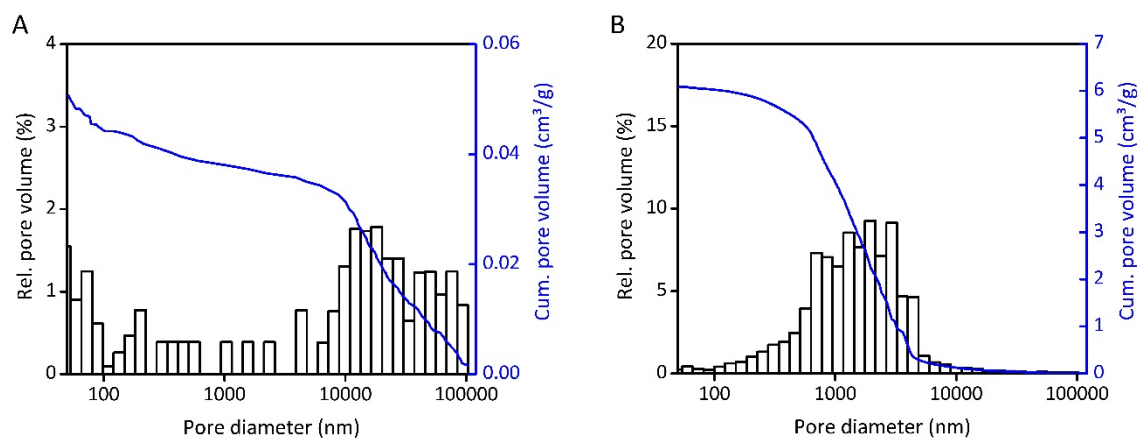


Fig. S1.6 Mercury intrusion measurements of FS5₁₇₅ (A) and FS5C₁₇₅ (B).

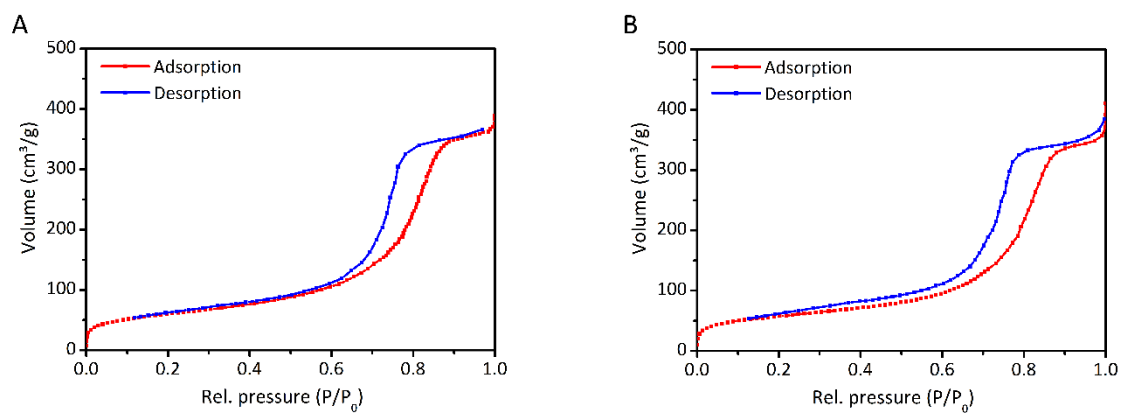


Fig. S1.7 Nitrogen adsorption isotherms of FS5c₁₂₅ (A) and FS5c₁₇₅ (B).

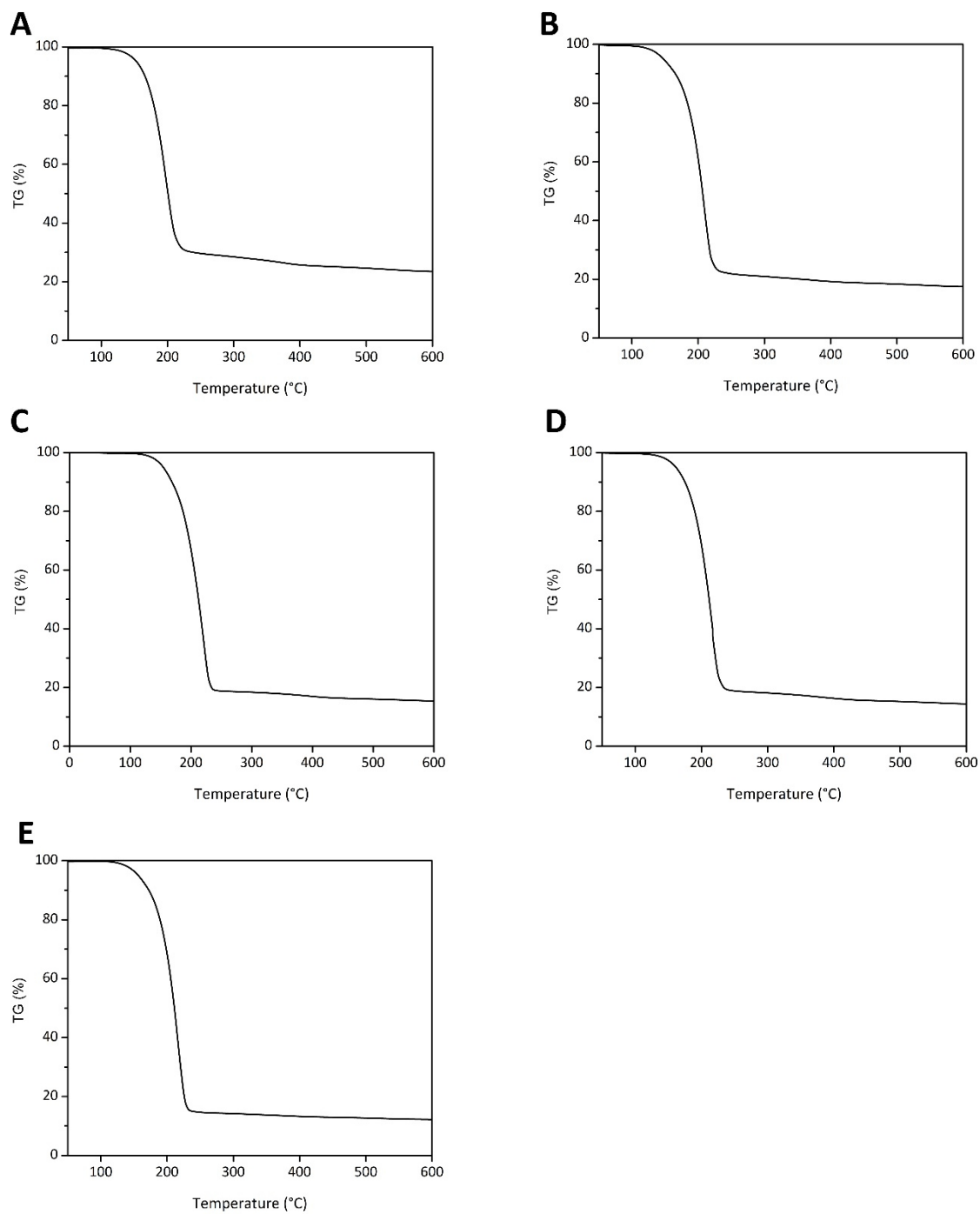


Fig. S1.8 TG curves of samples FS5100 (A), FS5125 (B), FS5150 (C), FS5175 (D) and FS5200 (E) measured with a heating rate of 1 °C min⁻¹.

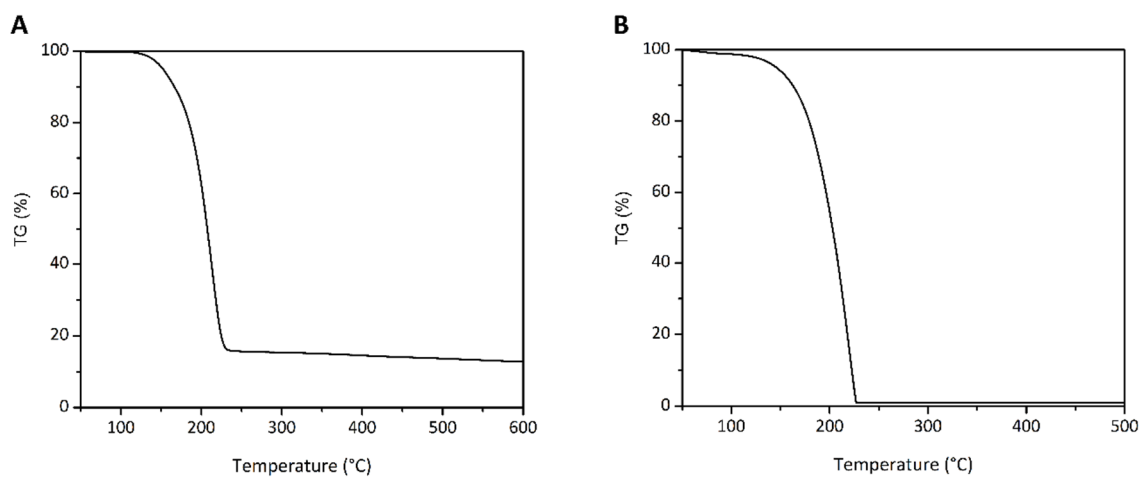


Fig. S1.9 TG curves of sample FS4 (A) and butyl stearate (B) measured with a heating rate of 1 °C min⁻¹.

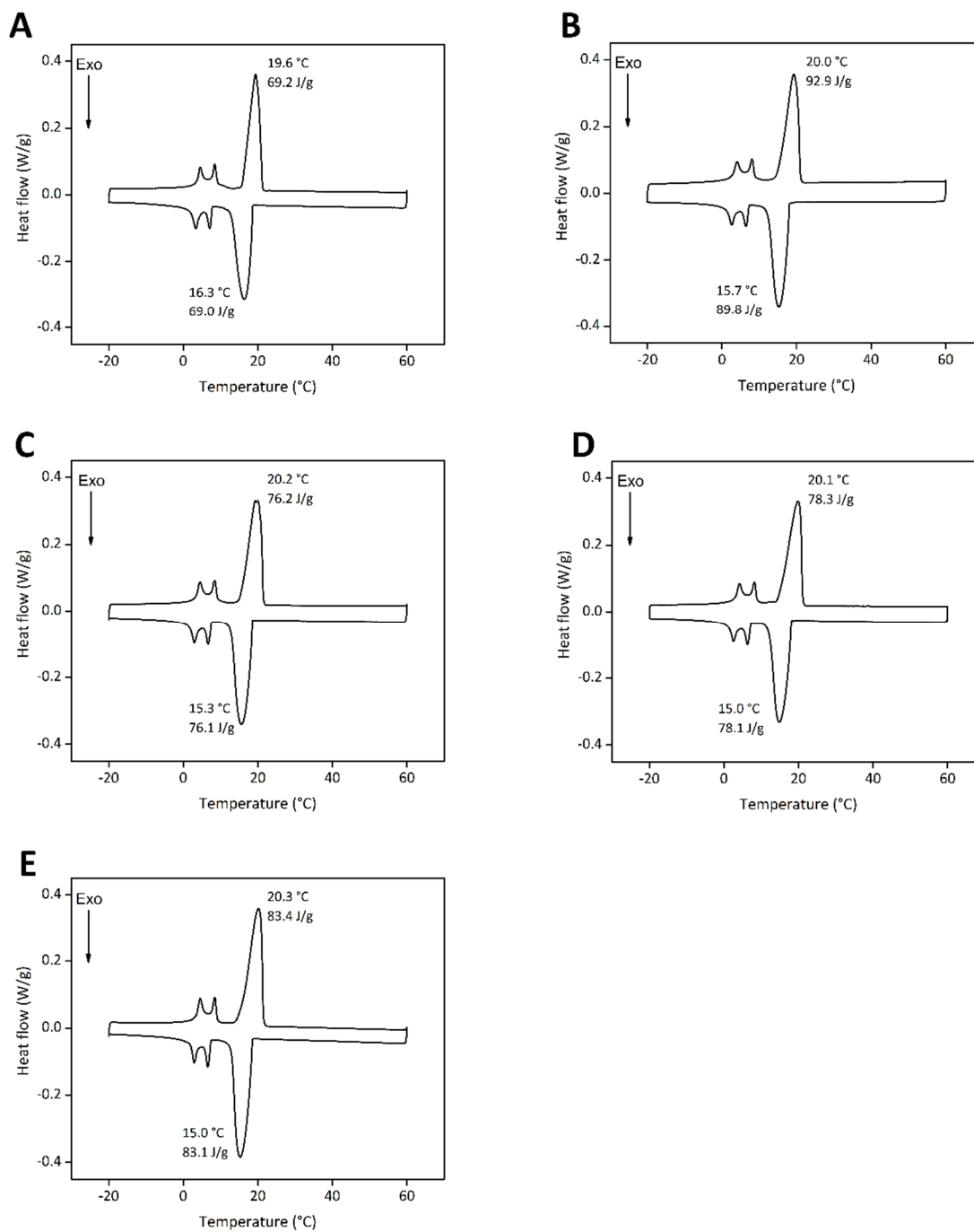


Fig. S1.10 DSC curves of ss-PCMs FS5₁₀₀ (A), FS5₁₂₅ (B), FS5₁₅₀ (C), FS5₁₇₅ (D) and FS5₂₀₀ (E) (heating rate: 1 °C min⁻¹).

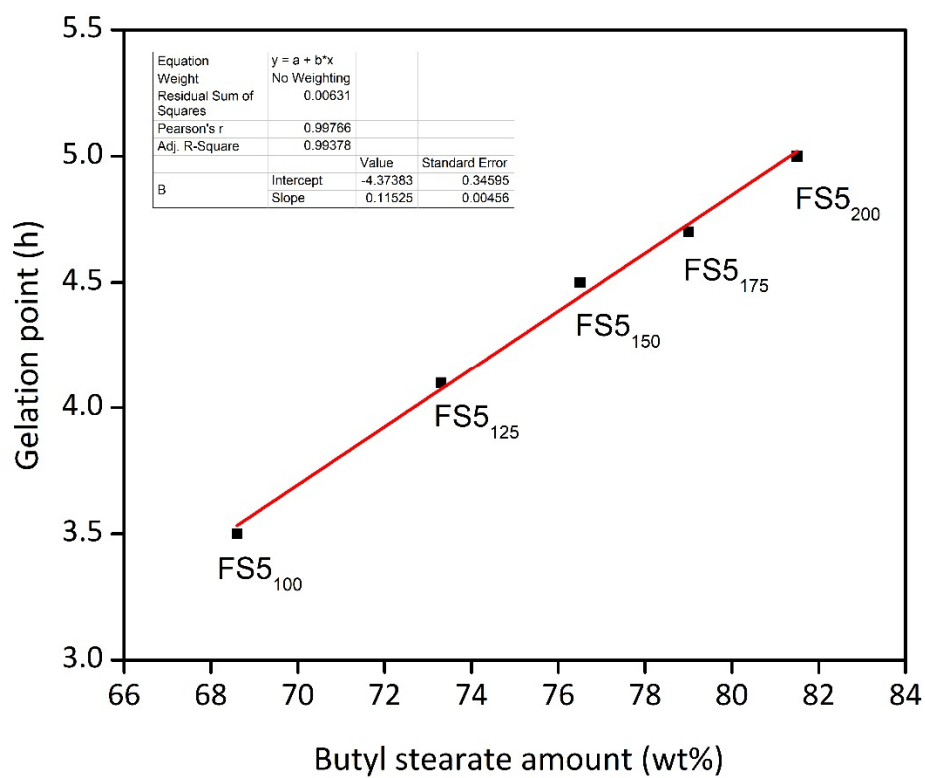


Fig. S1.11 Gelation points of samples FS5₁₀₀, FS5₁₂₅, FS5₁₅₀, FS5₁₇₅ and FS5₂₀₀.

Table S1.6 Thermal properties¹ of samples FS5₁₀₀ - FS5₂₀₀ and FS4 calculated via weighing and DSC measurements.

Sample	ΔH_{BS} (J/g)	ΔH_{total} (J/g)	T_m (°C)	ΔT_s (°C)	$Ma(PCM)_{DSC}$ (wt%)	$Ma(PCM)_{mass}$ (wt%)	$Ma(PCM)_{max}$ (wt%)	E_{DSC} (%)	E_{mass} (%)
FS5100	69	88	19.6	3.3	69.8	68.6	69.0	101	99
FS5125	73	93	20.0	4.3	73.8	73.3	73.5	100	100
FS5150	76	97	20.2	4.9	77.0	76.5	77.0	100	99
FS5175	78	100	20.1	5.1	79.6	79.0	79.5	100	99
FS5200	83	104	20.3	5.3	82.5	81.5	81.6	101	100
FS4	85	105	20.0	4.7	83.3	82.6	83.0	100	100

1: Melting enthalpy of BS signal ΔH_{BS} , melting enthalpy of whole ss-PCM ΔH_{total} , melting point of BS signal T_m , supercooling ΔT_s , mean value for effective mass fraction of PCM $Ma(PCM)_{DSC}$ (Eq. 1.1) and $Ma(PCM)_{mass}$ (Eq. 1.2), highest value for effective mass fraction of PCM $Ma(PCM)_{max}$ (Eq. 1.3) and corresponding PCM immobilization efficiencies E_{DSC} (Eq. 1.4) and E_{mass} (Eq. 1.5).

Movie S1.1

Different views of FS4.

Movie S1.2

Schematic presentation of each step to synthesize ss-PCMs via the *in situ* sol-gel process in this work.

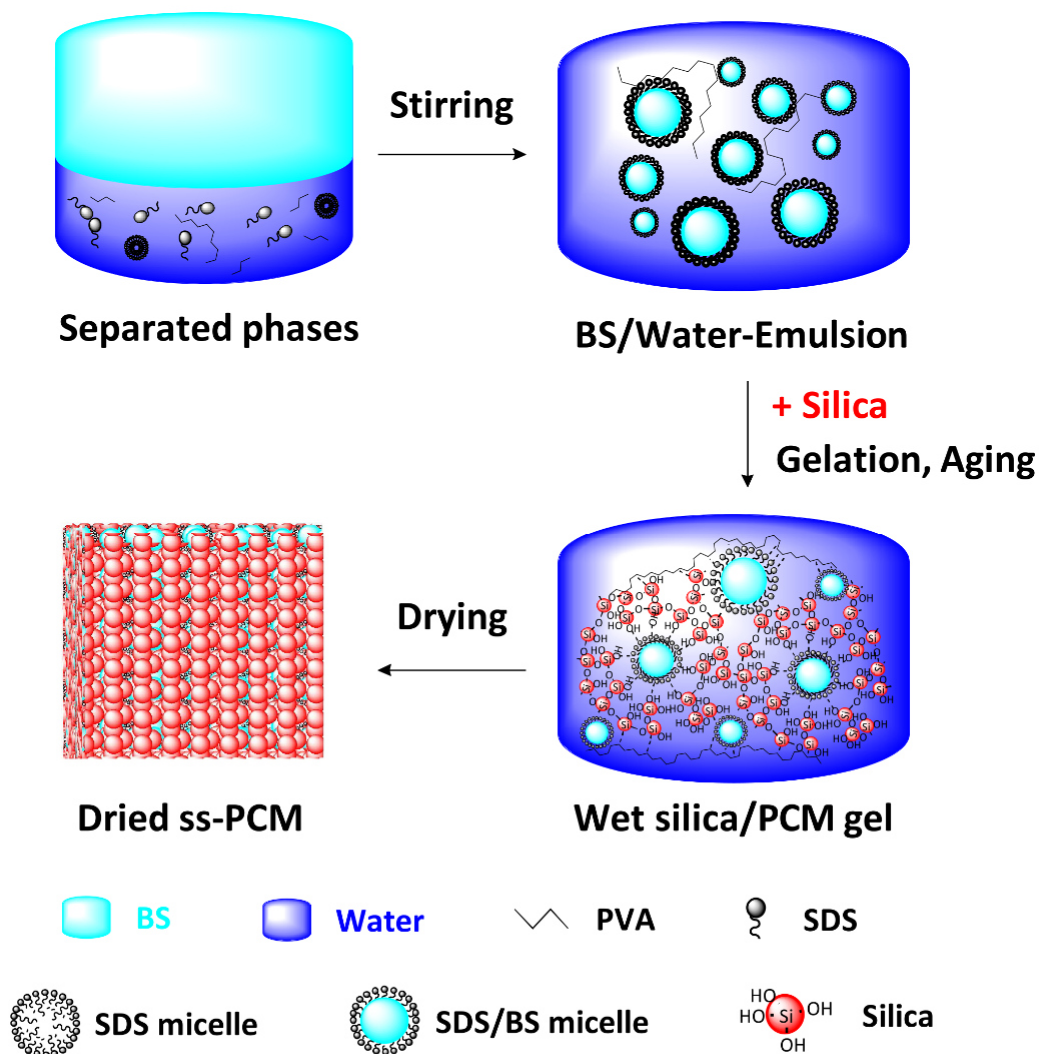
Movie S1.3

X-ray nanotomographic imaging of sample FS4 and visualization of sequential tomograms, showing the pores distribution from bottom to top.

Movie S1.4

Three-dimensional visualization of sample FS4. Segmentation of the silica framework is shown in yellow, while the filled pores are randomly coloured.

3.2 Influence of surfactants and organic polymers on monolithic shape-stabilized phase change materials synthesized via sol-gel route



Authors

Felix Marske¹, Joe Dasler¹, Caroline Haupt², Kirsten Bacia², Thomas Hahn¹ and Dirk Enke³

¹ Institute of Technical Chemistry, Martin Luther University of Halle-Wittenberg, 06120 Halle (Saale), Germany.

² Biophysical Chemistry, Institute of Chemistry and Charles-Tanford Protein Center, Martin Luther University of Halle-Wittenberg, 06120 Halle (Saale), Germany.

³ Institute of Chemical Technology, Universität Leipzig, 04109 Leipzig, Germany.

State of Publication

Accepted 25th January 2022 in *Journal of Energy Storage*

<https://doi.org/10.1016/j.est.2022.104127>

3.2.1 Abstract

Shape-stabilized phase change materials (ss-PCMs) can store up to five times more thermal energy than commercially available composite PCM boards based on core-shell PCMs, but have low mechanical stabilities. Therefore, we have recently synthesized ss-PCMs with high mechanical stability via a novel porogen-assisted sol-gel process. Here, we track the ss-PCM formation *in situ* and analyze the influence of the porogens sodium dodecyl sulfate (SDS) and poly(vinyl alcohol) (PVA) on ss-PCM properties. During gelation the silica scaffold is built around PCM droplets covered with SDS in an O/W emulsion. All ss-PCMs exhibit a high shape-stability (~100 %), a high long-term performance (> 2000 thermal cycles) and a high chemical stability, regardless of the amount of porogen used in the synthesis. Higher PVA amounts separate the emulsion in large hydrophilic and small hydrophobic regions and increase the silica macropore width in ss-PCMs from 1007 nm to 8801 nm due to silica fragmentation during drying. The silica fragmentation lowers the compressive strength (1.2 MPa) and thermal conductivity (0.37 W/mK) of the ss-PCMs by 50 % and by 17 % (10 °C), respectively. In contrast, low SDS amounts can not stabilize all PCM droplets in the emulsion from phase-separation, resulting in a partially fragmented silica phase. Too high SDS concentrations decrease the viscosity and hence, stability of the emulsion. Consequentially, the silica macropores collapse during drying, which lower the compressive strength (1.02 MPa) and thermal conductivity (0.37 W/mK) of ss-PCMs by 63 % and 25 % (10 °C), respectively.

3.2.2 Keywords

Thermal energy storage, Phase change material, Emulsion templating, Shape stabilization, Silica, Sol-gel

3.2.3 Introduction

The worldwide energy consumption and greenhouse emissions have increased by over 100 % since 1970 [1]. Approximately 22 % of the total primary energy [2] is used for space and water heating and cooling in buildings, which is why scientists focus increasingly on the development of thermal insulation and thermal energy storage materials (TES).

Promising thermal energy storage materials are organic phase change materials (PCMs), that are able to store large amounts of heat by phase transitions from solid to liquid at a certain temperature [3,4]. Typical organic PCMs are paraffins [5–7], alcohols [8–10], fatty acids [11–13], and polyethylene glycols [14–16] with high latent heats of 150 - 250 J/g. They are mostly used in photovoltaics [17], water- [18] and air-heating systems [19], wallboards [20], shutter [21], and ceilings [22] of energy-saving buildings. In contrast to inorganic PCMs, organic PCMs melt congruently and have sufficient crystallization rates during phase transition [23,24]. Incongruent melting can lead to a total loss of latent heat of the PCM after a few phase transitions. The crystallization rate of poorly self-nucleating PCMs slows down freezing and melting resulting in supercooling effects. However, organic PCMs are flammable [25], have low thermal conductivities [26,27], and can easily leak out of construction materials in liquid form [28]. To overcome these drawbacks, organic PCMs are encapsulated in micro- and nano-sized polymer-shells or porous carrier systems by capillary forces to form core-shell (cs) or shape-stabilized (ss) PCMs.

In cs-PCMs, the polymer shell acts as a physical barrier and prevents chemical reactions of the PCM core with its environment. A suitable polymer shell must be highly thermal conductive, mechanically stable and unreactive to its core material [29,30]. Silica [31–33], polyacrylates [34–36] and polyurethanes [37–39] are most widely used as shell materials according to the current literature.

PCMs must be monolithic for the application in energy-saving buildings. However, the direct incorporation of cs-PCMs or pure PCM in plaster, concrete and stones is limited to 5 - 30 wt%, drastically decreasing the overall latent heat [40]. For example, the overall latent heat of cs-PCM Micronal DS 5040 X (by Microtek Laboratories) decreases from 200 J/g for pure paraffin to 100 J/g [3] when encapsulated in a polyacrylate shell and to maximally 30 J/g when further added to construction materials [41]. Several studies have also shown a drastic loss of the overall compressive strength of construction materials after cs-PCM impregnation [42–44].

Shape-stabilized PCMs can be synthesized for example via melt infiltration under vacuum [45], macroencapsulation, sol-gel [14,16,46] and by addition of binder materials (cement [47], clay [48], graphite [5], vermiculite [49]) to produce blends as monoliths or fragments [50]. The

simplest synthesis of ss-PCMs is the impregnation of a porous structure with liquid PCM by melt infiltration, mostly assisted by vacuum [51]. For example, Xiangfa *et al.* [52] synthesized silica aerogels as porous carrier matrix via sol-gel and confined up to 85 wt% erythritol as PCM in the nanoporous silica structure by heating the PCM with the silica aerogel until all PCM was melted (melt infiltration). The silica carrier did not react with the PCM, indicating a high chemical stability of erythritol in silica structures. In comparison, blending and rapidly cooling methods enable the synthesis of ss-PCMs with higher PCM amounts of approximately 80 wt% via styrene-butadiene-styrene [50,53] or high-density polyethylene [54,55]. The liquid PCM and supporting material are mixed and cooled below the glass transition temperature of the supporting material until solidity is reached. The low thermal conductivity of the organic supporting materials without control over the PCM distribution is the major drawback of blending methods. Direct mixing of PCM with highly thermal conductive additives, such as expanded graphite [14], copper nanowires [56] or boron nitride [57], can increase the thermal conductivity of the PCM, but the mechanical stability and flammability of such ss-PCMs is still insufficient for many industrial applications. For a higher flame retardancy and mechanical stability of ss-PCMs, porous silica is a promising material due to its large specific surface area, low density, controllable pore structure, high adsorption capacity, high mechanical stability and high fire resistance [14,16,58,59].

In the past, ss-PCMs synthesized via sol-gel and silica as starting material were not monolithic without further extrusion techniques. The extrusion technique decreases, however, the long-term performance and increases the tendency of phase separation of silica and PCM by destroying the silica structure. Additionally, the mechanical and form stabilities of this ss-PCM class at higher PCM loadings were low or not characterized in these studies [14,46]. For example, Li *et al.* [14] synthesized a ss-PCM via sol-gel starting from tetraethyl orthosilicate (TEOS) as silica source and polyethylene glycol (PEG) as PCM with PCM mass fractions up to 80 wt%. Problematically, the ss-PCMs were not monolithic after shape-stabilization and the latent heat (50 wt% PCM) was 32.7 % lower after 3-times of melting and freezing of the PCM in the ss-PCM structure, indicating a low long-term performance. Via a novel CaCl₂-assisted sol-gel process, He *et al.* [46] synthesized broken ss-PCM pieces with PCM (PEG) mass fractions of ~80 wt% and grinded the product to powder for the usage of their product as additive. Despite the promising thermal properties and high PCM loading, the mechanical stability, long-term performance over 1000 thermal cycles and the silica pore structure were not analyzed in these studies.

In our recent studies, we were able to synthesize for the first-time silica-based ss-PCM as monolithic boards with high compressive strengths (1.2 MPa at 10 °C, 0.7 MPa at 30 °C), high long-term performances of 6000 melting and freezing cycles as well as high PCM loadings

(85 wt%) via a novel porogen-assisted *in situ* sol-gel process and stabilized silica sol for applications in need of a high mechanical stability, such as construction materials in buildings (roof, walls) [60]. These ss-PCMs consisted of a hierarchical and interconnected meso-macroporous silica structure with average pore diameters over 1000 nm, which showed no degradation reactions with the PCM and, thus, enables high chemical stabilities of the confined PCM. Additionally, we enhanced the thermal conductivity of our ss-PCMs by 345 % via hexagonal boron nitrides (20 wt%) to expand their application ratio, for example for the rapid cooling of batteries [61]. However, the *in situ* formation of the ss-PCMs were not analyzed and the role of the porogen was not fully understood in our previous studies, which is important for the development and improvement of novel or similar synthesized ss-PCMs in the future

For this reason, we further investigate the *in situ* ss-PCM formation mechanism and the function of the porogens sodium dodecyl sulfate (SDS) and poly(vinyl alcohol) (PVA) in the *in situ* sol-gel process by varying their amounts during synthesis. A novel confocal microscopy method is established to differentiate the PCM, silica and aqueous phase separately from each other and, thus, to track the *in situ* silica formation during gelation and aging in detail. This method and the used fluorescent dyes should be interesting for a deeper insight in the xero- or aerogel synthesis in sol-gel science, too. Moreover, we control for the first time the shape and width of silica pores formed around PCM droplets during ss-PCM synthesis and, thus, the mechanical and thermal properties of the resulting ss-PCMs. By adding higher amounts of SDS to the reaction mixture, we increased the compressive strength of our ss-PCMs by 150 % from 0.41 MPa (10 °C, 0.6 g SDS) to 1.02 MPa (10 °C, 1.2 g SDS). With the results from this study, the properties of ss PCMs synthesized via sol-gel can be adjusted for different applications field in need of a high mechanical stability or/and a high latent heat in the future.

3.2.4 Experimental

3.2.4.1 Materials

Butyl stearate (BS, technical grade product) and polyvinyl alcohol (PVA, 88 % hydrolyzed, average M.W. 22000) were purchased from Alfa Aesar and ACROS Organics, respectively. Sodium dodecyl sulfate (SDS, dust-free pellets, ≥99.0 % GC) and perylene were obtained by Sigma Aldrich. The stabilized silica sol Köstrosol 0730 was provided by Chemiewerk Bad Köstritz, Germany. Deionized water was used for all syntheses. AlexaFluor 488 hydrazide and FM1-43 (N-(3-Triethylammoniumpropyl)-4-(4-(Dibutylamino) Styryl) Pyridinium Dibromide) were purchased from ThermoFisher Scientific.

3.2.4.2 Preparation of ss-PCMs

1 g polyvinyl alcohol (PVA) was dissolved in 6.75 g water at 60 °C and added to a reaction mixture of 0.8 g sodium dodecyl sulfate (SDS) and 20 g butyl stearate (BS) in a polypropylene beaker. The suspension was heated to 50 °C for at least 6 h and stirred for 15 min at 700 rpm and 25 °C. Then, 9 g Köstrosol 0730 was added dropwise to the reaction mixture and stirred for another 15 min at 700 rpm and 25 °C. The polypropylene beakers were closed after the removal of the magnetic stirrer and heated to 40 °C for 3 days for gelation and aging. Afterwards, the wet gel was dried at 40 °C for 4 days and then at 100 °C for 20 h at ambient pressure in a circulating air oven to obtain monolithic ss-PCMs.

3.2.5 Characterization

Differential scanning calorimetry (DSC) was carried out on an 822e calorimeter by METTLER TOLEDO with a heating rate of 1 °C/min in a temperature range from -20 °C to 60 °C (holding times: 10 min). Every sample (15 mg) was measured at least five times. The peak integral was used to calculate the latent heat ΔH_{BS} (BS peak) and ΔH_{total} (all peaks). The average relative uncertainty of the latent heat was $\pm 3.22\%$. The highest and lowest temperature of the peak (peak maximum and minimum) of the DSC measurements were used to determine the melting and freezing points T_{m1} and T_{f1} . At the temperatures of T_{m1} and T_{f1} , the highest fraction of PCM is undergoing a phase transition in the silica structure of the ss-PCM from liquid to solid and vice versa. Additionally, the DSC onset temperatures of the melting and freezing peaks were taken as melting and freezing points T_{m2} and T_{f2} , respectively. These temperatures are the starting point of the melting and freezing process of BS and do not depend on the heating rate or mass fraction used for the measurements. To calculate the supercooling of PCM in the ss-PCM, the melting point T_{m1} (or T_{m2}) was subtracted from the freezing point T_{f1} (or T_{f2}).

Long-term performance tests of the ss-PCMs were carried out via a Primus 96 Thermal Cycler from MWG Biotech by heating the samples 2000-times between 8 °C and 60 °C. After thermal cycling, the samples were measured via DSC according to the already described procedure. The thermal conductivity was analyzed via a Hot Disk TPS 1500 thermal analyzer by Hot Disk AB based on a transient plane source method (TPS) at 10 °C and 30 °C. For sample preparation, all ss-PCM samples were sawed in the middle in two halves. The sensor and heater unit was put between the two halves of one sample and measured on three different spots in a sandwich-mode [61]. Every spot was measured three times (waiting period between measurements: 10 min) and the average values of the measurements were calculated for one sample. The average relative uncertainty of all measurements was $\pm 0.65\%$.

Thermogravimetric analysis (TG) of the samples was carried out on a STA 409 C/CD thermal analyzer by Netzsch to analyze the influence of SDS and PVA on the decomposition points of BS in the ss-PCMs. An amount of approximately 100 mg of the ss-PCMs was used for the measurements and heated up from room temperature to 700 °C with a heating rate of 1 °C/min under air atmosphere. The decomposition points were calculated via OriginLab 8.1 by the maximum of the first derivative of the TG curves.

The compressive strength of the ss-PCMs was measured on a TBH355 hardness tester by ERWEKA. Every sample with the same chemical composition was synthesized five times and measured at 10 °C and 30 °C for the mean compressive strength of the solid and liquid PCM in the solid ss-PCM, respectively. The average uncertainty over all measurements was $\pm 2.55\%$. For 'broken' samples, fragments were measured to determine a value for their compressive strengths. The pH value of the reaction mixture was measured with a Seven Easy pH electrode by METTLER TOLEDO. The gelation times were determined by turning the polypropylene beaker filled with gel upside down. This procedure was performed for 5 to 10 samples synthesized with the same amounts of chemicals. If the gel was not moving in this position, the gelation was considered as completed. The average values of all measurements had a relative uncertainty of approximately $\pm 5\%$. The shape-stability of the ss-PCM was determined by the difference of the weight before and after sample heating at 100 °C for 7 days.

Chemical degradation reactions of BS, PVA, silica and SDS were characterized via attenuated total reflection Fourier transform infrared (ATR-FTIR) spectroscopy. The samples were measured 32-times as pure substances between 4000 cm^{-1} to 200 cm^{-1} (resolution: 4 cm^{-1}) in a Tensor 27 spectroscope (Bruker) equipped with a diamond ATR unit.

The pore structure was analyzed for dried and calcined samples (600 °C, 10 h). About 100 mg sample was measured via mercury (Hg) intrusion on a Pascal140 (400 kPa) and Pascal440 (400 MPa) instruments (Porotec) to analyze macroporosity. The pore diameter (pore width) and pore volume were determined by calculations via the Washburn-equation, assuming a cylindrical pore model [62]. The contact angle of mercury was 141.3°. Nitrogen sorption (N_2) measurements were performed for each calcined sample (100 - 150 mg) at -196 °C using a Sorptomatic 1990 surface area analyzer (Porotec). The specific surface area, mesopore volume and mesopore diameter (width) of the calcined ss-PCM was calculated via the Brunauer-Emmett-Teller (BET) method [63]. Before measurements, all ss-PCM samples were dried at 120 °C under ultrahigh vacuum. The specific surface area was obtained using the linearized form of the BET equation (range of $0.05 \leq p/p_0 \leq 0.30$). The mesopore volume was determined at a relative pressure p/p_0 of 0.99. The mesopore volume calculated via N_2

sorption experiments was added to the macropore volume calculated via Hg measurements to obtain the total pore volume of the calcined ss-PCM.

Scanning electron microscope (SEM) images were taken on a Leo Gemini 1530 Zeiss scanning electron microscope with a secondary electron acceleration of 10 kV. The samples were placed on a conductive carbon tape for imaging. Confocal microscopy was performed on a Zeiss LSM 980 inverted microscope with an Airyscan detector (Carl Zeiss Microimaging, Jena, Germany) using 20× (LD Plan-Neofluar) and 50× (LD C-Epiplan-Apochromat) objectives with an N.A. of 0.4 and 0.6, respectively. Samples with a volume of 4 μL were prepared on glass coverslips equipped with a silicon ring as spacer and covered by a second coverslip. After gelation and aging, the upper coverslip was punctured and broken to allow for air-drying. Perylene (0.4 μM final concentration) was used to label the hydrophobic phase and was excited with a diode laser at 405 nm [64]. The water-soluble, green-fluorescent dye Alexa Fluor 488 hydrazide (a sulfonated derivative of Rhodamine Green) was used as a marker for the hydrophilic phase and the silica structures [65]. In a second approach, the amphiphilic, green-fluorescent dye FM1-43, previously described as a label for hydrophobic-hydrophilic interfaces, was added to the sol-gel reaction mixture [66]. Alexa Fluor 488 and FM1-43 containing samples (final concentration of 0.4 μM and 1 μM , respectively) were excited by a diode laser at 488 nm. Fluorescence emission was collected using the AiryScan detector. The two-color images were acquired in the line-wise multi-track mode.

3.2.6 Results and discussion

3.2.6.1 Tracking of ss-PCM formation via *in situ* sol-gel process

We emulsified the PCM phase as droplets in an aqueous phase in the first step of our sol-gel process. To obtain a stable PCM in water emulsion, we used the water-soluble surfactant SDS and the water-soluble polymer PVA.

To study the sol-gel synthesis of our ss-PCMs, we used confocal fluorescence laser scanning microscopy to visualize the formation of the ss-PCM PVA060 (Fig. 2.1), which is similar to sample FS4 in our previous study [57].

After 15 min of the gelation process (Fig. 2.1 (A, B)), the PCM phase has emulsified as droplets (blue) in a continuous aqueous phase (green). The PCM droplet size varies from approximately 0.5 μm to 10 μm . The PCM droplet size distribution as well as the electro-kinetic potential of the emulsion could not be analyzed by dynamic light scattering (DLS) and zeta-potential

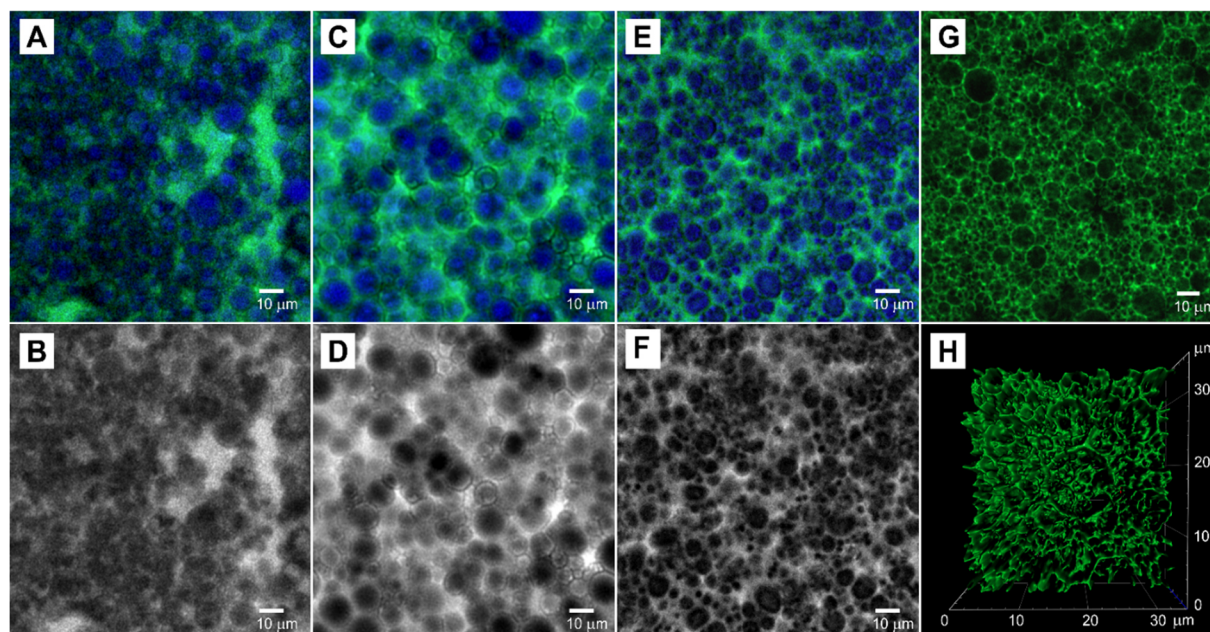


Fig. 2.1 Confocal fluorescence microscopy of the formation process of ss-PCM PVA060 after sol addition and a reaction time of 15 min (A, B), 48 h (C, D) and 72 h (E, F). The hydrophobic phase is labelled in blue with the dye perylene (A, C, E) and the hydrophilic phase is labelled with the soluble green dye Alexa Fluor 488 (A, C, E). For a detailed view of the behaviour of the aqueous phase during gelation and aging, single-color images of the hydrophilic Alexa Fluor 488 are shown (B, D, F). For a more precise analysis of the drying process after 4 d (G) and 8 d (H), the green fluorescent dye FM1-43 was added to the reaction mixture to probe only the silica matrix. (H) Three-dimensional surface rendering based on an axial stack of images.

measurements due to the individual components in the sol-gel synthesis and the high viscosity of the reaction mixture, respectively.

Emulsification of the PCM phase (approx. 65 vol%) as droplets is in line with the high Hydrophile-Lipophile Balance (HLB) value of SDS of 40 [62]. According to the Bancroft rule [63], a surfactant with a HLB value over 10 covers hydrophobic oil droplets in a continuous aqueous phase.

After 48 h (Fig. 2.1 (C, D)) the gelation of ss-PCM PVA060 (gelation time: 29 h) is already completed. All the PCM droplets are covered by black circles at this point in the fluorescence microscopy images. These black circles represent the silica polymer growing on top of the

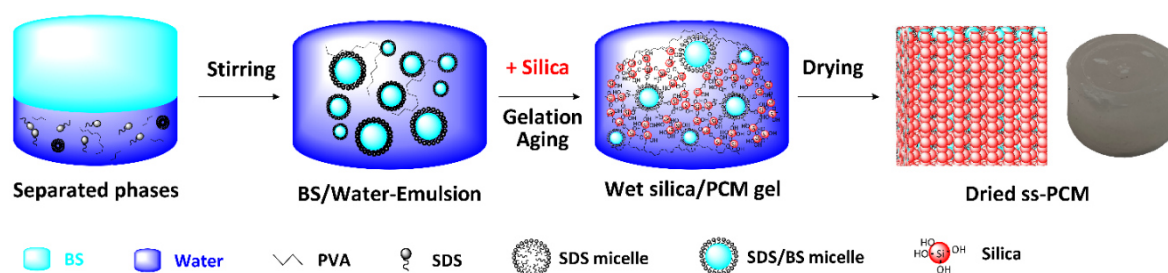


Fig. 2.2 Formation mechanism of monolithic ss-PCM via *in situ* sol-gel.

spherical PCM droplets and encapsulating the PCM in solution. Thus, the SDS-stabilized PCM droplets act as template for the silica structure during the sol-gel synthesis. All PCM droplets covered by the silica phase are connected to each other. In contrast to the emulsion after 15 min, the PCM droplets are separated by larger areas of the aqueous phase, which could be formed as a side effect of PVA. The water-soluble polymer PVA is expected to interact with the growing silica polymer in solution. Acting as a structure-directing agent, the PVA may decrease the solubility of the silica polymer in the aqueous phase, leading to a polymer-induced phase separation process [64]. After 72 h (Fig. 2.1 (E, F)) the spherical silica/PCM droplets have partially rearranged in the aging process and are arranged closer together, mainly due to synereses and Ostwald ripening effects. During drying the water evaporates from the water-filled porous channels, which are located between the spherical silica pores filled with PCM (Fig. 2.1 (G, H)). According to the literature [65], the drying process should be driven by film diffusion due to the low drying temperatures in our work. In this process the ss-PCM shrinks, the silica polymer is expected to form more siloxane bonds leading to a higher interconnectivity due to synereses effects, and the compressive strength of the ss-PCM increases from 10 kPa to 700 kPa at 30 °C. As a consequence, the silica structure shows no aqueous phase (green), and the different dyes, albeit only to a limited degree, are overlapping. The final silica structure is comparable to the SEM and XRM images of the similar synthesized sample FS4 from our previous study [57]. The surfactant SDS partitions to the interface of the PCM droplets and the surrounding aqueous phase. The silica polymer is formed around the SDS-coated PCM-droplets in the *in situ* sol-gel process, as illustrated in Fig. 2.2 and Movie S2.1.

3.2.6.2 Influence of PVA on physicochemical properties of ss-PCMs

We synthesized five different ss-PCMs with PVA amounts ranging from 0.6 g (PVA060) to 1.2 g (PVA120) via *in situ* sol-gel to investigate the influence of PVA on the silica structure and, thus, on the mechanical and thermal properties of our ss-PCMs. The SDS amount was kept constant at 0.8 g [60]. No strong chemical interactions or chemical degradation processes of SDS, BS and PVA in the silica phase of the ss-PCM were detected via attenuated total reflectance Fourier transform infrared spectroscopy (ATR-IR) (detailed analysis in supplementary, Fig. S2.1 - S2.4.). All ss-PCM samples were heated to 100 °C for 7 days to test the shape-stability and potential PCM leakage by weighing the ss-PCMs before and after heating. Samples PVA060 to PVA105 had the same weight before and after the heat treatment, pointing to a high shape-stability of approximately 100 %. In contrast, a thin PCM film covered the outer surface of ss-PCM PVA120 and the weight of PVA120 was 2 % lower after shape-stability tests, indicating PCM leakage for samples synthesized with 1.2 g PVA.

Table 2.1 Physicochemical properties¹ of ss-PCMs PVA060 - PVA120 synthesized with 9 g Köstrosol 0730, 0.8 g SDS, 6.75 g H₂O, 20 g BS and 0.6 g (PVA060) to 1.2 g (PVA120) PVA.

Sample	$M(PVA)$ (g)	ϕ (%) ^{a,b}	V_{total} (cm ³ /g) ^{a,b}	V_{macro} (cm ³ /g) ^a	V_{meso} (cm ³ /g) ^b	D_{macro} (nm) ^a	D_{meso} (nm) ^b	A_{meso} (m ² /g) ^b	pH	GT (h)	σ at 10 °C / 30 °C (MPa)	T_D (°C)
PVA060	0.60	5	0.025	0.025	-	250	-	-	9.2	29	1.24 / 0.68	216
PVA075	0.75	12	0.061	0.060	-	4412	-	-	9.0	18	1.12 / 0.55	210
PVA090	0.90	15	0.081	0.081	-	5253	-	-	8.8	10	0.95 / 0.42	209
PVA105	1.05	6	0.030	0.030	-	83	-	-	8.6	7	0.86 / 0.38	205
PVA120	1.20	12	0.064	0.064	-	27348	-	-	8.5	6	0.58 / 0.34	205
PVA060c ^c	0.60	95	7.80	6.98	0.82	1007	8	181	-	-	-	-
PVA075c ^c	0.75	95	7.79	7.02	0.77	1442	10	226	-	-	-	-
PVA090c ^c	0.90	95	8.10	7.39	0.71	1868	10	216	-	-	-	-
PVA105c ^c	1.05	95	8.00	7.32	0.68	2451	8	239	-	-	-	-
PVA120c ^c	1.20	95	8.09	7.55	0.54	8801	9	181	-	-	-	-

1: Mass of PVA $M(PVA)$ used in the synthesis of the ss-PCMs, porosity ϕ , total pore volume V_{total} , macropore volume V_{macro} , mesopore volume V_{meso} , mean macropore width/50% D_{macro} , mean mesopore width /50% D_{meso} , mesopore surface area A_{meso} , pH value, gelation time GT , compressive strength σ and decomposition point T_D of BS in ss-PCMs.

a: determined from mercury intrusion.

b: determined from nitrogen sorption.

c: ss-PCMs obtained after calcination for 10 h at 600 °C.

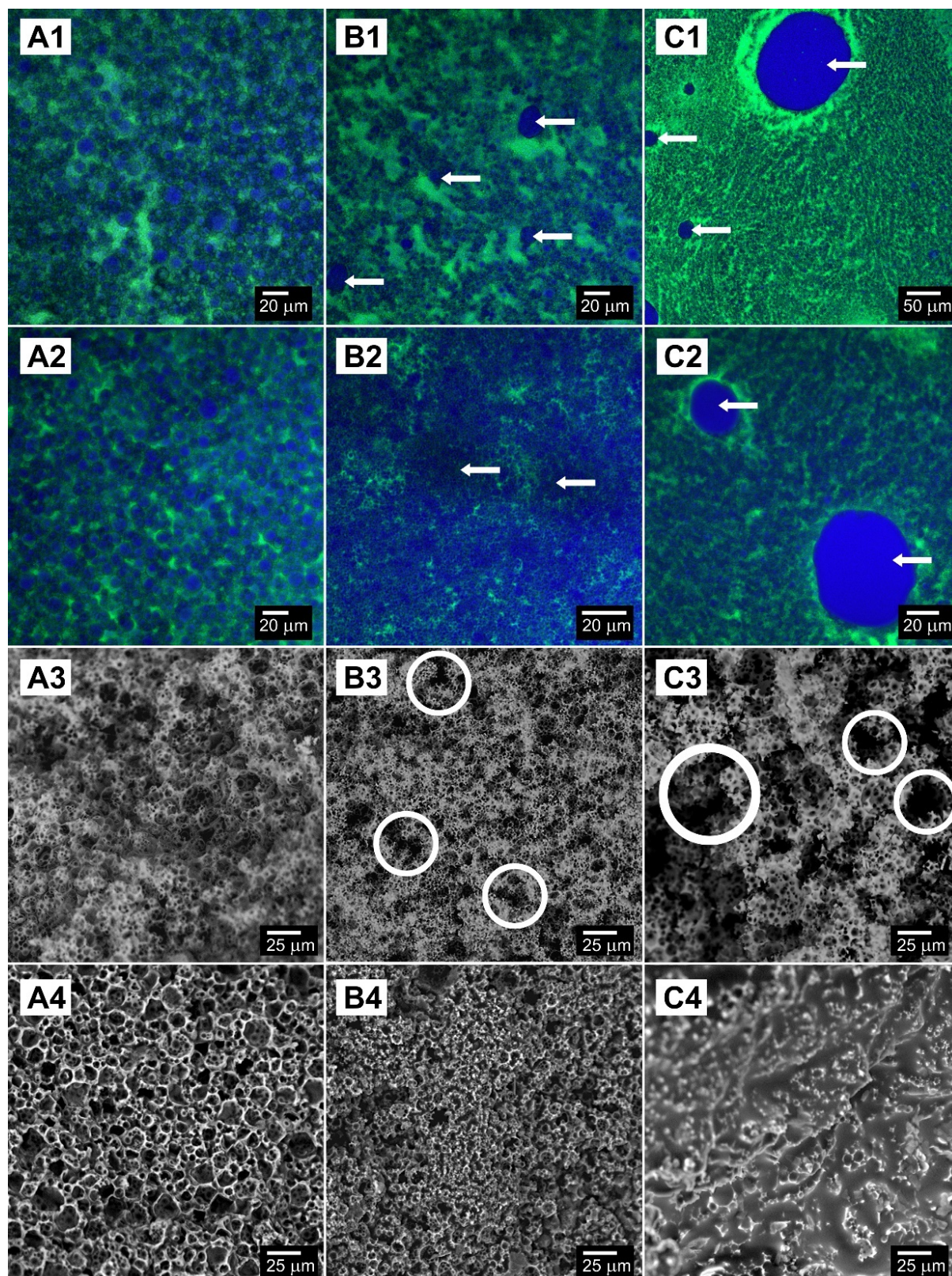


Fig. 2.3 Imaging of ss-PCM formation of PVA060 (A), PVA090 (B) and PVA120 (C) during gelation after 15 min (1) and 24 h (2) by confocal fluorescence microscopy, and after calcination (3) and drying (4) by scanning electron microscopy. In the fluorescence images, the hydrophobic phase is labelled in blue with perylene and the hydrophilic phase is labelled in green with Alexa Fluor 488. Areas with a higher PCM concentration are marked with an arrow in fluorescence microscopic images. Fragmented silica structures are circled in scanning electron microscopic images.

When PVA amounts lower than 0.6 g are used for the synthesis, the reaction mixture separates into macroscopic oil and aqueous phases. We reported earlier that fragmented ss-PCMs can be synthesized without PVA addition [60]. Therefore, low amounts of PVA seem to destabilize the BS/water-emulsion. When PVA amounts higher than 1.2 g are used for the synthesis, the color of the solution turns from translucent to opaque and the viscosity increases, indicating the start of gelation. However, a solid wet gel is not formed even after five days. To understand this effect, we analyzed the gelation and aging process of our samples by fluorescence microscopy. At a low PVA amount in ss-PCM (PVA060), the spherical PCM-droplets (blue) with a droplet width of $\sim 1 \mu\text{m}$ to $20 \mu\text{m}$ are covered by a silica phase (black) after gelation for 15 min (Fig. 2.3 (A1 - C1)). When the PVA amount is, however, increased from 0.6 g to 1.2 g, the aqueous phase (green) is more phase-separated from the hydrophobic PCM phase (blue) and the viscosity increases, resulting in small PCM droplets with widths below $1 \mu\text{m}$ and some bigger PCM droplets with widths up to $100 \mu\text{m}$ (PVA120). The viscosity of the reaction mixture is higher in sol-gel syntheses, when the gelation times are shorter or long-chain polymers are added [71]. Additionally, a decrease of the oil droplet diameter or lower temperatures increase the viscosity of o/w emulsions [72]. Therefore, the stirring rate during the synthesis of PVA120 is lower than of PVA060 due to the higher viscosity of PVA120.

Additionally, the distances between the phase-separated PCM droplets (PVA120) with widths above $20 \mu\text{m}$ vary strongly between $100 \mu\text{m}$ and $1000 \mu\text{m}$. Therefore, PVA acts as a typical structure-directing agent during the sol-gel synthesis and induces phase-separated, hydrophilic regions in the emulsion, which serves as templates for the pore structure during gelation. After 24 h during the gelation process (Fig. 2.3 (A2 - C2)), the PCM/silica-droplets of all samples coalesce to form “worm”-like PCM-patches. The higher the PVA amount in the samples, the stronger is the coalescence effect of the PCM-droplets to “worm”-like PCM-patches during gelation. According to the current literature [73,74], an increased amount of PVA results in a stronger phase separation tendency of emulsions and can disturb the gelation process by shielding silica aggregates via the formation of hydrogen-bonds with the silanol-groups of the silica phase. Therefore, the phase separation of the emulsion with PVA amounts above 1.2 g could be too fast compared to the gelation to form stable silica structures in our work.

During the drying process, the aqueous phase evaporates and the silica surrounding the PCM-droplets might form a strongly interconnected silica matrix through synereses effects and polycondensation reactions, which only consists of the spherical silica structures filled with PCM (Fig. S2.5). For the microstructure analysis of the dried ss-PCM, the samples PVA060 to PVA120 were calcined at $600 \text{ }^\circ\text{C}$ for 6 h to distinguish pores filled with air from pores filled with PCM and named PVA060c to PVA120c (Table 2.1). The mercury intrusion, nitrogen sorption

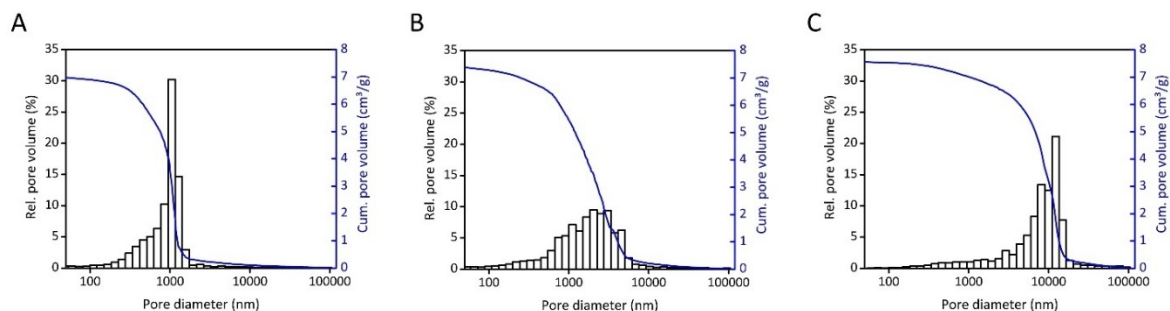


Fig. 2.4 Mercury intrusion measurements of calcined ss-PCM sample PVA060c (A), PVA090c (B) and PVA120c (C).

(Fig. S2.6), and scanning electron microscopy experiments showed for all calcined ss-PCM samples macro- and mesopores up to approximately 100 μm , which vary in pore widths and silica connectivity depending on the PVA concentration (Fig. 2.4).

Lowering the PVA amount used in the synthesis from 1.2 g (PVA120) to 0.6 g (PVA060) leads to a decrease of the mean macropore width from 8801 nm to 1007 nm, accompanied by an increase of the mesopore volume from 0.54 cm^3/g to 0.82 cm^3/g , respectively (Fig. 2.4, Table 2.1). The larger mean macropore width of PVA120c is probably a result of the increased amount of “broken” and fractured spherical silica pore structures in the micrometer range and the larger silica pores above 20 μm (Fig. 2.4 (C)). These “broken” silica pores should be the same silica structure as the “worm”-like silica patches in the fluorescence images (Fig. 2.3 (C2)).

The higher interconnectivity of the silica matrix at low PVA content appears to be the reason for the two-fold higher compressive strength σ of sample PVA060 ($\sigma = 0.68$ MPa at 30 $^\circ\text{C}$; $T_D = 216$ $^\circ\text{C}$) compared to sample PVA120 ($\sigma = 0.34$ MPa at 30 $^\circ\text{C}$; $T_D = 205$ $^\circ\text{C}$) (Table 2.1). Additionally, the decomposition point of BS in PVA060 ($T_D = 216$ $^\circ\text{C}$) is 11 $^\circ\text{C}$ higher than that of BS in PVA120 (Fig. S2.7, Table 2.1). PVA120 could have a lower thermal stability because of a higher mean macropore diameter of the silica structure (8801 nm) than PVA060 (1007 nm) (Fig. 2.4). Therefore, the evaporation of liquid PCM could be facilitated through larger silica pore channels during thermogravimetric analysis. In contrast to the mean macropore width, the total pore volume of samples PVA060c - PVA120c is nearly constant at 8 cm^3/g and appears, thus, not to be affected by the amount of PVA used for the synthesis. The gelation times are strongly influenced by the amount of PVA used for the ss-PCM synthesis. For example, the gelation process of PVA060 takes 23 h longer than that of PVA120 (Table 2.1). In accordance with our previous studies [60], the higher viscosity of the reaction mixture of sample PVA120 could accelerate the gelation process compared to PVA060.

In summary, the PVA amount used in the ss-PCM synthesis increases the width of BS droplets in water and decreases the pH-value. To our knowledge, the investigation of the influence of

PVA on pore widths constitutes the first example of controlling pore and silica structures in ss-PCMs synthesized via *in situ* sol-gel [75].

We further investigated the influence of PVA on the thermal properties of the ss-PCMs via differential scanning calorimetry (DSC) (Fig. 2.5), mass calculations (Table 2.2) and thermal conductivity measurements (Fig. 2.6). With an increased PVA mass fraction of the ss-PCMs, the thermal conductivity of PVA060 (366 mW/mK, 10 °C) to PVA120 (305 mW/mK, 10 °C) is decreased by 61 mW/mK (Fig. 2.6) and the supercooling ΔT_{s1} is increased by 0.8 °C, possibly due to the higher average macropore width of the silica phase and the lower compressive strength of PVA120 (Fig. 2.4, Table 2.1).

The supercooling of PCM ΔT_{s1} is calculated via the difference of the melting point T_{m1} and the freezing point T_{f1} , which are described as the temperature of the highest conversion rate of PCM from liquid to solid or vice versa during state transition. In contrast, the melting points T_{m2} calculated via the onset temperature of the DSC melting peak are independent from mass or heating rate changes during the measurements. The change of the melting points T_{m2} and the corresponding supercooling temperatures ΔT_{s2} of the PVA sample row (Table 2.2) are within the standard deviation of the DSC, indicating no effect of the PVA mass fraction on the melting points and supercooling temperatures of the PCM after shape-stabilization.

The melting enthalpies decreased from 85 J/g to 82 J/g for PVA060 to PVA120 as a result of the PVA addition without affecting the efficiencies E_{mass} and E_{DSC} (Table 2.2).

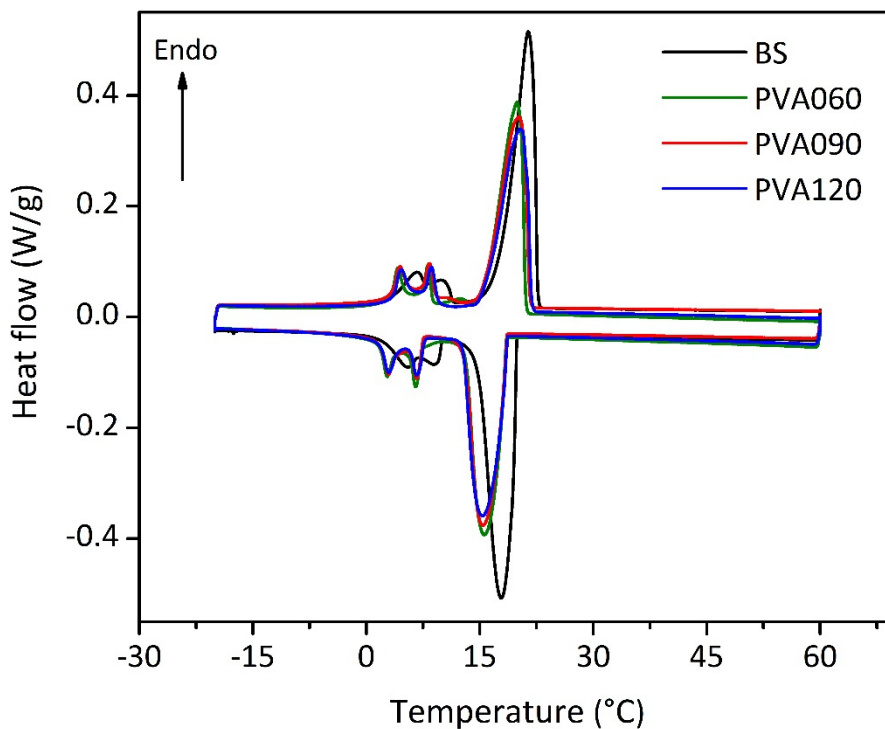


Fig. 2.5 DSC curves of BS (black), PVA060 (green), PVA090 (red) and PVA120 (blue).

Table 2.2 Thermal properties¹ of pure BS and samples PVA060 - PVA120 calculated via mass calculations and DSC measurements.

Sample	ΔH_{BS} (J/g)	ΔH_{total} (J/g)	T_{m1} (°C)	U_{Tm1} (%)	ΔT_{s1} (°C)	$U_{\Delta T_{s1}}$ (%)	T_{m2} (°C)	U_{Tm2} (%)	ΔT_{s2} (°C)	$U_{\Delta T_{s2}}$ (%)	$Ma(PCM)_{DSC}$ (wt%)	$Ma(PCM)_{mass}$ (wt%)	$Ma(PCM)_{max}$ (wt%)	E_{DSC} (%)	E_{mass} (%)
BS	102	126	21.7	0.32	4.1	0.51	17.7	0.13	2.5	0.20	-	-	-	-	-
PVA060	85	105	20.0	0.78	4.7	1.18	15.7	0.18	2.4	0.41	83.3	82.6	83.0	100.4	99.5
PVA075	84	104	19.6	0.91	4.9	1.24	15.6	0.37	2.4	0.62	82.5	82.1	82.5	100.0	99.5
PVA090	83	103	20.3	1.07	5.1	1.33	15.6	0.34	2.5	0.55	81.7	81.5	82.0	99.6	99.4
PVA105	83	102	19.7	0.63	5.2	1.65	15.8	0.25	2.6	0.41	81.1	80.9	81.5	99.5	99.3
PVA120	82	101	20.8	0.79	5.5	1.12	15.7	0.10	2.6	0.17	80.2	80.3	81.0	99.0	99.1

1: Melting enthalpy of BS signal ΔH_{BS} , melting enthalpy of whole ss-PCM ΔH_{total} , melting point of BS signal T_m calculated via temperature maximum (1) and onset (2), supercooling ΔT_s calculated via temperature maximum (1) and onset (2), mean value for effective mass fraction of PCM, relative uncertainty U of T_m and ΔT_s , $Ma(PCM)_{DSC}$ and $Ma(PCM)_{mass}$, highest value for effective mass fraction of PCM $Ma(PCM)_{max}$ and corresponding PCM immobilization efficiencies E_{DSC} and E_{mass} .

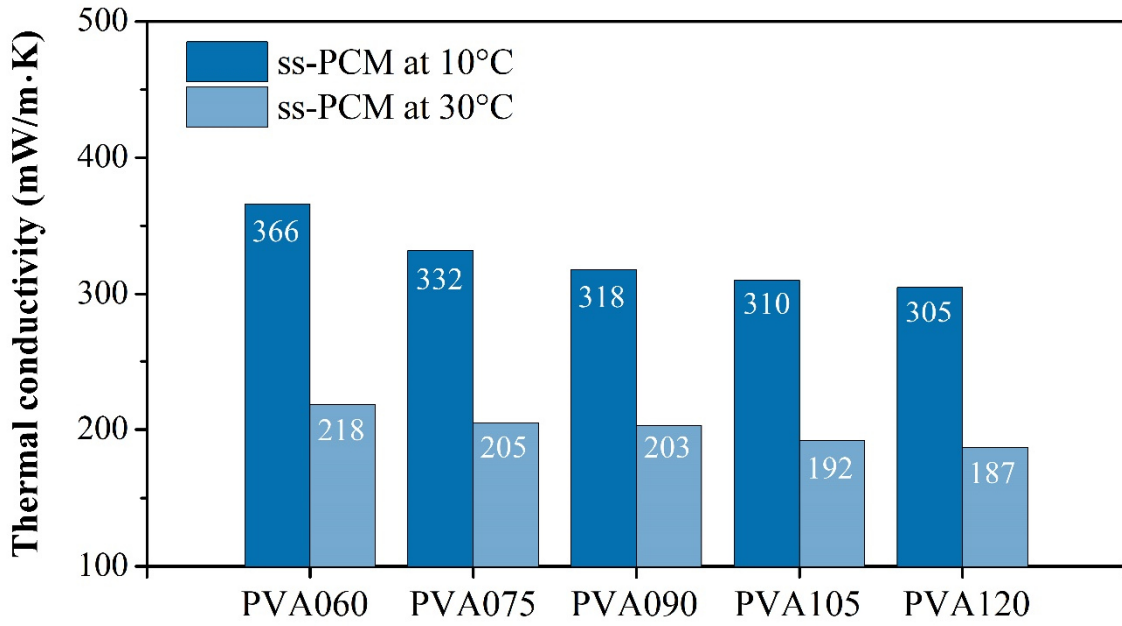


Fig. 2.6 Thermal conductivity of ss-PCMs PVA060, PVA075, PVA090, PVA105 and PVA120 measured below the freezing point (10 °C) and above the melting point (30°C) of pure PCM.

The effective mass fractions $Ma(PCM)_{DSC}$, $Ma(PCM)_{mass}$ and $Ma(PCM)_{max}$ and the corresponding PCM immobilization efficiencies E_{DSC} and E_{mass} are calculated according to Eq. 2.1 - 2.5 [60].

$$Ma(PCM)_{DSC} = \frac{\Delta_l^s H_m(ssPCM)}{\Delta_l^s H_m(PCM)} \cdot 100 \quad (\text{Eq. 2.1})$$

$$Ma(PCM)_{mass} = \frac{m_{ssPCM} - m_{Additives}}{m_{ssPCM}} \cdot 100 \quad (\text{Eq. 2.2})$$

$$Ma(PCM)_{max} = \frac{m_{PCM}}{m_{educts} - m_{H_2O}} \cdot 100 \quad (\text{Eq. 2.3})$$

$$E_{DSC} = \frac{Ma(PCM)_{DSC}}{Ma(PCM)_{max}} \cdot 100 \quad (\text{Eq. 2.4})$$

$$E_{mass} = \frac{Ma(PCM)_{mass}}{Ma(PCM)_{max}} \cdot 100 \quad (\text{Eq. 2.5})$$

where $Ma(PCM)_{DSC}$ and $Ma(PCM)_{mass}$ are the effective mass fractions of PCM obtained via DSC and by weight measurements, $\Delta_l^s H_m(ssPCM)$ and $\Delta_l^s H_m(PCM)$ are the melting enthalpies of ss-PCM, and pure PCM, m_{ssPCM} and $m_{Additives}$ are the masses of ss-PCM and educts

without water and PCM, $Ma(PCM)_{max}$ is the highest effective mass fraction of PCM without PCM leakage calculated by educt masses, m_{educts} is the mass of the complete educts, m_{H_2O} and m_{PCM} are the masses of water and BS, and E_{DSC} and E_{mass} are the confinement efficiencies calculated by DSC and weight measurements.

The value for $Ma(PCM)_{DSC}$ is calculated from DSC measurements and describes the mass fraction of the whole ss-PCM undergoing a state transition from solid to liquid and vice versa. In comparison, the effective mass fraction $Ma(PCM)_{mass}$ is obtained via sample weighing and is a measure for the amount of immobilized PCM in the ss-PCM. The effective mass fraction $Ma(PCM)_{max}$ depends only on the mass of the educts used for the synthesis and is the value of the highest possible mass fraction of PCM in the ss-PCM, if the whole PCM phase is shape-stabilized after synthesis.

The effective mass fractions $Ma(PCM)_{DSC}$, $Ma(PCM)_{mass}$ and $Ma(PCM)_{max}$ have nearly the same value (Table 2.2). Therefore, 100 % of the PCM mass used for the synthesis of samples PVA060 to PVA120 is immobilized (E_{mass}) in the silica structure as well as performing a state transition from solid to liquid and vice versa (E_{DSC}) during melting and freezing. As a consequence, the confined PCM should not be affected by possible physical and chemical interactions with the contents (SDS, SiO₂, PVA) or confinement effects in ss-PCMs during state transition. The melting enthalpies and effective mass fractions $Ma(PCM)_{DSC}$ and $Ma(PCM)_{mass}$ decrease from PVA060 to PVA120 only because of the increased mass fraction of PVA and, thus, decreased mass fraction of BS (Table 2.2).

For long-term performance tests, the ss-PCMs PVA060, PVA090 and PVA120 were heated above the melting point and cooled below the freezing point for up to 2000-times (Fig. S2.9). The thermal cycling number of 2000 cycles is comparable to the average value (1500) of this test in the current literature [76–78]. The latent heats differ only slightly after the thermal cycling tests and the values are within the relative uncertainty of the DSC measurements, indicating a high long-term performance and a high durability of the ss-PCMs. For building applications, every cycle represents a lifetime of one day. Thus, the ss-PCMs are stable for at least 2000 days.

3.2.6.3 Influence of SDS on physicochemical properties of ss-PCMs

We used 0.6 - 1.8 g SDS in the *in situ* sol-gel process to synthesize five ss-PCMs (SDS06 to SDS18) and to analyze the influence of SDS as surfactant on the physicochemical properties of the resulting ss-PCMs (Table 2.3, Fig. 2.7).

Table 2.3 Physicochemical properties¹ of ss-PCMs SDS06 to SDS18 synthesized with 9 g Köstrosol 0730, 1.0 g PVA, 6.75 g H₂O, 20 g BS and 0.6 g (SDS06) to 1.8 g (SDS18) SDS.

Sample	M (SDS) (g)	Φ (%) ^{a,b}	V_{total} (cm ³ /g) ^{a,b}	V_{macro} (cm ³ /g) ^a	V_{meso} (cm ³ /g) ^b	D_{macro} (nm) ^a	D_{meso} (nm) ^b	A_{meso} (m ² /g) ^b	pH	GT (h)	σ at 10 °C / 30 °C (MPa)	T_D (°C)
SDS06	0.6	4	0.017	0.017	-	66	-	-	8.7	11	0.41 / 0.14	210
SDS09	0.9	7	0.035	0.035	-	13617	-	-	8.7	3.5	0.91 / 0.41	212
SDS12	1.2	9	0.045	0.045	-	367	-	-	8.8	1.5	1.02 / 0.47	216
SDS15	1.5	7	0.032	0.032	-	72	-	-	8.9	0.8	0.69 / 0.26	212
SDS18	1.8	5	0.026	0.026	-	19243	-	-	8.9	0.5	0.38 / 0.12	209
SDS06c ^c	0.6	94	7.26	6.57	0.69	8070	9	197	-	-	-	-
SDS09c ^c	0.9	94	7.56	6.95	0.61	2281	8	232	-	-	-	-
SDS12c ^c	1.2	94	7.07	6.52	0.55	1332	7	212	-	-	-	-
SDS15c ^c	1.5	94	7.04	6.44	0.60	2090	7	241	-	-	-	-
SDS18c ^c	1.8	93	5.92	5.35	0.57	3231	9	201	-	-	-	-

1: Mass of SDS $M(SDS)$ used in the synthesis of the ss-PCMs, porosity Φ , total pore volume V_{total} , macropore volume V_{macro} , mesopore volume V_{meso} , mean macropore width/50% D_{macro} , mean mesopore width /50% D_{meso} , mesopore surface area A_{meso} , pH value, gelation time GT, compressive strength σ and decomposition point T_D of BS in ss-PCMs.

a: determined from mercury intrusion.

b: determined from nitrogen sorption.

c: ss-PCMs obtained after calcination for 10 h at 600 °C.

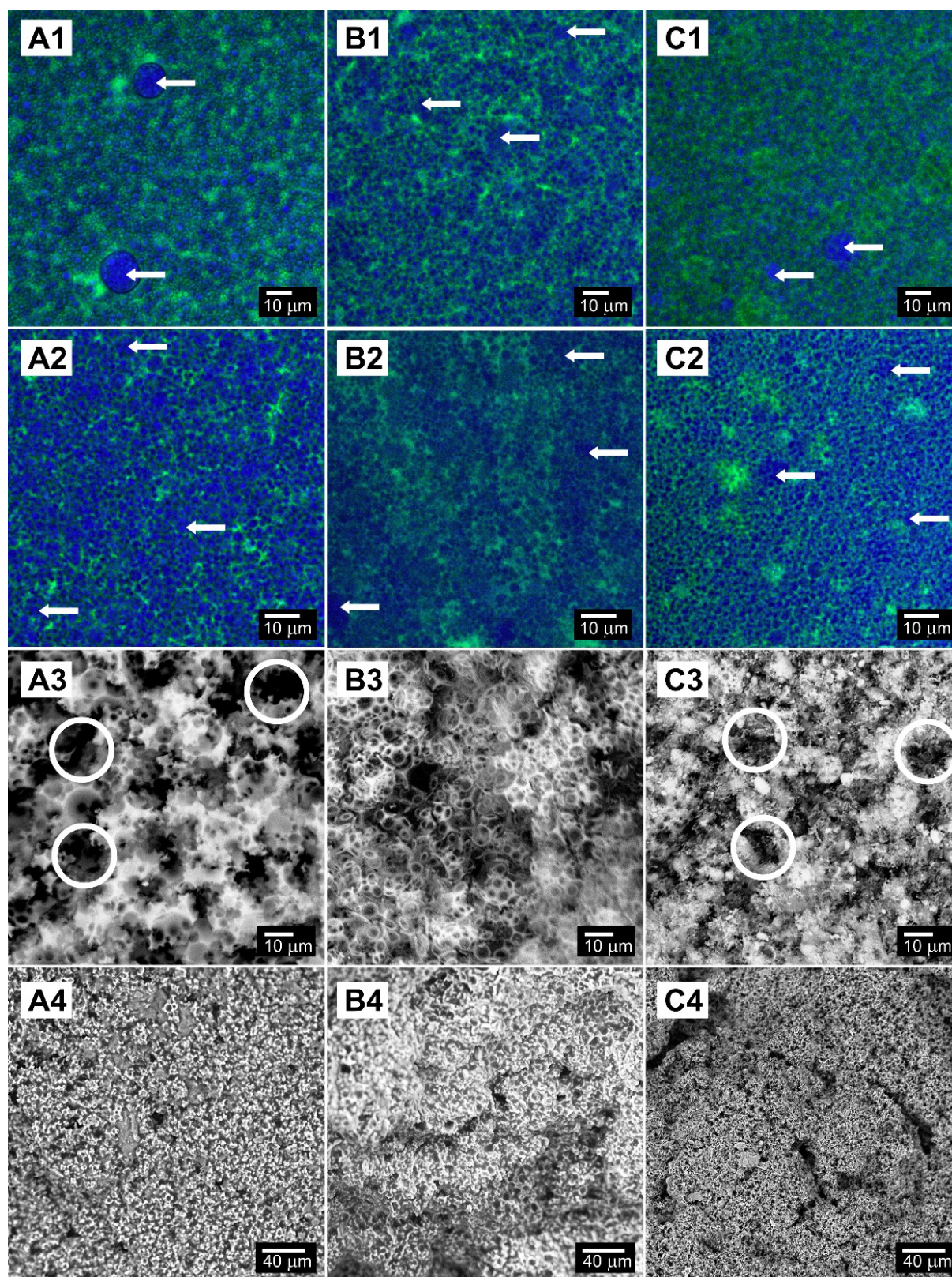


Fig. 2.7 Imaging of ss-PCM formation of SDS06(A), SDS12 (B) and SDS18(C) during gelation after 15 min (1) and approximately 50 h (2) by confocal fluorescence microscopy, and after calcination (3) and drying (4) by scanning electron microscopy. In the fluorescence images, the hydrophobic phase is marked in blue with perylene and the hydrophilic phase is marked in green with Alexa Fluor 488. Areas with a higher PCM concentration are marked with an arrow in fluorescence microscopic images. Fragmented silica structures are circled in scanning electron microscopic images.

The PVA amount was kept constant at 1.0 g during the synthesis. All samples showed the same absorption bands as the PVA sample row in ATR-IR spectra, indicating a high chemical stability of SDS, PVA and BS in the silica phase of the ss-PCMs (Fig. S2.10 – S2.11). After heating to 100 °C for 7 days, samples SDS09 to SDS15 had the same weight before and after heat treatment and, thus, a high shape-stability of approximately 100 %. In comparison, ss-PCMs SDS06 and SDS18 were both covered by a thin PCM film, had 1 % and 4 % lower weights, and a 99 % and 96 % shape-stability after heat treatment, respectively.

For fluorescence microscopy (Fig. 2.7), the aqueous phase was labelled with the green marker Alexa Fluor 488 and the PCM phase with the blue marker perylene. Samples SDS06 to SDS18 were calcined at 600 °C for pore structure analysis of the pure silica phase (SDS06c to SDS18c).

Using low SDS amounts (< 0.6 g) in the synthesis of the ss-PCMs caused the PCM phase to separate from the aqueous phase after stirring. As a result, the gelled silica particles accumulated in the aqueous phase at the bottom of the reaction vessel. We conclude that SDS amounts below 0.6 g are unable to stabilize the PCM-water-emulsion during the gelation process. In contrast, using high SDS amounts (> 1.2 g) still yielded ss-PCMs. However, the stability was reduced, as evidenced by a reduction in compressive strength of the synthesized ss-PCM monoliths at 30 °C from 0.47 MPa for sample SDS12 to 0.12 MPa for sample SDS18 and by a decrease of the decomposition points of the BS in the ss-PCMs from 216 °C for SDS12 to 209 °C for SDS18 (Table 2.3). Moreover, samples SDS15 to SDS18 were not monolithic. With an increasing SDS mass fraction, the gelation of samples SDS06 to SDS18 is accelerated from 11 h to 0.5 h and the pH-value is slightly increased by 0.2 (Table 2.3).

After 15 min during gelation (Fig. 2.7 (A1-C1)), the blue-labeled PCM phase is emulsified as droplets with droplet widths of ~1 µm in the continuous green-labeled, aqueous phase. The confocal microscopy images taken after 15 min and 50 h (Fig. 2.7)) differ only slightly from each other and trends cannot be evaluated as it was done for the different PVA concentrations. The SEM images (Fig. 2.7 (A3-C3)) show a partially fragmented spherical and a particulate, fragmented silica structure for SDS06c and SDS18c, respectively. The inter-particle space between the fragmented silica structures could be the reason for the higher mean macropore width of the silica phase of SDS06c (8070 nm) and SDS18c (3231 nm) compared to the interconnected silica structure in SDS12c (1332 nm) (Fig. 2.8, Table 2.3). Therefore, SDS12 with the higher interconnectivity of the silica structure has the highest value (0.47 MPa) of the compressive strength of the SDS sample row. Concomitantly, the decomposition temperatures of BS in the ss-PCMs increase from to 216 °C for SDS12, probably because of the highly interconnected silica structure and, thus, the decelerated PCM evaporation through smaller

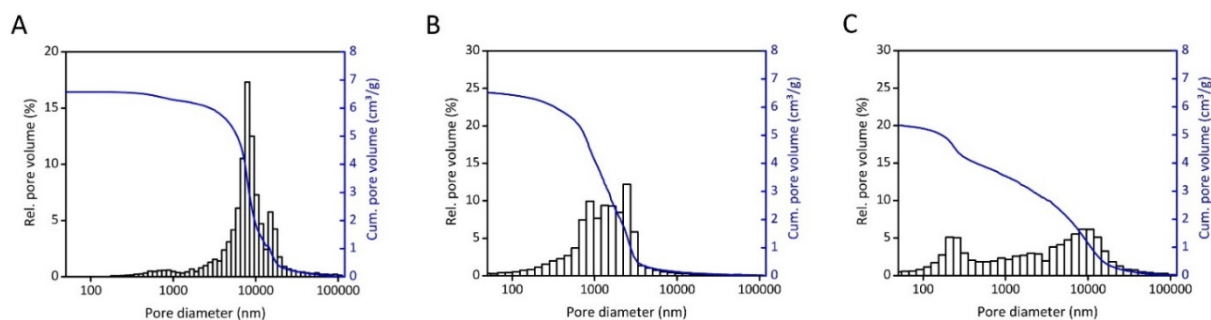


Fig. 2.8 Mercury intrusion measurements of calcined ss-PCM sample SDS06c (A), SDS12c (B) and SDS18c (C).

pore structures (Fig. S2.14, Table 2.3). In accordance to PVA06c - 12c, the samples SDS06c - 12c have nearly constant values for the porosity and total pore volumes. The mesopore volume and mean mesopore width of the samples are nearly constant and not affected by the SDS amount (Fig. S2.13, Table 2.3). The samples SDS06 to SDS18 show no N_2 sorption and are, compared to all the samples of the PVA concentration series, completely filled with PCM. These observations are in agreement with the current literature [79–83] and could be explained as follows. If the SDS concentration is too low (SDS06), the PCM phase cannot be fully covered by SDS molecules to form droplets and bigger (blue-labelled) PCM droplets without SDS-stabilization can form in the solution, as shown in Fig. 2.7 (A1). Therefore, the viscosity of the emulsion of SDS06 is smaller than for SDS12. The lower stabilization and viscosity of the PCM/water-emulsion of SDS06 could lead to the lower mechanical stability of the wet gel structure and, thus, a facilitated and accelerated breakage of the wet gel structure during drying (Fig. 2.7 (A3)).

At an SDS content of 1.2 g (SDS12), a region of maximum viscosity for the emulsion is reached and the wet gel structure seems to be stabilized sufficiently for a breakage-free drying process. If the SDS content is further increased (SDS18), the viscosity of the emulsion decreases again, probably because of reorganization of the interfacial layer [79]. At a certain point no more SDS molecules could be adsorbed to the SDS-covered PCM droplets. The increasing number of negatively charged SDS molecules in the sol can in turn bind to PVA and/or the silica structures. As a result, the network structure between SDS-PVA-silica could break up due to intrinsic electrostatic repulsion in the network leading to a decrease in viscosity. As a consequence, the wet gel structure of SDS18 differs clearly from SDS06 and the mechanical stability of the wet gel is not sufficient enough for a breakage-free drying process (Fig. 2.7 (C3)).

In summary, an increasing amount of SDS increases the number of SDS-stabilized PCM droplets in the PCM/water emulsion, which act as templates for the silica structure during the gelation process. The samples SDS12 and PVA06 with the smallest mean macropore width have the highest compressive strength and thermal stability.

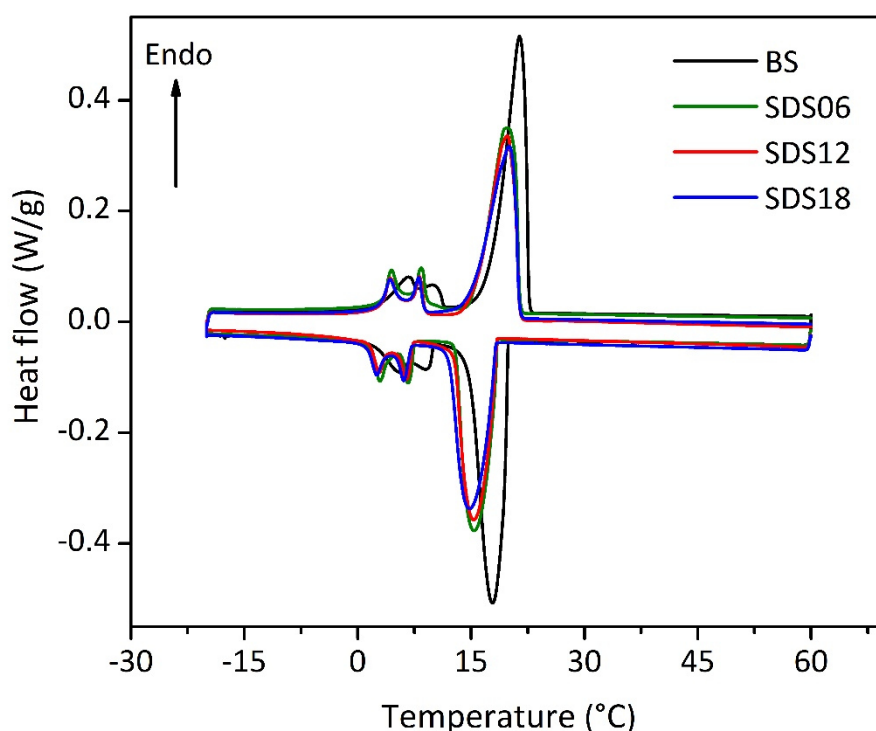


Fig. 2.9 DSC curves of BS (black), SDS06 (green), SDS12 (red) and SDS18 (blue).

To investigate the effect of SDS on the thermal properties, we characterized samples SDS06 to SDS18 with DSC (Fig. 2.9), mass calculations (Table 2.4) and thermal conductivity measurements (Fig. 2.10). The supercooling temperatures ΔT_{s1} and ΔT_{s2} as well as the melting temperatures of BS T_{m1} and T_{m2} are nearly constant and within the standard deviation of the DSC for the ss-PCMs of the SDS sample row (Fig. 2.10), indicating no influence of the SDS amount on these thermal properties. The thermal conductivity is higher for ss-PCM samples with higher compressive strengths (and lower average macropore widths) (Fig. 2.10). For example, sample SDS12 has the highest thermal conductivity (372 mW/mK, 10 °C) and the highest compressive strength (1.02 MPa, 10 °C) of the SDS sample row. The melting enthalpies of BS are decreased from 81 J/g for SDS06 to 79 J/g for SDS18 due to the higher mass fraction of SDS. The confinement efficiencies of PCM E_{DSC} and E_{mass} are both 100 % for the ss-PCMs of the SDS sample row and, thus, all PCM used for the synthesis is immobilized and the whole PCM phase performs a state transition during melting and freezing. Consequentially, neither physical and chemical reactions of SDS with BS and PVA nor confinement effects of the silica matrix should play a significant role for the sol-gel synthesis in this work. After 2000 heating and freezing cycles, the latent heats of SDS06 - SDS18 have the nearly the same values before and after the thermal cycling tests and the values are within the relative uncertainty of the DSC measurements (Fig. S2.15). Thus, the ss-PCMs are stable for ~2000 days in building applications.

Table 2.4 Thermal properties¹ of pure BS and samples SDS06 to SDS18 determined by mass calculations and DSC measurements.

Sample	ΔH_{BS} (J/g)	ΔH_{total} (J/g)	T_{m1} (°C)	U_{Tm1} (%)	ΔT_{s1} (°C)	$U_{\Delta T_{s1}}$ (%)	T_{m2} (°C)	U_{Tm2} (%)	ΔT_{s2} (°C)	$U_{\Delta T_{s2}}$ (%)	$Ma(PCM)_{DSC}$ (wt%)	$Ma(PCM)_{mass}$ (wt%)	$Ma(PCM)_{max}$ (wt%)	E_{DSC} (%)	E_{mass} (%)
SDS06	82	103	20.0	0.52	4.9	1.28	15.7	0.27	2.5	0.60	82.7	81.9	82.3	100.5	99.5
SDS09	82	103	20.3	0.71	5.1	1.62	15.7	0.38	2.5	0.58	82.1	80.7	81.3	101.0	99.3
SDS12	81	101	20.1	0.39	5.1	2.03	15.6	0.15	2.6	0.33	80.4	79.6	80.3	100.1	99.1
SDS15	80	100	20.1	0.88	5.1	1.71	15.5	0.16	2.8	0.46	79.6	78.3	79.4	100.3	98.6
SDS18	79	98	20.0	0.62	4.9	1.95	15.2	0.41	2.8	0.83	78.7	77.2	78.4	100.4	98.5

1: Melting enthalpy of BS signal ΔH_{BS} , melting enthalpy of whole ss-PCM ΔH_{total} , melting point of BS signal T_m calculated via temperature maximum (1) and onset (2), supercooling ΔT_s calculated via temperature maximum (1) and onset (2), mean value for effective mass fraction of PCM, relative uncertainty U of T_m and ΔT_s , $Ma(PCM)_{DSC}$ and $Ma(PCM)_{mass}$, highest value for effective mass fraction of PCM $Ma(PCM)_{max}$ and corresponding PCM immobilization efficiencies E_{DSC} and E_{mass} .

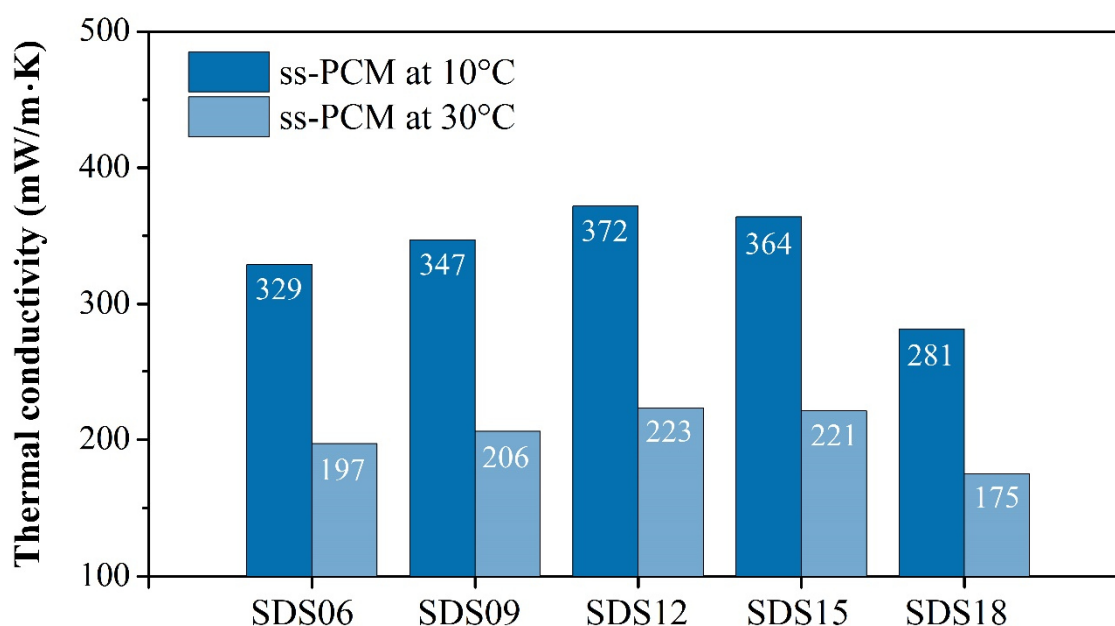


Fig. 2.10 Thermal conductivity of ss-PCMs SDS06, SDS09, SDS12, SDS15 and SDS18 measured below the freezing point (10 °C) and above the melting point (30°C) of pure PCM.

3.2.7 Conclusions

We studied the *in situ* ss-PCM formation during the sol-gel process and analyzed the influence of the porogens SDS and PVA on the physicochemical properties of ss-PCMs. The PCM droplets are emulsified and stabilized via SDS as surfactant in a continuous aqueous phase. These droplets act as templates for the silica pore structure in the ss-PCM during gelation. The PVA separates as structure-directing agent the PCM/water emulsion in a smaller hydrophobic and larger hydrophilic region, imaged as “worm”-like patches via confocal microscopy. The porogen concentration in the synthesized ss-PCMs does not affect the high shape-stability (~100 %), high long-term performance (> 2000 melting and freezing cycles) and high chemical stability of the ss-PCMs, but has a great impact on the silica structure, the thermal conductivity and mechanical strength of the ss-PCMs.

At high PVA concentrations, the silica macropore width in the ss-PCMs is increased up to eight times due to the fragmentation of silica pores during drying. The larger and partially fragmented silica pores lower the mechanical stability and the thermal conductivity of the ss-PCM from 1.2 MPa to 0.6 MPa and 0.37 W/mK to 0.31 W/mK at 10 °C, respectively. Moreover, the decomposition point of BS in the ss-PCM structure is lowered from 216 °C to 205 °C due to a facilitated PCM evaporation through larger silica pore channels.

In contrast, a higher amount of SDS increases the number of SDS-stabilized PCM droplets and, thus, the viscosity and stability of the emulsion, resulting in mechanically stable ss-PCMs during and after drying. At very high SDS concentration, the viscosity of the emulsion decreases and the silica structure collapses during drying, probably because of the increasing electrostatic repulsion between SDS-PVA and SDS-PVA-silica structures during gelation. As a consequence, the mechanical stability, the thermal conductivity and the decomposition point of BS in the ss-PCM are decreased from 1.0 MPa to 0.4 MPa (10 °C), 0.37 W/mK to 0.28 W/mK (10 °C) and 216 °C to 209 °C, respectively.

By minimizing the amount of PVA and using a higher amount of SDS, we could improve the thermal and mechanical properties of our ss-PCMs based on BS. With our findings, it should be possible to synthesize ss-PCMs with different hydrophobic PCMs, such as hexadecane, to increase the latent heat of our ss-PCMs (83 wt% PCM) from 100 J/g (BS) to 190 J/g (hexadecane) for future thermal energy storage applications in need of a high mechanical stability, such as energy-saving walls or battery cooling materials in electric vehicles.

3.2.8 Conflicts of interest

The authors declare that they have no financial or social conflict of interest, which could influence the work reported in this paper.

3.2.9 CRediT authorship contribution statement

Felix Marske: Conceptualization, Methodology, Validation, Formal analysis, Investigation, Data Curation, Writing - Original Draft, Visualization. **Joe Dasler:** Formal analysis. **Caroline Haupt:** Formal analysis, Resources, Writing - Review & Editing. **Kirsten Bacia:** Resources, Writing - Review & Editing. **Thomas Hahn:** Supervision, Project administration, Funding acquisition. **Dirk Enke:** Writing - Review & Editing, Supervision.

3.2.10 Acknowledgements

The authors of this paper thank Ms. Jenny Bienias for the mercury intrusion and nitrogen sorption measurements. Caroline Haupt and Kirsten Bacia acknowledge the funding from the Federal Ministry for Education and Research (BMBF, 03Z22HI2).

3.2.11 References

- [1] International Energy Agency, Key World Energy Statistics 2016 (2016) 1–80. https://doi.org/10.1787/key_energ_stat-2016-en.
- [2] International Energy Agency and the United Nations Environment Program, 2018 Global Status Report: towards a zero-emission, efficient and resilient buildings and construction sector. (2018) 1–73. <https://www.iea.org/reports/2018-global-status-report> (accessed 20 July 2021).
- [3] A. Sharma, V.V. Tyagi, C.R. Chen, D. Buddhi, Review on thermal energy storage with phase change materials and applications, *Renewable and Sustainable Energy Reviews* 13 (2009) 318–345. <https://doi.org/10.1016/j.rser.2007.10.005>.
- [4] E.M. Shchukina, M. Graham, Z. Zheng, D.G. Shchukin, Nanoencapsulation of phase change materials for advanced thermal energy storage systems, *Chemical Society Reviews* 47 (2018) 4156–4175. <https://doi.org/10.1039/c8cs00099a>.
- [5] M. Li, A nano-graphite/paraffin phase change material with high thermal conductivity, *Applied Energy* 106 (2013) 25–30. <https://doi.org/10.1016/j.apenergy.2013.01.031>.
- [6] G.V. Belessiotis, K.G. Papadokostaki, E.P. Favvas, E.K. Efthimiadou, S. Karellas, Preparation and investigation of distinct and shape stable paraffin/SiO₂ composite PCM nanospheres, *Energy Conversion and Management* 168 (2018) 382–394. <https://doi.org/10.1016/j.enconman.2018.04.059>.
- [7] G. Fang, Z. Chen, H. Li, Synthesis and properties of microencapsulated paraffin composites with SiO₂ shell as thermal energy storage materials, *Chemical Engineering Journal* 163 (2010) 154–159. <https://doi.org/10.1016/j.cej.2010.07.054>.
- [8] S.A. Memon, T.Y. Lo, S.A. Barbhuiya, W. Xu, Development of form-stable composite phase change material by incorporation of dodecyl alcohol into ground granulated blast furnace slag, *Energy and Buildings* 62 (2013) 360–367. <https://doi.org/10.1016/j.enbuild.2013.03.026>.
- [9] A. Solé, H. Neumann, S. Niedermaier, I. Martorell, P. Schossig, L.F. Cabeza, Stability of sugar alcohols as PCM for thermal energy storage, *Solar Energy Materials and Solar Cells* 126 (2014) 125–134. <https://doi.org/10.1016/j.solmat.2014.03.020>.
- [10] J. Zuo, W. Li, L. Weng, Thermal performance of caprylic acid/1-dodecanol eutectic mixture as phase change material (PCM), *Energy and Buildings* 43 (2011) 207–210. <https://doi.org/10.1016/j.enbuild.2010.09.008>.
- [11] A. Palacios, A. de Gracia, L. Haurie, L.F. Cabeza, A.I. Fernández, C. Barreneche, Study of the Thermal Properties and the Fire Performance of Flame Retardant-Organic PCM in Bulk Form, *Materials* 11 (2018). <https://doi.org/10.3390/ma11010117>.
- [12] H. Fauzi, H.S. Metselaar, T. Mahlia, H. Chyuan Ong, Nasruddin, H.M. Khanlou, Preparation and thermal characteristics of eutectic fatty acids/Shorea javanica composite

- for thermal energy storage, *Applied Thermal Engineering* 100 (2016) 62–67.
<https://doi.org/10.1016/j.applthermaleng.2016.01.146>.
- [13] Ş. Ince, Y. Seki, M. Akif Ezan, A. Turgut, A. Erek, Thermal properties of myristic acid/graphite nanoplates composite phase change materials, *Renewable Energy* 75 (2015) 243–248. <https://doi.org/10.1016/j.renene.2014.09.053>.
- [14] J. Li, L. He, T. Liu, X. Cao, H. Zhu, Preparation and characterization of PEG/SiO₂ composites as shape-stabilized phase change materials for thermal energy storage, *Solar Energy Materials and Solar Cells* 118 (2013) 48–53.
<https://doi.org/10.1016/j.solmat.2013.07.017>.
- [15] T. Qian, J. Li, H. Ma, J. Yang, The preparation of a green shape-stabilized composite phase change material of polyethylene glycol/SiO₂ with enhanced thermal performance based on oil shale ash via temperature-assisted sol–gel method, *Solar Energy Materials and Solar Cells* 132 (2015) 29–39. <https://doi.org/10.1016/j.solmat.2014.08.017>.
- [16] B. Tang, J. Cui, Y. Wang, C. Jia, S. Zhang, Facile synthesis and performances of PEG/SiO₂ composite form-stable phase change materials, *Solar Energy* 97 (2013) 484–492. <https://doi.org/10.1016/j.solener.2013.08.021>.
- [17] A.R. Abdulmunem, P.M. Samin, H.A. Rahman, H.A. Hussien, H. Ghazali, A novel thermal regulation method for photovoltaic panels using porous metals filled with phase change material and nanoparticle additives, *Journal of Energy Storage* 39 (2021) 102621. <https://doi.org/10.1016/j.est.2021.102621>.
- [18] H. Mousa, J. Naser, O. Houche, Using PCM as energy storage material in water tanks: Theoretical and experimental investigation, *Journal of Energy Storage* 22 (2019) 1–7. <https://doi.org/10.1016/j.est.2019.01.018>.
- [19] M. Dardir, K. Panchabikesan, F. Haghghat, M. El Mankibi, Y. Yuan, Opportunities and challenges of PCM-to-air heat exchangers (PAHXs) for building free cooling applications—A comprehensive review, *Journal of Energy Storage* 22 (2019) 157–175. <https://doi.org/10.1016/j.est.2019.02.011>.
- [20] D. Feldman, D. Banu, D.W. Hawes, Development and application of organic phase change mixtures in thermal storage gypsum wallboard, *Solar Energy Materials and Solar Cells* 36 (1995) 147–157. [https://doi.org/10.1016/0927-0248\(94\)00168-R](https://doi.org/10.1016/0927-0248(94)00168-R).
- [21] L. Cao, Di Su, Y. Tang, G. Fang, F. Tang, Properties evaluation and applications of thermal energy storage materials in buildings, *Renewable and Sustainable Energy Reviews* 48 (2015) 500–522. <https://doi.org/10.1016/j.rser.2015.04.041>.
- [22] M. Jaworski, P. Łapka, P. Furmański, Numerical modelling and experimental studies of thermal behaviour of building integrated thermal energy storage unit in a form of a ceiling panel, *Applied Energy* 113 (2014) 548–557.
<https://doi.org/10.1016/j.apenergy.2013.07.068>.

- [23] J. Pereira da Cunha, P. Eames, Thermal energy storage for low and medium temperature applications using phase change materials – A review, *Applied Energy* 177 (2016) 227–238. <https://doi.org/10.1016/j.apenergy.2016.05.097>.
- [24] A. de Gracia, L.F. Cabeza, Phase change materials and thermal energy storage for buildings, *Energy and Buildings* 103 (2015) 414–419. <https://doi.org/10.1016/j.enbuild.2015.06.007>.
- [25] Y. Cai, Y. Hu, L. Song, Y. Tang, R. Yang, Y. Zhang, Z. Chen, W. Fan, Flammability and thermal properties of high-density polyethylene/paraffin hybrid as a form-stable phase change material, *Journal of Applied Polymer Science* 99 (2006) 1320–1327. <https://doi.org/10.1002/app.22065>.
- [26] A. Karaipekli, A. Biçer, A. Sarı, V.V. Tyagi, Thermal characteristics of expanded perlite/paraffin composite phase change material with enhanced thermal conductivity using carbon nanotubes, *Energy Conversion and Management* 134 (2017) 373–381. <https://doi.org/10.1016/j.enconman.2016.12.053>.
- [27] N. Şahan, M. Fois, H. Paksoy, Improving thermal conductivity phase change materials—A study of paraffin nanomagnetite composites, *Solar Energy Materials and Solar Cells* 137 (2015) 61–67. <https://doi.org/10.1016/j.solmat.2015.01.027>.
- [28] F. Wang, S. Gao, J. Pan, X. Li, J. Liu, Short-Chain Modified SiO₂ with High Absorption of Organic PCM for Thermal Protection, *Nanomaterials* 9 (2019). <https://doi.org/10.3390/nano9040657>.
- [29] A. Jamekhorshid, S.M. Sadrameli, M. Farid, A review of microencapsulation methods of phase change materials (PCMs) as a thermal energy storage (TES) medium, *Renewable and Sustainable Energy Reviews* 31 (2014) 531–542. <https://doi.org/10.1016/j.rser.2013.12.033>.
- [30] G. Alva, Y. Lin, L. Liu, G. Fang, Synthesis, characterization and applications of microencapsulated phase change materials in thermal energy storage: A review, *Energy and Buildings* 144 (2017) 276–294. <https://doi.org/10.1016/j.enbuild.2017.03.063>.
- [31] Y. Lin, C. Zhu, G. Fang, Synthesis and properties of microencapsulated stearic acid/silica composites with graphene oxide for improving thermal conductivity as novel solar thermal storage materials, *Solar Energy Materials and Solar Cells* 189 (2019) 197–205. <https://doi.org/10.1016/j.solmat.2018.10.005>.
- [32] S. Imran Hussein, A. Ameelia Roseline, S. Kalaiselvam, Bifunctional nanoencapsulated eutectic phase change material core with SiO₂/SnO₂ nanosphere shell for thermal and electrical energy storage, *Materials & Design* 154 (2018) 291–301. <https://doi.org/10.1016/j.matdes.2018.05.046>.
- [33] F. Tang, L. Liu, G. Alva, Y. Jia, G. Fang, Synthesis and properties of microencapsulated octadecane with silica shell as shape-stabilized thermal energy storage materials, *Solar*

- Energy Materials and Solar Cells 160 (2017) 1–6.
<https://doi.org/10.1016/j.solmat.2016.10.014>.
- [34] J. Shi, X. Wu, R. Sun, B. Ban, J. Li, J. Chen, Nano-encapsulated phase change materials prepared by one-step interfacial polymerization for thermal energy storage, *Materials Chemistry and Physics* 231 (2019) 244–251.
<https://doi.org/10.1016/j.matchemphys.2019.04.032>.
- [35] A. Sarı, C. Alkan, A. Biçer, A. Altuntaş, C. Bilgin, Micro/nanoencapsulated n-nonadecane with poly(methyl methacrylate) shell for thermal energy storage, *Energy Conversion and Management* 86 (2014) 614–621. <https://doi.org/10.1016/j.enconman.2014.05.092>.
- [36] R. Altun-Anayurt, S. Alay-Aksoy, C. Alkan, S. Demirbag, M.S. Tözüm, Development of thermo-regulating fabrics using PCM microcapsules with poly(methyl methacrylate-co-2-hydroxy ethyl methacrylate) shell and n-alkane core, *International Journal of Clothing Science and Technology* 31 (2018) 65–79. <https://doi.org/10.1108/IJCST-09-2017-0145>.
- [37] G. Cui, J. Wang, X. Wang, W. Li, X. Zhang, Preparation and Properties of Narrowly Dispersed Polyurethane Nanocapsules Containing Essential Oil via Phase Inversion Emulsification, *Journal of Agricultural and Food Chemistry* 66 (2018) 10799–10807.
<https://doi.org/10.1021/acs.jafc.8b02406>.
- [38] M. Rahimi, J. Mokhtari, Fabrication of thermo-regulating hexadecane-polyurethane core-shell composite nanofibrous mat as advanced technical layer: Effect of coaxial nozzle geometry, *Journal of Industrial Textiles* 47 (2017) 1134–1151.
<https://doi.org/10.1177/1528083716676816>.
- [39] P. Felix De Castro, D.G. Shchukin, New polyurethane/docosane microcapsules as phase-change materials for thermal energy storage, *Chemistry* 21 (2015) 11174–11179.
<https://doi.org/10.1002/chem.201500666>.
- [40] Y. Konuklu, M. Ostry, H.O. Paksoy, P. Charvat, Review on using microencapsulated phase change materials (PCM) in building applications, *Energy and Buildings* 106 (2015) 134–155. <https://doi.org/10.1016/j.enbuild.2015.07.019>.
- [41] FB Errebai, L Derradji, M Amara, Optimum mass percentage of microencapsulated PCM mixed with gypsum for improved latent heat storage, *J. Energy Storage* (2021),
<https://doi.org/10.1016/j.est.2020.101910>.
- [42] T. Lecompte, P. Le Bideau, P. Glouannec, D. Nortershauser, S. Le Masson, Mechanical and thermo-physical behaviour of concretes and mortars containing phase change material, *Energy and Buildings* 94 (2015) 52–60.
<https://doi.org/10.1016/j.enbuild.2015.02.044>.
- [43] A. Figueiredo, J. Lapa, R. Vicente, C. Cardoso, Mechanical and thermal characterization of concrete with incorporation of microencapsulated PCM for applications in thermally

- activated slabs, *Construction and Building Materials* 112 (2016) 639–647.
<https://doi.org/10.1016/j.conbuildmat.2016.02.225>.
- [44] M. Hunger, A.G. Entrop, I. Mandilaras, H. Brouwers, M. Founti, The behavior of self-compacting concrete containing micro-encapsulated Phase Change Materials, *Cement and Concrete Composites* 31 (2009) 731–743.
<https://doi.org/10.1016/j.cemconcomp.2009.08.002>.
- [45] Y.E. Milián, A. Gutiérrez, M. Grágeda, S. Ushak, A review on encapsulation techniques for inorganic phase change materials and the influence on their thermophysical properties, *Renewable and Sustainable Energy Reviews* 73 (2017) 983–999.
<https://doi.org/10.1016/j.rser.2017.01.159>.
- [46] L. He, J. Li, C. Zhou, H. Zhu, X. Cao, B. Tang, Phase change characteristics of shape-stabilized PEG/SiO₂ composites using calcium chloride-assisted and temperature-assisted sol gel methods, *Solar Energy* 103 (2014) 448–455.
<https://doi.org/10.1016/j.solener.2014.02.042>.
- [47] B. Xu, Z. Li, Paraffin/diatomite composite phase change material incorporated cement-based composite for thermal energy storage, *Applied Energy* 105 (2013) 229–237.
<https://doi.org/10.1016/j.apenergy.2013.01.005>.
- [48] C. Cárdenas-Ramírez, F. Jaramillo, A.G. Fernández, L.F. Cabeza, M.A. Gómez, Influence of thermal treatments on the absorption and thermal properties of a clay mineral support used for shape-stabilization of fatty acids, *Journal of Energy Storage* 36 (2021) 102427. <https://doi.org/10.1016/j.est.2021.102427>.
- [49] X. Zhang, J. Qiao, W. Zhang, F. Cheng, Z. Yin, Z. Huang, X. Min, Thermal behavior of composite phase change materials based on polyethylene glycol and expanded vermiculite with modified porous carbon layer, *Journal of Materials Science* 53 (2018) 13067–13080. <https://doi.org/10.1007/s10853-018-2531-x>.
- [50] M. Xiao, B. Feng, K. Gong, Preparation and performance of shape stabilized phase change thermal storage materials with high thermal conductivity, *Energy Conversion and Management* 43 (2002) 103–108. [https://doi.org/10.1016/S0196-8904\(01\)00010-3](https://doi.org/10.1016/S0196-8904(01)00010-3).
- [51] D. Zhou, C.Y. Zhao, Y. Tian, Review on thermal energy storage with phase change materials (PCMs) in building applications, *Applied Energy* 92 (2012) 593–605.
<https://doi.org/10.1016/j.apenergy.2011.08.025>.
- [52] Z. Xiangfa, X. Hanning, F. Jian, Z. Changrui, J. Yonggang, Preparation, properties and thermal control applications of silica aerogel infiltrated with solid–liquid phase change materials, *Journal of Experimental Nanoscience* 7 (2012) 17–26.
<https://doi.org/10.1080/17458080.2010.497950>.

- [53] Y.P. Zhang, K.P. Lin, R. Yang, H.F. Di, Y. Jiang, Preparation, thermal performance and application of shape-stabilized PCM in energy efficient buildings, *Energy and Buildings* 38 (2006) 1262–1269. <https://doi.org/10.1016/j.enbuild.2006.02.009>.
- [54] V. Chalkia, N. Tachos, P.K. Pandis, A. Giannakas, M.K. Koukou, M.G. Vrachopoulos, L. Coelho, A. Ladavos, V.N. Stathopoulos, Influence of organic phase change materials on the physical and mechanical properties of HDPE and PP polymers, *RSC Advances* 8 (2018) 27438–27447. <https://doi.org/10.1039/C8RA03839B>.
- [55] A. Sarı, Form-stable paraffin/high density polyethylene composites as solid–liquid phase change material for thermal energy storage: Preparation and thermal properties, *Energy Conversion and Management* 45 (2004) 2033–2042. <https://doi.org/10.1016/j.enconman.2003.10.022>.
- [56] A. Sarı, A. Karaipekli, Preparation, thermal properties and thermal reliability of palmitic acid/expanded graphite composite as form-stable PCM for thermal energy storage, *Solar Energy Materials and Solar Cells* 93 (2009) 571–576. <https://doi.org/10.1016/j.solmat.2008.11.057>.
- [57] P.B. Wheelock, B.C. Cook, J.L. Haringa, A.M. Russell, Phase changes induced in hexagonal boron nitride by high energy mechanical milling, *Journal of Materials Science* 39 (2004) 343–347. <https://doi.org/10.1023/B:JMSE.0000008086.48380.01>.
- [58] J.-L. Zeng, F.-R. Zhu, S.-B. Yu, Z.-L. Xiao, W.-P. Yan, S.-H. Zheng, L. Zhang, L.-X. Sun, Z. Cao, Myristic acid/polyaniline composites as form stable phase change materials for thermal energy storage, *Solar Energy Materials and Solar Cells* 114 (2013) 136–140. <https://doi.org/10.1016/j.solmat.2013.03.006>.
- [59] R.-A. Mitran, S. Ioniță, D. Lincu, D. Berger, C. Matei, A Review of Composite Phase Change Materials Based on Porous Silica Nanomaterials for Latent Heat Storage Applications, *Molecules* 26 (2021). <https://doi.org/10.3390/molecules26010241>.
- [60] F. Marske, J. Martins de Souza e Silva, R.B. Wehrspohn, T. Hahn, D. Enke, Synthesis of monolithic shape-stabilized phase change materials with high mechanical stability via a porogen-assisted *in situ* sol–gel process, *RSC Advances* 10 (2020) 3072–3083. <https://doi.org/10.1039/C9RA10631F>.
- [61] F. Marske, T. Lindenberg, J. Martins de Souza e Silva, R.B. Wehrspohn, A.W. Maijenburg, T. Hahn, D. Enke, Size and surface effects of hexagonal boron nitrides on the physicochemical properties of monolithic phase change materials synthesized via sol–gel route, *Applied Thermal Engineering* 196 (2021) 117325. <https://doi.org/10.1016/j.applthermaleng.2021.117325>.
- [62] E.W. Washburn, Note on a Method of Determining the Distribution of Pore Sizes in a Porous Material, *Proceedings of the National Academy of Sciences of the United States of America* 7 (1921) 115–116. <https://doi.org/10.1073/pnas.7.4.115>.

- [63] S. Brunauer, P.H. Emmett, E. Teller, Adsorption of Gases in Multimolecular Layers, *Journal of the American Chemical Society* 60 (1938) 309–319. <https://doi.org/10.1021/ja01269a023>.
- [64] A. Margineanu, J. Hotta, R.A.L. Vallée, M. van der Auweraer, M. Ameloot, A. Stefan, D. Beljonne, Y. Engelborghs, A. Herrmann, K. Müllen, F.C. de Schryver, J. Hofkens, Visualization of membrane rafts using a perylene monoimide derivative and fluorescence lifetime imaging, *Biophysical Journal* 93 (2007) 2877–2891. <https://doi.org/10.1529/biophysj.106.100743>.
- [65] G.M. Funk, C.E. Hunt, D.E. Epps, P.K. Brown, Use of a rapid and highly sensitive fluorescamine-based procedure for the assay of plasma lipoproteins, *Journal of Lipid Research* 27 (1988) 792–795. [https://doi.org/10.1016/S0022-2275\(20\)38803-9](https://doi.org/10.1016/S0022-2275(20)38803-9).
- [66] U. Schote, J. Seelig, Interaction of the neuronal marker dye FM1-43 with lipid membranes, *Biochimica et Biophysica Acta (BBA) - Biomembranes* 1415 (1998) 135–146. [https://doi.org/10.1016/S0005-2736\(98\)00188-6](https://doi.org/10.1016/S0005-2736(98)00188-6).
- [67] Y. Zhang, X.Y. Zhang, J.L. Chai, X.C. Cui, J. Pan, J.W. Song, B. Sun, J.J. Lu, The phase behavior and solubilization of isopropyl myristate in microemulsions containing hexadecyl trimethyl ammonium bromide and sodium dodecyl sulfate, *Journal of Molecular Liquids* 244 (2017) 262–268. <https://doi.org/10.1016/j.molliq.2017.08.074>.
- [68] A.V. Sineva, D.S. Ermolat'ev, A.V. Pertsov, Structural transformations in a water-n-octane + chloroform-sodium dodecyl sulfate-n-pentanol microemulsion, *Colloid Journal* 69 (2007) 89–94. <https://doi.org/10.1134/S1061933X07010127>.
- [69] H. Nishino, R. Takahashi, S. Sato, T. Sodesawa, Phase separation in the solution of water glass and poly(vinyl alcohol), *Journal of Non-Crystalline Solids* 333 (2004) 284–290. <https://doi.org/10.1016/j.jnoncrysol.2003.12.046>.
- [70] U. Schubert, *Chemistry and Fundamentals of the Sol-Gel Process*, Wiley-VCH Verlag GmbH & Co. KGaA, 2015.
- [71] L. Klein, M. Aparicio, A. Jitianu (Eds.), *Handbook of Sol-Gel Science and Technology: Processing, Characterization and Applications*, 2nd ed., Springer International Publishing, Cham, 2018.
- [72] I. Anisa, A. Nour, Affect of Viscosity and Droplet Diameter on water-in-oil (w/o) Emulsions: An Experimental Study, *World Academy of Science, Engineering and Technology* 62 (2010). <https://doi.org/10.5281/zenodo.1328970>.
- [73] Shimio Sato, Tadahiro Murakata, Tohru Suzuki, Takashi Ohgawara, Control of pore size distribution of silica gel through sol-gel process using water soluble polymers as additives, *Journal of Materials Science* 25 (1990) 4880–4885. <https://doi.org/10.1007/BF01129956>.

- [74] J.K. Sakkos, D.P. Kieffer, B.R. Mutlu, L.P. Wackett, A. Aksan, Engineering of a silica encapsulation platform for hydrocarbon degradation using *Pseudomonas* sp. NCIB 9816-4, *Biotechnol. Bioengineering* 113 (2016) 513–521. <https://doi.org/10.1002/bit.25821>.
- [75] W. Aftab, X. Huang, W. Wu, Z. Liang, A. Mahmood, R. Zou, Nanoconfined phase change materials for thermal energy applications, *Energy and Environmental Science* 11 (2018) 1392–1424. <https://doi.org/10.1039/C7EE03587J>.
- [76] G. Ferrer, A. Solé, C. Barreneche, I. Martorell, L.F. Cabeza, Review on the methodology used in thermal stability characterization of phase change materials, *Renewable and Sustainable Energy Reviews* 50 (2015) 665–685. <https://doi.org/10.1016/j.rser.2015.04.187>.
- [77] A. Shukla, D. Buddhi, R.L. Sawhney, Thermal cycling test of few selected inorganic and organic phase change materials, *Renewable Energy* 33 (2008) 2606–2614. <https://doi.org/10.1016/j.renene.2008.02.026>.
- [78] M.K. Rathod, J. Banerjee, Thermal stability of phase change materials used in latent heat energy storage systems: A review, *Renewable and Sustainable Energy Reviews* 18 (2013) 246–258. <https://doi.org/10.1016/j.rser.2012.10.022>.
- [79] L.B. Petrovic, V.J. Sovilj, J.M. Katona, J.L. Milanovic, Influence of polymer-surfactant interactions on o/w emulsion properties and microcapsule formation, *Journal of Colloidal and Interface Science* 342 (2010) 333–339. <https://doi.org/10.1016/j.jcis.2009.10.077>.
- [80] X. Xin, H. Zhang, G. Xu, Y. Tan, J. Zhang, X. Lv, Influence of CTAB and SDS on the properties of oil-in-water nano-emulsion with paraffin and span 20/Tween 20, *Colloids and Surfaces A: Physicochemical and Engineering Aspects* 418 (2013) 60–67. <https://doi.org/10.1016/j.colsurfa.2012.10.065>.
- [81] H. Heinz, C. Pramanik, O. Heinz, Y. Ding, R.K. Mishra, D. Marchon, R.J. Flatt, I. Estrela-Lopis, J. Llop, S. Moya, R.F. Ziolo, Nanoparticle decoration with surfactants: Molecular interactions, assembly, and applications, *Surface Science Reports* 72 (2017) 1–58. <https://doi.org/10.1016/j.surfrep.2017.02.001>.
- [82] J. Lacava, A.-A. Ouali, B. Raillard, T. Kraus, On the behaviour of nanoparticles in oil-in-water emulsions with different surfactants, *Soft Matter* 10 (2014) 1696–1704. <https://doi.org/10.1039/c3sm52949e>.
- [83] T.F. Tadros, *Topics in Colloid and Interface Science*, first ed., Wiley-VCH Verlag, 2011.

3.2.12 Supporting Information

Additional Figures, Tables and Descriptions:

- Additional Figures for Section 3.2.6.1: Fig. S2.1 to S2.9
- Additional Figures for Section 3.2.6.3: Fig. S2.10 to S2.15
- Additional Description and QR code of Movie S2.1

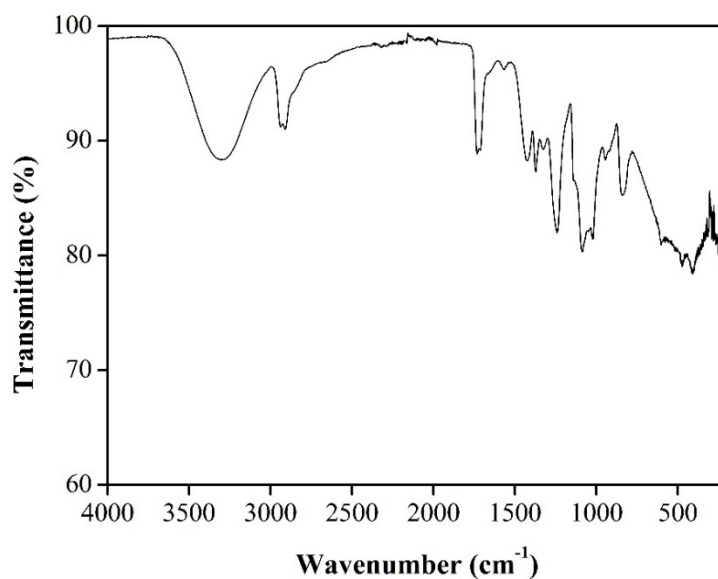


Fig. S2.1 ATR-IR spectrum of pure poly(vinyl alcohol) (PVA). ATR-IR peaks: 3600 - 3000 (m), 2939 (m), 2911 (m), 1731 (m), 1424 (m), 1241 (s), 1086 (s), 1022 (s), 841 (m) cm^{-1} .

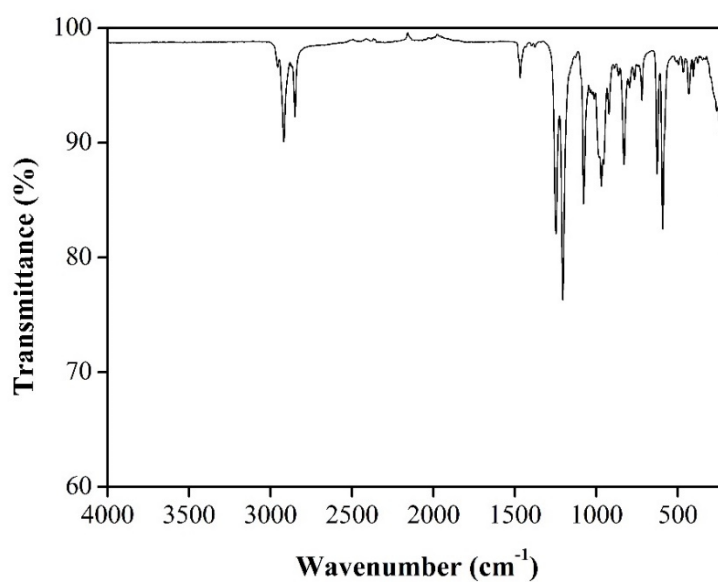


Fig. S2.2 ATR-IR spectrum of pure sodium dodecyl sulfate (SDS). ATR-IR peaks: 2957 (w), 2918 (m), 2850 (m), 1467 (w), 1205 (s), 1078 (s), 984 (s), 970 (m), 956 (m), 831 (m), 627 (m), 593 (s) cm^{-1} .

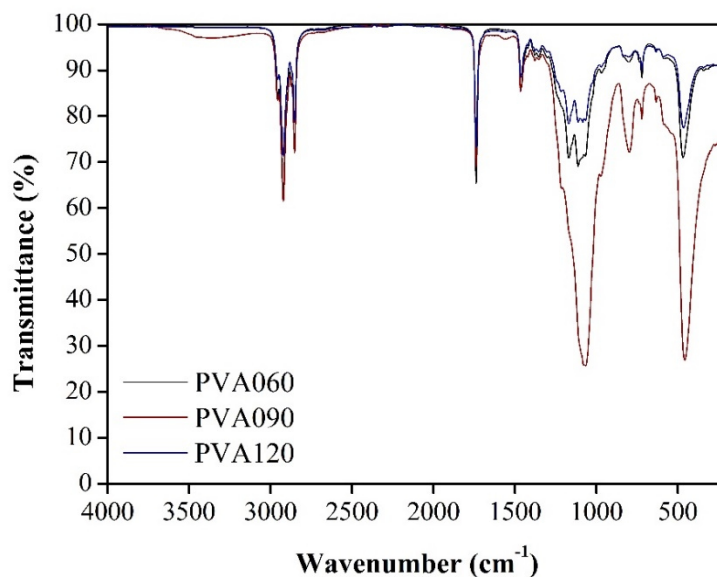


Fig. S2.3 ATR-IR spectra of ss-PCMs PVA060, PVA090 and PVA120. ATR-IR peaks: (PVA060) 2957 (s), 2922 (s), 2852 (s), 1738 (s), 1465 (m), 1170 (s), 1113 (s), 801 (w), 721 (w), 469 (s) cm^{-1} ; (PVA090) 2957 (s), 2922 (s), 2852 (s), 1738 (s), 1465 (m), 1214 (s), 1078 (s), 798 (w), 721 (w), 459 (s) cm^{-1} ; (PVA120) 2957 (s), 2922 (s), 2852 (s), 1738 (s), 1465 (m), 1217 (s), 1084 (s), 802 (w), 721 (w), 466 (s) cm^{-1} . All ss-PCMs show the same absorption band (IR peaks). Therefore, the SDS, PVA and BS should be chemically stable in the silica matrix and should have not reacted or interacted strongly with the silica matrix. Peak assignment for PVA060 (s: sharp; m: medium, w: weak) 2957 cm^{-1} (s), 2922 cm^{-1} (s) and 2852 cm^{-1} (s): $-\text{CH}_3$ and $-\text{CH}_2-$ stretching vibration of BS, SDS and PVA; 1738 cm^{-1} (s): C=O stretching vibration of the ester-group in BS and possible ketone-groups in PVA; 1465 cm^{-1} (m): $-\text{CH}_3$ and $-\text{CH}_2-$ bending vibration of BS, SDS and PVA; 1170 cm^{-1} (s) and 1113 cm^{-1} (s): antisymmetric stretching vibration of Si-O-Si; 801 (w): symmetric stretching vibration of Si-O-Si; 721 (w): $-\text{CH}_2-$ rocking vibration of BS, SDS and PVA; 469 cm^{-1} (s): transverse-optical rocking vibration (perpendicular to the Si-O-Si plane) of the oxygens of Si-O-Si.

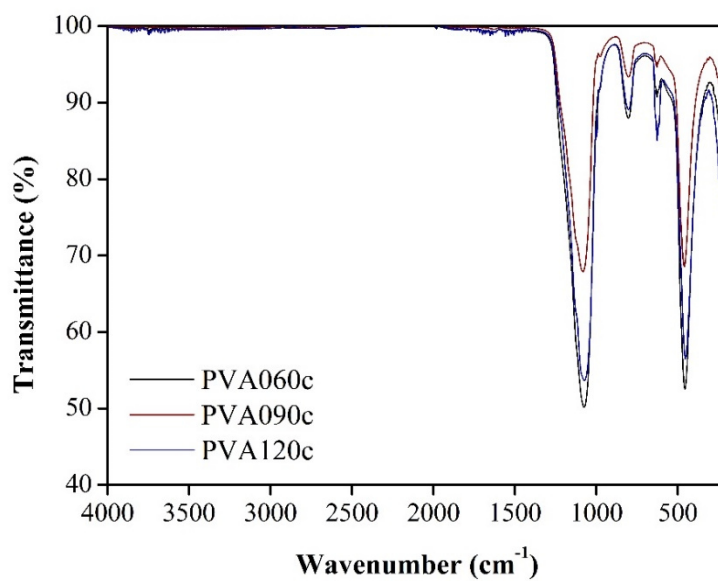


Fig. S2.4 ATR-IR spectra of calcined ss-PCMs PVA060c, PVA090c and PVA120c. ATR-IR peaks: (PVA060c) 1077 (s), 804 (w), 629 (w), 457 (s) cm⁻¹; (PVA090c) 1083 (s), 804 (w), 629 (w), 460 (s) cm⁻¹; (PVA120c) 1074 (s), 803 (w), 627 (w), 456 (s) cm⁻¹.

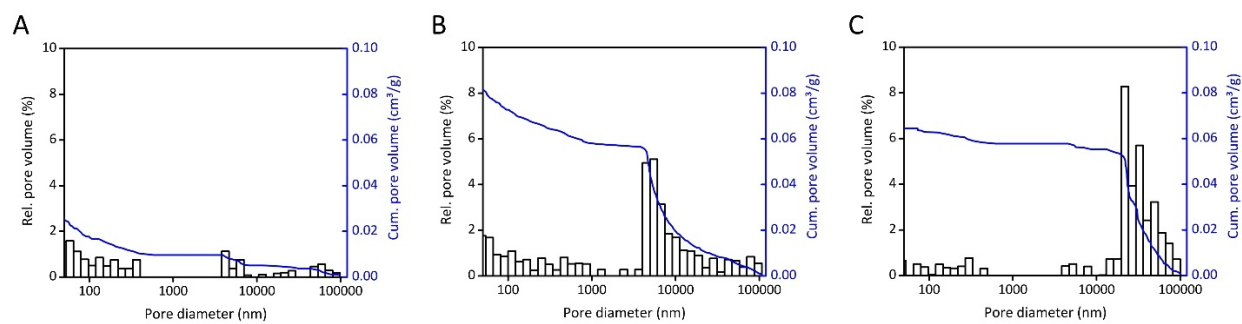


Fig. S2.5 Mercury intrusion measurements of ss-PCM samples PVA060 (A), PVA090 (B) and PVA120 (C).

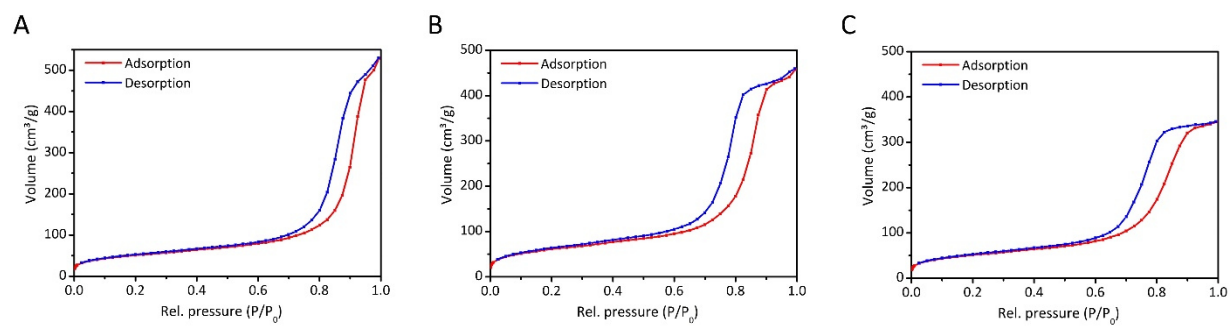


Fig. S2.6 Nitrogen adsorption isotherms of calcined ss-PCM samples PVA060c (A), PVA090c (B) and PVA120c (C).

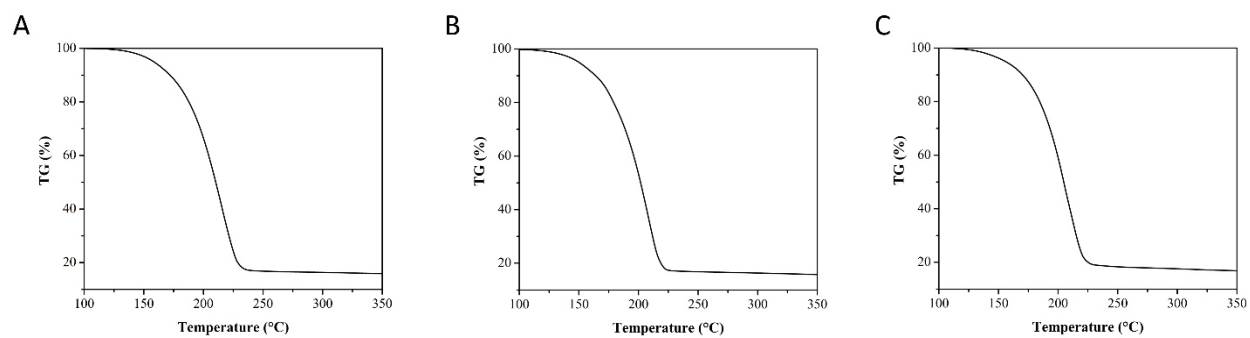


Fig. S2.7 TG curves of ss-PCM samples PVA060 (A), PVA090 (B) and PVA120 (C).

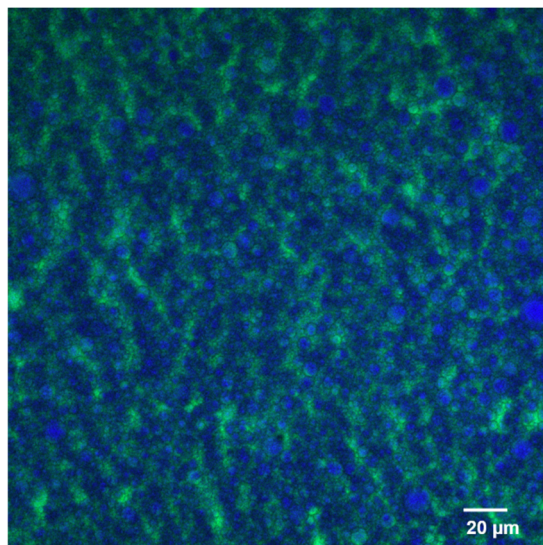


Fig. S2.8 Imaging of ss-PCM formation of PVA120 during gelation after 15 min by confocal fluorescence microscopy.

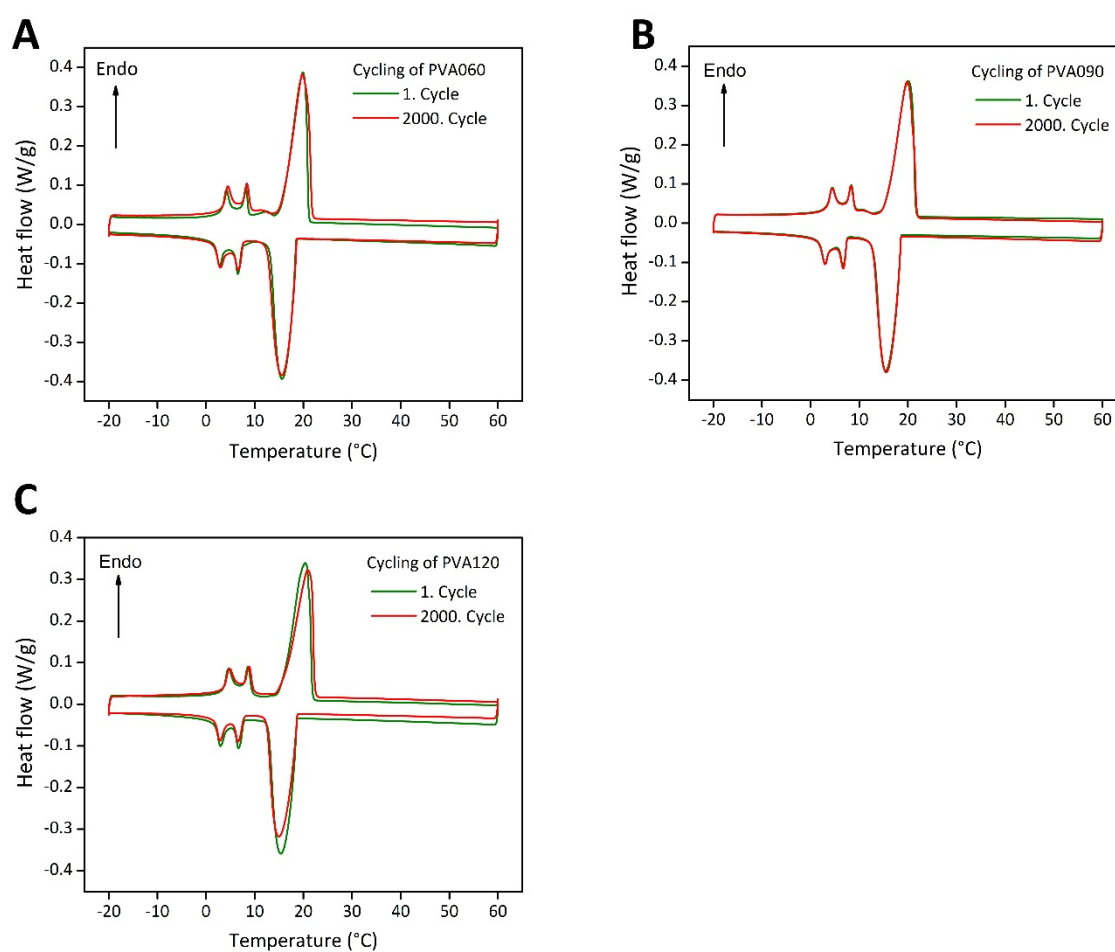


Fig. S2.9 DSC curves of ss-PCMs PVA060 (A), PVA090 (B) and PVA120 (C) before (1. Cycle) and after (2000. Cycle) thermal cycling experiments. The ss-PCM samples were heated above the melting point and cooled down below the freezing point for up to 2000-times (2000 cycles) to test the long-term performance and durability. For PCM in buildings, every cycle is assumed to express one day cycle of night time (PCM freezing) and day time (PCM melting). The samples PVA060 ($\pm 0.5\%$), PVA090 ($\pm 0.5\%$) and PVA120 ($\pm 3.0\%$) have nearly the same latent heat before and after the thermal cycling tests and the values for the latent heats are within the DSC uncertainty of $\pm 3.22\%$. Therefore, all samples have a high long-term performance. The silica phase seems to protect the BS efficiently from chemical degradation, reactions or interactions, which can lower the latent heat of pure BS during thermal cycling measurements.

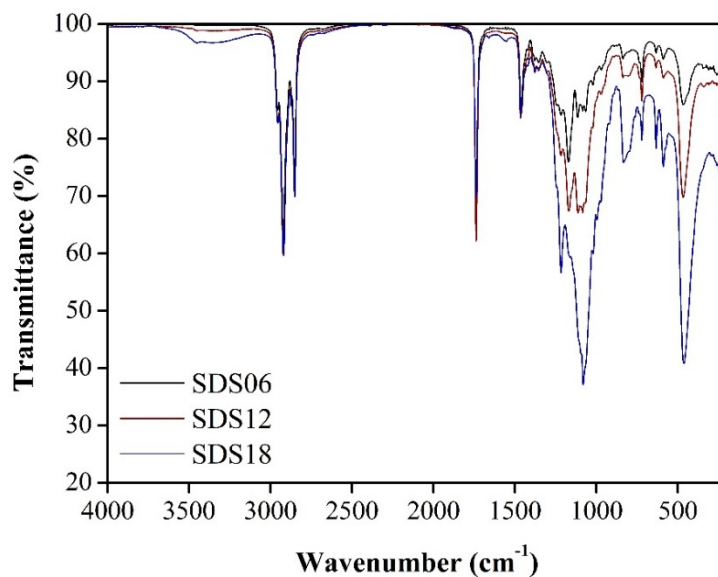


Fig. S2.10 ATR-IR spectra of ss-PCMs SDS06, SDS12 and SDS18. ATR-IR peaks: (SDS06) 2957 (s), 2922 (s), 2852 (s), 1738 (s), 1465 (m), 1171 (s), 1116 (s), 803 (w), 721 (w), 467 (s) cm^{-1} ; (SDS12) 2957 (s), 2922 (s), 2852 (s), 1738 (s), 1467 (m), 1216 (s), 1081 (s), 804 (w), 721 (w), 469 (s) cm^{-1} ; (SDS18) 2957 (s), 2919 (s), 2851 (s), 1738 (s), 1465 (m), 1217 (s), 1084 (s), 834 (w), 721 (w), 463 (s) cm^{-1} . All ss-PCMs have the same absorption band in ATR-IR spectra as sample row PVA (peak assignment: Fig. S3) and, thus, SDS, PVA, silica and BS should not chemically react or strongly interact with each other in the silica phase of the ss-PCM.

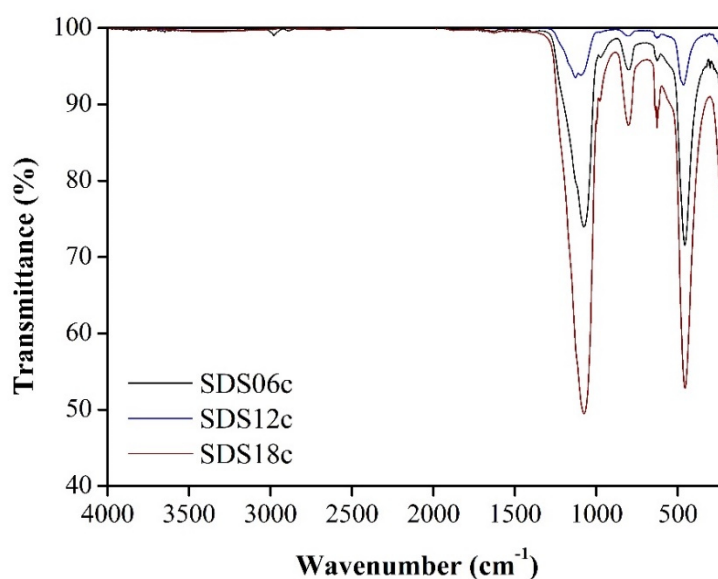


Fig. S2.11 ATR-IR spectra of calcined ss-PCMs SDS06c, SDS12c and SDS18c. ATR-IR peaks: (SDS06c) 1075 (s), 801 (w), 627 (w), 459 (s) cm^{-1} ; (SDS12c) 1096 (s), 806 (w), 629 (w), 466 (s) cm^{-1} ; (SDS18c) 1076 (s), 803 (w), 629 (w), 457 (s) cm^{-1} .

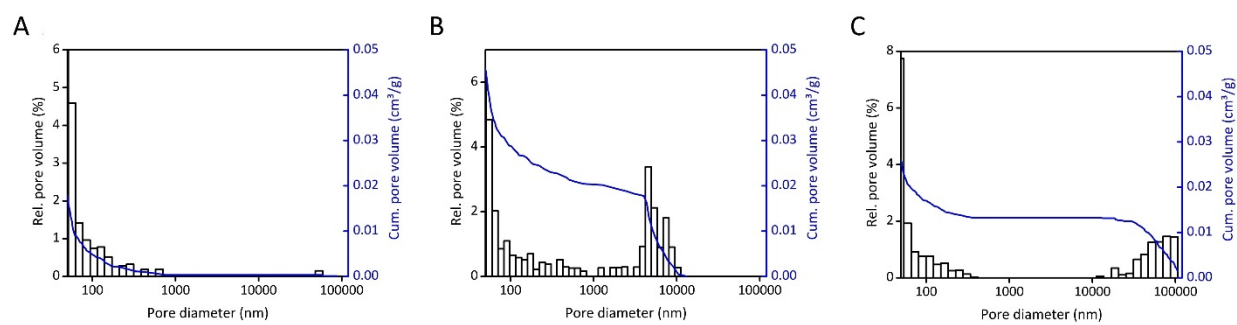


Fig. S2.12 Mercury intrusion measurements of ss-PCM samples SDS06 (A), SDS12 (B) and SDS18 (C).

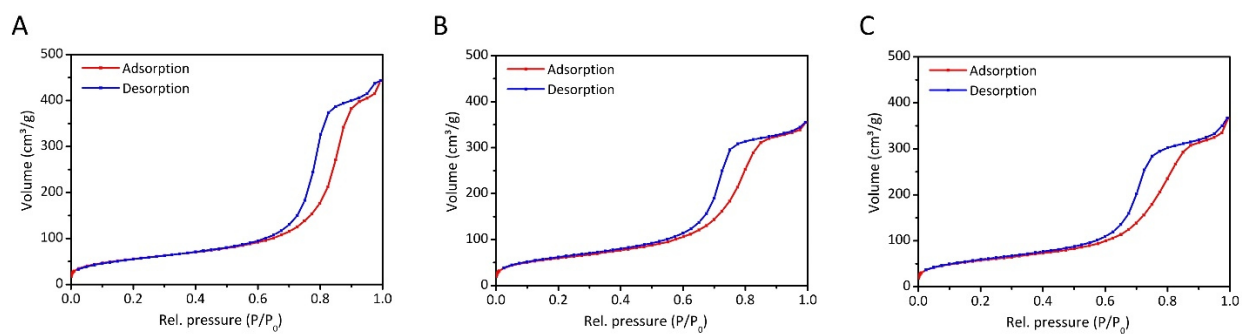


Fig. S2.13 Nitrogen adsorption isotherms of calcined ss-PCM samples SDS06c (A), SDS12c (B) and SDS18c (C).

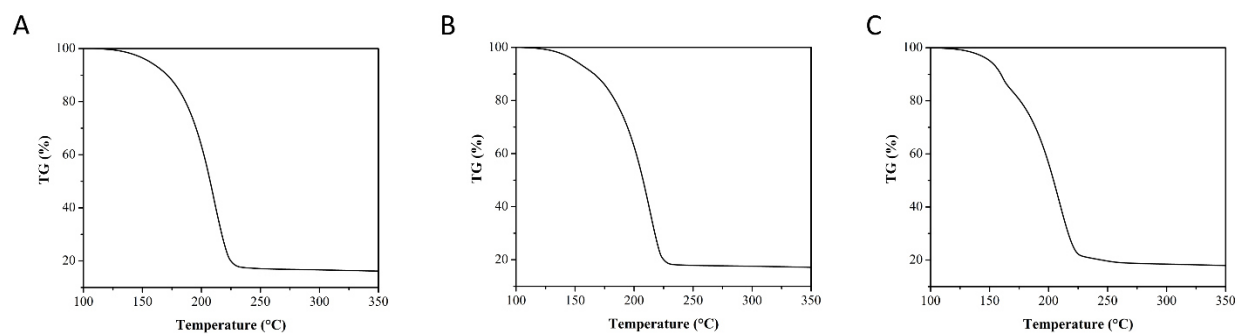


Fig. S2.14 TG curves of ss-PCM samples SDS06 (A), SDS12 (B) and SDS18 (C).

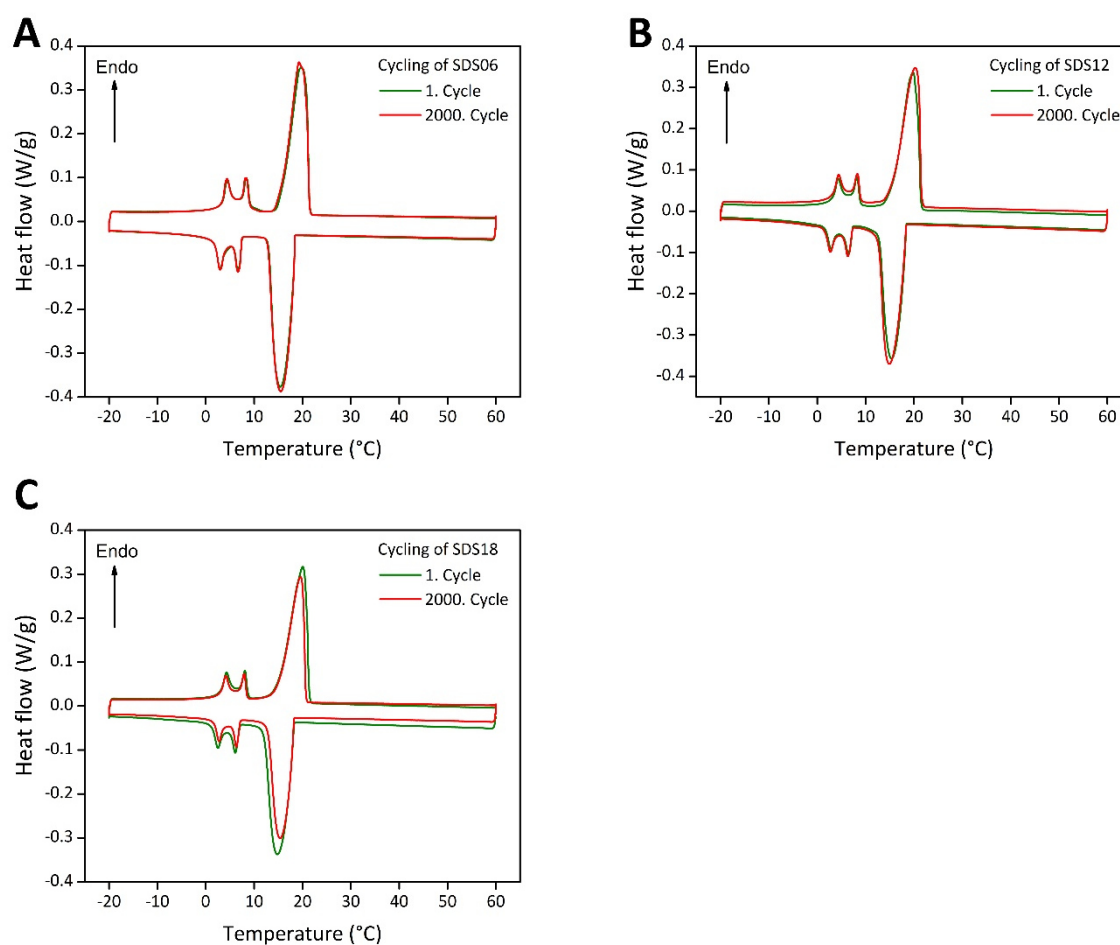
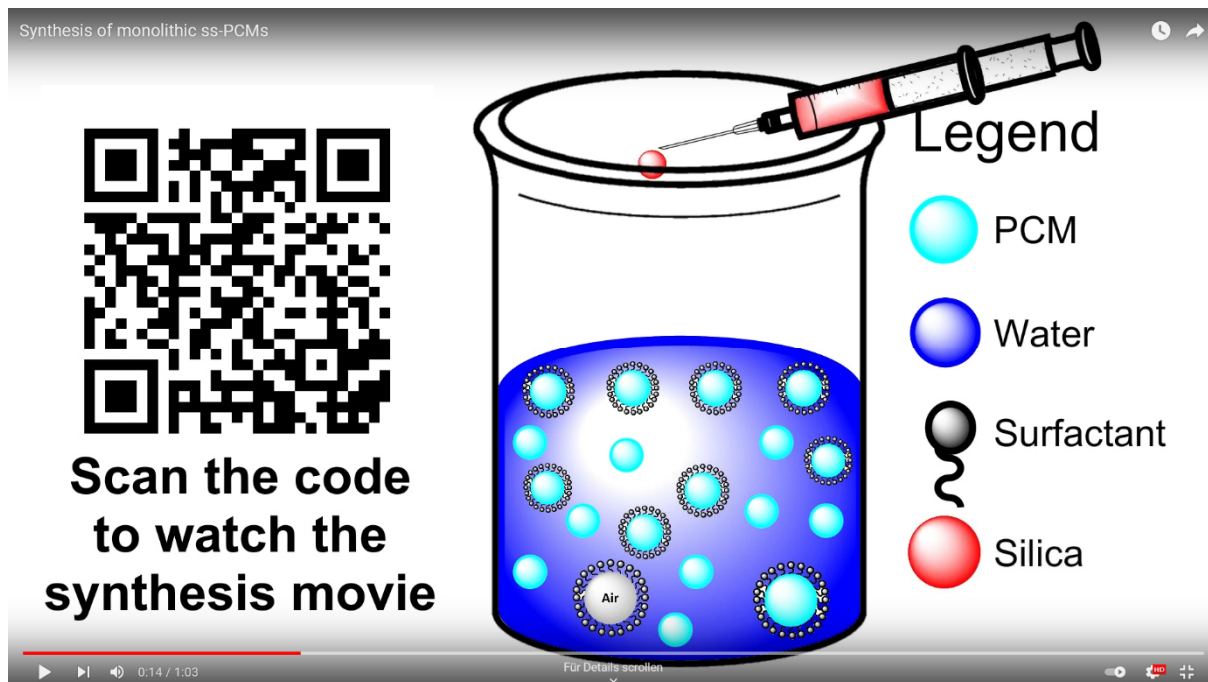


Fig. S2.15 DSC curves of ss-PCMs SDS06 (A), SDS12 (B) and SDS18 (C) before (1. Cycle) and after (2000. Cycle) thermal cycling experiments. The ss-PCM samples were heated above the melting point and cooled down below the freezing point for up to 2000-times (2000 cycles) to test the long-term performance and durability. The samples SDS06 ($\pm 0.2\%$), SDS12 ($\pm 0.2\%$) and SDS18 ($\pm 1.0\%$) have nearly the same latent heat before and after the thermal cycling tests and the values for the latent heat are within the DSC uncertainty of $\pm 3.22\%$. Thus, all samples have a high long-term performance of at least 2000 days in building applications. The silica phase seems to protect the BS efficiently from chemical degradation, reactions or interactions, which can lower the latent heat of pure BS during thermal cycling measurements.

Synthesis of monolithic ss-PCMs



Scan the code
to watch the
synthesis movie

Legend

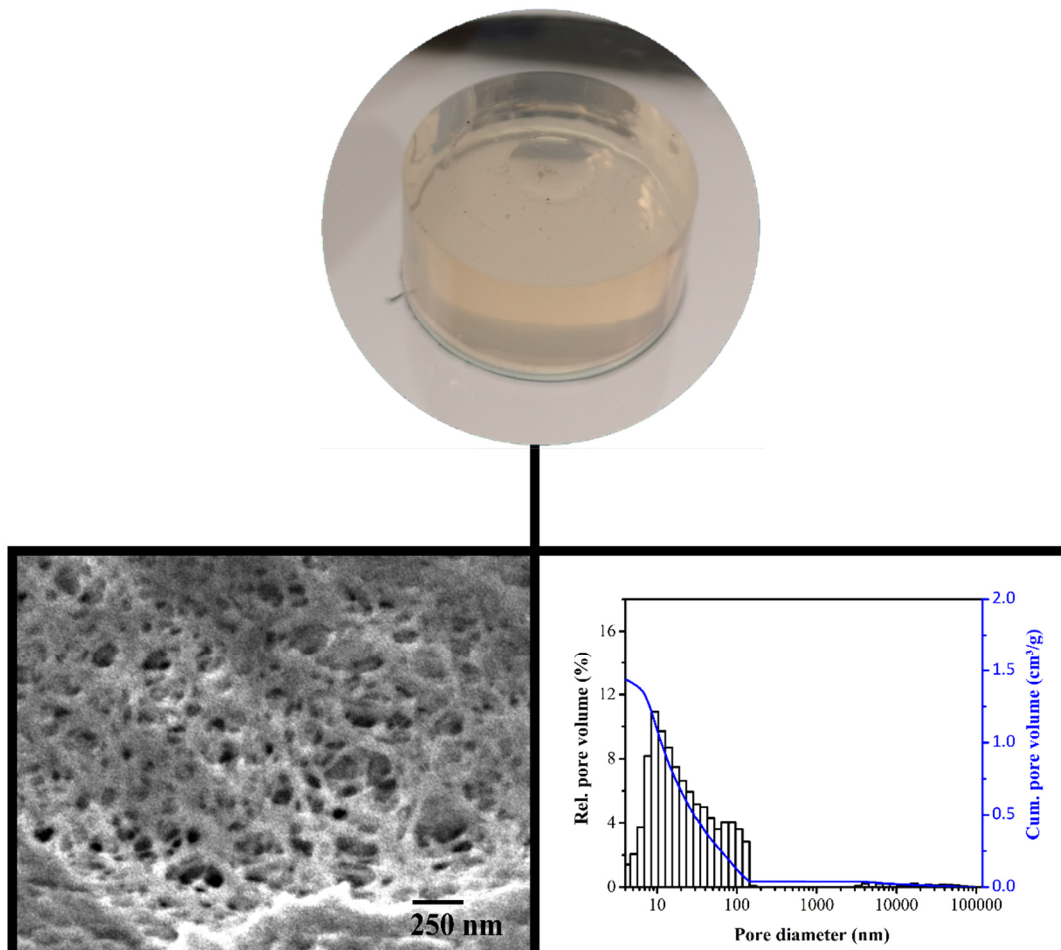
- PCM
- Water
- Surfactant
- Silica

0:14 / 1:03

Für Details scrolle...

Movie S2.1 Animated movie of the formation mechanism of ss-PCMs and the reaction steps. To watch the movie on Youtube, the QR code can be scanned. Link to movie: <https://youtu.be/drSIWO7IzTo>.

3.3 Shape stabilization of organic phase change materials as mechanical stable silica boards with high latent heats via sol-gel route



Authors

Felix Marske¹, Caroline Haupt², Claudia Birkemeyer³, Kirsten Bacia², Thomas Hahn¹ and Dirk Enke⁴

¹ Institute of Technical Chemistry, Martin Luther University of Halle-Wittenberg, 06120 Halle (Saale), Germany.

² Biophysical Chemistry, Institute of Chemistry and Charles-Tanford Protein Center, Martin Luther University of Halle-Wittenberg, 06120 Halle (Saale), Germany.

³ Institute of Analytical Chemistry, Leipzig University, 04103 Leipzig, Germany

⁴ Institute of Chemical Technology, Universität Leipzig, 04109 Leipzig, Germany.

State of Publication

Accepted 15th November 2022 in Journal of Building Engineering

<https://doi.org/10.1016/j.jobbe.2022.105198>

3.3.1 Abstract

Monolithic shape-stabilized phase change materials (ss-PCM) are of great interest for energy-saving construction materials, solar-water heating systems and passive cooling systems of batteries and photovoltaic cells. However, the application range of ss-PCMs is currently limited by either low mechanical stabilities or low heat storage capacities. Therefore, we have recently developed ss-PCMs based on silica and butyl stearate (BS) with high compressive strengths (1.2 MPa, 10 °C) and moderate latent heats (~100 J/g). Here, we synthesize ss-PCMs with high compressive strengths (1.2 MPa, 5 °C) as well as high latent heats (160 J/g) by combining mixtures of hexadecane (HD), octadecane (OD) and BS with our sol-gel route. Due to the well-interconnected silica matrix confining the paraffins, the ss-PCMs have 70 % higher thermal conductivities (0.43 W/mK, 5 °C) than pure paraffins, high shape-stabilities (~100 %), high PCM loadings (83 wt%), and high chemical and long-term stabilities (> 3000 thermal cycles). Moreover, they are thermally stable up to ~170 °C with PCM melting points of 17 °C and 22 °C. We also synthesize ss-PCMs with polyethylene glycol 600 (PEG600) and acetamide (Ac) to analyze the effect of non-paraffinic PCMs on the physicochemical properties of our ss-PCMs. These ss-PCMs had a ~30 % lower latent heat than expected because the PCM either reacted strongly by hydrogen bonding with the silica (PEG600) or was chemically degraded under the basic conditions during gelation (Ac). In contrast to the low compressive strength of shape-stabilized PEG600 (35 kPa, 5 °C), the ss-PCMs based on Ac have high compressive strengths (9.6 MPa, 5 °C). Moreover, they are translucent above the PCM melting point due to a nanoscopic silica matrix. The high supercooling effect (37 °C) and the moderate long-term stability (3000 thermal cycles, 20 % lower latent heat) of shape-stabilized Ac restrict its application to special, glassy materials.

Keywords:

Thermal energy storage, Phase change materials, Encapsulation, Sol-gel, Paraffin, Shape stability

3.3.2 Introduction

Due to the changing climate, humanity currently faces many social and environmental problems. In order to decelerate global warming but simultaneously meet global energy demands, the world desperately needs new energy technologies that are renewable, CO₂-neutral, and energy-efficient.

Currently, the building and transport sectors comprise 32 % and 35 % of the total global primary energy demand - a major share that needs to be drastically lowered in the coming years.[1]. Therefore, new energy-saving building materials and techniques with low CO₂-emission are of central interest. Because the cooling and heating applications are responsible for over 70 % of the energy consumption in buildings [1], the focus should lay on the development of new insulation materials [2–4], heat-pumps [5–7], geothermal [8,9], solar [10,11] and thermal energy systems [12–14]. Thermal energy systems based on latent heat storage (LHS) are particularly suited as future energy-saving building materials, as they can store 5 to 14-times more energy per volume as thermal energy than typical building construction materials made of bricks, concrete or gypsum [15]. The LHS materials are named phase change materials (PCM) because they store heat by a state transition and release it by the reverse state transition at a specific temperature, enabling passive heating and cooling, and, therein, reducing daily temperature fluctuations in living rooms [16]. For organic PCMs that undergo transition from solid to liquid state, the characteristic parameters are the melting and freezing points, which should be within the temperature comfort range of 18 - 30 °C for the usage as TES material in buildings.

Typical organic PCMs are polyethylene glycols [17–19], paraffins [20–22], fatty acids [23–25] and fatty acid esters [26–28]. These PCMs benefit from a moderate thermal stability, high chemical stability, low supercooling effects, no phase segregation effects and a low price, such as \$1.9/kg for paraffins and \$1.6/kg for fatty acids [29]. However, the application of organic PCMs in buildings is limited due to low thermal conductivity [30], low mechanical stability [31], and leakage issues in composite construction materials [32].

To overcome these problems, organic PCMs can be shape-stabilized by a wide range of different techniques: macro- and micro-encapsulation [33–35], vacuum-impregnation [36–38], and shape-stabilization as a blend with additives of high thermal conductivities [39–41]. The simplest immobilization technique of organic PCMs is the macroencapsulation of liquid PCM. In this technique, liquid PCM is filled in a suitable metal container, which is subsequently sealed to prevent leakage of liquid PCM. These shape-stabilized PCMs (ss-PCMs) have low thermal conductivities, resulting in high incongruent melting and supercooling effects [42,43]. Moreover, the metal container limits its application range in buildings. In the

microencapsulation approach liquid PCM is suspended in an aqueous solution as droplets. A polymeric shell is built around the PCM droplets to form a core-shell (cs) structure in solution. In these cs-PCMs, approximately 50 - 70 wt% PCM is immobilized due to volume expansion processes and additional thermal additives in the core [44]. The cs-PCMs are commercially available, for example by Microtek Labs as Micronal PCM [45], and have to be added as dry additives to construction materials for shape-stabilization as huge composite boards. To maintain its mechanical stability, the amount of cs-PCM is limited for different construction materials, for example to a maximum of 5 wt% for cementitious materials and 30 wt% for plaster [46].

For shape-stabilization of PCM by vacuum impregnation, nanoporous carrier monoliths are filled with liquid PCM under vacuum. High capillary forces often hinder complete vacuum infiltration of the porous monolithic material with PCM, resulting in low thermal conductivities and latent heats of these ss-PCMs [44,47,48]. In contrast, ss-PCM blends and suspensions yield higher latent heats and thermal conductivities than the ss-PCMs synthesized by vacuum-impregnation and microencapsulation. Following this approach, however, the mixing of liquid PCM with thermal additives, such as expanded graphite or copper nanoparticles, results in ss-PCMs with weakly connected molecular structures and thus, low mechanical stabilities [49–51]. Moreover, the ss-PCM blends are often fragmented after synthesis and not monolithic [44,51].

In summary, the perfect monolithic ss-PCM board that combines high latent heats, high thermal conductivities, high decomposition points and high mechanical stability is yet missing in the current literature. Additionally, most ss-PCMs can only be synthesized with one specific organic PCM class, limiting its application range [44,52].

Recently, we presented a novel sol-gel synthesis route to produce monolithic ss-PCMs with optimized thermal and mechanical properties [53]. By addition of hexagonal boron nitride particles for faster heat transfer, thermal conductivities could be improved while maintaining high mechanical stability and PCM loadings [54,55]. However, we created a shape-stabilized ss-PCM board made of only one fatty acid ester, butyl stearate, as PCM material. This ss-PCM turned out to be already quite efficient exhibiting a latent heat in the range of 100 J/g and a high compressive strength of 0.7 MPa (at 30 °C) at very high PCM loadings (86 wt%) [54]. Nevertheless, butyl stearate is a technical product with an in general relatively low latent heat of about 125 J/g, hindering its usage in industrial applications in contrast to paraffinic PCMs with latent heats above 200 J/g.

In this study, we aimed to extend the breadth of the recently introduced porogen-assisted sol-gel process [54] by using different organic PCMs, such as hexadecane, octadecane, PEG600

and acetamide, to further improve latent heat storage, and to enable wider commercial usage for example in heat-saving translucent window materials, walls, floor boards; or to increase the thermal storage capacity of electrical heaters and hot water storage systems in buildings. For the long-term performance and durability, we performed GC-MS, DSC and IR measurements to verify the chemical inertness of the paraffinic and non-paraffinic PCMs after shape-stabilization. Furthermore, we provide an in-depth analysis of the formation mechanism, the silica structure, the mechanical stability and the thermal properties of the ss-PCM.

3.3.3 Experimental

3.3.3.1 Materials

Köstrosol 0730 (30 wt% colloidal silica particles in water, 7 nm average particle diameter) was used as stabilized silica sol and purchased from *Chemiewerk Bad Köstritz*, Germany. Butyl stearate (technical grade product) and sodium dodecyl sulfate (SDS, ≥ 99.0 % GC, dust-free pellets) were obtained from *Alfa Aesar* and *Sigma-Aldrich*, respectively. Poly(vinyl alcohol) (PVA, 88 % hydrolyzed, average M.W. 22000) was purchased from *ACROS Organics*. The paraffins n-hexadecane (95 %) and n-octadecane (99 %) were both provided by *Alfa Aesar*. The non-paraffinic PCMs acetamide (99 %, GC) and poly(ethylene glycol) 600 (PEG, average M.W. 600) were obtained from *Sigma-Aldrich* and *ACROS Organics*, respectively. The fluorescent dye perylene was purchased from *Sigma Aldrich*, AlexaFluor 488 hydrazide and FM1-43 (N-(3-triethylammoniumpropyl)-4-(4-(dibutylamino) styryl) pyridinium dibromide) were purchased from *ThermoFisher Scientific*. Deionized water was used for all experiments.

3.3.3.2 Preparation of ss-PCMs

A total of 0.33 g poly(vinyl alcohol) (PVA) in 3.71 g water was heated to 60 °C until it was completely dissolved constituting the aqueous phase (5 h). The solution was added to a suspension of 0.44 g sodium dodecyl sulphate (SDS) and 11 g PCM. The PCM mass was varied from 11 g (standard) to 44 g in separate synthesis approaches to analyze the upper limit of shape-stability. Four different PCMs were used for the synthesis of ss-PCMs: n-hexadecane (HD), n-octadecane (OD), poly(ethylene glycol) 600 (PEG600) and acetamide (Ac). Each reaction mixture was heated to 50 °C in an oven for at least 12 h. For paraffin emulsification and dissolution of the non-paraffinic PCMs, the reaction mixtures were stirred for 15 min at 700 rpm and 40 °C. Afterwards, 4.95 g *Köstrosol 0730* was slowly transferred to the reaction mixtures and stirred for additional 15 min (700 rpm, 40 °C). The magnetic stirrers

were removed, the reaction vessels were closed with a cap and heated to 40 °C for 72 h. The cap was removed from the reaction vessels and the obtained wet gels were dried first at 40 °C for 7 days under ambient pressure, then at 60 °C for 2 days and finally at 100 °C for 24 h. In this work, the samples were prepared similar to the ss-PCMs based on butyl stearate as PCM from our previous studies [53,54].

3.3.3.3 Nomenclature of ss-PCMs

The ss-PCMs samples were named after the PCM used for the synthesis in this work. The paraffinic ss-PCMs Hexa and Octa were synthesized with a PCM mixture of 70 % hexadecane (HD) and 30 % butyl stearate (BS) and 70 % octadecane (OD) and 30 % butyl stearate, respectively. The ss-PCMs Acet and PEG were prepared with non-paraffinic PCMs acetamide (Ac) and polyethylene glycol 600 (PEG 600), respectively. The calcined ss-PCM samples were named PCM_c, for example Acet_c for ss-PCM Acet after calcination at 600 °C for 10 h.

3.3.3.4 Characterization methods

The macro- and mesoporosity of the silica matrix in ss-PCMs were analyzed by mercury (Hg) intrusion measurements (Pascal40 (400kPa) and Pascal440 (400 MPa), Porotec). The pore diameter (named also as pore width), pore volume and porosity were calculated by the Washburn-equation, using a cylindrical pore model [56]. The contact angle of mercury was 141.3°. Additionally, the micro- and mesoporosity were characterized by nitrogen sorption experiments (N₂) at -196 °C via a Sorptomatic 1990 surface area analyser by Porotec. About 100 mg of the ss-PCM sample was analyzed before and after calcination at 600 °C (10 h). The mesopore volume, mesopore diameter (width) and the specific surface area of the samples were obtained by calculations via the Brunauer-Emmett-Teller (BET) method [57]. The ss-PCMs were dried at 120 °C (48 h) under ultrahigh vacuum for each measurement to remove potentially adsorbed water. The specific surface area was determined by a linearized form of the BET equation in the pressure range of $0.05 \leq p/p_o \leq 0.30$. The mesopore volume was calculated at a relative pressure p/p_o of 0.99. The total pore volumes of the calcined ss-PCMs were obtained by adding the macro- (Hg) to the mesopore (N₂) volume.

High-resolution scanning electron microscopy (HRSEM, Merlin microscope, Zeiss) was performed to obtain high-resolution microscopic images of the ss-PCM and the silica structure in the ss-PCMs. The sample was fixated on a conductive carbon tape. For imaging, the secondary electron acceleration was set to 3 - 5 kV.

The gelation times were analyzed for 5 - 8 subsamples of every ss-PCM formulation and the average value was used as gelation time. Every ss-PCM was turned upside down during the gelation process before solidification. Gelation was considered as finished when the gel did not move during the upside down turn. The relative uncertainty of all measurements was approximately $\pm 5.0\%$.

The thermal conductivity was characterized by a TPS 1500 thermal analyzer by Hot Disk AB based on a transient plane source (TPS) method via sandwich-mode at 5 °C and 40 °C (90 °C for sample Acet). Each sample was sawed in two halves and used to cover the sensor and heater unit (platelet form) [54]. The sensor and heater unit was used to measure the thermal conductivity on three different spots between the ss-PCM halves for three times with a waiting interval of 10 min between each measurement and the average value was calculated for each ss-PCM sample (average relative uncertainty: $\pm 0.76\%$). The thermal properties of the ss-PCMs, such as the latent heat and supercooling effect, were measured by an 822e calorimeter from METTLER TOLEDO in a DSC analysis system with a heating rate of 1 °C/min, running from -20 to 60 °C (Acet: 0 – 100 °C) and vice versa under air atmosphere with holding times of 10 min at -20 and 60 °C (temperature range of Acet: 0 and 100 °C; average relative uncertainty for all latent heats ΔH_{total} was $\pm 2.9\%$ as calculated by integration of the DSC peak area of the DSC curves). A constant amount of ss-PCM of 15 mg was used for the measurements to minimize the dependence on the mass. The peak maximum and minimum of the DSC measurements of each ss-PCM were used to determine and define the melting and freezing points T_m and T_f of the PCMs and ss-PCMs. At these specific temperatures, most of the PCM phase is undergoing a phase transition during measurements. The melting point was subtracted from the freezing point to obtain the supercooling temperature of PCM ΔT_s .

Long-term performance tests were performed as described for the DSC measurements between 8 °C and 60 °C (100 °C for Acet) at a heating rate of 10 °C/min until the ss-PCMs were melted and frozen 3000 × (heating rate of 1 °C/min for 3000. cycle). The thermal stability of the ss-PCM samples was characterized by thermogravimetry (TG) using a STA 409 C/CD thermal analyser (Netzsch). Each ss-PCM sample (50 mg) was heated from 25 °C to 500 °C (heating rate: 2 °C/min). The decomposition points were calculated by the minimum value of the first derivative of the TG curves using the OriginPro 8.1 (OriginLab Corporation, Northampton, MA, USA) software (standard deviation: $\pm 2.0\%$).

The PCM leakage of the ss-PCMs was used to characterize the shape-stability and was calculated via the mass percentage difference before and after heating the sample at 100 °C for 1 week. The average uncertainty of this method was approximately $\pm 5.0\%$. The average comprehensive strength of each ss-PCM sample with the same composition was measured

five times on a TBH355 hardness tester from ERWEKA at 10 °C (solid silica matrix, solid PCM) and 40 °C (solid silica matrix, liquid PCM). The average relative uncertainty of the compressive strength measurements was $\pm 2.0\%$. The sample Acet was measured at 90 °C instead of 40 °C because of the higher melting point of acetamide.

To characterize the chemical stability of the pure PCM and the ss-PCM, samples were analyzed by attenuated total reflection Fourier transform infrared (ATR-FTIR) spectroscopy between 200 cm^{-1} to 4000 cm^{-1} in a Tensor 27 spectroscope by *Bruker* equipped with a diamond ATR unit (resolution: 4 cm^{-1}). Measurements were repeated 32-times.

To visualize gelation and aging processes of the ss-PCMs, confocal microscopy was performed on a Zeiss LSM 980 inverted microscope with an Airyscan detector using an LD Plan-Neofluar 20 \times , N.A. 0.4 objective, an LD C-Epiplan-Apochromat 50 \times , N.A. 0.6 objective and a Plan-Apochromat 63 \times , N.A. 1.4 oil-immersion objective. The wet ss-PCM mixtures (4 μL) were placed on glass coverslips equipped with a silicon ring as spacer. A second coverslip was put on top to get a closed microscopic chamber. The hydrophobic phase of the paraffinic ss-PCMs was marked with perylene (0.4 μM), which was excited with a diode laser at 405 nm [58]. The hydrophilic phase and the silica structure of all ss-PCMs were labelled with the water-soluble, green-fluorescent dye Alexa Fluor 488 hydrazide (a sulfonated derivative of Rhodamine Green) [59]. To further analyze the shape-stabilization process of non-paraffinic PCM PEG600, the green-fluorescent dye FM1-43, previously described as a label for hydrophobic-hydrophilic interfaces [60], was added to the sol-gel reaction mixture in a second approach. Alexa Fluor 488 as well as FM1-43 containing ss-PCMs (final concentration of 0.4 μM and 1 μM , respectively) were excited by a diode laser at 488 nm and the fluorescence emission was collected using the AiryScan detector. The two-color images were obtained using the line-wise multi-track mode.

The chemical stability was also characterized using mass spectrometry. A method for the analysis of volatile compounds was developed using thermal desorption in a headspace injector (HS-20) coupled to a Shimadzu QP-2010 GC-EI-quadrupole-MS (all modules from Shimadzu, Kyoto, Japan) equipped with a DB5-MS capillary column (J&W Fisher, 30 m, 0.25 mM id, 0.25 μM film). Headspace injection was done in loop mode (2 min load time and 1 min injection time) with helium as carrier gas at a column flow of 0.96 mL/min and a split of 10:1. The headspace oven was set to 80 °C, sample and transfer line to 160 °C with a pressurising gas pressure of 76 kPa and 1 min pressurising time. The GC programme started at 30 °C, held for 5 min and ramped with 6 °C/min to 150 °C. The electron impact ionization source operated at 200 °C and 70 eV, scanning from m/z 34 - 400. Analysis of polar substances was pursued using electrospray ionization on an ESI-qTOF Impact II (Bruker Daltonik GmbH) operated by

Control 4.0. For a sample delivery flow of 200 $\mu\text{L/h}$, nebulizer pressure was adjusted to 0.3 bar (4.4 psi) and dry gas was set to 4 L/min (both nitrogen) and 200°C. Ion signals were acquired in positive mode, with optimized parameters for detection between m/z 700 - 3000 (RF Funnel 1 400 / Funnel 2 600 / Hexapole 800 Vpp; ion energy 4 eV; low mass m/z 400; collision energy 10 eV, collision RF 1600 Vpp; transfer time 160 μs ; pre pulse storage 15 μs).

3.3.4 Results and discussion

In this work, we shape-stabilized the PCMs hexadecane (HD), octadecane (OD), acetamide (Ac), and polyethylene glycol 600 (PEG600) via our recently reported *in situ* sol-gel process to analyze the effect of paraffinic and non-paraffinic PCMs on the physicochemical properties of ss-PCMs. However, the hydrophobic phase of HD and OD separated from the hydrophilic aqueous phase after 5 - 10 min during ss-PCM gelation. To lower the hydrophobicity of the paraffins, 30 % BS was mixed with 70 % HD or OD. The HD/BS and OD/BS mixtures were used to synthesize the monolithic and crack-free ss-PCMs Hexa and Octa, respectively (Fig. 3.1). The non-paraffinic PCMs PEG 600 and Ac were shape-stabilized as monolithic ss-PCMs PEG and Acet (Fig. 3.1). The ss-PCM PEG is a yellowish monolith with a wet surface, indicating PCM leakage at the silica surface of the dried ss-PCM. In contrast, the ss-PCM Acet is shape-stabilized without any macroscopically visible PCM leakage on the outer surface. Moreover, Acet is opaque below the freezing point of pure Ac (Fig. 3.1 D) and translucent above the melting point of pure Ac (Fig. 3.1 E). The translucent color of Acet is an indicator for silica pore size distribution below 50 nm and could make Acet an interesting novel heat-saving glass material for buildings (e.g. for dormer windows) [61–64]. To the best of our knowledge, Acet is the first reported translucent ss-PCM which is not synthesized by macroencapsulation techniques [61–64].

To characterize the shape-stability of the ss-PCMs, PCM leakage was determined by comparing the overall mass of the ss-PCMs before and after keeping the samples at 100 °C for 1 week. If no leakage occurs, the shape-stability should be 100 % according to Eq. 3.1.

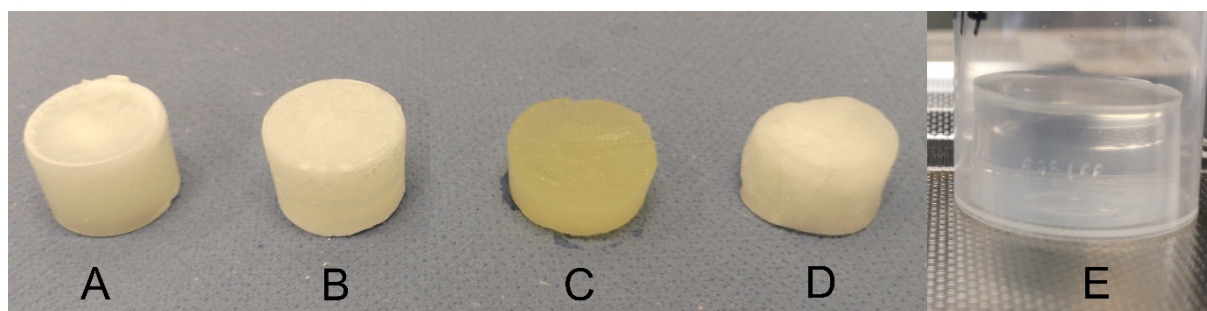


Fig. 3.1 Images of the ss-PCMs Hexa (A), Octa (B), PEG (C) and Acet (D, E). The ss-PCM Acet is milky-white below the freezing point of pure acetamide (D) and translucent above the melting point of pure acetamide (E).

$$S = \frac{m_{ssPCM100}}{m_{ssPCM}} \cdot 100 \% \quad (\text{Eq. 3.1})$$

where S is the shape-stability of the ss-PCM, m_{ssPCM} is the mass of ss-PCM and $m_{ssPCM100}$ is the mass of the ss-PCM after shape-stability tests at 100°C for 1 week.

The ss-PCMs Hexa, Octa and Acet have an S value of approximately 100 % indicating that no PCM leakage occurred during heating. In contrast, the sample PEG has an S value of 95 % and a thin PCM film could be observed on the surface of the sample, indicating marginal PCM leakage.

Another way to map PCM leakage is to compare the effective mass fraction of PCM $Ma(PCM)_{mass}$ (Eq. 3.3) of ss-PCMs in relation to the maximum possible effective mass fraction of PCM $Ma(PCM)_{max}$ (Eq. 3.2) of ss-PCMs, calculated by initially deployed educts in the ss-PCM synthesis except for water [53].

$$Ma(PCM)_{max} = \frac{m_{PCM}}{m_{educts} - m_{H_2O}} \cdot 100 \% \quad (\text{Eq. 3.2})$$

$$Ma(PCM)_{mass} = \frac{m_{ssPCM} - m_{additives}}{m_{ssPCM}} \cdot 100 \% \quad (\text{Eq. 3.3})$$

where $Ma(PCM)_{max}$ is the highest possible value for the effective mass fraction of PCM, $Ma(PCM)_{mass}$ is the effective mass fractions of PCM calculated by weight (mass), S is the shape-stability of the ss-PCM, m_{ssPCM} is the mass of ss-PCM, $m_{additives}$ is the mass of the educts without water and PCM, in particular the mass of SDS, PVA and silica, m_{H_2O} and m_{PCM} are the masses of water and PCM used for the synthesis of ss-PCMs, and m_{educts} is the total mass of all used educts for the syntheses (PCM, H₂O, SDS, PVA, silica).

Both values should match in case of no leakage. Because all ss-PCMs were synthesized similarly using the same amounts of educts, they all have a $Ma(PCM)_{max}$ of 83 wt%. We then determined the effective mass fraction of PCM $Ma(PCM)_{mass}$ by simply weighing the ss-PCM monoliths. For Hexa and Octa, as expected due to no observed leakage, $Ma(PCM)_{mass}$ has values of around 83 wt%. PEG has a $Ma(PCM)_{mass}$ value of 81 wt%, which comes along with the marginal visible leakage of PEG600 on the sample surface. Interestingly, ss-PCM Acet has a lower weight after synthesis than expected and, thus, a lower $Ma(PCM)_{mass}$ of 54 wt%. The reason for this loss of PCM could be attributed to a possible chemical degradation of acetamide to acetic acid due to the basic synthesis conditions, which then evaporated during subcritical drying in the sol-gel process [65].

In addition, we studied the maximum proportion of PCM that can be shape-stabilized. The paraffinic ss-PCMs Hexa and Octa are both monolithic and 100 % shape-stable up to a PCM mass percentage $Ma(PCM)_{max}$ of 86 wt%. At mass fractions of approximately 93 wt% they lose their form and shape-stability, which is comparable to ss-PCMs based on BS [53]. For PEG, the application of 84 wt% PCM leads to deformed ss-PCMs with an S value of 80 %. With higher PCM (PEG600) amounts above 86 - 87 wt%, no ss-PCMs can be synthesized. The ss-PCM Acet is shape-stable and monolithic up to a $Ma(PCM)_{max}$ of 85 wt% (the respective $Ma(PCM)_{mass}$ value was 56 wt%). But it fragments into small pieces at a $Ma(PCM)_{max}$ of 88 wt% ($Ma(PCM)_{mass}$: 58 wt%) due to the formation of needle-shaped Ac crystals after freezing.

The ss-PCMs with $Ma(PCM)_{mass}$ values higher than 83 wt% PCM are not further characterized because of 50 to 85 % lower compressive strengths for samples with 86 wt% PCM based on HD and OD, or rather 56 wt% PCM and 84 wt% PCM based on Ac and PEG600, respectively. The compressive strengths of ss-PCM Hexa, Octa, PEG and Acet are listed in Table 3.1 and are discussed together with the structural properties of the ss-PCM in detail (3.3.4.3).

3.3.4.1 FTIR and GC/MS analysis of ss-PCMs

We examined possible chemical degradation reactions of the PCM after shape-stabilization by attenuated total reflection Fourier transform infrared spectroscopy (Fig. 3.2, Fig. S3.1 - S3.3) [66]. In the IR spectra of PEG and Acet, the broad transmission bands at 3700 - 3000 cm^{-1} (PEG) and 3750 - 3000 cm^{-1} (Acet) indicate vibrations of hydrogen bonding between -OH and

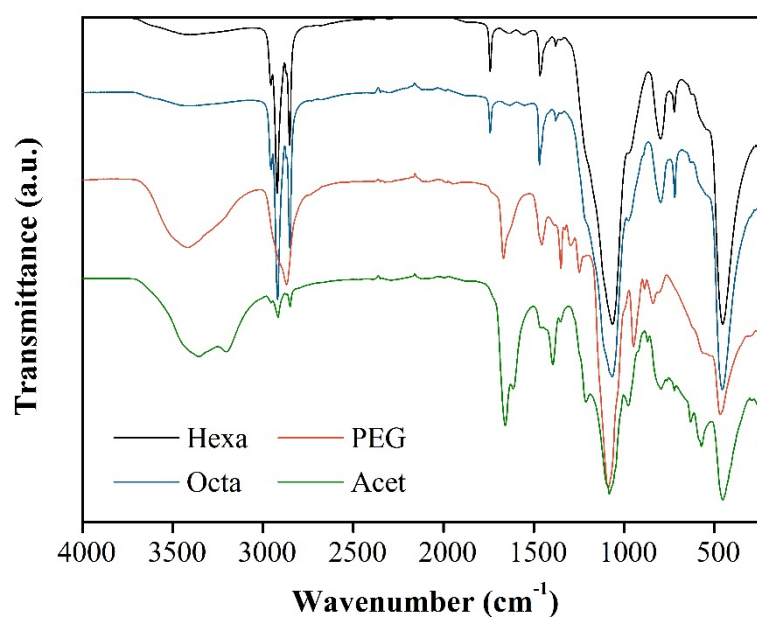


Fig. 3.2 ATR-FTIR spectra of ss-PCMs Hexa, Octa, PEG and Acet.

-NH₂ groups. In comparison to pure Ac (Fig. S3.1), the transmission bands of Acet are shifted by 150 cm⁻¹ to higher values, possibly due to hydrogen bonding and partial chemical degradation of Ac (27 % lower $Ma(PCM)_{mass}$ (56 wt%) of ss-PCM Acet than expected) [65]. The ss-PCMs Hexa and Octa have similar IR spectra with medium (m) to strong (s) transmission bands at 2957 cm⁻¹ (m), 2921 cm⁻¹ (s) and 2852 cm⁻¹ (s) due to -CH₃ and -CH₂- stretching and weak transmission bands at 1465 cm⁻¹ caused by bending vibrations in BS, Octa, Hexa, SDS and PVA (Fig. 3.2, Fig. S3.2). The transmission bands for -CH₃ and -CH₂ stretching vibrations are overlapping for the non-paraffinic ss-PCMs PEG (polymeric nature of PEG600), for Acet they only pronounce a weak intensity (only one -CH₃ group in Ac). The small transmission band at 1741 cm⁻¹ (Hexa, Octa) and the strong transmission band at 1657 cm⁻¹ (Acet) correspond to the C=O and C-O stretching vibrations of the ester-group in BS, ketone-groups in Ac (and/or possible acid groups of acetic acid) and hydroxyl-groups in PVA. The strong transmission band of Acet at 1613 cm⁻¹ indicates -NH₂ stretching vibrations. Compared to the IR spectrum of pure PEG600 (Fig. S3.1) shape-stabilized PEG600 shows a novel medium transmission band at 1667 cm⁻¹ (Fig. 3.2), which indicates C=O and C-O stretching vibrations, possibly from PVA.

The silica matrix of all samples is represented by two transmission bands at 1063 cm⁻¹ (s) and 797 cm⁻¹ (w) for the antisymmetric and symmetric stretching vibration of Si-O-Si, and one strong transmission band at 452 cm⁻¹ (partially overlapped for PEG and Acet) for the transverse-optical rocking vibration of the oxygen in Si-O-Si bonds, which is perpendicular to the Si-O-Si plane [67].

In summary, the ss-PCMs Hexa, Octa and PEG show the same transmission bands as the pure educts (Fig. S3.1) and should thus be chemically stable in the silica matrix. In contrast, the non-paraffinic ss-PCM Acet might be chemically degraded. Moreover, the novel transmission band at 1667 cm⁻¹ after PEG600 confinement in ss-PCM PEG could represent not only the C-O and C=O stretching vibrations of PVA but also of ethylene glycol (EG) from a possible PEG600 hydrolysis during synthesis.

To verify our assumptions, we have further analyzed our samples by electrospray ionization mass spectrometry (ESI MS) to possibly detect hydrolyzation products of PEG 600 and by gas chromatography electron ionisation mass spectrometry (GC EI MS) to characterize putative volatile compounds evolved during heating, such as acetic acid or ethylene glycol. The ss-PCMs Hexa, Octa and PEG show the same signals as the educts of the synthesis approach, as detected by GC EI MS (detailed analysis in supplementary, Fig. S3.4 - S3.5). Thus, the paraffins HD and OD should be confined in the silica structure without chemical degradation during and after the shape-stabilization process. Moreover, ESI MS analysis suggested that

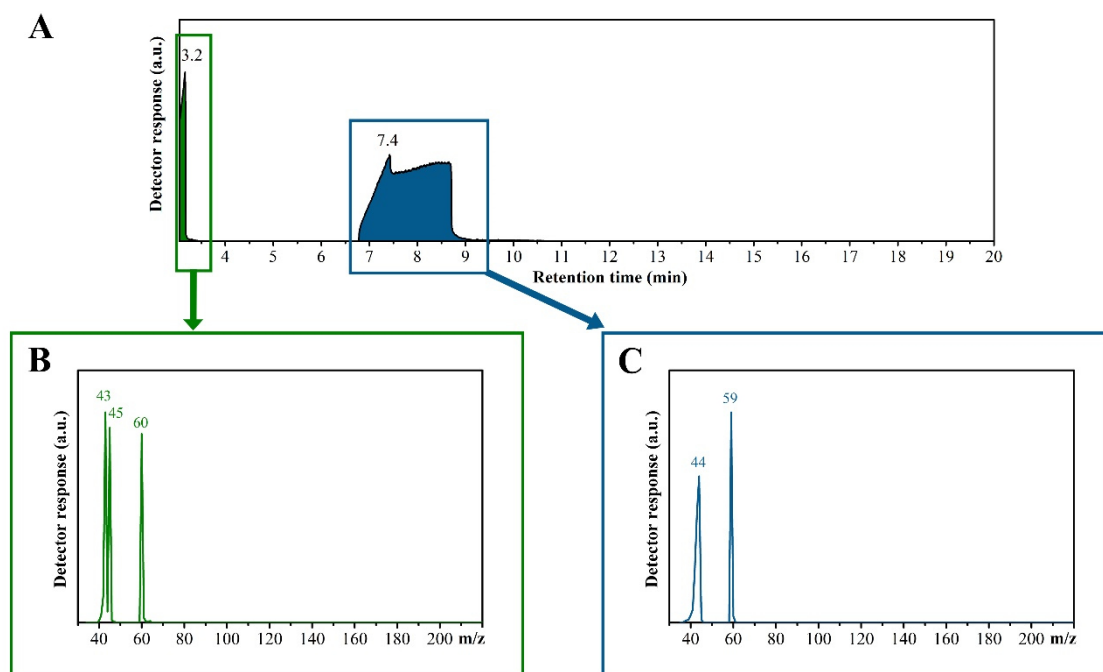


Fig. 3.3 Gas chromatogram of ss-PCM Acet (A). Mass spectra of the two abundant peaks in the GC chromatogram of ss-PCM Acet at the retention times of 3.2 min (B) and 7.4 min (C), respectively, recorded by EI MS.

the mass distribution of the polymer PEG600 before and after shape-stabilization is preserved, indicating that there is no chemical degradation reaction (Fig. S3.6 - S3.7).

Hence, the PCM PEG600 should have not been hydrolyzed during the synthesis and the transmission band at 1667 cm^{-1} for C-O and C=O stretching vibrations in the spectrum of the ATR-FTIR analysis only originate from PVA. In contrast, the mass spectra of two abundant peaks in the GC EI MS analysis of ss-PCM Acet show intense signals at m/z values of 59 (the very broad peak between 7 to 9 min retention time) and 60 (peak at 3.2 min retention time) representing the masses of Ac (59 g/mol) and acetic acid (60 g/mol), respectively (Fig. 3.3). Signals at an m/z of 45 (Fig. 3.3 B) and 44 (Fig. 3.3 C) can be assigned to the loss of the methyl group and decarboxylation of the carboxyl group after highly energetic electron ionization; also, peak identity was confirmed by mass spectral match with the NIST reference library. As expected by the mass loss of ss-PCM Acet (reduced $Ma(PCM)_{mass}$) and the characteristic smell during sol-gel synthesis, GC EI MS analysis provided evidence that PCM Ac is partially hydrolyzed to acetic acid and ammonia, possibly reinforced by the basic pH of ~ 9 . Consequently, it can be expected that acetic acid as well as ammonia mostly evaporated during the drying process.

3.3.4.2 Formation mechanism of ss-PCMs

To track the *in situ* formation of the ss-PCMs, we imaged the ss-PCMs during gelation and aging by confocal fluorescence laser scanning microscopy (FLSM) (Fig. 3.4). For the paraffinic ss-PCM samples, the hydrophobic PCM phase was labelled with the dye perylene and is depicted in blue in the fluorescence microscopic images, whereas the aqueous phase (PVA, SDS, water) was labelled with the hydrophilic dye Alexa Fluor 488 and is depicted in green (Fig. 3.4 (A, B)). The solid silica structures at early time points (during gelation) are visible as black circles in the images due to the absence of any fluorescent stain (Fig. 3.4 A1, B1, A2). Black shadows and black spots can be correlated with putative air inclusions. Due to the high viscosity of the emulsions dynamic light scattering (DLS) and zeta-potential measurements failed to analyze the PCM droplet size distribution as well as the electro-kinetic potential of the emulsion.

After 15 min of gelation of samples Hexa and Octa, a macroemulsion with PCM droplets (diameters: ~ 0.5 to $10\ \mu\text{m}$, blue) in an aqueous continuous phase (green) is formed. The PCM droplet form and size in the macroemulsions are comparable to those based solely on BS as PCM [68]. After the gelation process of Hexa (13 h) and Octa (20 h) has finished, the PCM droplets are covered by spherical silica structure synthesized during gelation and aging (72 h), which are displayed as black circles due to the absence of a fluorescent stain (Fig. 3.4 (A2, B2), Fig. S3.8).

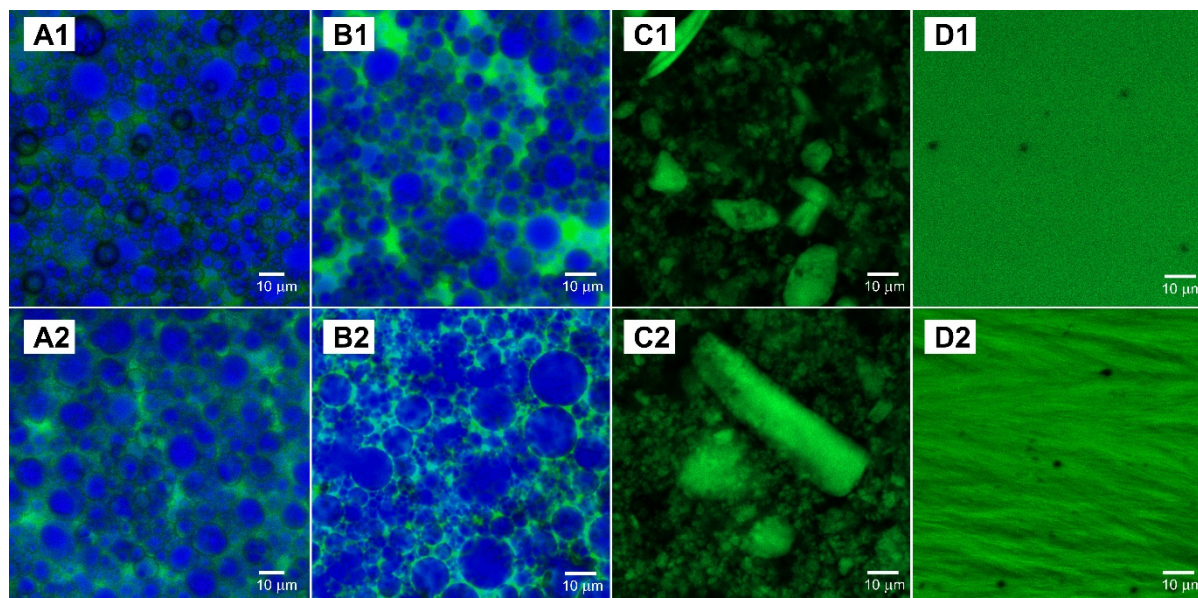


Fig. 3.4 Confocal fluorescence microscopy of the formation process of ss-PCM Hexa (A), Octa (B), PEG (C) and Acet (D) after a reaction time of 15 min (1) and 72 h (2). The hydrophobic phase is labelled in blue with the dye perylene (A, B) and the hydrophilic phase is labelled with the green dye Alexa Fluor 488 (A, B, D). The black lines and spots represent the growing silica phase and air inclusions during the sol-gel synthesis. The non-paraffinic ss-PCM PEG was labelled with the green- fluorescent dye FM1-43.

Like ss-PCMs based on BS [68], the type of emulsion (o/w or w/o) depends mostly on the high Hydrophile-Lipophile Balance (HLB) value of the surfactant SDS of 40 [69] and not on the large volume of PCM compared to water. Surfactants with $HLB > 10$ tend to build oil (PCM) in water emulsions according to the Bancroft rule [70]. As a consequence, the hydrophobic paraffin/BS mixtures form PCM in water (o/w) emulsions during synthesis, in which the PCM droplets are covered by SDS molecules and act as templates for the silica pore structure of the ss-PCM. For a stable emulsion, the hydrophobicity of the PCM must be relatively low and the viscosity of the reaction mixture should be high to prevent phase separation effects. If however, the hydrophobicity of the PCM is too high - such as for pure HD and OD - and the viscosity is too low, the macroemulsion is thermodynamically and kinetically unstable and separates into two macroscopic phases [71–75]. In case pure paraffins are used to obtain ss-PCMs, we propose to increase the viscosity of the macroemulsion before silica addition, for example by adding more high-molecular weight polymers to the reaction mixture.

The silica matrix in the non-paraffinic ss-PCMs PEG is depicted in green in the FLSM images (Fig. 3.4 (C), Fig. S3.9 (C, D), Fig. S3.10). Using Alexa Fluor 488 as a fluorescent dye to probe the gelation process in PEG, only homogeneously distributed green fluorescence could be monitored, which was expectable due to the hydrophilic character of PEG600, PVA, SDS and silica. Therefore, we used the green-fluorescent dye FM1-43 that is known to probe silica matrices in ss-PCMs [68]. Immediately, after 15 min of gelation, differently sized silica aggregates and particles were visible, indicating a high degree of silica aggregation. These silica particles and aggregates expand during the gelation (70 h) and aging process likely due to agglomeration of PEG molecules to the silica particles (Fig. S3.11). The high degree of aggregation could inhibit the formation of a well interconnected silica phase in sample PEG.

The non-paraffinic sample Acet also has a long gelation time of 65 h due to missing hydrophobic droplets (templates), which typically accelerate the gelation process. During the gelation process, a continuous hydrophilic phase with some black spots is observed in the fluorescence images of sample Acet (Fig. 3.4 (D), Fig. S3.9 (A, B)). The black spots putatively represent air bubbles, possibly introduced by stirring. Due to the resolution limit of confocal fluorescence laser scanning microscopy no silica structures with the small pore sizes of less than 100 nm (mean macropore width: 68 nm as determined by mercury intrusion experiments, Table 3.1, Fig. 3.5 (D)) could be detected in the ss-PCM Acet.

3.3.4.3 Structural and mechanical properties of ss-PCMs

Small silica pore sizes and a high interconnectivity of the silica phase are the desirable key parameters in a sol-gel synthesis to achieve mechanically stable ss-PCM with a high thermal conductivity, high compressive strength and less supercooling effects [53].

Table 3.1 Structural properties^a of samples Hexa, Octa, Acet and PEG before and after calcination at 600 °C, named here Hexa_c, Octa_c, Acet_c and PEG_c.

Sample	$\phi^{b,c}$ (%)	$V_{total}^{b,c}$ (cm ³ /g)	V_{macro}^b (cm ³ /g)	V_{meso}^c (cm ³ /g)	D_{macro}^b (nm)	D_{meso}^c (nm)	A_{meso}^c (m ² /g)	σ at 5 °C (kPa)	σ at 40 °C ^d (kPa)
Hexa	3	0.013	0.013	-	78	-	-	1188	642
Octa	7	0.034	0.034	-	4256	-	-	1174	746
PEG	5	0.022	0.022	-	24798	-	-	35	6
Acet	1	0.005	0.005	-	68	-	-	9614	6082
Hexa_c	95	8.04	7.15	0.89	921	10	187	-	-
Octa_c	95	9.26	8.43	0.83	2327	10	192	-	-
PEG_c	95	8.68	7.83	0.85	9704	15	234	-	-
Acet_c	74	1.28	0.42	0.86	88	24	250	-	-

a: Porosity ϕ , total pore volume V_{total} , macropore volume V_{macro} , mesopore volume V_{meso} , mean macropore diameter/50% D_{macro} , mean mesopore diameter/50% D_{meso} , BET surface area A_{meso} and the compressive strength σ at 5 °C and 40 °C of the ss-PCMs before and after calcination at 600 °C.

b: calculated via mercury intrusion.

c: calculated via nitrogen sorption.

d: sample Acet was measured at 90 °C instead of 40 °C due to the higher melting point.

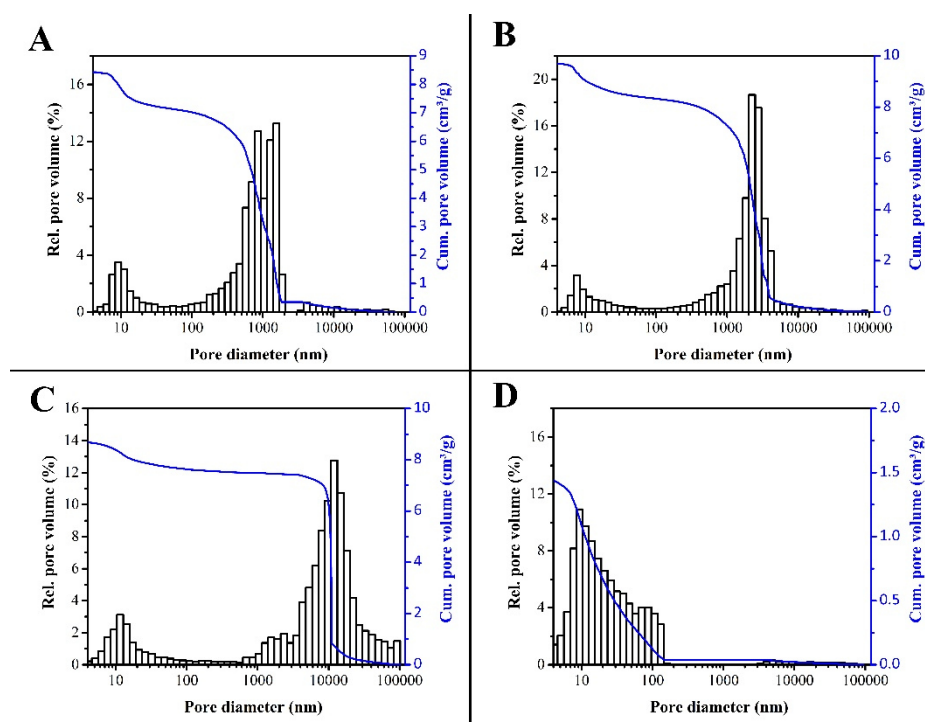


Fig. 3.5 Mercury intrusion measurements of sample Hexa_c (A), Octa_c (B), PEG_c (C) and Acet_c (D).

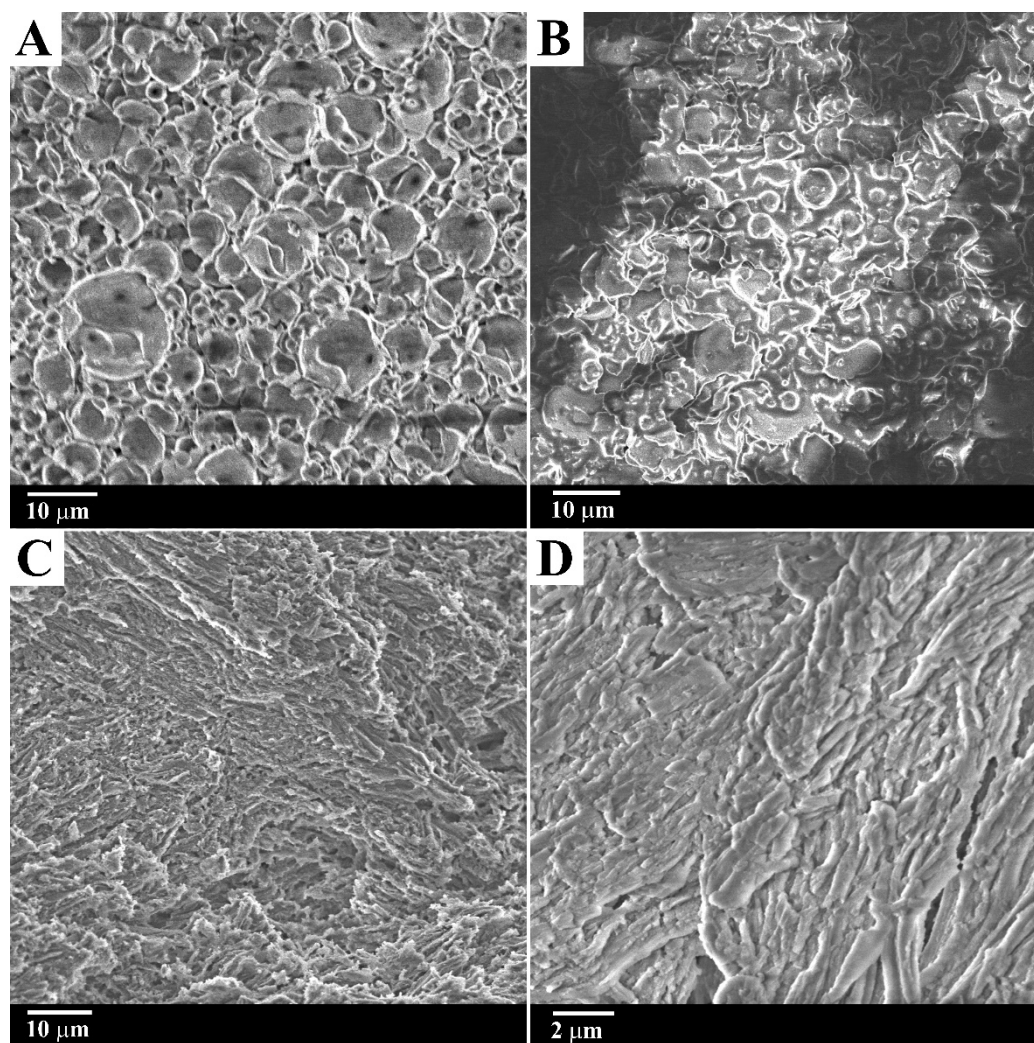


Fig. 3.6 SEM images of ss-PCMs Hex (A), Oct (B), PEG (C) and Acet (D).

To characterize the properties of the ss-PCMs, we analyzed the micro- and mesoporosity of our ss-PCMs by nitrogen adsorption (N_2), the meso- and macroporosity by mercury intrusion porosimetry (Hg) and the interconnectivity and geometrical form of the silica phase by scanning electron microscopy (SEM) (Table 3.1, Fig. 3.5, 3.6). Every sample was calcinated for 6 h at 600 °C to analyze the pure silica pore structure of the ss-PCMs. All calcined samples Octa_c, Hexa_c, PEG_c and Acet_c show type IV isotherms with H1/H2 hysteresis in nitrogen adsorption measurements, typical for mesoporous systems (Fig. S3.14). In contrast, the N_2 adsorption measurements of the ss-PCMs Hexa, Octa, PEG and Acet show no uptake of N_2 , thus, the silica mesopores should be completely filled with PCM. The macroporosity of all ss-PCMs is around 1 – 7 % (Fig. S3.13), possibly because of Hg detection limits for porous carrier systems filled with liquids. Moreover, we could not detect empty silica pores of our samples by SEM in this work (Fig. 3.6). The meso- and macropore volumes of the different calcinated ss-PCMs strongly depend on the PCM used in the sol-gel synthesis.

The calcined ss-PCMs Hexa_c and Octa_c have macropore volumes of $8.43 \text{ cm}^3/\text{g}$ and $7.15 \text{ cm}^3/\text{g}$ and an average macropore width (diameter) of 921 nm and 2327 nm, respectively.

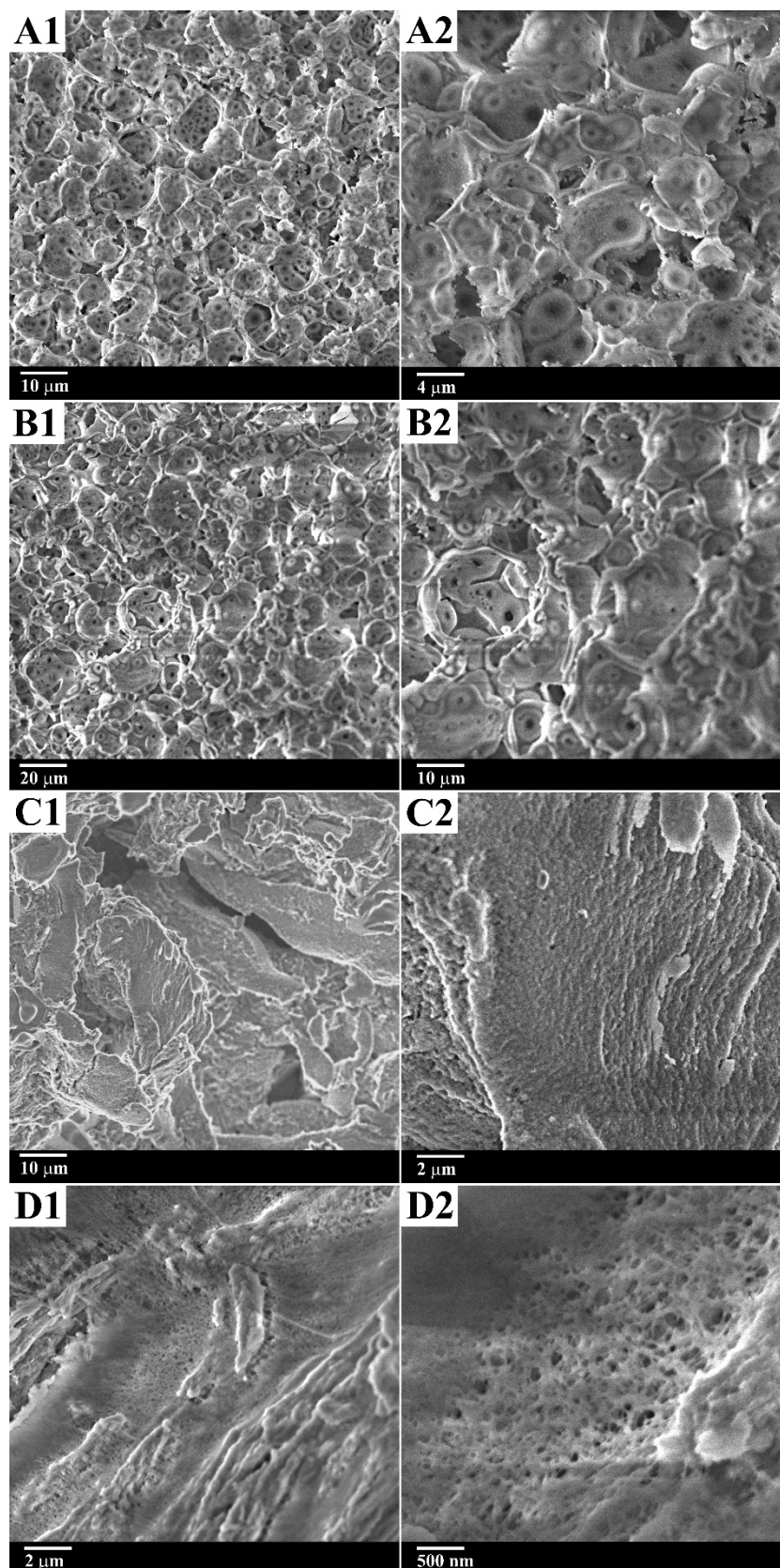


Fig. 3.7 SEM images of calcined ss-PCMs Hex_c (A), Oct_c (B), PEG_c (C) and Acet_c (D).

The silica pore width distribution (Fig. 3.5) and the spherical silica pore shape (Fig. 3.7) of Octa_c and Hexa_c are similar to the calcined ss-PCM based on BS from our previous study (FS4) [53], which has an average macropore width of 1007 nm and a macropore volume of 7.80 cm³/g. The average macropore width of the silica matrix should be higher for Octa_c than for Hexa_c due to the higher hydrophobicity, longer hydrocarbon chain and, thus, larger pore template size of OD in the sol-gel synthesis [76].

The microscopic images of Hexa_c and Octa_c (Fig. 3.7) show well interconnected spherical silica pores around 0.5 - 10 μm (Hexa_c) and 1 - 20 μm (Octa_c), which are covered by smaller silica pores below 1 μm. Additionally, the images are similar to the ones of the mechanical stable ss-PCMs based on pure BS [53]. For this reason, the ss-PCMs Octa_c and Hexa_c have compressive strengths of 0.64 MPa and 0.75 MPa at 40 °C similar to those of ss-PCMs based on pure BS, respectively (Table 3.1).

If ss-PCMs are, however, synthesized with PEG600 as PCM, the average macropore width is increased to 9704 nm, which is more than 8700 nm larger compared to Hexa_c (Table 3.1). The porosity of 95 % and the macropore volume of 8.68 cm³/g of PEG_c have nearly the same values as for Hexa_c and Octa_c, mainly due to the same amount of PCM used for the synthesis.

The silica structure of PEG_c (Fig. 3.7) is completely different from that of Hexa_c and is built of thick silica particle structures, which are parted from each other via “worm”-like interparticular spaces. Therefore, the macropore volume of PEG detected by Hg intrusion measurements characterizes the space between these silica particles. The weak interconnections between the bigger silica particles should be the reason for the low compressive strength of 6 kPa for PEG samples at 40 °C (Table 3.1). The silica structure not only consists of interparticular space but also on spherical silica pores with widths below 100 nm located on top of the thick silica particles. These spherical pores of PEG_c are comparable to the ones of Hexa_c and Octa_c and should be generated by structure-directing effects of SDS, PVA and silica in the aqueous phase. According to Feinle *et al.* [77], silica particles act as structure-directing agent and form mesoporous silica structures by itself during gelation. We assume that the mesopores of ss-PCM PEG_c as well as of Acet_c, Hexa_c and Octa_c are caused by a similar self-organization effect.

As reported by Vong *et al.* [78] for silica sols prepared from TEOS, PEG600 strongly interacts with the growing silica polymer by a large number of hydroxyl groups by forming hydrogen bonds during gelation. The hydrogen bonding of PEG600 should shield silica particles from each other at a certain secondary silica particle size during gelation, and thus disturbing the formation of an interconnected silica structure. As a consequence, silica sols tend to aggregate

after PEG600 addition [78]. The total pore volume of Acet_c ($1.28 \text{ cm}^3/\text{g}$) is reduced up to 84 % compared to the paraffinic ss-PCM Hexa_c ($8.04 \text{ cm}^3/\text{g}$) (Table 3.1). The porosity of Acet_c (74 %) as well is reduced up to 21 %.

As our results from GC-MS analysis (Fig. 3.3) suggest, sample Acet exhibits a smaller pore volume because of the chemical degradation of acetamide to acetic acid and the evaporation of acetic acid during drying. According to previous studies [79,80], Ac only forms hydrogen bonds to silanoyl-groups of the silica matrix and does not form Si-O-C covalent bonds with the silica particles, which is also in line with the results of the IR studies (Fig. 3.2). Ac is a small molecule and highly soluble in water. In sol-gel chemistry, Ac is used as a drying chemical control agent (DCCA) to widen smaller pores, for example of monomodal silica gels based on tetramethyl orthosilicate (TMOS) [79]. This effect is based on hydrogen bonding and electrostatic interactions with the growing silica phase during gelation and leads to the observed increased average silica mesopore width of Acet (24 nm) in comparison to Hexa (10 nm) (Table 3.1).

As a consequence, ss-PCM Acet consists of a mesoporous, highly interconnected silica matrix without macroporous structures (Fig. 3.7) and is translucent above the melting point. Additionally, the compressive strength of Acet is 6.1 MPa at 90 °C and 9.6 MPa at 5 °C (Table 3.1). To the best of our knowledge, the in this work stated compressive strengths of Acet are the highest reported values for ss-PCMs consisting of over 20 wt% PCM.

3.3.4.4 Thermal properties of ss-PCMs

After PCM immobilization, the well interconnected silica matrix increases the thermal conductivity (5 °C) of Hexa and Octa by 62 % and 78 % compared to the pure PCM HD (264 mW/mK) and OD (244 mW/mK) (Fig. 3.8). The relative thermal conductivity increase is similar to that of ss-PCMs based on BS (84 %) [54]. Due to the high interfacial resistance of the liquid state, the thermal conductivity of solid PCMs differs from liquid PCMs [81]. In comparison, the thermal conductivity of PEG600 (334 mW/mK) at 5 °C is increased only by 23 % in ss-PCM PEG (410 mW/mK), probably due to the weak interconnected silica matrix and the larger macroporous silica channels between the silica particles (Fig. 3.5, Fig. 3.7). Sample Acet had 29 wt% less PCM immobilized in the silica structure and, thus, a higher ratio of silica to PCM, resulting in a 102 % higher thermal conductivity (617 mW/mK, 5 °C) compared to Ac (307 mW/mK, 5 °C) (Fig. 3.8).

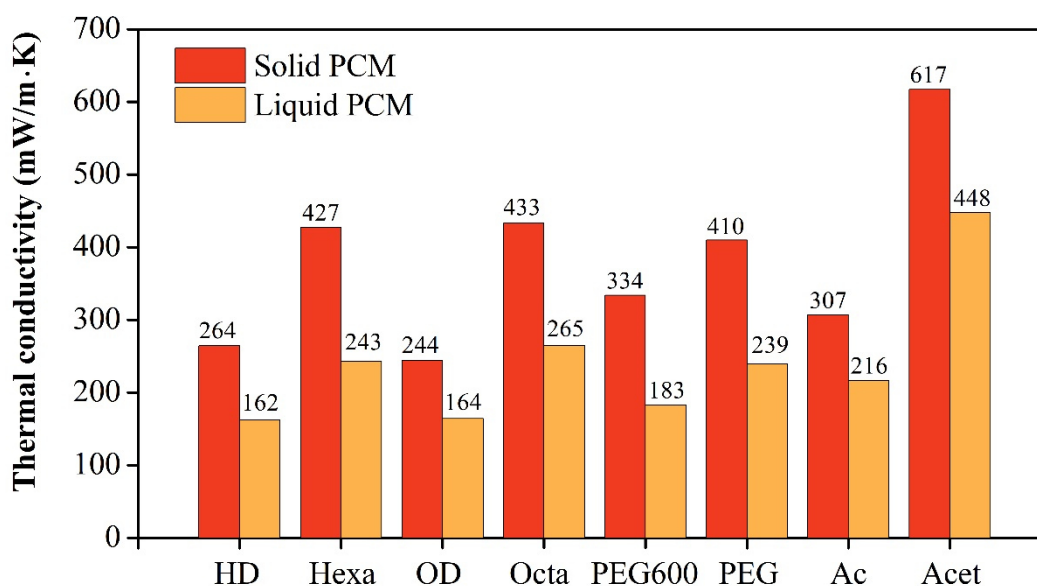


Fig. 3.8 Thermal conductivity of the pure PCMs hexadecane (HD), octadecane (OD), PEG600 and acetamide (Ac) and of the ss-PCMs Hexa, Octa, PEG and Acet measured above the melting point (liquid PCM) and below the freezing point (solid PCM) of PCM.

For the paraffinic ss-PCM samples Hexa and Octa, the DSC peaks of the melting points at 16.5 °C and 27.6 °C shift to higher temperatures in comparison to the pure PCMs with melting points of 15.3 °C and 26.1 °C, respectively (Table 3.2, Fig. 3.9). The opposite trend is observed for the peaks of the freezing points for Hexa and Octa with 10.8 °C and 21.8 °C, resulting in an increased supercooling effect (difference between melting and freezing point) of both samples. A similar trend is observed, when the melting points and supercooling temperatures are determined by the on-set temperature of the DSC peaks (Table S3.1). If the melting points of the paraffins are shifted to lower values, the thermal conductivity of the ss-PCM will be increased relative to the pure substance [82–85]. Additionally, smaller silica pore size structures can increase the melting point and lower the freezing point of immobilized PCM due to increased capillary forces in smaller pore systems. The silica pore size may be the predominant effect for the higher supercooling of the confined PCM.

Finally, the PCM confinement was elucidated. To calculate the percentage of PCM performing the phase transition from liquid to solid, the efficiency E_{DSC} (Eq. 3.5) is defined as the effective PCM mass fraction $Ma(PCM)_{DSC}$ (Eq. 3.4) undergoing the phase transition as determined by DSC measurements relative to the maximum possible mass fraction of PCM as deployed in the synthesis, $Ma(PCM)_{max}$ (83 wt% for Hexa, Octa and PEG, Eq. 3.2).

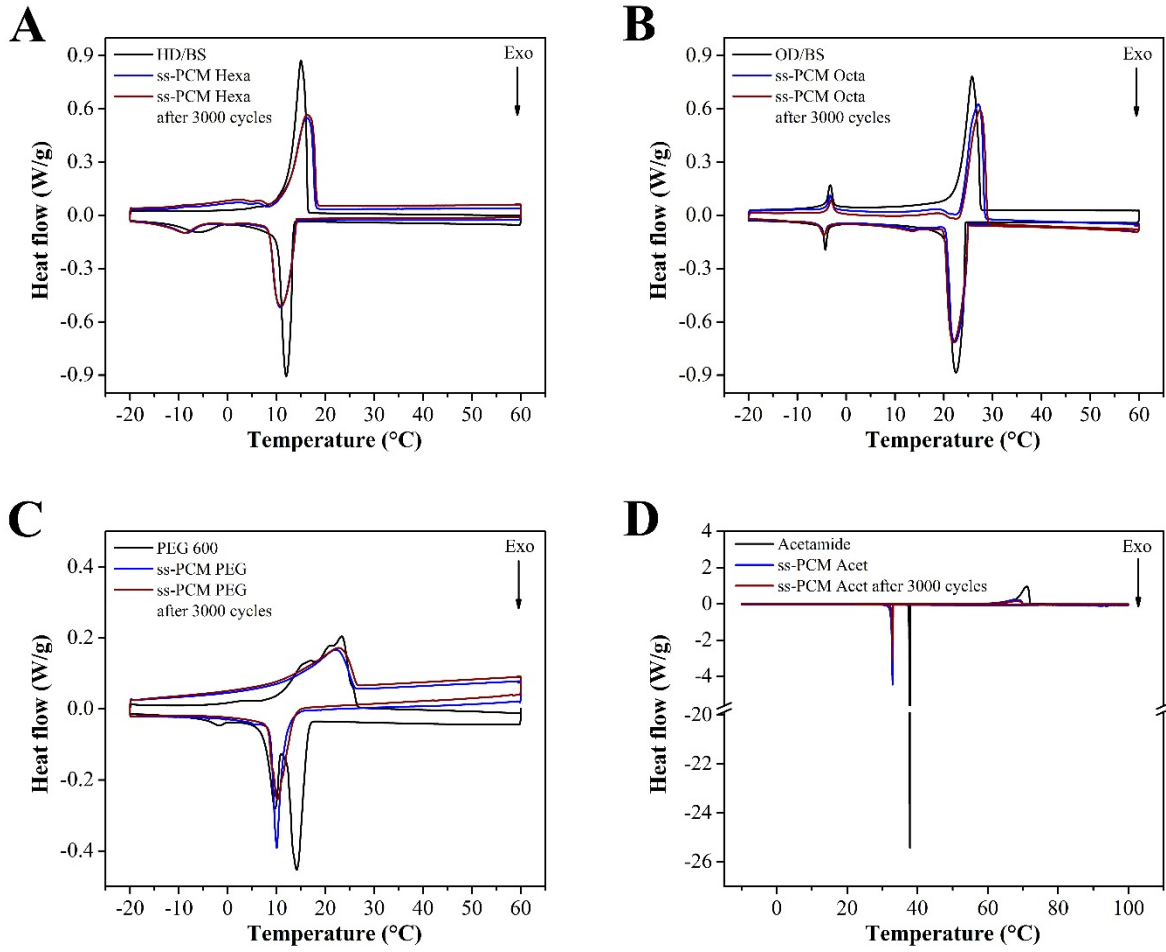


Fig. 3.9 DSC curves and long-term performance tests for ss-PCMs Hexa (A), Octa (B), PEG (C) and Acet (D). For the long-term performance tests and to evaluate the durability, the samples were melted and frozen up to 3000 times via DSC measurements.

The immobilization rate of PCM is defined as E_{mass} (Eq. 3.6) by determining the mass fraction of the immobilized pure PCM in the ss-PCM, $Ma(PCM)_{mass}$ (Eq. 3.3), relative to the maximum possible PCM mass fraction $Ma(PCM)_{max}$ (Eq. 3.2) as applied in the synthesis [53].

$$Ma(PCM)_{DSC} = \frac{\Delta_l^s H_m(ssPCM)}{\Delta_l^s H_m(PCM)} \cdot 100 \% \quad (\text{Eq. 3.4})$$

$$E_{DSC} = \frac{Ma(PCM)_{DSC}}{Ma(PCM)_{max}} \cdot 100 \% \quad (\text{Eq. 3.5})$$

$$E_{mass} = \frac{Ma(PCM)_{mass}}{Ma(PCM)_{max}} \cdot 100 \% \quad (\text{Eq. 3.6})$$

where $Ma(PCM)_{DSC}$ is the effective mass fraction of PCM obtained by DSC measurements, $\Delta_l^s H_m(ssPCM)$ and $\Delta_l^s H_m(PCM)$ are the melting enthalpies of ss-PCM and pure PCM,

$Ma(PCM)_{max}$ is the highest effective mass fraction of PCM without PCM leakage calculated by Eq. 3.2, $Ma(PCM)_{mass}$ is the effective mass fractions of PCM calculated by weight (mass) (Eq. 3.3), which also takes chemical degradation and chemical stability into account, and E_{DSC} and E_{mass} are the confinement efficiencies calculated by DSC and mass measurements, respectively.

The effective mass fractions $Ma(PCM)_{DSC}$ of Hexa and Octa have nearly the same value as the mass fraction $Ma(PCM)_{mass}$. Consequentially, 99.6 % or rather 99.5 % PCM of the PCM used in the synthesis are immobilized in the ss-PCM (Table 3.2) and almost 100 % of this immobilized PCM phase is performing the phase transition during the recurrent melting and freezing cycles in the ss-PCM (98.4 % and 99.6 %, respectively, Table 3.2). After 3000 phase transition cycles, the ss-PCMs Hexa and Octa have nearly the same latent heat as before and, thus, a very high thermal cycling stability and durability (Fig. 3.9). If the ss-PCM will be used as thermal storage materials in buildings, Octa and Hexa would last for at least 3000 days without losing latent heat.

The melting point of PEG600 in ss-PCM PEG is indicated by a broad DSC peak ranging from approximately 12 to 28 °C with a maximum at 22.5 °C due to the polymeric nature of PEG600, which is comparable to the DSC peak for the melting point of pure PEG600 (Fig. 3.9). The melting point of PEG600 in ss-PCM PEG is indicated by a broad DSC peak ranging from approximately 12 to 28 °C with a maximum at 22.5 °C due to the polymeric nature of PEG600, which is comparable to the DSC peak for the melting point of pure PEG600 (Fig. 3.9).

In contrast, the DSC peak for the freezing point of PEG600 at 14 °C is lowered by approximately 4 °C after the shape-stabilization, increasing the supercooling temperature from 9.4 °C (pure PCM) to 12.2 °C (immobilized PCM). The supercooling temperature is higher for PEG than for Hexa and Octa, likely due to the stronger interaction of PEG600 by hydrogen bonding with the silica surface whereas the paraffinic PCMs interact only weakly with the silica surface. The immobilization efficiencies of PEG are nearly 100 % regarding the effective mass fractions in the synthesis (E_{mass}) and 67 % (E_{DSC}) when looking at the calorimetric properties (Table 3.2). This implies that the entire PCM used in the synthesis of PEG is immobilized (E_{mass} : 98.1 %), but only 67 % of the immobilized PEG600 is performing the phase transition from liquid to solid and vice versa (E_{DSC} : 67 %), possibly due to strong ionic interactions and hydrogen bonding between PEG600 and the silica surface. After 3000 thermal cycles, the PEG600 in PEG has a 15 % lower latent heat (Fig. 3.9). We assume that the multiple heating and freezing cycles of sample PEG affect the silica structure and enables more hydrogen bonding between PEG600 and the silica surface, resulting in a lower latent heat of sample PEG.

Table 3.2 Thermal properties¹ of pure PCMs hexadecane (HD), octadecane (OD), polyethylene glycol 600 (PEG600), acetamide (Ac), HD/BS mixture (7:3), OD/BS mixtures (7:3) and of the corresponding ss-PCMs calculated by DSC and TG measurements. Effective mass fractions of PCM calculated via weighing of educts and the ss-PCMs (Eq. 3.2, Eq. 3.3) are also listed.

Sample	ΔH_{total} (J/g)	$U_{\Delta H}$ (%)	T_m (°C)	T_f (°C)	ΔT_s (°C)	$U_{\Delta T_s}$ (%)	m (g)	$Ma(PCM)_{DSC}$ (wt%)	$Ma(PCM)_{mass}$ (wt%)	$Ma(PCM)_{max}$ (wt%)	E_{DSC} (%)	E_{mass} (%)	T_D (°C)
HD	206	0.74	20.2	15.0	5.2	1.83	-	-	-	-	-	-	169
OD	224	0.45	31.6	25.4	6.2	1.22	-	-	-	-	-	-	184
PEG600 ²	146	1.21	23.4	14.0	9.4	0.78	-	-	-	-	-	-	199
Ac	192	0.81	72.7	38.3	34.2	1.38	-	-	-	-	-	-	140
HD/BS	180	0.67	15.3	11.7	3.6	2.32	-	-	-	-	-	-	168/221
OD/BS	191	0.93	26.1	22.1	4.0	1.94	-	-	-	-	-	-	196 /224
Hexa	147	2.11	16.5	10.8	5.7	1.77	13.2	81.7	82.7	83.0	98.4	99.6	169/ 223
Octa	158	1.79	27.6	21.8	5.8	1.88	13.2	82.7	82.6	83.0	99.6	99.5	192/226
PEG	81	3.88	22.5	10.3	12.2	1.91	13.1	55.5	81.4	83.0	66.9	98.1	252
Acet	101	3.52	68.7	31.5	37.2	1.03	5.0	52.6	54.4	83.0	63.4	65.5	127

1: Melting enthalpy ΔH_{total} , relative uncertainty $U_{\Delta H}$ of ΔH_{total} , melting point of PCM T_m , freezing point of PCM T_f , supercooling ΔT_s , relative uncertainty $U_{\Delta T}$ of ΔT_s , mass of ss-PCM m , mean value for effective mass fraction of PCM $Ma(PCM)_{DSC}$ and $Ma(PCM)_{mass}$, highest value for effective mass fraction of PCM $Ma(PCM)_{max}$, PCM immobilization efficiencies E_{DSC} and E_{mass} and decomposition point T_D of PCM.

2: T_D of PEG600: Broad peak area with maximum at 199 °C (On set: 89 °C, end set: 219 °C).

The freezing point (38 °C) and the melting point (73 °C) of Ac are lowered by approximately 7 °C and 4 °C after immobilization in sample Acet (Table 3.2). As a consequence, the supercooling temperature of Ac is increased by 3 °C in sample Acet, which is in line to the supercooling increase of sample PEG. The effective mass fraction of PCM $Ma(PCM)_{mass}$ is 29 wt% lower than $Ma(PCM)_{max}$ for ss-PCM Acet and, thus, only ~30 wt% Ac used for the synthesis is immobilized during the synthesis in the ss-PCM structure (E_{mass}) due to the chemical degradation and subsequent evaporation of Ac as acetic acid and ammonia during drying (Fig. 3.2, Fig. 3.3). However, approximately 97 % of the immobilized Ac is performing the phase transition from liquid to solid and vice versa (E_{DSC} relative to E_{mass}). Additionally, the latent heat of sample Acet is decreased by 20 % after 3000 freezing and melting cycles, pointing to a moderate degradation rate of Ac in the pure silica phase without remaining water.

The decomposition points of the PCMs in the paraffinic ss-PCM samples Octa and Hexa are within the standard deviation (± 2.0 %) of the thermal gravimetric analysis before and after immobilization, underlining the high thermal stability and chemical inertness of BS, HD and OD during and after shape-stabilization (Table 3.2, Fig. S3.17). In comparison, Ac has a slightly lower decomposition point of 127 °C after shape-stabilization due to a higher thermal conductivity. The PCM PEG600 has a broad temperature range of the PCM decomposition from 130 °C to 330 °C and from 240 °C to 330 °C (melting point: ~252 °C) after shape-stabilization (Fig. S3.17). The temperature range of the PEG600 decomposition in ss-PCM PEG is narrower, possibly due to a faster heat transfer in the small silica pore system. By heating the sample to 500 °C, the ss-PCMs Octa, Hexa and PEG600 have lost 87 - 90 wt% of their mass, which represent the mass fraction of the organic compound PCM as well as SDS and PVA after the removal of water. In contrast, ss-PCM Acet has a higher mass loss of 68 wt% after TG measurements due to its chemical degradation (Fig. S3.17).

3.3.5 Conclusions

We synthesized ss-PCMs based on hexadecane (HD), octadecane (OD), polyethylene glycol 600 (PEG600) and acetamide (Ac) to validate the applicability of our porogen-assisted sol-gel process to other organic PCMs apart from butyl stearate (BS). We showed that the here investigated ss-PCMs have a higher latent heat of up to 160 J/g compared to 100 J/g for the BS ss-PCM [54,55,68]. Moreover, the PCMs used for the synthesis differ in their hydrophilicity, thermal and chemical stability, and have melting points (MP) ranging from 15 to 73 °C, broadening the application range of the here introduced ss-PCMs.

The PCMs HD and OD separate from the aqueous phase during gelation due to their high hydrophobicity. Using a less hydrophobic mixture of HD or OD together with BS (70:30 (w/w)), monolithic ss-PCMs (83 wt% PCM) are synthesized with a shape-stability of up to 93 wt% PCM, with high compressive strengths (1.2 MPa, 5 °C), high durability (~3000 thermal cycles), and high chemical stability by confining the paraffin/BS mixture as droplets in a spherical silica structure with average macropore widths of 1 - 2 μm during gelation. The physicochemical properties of these ss-PCMs differ only slightly as they show comparable latent heats (150 - 160 J/g), thermal stabilities (~170 °C) and MPs of 17 °C and 22 °C, which is based on their chemical nature and mass fraction of the confined PCM. In their overall constitution they are quite similar. Therefore, paraffinic ss-PCMs with different latent heats and MPs can be synthesized with the same high mechanical stabilities as ss-PCMs based solely on BS. The paraffinic ss-PCMs are the first reported ss-PCMs with such high latent heats as well as high compressive strengths, making them interesting as novel energy-saving construction materials for buildings or as cooling medium in photovoltaic and battery systems.

In comparison, the latent heats of PEG600 and Ac are ~30 % lower after shape-stabilization than expected. Strong ionic interactions and hydrogen bonding to the silica structure seem to hinder the complete melting and freezing of PEG600 during the phase transitions. The PCM Ac is hydrolyzed under the basic conditions during synthesis to acetic acid and ammonia (Ac), which evaporates during drying of the ss-PCM.

The shape-stabilized PEG600 consists of a fragmented silica structure because PEG600 disturbs the gelation of silica and promotes silica aggregation. Consequentially, the compressive strength (35 kPa, 5 °C), the shape-stability (5 wt% PCM leakage) and the latent heats of these ss-PCMs are low (81 J/g). After drying, the shape-stabilized Ac has only a moderate latent heat (101 J/g), a moderate durability (after 3000 thermal cycles 20 % lower latent heat) and a high supercooling temperature (37 °C), also in combination with a high compressive strength (9.6 MPa, 5 °C). Interestingly, these ss-PCMs are translucent above the MP of Ac due to a well-interconnected mesoporous silica matrix with an average pore width of 24 nm. To the best of our knowledge, the shape-stabilized Ac has the highest reported compressive strength for ss-PCMs with >10 wt% PCM and is the first translucent ss-PCM. We think our sol-gel process is best suited for immobilizing hydrophobic PCMs (paraffins, fatty acid esters), but could also be of interest for the future development of highly mechanically stable and translucent ss-PCMs, given the chemical stability of the hydrophilic PCMs during synthesis.

3.3.6 Conflicts of interest

There are no conflicts of any authors to declare.

3.3.7 CRediT author contribution statement

Felix Marske: Conceptualization, Methodology, Validation, Formal analysis, Investigation, Data Curation, Writing - Original Draft, Visualization. **Caroline Haupt:** Formal analysis, Resources, Writing - Review & Editing. **Claudia Birkemeyer:** Formal analysis, Writing - Review & Editing. **Kirsten Bacia:** Resources, Writing - Review & Editing. **Thomas Hahn:** Supervision, Project administration, Funding acquisition. **Dirk Enke:** Writing - Review & Editing, Supervision.

3.3.8 Acknowledgements

The authors thank Mr. Jaques-Christopher Schmidt for sample preparation help and for the determination of gelation times and thermal conductivities. Special thanks to Mr. Eric Matthes for TG measurements, Mr. Florian Himmelstein for the sample imaging by SEM and Ms. Jenny Bienias for the mercury intrusion and nitrogen sorption measurements. Caroline Haupt and Kirsten Bacia acknowledge the funding from the Federal Ministry for Education and Research (BMBF, 03Z22HI2). We thank Ramona Oehme and Georg Pönisch from the MS Core Facility MS UL of the University of Leipzig for technical support. Claudia Birkemeyer acknowledges funding from the European Fund for Regional Structure Development, EFRE (“Europe funds Saxony”, grant no. 22137019).

3.3.9 References

- [1] International Energy Agency and the United Nations Environment Programme, 2018 Global Status Report: Towards a Zero-Emission, Efficient and Resilient Buildings and Construction Sector, International Energy Agency and the United Nations Environment Programme, 2018, pp. 1–73. <https://www.iea.org/reports/2018-global-status-report>. accessed 9 February 2022.
- [2] Llantoy N, Chàfer M, Cabeza LF. A comparative life cycle assessment (LCA) of different insulation materials for buildings in the continental Mediterranean climate. *Energy and Buildings* 2020;225:110323. <https://doi.org/10.1016/j.enbuild.2020.110323>.
- [3] Rojas C, Cea M, Iriarte A, Valdés G, Navia R, Cárdenas-R JP. Thermal insulation materials based on agricultural residual wheat straw and corn husk biomass, for

- application in sustainable buildings. *Sustainable Materials and Technologies* 2019;20:e00102. <https://doi.org/10.1016/j.susmat.2019.e00102>.
- [4] Shang L, Lyu Y, Han W. Microstructure and Thermal Insulation Property of Silica Composite Aerogel. *Materials (Basel)* 2019;12(6). <https://doi.org/10.3390/ma12060993>.
- [5] Gross R, Hanna R. Path dependency in provision of domestic heating. *Nature Energy* 2019;4(5):358–64. <https://doi.org/10.1038/s41560-019-0383-5>.
- [6] Bergamini R, Jensen JK, Elmegaard B. Thermodynamic competitiveness of high temperature vapor compression heat pumps for boiler substitution. *Energy* 2019;182:110–21. <https://doi.org/10.1016/j.energy.2019.05.187>.
- [7] Pieper H, Ommen T, Elmegaard B, Brix Markussen W. Assessment of a combination of three heat sources for heat pumps to supply district heating. *Energy* 2019;176:156–70. <https://doi.org/10.1016/j.energy.2019.03.165>.
- [8] Bonamente E, Aquino A. Environmental Performance of Innovative Ground-Source Heat Pumps with PCM Energy Storage. *Energies* 2020;13(1):117. <https://doi.org/10.3390/en13010117>.
- [9] Templeton JD, Hassani F, Ghoreishi-Madiseh SA. Study of effective solar energy storage using a double pipe geothermal heat exchanger. *Renewable Energy* 2016;86:173–81. <https://doi.org/10.1016/j.renene.2015.08.024>.
- [10] Akter MN, Mahmud MA, Oo AM. Comprehensive economic evaluations of a residential building with solar photovoltaic and battery energy storage systems: An Australian case study. *Energy and Buildings* 2017;138:332–46. <https://doi.org/10.1016/j.enbuild.2016.12.065>.
- [11] Castillo-Calzadilla T, Macarulla AM, Kamara-Esteban O, Borges CE. A case study comparison between photovoltaic and fossil generation based on direct current hybrid microgrids to power a service building. *Journal of Cleaner Production* 2020;244:118870. <https://doi.org/10.1016/j.jclepro.2019.118870>.
- [12] Alva G, Lin Y, Fang G. An overview of thermal energy storage systems. *Energy* 2018;144:341–78. <https://doi.org/10.1016/j.energy.2017.12.037>.
- [13] Lin Y, Jia Y, Alva G, Fang G. Review on thermal conductivity enhancement, thermal properties and applications of phase change materials in thermal energy storage. *Renewable and Sustainable Energy Reviews* 2018;82:2730–42. <https://doi.org/10.1016/j.rser.2017.10.002>.
- [14] Stropnik R, Koželj R, Zavrl E, Stritih U. Improved thermal energy storage for nearly zero energy buildings with PCM integration. *Solar Energy* 2019;190:420–6. <https://doi.org/10.1016/j.solener.2019.08.041>.

-
- [15] Sharma A, Tyagi VV, Chen CR, Buddhi D. Review on thermal energy storage with phase change materials and applications. *Renewable and Sustainable Energy Reviews* 2009;13(2):318–45. <https://doi.org/10.1016/j.rser.2007.10.005>.
- [16] Shchukina EM, Graham M, Zheng Z, Shchukin DG. Nanoencapsulation of phase change materials for advanced thermal energy storage systems. *Chemical Society Reviews* 2018;47(11):4156–75. <https://doi.org/10.1039/c8cs00099a>.
- [17] Chen G, Shi T, Zhang X, Cheng F, Wu X, Leng G et al. Polyacrylonitrile/polyethylene glycol phase-change material fibres prepared with hybrid polymer blends and nano-SiC fillers via centrifugal spinning. *Polymer* 2020;186:122012. <https://doi.org/10.1016/j.polymer.2019.122012>.
- [18] Tang L-S, Yang J, Bao R-Y, Liu Z-Y, Xie B-H, Yang M-B et al. Polyethylene glycol/graphene oxide aerogel shape-stabilized phase change materials for photo-to-thermal energy conversion and storage via tuning the oxidation degree of graphene oxide. *Energy Conversion and Management* 2017;146:253–64. <https://doi.org/10.1016/j.enconman.2017.05.037>.
- [19] Wang W, Yang X, Fang Y, Ding J. Preparation and performance of form-stable polyethylene glycol/silicon dioxide composites as solid–liquid phase change materials. *Applied Energy* 2009;86(2):170–4. <https://doi.org/10.1016/j.apenergy.2007.12.003>.
- [20] Ye S, Zhang Q, Hu D, Feng J. Core–shell-like structured graphene aerogel encapsulating paraffin: Shape-stable phase change material for thermal energy storage. *Journal of Materials Chemistry A* 2015;3(7):4018–25. <https://doi.org/10.1039/C4TA05448B>.
- [21] Feliński P, Sekret R. Experimental study of evacuated tube collector/storage system containing paraffin as a PCM. *Energy* 2016;114:1063–72. <https://doi.org/10.1016/j.energy.2016.08.057>.
- [22] Giro-Paloma J, Barreneche C, Delgado M, Martínez M, Fernández AI, Cabeza LF. Physicochemical and Thermal Study of a MPCM of PMMA Shell and Paraffin Wax as a Core. *Energy Procedia* 2014;48:347–54. <https://doi.org/10.1016/j.egypro.2014.02.040>.
- [23] He H, Zhao P, Yue Q, Gao B, Yue D, Li Q. A novel polynary fatty acid/sludge ceramsite composite phase change materials and its applications in building energy conservation. *Renewable Energy* 2015;76:45–52. <https://doi.org/10.1016/j.renene.2014.11.001>.
- [24] Sleiti AK, Naimaster EJ. Application of Fatty Acid Based Phase-Change Material to Reduce Energy Consumption From Roofs of Buildings. *Journal of Solar Energy Engineering* 2016;138(5):186. <https://doi.org/10.1115/1.4033574>.
- [25] Prasanna P, Ramkumar R, Sunilkumar K, Rajasekar R. Experimental study on a binary mixture ratio of fatty acid-based PCM integrated to PV panel for thermal regulation on a

- hot and cold month. *International Journal of Sustainable Energy* 2020;11(22):1–17.
<https://doi.org/10.1080/14786451.2020.1801682>.
- [26] Ravotti R, Fellmann O, Lardon N, Fischer L, Stamatiou A, Worlitschek J. Analysis of Bio-Based Fatty Esters PCM's Thermal Properties and Investigation of Trends in Relation to Chemical Structures. *Applied Sciences* 2019;9(2):225.
<https://doi.org/10.3390/app9020225>.
- [27] Wi S, Seo J, Jeong S-G, Chang SJ, Kang Y, Kim S. Thermal properties of shape-stabilized phase change materials using fatty acid ester and exfoliated graphite nanoplatelets for saving energy in buildings. *Solar Energy Materials and Solar Cells* 2015;143:168–73. <https://doi.org/10.1016/j.solmat.2015.06.040>.
- [28] Zhang H, Zhang L, Li Q, Huang C, Guo H, Xiong L et al. Preparation and characterization of methyl palmitate/palygorskite composite phase change material for thermal energy storage in buildings. *Construction and Building Materials* 2019;226:212–9. <https://doi.org/10.1016/j.conbuildmat.2019.07.152>.
- [29] Kosny J, Shukla N, Fallahi A. Cost Analysis of Simple PCM-Enhanced Building Envelopes in Southern U.S. Climates. United States. <https://www.osti.gov/biblio/1219890>. accessed 20 February 2022
- [30] Zhou D, Zhao CY, Tian Y. Review on thermal energy storage with phase change materials (PCMs) in building applications. *Applied Energy* 2012;92:593–605.
<https://doi.org/10.1016/j.apenergy.2011.08.025>.
- [31] Lecompte T, Le Bideau P, Glouannec P, Nortershauser D, Le Masson S. Mechanical and thermo-physical behaviour of concretes and mortars containing phase change material. *Energy and Buildings* 2015;94:52–60.
<https://doi.org/10.1016/j.enbuild.2015.02.044>.
- [32] Marani A, Nehdi ML. Integrating phase change materials in construction materials: Critical review. *Construction and Building Materials* 2019;217:36–49.
<https://doi.org/10.1016/j.conbuildmat.2019.05.064>.
- [33] Liu Y, Wang M, Cui H, Yang L, Liu J. Micro-/macro-level optimization of phase change material panel in building envelope. *Energy* 2020;195:116932.
<https://doi.org/10.1016/j.energy.2020.116932>.
- [34] Hassan A, Shakeel Laghari M, Rashid Y. Micro-Encapsulated Phase Change Materials: A Review of Encapsulation, Safety and Thermal Characteristics. *Sustainability* 2016;8(10):1046. <https://doi.org/10.3390/su8101046>.
- [35] Wijesuriya S, Tabares-Velasco PC. Experimental apparatus and methodology to test and quantify thermal performance of micro and macro-encapsulated phase change materials in building envelope applications. *Journal of Energy Storage* 2020;32:101770.
<https://doi.org/10.1016/j.est.2020.101770>.

-
- [36] Nomura T, Okinaka N, Akiyama T. Impregnation of porous material with phase change material for thermal energy storage. *Materials Chemistry and Physics* 2009;115(2):846–50. <https://doi.org/10.1016/j.matchemphys.2009.02.045>.
- [37] Kang Y, Jeong S-G, Wi S, Kim S. Energy efficient Bio-based PCM with silica fume composites to apply in concrete for energy saving in buildings. *Solar Energy Materials and Solar Cells* 2015;143:430–4. <https://doi.org/10.1016/j.solmat.2015.07.026>.
- [38] Wi S, Chang SJ, Kim S. Improvement of thermal inertia effect in buildings using shape stabilized PCM wallboard based on the enthalpy-temperature function. *Sustainable Cities and Society* 2020;56:102067. <https://doi.org/10.1016/j.scs.2020.102067>.
- [39] Cárdenas-Ramírez C, Jaramillo F, Gómez M. Systematic review of encapsulation and shape-stabilization of phase change materials. *Journal of Energy Storage* 2020;30:101495. <https://doi.org/10.1016/j.est.2020.101495>.
- [40] Fang Y, Ding Y, Tang Y, Liang X, Jin C, Wang S et al. Thermal properties enhancement and application of a novel sodium acetate trihydrate-formamide/expanded graphite shape-stabilized composite phase change material for electric radiant floor heating. *Applied Thermal Engineering* 2019;150:1177–85. <https://doi.org/10.1016/j.applthermaleng.2019.01.069>.
- [41] Qu Y, Wang S, Tian Y, Zhou D. Comprehensive evaluation of Paraffin-HDPE shape stabilized PCM with hybrid carbon nano-additives. *Applied Thermal Engineering* 2019;163:114404. <https://doi.org/10.1016/j.applthermaleng.2019.114404>.
- [42] Liu Z, Yu Z, Yang T, Di Qin, Li S, Zhang G et al. A review on macro-encapsulated phase change material for building envelope applications. *Building and Environment* 2018;144:281–94. <https://doi.org/10.1016/j.buildenv.2018.08.030>.
- [43] Rathore PKS, Shukla SK. Potential of macroencapsulated PCM for thermal energy storage in buildings: A comprehensive review. *Construction and Building Materials* 2019;225:723–44. <https://doi.org/10.1016/j.conbuildmat.2019.07.221>.
- [44] Aftab W, Huang X, Wu W, Liang Z, Mahmood A, Zou R. Nanoconfined phase change materials for thermal energy applications. *Energy and Environmental Science* 2018;11(6):1392–424. <https://doi.org/10.1039/C7EE03587J>.
- [45] Navarro L, Solé A, Martín M, Barreneche C, Olivieri L, Tenorio JA et al. Benchmarking of useful phase change materials for a building application. *Energy and Buildings* 2019;182:45–50. <https://doi.org/10.1016/j.enbuild.2018.10.005>.
- [46] Errebai FB, Derradji L, Amara M, Optimum mass percentage of microencapsulated PCM mixed with gypsum for improved latent heat storage, *Journal of Energy Storage* (2021), <https://doi.org/10.1016/j.est.2020.101910>.

-
- [47] Zhou D, Zhao CY, Tian Y. Review on thermal energy storage with phase change materials (PCMs) in building applications. *Applied Energy* 2012;92:593–605. <https://doi.org/10.1016/j.apenergy.2011.08.025>.
- [48] Qian T, Li J, Min X, Guan W, Deng Y, Ning L. Enhanced thermal conductivity of PEG/diatomite shape-stabilized phase change materials with Ag nanoparticles for thermal energy storage. *Journal of Materials Chemistry A* 2015;3(16):8526–36. <https://doi.org/10.1039/C5TA00309A>.
- [49] Yang J, Yu P, Tang L-S, Bao R-Y, Liu Z-Y, Yang M-B et al. Hierarchically interconnected porous scaffolds for phase change materials with improved thermal conductivity and efficient solar-to-electric energy conversion. *Nanoscale* 2017;9(45):17704–9. <https://doi.org/10.1039/c7nr05449a>.
- [50] Wen R, Huang Z, Huang Y, Zhang X, Min X, Fang M et al. Synthesis and characterization of lauric acid/expanded vermiculite as form-stabilized thermal energy storage materials. *Energy and Buildings* 2016;116:677–83. <https://doi.org/10.1016/j.enbuild.2016.01.023>.
- [51] Jeong S-G, Lee J-H, Seo J, Kim S. Thermal performance evaluation of Bio-based shape stabilized PCM with boron nitride for energy saving. *International Journal of Heat and Mass Transfer* 2014;71:245–50. <https://doi.org/10.1016/j.ijheatmasstransfer.2013.12.017>.
- [52] Huang X, Chen X, Li A, Atinafu D, Gao H, Dong W. Shape-stabilized phase change materials based on porous supports for thermal energy storage applications. *Chemical Engineering Journal* 2019;356:641–61. <https://doi.org/10.1016/j.cej.2018.09.013>.
- [53] Marske F, Martins de Souza e Silva J, Wehrspohn RB, Hahn T, Enke D. Synthesis of monolithic shape-stabilized phase change materials with high mechanical stability via a porogen-assisted in situ sol–gel process. *RSC Advances* 2020;10(6):3072–83. <https://doi.org/10.1039/C9RA10631F>.
- [54] Marske F, Lindenberg T, Martins de Souza e Silva J, Wehrspohn RB, Maijenburg AW, Hahn T. Size and surface effects of hexagonal boron nitrides on the physicochemical properties of monolithic phase change materials synthesized via sol–gel route. *Applied Thermal Engineering* 2021;196:117325. <https://doi.org/10.1016/j.applthermaleng.2021.117325>.
- [55] Marske F, Lindenberg T, Souza e Silva JM de, Wehrspohn RB, Maijenburg AW, Hahn T. Experimental data showing the influence of different boron nitride particles on the silica network, the butyl stearate and the porogens in shape-stabilized phase change materials. *Data in Brief* 2021:107428. <https://doi.org/10.1016/j.dib.2021.107428>.
- [56] Washburn EW. Note on a Method of Determining the Distribution of Pore Sizes in a Porous Material. *Proceedings of the National Academy of Sciences of the United States of America* 1921;7(4):115–6. <https://doi.org/10.1073/pnas.7.4.115>.

-
- [57] Brunauer S, Emmett PH, Teller E. Adsorption of Gases in Multimolecular Layers. *Journal of American Chemical Society* 1938;60(2):309–19. <https://doi.org/10.1021/ja01269a023>.
- [58] Margineanu A, Hotta J, Vallée RAL, van der Auweraer M, Ameloot M, Stefan A. Visualization of membrane rafts using a perylene monoimide derivative and fluorescence lifetime imaging. *Biophysical Journal* 2007;93(8):2877–91. <https://doi.org/10.1529/biophysj.106.100743>.
- [59] Funk GM, Hunt CE, Epps DE, Brown PK. Use of a rapid and highly sensitive fluorescamine-based procedure for the assay of plasma lipoproteins. *Journal of Lipid Research* 1988;27(7):792–5. [https://doi.org/10.1016/S0022-2275\(20\)38803-9](https://doi.org/10.1016/S0022-2275(20)38803-9).
- [60] Schote U, Seelig J. Interaction of the neuronal marker dye FM1-43 with lipid membranes. *Biochimica et Biophysica Acta (BBA) - Biomembranes* 1998;1415(1):135–46. [https://doi.org/10.1016/S0005-2736\(98\)00188-6](https://doi.org/10.1016/S0005-2736(98)00188-6).
- [61] Li S, Zhong K, Zhou Y, Zhang X. Comparative study on the dynamic heat transfer characteristics of PCM-filled glass window and hollow glass window. *Energy and Buildings* 2014;85:483–92. <https://doi.org/10.1016/j.enbuild.2014.09.054>.
- [62] Ismail KA, Salinas CT, Henriquez JR. Comparison between PCM filled glass windows and absorbing gas filled windows. *Energy and Buildings* 2008;40(5):710–9. <https://doi.org/10.1016/j.enbuild.2007.05.005>.
- [63] Zhong K, Li S, Sun G, Li S, Zhang X. Simulation study on dynamic heat transfer performance of PCM-filled glass window with different thermophysical parameters of phase change material. *Energy and Buildings* 2015;106:87–95. <https://doi.org/10.1016/j.enbuild.2015.05.014>.
- [64] Li D, Wu Y, Wang B, Liu C, Arıcı M. Optical and thermal performance of glazing units containing PCM in buildings: A review. *Construction and Building Materials* 2020;233:117327. <https://doi.org/10.1016/j.conbuildmat.2019.117327>.
- [65] Breitmaier E, Jung G. *Organische Chemie: Grundlagen, Verbindungsklassen, Reaktionen, Konzepte, Molekülstruktur, Naturstoffe ; 133 Tabellen*. 6th ed. Stuttgart: Georg Thieme Verlag; 2009.
- [66] Hesse M, Meier H, Zeeh B. *Spectroscopic methods in organic chemistry: 100 tables*. 2nd ed. Stuttgart: Thieme; 2008.
- [67] Innocenzi P. Infrared spectroscopy of sol–gel derived silica-based films: a spectro-microstructure overview. *Journal of Non-Crystalline Solids* 2003;316(2-3):309–19. [https://doi.org/10.1016/S0022-3093\(02\)01637-X](https://doi.org/10.1016/S0022-3093(02)01637-X).
- [68] Marske F, Dasler J, Haupt C, Bacia K, Hahn T, Enke D. Influence of surfactants and organic polymers on monolithic shape-stabilized phase change materials synthesized via sol-gel route. *Journal of Energy Storage* 2022;49:104127. <https://doi.org/10.1016/j.est.2022.104127>.

-
- [69] Zhang Y, Zhang XY, Chai JL, Cui XC, Pan J, Song JW et al. The phase behavior and solubilization of isopropyl myristate in microemulsions containing hexadecyl trimethyl ammonium bromide and sodium dodecyl sulfate. *Journal of Molecular Liquids* 2017;244:262–8. <https://doi.org/10.1016/j.molliq.2017.08.074>.
- [70] Sineva AV, Ermolat'ev DS, Pertsov AV. Structural transformations in a water-n-octane + chloroform-sodium dodecyl sulfate-n-pentanol microemulsion. *Colloid Journal* 2007;69(1):89–94. <https://doi.org/10.1134/S1061933X07010127>.
- [71] Wright JD, Sommerdijk NAJM. *Sol-Gel Materials: Chemistry and Applications*. Boca Raton: Chapman and Hall/CRC; 2014.
- [72] Feng H, Verstappen NAL, Kuehne AJC, Sprakel J. Well-defined temperature-sensitive surfactants for controlled emulsion coalescence. *Polym. Chem.* 2013;4(6):1842. <https://doi.org/10.1039/C2PY21007J>.
- [73] Lins RF, Alves-Rosa MA, Pulcinelli SH, Santilli CV. Formation of TiO₂ ceramic foams from the integration of the sol–gel method with surfactants assembly and emulsion. *Journal of Sol-Gel Science and Technology* 2012;63(2):224–9. <https://doi.org/10.1007/s10971-012-2700-3>.
- [74] Pham Q-T, Yao Z-H, Wang Y-T, Wu Y-T, Chern C-S. Preparation and characterization of monodisperse silica nanoparticles via miniemulsion sol–gel reaction of tetraethyl orthosilicate. *Journal of Materials Science* 2017;52(21):12706–16. <https://doi.org/10.1007/s10853-017-1402-1>.
- [75] Oh SG, Shah DO. Effect of counterions on the interfacial tension and emulsion droplet size in the oil/water/dodecyl sulfate system. *Journal of Physical Chemistry* 1993;97(2):284–6. <https://doi.org/10.1021/j100104a003>.
- [76] Oliver RC, Lipfert J, Fox DA, Lo RH, Doniach S, Columbus L. Dependence of micelle size and shape on detergent alkyl chain length and head group. *PLoS ONE* 2013;8(5):e62488. <https://doi.org/10.1371/journal.pone.0062488>.
- [77] Feinle A, Elsaesser MS, Hüsing N. Sol-gel synthesis of monolithic materials with hierarchical porosity. *Chemical Society Reviews* 2016;45(12):3377–99. <https://doi.org/10.1039/c5cs00710k>.
- [78] Vong M, Bazin N, Sermon PA. Chemical Modification of Silica Gels. *Journal of Sol-Gel Science and Technology* 1997;8(1/2/3):499–505. <https://doi.org/10.1023/A:1018350227105>.
- [79] Chan JB, Jonas J. Effect of various amide additives on the tetramethoxysilane sol-gel process. *Journal of Non-Crystalline Solids* 1990;126(1-2):79–86. [https://doi.org/10.1016/0022-3093\(90\)91025-M](https://doi.org/10.1016/0022-3093(90)91025-M).

-
- [80] Chen C, Wang A, Xu G, Ni C. High-Performance Phase Change Composite of Acetamide/Silica-Network for Thermal Storage. *Nanoscience and Nanotechnology Letters* 2013;5(1):84–8. <https://doi.org/10.1166/nnl.2013.1416>.
- [81] Qureshi ZA, Ali HM, Khushnood S. Recent advances on thermal conductivity enhancement of phase change materials for energy storage system: A review. *International Journal of Heat and Mass Transfer* 2018;127:838–56. <https://doi.org/10.1016/j.ijheatmasstransfer.2018.08.049>.
- [82] Karaipekli A, Sarı A. Capric–myristic acid/vermiculite composite as form-stable phase change material for thermal energy storage. *Solar Energy* 2009;83(3):323–32. <https://doi.org/10.1016/j.solener.2008.08.012>.
- [83] Wang Y, Xia TD, Zheng H, Feng HX. Stearic acid/silica fume composite as form-stable phase change material for thermal energy storage. *Energy and Buildings* 2011;43(9):2365–70. <https://doi.org/10.1016/j.enbuild.2011.05.019>.
- [84] Radhakrishnan R, Gubbins KE. Free energy studies of freezing in slit pores: an order-parameter approach using Monte Carlo simulation. *Molecular Physics* 1999;96(8):1249–67. <https://doi.org/10.1080/00268979909483070>.
- [85] Radhakrishnan R, Gubbins KE, Watanabe A, Kaneko K. Freezing of simple fluids in microporous activated carbon fibers: Comparison of simulation and experiment. *The Journal of Chemical Physics* 1999;111(19):9058–67. <https://doi.org/10.1063/1.480261>.

3.3.10 Supporting Information

Additional Figures, Tables and Descriptions:

- Additional Figures: Fig. S3.1 to Fig. S3.17
- Additional Tables: Table S3.1
- Captions for Movie S3.1

Other Supplementary Materials for this manuscript include:

- Movie S3.1

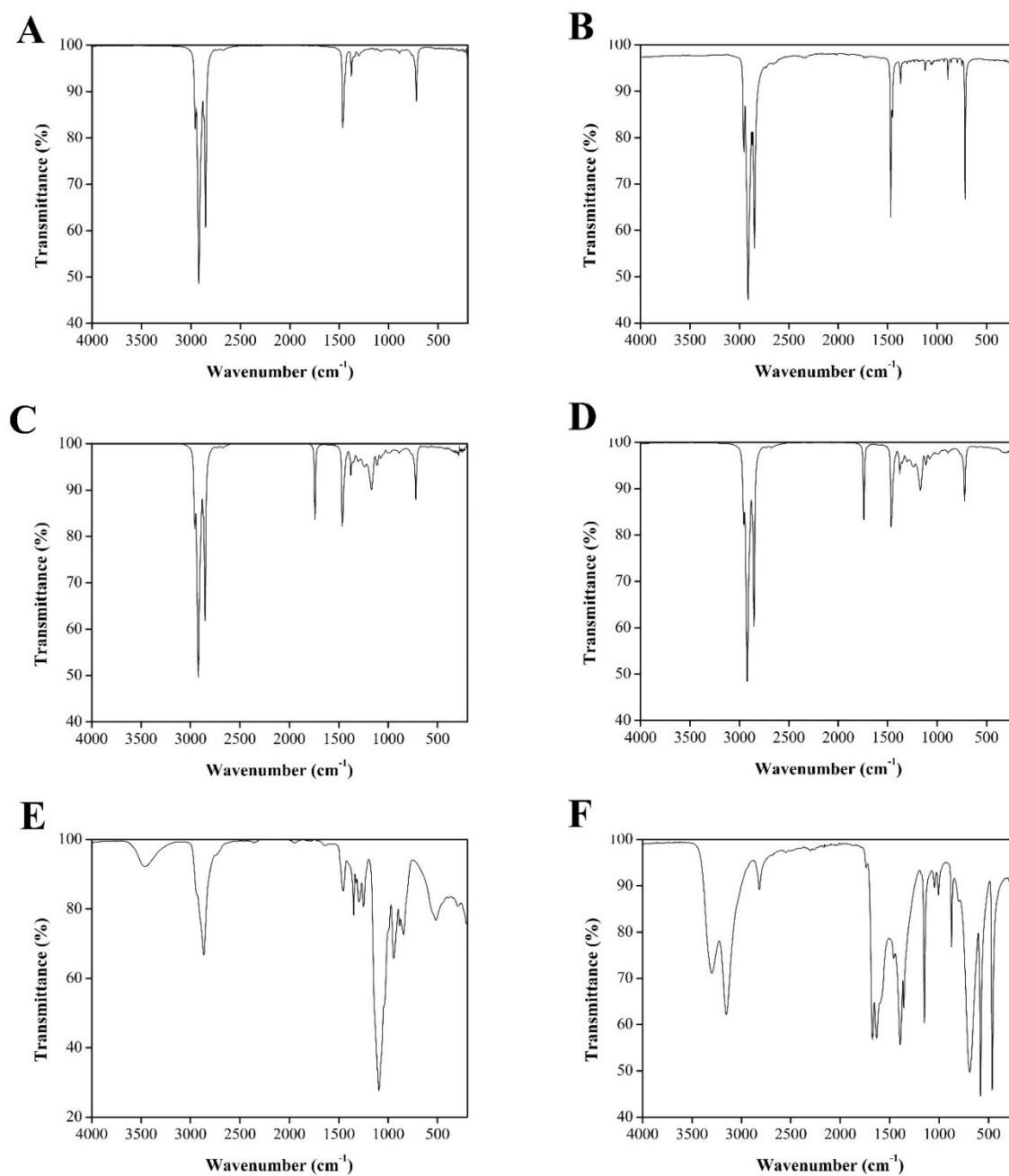


Fig. S3.1 ATR-FTIR spectra of the pure PCMs hexadecane (A), octadecane (B), polyethylene glycol 600 (E), acetamide (F) and the PCM mixtures (70:30) of hexadecane/butyl stearate (C) and octadecane/butyl stearate (D). ATR-FTIR peaks: (A) 2957 (m), 2921 (s), 2852 (s), 1465 (m), 721 (m) cm^{-1} ; (B) 2954 (m), 2912 (s), 2847 (s), 1470 (s), 717 (s) cm^{-1} ; (C) 2957 (m), 2921 (s), 2852 (s), 1741 (m), 1465 (m), 1168 (w), 721 (m) cm^{-1} ; (D) 2957 (m), 2921 (s), 2852 (s), 1741 (m), 1465 (m), 1168 (w), 721 (m) cm^{-1} ; (E) 3650 - 3150 (broad), 2865 (s), 1455 (m), 1348 (m), 1296 (m), 1248 (m), 1094 (s), 944 (s), 846 (s), 518 (m) cm^{-1} ; (F) 3298 (s, broad), 3152 (s, broad), 2818 (m), 1673 (s), 1631 (s), 1460 (s), 1393 (s), 1357 (s), 1148 (s), 1046 (m), 1006 (m), 874 (m), 690 (s), 581 (s), 463 (s) cm^{-1} .

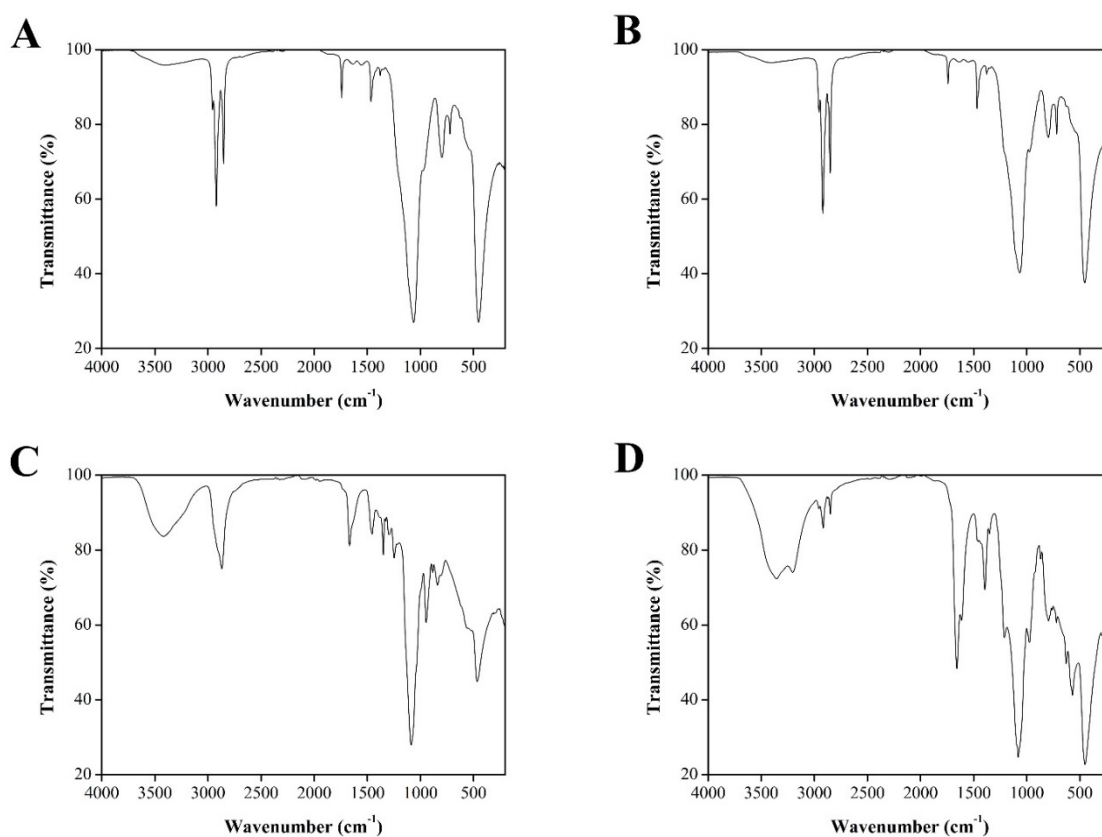


Fig. S3.2 ATR-FTIR spectra of ss-PCMs Hexa (A), Octa (B), PEG (C) and Acet (D). ATR-FTIR peaks: (A) 2957 (m), 2921 (s), 2852 (s), 1741 (w), 1465 (w), 1063 (s), 797 (s), 721 (m), 453 (s) cm^{-1} ; (B) 2955 (m), 2920 (s), 2851 (s), 1741 (w), 1468 (w), 1064 (s), 796 (m), 718 (m), 454 (s) cm^{-1} ; (C) 3700 - 3000 (broad), 2870 (m), 1667 (m), 1454 (m), 1348 (m), 1296 (m), 1247 (m), 1087 (s), 947 (s), 838 (m), 523 (s), 466 (s) cm^{-1} ; (D) 3354 (m, broad), 3204 (m, broad), 2955 (w), 2917 (w), 2850 (w), 1657 (s), 1613 (s), 1466 (m), 1394 (m), 1211 (s), 1080 (s), 974 (s), 794 (s), 720 (s), 630 (s), 570 (s), 451 (s) cm^{-1} .

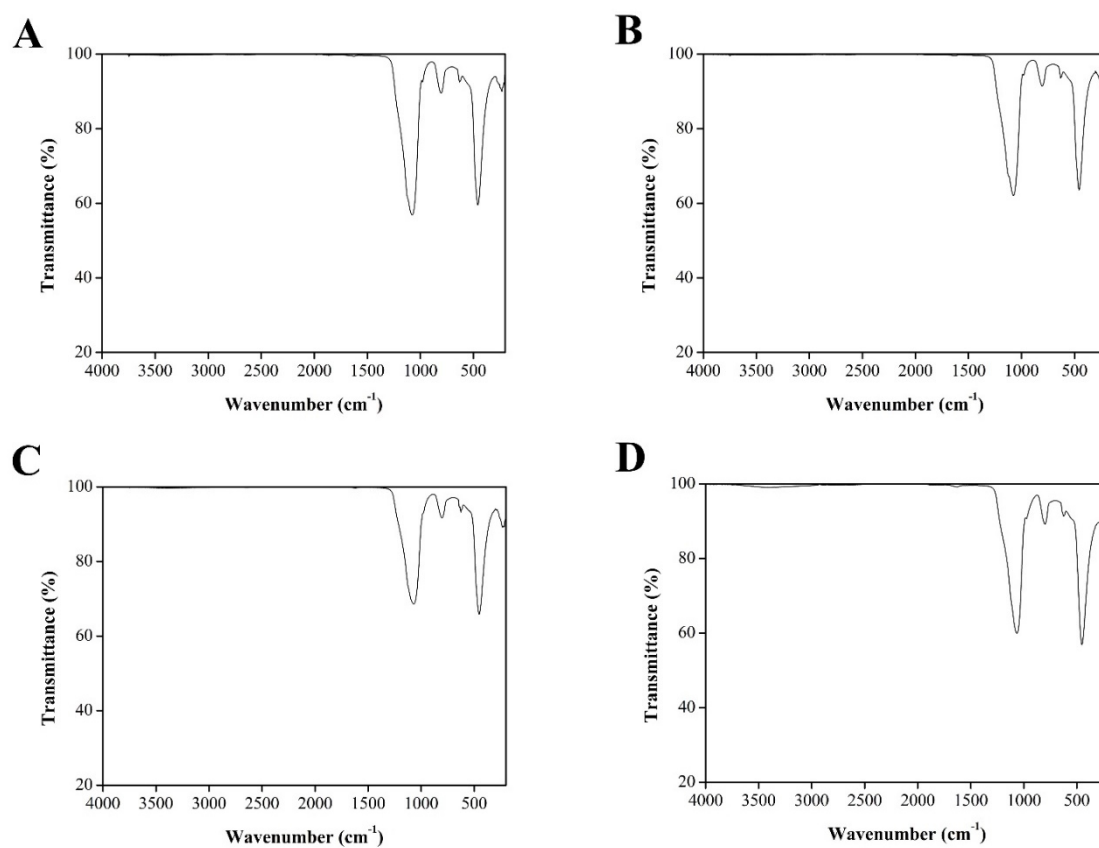


Fig. S3.3 ATR-FTIR spectra of calcined ss-PCMs Hexa_c (A), Octa_c (B), PEG_c (C) and Acet_c (D). ATR-FTIR peaks: (A) 1078 (s), 806 (w), 631 (w), 459 (s) cm⁻¹; (B) 1076 (s), 804 (w), 631 (w), 457 (s) cm⁻¹; (C) 1070 (s), 804 (w), 626 (w), 454 (s) cm⁻¹; (D) 1066 (s), 801 (w), 625 (w), 453 (s) cm⁻¹

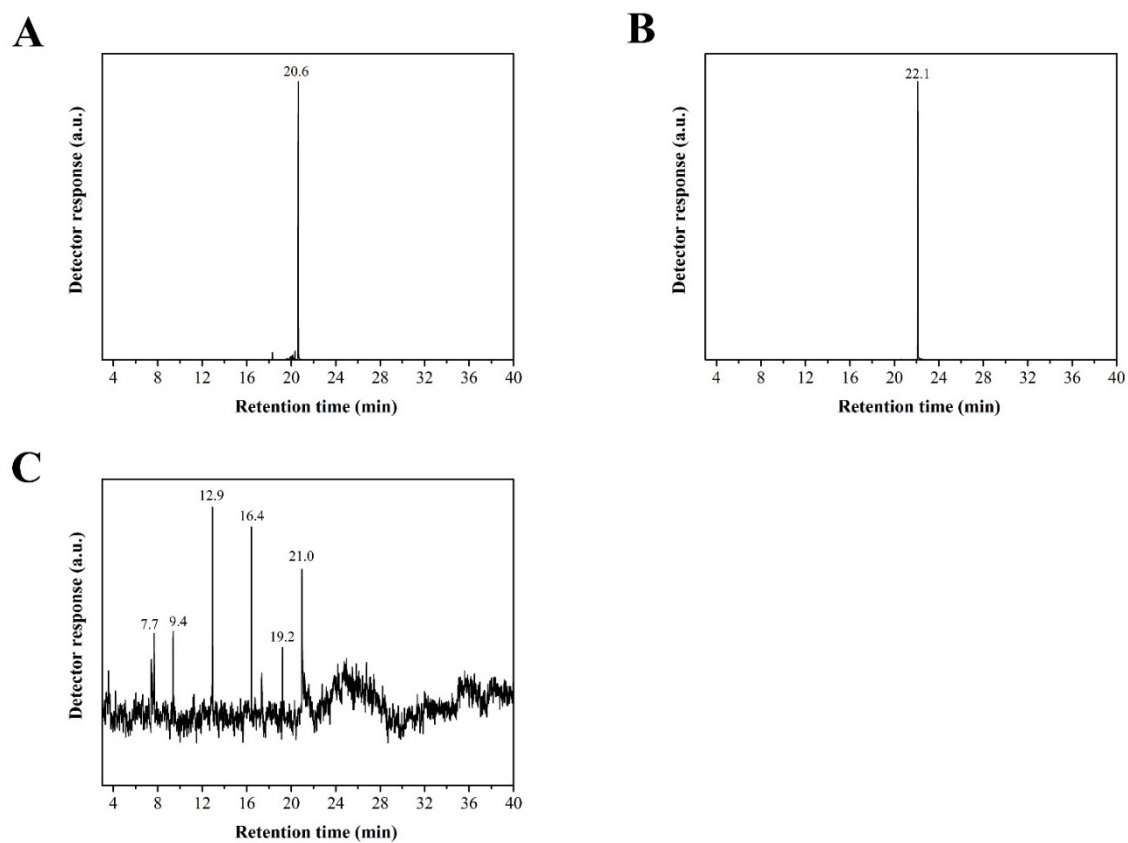


Fig. S3.4 Gas chromatograms of the pure PCMs HD (A), OD (B) and PEG600 (C). HD and OD elute as a single peak at retention times of 20.6 min and 22.1 min, respectively. The chromatogram of PEG600 shows multiple peaks due to the polymeric nature of PEG600.

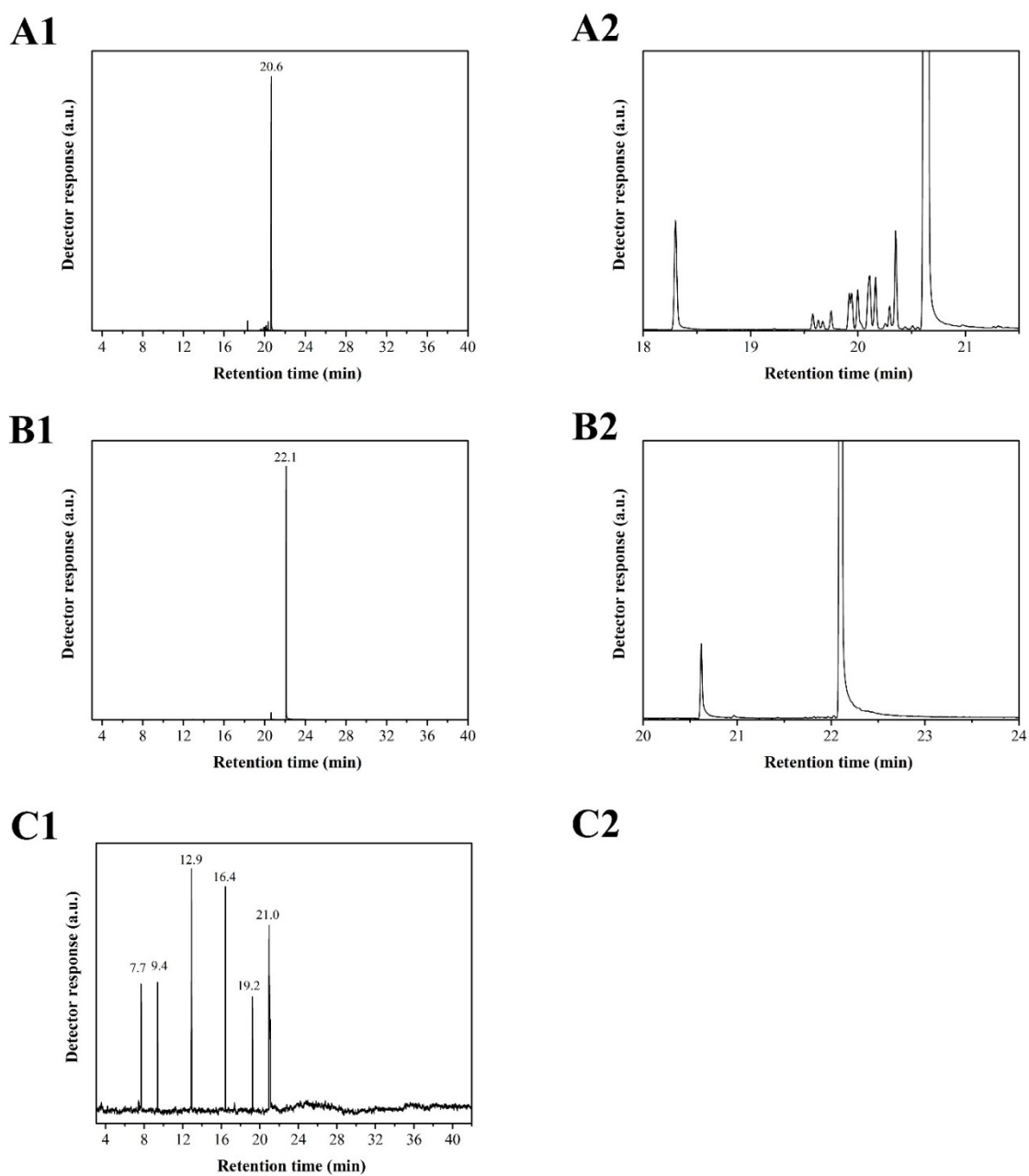


Fig. S3.5 Chromatograms of ss-PCMs Hexa (A1), Octa (B1) and PEG (C1) derived from gas chromatographic measurements. Expanded regions of A1 and B1 are shown in A2 und B2, respectively. The retention times in the chromatograms of all ss-PCMs have the same values as the pure PCMs in Fig. S3.4.

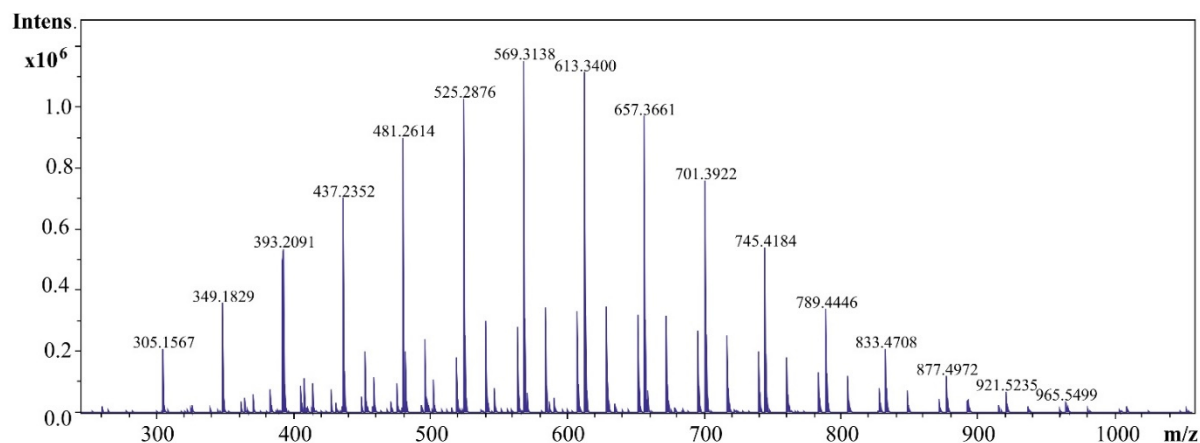


Fig. S3.6 Mass spectrum of pure PCM PEG600 obtained by electrospray ionization MS.

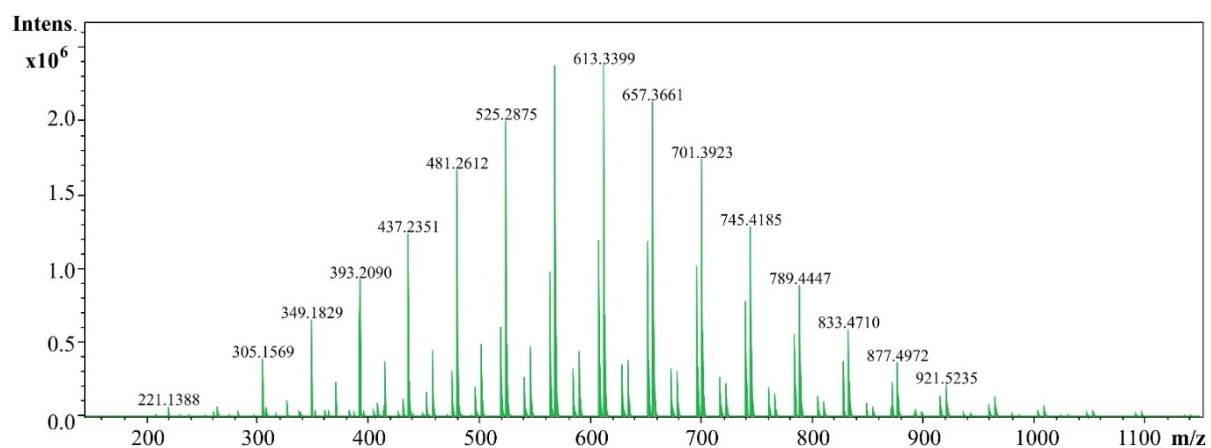


Fig. S3.7 Mass spectrum (MS) of ss-PCM PEG obtained by electrospray ionization MS. The MS peak distribution of ss-PCM PEG is nearly identical to the one of pure PEG600 (Fig. S3.6) and, thus, the PEG600 should not have been hydrolyzed to smaller polymeric units or ethylene glycol during and after shape-stabilization.

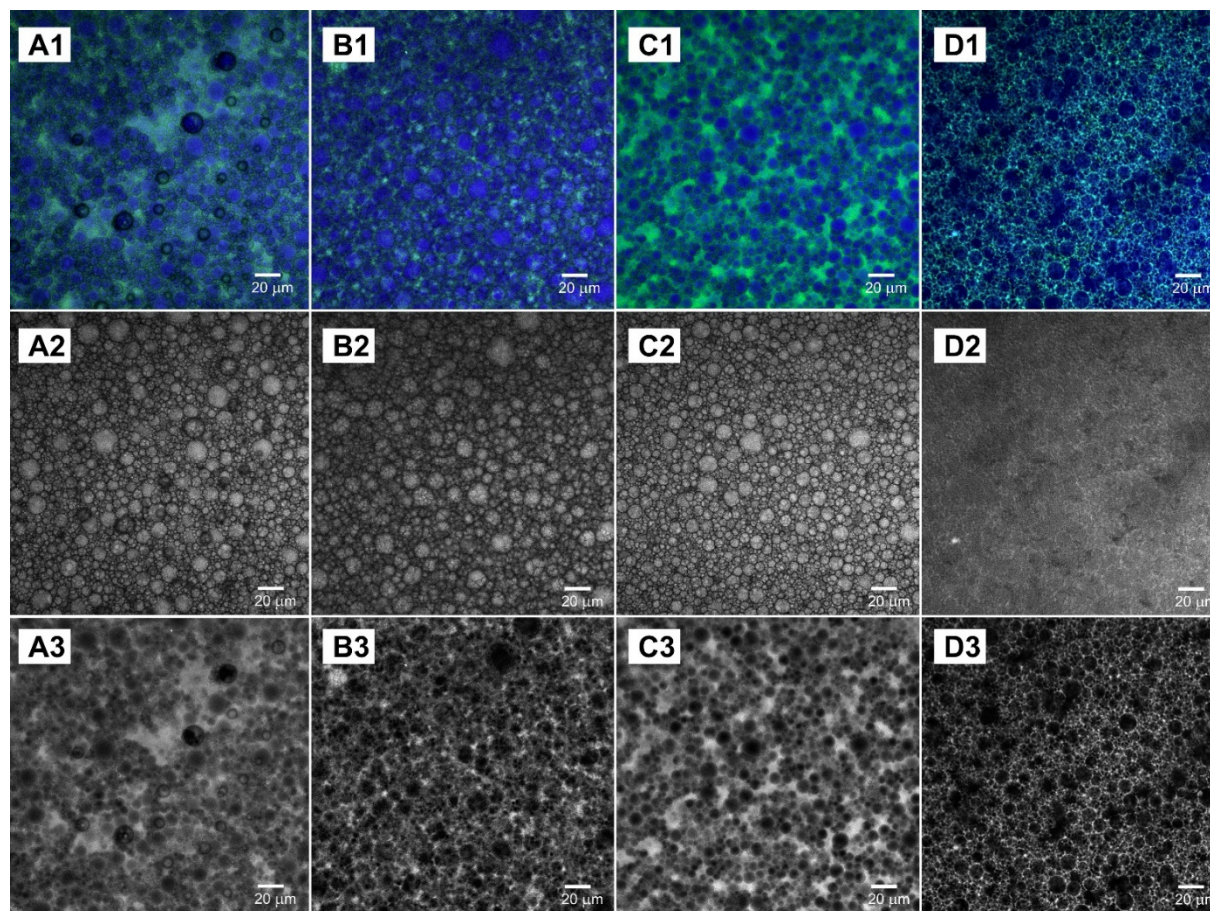


Fig. S3.8 Confocal fluorescence microscopy of the formation process of paraffinic ss-PCM Hexa (A, B) and Octa (C, D) after a reaction time of 15 min (A, C) and 72 h (B, D). The hydrophobic phase is labelled in blue with the dye perylene and the hydrophilic phase is labelled with the green-fluorescent dye Alexa Fluor 488 (1). The black lines and spots (absence of fluorescence stain) represent the growing silica phase and air inclusions during the sol-gel synthesis (1). For a more accurate analysis of the droplet size distribution (2) and the formation of the silica matrix (3), both fluorescent channels are depicted separately (blue channel (2), green channel (3)). Scale bars: 20 μm.

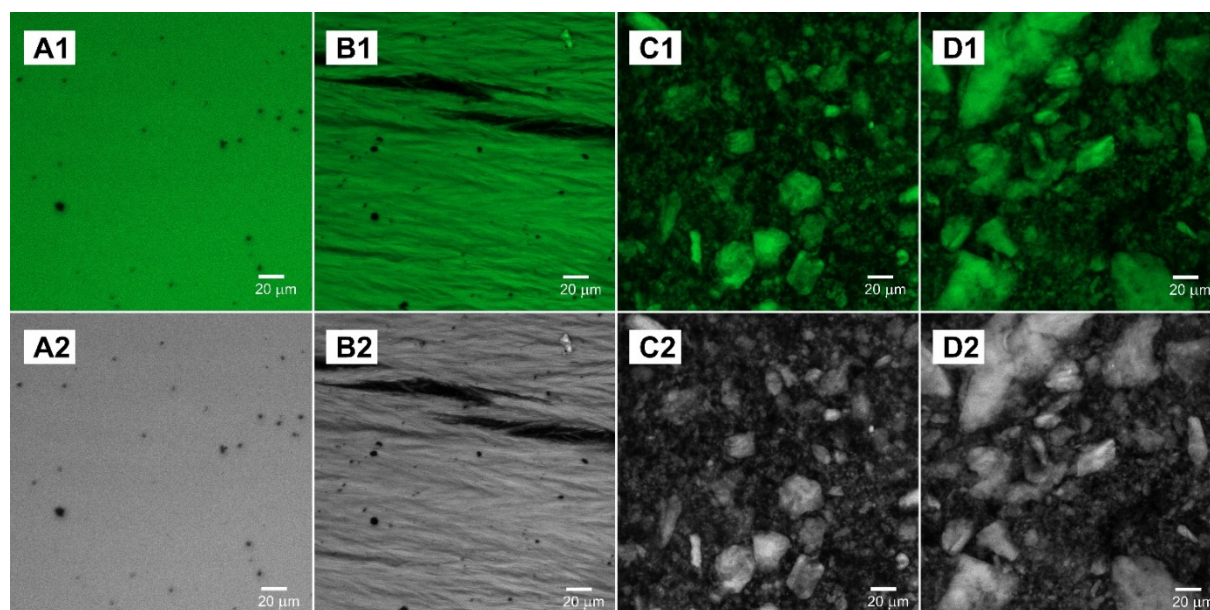


Fig. S3.9 Confocal fluorescence microscopy of the formation process of non-paraffinic ss-PCM Acet (A, B) and PEG (C, D) after a reaction time of 15 min (A, C) and 72 h (B, D). The hydrophilic phase is either labelled with the green-fluorescent dye Alexa Fluor 488 (A, B) or FM1-43 (C, D). For an unaltered viewing, fluorescence images are also shown in black and white.

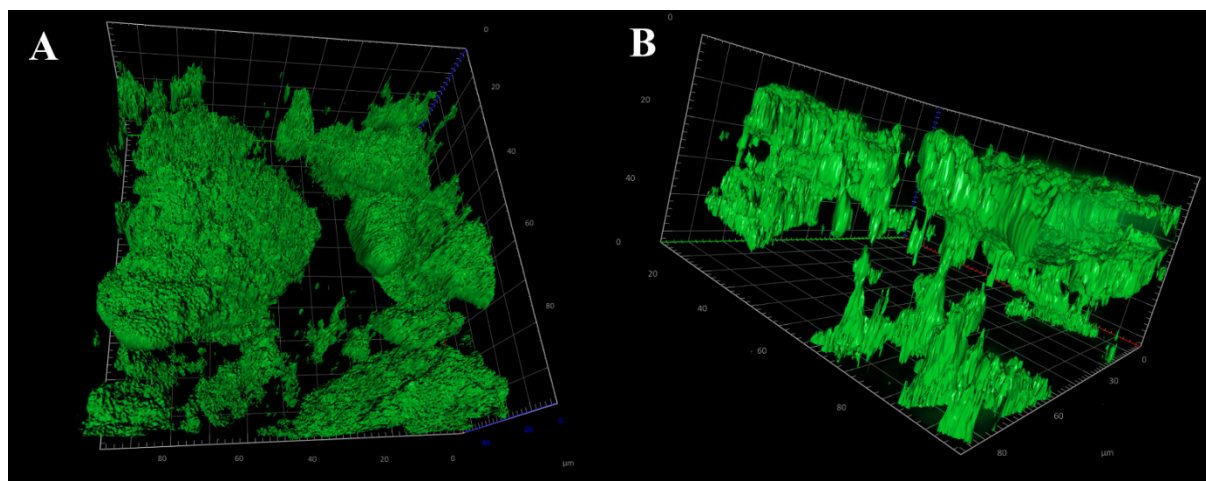


Fig. S3.10 3D reconstructions of an axial series of confocal slices of the ss-PCM PEG after a reaction time of 72 h (A) and after drying (B). FM1-43 was used to label the silica matrix (green).

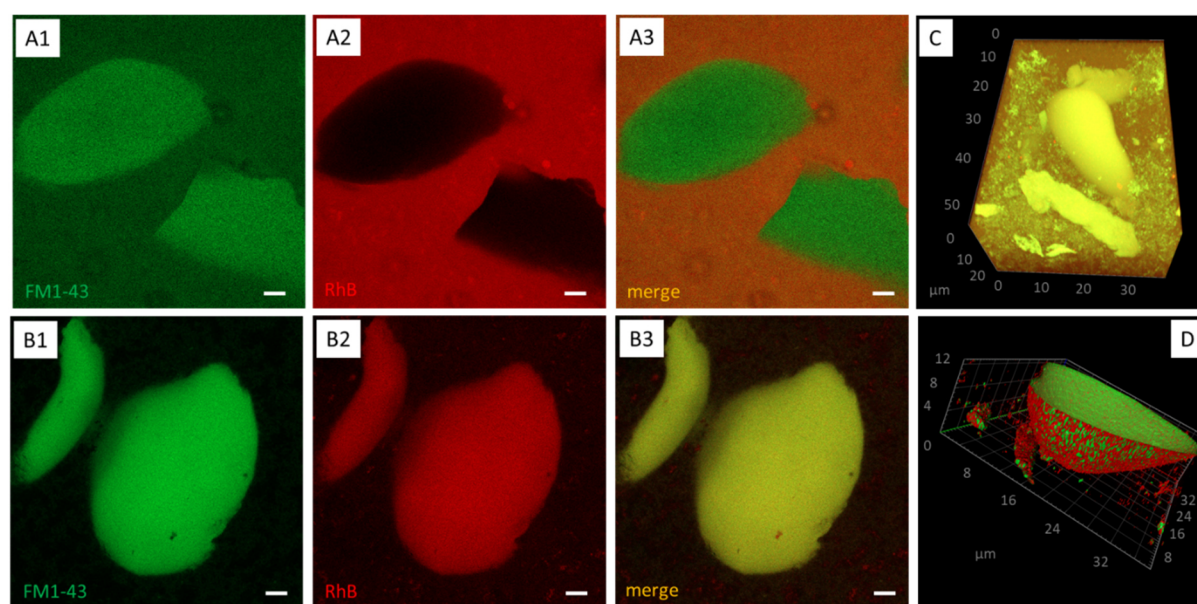


Fig. S3.11 Dual-color confocal fluorescence microscopy of ss-PCM PEG. To directly probe the PEG phase during gelation in the sol-gel process, Rhodamine B-labeled PEG at a final concentration of 0.4 mM was applied (mPEG-Rhodamine, Creative PEGWorks, NC, USA). Rhodamine (5(6)-carboxytetramethylrhodamine) is a red-fluorescent dye, excited at 561 nm, fluorescence emission was collected from 573 nm to 627 nm using the AiryScan detector. The silica matrix was simultaneously monitored using FM1-43, excited at 488 nm, fluorescence emission was collected from 499 nm to 549 nm using the AiryScan detector. Gelation progress after 15 min (A) and 72 h (B), separated into the different fluorescence channels (green: 1, red: 2) as well as the overlay (3). Immediately after reaction start silica aggregates are formed (green particles, A1), whereas PEG is still uniformly distributed in the aqueous phase (red, A2). As the gelation progresses, PEG agglomerates with the silica particles as proven by co-localization of the two fluorescent dyes. Scale bars: 10 μm . (C, D) 3D reconstructions of an axial series of confocal slices of the ss-PCM PEG after drying as volume representation (C) and as surface representation (D). Channel representation as in (B3).

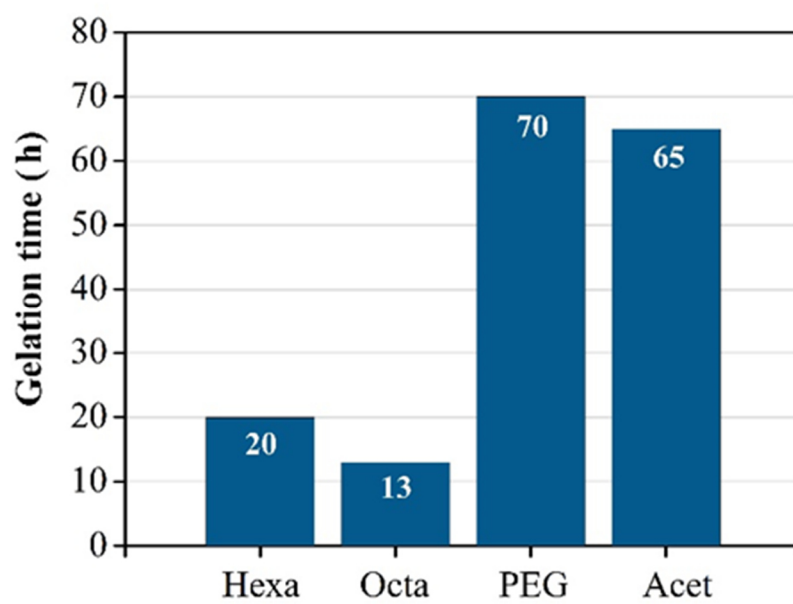


Fig. S3.12 Gelation times of ss-PCMs Hexa, Octa, PEG and Acet synthesized via sol-gel route.

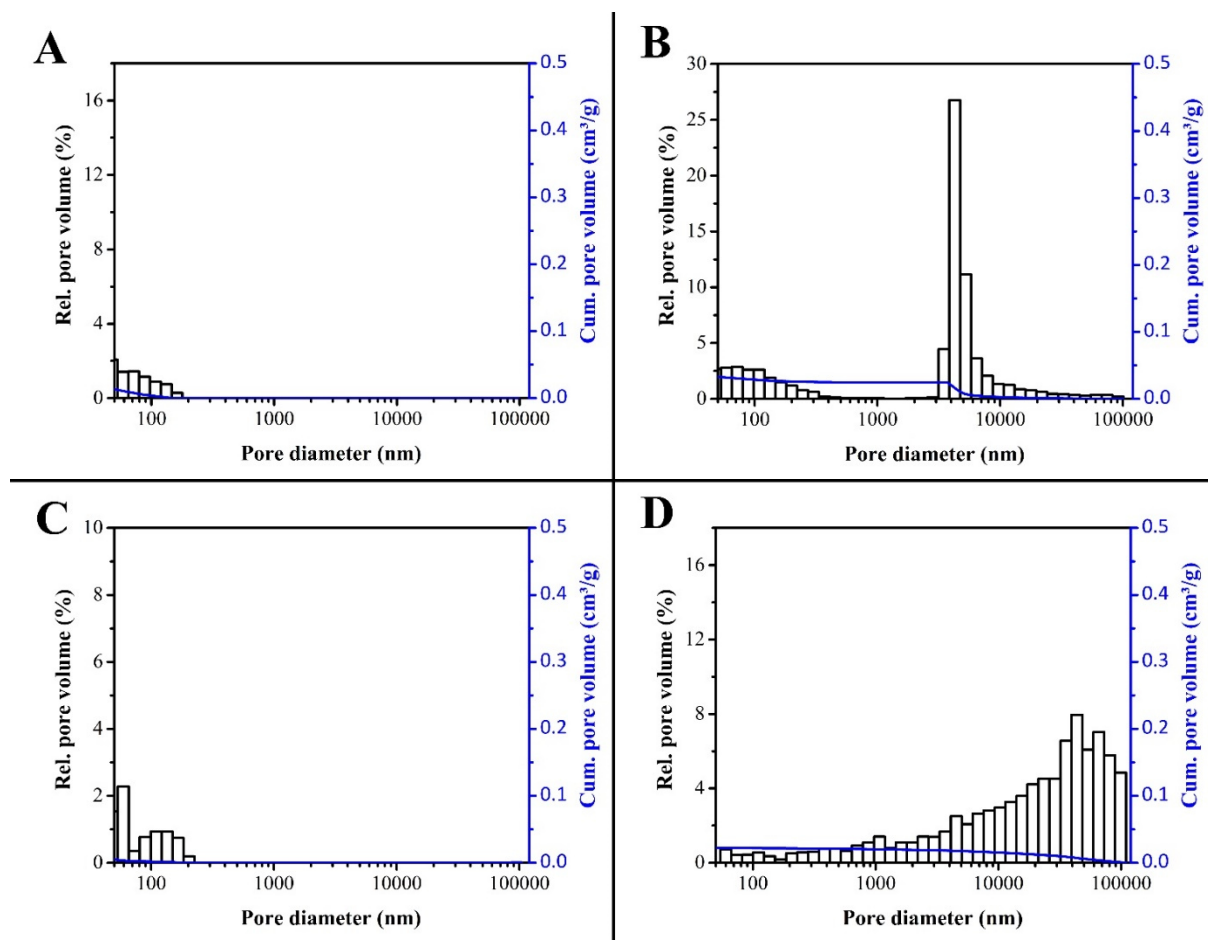


Fig. S3.13 Mercury intrusion measurements of ss-PCMs Hexa (A), Octa (B), PEG (C) and Acet (D).

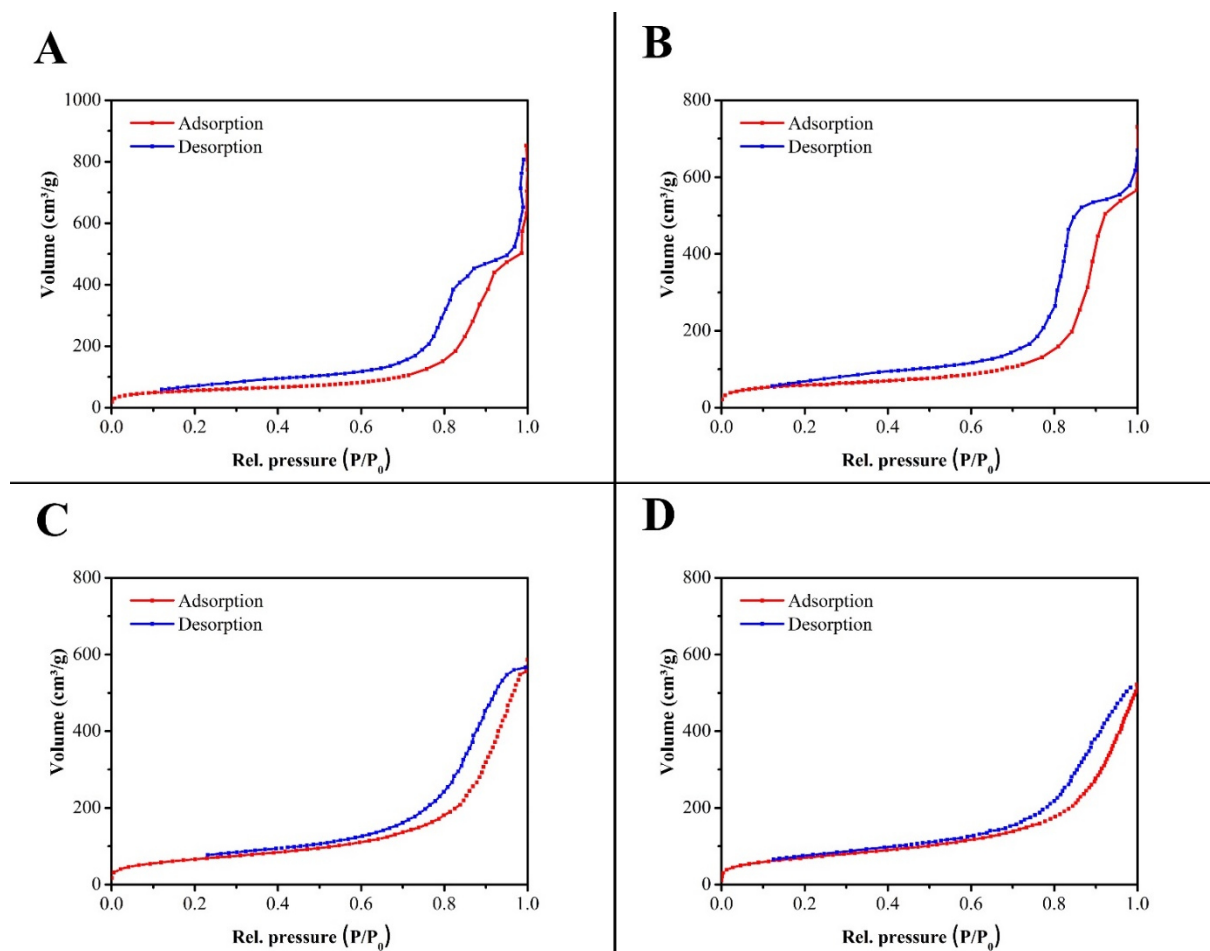


Fig. S3.14 Nitrogen adsorption and desorption isotherms of calcined ss-PCMs Hexa_c (a), Octa_c (B), PEG_c (C) and Acet_c (D).

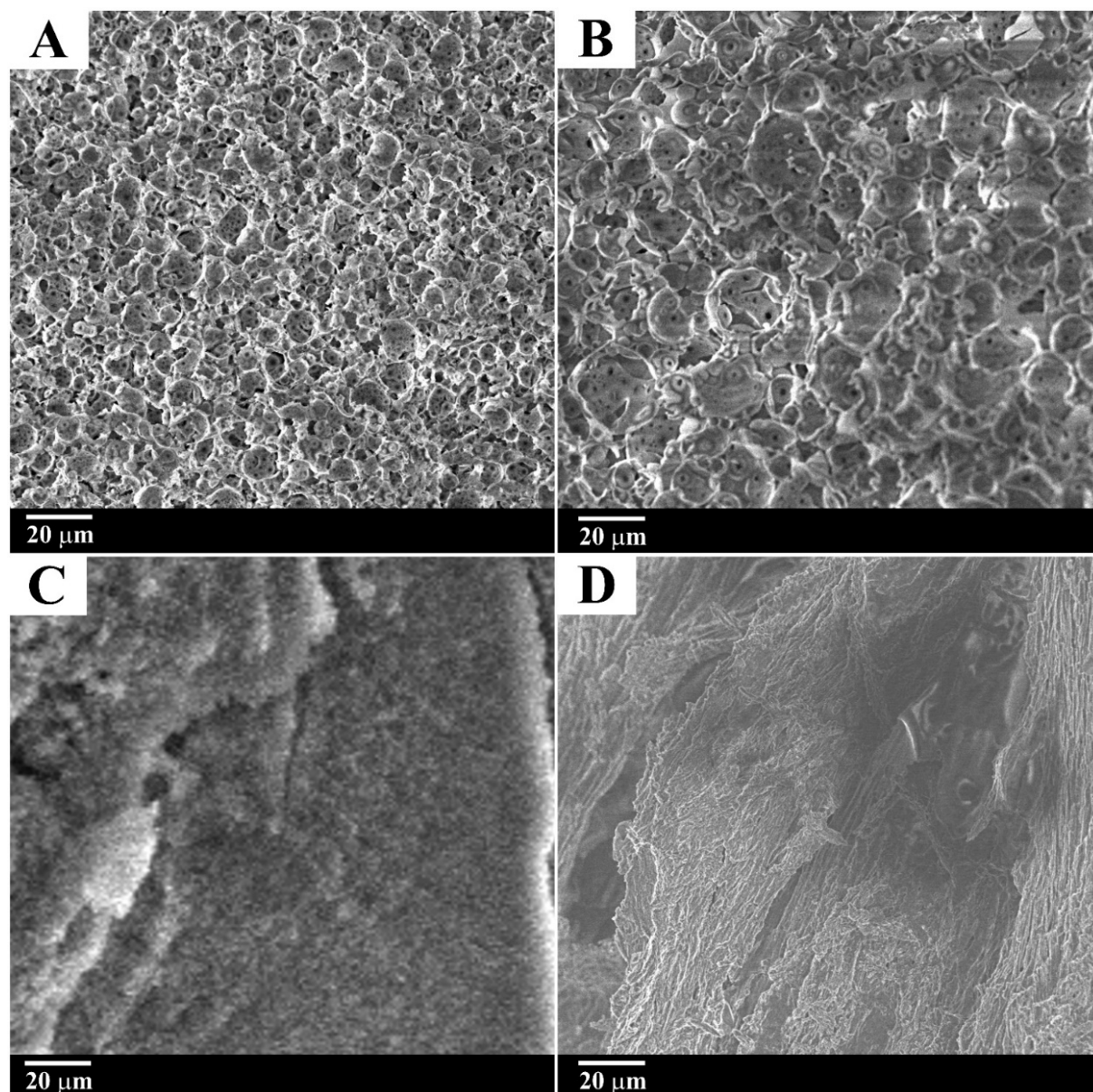


Fig. S3.15 SEM images of calcined ss-PCMs Hexa_c (A), Octa_c (B), PEG_c (C) and Acet_c (D).

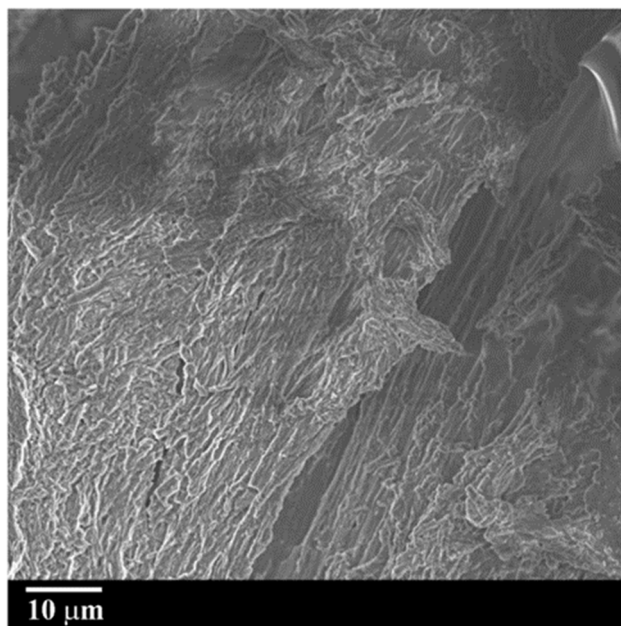


Fig. S3.16 SEM image of calcined ss-PCM Acet_c.

Table S3.1 Melting points and supercooling temperatures of pure PCMs hexadecane (HD), octadecane (OD), polyethylene glycol 600 (PEG600), acetamide (Ac), HD/BS mixture (7:3), OD/BS mixtures (7:3) and of the corresponding ss-PCMs calculated via the on-set and end-set temperature of the DSC peaks.

Sample	T_{m2} (°C)	T_{mw} (°C)	T_{f2} (°C)	T_{fw} (°C)	ΔT_{s2} (°C)	$U_{\Delta T_{s2}}$ (%)
HD	17.5	3.6	13.7	2.6	3.8	0.43
OD	28.2	4.4	24.6	2.4	3.6	0.67
PEG600 ²	15.1	10.5	11.3	4.0	3.8	0.72
Ac	59.5	12.5	36.0	1.6	23.5	0.31
HD/BS	12.5	3.9	10.2	3.1	2.3	0.22
OD/BS	22.9	4.5	20.5	3.9	2.4	0.84
Hexa	12.8	4.9	9.1	4.9	3.7	0.92
Octa	23.5	5.3	19.8	5.0	3.7	0.97
PEG	13.4	15.4	8.4	5.0	5.0	0.73
Acet	64.3	6.5	32.2	0.7	32.1	0.61

1: Melting point of BS T_{m2} , peak wide T_{mw} of DSC melting peak, freezing point of BS T_{f2} , peak wide T_{fw} of DSC melting peak, supercooling temperature ΔT_{s2} calculated via T_{m2} and T_{f2} , and the relative uncertainty $U_{\Delta T}$ of ΔT_{s2} . All values were obtained via the on-set /end-set temperature of the melting/freezing peaks in the DSC measurement. The peak width was calculated by the difference of on-set and end-set temperature of the DSC peaks

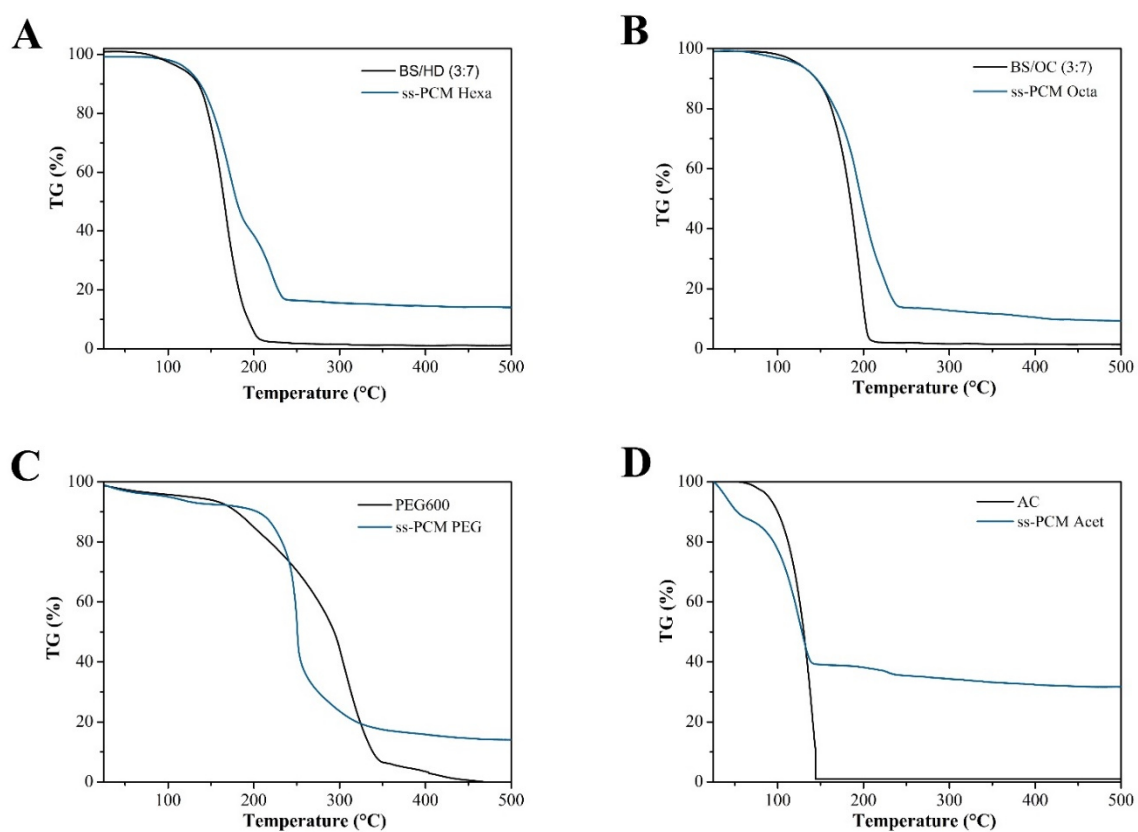


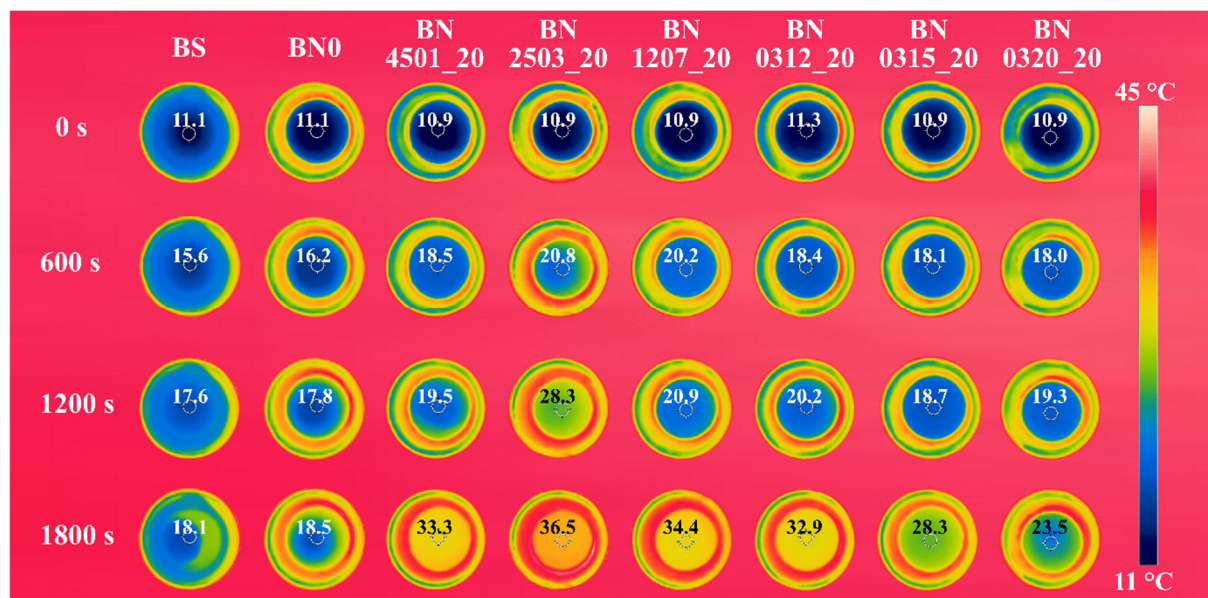
Fig. S3.17 TG curves of pure PCMs butyl stearate/hexadecane (3:7) (A), butyl stearate/octadecane (3:7) (B), PEG600 (C) and acetamide (D) (black curves) compared to ss-PCM Hexa (A), Octa (B), PEG (C) and Acet (D) (blue curves).

Caption and Description of Movie S3.1

Movie S3.1

Movie S3.1 shows the solidification process of the confined PCM (acetamide) in the ss-PCM Acet. The ss-PCM Acet is translucent above and milky-white below the freezing point of confined acetamide.

3.4 Size and surface effects of hexagonal boron nitrides on the physicochemical properties of monolithic phase change materials synthesized via sol-gel route



Authors

Felix Marske ^a, Titus Lindenberg ^b, Juliana Martins de Souza e Silva ^{c, d}, Ralf B. Wehrspohn ^c, A. Wouter Maijenburg ^b, Thomas Hahn ^a, Dirk Enke ^e

^a Institute of Technical Chemistry, Martin Luther University of Halle-Wittenberg, Halle (Saale) 06120, Germany

^b Center for Innovation Competence SiLi-nano, Martin Luther University of Halle-Wittenberg, Halle (Saale) 06120, Germany

^c Institute of Physics, Martin Luther University of Halle-Wittenberg, Halle (Saale) 06120, Germany

^d Fraunhofer Institute for Microstructure of Materials and Systems (IMWS), Halle (Saale) 06120, Germany

^e Institute of Chemical Technology, Leipzig University, Leipzig 04109, Germany

State of Publication

Accepted 2nd July 2021 in *Applied Thermal Engineering*

doi.org/10.1016/j.applthermaleng.2021.117325

3.4.1 Abstract

Monolithic shape-stabilized phase change materials (ss-PCMs) are among the most promising materials to store large amounts of solar energy, waste heat and off-peak electricity as heat in energy-saving buildings, battery- and water-heating systems. Generally, graphite-like additives, such as hexagonal boron nitride platelets (BN), are used to increase the thermal conductivity of ss-PCMs. However, it is still unknown which particle size and surface type of graphite-like additives increase the thermal conductivity of ss-PCMs to the highest extent. Here, we present the first experimental study about the influence of BN with different particle sizes and specific surface areas on the physicochemical properties of ss-PCMs synthesized via the sol-gel route. With a BN particle size of 25 μm , the average thermal conductivity of ss-PCMs containing 5 - 20 wt% BN increased by 57 % when compared to the same ss-PCMs prepared with smaller BN particles (3 μm). This effect possibly results from the stronger exfoliation of the larger BN particles during synthesis and a larger amount of BN particles ordered in the same alignment in the silica structure. BN particles larger than 25 μm hinder the formation of mechanically stable silica structures. Smaller BN particles lead to higher viscous reaction mixtures with shorter gelation times and, thus, result in smaller silica macropores with diameters below 1 μm and higher compressive strengths of ss-PCMs up to 2.4 MPa at 10 °C and 1.7 MPa at 30 °C. An increasing specific surface area of BN up to 20 m^2/g decreases the thermal conductivity by 0.11 W/mK (30 °C) and the compressive strength by 0.28 MPa (30 °C) of ss-PCMs with 20 wt% BN because of more BN agglomeration. Therefore, ss-PCMs containing 20 wt% BN with a particle size of 25 μm and a specific surface area of 3 m^2/g have the highest thermal conductivity of 1.14 W/mK at 10 °C and 0.62 W/mK at 30 °C, but a 0.7 - 0.3 MPa lower compressive strength (10 °C) than the ss-PCM synthesized using 3 μm sized BN particles and specific surface areas of 12 - 20 m^2/g .

3.4.2 Keywords

Thermal energy storage, Phase change materials, Encapsulation, Sol-gel, Boron nitride, Shape stability

3.4.3 Introduction

The rapidly growing population worldwide, which is expected to increase to 9.7 billion humans in 2050 [1], is one of the major problems of the human kind, with consequences such as higher demands of food, water, ground and energy. Therefore, new energy storage systems must be developed to decrease the worldwide energy demand and greenhouse gas emission. Organic phase change materials (PCMs) are among the most promising materials to store huge amounts of thermal energy by a state transition from liquid to solid at a constant temperature [2]. They are generally non-toxic and non-explosive, have low volume expansions during melting process, are non-corrosive to metal containers, are chemical and thermal stable after multiple freezing and melting cycles, and are available in large quantities [3–5]. Moreover, organic PCMs are easy to handle, and show low supercooling and phase separation effects [6–8]. These properties make organic PCMs perfectly suited for waste-heat recovery, drying technology, cold storage, domestic hot water and off-peak electricity applications [9–11]. However, the low thermal conductivity of pure PCMs is not sufficient for many applications. For example, liquid-cooling and air-cooling via fans, pipes, and pumps of batteries in electric vehicles (EV) is currently too bulky, expensive, and limited to specific charging rates due to overheating problems [12,13]. Therefore, Kizilel and Al Hallaj [14] used PCM in a highly thermal conductive graphite matrix as passive thermal energy storage (TES) system for Li-ion batteries, which were rapidly discharged (2.08 C, 20 A) at 45 °C. Because of the graphite, the melting point of the PCM in the battery system was reached after short time and the temperature maintained at 55 °C over a longer time than without PCM, demonstrating PCM to be useful as cooling medium in batteries. In photovoltaic systems, the PV conversion efficiency of light into electricity is decreased by a higher temperature, resulting in a 0.2 - 0.5% loss of output power per 1 K increase in the PV panel temperature [15]. Therefore, scientists integrated PCM with thermal conductive materials, such as Al₂O₃ [16], as passive cooling unit in PV-systems to increase the thermal conductivity and to prevent overheating of PV and increase the thermal efficiency of the system [17]. With the usage of nanoscopic silicon carbide as thermal conductive additive and paraffin as cooling unit, Al-Waeli *et al.* [18] could increase the electrical efficiency of their hybrid PV and solar collector (Photovoltaic-Thermal) system from 7.1% to 13.7%.

In buildings, PCM can be integrated in sandwich glazed structures, such as windows or glass facades, to increase the thermal comfort in rooms and to decrease the energy needed for heating due to passive heating of PCM via sunlight during daytime. The low thermal conductivity of these glass-PCM structures is mostly too low for an adequate heat transfer between air and PCM [19–21]. Therefore, thermal conductive additives are needed which do not decrease the transmission of the glass-PCM-structures and increase the photothermal

efficiency of the system to collect solar energy. With ZnO and CuO as nanoparticles, Yang *et al.* [22] could increase the thermal conductivity of their glass-paraffin system by 8.44 % and 13.12% at low volume percentages of nanoparticles (1.5×10^{-3} vol%), respectively.

In general, conducting fins [23–27], metal nanoparticles [28–30] and carbon nanotubes, sheets and platelets [31–34] are homogeneously dispersed in liquid PCM to increase the thermal conductivity of PCMs via small additives available as powder. Additionally, the insertion of macroscopic metallic foams with open pore structures in liquid PCM is a promising method to increase the thermal conductivity of PCMs [35–39], too. For example, Mancini *et al.* [40] incorporated liquid PCM in a copper foam structure and increased the overall heat transfer rate of paraffins with melting points between 53 °C to 59 °C by a factor of 4 to 8. Expanded graphite (EG) and similar structured materials, such as hexagonal boron nitride platelets (BN), have the highest thermal conductivities known and, thus, are widely studied in the current PCM research [41–43]. They are also chemically and thermally stable, and have high inner surfaces, enabling a faster heat transfer rate in PCMs. Their properties strongly depend on the aspect ratio of particle size to particle thickness [44]. The particle size is defined as the in-plane diameter of the whole 2D ring structure. The particle thickness is measured in the perpendicular direction to the particle size and characterizes the sum of all single-layered nanosheets, which are stacked on top of each other in the BN platelet. For example, the in-plane thermal conductivity of one single-layered BN has a value of 600 W/mK (27 °C), whereas bulk BN with five nanosheets stacked on top of each other and the same particle size has a lower value of 390 W/mK (27 °C) because of a slower heat transfer rate between the 2D nanosheets [45].

For a homogeneous suspension, the PCM is melted, mixed with the layered additive, stirred vigorously and sonicated for separation of the plates [46–48]. However, several studies have reported precipitation and aggregation of graphite-like additives and leakage from graphite-like additives after multiple melting and freezing cycles of the nano-enhanced PCM (NePCM), lowering the thermal conductivity over time [42,49,50]. To prevent aggregation and leakage effects, cellulose [51], graphite oxide [52], wood's alloy [53] and betonite [54] can be added as a binder. NePCMs that keep their shape during at least one state transition are named shape-stabilized PCMs (ss-PCMs). For example, Jiang *et al.* [55] impregnated porous graphite with paraffin and increased the thermal conductivity of the composite material to one of the highest reported values of 13.85 W/mK by using 30 wt% EG. For the application as battery thermal management system (BTES), they pressed the EG/paraffin powder to a ss-PCM block. Though its promising battery cooling ability during battery charging, 21 wt% paraffin leaked out of the ss-PCM (9 wt% EG), already after heating the ss-PCM 10-times above the melting point, pointing to a low durability and limiting its application.

Therefore, a high mechanical stability can be more important than a high thermal conductivity for ss-PCMs used in building construction materials [56] and BTES for electric vehicles [57]. However, only few studies address the improvement of the mechanical stability as well as the thermal conductivity of ss-PCMs in the current literature [58]. For example, Yang *et al.* have synthesized ss-PCMs via an ice-templated assembly strategy with graphite oxide as a binder and hexagonal boron nitride platelets (BN) as graphite-like additive [59]. The cylindrical samples had a high thermal conductivity of 1.84 W/mK at relatively low BN amount (19.2 wt%), but only a low compressive strength of approximately 5 kPa, which was measured by calibration weights and not in a specific mechanical strength tester.

Additionally, the influence of the particle size and specific surface area of BN and expanded graphite on the physicochemical properties of ss-PCMs is still not understood in the current literature, resulting in a wide range of incomparable experimental studies about graphite-like additives in ss-PCMs. In contrast to EG, BN is not electrically conductive and is, thus, preferred as thermal additive for ss-PCMs synthesized as thermal management system material for electric devices and batteries [60]. Therefore, an experimental analysis of BN with different particle sizes and specific surface areas in ss-PCMs is required to find the BN best suited for an increase of the thermal conductivity of ss-PCMs.

With the purpose to fulfil this need and enable faster progress in the development of efficient ss-PCMs, we analysed the effect of randomly distributed BN on the physicochemical properties of our recently reported and mechanically stable ss-PCMs [61]. We achieved to increase both the thermal conductivity and mechanical stability of our ss-PCMs (0.7 MPa, 30 °C) based on silica as the carrier matrix and butyl stearate as the PCM using BNs with different particle sizes and specific surface areas.

3.4.4 Experimental

3.4.4.1 Materials

The stabilized silica sol Köstrosol 0730 (30 wt% colloidal silica particles in water, 7 nm average particle diameter) was provided by Chemiewerk Bad Köstritz, Germany. Butyl stearate (technical grade product) and poly(vinyl alcohol) (PVA, 88 % hydrolyzed, average M.W. 22000) were purchased by Alfa Aesar and ACROS Organics, respectively. Sodium dodecyl sulfate (SDS, ≥ 99.0 % GC, dust-free pellets) was obtained from Sigma-Aldrich. Hexagonal boron nitride platelets (HeBoFill: 510, 490, 641, 110, 230, 205) were provided by Henze Boron Nitride Products AG, Germany. Deionized water was used for all experiments.

3.4.4.2 Preparation of ss-PCMs

An amount of 0.33 g poly(vinyl alcohol) (PVA) was dissolved in 3.71 g water, heated to 60 °C for 5 h and added to a suspension of 0.44 g sodium dodecyl sulfate (SDS) and 11.00 g butyl stearate (BS). After preparing 24 suspensions, an amount of 0.70 g (5 wt%), 1.47 g (10 wt%), 2.34 g (15 wt%) and 3.31 g (20 wt%) of each type of HeBoFill hexagonal boron nitride platelets was added separately to the suspensions, heated to 50 °C and left at this temperature for at least 12 h. After stirring for 15 min at 700 rpm and 25 °C, 4.95 g Köstrosol 0730 was added dropwise to the reaction mixtures and stirred for another 15 min at 700 rpm and 25 °C. Then, the magnetic stirrers were removed and the beakers containing the reaction mixtures were closed. After heating the suspensions for 72 h at 40 °C, the beakers were opened, and the wet gels dried at ambient pressure first at 40 °C for 4 days and then at 100 °C for 20 h (sample pictures in Fig. S4.1). A reference sample was synthesized without BN and named BN0 (equivalent to sample FS4 from our previous study [61]).

3.4.4.3 Nomenclature of ss-PCMs

The different ss-PCM samples were named after their chemical nature as BN followed by two numbers marking the particle size (μm) and particle surface area (m^2/g) of the immobilized BN, respectively. The last two numbers of the ss-PCM name represent the amount of BN used in the synthesis of the ss-PCM (wt%). For example, ss-PCM BN2503_10 was synthesized with 10 wt% HeboFill 490, which has an average particle size D_{50} of 25 μm and a specific surface area S_m (BET) of 3 m^2/g (Fig. 4.1, Table 4.1). The name of the calcined ss-PCMs were marked with a “c” after the particle surface area (e.g. BN2503c_10).

Table 4.1 Average particle size D_{50} , particle thickness Δ and specific surface area S_m of hexagonal boron nitride of type HeBoFill used in the ss-PCM synthesis.

	HeBoFill 510	HeBoFill 490	HeBoFill 641	HeBoFill 110	HeBoFill 230	HeBoFill 205
D_{50} (μm)	45	25	12	3	3	3
Δ (nm)	177	145	124	69	68	64
S_m (m^2/g)	1	3	7	12	15	20

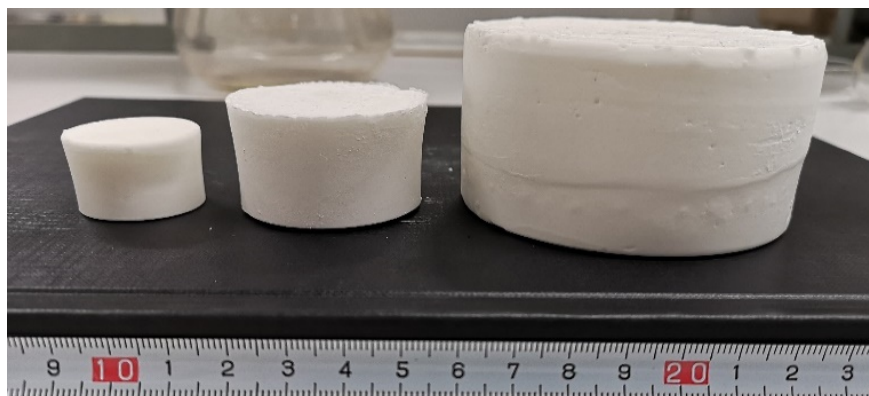


Fig. 4.1 Upscaling of ss-PCM BN2503_10 in three different sizes.

3.4.5 Characterization of ss-PCMs

The thermal properties of the ss-PCMs were analysed by DSC measurements using an 822e calorimeter from METTLER TOLEDO with a heating rate of 1 °C/min, running from -20 °C to 60 °C under air atmosphere with holding times of 10 min. The accuracy of the DSC temperature measurement was within ± 0.01 °C. The average relative uncertainty of all latent heats ΔH_{total} and of all values for supercooling ΔT_s calculated via DSC measurements was ± 3.73 % and ± 1.71 %, respectively. For long-term performance tests, the ss-PCM samples were melted and frozen 1000-times via a Primus 96 Thermal Cycler from MWG Biotech Inc. between 8 °C and 60 °C and measured via DSC afterwards. To measure the heat transfer rates during PCM melting, the ss-PCM samples were put in a metallic vessel and cooled down to 11 °C (Fig. S4.2). Afterwards, the vessel was heated in a water bath at 45 °C and the temperature was tracked every 15 s using a C3 thermal imaging camera from FLIR. The thermal conductivity was measured using a Hot Disk TPS 1500 thermal analyser from Hot Disk AB based on a transient plane source (TPS) method. The samples were measured in sandwich-mode at 10 °C and at 30 °C (Fig. S4.3). For the measurement, two ss-PCM samples synthesized with the same ingredients were sawed in the middle in two halves and the sensor, which acted also as heater, was put on three different spots between the two halves of each ss-PCM sample. Every spot was measured a total time of three times with a waiting period of 10 min between each measurement and the thermal conductivity value of these measurements was calculated by dividing the thermal conductivity values by the number of measurements. The average relative uncertainty for the thermal conductivity measurements of all samples was ± 0.87 % (Table S4.2). To calculate the average thermal conductivity of a sample row, the thermal conductivity of all ss-PCMs of a sample row were summed and divided by the number of samples (4).

The average compressive strength of five ss-PCMs with the same composition was measured using a TBH355 hardness tester from ERWEKA at 10 °C (solid silica matrix, solid PCM) and at 30 °C (solid silica matrix, liquid PCM). The average relative uncertainty of all measurements was ± 2.23 % (Table S4.5). After the measurements, a value of the physical force was obtained, which induces microscopic cracks in the ss-PCM. The physical force was divided by the area of the ss-PCM to calculate the value for the compressive strength.

To prove the completion of the gelation process and, thus, the gelation times, 5 - 8 samples of every ss-PCM were synthesized and turned upside down after some time during gelation. If the wet gel was solid and not moving, the gelation was finished. The relative uncertainty of this measurement method was approximately ± 5 %.

The macro- and mesoporosity of the ss-PCMs and silica matrix were characterized by mercury (Hg) intrusion measurements (Pascal140 (400 kPa) and Pascal440 (400 MPa), Porotec) and by nitrogen sorption measurements at -196 °C (Sorptomatic 1990 surface area analyser, Porotec), respectively. For the measurements, the ss-PCM sample (100 mg) was analysed before and after the calcination of the ss-PCM at 600 °C for 10 h. The pore diameter is defined as the width (size) of one silica pore in this work. The pore diameter is calculated via the direct measurement of mercury intrusion for macropores with pore diameters above 50 nm and via nitrogen-adsorption measurements for mesopores below 50 nm.

High-resolution microscopic images of the silica structure in ss-PCMs were taken via scanning electron microscopy (SEM) using a Merlin HRSEM from Zeiss. For this, the samples were attached onto a conductive carbon tape and the accelerating voltage was set to 3 - 5 kV. X-ray microscopy experiments were carried out with a Carl Zeiss Xradia 810 Ultra (Cr X-ray source, 5.4 keV). For this, a total of 901 projections (field-of-view: $65 \times 65 \mu\text{m}^2$) was acquired over 180° using Zernike phase-contrast imaging, with an exposure time of 10 s per projection, a detector binning of 2 resulting in an isotropic voxel size of 128 nm in the final images. The images were reconstructed with filtered back-projection algorithm using the XMReconstructor software and three-dimensionally visualized with TXM3DViewer software, both integrated into the Xradia 810 Ultra. Avizo (Thermo Fisher Scientific version 9.4.0) was used for the three-dimensional rendering after applying a non-local means filter.

For the chemical analysis of BN, the ss-PCM samples were calcined at 600 °C for 24 h and measured via X-ray powder diffraction (XRD) using a D8 advanced X-Ray diffractometer from Bruker AXS, working with a Cu K α source ($\lambda = 0.15406$ nm) in a 2θ range of $5 - 80^\circ$ (counting time per step: 0.5 s).

3.4.6 Results and discussion

To understand the effect of particle size and specific surface area on the physicochemical properties of the ss-PCM samples, we synthesised thermally enhanced ss-PCMs using six types of hexagonal boron nitride platelets (BN), each with a different particle size and specific surface area (Table 4.1), and we used four different amounts of BN (5 - 20 wt%), resulting in a total of 24 samples. After the ss-PCM synthesis, we tested the shape-stability of all ss-PCMs by a simple PCM leakage test at a temperature of 100 °C for 1 month. We could not observe any PCM leakage or mass loss during this time. The FTIR and ²⁹Si MAS NMR analyses of all ss-PCMs show that there is no significant influence of BN on the hydrolysis degree of the silica network and that the surfactant SDS and the organic copolymer PVA are chemically inert during the syntheses (Publication 5 (Fig. 5.1 to 5.5)).

3.4.6.1 Influence of BN on the thermal properties of ss-PCMs

The relative thermal conductivity enhancement K is a good indicator to compare results from studies performed with different measurement methods and different PCMs, and is calculated as follows:

$$K = \left(\frac{k_{eff} - k_{BN0}}{k_{BS}} \right) \cdot 100 \quad \text{Eq. (4.7)}$$

where k_{eff} is the thermal conductivity of the sample, k_{BS} is the thermal conductivity of the pure PCM butyl stearate (BS) and k_{BN0} is the thermal conductivity of ss-PCM sample BN0 synthesized without BN addition. The thermal conductivities of the pure BS and ss-PCM BN0 k_{BN0} are 0.363 W/mK at 10 °C (0.215 W/mK at 30 °C) and 0.220 W/mK at 10 °C (0.117 W/mK at 30 °C). The thermal conductivity enhancement ratio is smaller in a liquid state than in a solid state because of high interfacial resistance of the liquid state [62]. Therefore, the thermally enhanced ss-PCMs were measured at 10 °C with BS in the solid phase and at 30 °C with BS in the liquid phase, which was shape-stabilized by solid SDS, PVA, BN and the well-interconnected silica matrix (Fig. 4.2, Table S4.2). With an increasing mass fraction of BN from 5 wt% to 20 wt%, the thermal conductivity of all samples also increased. For example, by duplicating the amount of BN in sample BN0312 (BN0312_10 vs. BN0312_20) the thermal enhancement rises from 66% to 222%. This increase probably occurs because of a higher contact area between BN particles and, thus, a better heat transfer (Fig. 4.2, Table S4.2), which is in agreement with previous studies [52,59].

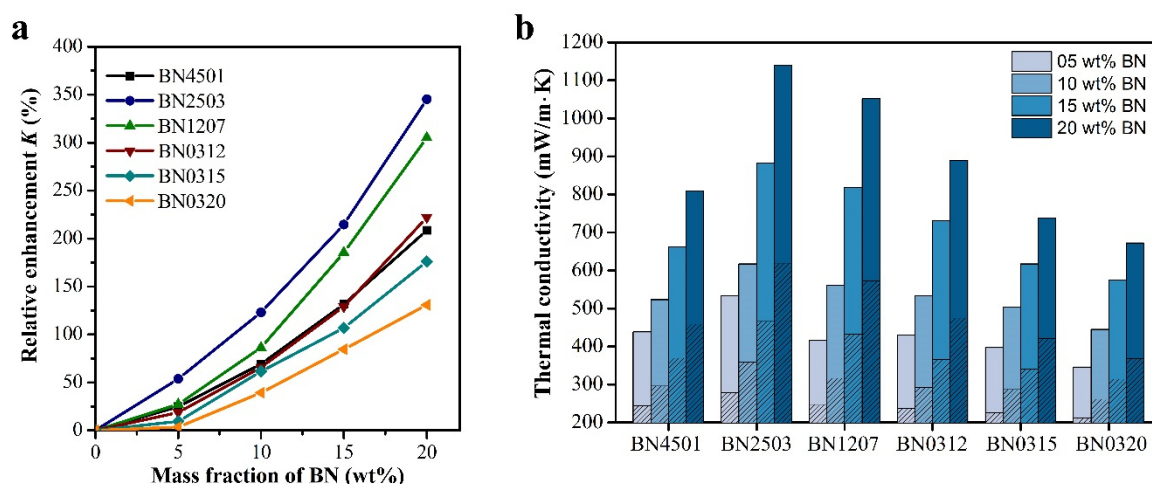


Fig. 4.2 a) Relative enhancement K of the thermal conductivity of BS measured at 30 °C in dependence of the mass fraction of BN in the ss-PCM samples BN4501, BN2503, BN1207, BN0312, BN0315 and BN0320. The relative thermal enhancement K was calculated by Eq. 4.1 (thermal conductivities (30 °C) of BS (0.117 W/mK) and BN0 (0.215 W/mK)). b) Thermal conductivities of ss-PCM sample rows BN4501, BN2502, BN1207, BN0312, BN0315 and BN0320 synthesized with 5 - 20 wt% BN. The thermal conductivities of the ss-PCMs were measured below the freezing point of BS at 10 °C (filled) and above the melting point of BS at 30 °C (dense).

The thermal conductivity of sample BN0312_05 is increased by 103% compared to pure BS (0.117 W/mK at 30 °C) and by 19% compared to sample BN0 synthesized without BN (0.215 W/mK at 30 °C) (Fig. 4.2a). When comparing samples with the same particle size but different specific surface areas (samples BN0312, BN0315 and BN0320), we observe a lower thermal conductivity for the samples with a higher specific surface area of BN particles immobilized in the ss-PCMs.

In the current literature, thermal conductive particles with high specific surface areas and large aspect ratios, such as single wall carbon nanotubes [63], have a higher thermal conductivity than the ones with lower specific surface areas and smaller aspect ratios, such as larger multi-wall carbon nanotubes. In this work, however, we observe the exact opposite trend (Fig. 4.2b). One hypothesis is that, with increasing specific surface area, BN can interact more via weak dipole-dipole interactions with its surrounding chemical environment, increasing the viscosity of the reaction mixture and, thus, the BN agglomeration during gelation processes. The agglomeration of BN particles could be a negative side effect of using BN particles with high specific surface areas in the sol-gel process and overweigh the positive effect of the higher contact areas between BN and PCM, resulting in lower thermal conductivities for sample series BN0320 in comparison to BN0312. The relative enhancement of the thermal conductivity K from BN0312_20 (222%) to BN2503_20 (345%) (Fig. 4.2a) corresponds to an increase of the average particle size from 3 μm to 25 μm and a lowering of the specific surface area from 12 m^2/g to 3 m^2/g . Larger particles of BN seem to increase the thermal conductivity of ss-PCMs to a higher extent than smaller particles. However, the sample group BN4501, with the highest

average particle size of 45 μm and the lowest specific surface area of 1 m^2/g , has a lower average thermal conductivity than samples BN2503 and BN1207, which is comparable to the one of BN0312. Additionally, two out of four samples of BN4501_10 were broken in two pieces after drying and sample BN4501_20 was partially broken, indicating an upper limit of the BN particle size in the *in situ* sol gel process used in this work. A large particle size could inhibit the formation of a stable, thermally conductive silica matrix around the BS droplets during gelation, which could be the reason for the lower average thermal conductivity of sample series BN4501 with 5 wt% to 20 wt% BN.

Next, we compared the thermal conductivity enhancement K of the ss-PCMs in this work with six studies in the literature [64–69] about thermally enhanced form-stable PCM blends (fs-PCM) (Fig. 4.3). The thermal conductivity enhancement K of the ss-PCMs is referred to the thermal conductivity of sample BN0 at 30 °C (0.215 W/mK). The ss-PCM were measured above the melting point of the PCM in all literature studies. The PCMs are not encapsulated

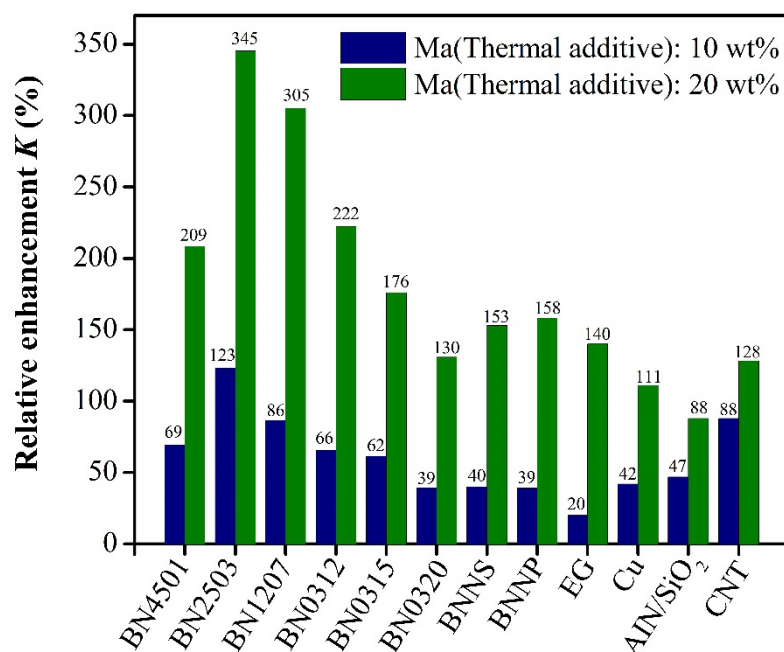


Fig. 4.3 Relative enhancement K of the thermal conductivity of PCMs in ss-PCMs synthesized in this work and in form-stable (fs) PCM blends synthesized in the literature with 10 wt% and 20 wt% thermal additives. The fs-PCMs are named after the thermal additive, which was used in their synthesis to increase the thermal conductivity, such as Cu for copper nanowires or EG for expanded graphite. The relative enhancement K is referred to sample BN0 (0.215 W/mK, 30°C) for samples in this study (Eq. 1) and to pure PCM for the literature samples. All thermal conductivities were measured above the melting point of the pure PCM. The fs-PCM blends were synthesized with the following thermal additives and PCMs in the literature: BN nanosheets and polysiloxane (solid: 0.11 W/mK) (BNNS [64]), BN and poly(ethylene glycol) (solid: 0.30 W/mK) (BNNP [65]), expanded graphite and palmitic acid (solid: 0.25 W/mK) (EG [66]), copper nanowires and tetradecanol (solid: 0.32 W/mK) (Cu [67]), aluminium nitride, silica and poly(ethylene glycol) (solid: 0.30 W/mK) (AlN/SiO₂ [68]), carbon nanotubes and beeswax (solid: 0.32 W/mK) (CNT [69]).

by a covalent-connected carrier matrix in these studies, but maintain their shape at higher temperatures and should, therefore, be comparable to the ss-PCMs in this work. Moreover, Yang *et al.* (BNNP) [65], Zheng *et al.* (Cu) [67] and Wang *et al.* (AlN/SiO₂) [68] have used the same transient plane source technique to measure the thermal conductivities in their studies as in this work.

The well covalent-connected silica matrix in ss-PCM BN0 enables a 37% higher thermal conductivity enhancement than fs-PCM AlN/SiO₂ with the same amount of immobilized PCM (84 wt%) and silica (10 wt%) [68] (Fig. 4.3). The highest thermal conductivity enhancements are obtained for the fs-PCMs thermally enhanced with boron nitride nanosheets (BNNS) [64] and nanoparticles (BNNP) [65], followed by the similarly structured additive expanded graphite [66], which is comparable to our ss-PCM series BN0315 and BN0320 due to a similar average particle size (3 μm) to the BN in sample BNNP (1 - 2 μm) and BNNS (10 - 15 μm). However, our ss-PCMs BN1207_20 and BN2503_20 with larger BN particle sizes have a 147 % and 187 % higher thermal conductivity enhancement than fs-PCM BNNP with the highest thermal conductivity enhancement (158 %) (Fig. 4.3). Therefore, large BN particles should be more efficient to increase the thermal conductivity of PCMs.

Additionally, we measured the temperature evolution of pure BS, BN0 and the thermally enhanced ss-PCMs BN4501 - BN0320 from 11 $^{\circ}\text{C}$ to 40 $^{\circ}\text{C}$ to analyse the heat transfer under real conditions (Table 4.2, Fig. 4.4). A comprehensive overview of the temperature evolution of all 24 ss-PCMs is given in the supplementary info (Table S4.1, Movies S4.1 - S4.4).

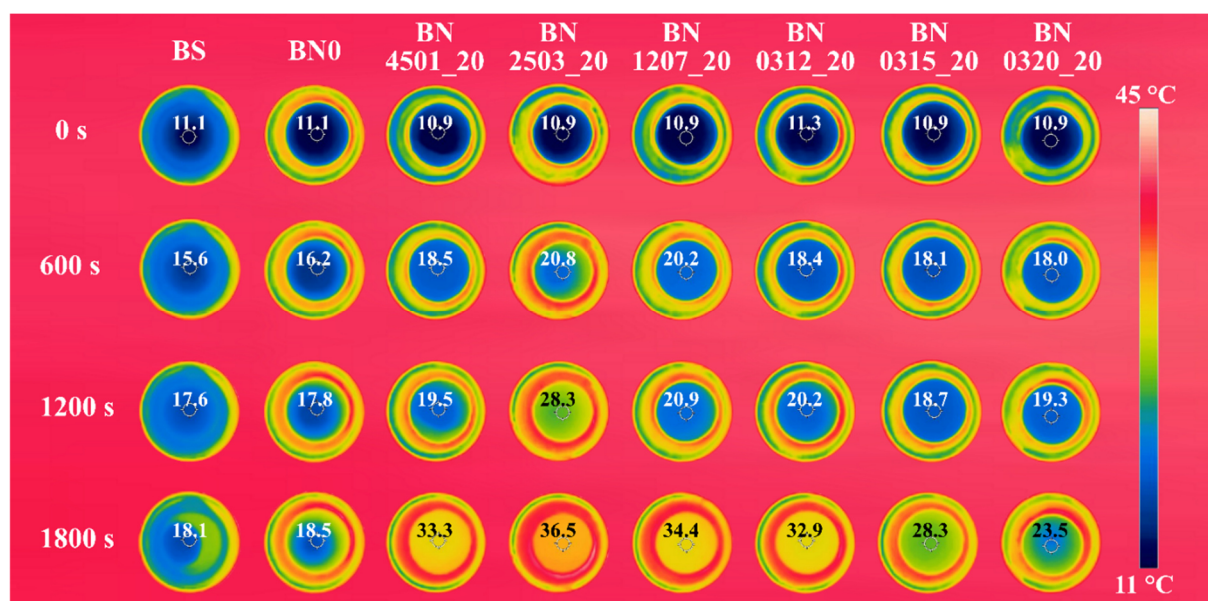


Fig. 4.4 Temperature evolution of pure BS and the ss-PCMs synthesized without BN (BN0) and with BN (BN4501_20 - BN0320_20). The samples were heated in a vessel in a water bath from 11 $^{\circ}\text{C}$ to 45 $^{\circ}\text{C}$.

Table 4.2 Temperature evolution of pure BS and thermally enhanced ss-PCMs from 11 °C to 33 °C in a vessel at 45 °C (water bath). The time to heat the solid from 11 °C to 17 °C, to perform the state transition from solid to liquid of the immobilized PCM (17 - 23 °C) and to heat the liquid from 23 °C to 33 °C were measured via thermal imaging.

Temp. (°C)	BS (s)	BN0 (s)	BN4501_20 (s)	BN2503_05 (s)	BN2503_10 (s)	BN2503_15 (s)	BN250_3_20 (s)	BN120_7_20 (s)	BN031_2_20 (s)	BN031_5_20 (s)	BN0320_20 (s)
11 - 17	1020	600	441	330	285	240	180	210	255	270	330
17 - 23	2730	2100	1485	1905	1650	1440	1110	1380	1455	1560	1755
23 - 33	3435	2760	1755	2220	2025	1800	1365	1650	1830	1905	2220

The sample with the highest thermal conductivity (BN2503_20, 0.62 W/mK (30 °C), 1.14 W/mK (10 °C), Fig. 4.2) heats 146 % and 89 % faster at 23 °C than the pure BS and BN0 (Table 4.2), respectively. After 1800 s in the water bath, sample BN2503_20 reached the highest temperature of 36.5 °C (Fig. 4.4). The sample BN0320_20 with a small average particle size of 3 µm needs 855 s longer to reach 33 °C than BN2503_20 with an average particle size of 25 µm (Table 4.2), suggesting a strong influence of the average particle size of BN on the heat transfer rate. With a decreasing specific surface area of BN from 20 m²/g to 12 m²/g (BN0312_20, BN0320_20), the heat transfer rate increased by 21 % (390 s), which is similar to the increase of the thermal conductivity (Fig. 4.2). The thermal image of pure BS shows incongruent melting after 1800 s (solid BS: blue, liquid BS: yellow, Fig. 4.4). Even after 3200 s and at approximately 30 °C, one part of the pure BS remains solid (Movie S4.4). However, the ss-PCMs BN0 and BN4501 - BN0320 show no incongruent melting, which represents a great improvement of BS as thermal energy storage unit in buildings, batteries, or in domestic hot water storage.

We analysed the thermal properties of our samples (Fig. 4.5, Table 4.3) via weighing of the dried samples and DSC/TG measurements. Moreover, we calculated the effective mass fraction $Ma(PCM)_{mass}$ and $Ma(PCM)_{DSC}$, and the immobilization efficiencies E_{mass} and E_{DSC} according to our previous study (all 24 ss-PCM samples are listed in Table S4.3) [34]. If higher amounts of BN are added to the reaction mixture, the latent heats of the ss-PCMs are decreased due to a lower mass fraction of pure PCM performing a phase change at the melting and freezing point in the ss-PCM. The effective mass fractions $Ma(PCM)_{mass}$ and $Ma(PCM)_{DSC}$ have approximately the same value as $Ma(PCM)_{max}$ and, thus, have values of 100% for PCM immobilization efficiencies E_{mass} and E_{DSC} (Table 4.3).

A PCM immobilization efficiency of 100 % is an indicator that all PCM used in the synthesis is immobilized in the silica pore structures of the thermally enhanced ss-PCMs (E_{mass}) and that 100% of the PCM amount in the ss-PCM is performing the state transition from liquid to solid and vice versa (E_{DSC}). Therefore, all synthesized ss-PCMs show no confinement effects of the

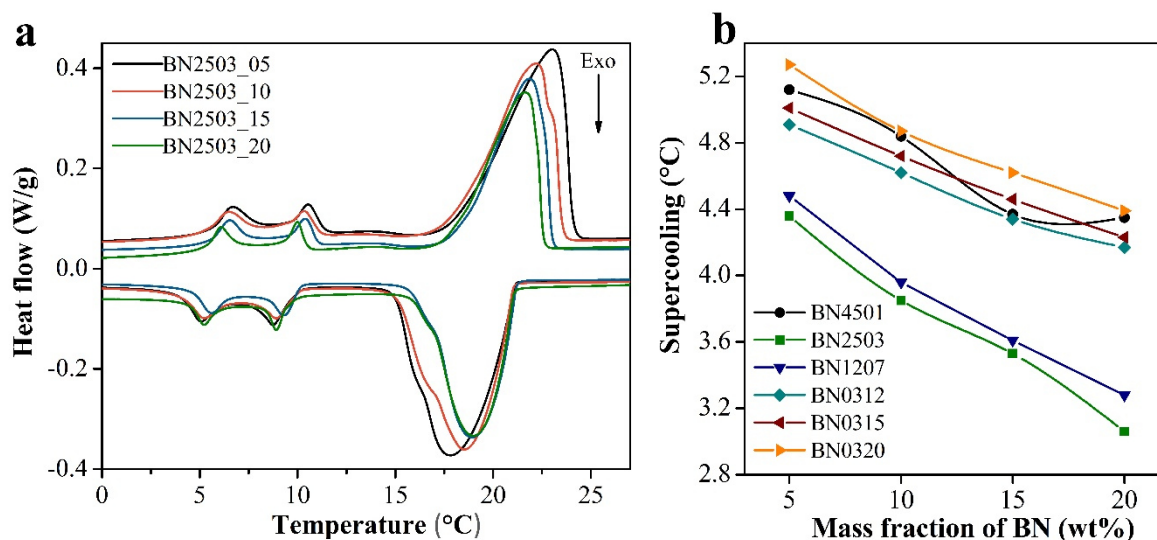


Fig. 4.5 (a) DSC curves of ss-PCMs BN2503 with different BN mass fraction (BN2503_05–BN2503_20), and (b) supercooling of samples BN4501 to BN0320 as a function of the BN mass fraction.

silica matrix or strong interaction effects with the BN structure, which would inhibit the state transition of the immobilized PCM and lower the latent heat of the ss-PCM.

The value of $Ma(PCM)_{mass}$ of the samples is approximately 1 % lower than $Ma(PCM)_{max}$ because of ss-PCM loss gelled at the reaction vessel surface. This effect is more pronounced at higher BN mass fractions and smaller particle sizes because of an increased viscosity of the reaction mixture. The difference between the melting and freezing points T_m and T_f is the supercooling of the sample T_s (Table 4.3). The supercooling of BN0 is 0.6 °C higher than the supercooling of BS, mainly due to the weakly attractive interactions between BS and silica. For samples BN2503 with the highest thermal conductivities, the supercooling of BN2503_10 (3.9 °C) to BN2503_20 (3.0 °C) is smaller than the supercooling of pure BS because of a higher thermal conductivity (Fig. 4.5a, Table 4.3). Additionally, the melting peak width of the BN2503 samples (22°C to 23°C) is decreased due to a higher thermal conductivity with a decreased BS mass fraction (Fig. 4.5a). With a decreasing specific surface area for samples BN0320 to BN0312, the average thermal conductivity is increased and the supercooling decreased (Fig. 4.5b). Larger BN particles (except for boron nitride particles larger than 25 μm (BN4501)) show higher thermal conductivities and, thus, lower supercooling effects. The supercooling is strongly influenced by the thermal conductivity of the sample and the particle size.

The average decomposition points of all ss-PCMs are decreased by an increased mass fraction of BN from 5 wt% to 20 wt%, because of a higher heat transfer rate due to BN during the TG measurement (Table 4.3, Publication 5 (Fig. 5.6 - 5.9)). In contrast, the effect of particle size and specific surface area of BN on the decomposition points of the ss-PCMs is so small that the temperature difference is within the TG detection limit.

Table 4.3 Thermal properties¹ of pure BS, BN0 and samples BN4501_10/20 - BN0320 BN_10/20 calculated via weighing, DSC and TG measurements.

Sample	ΔH_{BS} (J/g)	ΔH_{total} (J/g)	$U_{\Delta H}$ (%)	T_m (°C)	T_f (°C)	ΔT_s (°C)	$U_{\Delta T}$ (%)	m_{ss-PCM} (g)	$Ma(PCM)_{DSC}$ (wt%)	$Ma(PCM)_{mass}$ (wt%)	$Ma(PCM)_{max}$ (wt%)	E_{DSC} (%)	E_{mass} (%)	T_D (°C)
BS	102	126	0.87	21.7	17.6	4.1	0.51	-	100.0	100.0	100.0	100.0	100.0	218
BN0	85	105	2.82	20.0	15.3	4.7	1.28	13.26	83.3	82.6	83.0	100.4	99.5	216
BN4501_10	72	93	3.59	22.7	17.8	4.9	1.34	14.39	74.2	74.1	74.7	99.3	99.2	230
BN4501_20	65	84	4.94	22.5	18.1	4.4	1.19	15.99	66.9	65.2	66.4	100.8	99.1	226
BN2503_05	78	99	2.60	22.6	18.2	4.4	1.74	13.78	79.2	78.6	78.8	100.5	99.7	228
BN2503_10	73	93	3.32	22.3	18.4	3.9	1.96	14.59	74.1	74.4	74.7	99.3	99.7	226
BN2503_15	69	89	3.61	22.2	18.8	3.4	1.78	15.22	70.9	69.8	70.7	100.2	98.8	223
BN2503_20	65	83	2.89	22.0	19.0	3.0	1.45	15.99	66.3	65.2	66.4	99.9	99.1	220
BN1207_10	74	94	4.11	22.2	18.2	4.0	1.61	14.33	75.2	74.0	74.7	100.7	99.0	232
BN1207_20	64	83	2.17	21.9	18.6	3.3	1.36	15.93	66.5	65.0	66.4	100.0	98.0	221
BN0312_10	74	95	4.54	22.5	17.9	4.6	1.61	14.68	75.7	74.6	74.7	101.4	99.9	225
BN0312_20	64	83	5.95	22.4	18.3	4.1	2.65	15.85	66.2	64.9	66.4	99.6	97.7	219
BN0315_10	74	93	2.83	22.6	17.8	4.8	1.09	14.26	74.6	73.9	74.7	99.9	98.9	228
BN0315_20	69	83	3.68	22.8	18.2	4.6	1.72	15.50	66.0	64.1	66.4	99.4	96.5	225
BN0320_10	72	94	3.38	22.5	17.7	4.8	1.38	14.60	75.0	74.5	74.7	100.4	99.7	233
BN0320_20	68	84	3.30	22.5	18.0	4.4	1.32	15.74	67.4	64.6	66.4	101.5	97.3	228

1: Melting enthalpy of BS ΔH_{BS} , melting enthalpy of whole ss-PCM ΔH_{total} , relative uncertainty $U_{\Delta H}$ of ΔH_{total} , melting point of BS T_m , freezing point of BS T_f , supercooling ΔT_s , relative uncertainty $U_{\Delta T}$ of ΔT_s , mass of ss-PCM m_{ss-PCM} , mean value for effective mass fraction of PCM $Ma(PCM)_{DSC}$ and $Ma(PCM)_{mass}$, highest value for effective mass fraction of PCM $Ma(PCM)_{max}$, PCM immobilization efficiencies E_{DSC} and E_{mass} and decomposition point T_D of BS.

For long-term performance tests, the ss-PCMs containing 20 wt% BN (BN4501_20 to BN0320_20) were 1000-times cooled to 8 °C and heated to 60 °C to perform multiple melting and solidification cycles. The values of all latent heats before and after the long-term performance tests remain similar (within the standard variation of the DSC) and, thus, indicate a high longevity and durability of the ss-PCMs (Fig. S4.5).

In summary, ss-PCM sample BN2503_20 has the highest thermal conductivity (0.62 W/mK (30 °C), 1.14 W/mK (10 °C)) and the lowest supercooling effect (3 °C) in this work. In comparison to smaller BN particles (3 µm), BN of type HeBoFill 490 with a particle size of 25 µm and specific surface area of 3 m²/g increases the thermal conductivity of the ss-PCMs to a 2-times higher value and, thus, is best suited for the increase of the thermal conductivity of ss-PCMs. We expect that bigger BN particles should also increase the thermal conductivity of polymers to the highest extent, which were synthesized with *in situ* polymerization methods similar to sol-gel, such as the heat exchange polymers polyamide 66 in electronic devices [70,71] and poly(methyl methacrylate) in light emitting diodes [72].

3.4.6.2 Influence of BN on the mechanical properties of ss-PCMs

We found that larger BN particles increase the thermal conductivity of the ss-PCMs, whereas BN particles with a higher specific surface area (i.e. smaller BN particles) decrease the thermal conductivity of the ss-PCMs. To understand these trends, the interconnectivity and pore structure of the silica matrix in the ss-PCMs were analysed via mercury intrusion porosimetry (Hg), nitrogen adsorption (N₂), scanning electron microscopy (SEM) and three-dimensional (3D) high-resolution X-ray microscopy (XRM) (Fig. 4.6, 4.7, Fig. S4.6 - S4.11). To simplify, the mean macropore diameter/50% D_{total} is abbreviated as macropore diameter in the following discussion.

To compare the silica pores filled with PCM with the silica pores filled with air, the ss-PCM samples were all calcined at 600 °C for 6 h. All samples BN4501 - BN0320 show no nitrogen sorption, as it was also observed for the ss-PCMs without additional BN from our previous study [61]. Therefore, the silica matrix in our ss-PCMs should be completely filled with PCM. In contrast, macropores of samples BN4501 to BN0320 are detected via mercury intrusion with an average macropore volume of 0.11 cm³/g for all samples containing BN (Table S4.5). The constant, low volume of macropores detected is not influenced by the specific type of BN and neither by the amount of BN used in the synthesis, indicating a detection limitation of mercury intrusion for small pores due to the high pressure applied during the measurement.

Table 4.4 Textural properties^a of samples BN0, BN2503 and BN4501_10/20 - BN0320 BN_10/20 after calcination at 600 °C, named here BN0c and BN4501c - BN0320c.

Sample	$\Phi^{b,c}$ (%)	$V_{total}^{b,c}$ (cm ³ /g)	V_{macro}^b (cm ³ /g)	V_{meso}^c (cm ³ /g)	D_{macro}^b (nm)
BN0	95	7.80	6.98	0.82	1007
BN4501c_10	89	3.75	3.17	0.59	1384
BN4501c_20	84	2.31	2.01	0.30	757
BN2503c_05	92	5.45	4.82	0.64	1492
BN2503c_10	89	3.93	3.49	0.44	1222
BN2503c_15	88	3.47	3.15	0.33	1147
BN2503c_20	85	2.78	2.40	0.38	685
BN1207c_10	89	3.75	3.31	0.44	749
BN1207c_20	84	2.31	2.05	0.26	512
BN0312c_10	89	3.88	3.37	0.51	800
BN0312c_20	85	2.63	2.27	0.36	373
BN0315c_10	90	4.07	3.55	0.52	614
BN0315c_20	86	2.78	2.41	0.37	335
BN0320c_10	90	4.03	3.53	0.50	556
BN0320c_20	85	2.68	2.27	0.41	323

^a Porosity Φ , total pore volume V_{total} , macropore volume V_{macro} , mesopore volume V_{meso} and mean macropore diameter/50% D_{macro} of calcined ss-PCMs. ^b calculated via mercury intrusion. ^c calculated via nitrogen sorption.

Additionally, macropores cannot be seen in the SEM images of the samples BN4501 to BN0320 (Fig. 4.7 (A1 - D1)) and, thus, the whole silica structure in all ss-PCMs should be completely filled with PCM. The average meso- and macropore volumes of the calcined sample series BN4501c to BN0320c are similar for ss-PCMs with the same BN mass fraction, respectively. Therefore, the specific surface area and particle size of BN seem to have no effect on the total pore volume of calcined ss-PCMs, which have a uniform macropore/mesopore ratio of 87:13. With an increased BN mass fraction from 5 wt% to 20 wt%, the average total pore volume of the silica matrix is decreased from approximately 5.45 cm³/g for sample series BN4501c_05 - BN0320c_05 to 2.24 cm³/g for BN4501c_20 to BN0320c_20 (Table S4.4).

In contrast, the macropore diameter of the silica matrix in the ss-PCMs is strongly influenced by the particle size and the specific surface area of the BN used for the synthesis (Fig. 4.6). With an increasing particle size of BN from 3 μ m to 45 μ m, the macropore diameter of the silica structure of samples BN0320c_10 to BN4501c_10 is increased from an average value of 556 nm to 1384 nm, and from sample BN1207c_10 to BN4501c_10 from 749 nm to 1384 nm. The lower specific surface area of BN in BN0312c_10 results in a 44 % higher silica macropore diameter as compared to BN0320c_10 (Fig. 4.6 (b)). The same trend is obtained for the

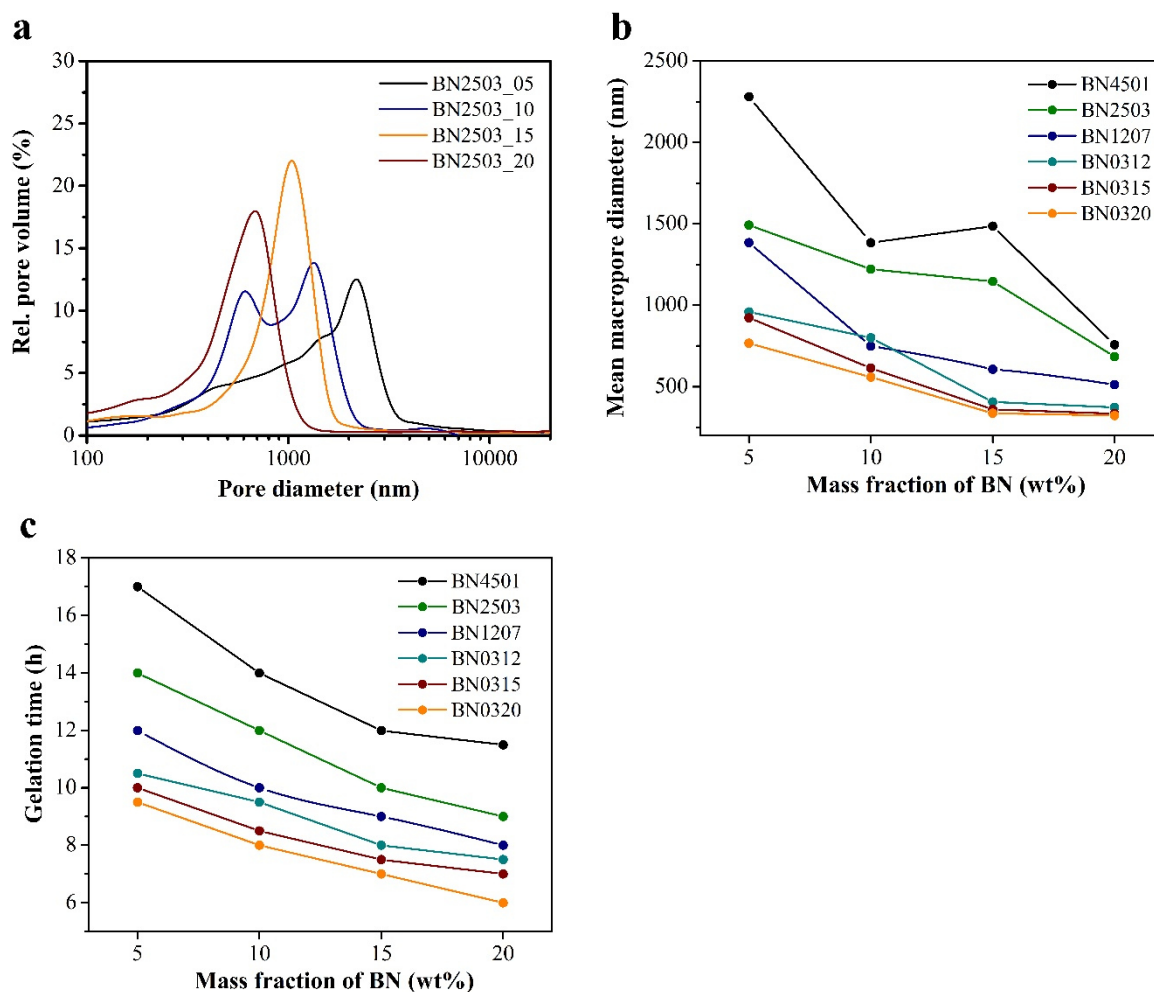


Fig. 4.6 Relative pore volume in dependence of the pore diameter of samples BN2503_05 to BN2503_20 (a), mean macropore diameter/50% of the calcined ss-PCMs as a function of the BN mass fraction (b) and gelation time of all ss-PCMs in dependence of the BN mass fraction (c). (a) and (b) was calculated via direct measuring of mercury intrusion.

samples synthesized with 5 wt%, 15 wt% and 20 wt% BN (Table S4.4). The reason for this trend should be the viscosity and the gelation times of the PCM/water-emulsion. A high viscosity of the reaction mixture should stabilize the PCM/water-emulsion from phase separation and accelerates the sol-gel process, resulting in a faster gelation process and shorter gelation times (Fig. 4.6 (c)). The fastest gelation process was obtained after 6 h for the synthesis of BN0320_20 (Fig. 4.6 (c)). Smaller particles with higher specific surface areas increase the viscosity of a reaction mixture to a higher extent than the particles with smaller specific surface areas and larger particle sizes [73–75]. Therefore, an increasing particle size and decreasing specific surface area of BN should increase the silica macropore diameter and, thus, lower the compressive strength of the ss-PCM. For this reason, ss-PCM BN0312_20 synthesized with HeBoFill 110 has the highest compressive strength (2.4 MPa, 10 °C) in this work (Fig. 4.6, Fig. 4.9).

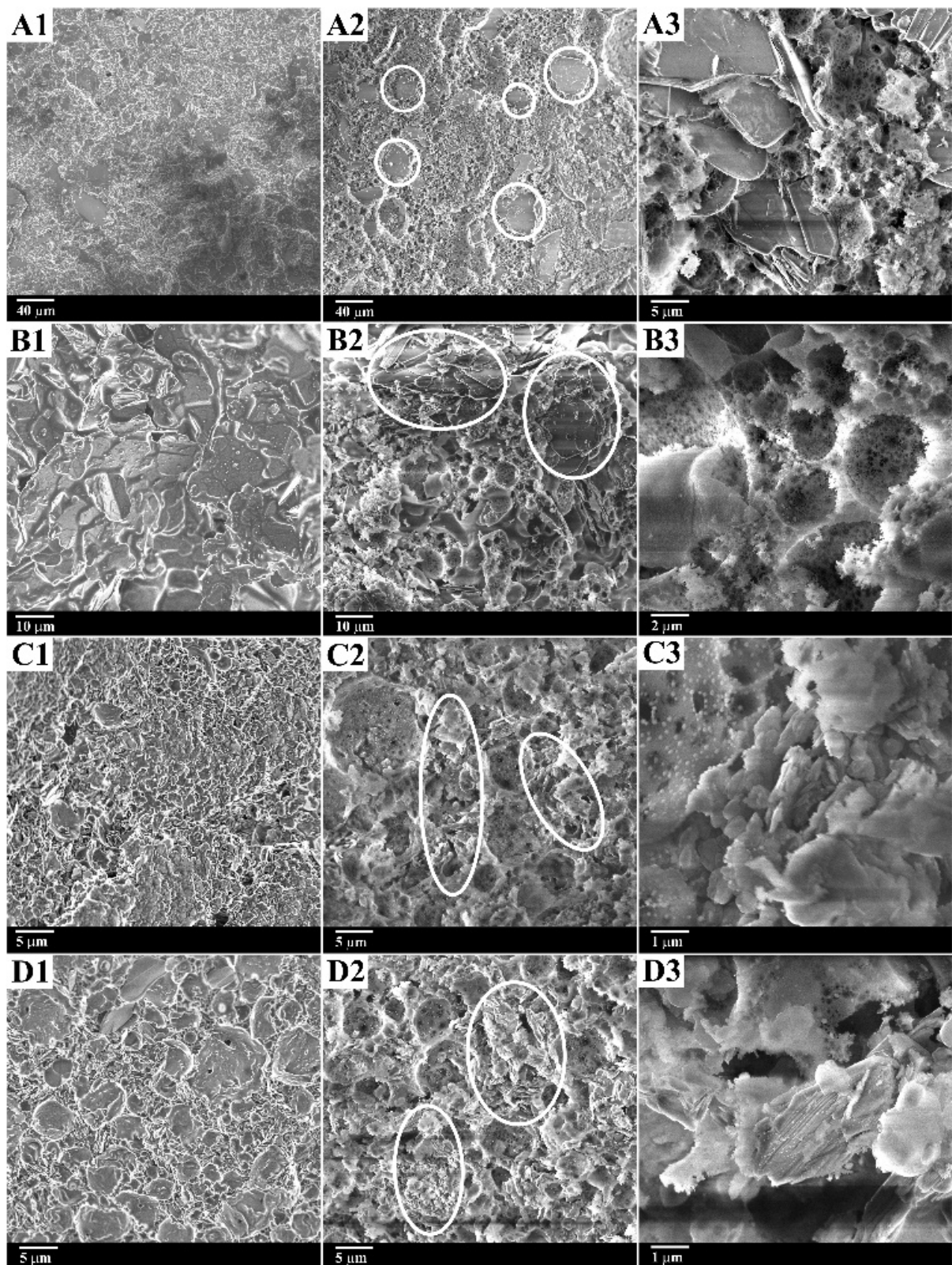


Fig. 4.7 SEM images of ss-PCM samples BN4501_20 (A), BN2503_20 (B), BN0312_20 (C) and BN0320_20 (D) dried at 100 °C (1) and calcined at 600 °C (2, 3). Boron nitride platelets are marked with a white cycle.

This value is 40 % higher than the compressive strength of sample BN2503_20 synthesized with HeBoFill 490 with the highest thermal conductivity.

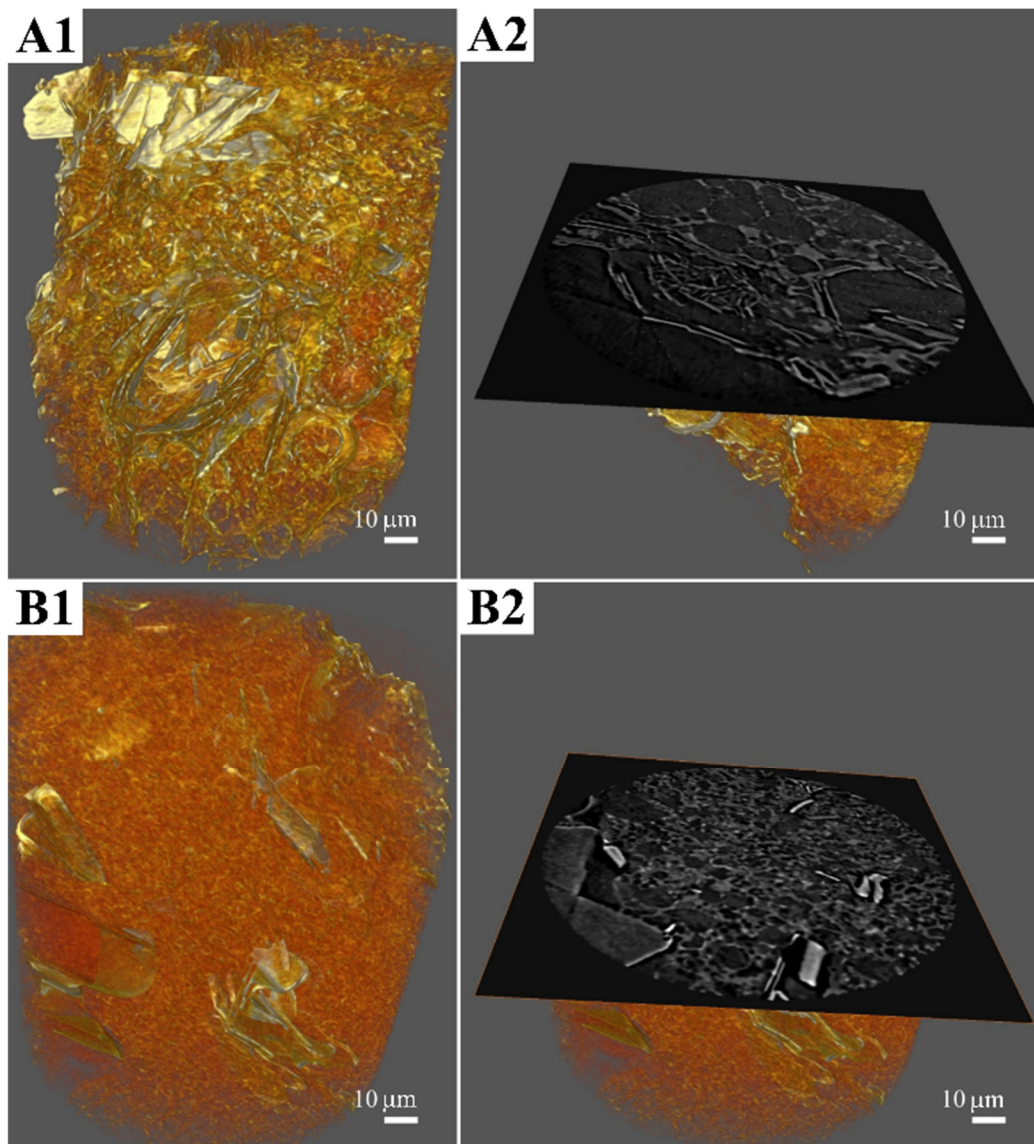


Fig. 4.8 The respective volumetric XRM representation of the samples BN4501_20 (A) and BN2503_20 (B). BN and silica structure are marked in silver.

Especially for walls, roof tops or floors the mechanical stability of ss-PCMs is more important than a high thermal conductivity. The BN of type HeBoFill 110 should, therefore, be preferred to HeBoFill 490 for the synthesis of mechanical stable ss-PCM boards for building applications in the future.

By an increased mass fraction of BN from 5 wt% to 20 wt%, the silica macropore diameter in all ss-PCMs is decreased because of a higher viscosity and a faster gelation process. However, by adding more BN to the synthesis mixture of ss-PCMs, the smaller macropore diameter does not lead to a linear increase of the compressive strength (Fig. 4.9).

The compressive strength of the ss-PCM depends on the mechanical stability of the silica matrix and the viscosity of the PCM. With a higher BN mass fraction, the silica structure should

loose interconnectivity and mechanical stability, whereas the PCM viscosity is increased (Fig. 4.7 - Fig. 4.9). From 5 wt% to 15 wt% BN, the increase of the compressive strength by an increased viscosity could be predominant. With a BN mass fraction above 15 wt%, the negative impact of the BN on the interconnectivity of the silica structure could be predominant, resulting in a non-linear increase of the compressive strength of the ss-PCMs containing 5 - 20 wt% BN (Fig. 4.9).

In comparison, the specific surface areas of BN in sample series BN0312 - BN0320 have a smaller impact on the silica structure of the ss-PCMs than the particle size of BN. For example, the average macropore diameter of samples BN0312c_05 to BN0312c_20 is only slightly higher (28 %) than the average macropore diameter of samples BN0320c_05 to BN0320c_20 (Table S4.4). The higher specific surface area of BN should lead to a stronger BN agglomeration, resulting in a more inhomogenous distribution of BN during gelation (Fig. 4.7 (C2- D2)). For this reason, the thermal conductivity and compressive strength should be higher for sample series BN0312 than for BN0320, which is indeed the case (Fig. 4.2, Fig. 4.9).

Despite the slightly higher BN agglomeration, the SEM images of the samples BN0312_20 to BN0320_20 (Fig. 4.7, Fig. S4.10 - S4.11) show well interconnected spherical silica structures similar to the silica structure in BN0 and FS4 from our previous study [61].

In contrast, the larger BN particles in samples BN4501c_20 to BN1207c_20 are more homogeneously distributed in the silica matrix as single platelets (Fig. 4.7 (A - B)). The respective volumetric representations of BN4501_20 to BN2503_20 (Fig. 4.8) enables us to

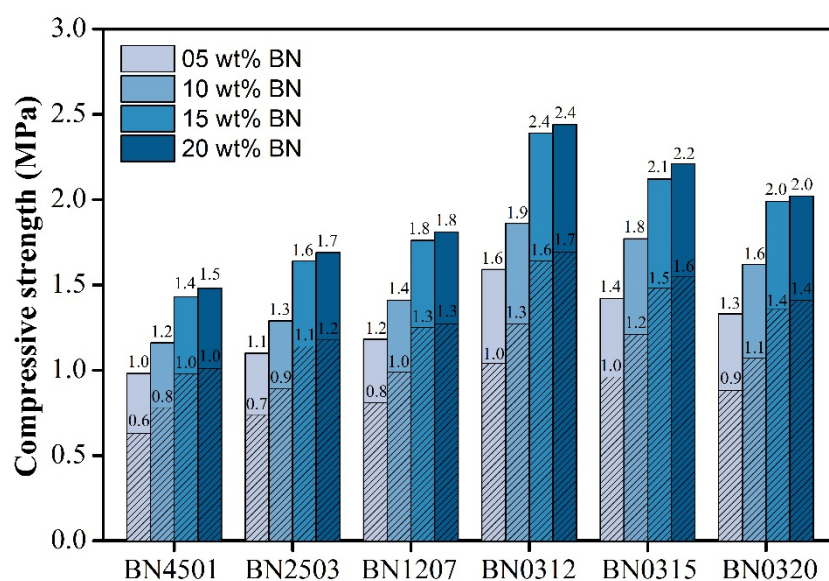


Fig. 4.9 Compressive strength of all ss-PCMs measured below the freezing point of BS at 10 °C (filled) and above the melting point of BS at 30 °C (dense)

observe BN platelets with different 3D orientations in the silica matrix. The different orientation of BN particles in the silica matrix is expected to lower the thermal conductivity and heat transfer of the ss-PCM and should, thus, be avoided in future studies.

From the SEM images with a higher resolution (Fig. 4.7 (A3, B3)), it can be seen that BN2503c_20 shows more spherical pores below 500 nm than BN4501c_20, resulting in a 72 nm smaller mean macropore diameter (Table 4.4). The presence of more broken silica structures in BN4501c_20 (Fig. 4.7) could be the reason for the lower mechanical stability and thermal conductivity of BN4501_20 in comparison to BN2503_20 (Fig. 4.2, Fig. 4.9). Therefore, the BN particles seem to have an upper limit of the particle size of above 25 μm for the synthesis of ss-PCMs with high compressive strength and thermal conductivity.

To analyse a possible BN exfoliation by magnetic stirring during synthesis [76,77], XRD studies of the calcined ss-PCMs were carried out (Table S4.6 - S4.7). In the XRD patterns (Fig. 4.10 (a), Fig. S4.12), the pure hexagonal BN particles BN4501 - BN0320 (lattice constants: $a=b=2.504$, $c=6.656$; lattice spacing: ~ 0.55 nm; JCPDS 45-0893) show four characteristic diffraction peaks at approximately 26.8° , 41.6° , 50.2° and 55.1° , which correspond to the (002), (100), (102) and (004) planes, respectively. All ss-PCM samples show the same diffraction peaks as the pure BN particles and differ in their absolute intensities (Fig. 4.10, Fig. S4.12). The diffraction peak at 26.6° of BN powder HeBoFill 490 is shifted by 0.3° to higher degrees after immobilization in the silica matrix of BN2503_20, pointing to a higher separation of BN during synthesis.

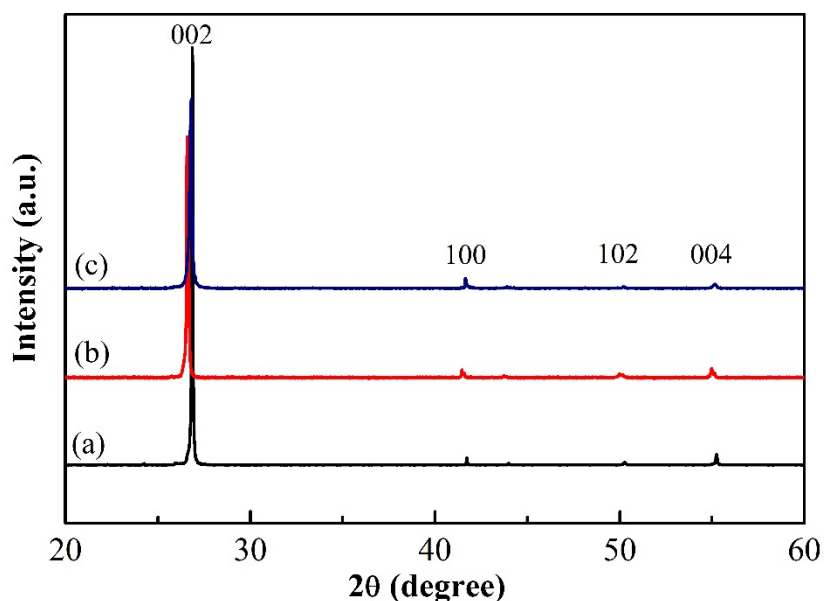


Fig. 4.10 XRD patterns of pure BN powder HeBoFill 490 (a) in comparison to BN in calcined ss-PCMs BN2503c_20 (b) and BN0312c_20 (c).

We used Eq. 4.2 and the diffraction peak with the highest intensity at 26.8° (002) to calculate the BN particle thickness L_c , before and after BN addition to the synthesis of the ss-PCMs (Fig. 4.11).

$$L_c = \frac{K \cdot \lambda}{\beta \cdot \cos\theta} \quad \text{Eq. (4.8)}$$

with K as the Scherrer constant, λ as the wavelength of CuK α radiation (1.54), β as full width at half maximum and θ as the scattering angle.

The 40 % to 25% smaller particle thickness of BN after ss-PCM synthesis suggests that the BN platelets are partially exfoliated to nanosheets during gelation, resulting in an increased contact area of the BN surface with the PCM (Fig. 4.11). The higher aspect ratio of exfoliated BN platelets could have two different effects on the ss-PCM properties. For sample series BN0312 to BN0320, the exfoliation of BN should enhance the effect of the specific surface area and could, thus, lower the thermal conductivity and mechanical stability by formation of more BN agglomerates.

In contrast, the ss-PCMs of sample series BN4501 to BN1207 with low specific surface areas show less BN agglomeration in the SEM images (Fig. 4.7 (A, B), Fig. S.4.10). For this reason, the effect of the increased contact area between PCM and BN could be higher in these samples than the effect of BN agglomeration during synthesis, resulting in higher thermal conductivities by BN exfoliation.

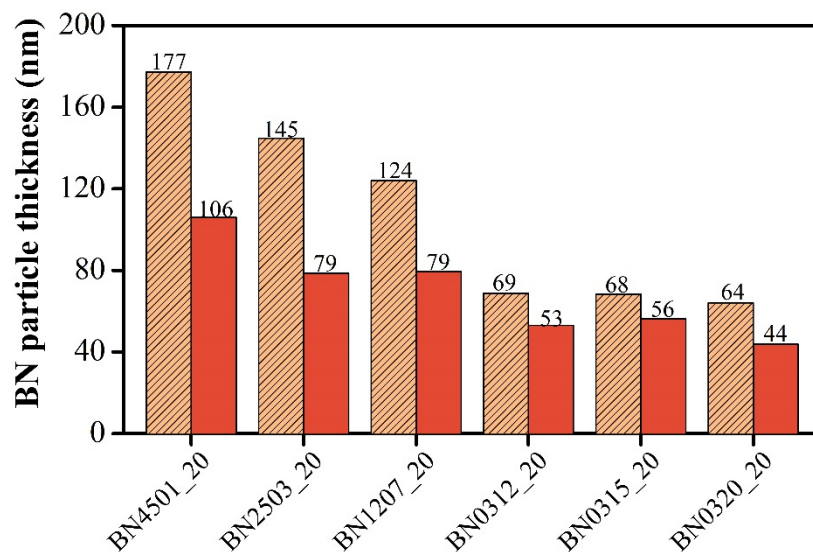


Fig. 4.11 Average BN particle thickness before (dense) and after (filled) BN addition to the synthesis of ss-PCMs BN4501_20 to BN0320_20.

3.4.7 Conclusions

In this work, we analysed the influence of the particle size and specific surface area of different BN particles on the chemical, mechanical and thermal properties of ss-PCMs synthesized via the sol-gel route. The BN particles used in the ss-PCM synthesis differ in their particle size from 3 μm to 45 μm , and in their specific surface area from 1 m^2/g to 20 m^2/g .

Large BN particles (25 μm) increase the thermal conductivity of the ss-PCM to the highest extent (1.14 W/mK at 10 $^{\circ}\text{C}$, 0.62 W/mK at 30 $^{\circ}\text{C}$) and decrease the supercooling of BS from approximately 5 $^{\circ}\text{C}$ to 3 $^{\circ}\text{C}$ due to reduced BN agglomeration and a slightly higher BN exfoliation ratio. However, large BN particles (25 μm) disturb the gelation of the silica polymer during the sol-gel process, resulting in more broken silica pores with two times higher macropore diameter (685 nm) and a 40 % lower compressive strength (1.7 MPa at 10 $^{\circ}\text{C}$, 1.2 MPa at 30 $^{\circ}\text{C}$) as compared to ss-PCMs synthesized with smaller BN particles (3 μm). Additionally, ss-PCMs monoliths containing BN particles larger than 25 μm were partially broken.

In contrast, a lower specific surface area of BN from 20 m^2/g to 12 m^2/g at the same particle size increases both the thermal conductivity and the compressive strength by approximately 90 % (0.89 W/mK at 10 $^{\circ}\text{C}$, 0.48 W/mK at 30 $^{\circ}\text{C}$) and 20 % (2.4 MPa at 10 $^{\circ}\text{C}$, 1.7 MPa at 30 $^{\circ}\text{C}$), respectively, because of a lower viscosity of the reaction mixture. A high viscosity of the reaction mixture hinders the separation of BN particles during stirring and, thus, increases the BN agglomeration, which is disadvantageous for the thermal conductivity, as well as for the mechanical stability of the resulting ss-PCM.

Large BN particles (25 μm) with low specific surface areas (3 m^2/g) are best suited for the increase of the thermal conductivity of ss-PCMs, whereas smaller BN particles (3 μm) with lower specific surface areas (12 m^2/g) increase the mechanical stability to a higher extent. However, a prevented agglomeration of smaller BN particles with higher specific surface areas could increase both the thermal conductivity and the mechanical stability of ss-PCMs in future studies, if the sol-gel synthesis is not disturbed, e.g. due to stirring via higher shear forces. The optimal BN particle size and specific surface area should, therefore, be chosen depending on the synthesis conditions of the thermally enhanced polymer, such as our ss-PCM, and the importance of the thermal conductivity in comparison to the mechanical stability.

3.4.8 CRediT authorship contribution statement

Felix Marske: Conceptualization, Methodology, Validation, Formal analysis, Investigation, Data curation, Writing – original draft, Visualization. **Titus Lindenberg:** Formal analysis, Resources. **Juliana Martins Souza e Silva:** Formal analysis, Resources, Writing – review & editing. **Ralf B. Wehrspohn:** Resources, Writing – review & editing. **A. Wouter Maijenburg:** Writing – review & editing, Resources. **Thomas Hahn:** Supervision, Project administration, Funding acquisition. **Dirk Enke:** Writing – review & editing, Supervision.

3.4.9 Declaration of Competing Interest

The authors declare that they have no known competing financial interests or personal relationships that could have appeared to influence the work reported in this paper.

3.4.10 Acknowledgements

The authors of this paper thank Mr. Eik Koslowski for XRD measurements, Mr. Alexey G. Krushelnitsky for ²⁹Si NMR measurements, Mr. Jaques Schmidt for ATR-IR measurements and Ms. Jenny Bienias for the mercury intrusion and nitrogen sorption measurements. Juliana Martins de Souza e Silva and Ralf B. Wehrspohn acknowledge the DFG for the granted project WE 4051/21-1. Additionally, Titus Lindenberg and A. Wouter Maijenburg acknowledge financial support from the BMBF (grant no. FKZ:03Z22HN11).

3.4.11 References

- [1] United Nations, Department of Economic and Social Affairs, Population Division (2019), World Population Prospects 2019, Online Edition., 2019, <https://population.un.org/wpp/Download/Probabilistic/Population/>.
- [2] A.K. Pandey, M.S. Hossain, V.V. Tyagi, N. Abd Rahim, J.A. Selvaraj, A. Sari, Novel approaches and recent developments on potential applications of phase change materials in solar energy, *Renewable and Sustainable Energy Reviews* 82 (2018) 281–323.
- [3] E.M. Shchukina, M. Graham, Z. Zheng, D.G. Shchukin, Nanoencapsulation of phase change materials for advanced thermal energy storage systems, *Chemical Society reviews* 47 (2018) 4156–4175.

-
- [4] P.K.S. Rathore, S.K. Shukla, Potential of macroencapsulated PCM for thermal energy storage in buildings: A comprehensive review, *Construction and Building Materials* 225 (2019) 723–744.
- [5] S. Rostami, M. Afrand, A. Shahsavari, M. Sheikholeslami, R. Kalbasi, S. Aghakhani, M.S. Shadloo, H.F. Oztop, A review of melting and freezing processes of PCM/nano-PCM and their application in energy storage, *Energy* 211 (2020) 118698.
- [6] J. Pereira da Cunha, P. Eames, Thermal energy storage for low and medium temperature applications using phase change materials – A review, *Applied Energy* 177 (2016) 227–238.
- [7] A. Sharma, V.V. Tyagi, C.R. Chen, D. Buddhi, Review on thermal energy storage with phase change materials and applications, *Renewable and Sustainable Energy Reviews* 13 (2009) 318–345.
- [8] M.C. Browne, B. Norton, S.J. McCormack, Phase change materials for photovoltaic thermal management, *Renewable and Sustainable Energy Reviews* 47 (2015) 762–782.
- [9] L. Cao, Di Su, Y. Tang, G. Fang, F. Tang, Properties evaluation and applications of thermal energy storage materials in buildings, *Renewable and Sustainable Energy Reviews* 48 (2015) 500–522.
- [10] A.A. Al-Abidi, S. Bin Mat, K. Sopian, M.Y. Sulaiman, A.T. Mohammed, CFD applications for latent heat thermal energy storage: A review, *Renewable and Sustainable Energy Reviews* 20 (2013) 353–363.
- [11] M.S. Naghavi, B.C. Ang, B. Rahmanian, S. Naghavi, S. Bazri, R. Mahmoodian, H. Metselaar, On-demand dynamic performance of a thermal battery in tankless domestic solar water heating in the tropical region, *Applied Thermal Engineering* 167 (2020) 114790.
- [12] J. Jaguemont, N. Omar, P. van den Bossche, J. Mierlo, Phase-change materials (PCM) for automotive applications: A review, *Applied Thermal Engineering* 132 (2018) 308–320.
- [13] J. Kim, J. Oh, H. Lee, Review on battery thermal management system for electric vehicles, *Applied Thermal Engineering* 149 (2019) 192–212.
- [14] R. Kizilel, A. Lateef, R. Sabbah, M.M. Farid, J.R. Selmán, S. Al-Hallaj, Passive control of temperature excursion and uniformity in high-energy Li-ion battery packs at high current and ambient temperature, *Journal of Power Sources* 183 (2008) 370–375.
- [15] C.-Y. Huang, H.-C. Sung, K.-L. Yen, Experimental Study of Photovoltaic/Thermal (PV/T) Hybrid System, *SGCE 2* (2013) 148–151.
- [16] M.R. Salem, M.M. Elsayed, A.A. Abd-Elaziz, K.M. Elshazly, Performance enhancement of the photovoltaic cells using Al₂O₃/PCM mixture and/or water cooling-techniques, *Renewable Energy* 138 (2019) 876–890.

-
- [17] T. Ma, Z. Li, J. Zhao, Photovoltaic panel integrated with phase change materials (PV-PCM): technology overview and materials selection, *Renewable and Sustainable Energy Reviews* 116 (2019) 109406.
- [18] A.H. Al-Waeli, K. Sopian, M.T. Chaichan, H.A. Kazem, A. Ibrahim, S. Mat, M.H. Ruslan, Evaluation of the nanofluid and nano-PCM based photovoltaic thermal (PVT) system: An experimental study, *Energy Conversion and Management* 151 (2017) 693–708.
- [19] Y. Zhu, B. Wang, Q. Zhang, H. Wang, J. Zhu, Y. Liu, Y. Zhang, X. Sun, X. Zhang, S. Yun, H. Jiang, F. Gao, L. Kang, Paraffin wax–Cs_{0.33}WO₃ composite windows with excellent near infrared shielding and thermal energy storage abilities, *Chem. Pap.* 73 (2019) 1677–1684.
- [20] D. Li, Y. Zheng, Z. Li, H. Qi, Optical properties of a liquid paraffin-filled double glazing unit, *Energy and Buildings* 108 (2015) 381–386.
- [21] D. Li, T. Ma, C. Liu, Y. Zheng, Z. Wang, X. Liu, Thermal performance of a PCM-filled double glazing unit with different optical properties of phase change material, *Energy and Buildings* 119 (2016) 143–152.
- [22] R. Yang, D. Li, S.L. Salazar, Z. Rao, M. Arıcı, W. Wei, Photothermal properties and photothermal conversion performance of nano-enhanced paraffin as a phase change thermal energy storage material, *Solar Energy Materials and Solar Cells* 219 (2021) 110792.
- [23] R. Baby, C. Balaji, Thermal optimization of PCM based pin fin heat sinks: An experimental study, *Applied Thermal Engineering* 54 (2013) 65–77.
- [24] V. Shatikian, G. Ziskind, R. Letan, Numerical investigation of a PCM-based heat sink with internal fins, *International Journal of Heat and Mass Transfer* 48 (2005) 3689–3706.
- [25] S. Mat, A.A. Al-Abidi, K. Sopian, M.Y. Sulaiman, A.T. Mohammad, Enhance heat transfer for PCM melting in triplex tube with internal–external fins, *Energy Conversion and Management* 74 (2013) 223–236.
- [26] U. Stritih, An experimental study of enhanced heat transfer in rectangular PCM thermal storage, *International Journal of Heat and Mass Transfer* 47 (2004) 2841–2847.
- [27] J.M. Mahdi, E.C. Nsofor, Solidification enhancement of PCM in a triplex-tube thermal energy storage system with nanoparticles and fins, *Applied Energy* 211 (2018) 975–986.
- [28] Q. Ren, F. Meng, P. Guo, A comparative study of PCM melting process in a heat pipe-assisted LHTES unit enhanced with nanoparticles and metal foams by immersed boundary-lattice Boltzmann method at pore-scale, *International Journal of Heat and Mass Transfer* 121 (2018) 1214–1228.

-
- [29] M. Sheikholeslami, O. Mahian, Enhancement of PCM solidification using inorganic nanoparticles and an external magnetic field with application in energy storage systems, *Journal of Cleaner Production* 215 (2019) 963–977.
- [30] M. Liu, Y. Ma, H. Wu, R.Y. Wang, Metal matrix-metal nanoparticle composites with tunable melting temperature and high thermal conductivity for phase-change thermal storage, *ACS nano* 9 (2015) 1341–1351.
- [31] S.-G. Jeong, J.-H. Lee, J. Seo, S. Kim, Thermal performance evaluation of Bio-based shape stabilized PCM with boron nitride for energy saving, *International Journal of Heat and Mass Transfer* 71 (2014) 245–250.
- [32] M. Li, Q. Guo, S. Nutt, Carbon nanotube/paraffin/montmorillonite composite phase change material for thermal energy storage, *Solar Energy* 146 (2017) 1–7.
- [33] D. Zou, X. Ma, X. Liu, P. Zheng, Y. Hu, Thermal performance enhancement of composite phase change materials (PCM) using graphene and carbon nanotubes as additives for the potential application in lithium-ion power battery, *International Journal of Heat and Mass Transfer* 120 (2018) 33–41.
- [34] Z. Zhang, N. Zhang, J. Peng, X. Fang, X. Gao, Y. Fang, Preparation and thermal energy storage properties of paraffin/expanded graphite composite phase change material, *Applied Energy* 91 (2012) 426–431.
- [35] M. Esapour, A. Hamzehnezhad, A.A. Rabienataj Darzi, M. Jourabian, Melting and solidification of PCM embedded in porous metal foam in horizontal multi-tube heat storage system, *Energy Conversion and Management* 171 (2018) 398–410.
- [36] P.T. Sardari, R. Babaei-Mahani, D. Giddings, S. Yasserli, M.A. Moghimi, H. Bahai, Energy recovery from domestic radiators using a compact composite metal Foam/PCM latent heat storage, *Journal of Cleaner Production* 257 (2020) 120504.
- [37] M. Iasiello, M. Mameli, S. Filippeschi, N. Bianco, Metal foam/PCM melting evolution analysis: Orientation and morphology effects, *Applied Thermal Engineering* 187 (2021) 116572.
- [38] M. Iasiello, M. Mameli, S. Filippeschi, N. Bianco, Simulations of paraffine melting inside metal foams at different gravity levels with preliminary experimental validation, *J. Phys.: Conf. Ser.* 1599 (2020) 12008.
- [39] L.J. Gibson, M.F. Ashby, *Cellular solids: Structure and properties*, 2nd ed., Cambridge Univ. Press, Cambridge, 2010.
- [40] S. Mancin, A. Diani, L. Doretto, K. Hooman, L. Rossetto, Experimental analysis of phase change phenomenon of paraffin waxes embedded in copper foams, *International Journal of Thermal Sciences* 90 (2015) 79–89.

-
- [41] Deepika, L.H. Li, A.M. Glushenkov, S.K. Hait, P. Hodgson, Y. Chen, High-efficient production of boron nitride nanosheets via an optimized ball milling process for lubrication in oil, *Scientific reports* 4 (2014) 7288.
- [42] X. Fang, L.-W. Fan, Q. Ding, X.-L. Yao, Y.-Y. Wu, J.-F. Hou, X. Wang, Z.-T. Yu, G.-H. Cheng, Y.-C. Hu, Thermal energy storage performance of paraffin-based composite phase change materials filled with hexagonal boron nitride nanosheets, *Energy Conversion and Management* 80 (2014) 103–109.
- [43] L. Liu, Di Su, Y. Tang, G. Fang, Thermal conductivity enhancement of phase change materials for thermal energy storage: A review, *Renewable and Sustainable Energy Reviews* 62 (2016) 305–317.
- [44] Q. Weng, X. Wang, X. Wang, Y. Bando, D. Golberg, Functionalized hexagonal boron nitride nanomaterials: Emerging properties and applications, *Chemical Society reviews* 45 (2016) 3989–4012.
- [45] L. Lindsay, D.A. Broido, Enhanced thermal conductivity and isotope effect in single-layer hexagonal boron nitride, *Phys. Rev. B* 84 (2011).
- [46] Y. Zeng, L.-W. Fan, Y.-Q. Xiao, Z.-T. Yu, K.-F. Cen, An experimental investigation of melting of nanoparticle-enhanced phase change materials (NePCMs) in a bottom-heated vertical cylindrical cavity, *International Journal of Heat and Mass Transfer* 66 (2013) 111–117.
- [47] L.-W. Fan, X. Fang, X. Wang, Y. Zeng, Y.-Q. Xiao, Z.-T. Yu, X. Xu, Y.-C. Hu, K.-F. Cen, Effects of various carbon nanofillers on the thermal conductivity and energy storage properties of paraffin-based nanocomposite phase change materials, *Applied Energy* 110 (2013) 163–172.
- [48] R.J. Warzoha, R.M. Weigand, A.S. Fleischer, Temperature-dependent thermal properties of a paraffin phase change material embedded with herringbone style graphite nanofibers, *Applied Energy* 137 (2015) 716–725.
- [49] R.D. Weinstein, T.C. Kopec, A.S. Fleischer, E. D'Addio, C.A. Bessel, The Experimental Exploration of Embedding Phase Change Materials With Graphite Nanofibers for the Thermal Management of Electronics, *J. Heat Transfer* 130 (2008) 42405.
- [50] J.M. Khodadadi, L. Fan, H. Babaei, Thermal conductivity enhancement of nanostructure-based colloidal suspensions utilized as phase change materials for thermal energy storage: A review, *Renewable and Sustainable Energy Reviews* 24 (2013) 418–444.
- [51] R.M. Saeed, J.P. Schlegel, C. Castano, R. Sawafta, Preparation and enhanced thermal performance of novel (solid to gel) form-stable eutectic PCM modified by nano-graphene platelets, *Journal of Energy Storage* 15 (2018) 91–102.

- [52] J. Yang, P. Yu, L.-S. Tang, R.-Y. Bao, Z.-Y. Liu, M.-B. Yang, W. Yang, Hierarchically interconnected porous scaffolds for phase change materials with improved thermal conductivity and efficient solar-to-electric energy conversion, *Nanoscale* 9 (2017) 17704–17709.
- [53] Z. Huang, Z. Luo, X. Gao, X. Fang, Y. Fang, Z. Zhang, Preparation and thermal property analysis of Wood's alloy/expanded graphite composite as highly conductive form-stable phase change material for electronic thermal management, *Applied Thermal Engineering* 122 (2017) 322–329.
- [54] X. Huang, G. Alva, L. Liu, G. Fang, Preparation, characterization and thermal properties of fatty acid eutectics/bentonite/expanded graphite composites as novel form-stable thermal energy storage materials, *Solar Energy Materials and Solar Cells* 166 (2017) 157–166.
- [55] G. Jiang, J. Huang, Y. Fu, M. Cao, M. Liu, Thermal optimization of composite phase change material/expanded graphite for Li-ion battery thermal management, *Applied Thermal Engineering* 108 (2016) 1119–1125.
- [56] M. Ren, Y. Liu, X. Gao, Incorporation of phase change material and carbon nanofibers into lightweight aggregate concrete for thermal energy regulation in buildings, *Energy* 197 (2020) 117262.
- [57] Q. Huang, X. Li, G. Zhang, J. Deng, C. Wang, Thermal management of Lithium-ion battery pack through the application of flexible form-stable composite phase change materials, *Applied Thermal Engineering* 183 (2021) 116151.
- [58] U.B. Shahid, A. Abdala, A critical review of phase change material composite performance through Figure-of-Merit analysis: Graphene vs Boron Nitride, *Energy Storage Materials* 34 (2021) 365–387.
- [59] J. Yang, L.-S. Tang, R.-Y. Bao, L. Bai, Z.-Y. Liu, W. Yang, B.-H. Xie, M.-B. Yang, An ice-templated assembly strategy to construct graphene oxide/boron nitride hybrid porous scaffolds in phase change materials with enhanced thermal conductivity and shape stability for light-thermal-electric energy conversion, *J. Mater. Chem. A* 4 (2016) 18841–18851.
- [60] W. Han, C. Ge, R. Zhang, Z. Ma, L. Wang, X. Zhang, Boron nitride foam as a polymer alternative in packaging phase change materials: Synthesis, thermal properties and shape stability, *Applied Energy* 238 (2019) 942–951.
- [61] F. Marske, J. Martins de Souza e Silva, R.B. Wehrspohn, T. Hahn, D. Enke, Synthesis of monolithic shape-stabilized phase change materials with high mechanical stability via a porogen-assisted *in situ* sol-gel process, *RSC Adv.* 10 (2020) 3072–3083.

- [62] Z.A. Qureshi, H.M. Ali, S. Khushnood, Recent advances on thermal conductivity enhancement of phase change materials for energy storage system: A review, *International Journal of Heat and Mass Transfer* 127 (2018) 838–856.
- [63] A. Nasiri, M. Shariaty-Niasar, A.M. Rashidi, R. Khodafarin, Effect of CNT structures on thermal conductivity and stability of nanofluid, *International Journal of Heat and Mass Transfer* 55 (2012) 1529–1535.
- [64] H.-B. Cho, Y. Tokoi, S. Tanaka, H. Suematsu, T. Suzuki, W. Jiang, K. Niihara, T. Nakayama, Modification of BN nanosheets and their thermal conducting properties in nanocomposite film with polysiloxane according to the orientation of BN, *Composites Science and Technology* 71 (2011) 1046–1052.
- [65] J. Yang, L.-S. Tang, R.-Y. Bao, L. Bai, Z.-Y. Liu, W. Yang, B.-H. Xie, M.-B. Yang, Largely enhanced thermal conductivity of poly (ethylene glycol)/boron nitride composite phase change materials for solar-thermal-electric energy conversion and storage with very low content of graphene nanoplatelets, *Chemical Engineering Journal* 315 (2017) 481–490.
- [66] A. Sarı, A. Karaipekli, Preparation, thermal properties and thermal reliability of palmitic acid/expanded graphite composite as form-stable PCM for thermal energy storage, *Solar Energy Materials and Solar Cells* 93 (2009) 571–576.
- [67] J.-L. Zeng, F.-R. Zhu, S.-B. Yu, L. Zhu, Z. Cao, L.-X. Sun, G.-R. Deng, W.-P. Yan, L. Zhang, Effects of copper nanowires on the properties of an organic phase change material, *Solar Energy Materials and Solar Cells* 105 (2012) 174–178.
- [68] W. Wang, X. Yang, Y. Fang, J. Ding, J. Yan, Enhanced thermal conductivity and thermal performance of form-stable composite phase change materials by using β -Aluminum nitride, *Applied Energy* 86 (2009) 1196–1200.
- [69] N. Putra, S. Rawi, M. Amin, E. Kusriani, E.A. Kosasih, T.M. Indra Mahlia, Preparation of beeswax/multi-walled carbon nanotubes as novel shape-stable nanocomposite phase-change material for thermal energy storage, *Journal of Energy Storage* 21 (2019) 32–39.
- [70] X. Fu, C. Yao, G. Yang, Recent advances in graphene/polyamide 6 composites: A review, *RSC Adv.* 5 (2015) 61688–61702.
- [71] S. Zhou, L. Yu, X. Song, J. Chang, H. Zou, M. Liang, Preparation of highly thermally conducting polyamide 6/graphite composites via low-temperature *in situ* expansion, *J. Appl. Polym. Sci.* 131 (2014) n/a-n/a.
- [72] H. Oh, J. Kim, Fabrication of polymethyl methacrylate composites with silanized boron nitride by in-situ polymerization for high thermal conductivity, *Composites Science and Technology* 172 (2019) 153–162.

-
- [73] H.D. Koca, S. Doganay, A. Turgut, I.H. Tavman, R. Saidur, I.M. Mahbubul, Effect of particle size on the viscosity of nanofluids: A review, *Renewable and Sustainable Energy Reviews* 82 (2018) 1664–1674.
- [74] A. Sergis, Y. Hardalupas, Anomalous heat transfer modes of nanofluids: A review based on statistical analysis, *Nanoscale research letters* 6 (2011) 391.
- [75] E.V. Timofeeva, J.L. Routbort, D. Singh, Particle shape effects on thermophysical properties of alumina nanofluids, *Journal of Applied Physics* 106 (2009) 14304.
- [76] W. Luo, Y. Wang, E. Hitz, Y. Lin, B. Yang, L. Hu, Solution Processed Boron Nitride Nanosheets: Synthesis, Assemblies and Emerging Applications, *Adv. Funct. Mater.* 27 (2017) 1701450.
- [77] Y. Wen, Y. Xue, X. Li, H. Pei, X. Zhou, Y. Feng, Y. Ye, X. Xie, Y.-W. Mai, In-situ shear exfoliation and thermal conductivity of SBS/Graphite nanoplatelet nanocomposites, *Composites Part B: Engineering* 197 (2020) 108172.

3.4.12 Supporting Information

Additional Figures, Tables and Descriptions:

- Additional Figures for Chapter 3.4.5.: Fig. S4.1 to S4.3
- Additional Figures & Tables for Chapter 3.4.6.1: Fig. S4.4 to S4.5, Table S4.1 to S4.3
- Additional Figures & Tables for Chapter 3.4.6.2: Fig. S4.6 to S4.12, Table S4.4 to S4.7
- Captions for Movie S4.1 to S4.4

Other Supplementary Materials for this manuscript include:

- Movie S4.1 to S4.4

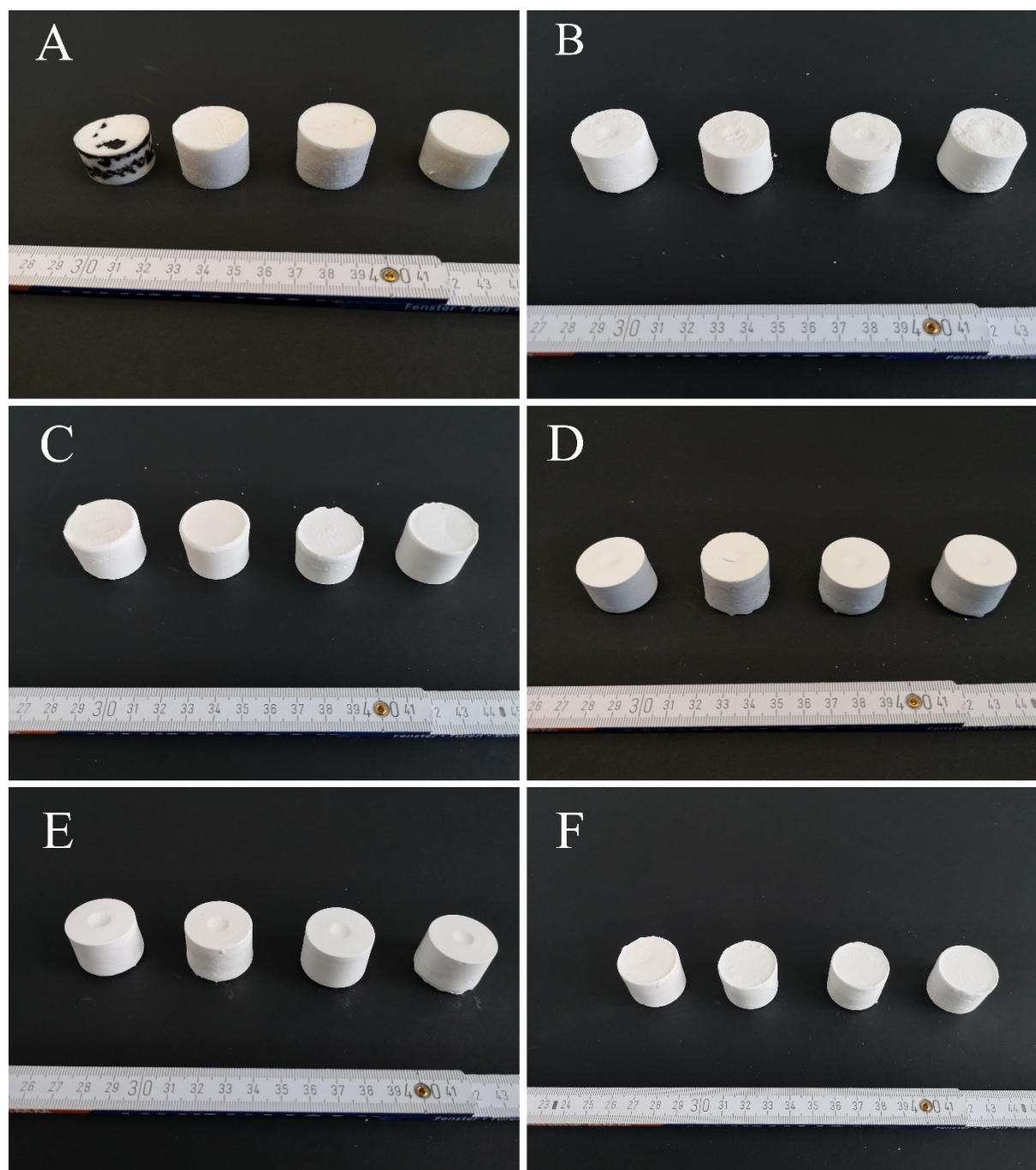


Fig. S.4.1 Pictures of four ss-PCM monoliths of each sample BN4501_20 (A), BN2503_20 (B), BN1207_20 (C), BN0312_20 (D), BN0315_20 (E) and BN0320_20 (F). Samples BN4501_20 are the only ss-PCMs containing 20 wt% BN that are partially cracked.



Fig. S4.2 Pictures of the construction of the thermal imaging experiment. The sample was cooled to 11 °C and put in a metallic vessel. The sample inside the metallic vessel was put in a water bath at 45 °C. The temperature of the sample was tracked via a thermal imaging camera every 15 s. Video files about the temperature evolution in the ss-PCMs containing 5 wt%, 10 wt%, 15 wt% and 20 wt% hBN are marked as Movie S4.1 - S4.4.

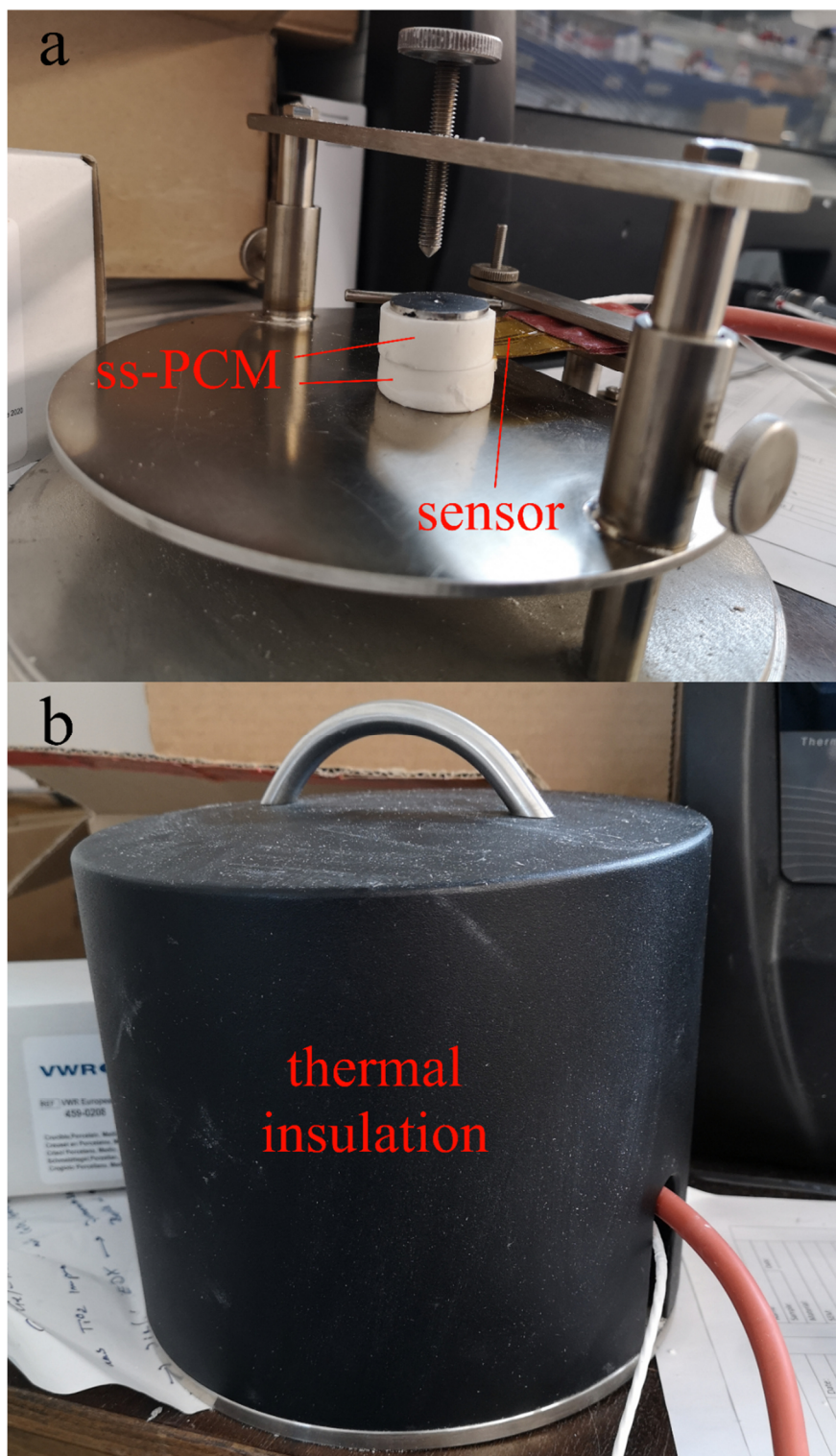


Fig. S4.3 Experimental setup for the thermal conductivity measurements of the ss-PCM samples. The samples were sawed in the middle in two halves. The sensor (yellow) for heating and detecting was placed between the two halves (sandwich-mode) (a) and a metallic cap was put on top of the setup for the thermal insulation during measurements (b). The measurements were performed at 30 °C and at 10 °C to calculate the thermal conductivity of ss-PCMs above the melting point and below the freezing point of the immobilized PCM inside the ss-PCM, respectively.

Table S4.1 Temperature evolution of pure BS and thermally enhanced ss-PCMs from 11 °C to 33 °C in a vessel placed at 45 °C (water bath). The time to heat the solid from 11 °C to 17 °C, to perform the state transition from solid to liquid of the immobilized PCM (17 - 23 °C) and to heat the liquid from 23 °C to 33 °C was measured via thermal imaging technique. Experimental details are shown in Fig. S4.3.

Sample\Time	Heated from 11 °C to 17 °C (s)	Heated from 17 °C to 23 °C (s)	Heated from 23 °C to 33 °C (s)
BS	1020	2730	3435
BN0	600	2100	2760
BN4501_05	495	2025	2475
BN4501_10	441	1800	2130
BN4501_15	330	1620	2025
BN4501_20	315	1485	1755
BN2503_05	330	1905	2220
BN2503_10	285	1650	2025
BN2503_15	240	1440	1800
BN2503_20	180	1110	1365
BN1207_05	345	1920	2295
BN1207_10	300	1695	2010
BN1207_15	240	1455	1725
BN1207_20	210	1380	1650
BN0312_05	405	2100	2625
BN0312_10	345	1875	2400
BN0312_15	300	1650	2025
BN0312_20	255	1455	1830
BN0315_05	405	2145	2640
BN0315_10	360	1890	2190
BN0315_15	315	1545	1905
BN0315_20	270	1655	1860
BN0320_05	510	2220	2700
BN0320_10	360	1920	2325
BN0320_15	330	1755	2220
BN0320_20	330	1725	2055

Table S4.2 The thermal conductivity and the relative enhancement K of the thermal conductivity of ss-PCM samples BN4501, BN2503, BN1207, BN0312, BN0315 and BN0320 and the corresponding uncertainty. The relative thermal enhancement K was calculated by Eq. 4.1 and is referred to the thermal conductivity λ of sample BN0 synthesized without BN addition.

Sample	Thermal conductivity λ_l at 30 °C (W/mK)	Uncertainty of λ_l (%)	Relative enhancement K at 30 °C (%)	Thermal conductivity λ_s at 10 °C (W/mK)	Uncertainty of λ_s (%)	Relative enhancement K at 10 °C (%)
BS	0.117	0.32	-	0.220	0.61	-
BN0	0.215	0.21	0	0.363	1.14	0
BN4501_05	0.244	1.33	25	0.438	0.55	34
BN4501_10	0.296	1.21	69	0.523	0.89	73
BN4501_15	0.369	0.89	132	0.661	0.74	135
BN4501_20	0.459	0.57	209	0.809	1.03	203
BN2503_05	0.278	0.93	54	0.534	1.88	78
BN2503_10	0.359	0.45	123	0.617	0.32	115
BN2503_15	0.466	0.32	215	0.883	0.22	236
BN2503_20	0.619	0.30	345	1.140	0.93	353
BN1207_05	0.247	0.67	27	0.419	0.95	25
BN1207_10	0.316	1.22	86	0.561	1.18	90
BN1207_15	0.432	1.62	185	0.819	1.75	207
BN1207_20	0.572	0.48	305	1.052	0.63	313
BN0312_05	0.237	0.22	19	0.430	0.84	30
BN0312_10	0.292	0.67	66	0.534	0.37	78
BN0312_15	0.366	0.62	129	0.731	0.43	167
BN0312_20	0.475	0.74	222	0.890	0.48	240
BN0315_05	0.226	1.18	9	0.408	0.41	20
BN0315_10	0.287	0.39	62	0.503	1.01	64
BN0315_15	0.340	0.84	107	0.617	0.79	115
BN0315_20	0.421	0.59	176	0.738	1.09	170
BN0320_05	0.218	0.46	3	0.399	1.59	16
BN0320_10	0.261	0.81	39	0.445	0.88	37
BN0320_15	0.314	0.99	85	0.575	1.91	96
BN0320_20	0.368	1.29	131	0.672	2.24	140

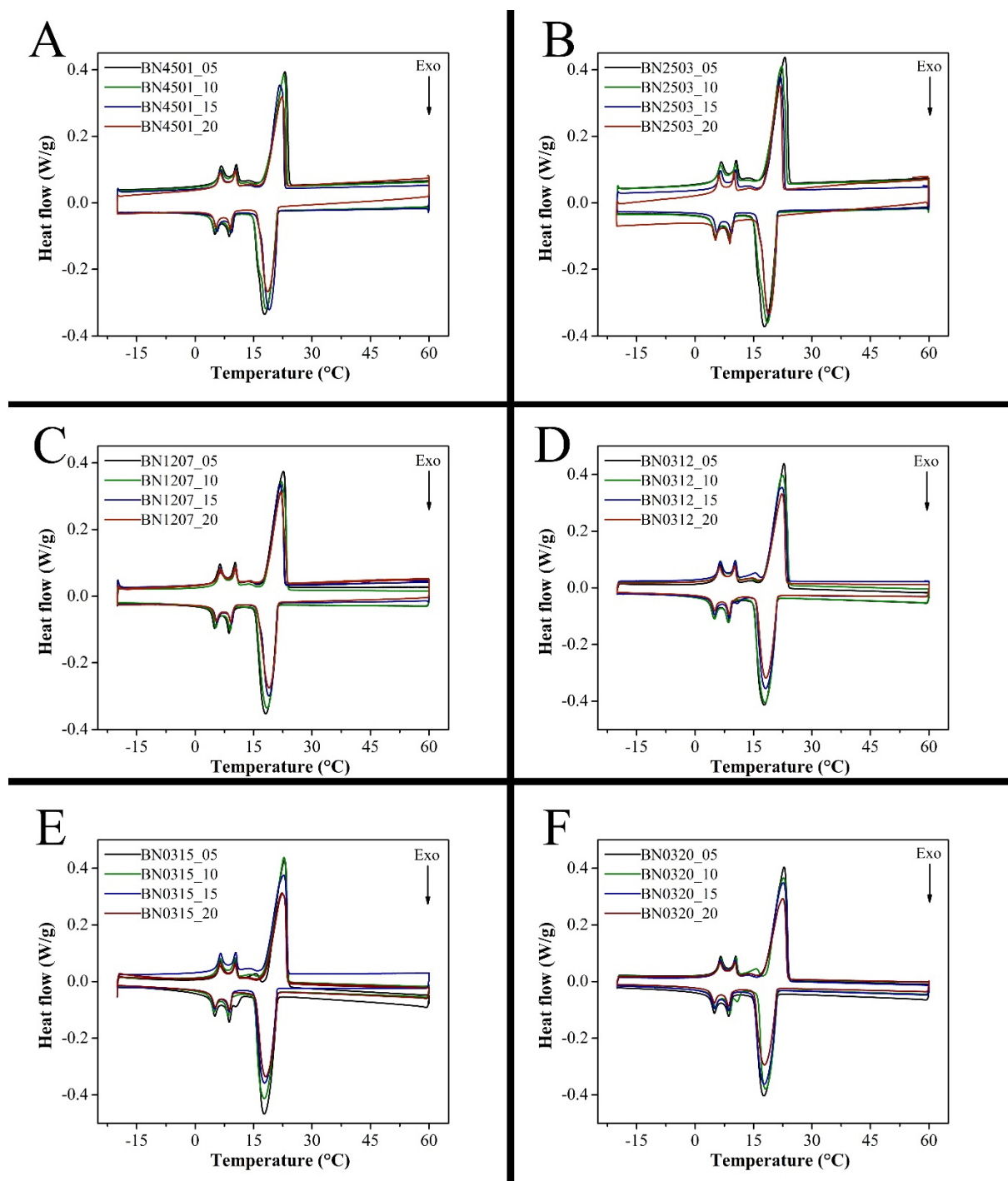


Fig. S4.4 DSC curves of ss-PCMs BN4501 (A), BN2503 (B), BN1207 (C), BN0312 (D), BN0315 (E) and BN0320 (F) containing 5 wt% 10 wt%, 15 wt% and 20 wt% hexagonal boron nitride.

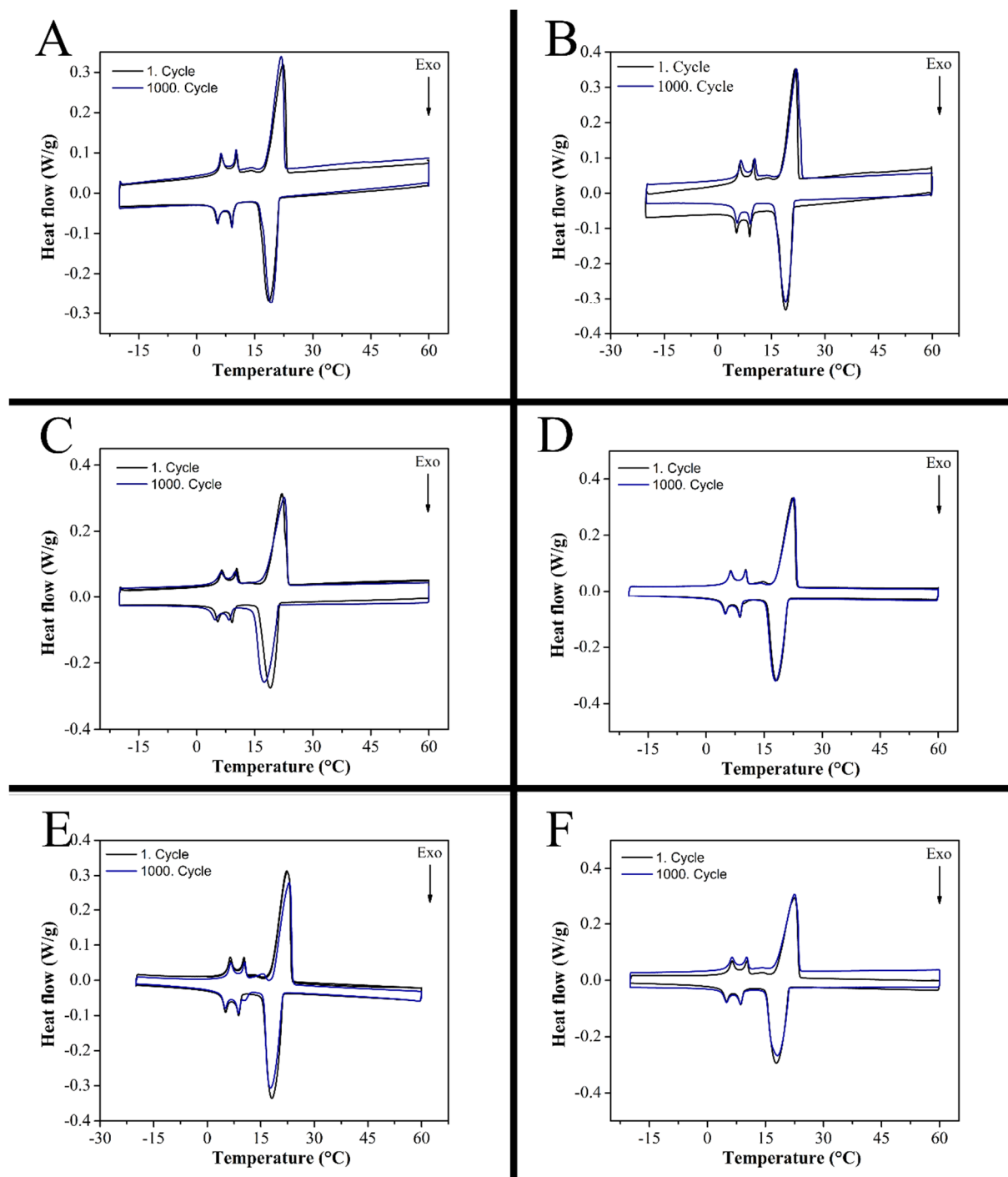


Fig. S4.5 DSC curves of the thermal cycling experiments of ss-PCMs BN04501_20 (A), BN2503_20 (B), BN1207_20 (C), BN0312_20 (D), BN0315_20 (E) and BN0320_20 (F). The ss-PCMs were melted and freed for 1000-times via a Primus 96 Thermal Cycler by MWG Biotech Inc between 8 °C and 60 °C. After the cycling experiment, the ss-PCMs were measured via DSC again. The deviation of the latent heats of all ss-PCM after the 1. Cycle and the 1000. Cycle is within the standard variation of the DSC device, pointing to a high longevity of the ss-PCMs.

Table S4.3.1 Thermal properties¹ of pure BS, BN0 and ss-PCMs BN4501 - BN0320 calculated via weighing and DSC measurements (part 1).

Sample	ΔH_{BS} (J/g)	ΔH_{total} (J/g)	$U_{\Delta H}$ (%)	T_m (°C)	T_f (°C)	ΔT_s (°C)	$U_{\Delta T}$ (%)	M_{ss-PCM} (g)	$Ma(PCM)_{DSC}$ (wt%)	$Ma(PCM)_{mass}$ (wt%)	$Ma(PCM)_{max}$ (wt%)	E_{DSC} (%)	E_{mass} (%)
BS	102.2	125.0	0.87	21.7	17.6	4.1	0.51	-	-	-	-	-	-
BN0	85.4	105.3	2.82	20.0	15.3	4.7	1.28	13.261	83.3	82.6	83.0	100.4	99.5
BN4501_05	76.2	98.8	2.60	22.6	17.5	5.1	3.06	13.297	79.0	77.8	78.8	100.3	98.7
BN4501_10	71.9	92.8	3.32	22.7	17.8	4.9	1.34	14.391	74.2	74.1	74.7	99.3	99.2
BN4501_15	68.8	88.1	3.61	22.4	18.0	4.4	1.69	15.113	70.4	69.6	70.7	99.6	98.4
BN4501_20	65.0	83.7	2.89	22.5	18.1	4.4	1.19	15.989	66.9	65.2	66.4	100.8	98.1
BN2503_05	77.5	99.0	3.79	22.6	18.2	4.4	1.74	13.782	79.2	78.6	78.8	100.5	99.7
BN2503_10	73.3	92.8	4.11	22.3	18.4	3.9	1.96	14.585	74.1	74.4	74.7	99.3	99.7
BN2503_15	68.7	88.6	4.46	22.2	18.8	3.4	1.78	15.221	70.9	69.8	70.7	100.2	98.8
BN2503_20	64.6	82.9	2.17	22.0	19.0	3.0	1.45	15.987	66.3	65.2	66.4	99.9	98.1
BN1207_05	77.0	98.0	4.02	22.5	18.0	4.5	2.15	13.562	78.4	78.2	78.8	99.5	99.3
BN1207_10	74.3	94.	3.59	22.2	18.2	4.0	1.61	14.329	75.2	74.0	74.7	100.7	99.0
BN1207_15	66.9	88.1	2.01	22.2	18.0	4.2	1.82	15.158	70.5	69.7	70.7	99.7	98.6
BN1207_20	63.8	83.1	4.94	21.9	18.6	3.3	1.36	15.933	66.5	65.0	66.4	100.0	98.0

1: Melting enthalpy of BS signal ΔH_{BS} , melting enthalpy of whole ss-PCM ΔH_{total} , relative uncertainty $U_{\Delta H}$ of ΔH_{total} , melting point of BS signal T_m , supercooling ΔT_s , relative uncertainty $U_{\Delta T}$ of ΔT_s , mean value for effective mass fraction of PCM $Ma(PCM)_{DSC}$ (Eq. 1.1) and $Ma(PCM)_{mass}$ (Eq. 1.2), highest value for effective mass fraction of PCM $Ma(PCM)_{max}$ (Eq. 1.3) and corresponding PCM immobilization efficiencies E_{DSC} (Eq. 1.4) and E_{mass} (Eq. 1.5).

Table S4.3.2 Thermal properties¹ of pure BS, BN0 and ss-PCMs BN4501 - BN0320 calculated via weighing and DSC measurements (part 2).

Sample	ΔH_{BS} (J/g)	ΔH_{total} (J/g)	$U_{\Delta H}$ (%)	T_m (°C)	T_f (°C)	ΔT_s (°C)	$U_{\Delta T}$ (%)	M_{ss-PCM} (g)	$Ma(PCM)_{DSC}$ (wt%)	$Ma(PCM)_{mass}$ (wt%)	$Ma(PCM)_{max}$ (wt%)	E_{DSC} (%)	E_{mass} (%)
BN0312_05	76.2	97.4	5.60	22.8	17.9	4.9	1.29	13.671	77.9	78.4	78.8	98.9	99.5
BN0312_10	74.4	94.7	3.38	22.5	17.9	4.6	1.61	14.681	75.7	74.6	74.7	101.4	99.9
BN0312_15	71.5	89.2	2.71	22.7	18.4	4.3	1.77	14.839	71.3	69.0	70.7	100.9	97.7
BN0312_20	63.8	82.7	3.30	22.4	18.3	4.1	2.65	15.849	66.2	64.9	66.4	99.6	97.7
BN0315_05	76.3	99.5	4.06	22.6	17.5	5.1	1.58	13.891	79.6	78.7	78.8	101.0	99.9
BN0315_10	73.9	93.3	4.54	22.6	17.8	4.8	1.09	14.261	74.6	73.9	74.7	99.9	98.9
BN0315_15	70.9	90.8	5.72	22.7	18.0	4.7	1.53	15.054	72.6	69.5	70.7	102.7	98.3
BN0315_20	69.1	82.5	5.95	22.8	18.2	4.6	1.72	15.504	66.0	64.1	66.4	99.4	96.5
BN0320_05	76.7	98.6	3.51	22.8	17.6	5.2	2.25	13.804	78.9	78.6	78.8	100.1	99.8
BN0320_10	71.6	93.8	2.83	22.5	17.7	4.8	1.38	14.601	75.0	74.5	74.7	100.4	99.7
BN0320_15	69.8	89.5	2.82	22.6	18.0	4.6	1.64	15.154	71.6	69.7	70.7	101.3	98.6
BN0320_20	67.5	84.3	3.68	22.5	18.0	4.4	1.32	15.743	67.4	64.6	66.4	101.5	97.3

1: Melting enthalpy of BS signal ΔH_{BS} , melting enthalpy of whole ss-PCM ΔH_{total} , relative uncertainty $U_{\Delta H}$ of ΔH_{total} , melting point of BS signal T_m , supercooling ΔT_s , relative uncertainty $U_{\Delta T}$ of ΔT_s , mean value for effective mass fraction of PCM $Ma(PCM)_{DSC}$ (Eq. 1.1) and $Ma(PCM)_{mass}$ (Eq. 1.2), highest value for effective mass fraction of PCM $Ma(PCM)_{max}$ (Eq. 1.3) and corresponding PCM immobilization efficiencies E_{DSC} (Eq. 1.4) and E_{mass} (Eq. 1.5).

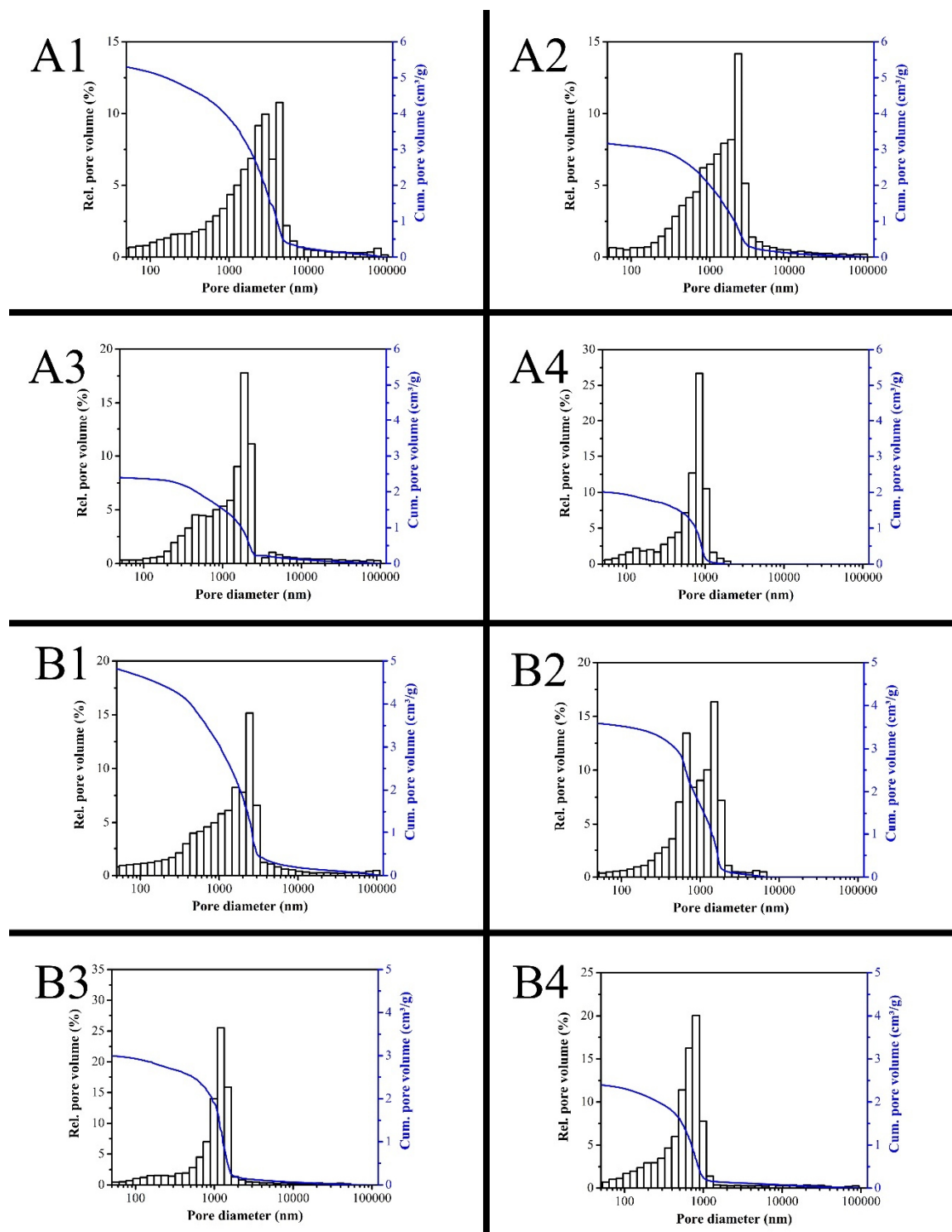


Fig. S4.6.1 Mercury intrusion measurements of calcined ss-PCMs BN4501c (A), BN2503c (B), BN1207c (C), BN0312c (D), BN0315c (E) and BN0320c (F) containing 5 wt% (1), 10 wt% (2), 15 wt% (3) and 20 wt% (4) hexagonal boron nitride (part 1).

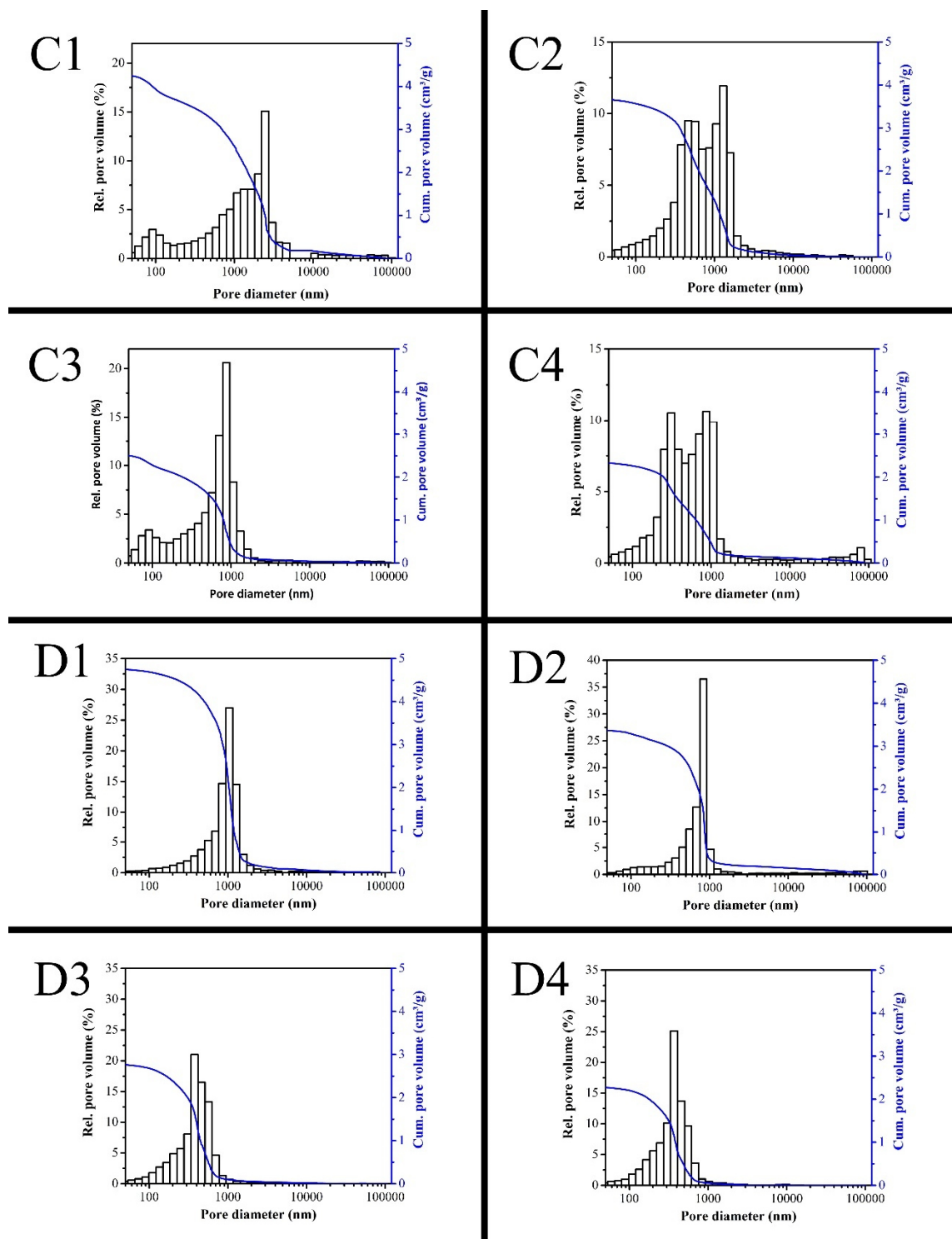


Fig. S4.6.2 Mercury intrusion measurements of calcined ss-PCMs BN4501c (A), BN2503c (B), BN1207c (C), BN0312c (D), BN0315c (E) and BN0320c (F) containing 5 wt% (1), 10 wt% (2), 15 wt% (3) and 20 wt% (4) hexagonal boron nitride (part 2).

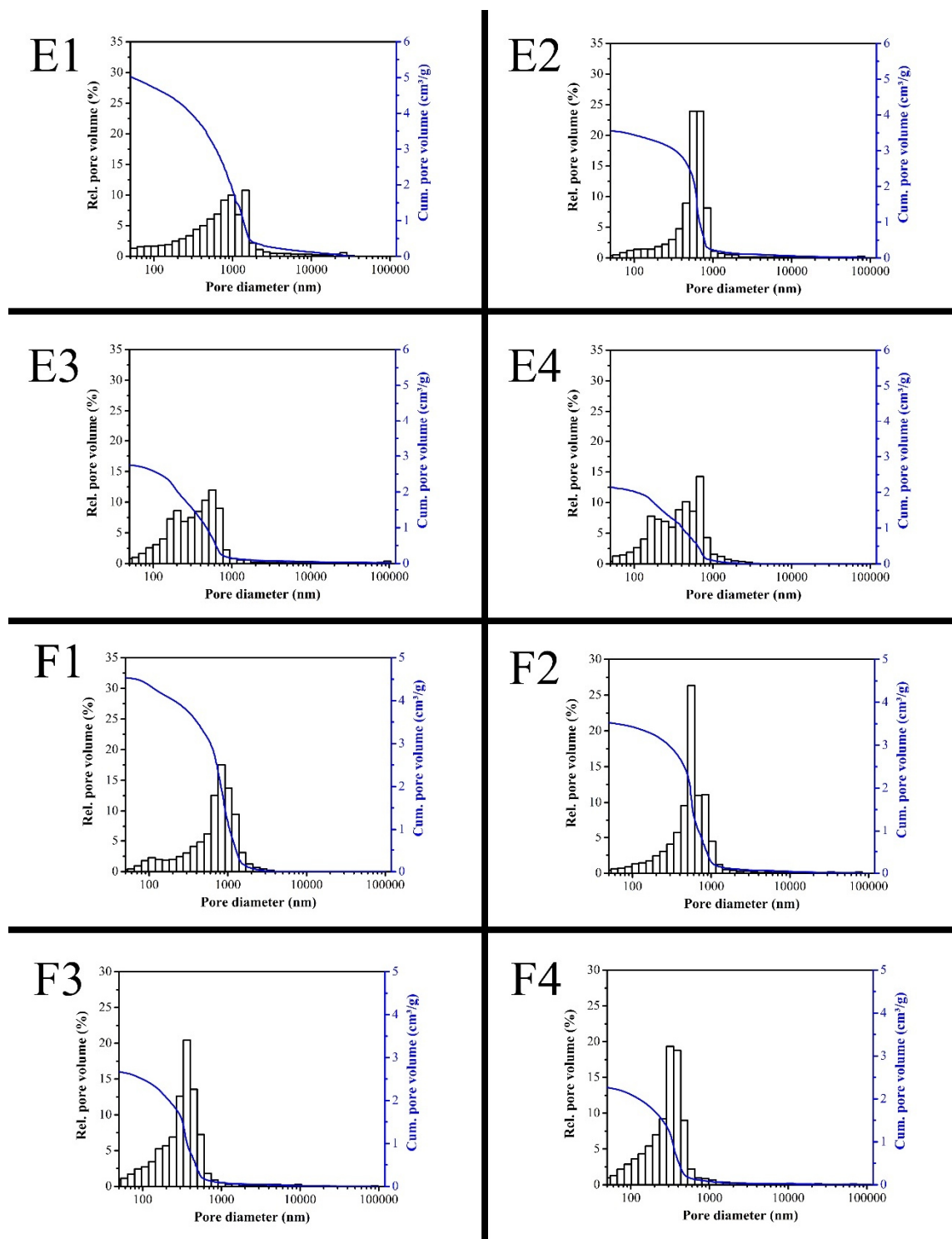


Fig. S4.6.3 Mercury intrusion measurements of calcined ss-PCMs BN4501c (A), BN2503c (B), BN1207c (C), BN0312c (D), BN0315c (E) and BN0320c (F) containing 5 wt% (1), 10 wt% (2), 15 wt% (3) and 20 wt% (4) hexagonal boron nitride (part 3).

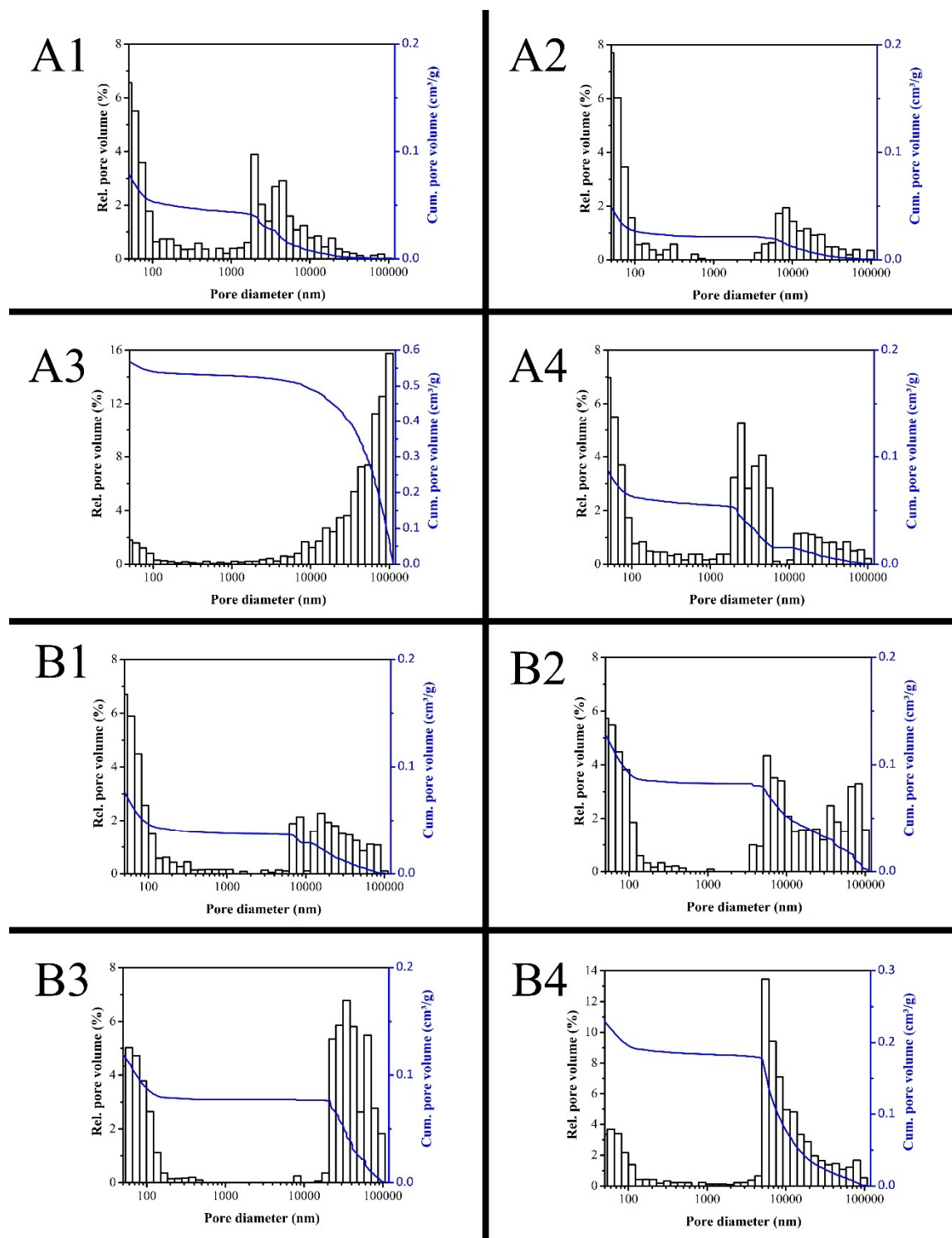


Fig. S4.7.1 Mercury intrusion measurements of ss-PCMs BN4501 (A), BN2503 (B), BN1207 (C), BN0312 (D), BN0315 (E) and BN0320 (F) containing 5 wt% (1), 10 wt% (2), 15 wt% (3) and 20 wt% (4) hexagonal boron nitride (part 1).

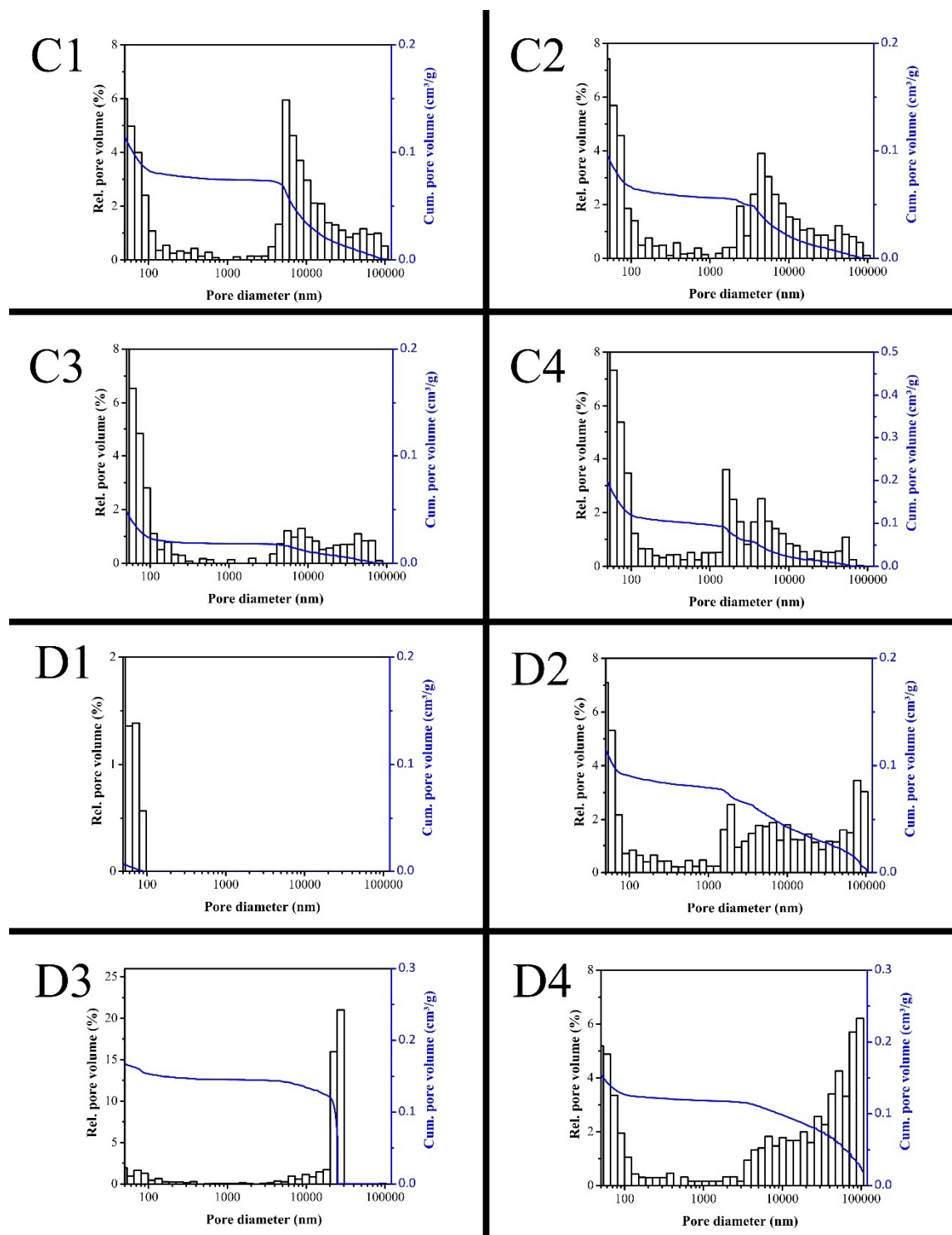


Fig. S4.7.2 Mercury intrusion measurements of ss-PCMs BN4501 (A), BN2503 (B), BN1207 (C), BN0312 (D), BN0315 (E) and BN0320 (F) containing 5 wt% (1), 10 wt% (2), 15 wt% (3) and 20 wt% (4) hexagonal boron nitride (part 2).

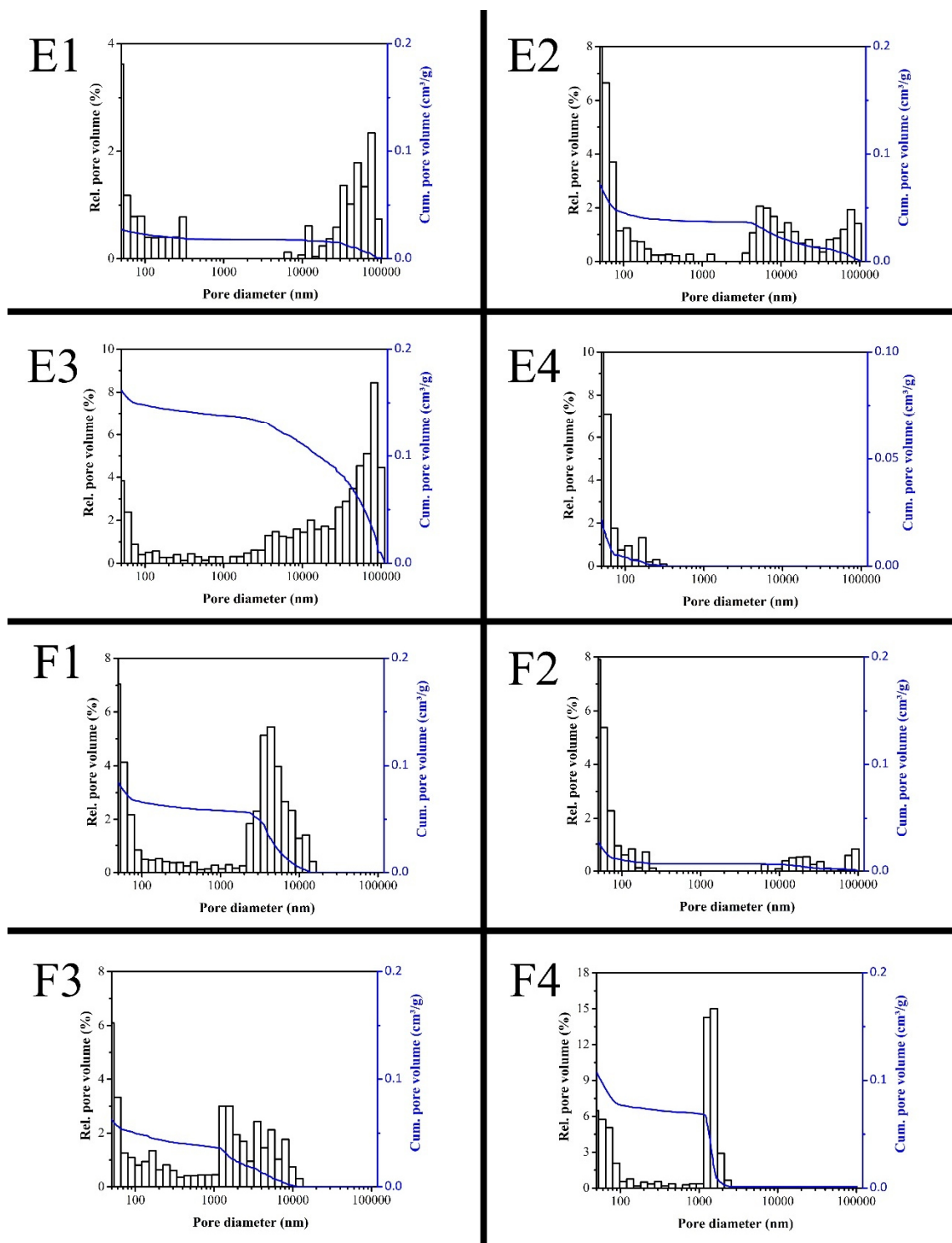


Fig. S4.7.3 Mercury intrusion measurements of ss-PCMs BN4501 (A), BN2503 (B), BN1207 (C), BN0312 (D), BN0315 (E) and BN0320 (F) containing 5 wt% (1), 10 wt% (2), 15 wt% (3) and 20 wt% (4) hexagonal boron nitride (part 3).

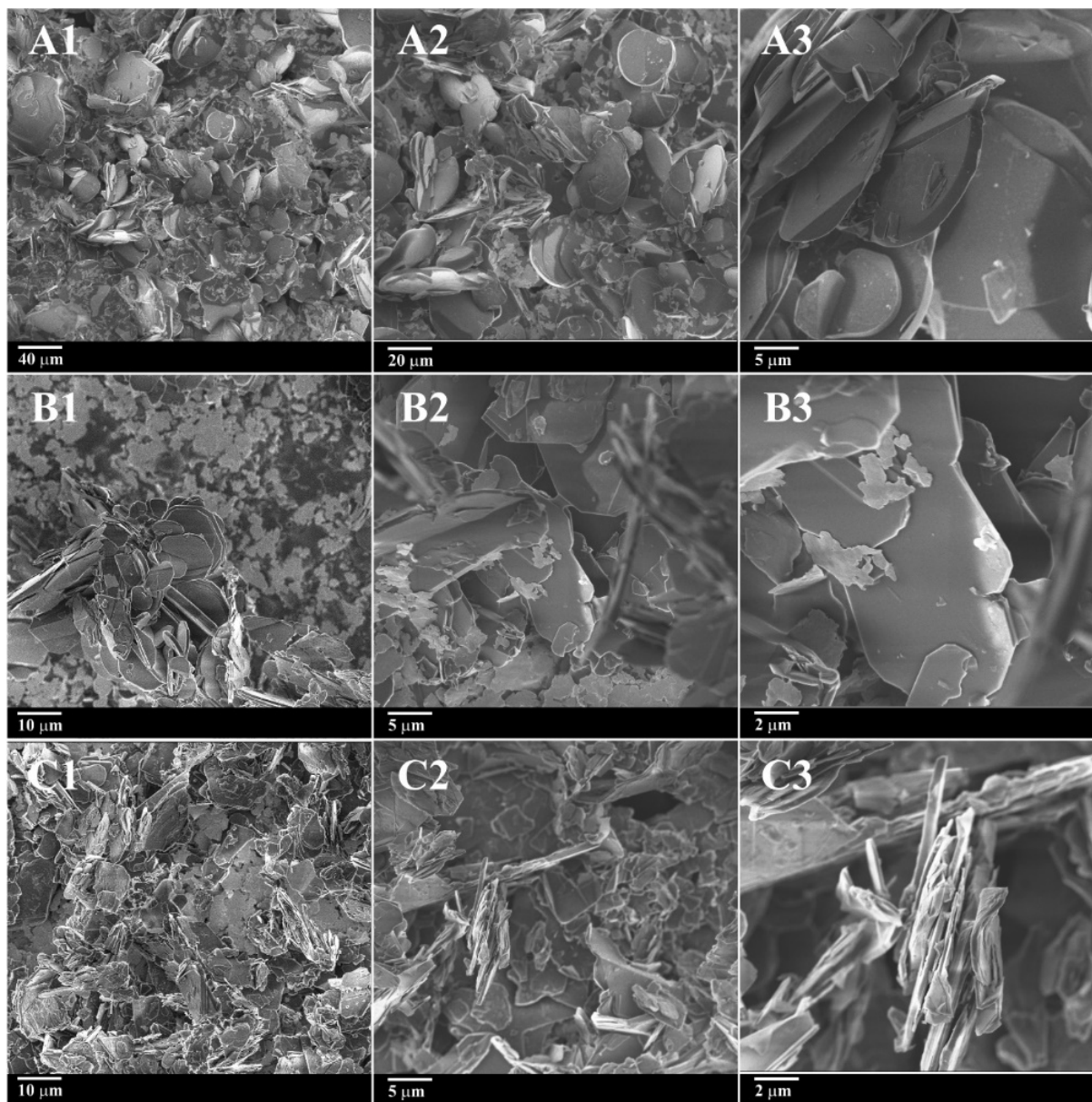


Fig. S4.8.1 Microscopic SEM images of pure hBNs HeBoFill 501 (A), HeBoFill 491 (B), HeBoFill 641 (C), HeBoFill 110 (D), HeBoFill 230 (E) and HeBoFill 205 (F) (part 1).

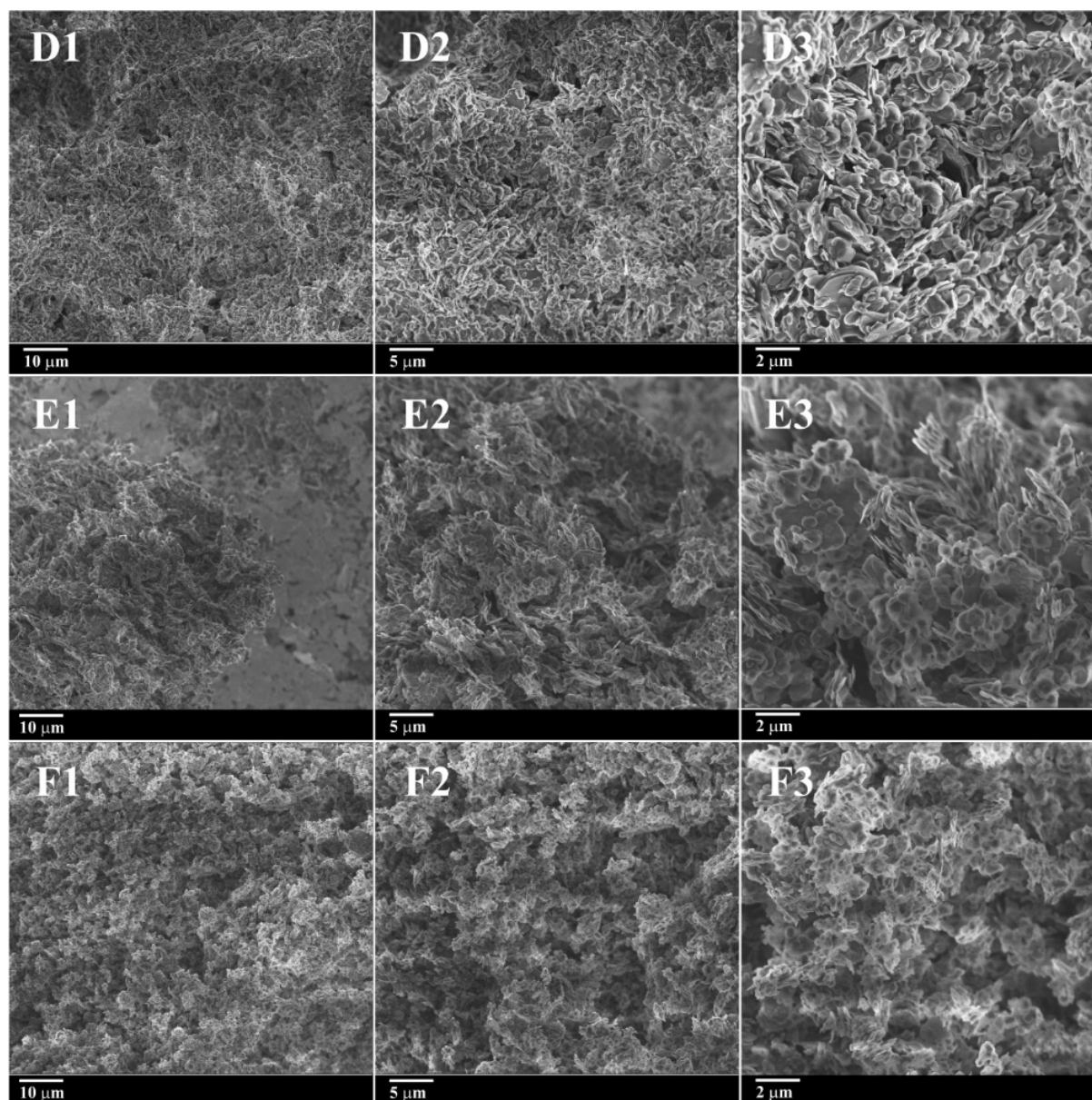


Fig. S4.8.2 Microscopic SEM images of pure hBNs HeBoFill 501 (A), HeBoFill 491 (B), HeBoFill 641 (C), HeBoFill 110 (D), HeBoFill 230 (E) and HeBoFill 205 (F) (part 2).

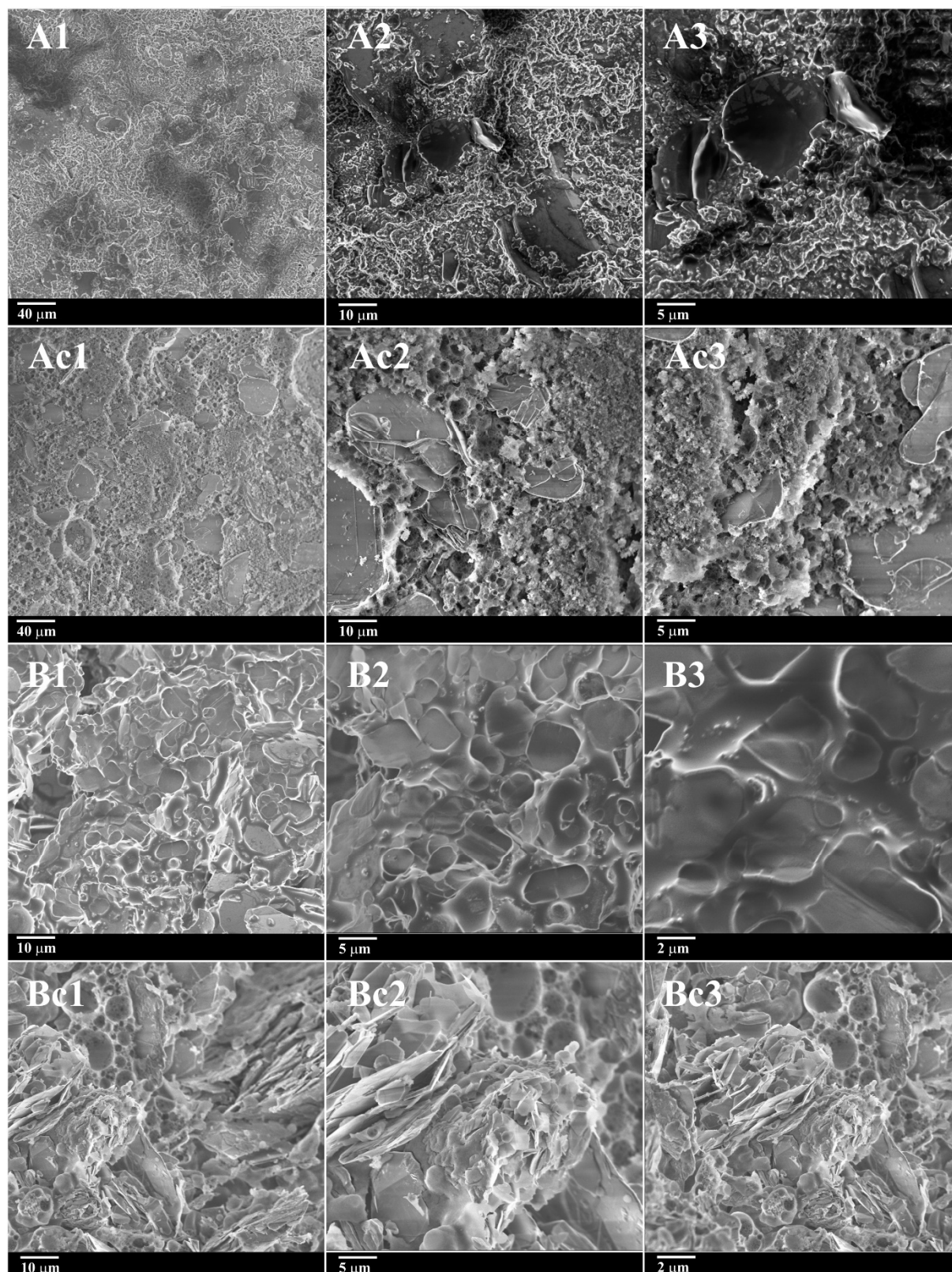


Fig. S4.9 Microscopic SEM images of ss-PCM samples BN4501_20 (A), BN4501c_20 (Ac), BN2503_20 (B) and BN2503c_20 (Bc).

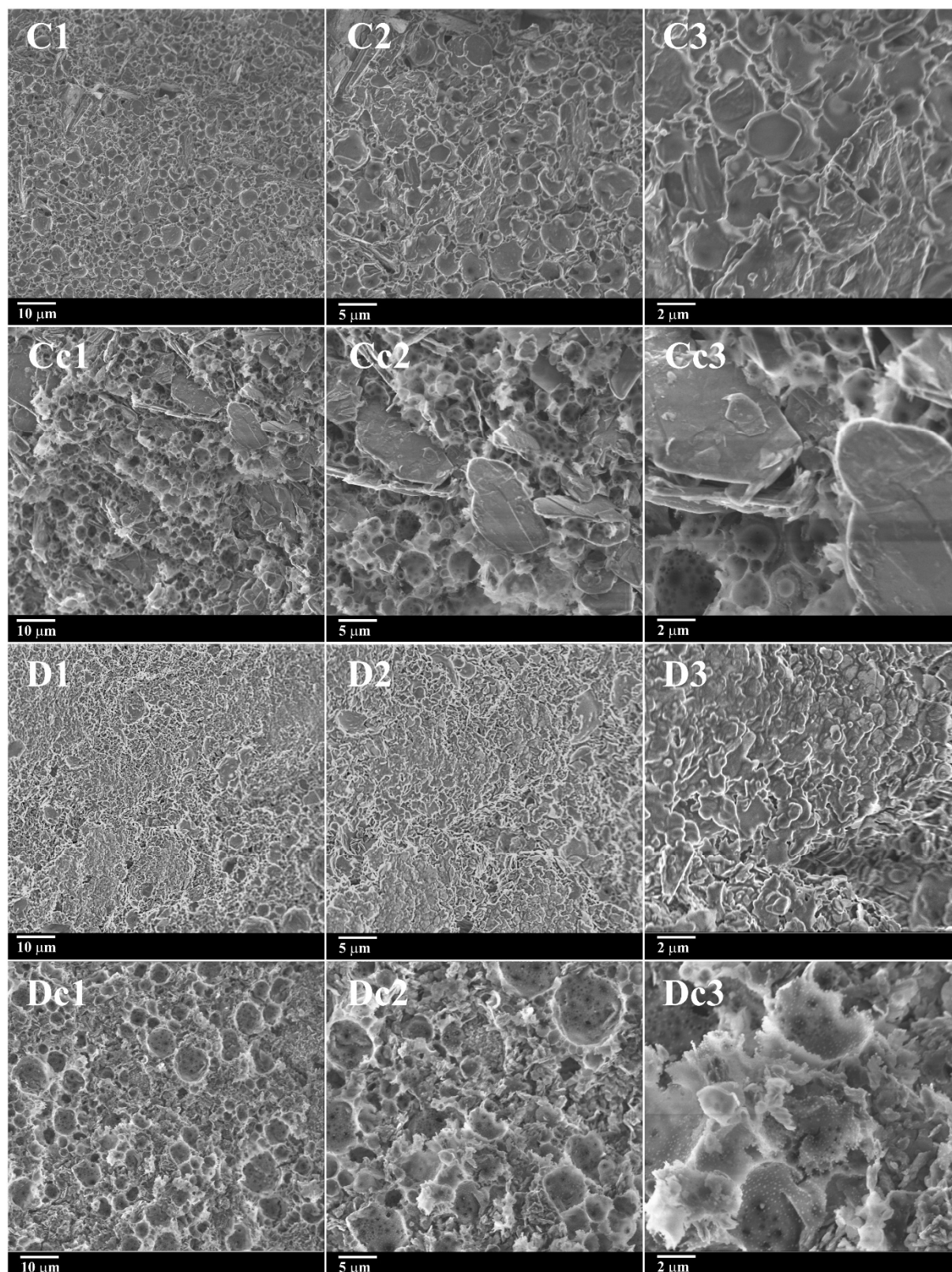


Fig. S4.10 Microscopic SEM images of ss-PCM samples BN1207_20 (C), BN1207c_20 (Cc), BN0312_20 (D) and BN0312c_20 (Dc).

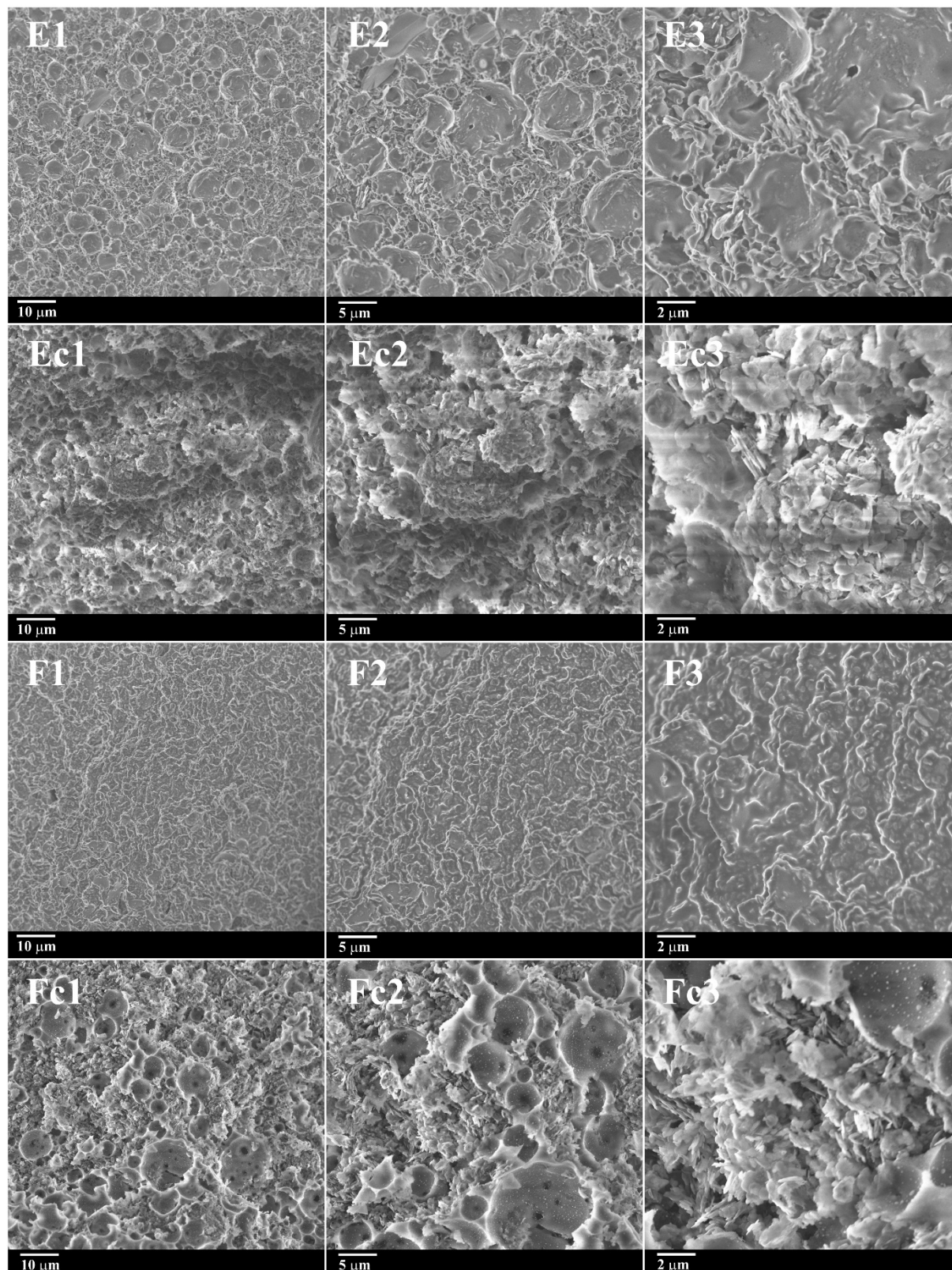


Fig. S4.11 Microscopic SEM images of ss-PCM samples BN0315_20 (E), BN0315c_20 (Ec), BN0320_20 (F) and BN0320c_20 (Fc).

Table S4.4 Structural properties^a of calcined samples BN0c, BN4501c, BN2503c, BN1207c, BN0312c, BN0315c and BN0320c.

Sample	$\phi^{b,c}$ (%)	$V_{total}^{b,c}$ (cm ³ /g)	V_{macro}^b (cm ³ /g)	V_{meso}^c (cm ³ /g)	D_{macro}^b (nm)	A_{meso}^c (m ² /g)
BN4501_05c	93	6.013	5.298	0.715	2281	171
BN4501_10c	89	3.751	3.166	0.585	1384	132
BN4501_15c	86	2.904	2.398	0.506	1486	98
BN4501_20c	84	2.309	2.010	0.299	757	78
BN2503_05c	92	5.454	4.818	0.636	1492	174
BN2503_10c	89	3.927	3.486	0.441	1222	115
BN2503_15c	88	3.473	3.146	0.327	1147	87
BN2503_20c	85	2.774	2.395	0.379	685	74
BN1207_05c	91	4.926	4.251	0.675	1385	170
BN1207_10c	89	3.749	3.309	0.440	749	111
BN1207_15c	86	2.871	2.503	0.368	606	97
BN1207_20c	84	2.311	2.052	0.259	512	82
BN0312_05c	92	5.356	4.751	0.605	958	137
BN0312_10c	89	3.881	3.366	0.515	800	115
BN0312_15c	87	3.290	2.762	0.528	406	98
BN0312_20c	85	2.630	2.274	0.356	373	67
BN0315_05c	93	5.818	5.217	0.601	922	139
BN0315_10c	90	4.073	3.554	0.519	614	112
BN0315_15c	87	3.245	2.749	0.496	361	105
BN0315_20c	86	2.779	2.412	0.367	335	70
BN0320_05c	92	5.129	4.534	0.595	766	133
BN0320_10c	90	4.031	3.525	0.506	559	119
BN0320_15c	87	3.164	2.671	0.493	337	98
BN0320_20c	85	2.673	2.266	0.407	323	86

^a Porosity ϕ , total pore volume V_{total} , macropore volume V_{macro} , mesopore volume V_{meso} , mean macropore diameter/50% D_{total} , mesopore surface area A_{meso} of calcined ss-PCMs. ^b calculated via mercury intrusion. ^c calculated via nitrogen sorption. Notes: All samples were calcined at 600 °C.

Table S4.5 Structural properties^a of samples BN0, BN4501, BN2503, BN1207, BN0312, BN0315 and BN0320.

Sample	Φ (%)	V_{total} (cm ³ /g)	D_{macro} (nm)	σ_s at 10 °C (MPa)	U_s (%)	σ_l at 30 °C (MPa)	U_l (%)
BN0	5	0.027	250	0.69	1.88	1.21	1.35
BN4501_05	15	0.079	1984	0.98	2.93	0.63	2.23
BN4501_10	10	0.049	147	1.16	2.55	0.78	2.81
BN4501_15	57	0.568	55118	1.43	2.78	0.98	1.87
BN4501_20	16	0.087	2492	1.48	2.02	1.01	2.11
BN2503_05	14	0.079	743	1.1	2.29	0.74	1.27
BN2503_10	22	0.128	7092	1.29	2.75	0.89	1.48
BN2503_15	21	0.119	27503	1.64	1.01	1.14	1.33
BN2503_20	34	0.229	7029	1.69	2.66	1.18	1.10
BN1207_05	20	0.115	6003	1.18	1.62	0.81	2.18
BN1207_10	17	0.096	3684	1.41	3.35	0.99	2.74
BN1207_15	10	0.049	92	1.76	2.88	1.25	1.76
BN1207_20	24	0.152	742	1.81	3.01	1.27	1.48
BN0312_05	2	0.007	67	1.59	3.28	1.04	2.21
BN0312_10	20	0.114	4706	1.86	2.44	1.27	2.01
BN0312_15	27	0.167	24147	2.39	1.52	1.64	3.03
BN0312_20	24	0.153	341	2.44	1.79	1.69	2.57
BN0315_05	6	0.027	33304	1.42	3.08	0.96	1.85
BN0315_10	14	0.072	3953	1.77	3.15	1.21	1.81
BN0315_15	26	0.162	32888	2.12	2.48	1.48	2.36
BN0315_20	5	0.022	62	2.21	2.99	1.55	1.41
BN0320_05	16	0.058	3681	1.33	1.37	0.88	2.72
BN0320_10	6	0.027	71	1.62	2.03	1.07	2.31
BN0320_15	12	0.063	1410	1.99	2.07	1.36	3.31
BN0320_20	19	0.107	1315	2.02	1.39	1.41	2.79

^a Porosity Φ , total pore volume V_{total} and mean macropore diameter/50% D_{total} calculated via mercury intrusion, compressive strength σ_s at 10 °C, compressive strength σ_l at 30 °C, uncertainty U_s of σ_s , and uncertainty U_l of σ_l .

Notes: Nitrogen sorption experiments showed no signal for the ss-PCMs. Therefore, the mesopore volume of the silica matrix in the ss-PCMs should be fully filled with PCM. The ss-PCMs have just a small pore volume left. This macropore volume could be detected because of mercury intrusion limits (destruction and compression of liquid PCM at higher pressures by mercury).

Table S4.6 XRD diffraction peaks of pure boron nitride (BN) powder HeBoFill 501 to HeBoFill 205 and calcined ss-PCMs BN4501c_20 to BN0320c_20.

NamePlane	002 (°)	100 (°)	102 (°)	004 (°)
HeBoFill501	26.80	41.67	50.22	55.18
BN4501c_20	26.78	41.59	50.14	55.10
HeBoFill491	26.87	41.73	50.29	55.24
hBN2503c_20	26.59	41.47	50.00	54.98
HeBoFill 64	26.71	41.56	50.13	55.10
BN1207c_20	26.71	41.57	50.17	55.09
HeBoFill 110	26.80	41.67	50.26	55.18
BN0312c_20	26.67	41.67	-	55.06
HeBoFill 230	26.76	41.63	-	55.15
BN0315c_20	26.78	41.63	-	55.15
HeBoFill 205	26.66	41.55	-	55.01
BN0320c_20	26.82	41.78	-	55.22

Table S4.7 XRD data of pure boron nitride (BN) powder HeBoFill 501 to HeBoFill 205 and calcined ss-PCMs BN4501c_20 to BN0320c_20. The layer height of BN particles, lattice space of BN particles and number of BN layers were calculated via Debye-Scherrer equation (Eq. 4.2). All BN particles are exfoliated during the sol-gel synthesis.

Name	Scherrer Constant K	Wavelength λ (Cu) (Å)	Scatter Angle 2θ (°)	Fill Half Maximum $FWHM$	Wide Peak Width at Half-Hight b^2 (device)	Layer height N (nm)	Lattice space d_{002} (nm)	Number of BN layers L
HeBoFill 501	0.91	1.5418	26.80295	0.0676	0.00239	177.3	0.572	311
BN4501c_20	0.91	1.5418	26.77671	0.1114	0.00239	106.0	0.565	189
HeBoFill491	0.91	1.5418	26.86854	0.0859	0.00239	144.8	0.588	247
hBN2503c_20	0.91	1.5418	26.59305	0.1372	0.00239	78.6	0.514	154
HeBoFill 64	0.91	1.5418	26.71112	0.0919	0.00239	124.2	0.547	228
BN1207c_20	0.91	1.5418	26.71112	0.1436	0.00239	79.4	0.547	146
HeBoFill 110	0.91	1.5418	26.80295	0.1740	0.00239	68.8	0.572	121
BN0312c_20	0.91	1.5418	26.67176	0.2107	0.00239	53.1	0.536	100
HeBoFill 230	0.91	1.5418	26.76359	0.1716	0.00239	68.3	0.561	123
BN0315c_20	0.91	1.5418	26.77671	0.2096	0.00239	56.3	0.565	101
HeBoFill 205	0.91	1.5418	26.65864	0.2517	0.00239	44.2	0.533	84
BN0320c_20	0.91	1.5418	26.81607	0.2756	0.00239	43.8	0.575	77

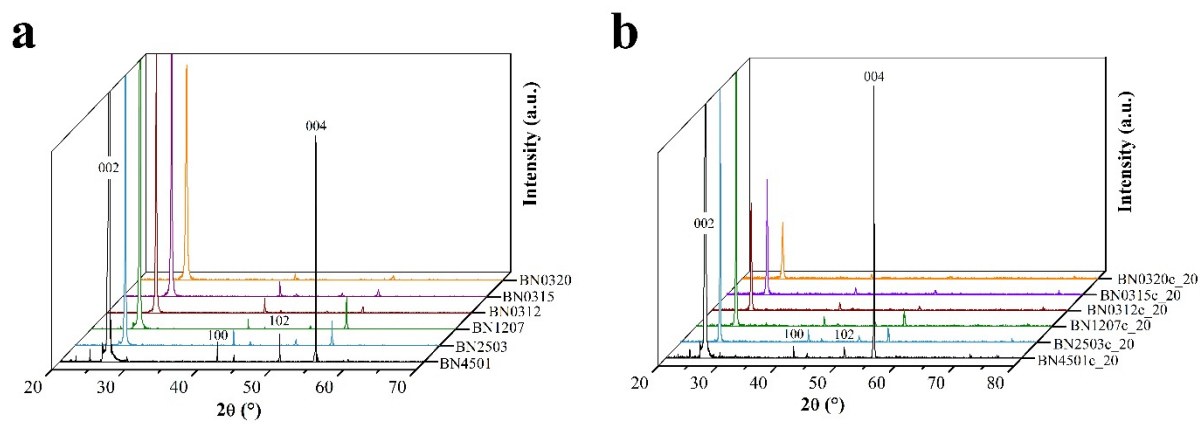


Fig. S4.12 XRD patterns of pure boron nitride (BN) powder HeBoFill 501 (BN4501) to HeBoFill 205 (BN0320) (a) and calcined ss-PCMs BN4501c_20 to BN0320c_20 (b).

Thermal Imaging Movies

Movie S4.1

Temperature evolution of BN4501_05, BN2503_05, BN1207_05, BN0312_05, BN0315_05 and BN0320_05 in a water bath at 45 °C for 40 min. Experimental details are shown in Fig. S.4.3.

Movie S4.2

Temperature evolution of BN4501_10, BN2503_10, BN1207_10, BN0312_10, BN0315_10 and BN0320_10 in a water bath at 45 °C for 40 min. Experimental details are shown in Fig. S.4.3.

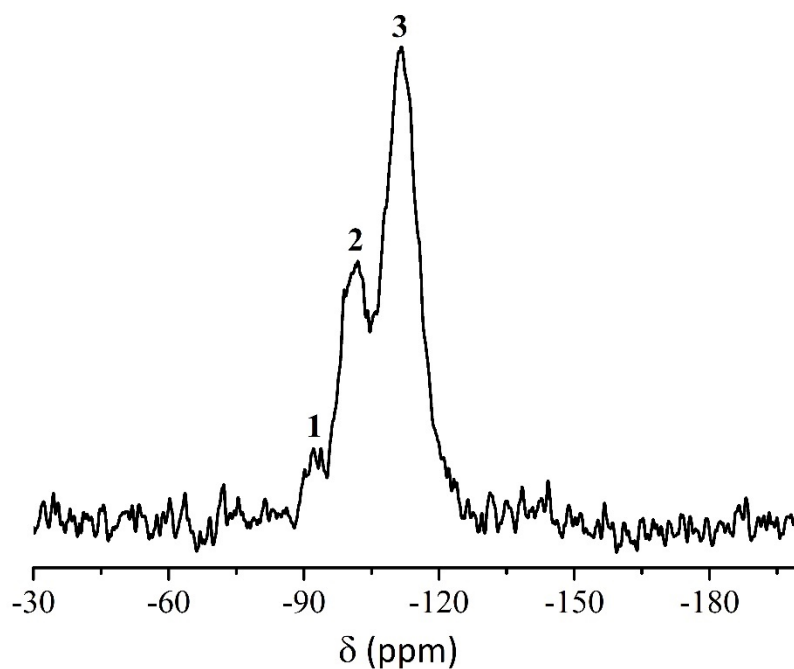
Movie S4.3

Temperature evolution of BN4501_15, BN2503_15, BN1207_15, BN0312_15, BN0315_15 and BN0320_15 in a water bath at 45 °C for 40 min. Experimental details are shown in Fig. S.4.3.

Movie S4.4

Temperature evolution of BN4501_20, BN2503_20, BN1207_20, BN0312_20, BN0315_20 and BN0320_20 in a water bath at 45 °C for 40 min. Experimental details are shown in Fig. S.4.3.

3.5 Experimental data showing the influence of different boron nitride particles on the silica network, the butyl stearate and the porogens in shape-stabilized phase change materials



Authors

Felix Marske ^a, Titus Lindenberg ^b, Juliana Martins de Souza e Silva ^{c,d}, Ralf B. Wehrspohn ^c,
A. Wouter Maijenburg ^b, Thomas Hahn ^a, Dirk Enke ^e

^a Institute of Technical Chemistry, Martin Luther University of Halle-Wittenberg, Halle (Saale) 06120, Germany

^b Center for Innovation Competence SiLi-nano, Martin Luther University of Halle-Wittenberg, Halle (Saale) 06120, Germany

^c Institute of Physics, Martin Luther University of Halle-Wittenberg, Halle (Saale) 06120, Germany

^d Fraunhofer Institute for Microstructure of Materials and Systems (IMWS), Halle (Saale) 06120, Germany

^e Institute of Chemical Technology, Leipzig University, Leipzig 04109, Germany

State of Publication

Co-Submission to Publication 4, Accepted 22th September 2021 in *Data in Brief*

doi.org/10.1016/j.dib.2021.107428

3.5.1 Abstract

Shape-stabilized phase change materials (ss-PCMs) based on silica and butyl stearate were thermally enhanced via the addition of different hexagonal boron nitride particles (BN) to the *in situ* sol-gel synthesis. The dataset is used in conjunction with the experimental data of the influence of the particle size and surface area of BN on the thermal and mechanical properties of ss-PCMs discussed in Marske *et al.* [1]. To study the effect of the different BN particles on the hydrolysis degree of the silica network and on the chemical nature of the porogens sodium dodecyl sulfate and poly(vinyl alcohol) used for the ss-PCM synthesis, the ss-PCM samples are measured via High Power Decoupling (HPDEC) Magic Angle Spinning (MAS) ^{29}Si NMR and attenuated total reflection-Fourier transform infrared (ATR-FTIR) spectroscopy, respectively. Additionally, data of the influence of BN on the thermal properties is presented as thermogravimetric analysis (TG). The ^{29}Si MAS NMR spectra are referenced to tetramethylsilane and show the different silica species in ppm. The different value of wavenumber and intensity of each reference and ss-PCM sample is listed in the IR spectra. The decomposition points of the ss-PCMs are calculated from the TG data via OriginLab. The spectra and data can be used as a reference for other researchers and engineers to use in synthesizing ss-PCMs based on silica and other polymeric materials or as reference for pure BN, SDS, stabilized silica sol and PVA.

3.5.2 Keywords

Phase change materials, PCM, Boron nitride, Shape-stabilization, Sol-gel, Thermal energy storage

3.5.3 Specifications Table

Subject	Thermal energy storage
Specific subject area	Shape-stabilized phase change materials, hexagonal boron nitride, thermal conductivity enhancement
Type of data	Figure, Table
How data were acquired	<p>High Power Decoupling (HPDEC) Magic Angle Spinning (MAS) ^{29}Si NMR using a Bruker DRX-400 WB NMR spectrometer (Bruker Biospin, Karlsruhe, Germany) equipped with a 4-mm double-resonance MAS probe maintained at $-10\text{ }^{\circ}\text{C}$ by a temperature control unit.</p> <p>Attenuated total reflection-Fourier transform infrared (ATR-FTIR) spectroscopy using a Tensor 27 spectroscope equipped with a diamond ATR unit from Bruker.</p> <p>Thermogravimetry (TG) using a <i>STA 409 C/CD</i> thermal analyser from Netzsch.</p>
Data format	Raw, Analyzed
Parameters for data collection	ss-PCM samples were synthesized with silica, sodium dodecyl sulfate, poly(vinyl alcohol), butyl stearate, water, and BN of type HeBoFill with different particle sizes and specific surface areas via a specific sol-gel process
Description of data collection	<p>For ^{29}Si MAS NMR, the ss-PCM sample scanning was carried at a radio-frequency field strength of 42 kHz as a $\pi/2$ pulse during an acquisition time of 25 ms (Larmor frequency of 79.49 MHz, spinning speed of 10 kHz, repetition delay of 40 s, number of scans between 2000 - 3500, and using tetramethylsilane as s reference).</p> <p>The ss-PCMs were scanned 60-times via ATR-FTIR instrument as pure substance at the range of 4000 cm^{-1} to 400 cm^{-1} wavenumbers.</p> <p>An amount of 100 mg ss-PCM sample was heated from 25 to $400\text{ }^{\circ}\text{C}$ in thermogravimetric analysis (heating rate of $1\text{ }^{\circ}\text{C}/\text{min}$).</p>

Data source location	Institution: Martin Luther University of Halle-Wittenberg City/Town/Region: Halle (Saale) / Saxony-Anhalt Country: Germany
Data accessibility	With the article
Related research article	F. Marske, T. Lindenberg, J. Martins de Souza e Silva, R. B. Wehrspohn, A. W. Maijenburg, T. Hahn and D. Enke, Size and surface effects of hexagonal boron nitrides on the physicochemical properties of monolithic phase change materials synthesized via sol-gel route, Appl. Therm. Eng. 196 (2021), 117325.

3.5.4 Value of the Data

- It is of great interest to find the boron nitride best suited to increase the mechanical stability, thermal conductivity, and durability of polymers, such as ss-PCMs, to the highest extent.
- The researcher can use the data to compare or develop ss-PCMs based on silica and boron nitride with higher decomposition points of PCMs and, thus, broaden the application range of different polymers.
- The data help to understand the relationship between boron nitride with different particle sizes and specific surface areas in sol-gel processes.
- The data of the pure substances before and after immobilization in the silica network enables a proper comparison with similar materials, such as graphite, carbon nanotubes and boron nitride nanosheets.

3.5.5 Data Description

The dataset is based on the analysis of ss-PCM samples synthesized with [1] and without BN particles [2]. The ss-PCM samples were measured via High Power Decoupling (HPDEC) Magic Angle Spinning (MAS) ^{29}Si NMR, Attenuated total reflection-Fourier transform infrared (ATR-FTIR) spectroscopy and thermogravimetry (TG). The thermally enhanced ss-PCM samples were synthesized with six types of hexagonal boron nitride platelets (BN). A total of four different amounts of BN of each BN type (5 - 20 wt%) was used for the ss-PCM synthesis, resulting in a total of 24 different ss-PCM samples. The particle size, particle thickness and

specific surface area of each BN type is listed in our recent publication [1]. The raw data of all figures is given in the supplementary data of this paper.

Because a well-interconnected silica network is a key property of mechanical stable ss-PCMs, we analyzed the influence of BN with different particle sizes and specific surface areas on the hydrolysis degree of the pure silica sol and the silica network in our ss-PCM samples via ^{29}Si MAS NMR in Fig. 5.1. The ^{29}Si MAS NMR spectra of the stabilized silica sol show three peaks in Fig. 5.1 (A). In Fig. 5.1 (B-H), the ^{29}Si MAS NMR spectra of the ss-PCMs BN0 (B), BN4501_20 (C), BN2503_20 (D), BN1207_20 (E), BN0312_20 (F), BN0315_20 (G) and BN0320_20 (H) show three partially overlapping peaks with a decreased peak intensity of peak 2 in comparison to Fig. 5.1 (A).

Physical and chemical interactions between the surfactant sodium dodecyl sulfate (SDS), the co-polymer poly(vinyl alcohol) (PVA), silica, butyl stearate and BN were analyzed via attenuated total reflection-Fourier transform infrared (ATR-FTIR) spectroscopy. Fig. 5.2 shows the ATR-IR spectra of the educts stabilized silica sol (A), butyl stearate (B), SDS (C) and PVA (D). Fig. 5.3 shows the combination of six ATR-IR spectra of the pure BN particles of the type HeBoFill501 (BN4501), HeBoFill 491 (BN2503), HeBoFill64 (BN1207), HeBoFill1111 (BN0312), HeBoFill230 (BN0315) and HeBoFill205 (BN0320). Fig. 5.4 shows the sample row BN2503 (A1) and BN0312 (B1) with four different BN amounts used in the ss-PCM synthesis after drying at 100 °C for 24 h (A1, B1) and calcination at 600 °C for 6 h (A2, B2). Fig. 5.5 shows a combination of the ATR-IR spectra of all ss-PCM samples containing 20 wt% BN after drying at 100 °C for 24 h (A1) and calcination at 600 °C for 6 h (A2).

The effect of the particle size and specific surface area of BN on the decomposition points of the ss-PCMs was analyzed via thermogravimetry (TG). The TG curves of the sample rows BN4501 (A), BN2503 (B), BN1207 (C), BN0312 (D), BN0315 (E) and BN0320 (F) are shown in Fig. 5.6 - 5.8. For the determination of the decomposition points, the maximum of the first derivative of the TG curves (Fig. 5.6 - 5.8) was calculated via OriginLab 8.1. All decomposition points in dependence of the BN type and the BN mass fraction are listed in Table 5.1 and shown in Fig. 5.9.

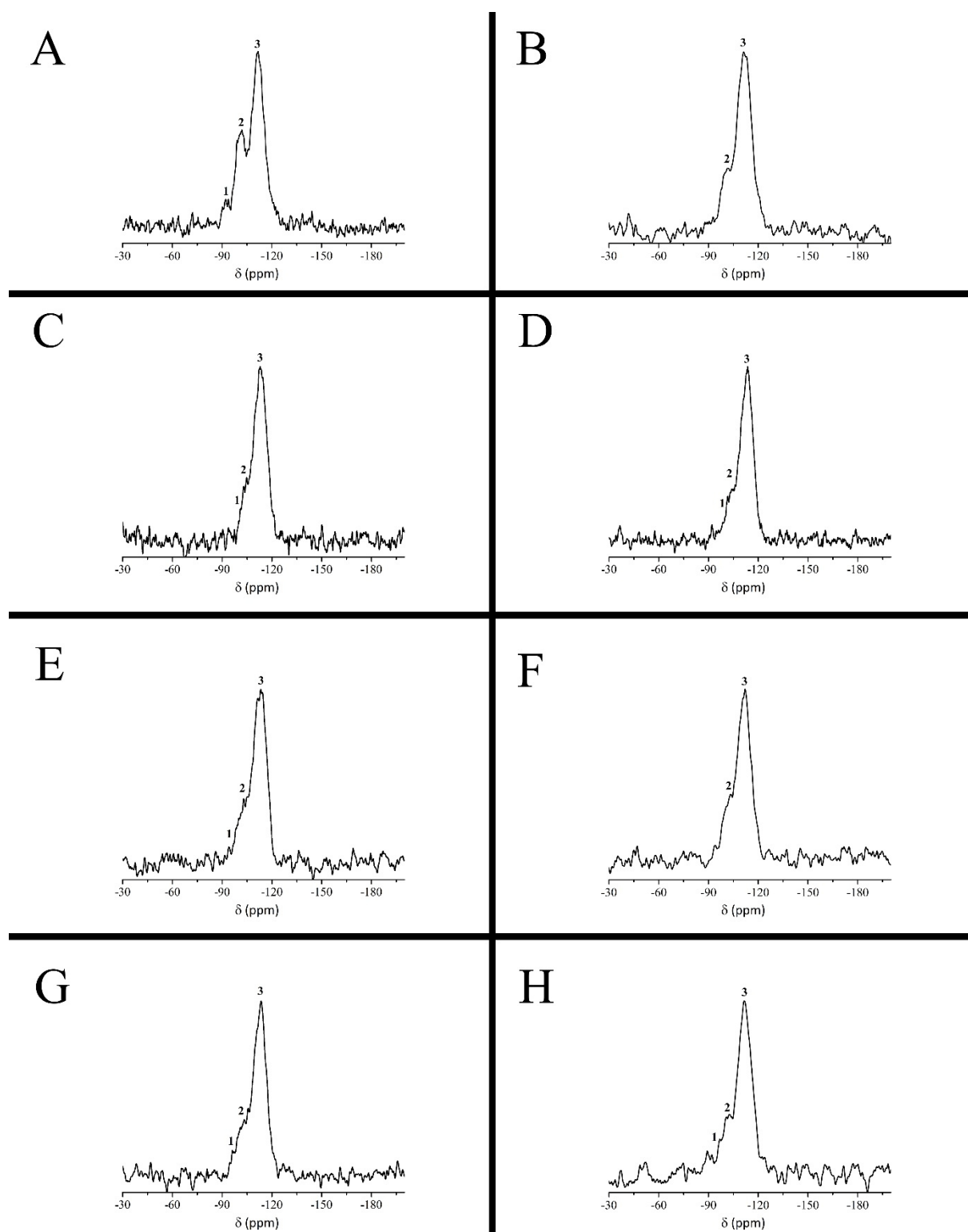


Fig. 5.1 ^{29}Si MAS NMR spectra of stabilized silica sol (A), ss-PCM BN0 (B) synthesized without BN and ss-PCM samples BN4501_20 (C), BN2503_20 (D), BN1207_20 (E), BN0312_20 (F), BN0315_20 (G) and BN0320_20 (H). 1 = $(\text{Si-O})_2\text{Si}(\text{OH})_2$ (Q^2); 2 = $(\text{Si-O})_2\text{Si}(\text{O-Si})(\text{OH})$ (Q^3); 3 = $(\text{Si-O})_2\text{Si}(\text{O-Si})_2$ (Q^4).

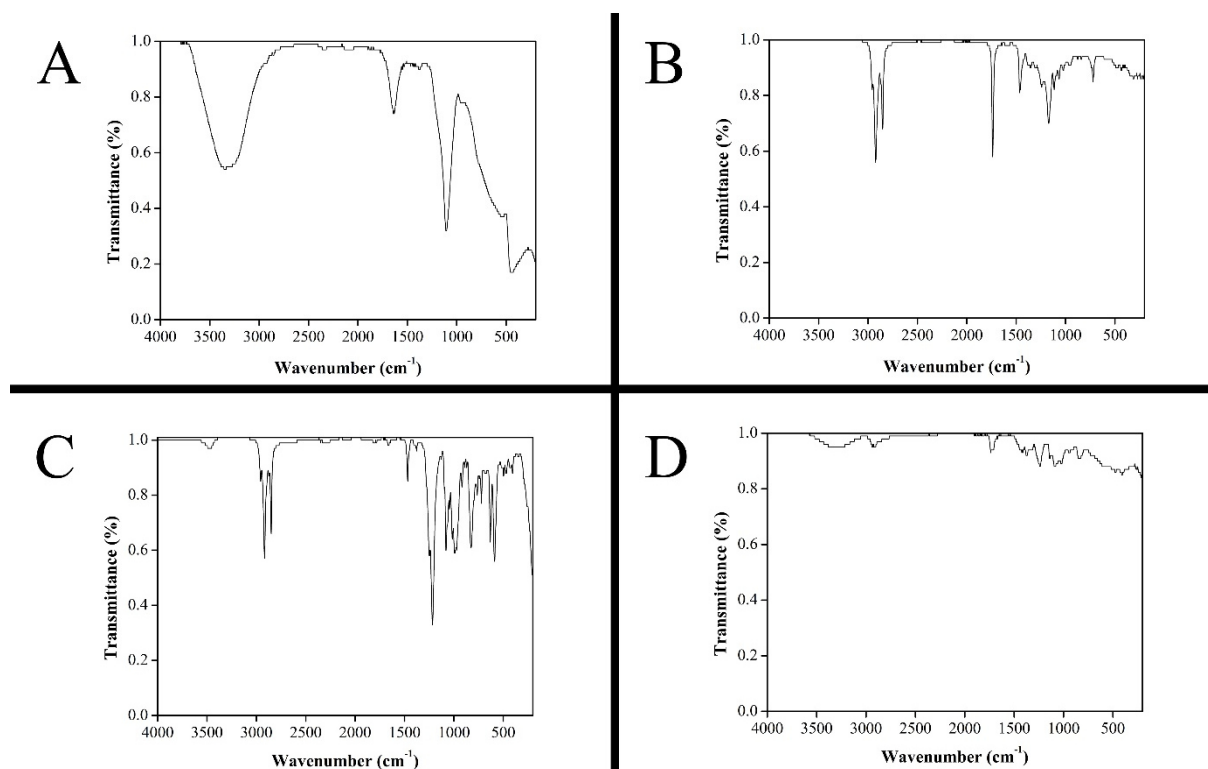


Fig. 5.2 ATR-IR spectra of educts silica sol (A), butyl stearate (B), sodium dodecyl sulfate (C) and poly(vinyl alcohol) (D). ATR-IR peaks: (A) 3700 - 2900, 1647, 1110, 456 cm^{-1} ; (B) 2922, 2854, 1738, 1465, 1174, 721 cm^{-1} ; (C) 2958, 2917, 2849, 1468, 1218, 1081, 1017, 994, 9973, 828, 633, 591 cm^{-1} ; (D) 3350 - 3000, 2942, 1741, 1424, 1244, 1096, 853 cm^{-1} .

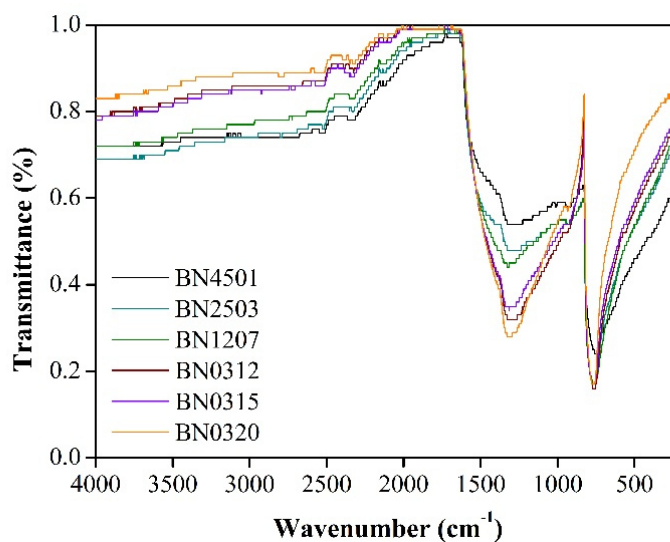


Fig. 5.3 ATR-IR spectra of pure hBN HeBoFill501 (BN4501), HeBoFill 491 (BN2503), HeBoFill64 (BN1207), HeBoFill111 (BN0312), HeBoFill230 (BN0315) and HeBoFill205 (BN0320). ATR-IR peaks of BN2503: 1316, 770 cm^{-1} .

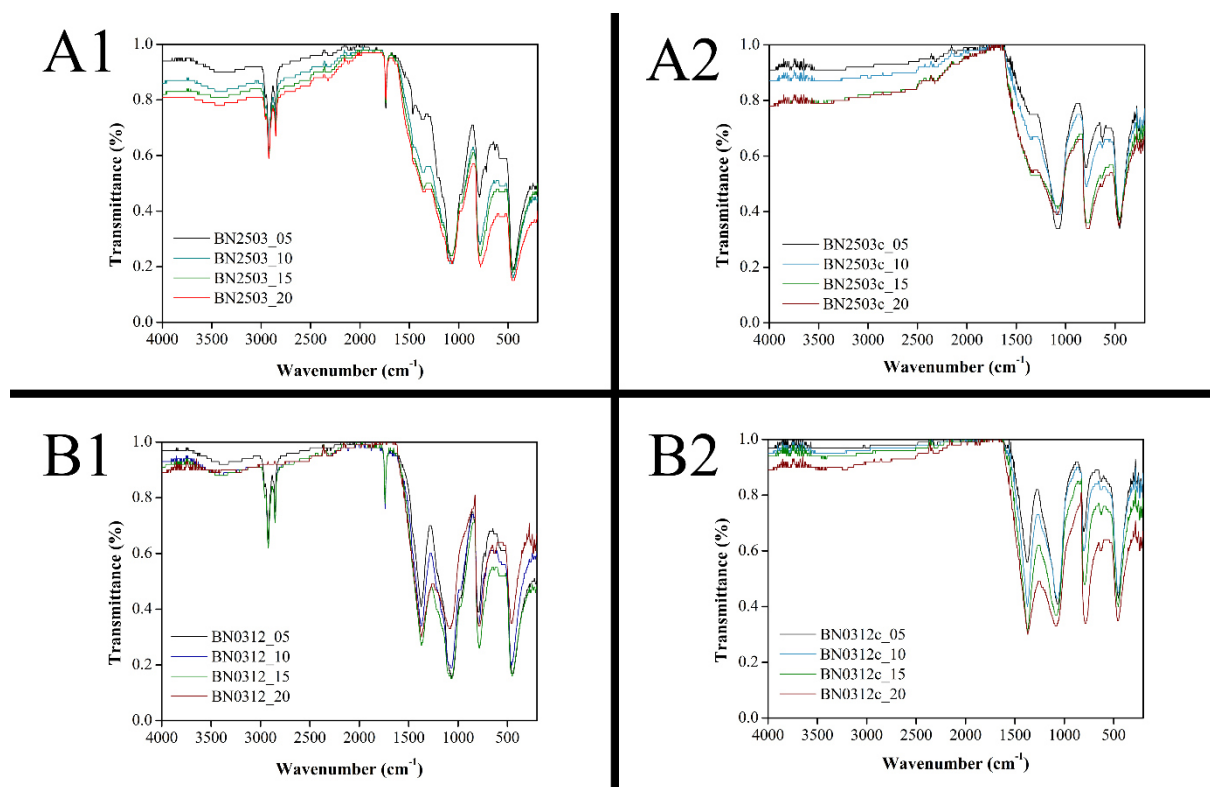


Fig. 5.4 ATR-IR spectra of ss-PCMs BN2503 (A1), BN2503c (A2), BN0312 (B1) and BN0312c (B2). The ss-PCMs marked with a “c” are calcined at 600 °C for 6 h and represent the pure silica network with boron nitride in the ss-PCM. ATR-IR peaks: (A1, BN2503_20) 2924, 2854, 1383, 1071, 789, 461 cm^{-1} ; (A2, BN2503c_20) 1381, 1098, 790, 464 cm^{-1} ; (B1, BN0312_20) 2923, 2854, 1740, 1378, 1092, 792, 457 cm^{-1} ; (B2, BN0312c_20) 1370, 1095, 793, 462 cm^{-1} .

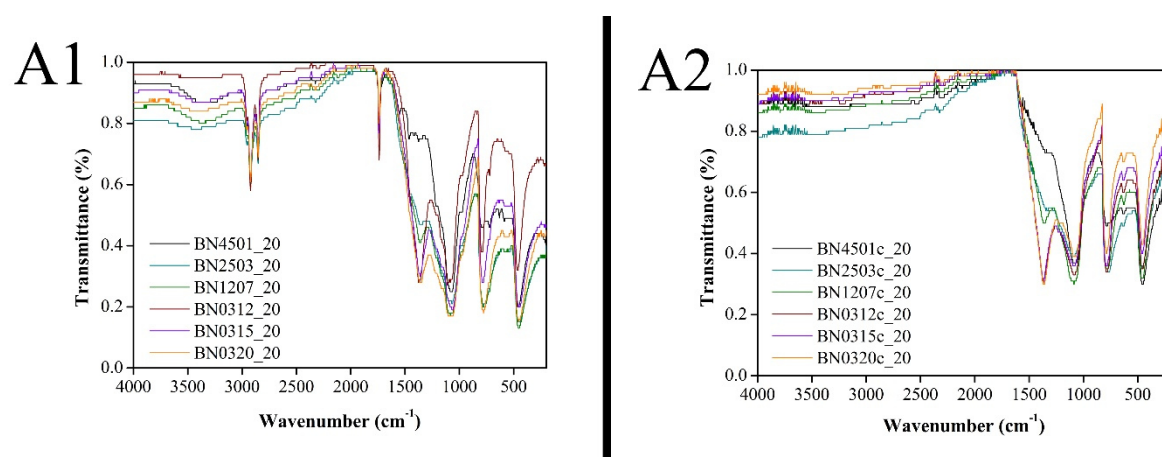


Fig. 5.5 ATR-IR spectra of all samples from BN4501_20 to BN0320_20 (A1) and all calcined samples from BN4501c_20 to BN0320c_20 (A2). The ss-PCMs marked with a “c” are calcined at 600 °C for 6 h and represent the pure silica network with boron nitride in the ss-PCM. ATR-IR peaks: (A1, BN2503_20) 2924, 2854, 1383, 1071, 789, 461 cm^{-1} ; (A2, BN2503c_20) 1381, 1098, 790, 464 cm^{-1} .

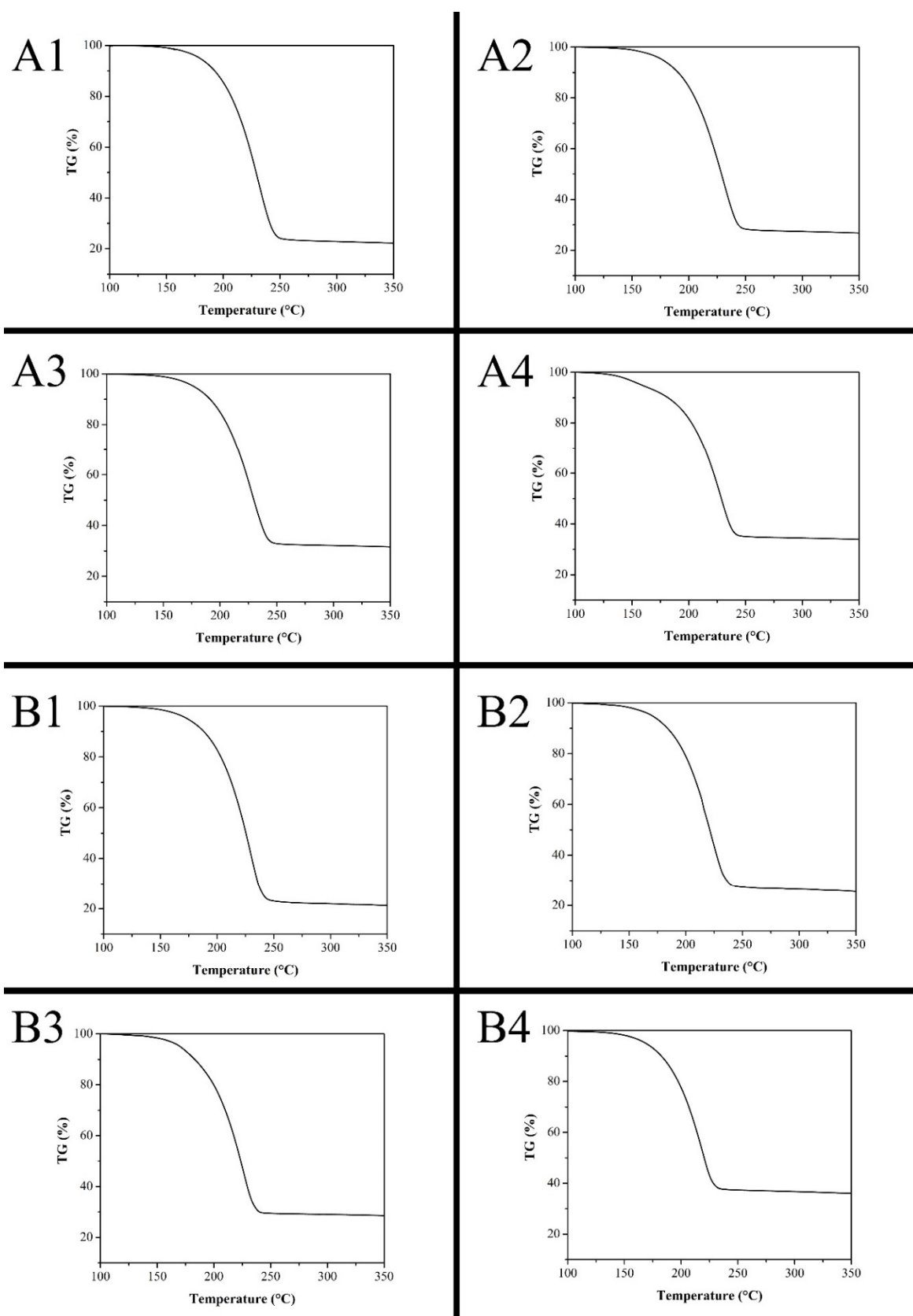


Fig. 5.6 TG curves of ss-PCMs BN04501_05 (A1), BN4501_10 (A2), BN4501_15 (A3), BN4501_20 (A4), BN2503_05 (B1), BN2503_10 (B2), BN2503_15 (B3) and BN2503_20 (B4).

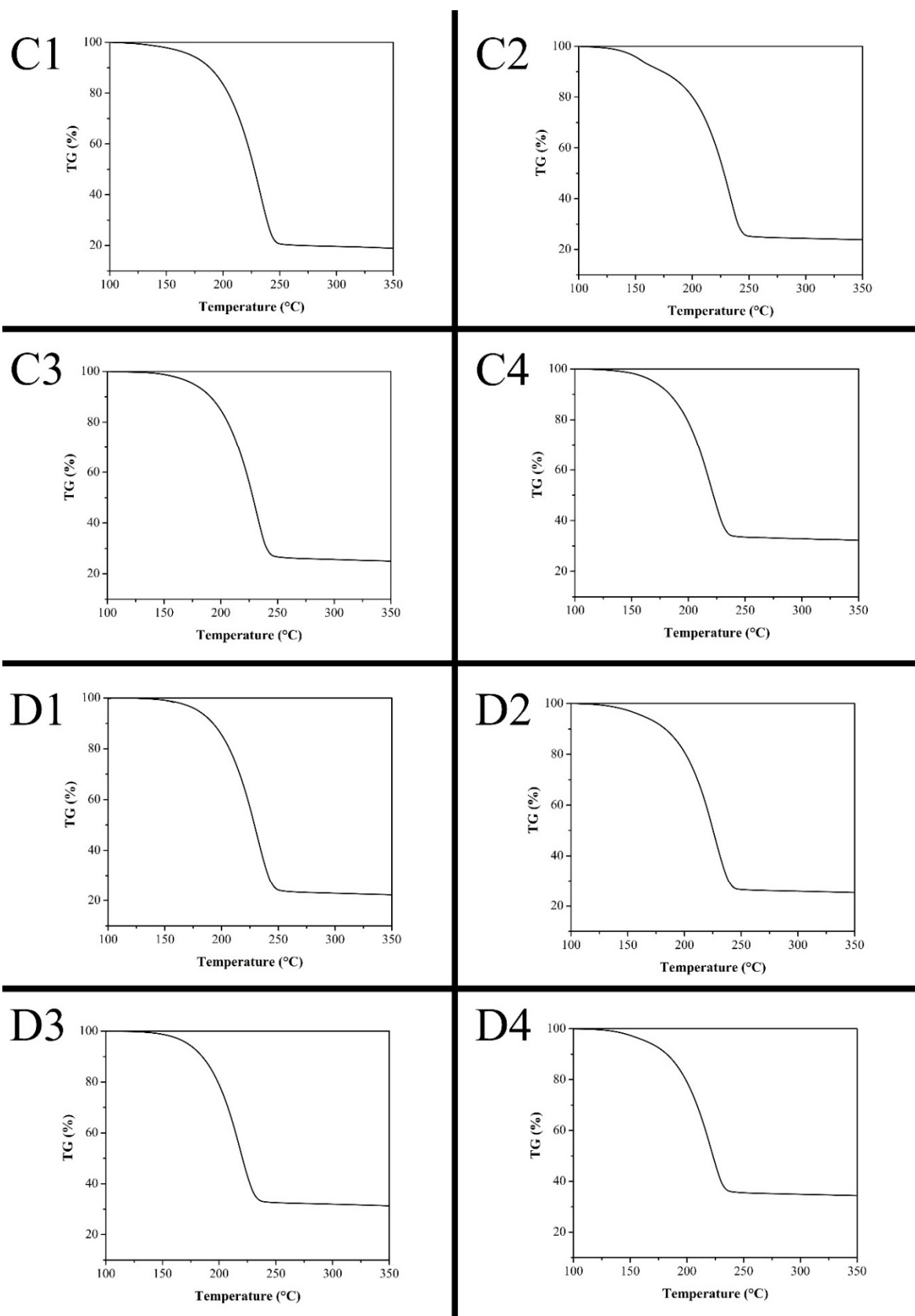


Fig. 5.7 TG curves of ss-PCMs BN1207_05 (C1), BN1207_10 (C2), BN1207_15 (C3), BN1207_20 (C4), BN0312_05 (D1), BN0312_10 (D2), BN0312_15 (D3) and BN0312_20 (D4).

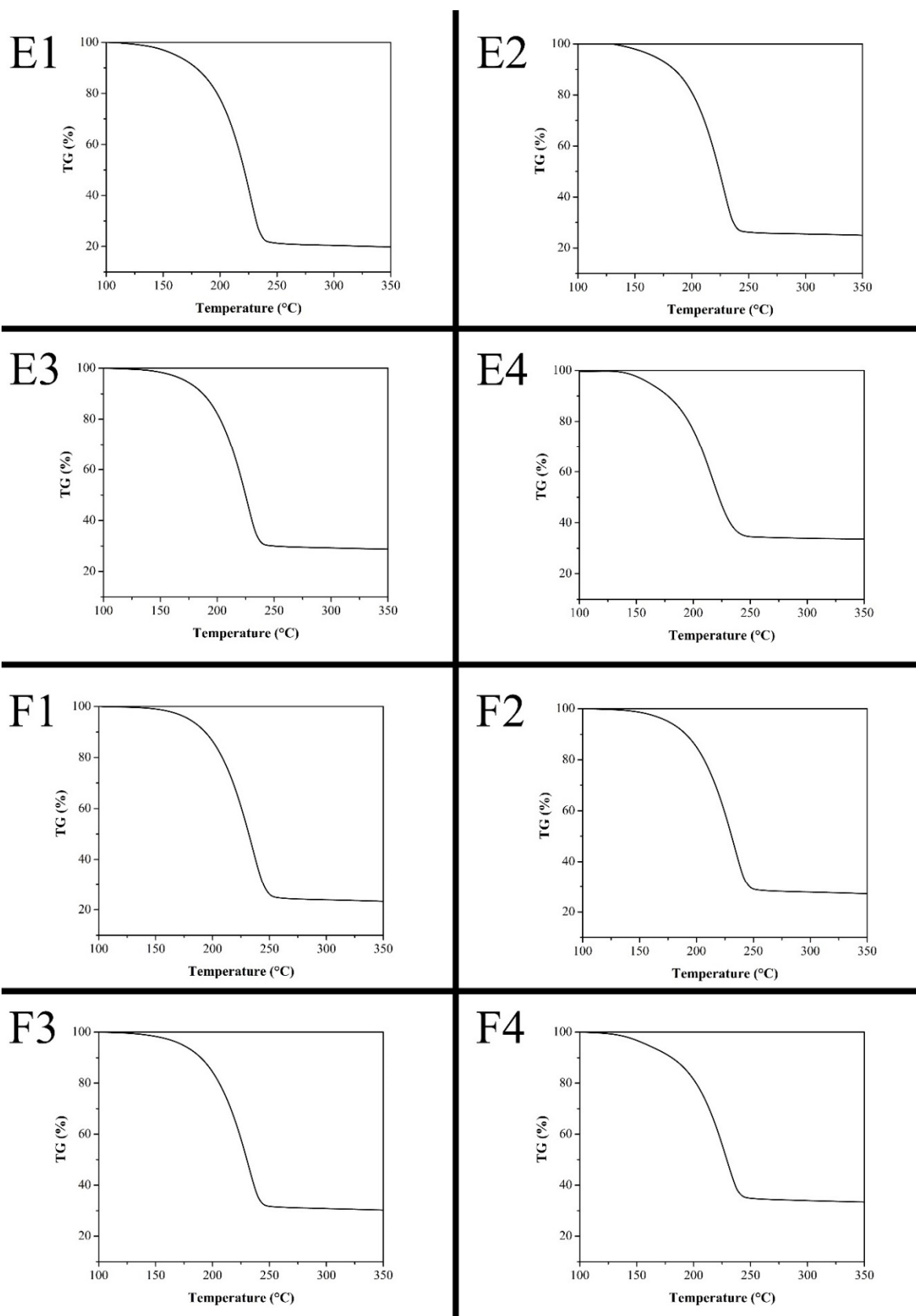


Fig. 5.8 TG curves of ss-PCMs BN0315_05 (E1), BN0315_10 (E2), BN0315_15 (E3), BN0315_20 (E4), BN0320_05 (F1), BN0320_10 (F2), BN0320_15 (F3) and BN0320_20 (F4).

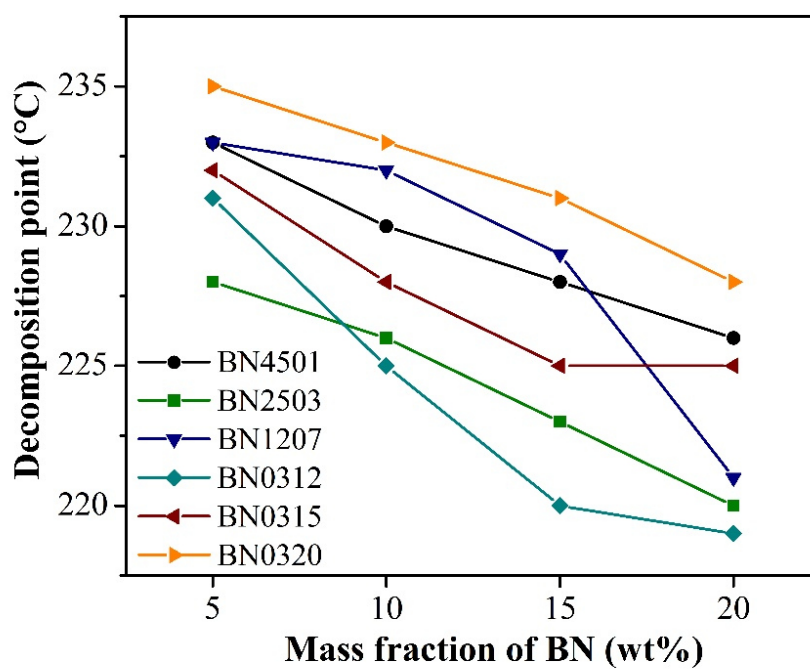


Fig. 5.9 Decomposition points of ss-PCM sample row BN4501, BN2503, BN1207, BN0312, BN0315 and BN0320 in dependence of the BN mass fraction. Data of the decomposition points of ss-PCM sample row BN2503 and ss-PCMs of the sample row BN4501 - BN0320 containing 10 wt% and 20 wt% BN are taken from our related research article [1].

Table 5.1 Decomposition points of pure BS, sample BN0 and ss-PCMs BN4501 - BN0320 measured via TG. TG data was processed via OriginLab 8.1 to calculate the decomposition points. Data of the decomposition points T_G of BS, BN0, ss-PCM sample row BN2503 and ss-PCMs of the sample row BN4501 - BN0320 containing 10 wt% and 20 wt% BN are taken from our related research article [1].

Sample	T_G (°C)
BS	218
BN0	216
BN4501_05	233
BN4501_10	230
BN4501_15	228
BN4501_20	226
BN2503_05	228
BN2503_10	226
BN2503_15	223
BN2503_20	220
BN1207_05	233
BN1207_10	232
BN1207_15	229
BN1207_20	221
BN0312_05	231
BN0312_10	225
BN0312_15	220
BN0312_20	219
BN0315_05	232
BN0315_10	228
BN0315_15	225
BN0315_20	225
BN0320_05	235
BN0320_10	233
BN0320_15	231
BN0320_20	228

3.5.6 Experimental Design, Materials and Methods

3.5.6.1 Materials

The stabilized silica sol of type Köstrosol 0730 is a suspension of 30 wt% colloidal silica particles with a 7 nm average particle diameter in water, and was obtained by *Chemiewerk Bad Köstritz*, Germany. Butyl stearate (BS) is a technical grade product (40 - 60%) and was purchased by *Alfa Aesar*. The co-polymer poly(vinyl alcohol) (PVA) has an average molecular weight of 22000 and is hydrolyzed by 88 % (PVA, 88 % hydrolyzed, average M.W. 22000). PVA was purchased by *ACROS Organics*. The surfactant sodium dodecyl sulfate (SDS) was purchased as dust-free pellets with a purity over 99 % (GC) by *Sigma-Aldrich*. The different hexagonal boron nitride platelets (BN) of HeBoFill type (510, 490, 641, 110, 230, 205) were obtained by *Henze Boron Nitride Products AG*, Germany. The BN of HeBoFill type have the following particle sizes and specific surface areas: 45 μm , 1 m^2/g (HeBoFill 510); 25 μm , 3 m^2/g (HeBoFill 490); 12 μm , 7 m^2/g (HeBoFill 641); 3 μm , 12 m^2/g (HeBoFill 110); 3 μm , 15 m^2/g (HeBoFill 230); 3 μm , 20 m^2/g (HeBoFill 205). Tetramethylsilane was purchased by *Sigma-Aldrich*. Deionized water was in our study.

3.5.6.2 Methods

High Power Decoupling (HPDEC) Magic Angle Spinning (MAS) ^{29}Si NMR was analyzed on a Bruker DRX-400 WB NMR spectrometer by *Bruker Biospin* (Karlsruhe, Germany). The spectrometer was equipped with a 4-mm double-resonance MAS probe maintained at $-10\text{ }^\circ\text{C}$ by a temperature control unit. The Larmor frequency was set to 79.49 MHz and the spinning speed was set to 10 kHz. It was worked with a repetition delay of 40 s. A total of 2000 to 3500 scans were performed for each sample. Tetramethylsilane (TMS) was used as external reference and the ss-PCM sample scanning was carried at a radio-frequency field strength of 42 kHz as a $\pi/2$ pulse during an acquisition time of 25 ms. The liquid stabilized sol was measured via ^{29}Si NMR without MAS at $20\text{ }^\circ\text{C}$ and the measurement settings were changed as followed: repetition delay of 15 s, number of scans of 12000, acquisition time during a $\pi/2$ pulse of 30 μs .

Attenuated total reflection infrared spectroscopy (ATR-IR) was carried out via a Tensor 27 spectroscope equipped with a diamond ATR unit from *Bruker* at room temperature ($25\text{ }^\circ\text{C}$).

The samples were put directly on the diamond ATR unit and were scanned for a total of 60-times. The peaks of the signals were determined via the peak analyzer option in *OriginLab 8.1*.

The thermal stability was analysed via thermogravimetry (TG) using a STA 409 C/CD thermal analyser from *Netzsch*. An average amount of 100 mg of every ss-PCM sample was measured and heated from 25 °C to 400 °C at a heating rate of 1 °C/min. The raw data was exported and processed via *OriginLab 8.1*. For the calculation of the decomposition points, the first derivative of the TG curve was calculated and the value of the maximum of the first derivative curve was determined.

3.5.7 Ethics Statement

The authors have both collected the presented data and written this article according to generally standards of ethical behavior in scientific publishing.

3.5.8 CRediT authorship contribution statement

Felix Marske: Conceptualization, Methodology, Validation, Formal analysis, Investigation, Data curation, Writing – original draft, Visualization. **Titus Lindenberg:** Formal analysis, Resources. **Juliana Martins Souza e Silva:** Formal analysis, Resources, Writing – review & editing. **Ralf B. Wehrspohn:** Resources, Writing – review & editing. **A. Wouter Maijenburg:** Writing – review & editing, Resources. **Thomas Hahn:** Supervision, Project administration, Funding acquisition. **Dirk Enke:** Writing – review & editing, Supervision.

3.5.9 Acknowledgments

The authors of this paper thank Mr. Alexey G. Krushelnitsky for ²⁹Si NMR measurements and Mr. Jaques Schmidt for ATR-IR measurements. The authors of this paper acknowledge the financial support of the Open Access Publication Fund of the Martin-Luther-University Halle-Wittenberg. Juliana Martins de Souza e Silva and Ralf B. Wehrspohn acknowledge the DFG for the granted project WE 4051/21-1. Additionally, Titus Lindenberg and A. Wouter Maijenburg acknowledge financial support from the BMBF (grant no. FKZ:03Z22HN11).

3.5.10 Declaration of Competing Interest

The authors declare that they have no known competing financial interests or personal relationships which have or could be perceived to have influenced the work reported in this article.

3.5.11 References

- [1] F. Marske, T. Lindenberg, J. Martins de Souza e Silva, R. B. Wehrspohn, A. W. Maijenburg, T. Hahn and D. Enke, Size and surface effects of hexagonal boron nitrides on the physicochemical properties of monolithic phase change materials synthesized via sol-gel route, *Appl. Therm. Eng.* 196 (2021), 117325.
- [2] F. Marske, J. Martins de Souza e Silva, R. B. Wehrspohn, T. Hahn and D. Enke, Synthesis of monolithic shape-stabilized phase change materials with high mechanical stability via a porogen-assisted *in situ* sol-gel process, *RSC Adv.* 10 (2020), 3072–3083.

4 Summarizing Discussion

The characterization methods, the synthesis approach and the thermal conductivity enhancement strategies presented in the five publications are discussed and situated in their literary and scientific context. Interpretations of the main results are described, including advantages, disadvantages and limitations of the synthesis approaches, the ss-PCMs and analytical methods developed and used in this work. Additional information are given about the influence of the pH value, the chemical nature of surfactants and the molecular mass of PVA during gelation, which are not presented in the five publications. Moreover, ss-PCMs based on CrodaTherm™ 21 as bio-based PCM and expanded graphite (EG) as substitute of BS as PCM and boron nitride (BN) as thermal conductive additive have been synthesized and are analyzed as well.

4.1 Synthesis of ss-PCMs

The novel porogen-assisted sol-gel synthesis was developed step by step starting from stabilized silica sol and pure butyl stearate (BS). Stabilized silica sol is non-toxic and inflammable, has an adjustable particle size distribution and is available for a low market price [1,2]. However, only two master theses were published so far about the synthesis of monolithic and crack-free silica monoliths based on stabilized silica sol by subcritical drying [3,4]. The herein described silica monoliths were filled with air and should be used as thermal insulation material in the future. Stabilized silica sols with small particle sizes (7 nm, 30 wt% silica) were applied in these studies because they were best suited to build small pore structures [3] and, thus, are taken as starting material for the synthesis of ss-PCMs in the present work. Educts, polymer-induced phase separation strategies and conditions (temperature, pH, stirring rates) of the sol-gel process in these studies strongly differ from this work. Generally, alkyl silicates or water glass are used as silica precursors for the subcritical synthesis of silica monoliths. Therefore, the development of sol-gel syntheses based on stabilized silica sol is highly attractive for the sol-gel science as well as getting a deeper insight into the stepwise process of these syntheses.

Regarding the pure silica sol, the gelation of the silica particles in the stabilized sol is prevented by small amounts of cations, such as sodium, located on the outer surface of the silica particles. Longer times of heating (80 °C, 7 - 14 days) induce the gelation process, possibly due to a higher rate of molecular Brownian motion of the silica particles and aggregates. After

gelation, the wet silica gel is completely transparent, pointing to a micro- and mesoporous silica structure. The subcritical drying process destroys the monolithic form of the silica gel and a silica powder is obtained. So, a careful selection of the process parameters is mandatory.

Butyl stearate as organic PCM is a typical example of a fatty acid ester, which was found in many PCM studies before because of its high chemical stability and high decomposition point compared to paraffins [5]. Butyl stearate is, however, only available as technical grade product for an affordable market price and provides low latent heats of 125 J/g compared to pure paraffins (> 200 J/g).

If higher amounts of BS (>20 wt%) are mixed with the silica sol and heated to at least 40 °C, the emulsion is separated after some seconds and the silica particles start to gel in the aqueous phase on the bottom of the reaction vessel due to facilitated silica condensation reactions at the interface between aqueous and PCM phase. To stop macroscopic phase separations during gelation, the viscosity of the reaction mixture is increased by poly(vinyl alcohol) (PVA) and the emulsion is stabilized by a surfactant, sodium dodecyl sulfate (SDS), with a high hydrophilic lipophilic balance (HLB) value above 10 (HLB: 40) to obtain PCM (droplets) in water (continuous phase) emulsions. With these porogens, mechanically stable ss-PCM monoliths with up to 86 wt% PCM, high chemical stabilities, high long-term performances of at least 6000 melting and freezing cycles and compressive strengths of up to 1.2 MPa at 10 °C (0.7 MPa at 30 °C) could have been synthesized. The ss-PCMs can be synthesized without PVA, but not without SDS, underlining the importance of the surfactant for the sol-gel synthesis. However, the ss-PCMs without PVA have a much lower compressive strength of 6 kPa at 10 °C (2 kPa, 30 °C).

The SDS molecules seem to cover the surface of the PCM droplets in the emulsion and, thus, hinder the emulsion from macroscopic phase separation (Fig. 2.1, Fig. 2.2). By magnetic stirring with higher shear forces (> 700 rpm), air inclusions are stabilized as bubbles during synthesis, too. During gelation, silica builds an interconnected spherical silica structure on top of the PCM droplets that are covered by SDS or on top of air bubbles, which both act as a typical template structure during synthesis (Fig. 2.1). The inclusion of air should be minimized by stirring with lower shear forces (600 - 700 rpm) because of the low thermal conductivity of air, which would otherwise affect the quality of the ss-PCM. The concentration of the surfactant SDS in the solution is highly important to cover the whole PCM phase in the emulsion with SDS molecules. By varying the SDS amount it could have been shown that 5 wt% SDS (0.32 mol/l) seem to cover the BS phase (83 wt%) to the highest extent because the silica pore structures in the ss-PCMs had the lowest average macropore diameter (Table 2.3). A smaller

dimension of the spherical silica structure always increases the thermal conductivity and the compressive strength as revealed in the present study. Thus, ss-PCMs synthesized with 5 wt% (0.32 mol/l) SDS have the highest compressive strength of the SDS sample row (Fig. 2.10). Higher SDS concentrations decrease the viscosity of the emulsion and the silica structure is fractured during drying (Fig. 2.7). Consequentially, the compressive strength and the thermal conductivity of BS in the ss-PCM are decreased from 1.0 MPa to 0.4 MPa (10 °C) and 0.37 W/mK to 0.28 W/mK (10 °C), respectively. Moreover, a higher thermal conductivity and a higher heat transfer in the PCM phase result always in lower decomposition points of PCM. By increasing the SDS amount from 2.5 wt% to 7 wt%, the decomposition point of BS in the ss-PCM structure is decreased by 7 °C to 209 °C (Table 2.3). Reasons for the low emulsion viscosity at high SDS concentrations could be hydrogen bonding and electrostatic interactions of excess SDS molecules in solution, which are not attached to the surface of the PCM droplets and interact with PVA and silica structures by electrostatic repulsion effects during gelation. Therefore, the excess SDS in the aqueous phase should act as a structure-directing agent and alter the dimension and interconnectivity of the silica structure.

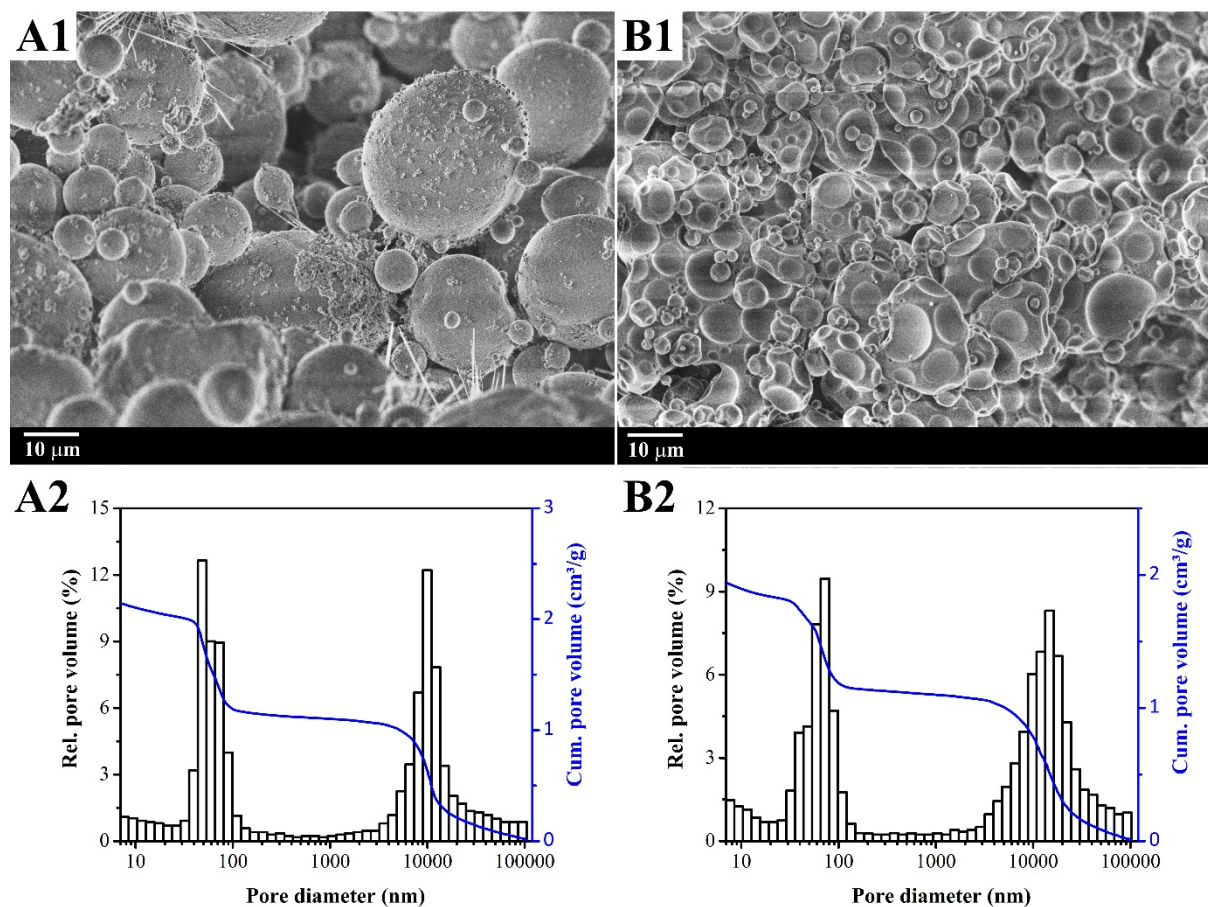


Fig. D1 SEM images (1) and mercury intrusion measurements (2) of the calcined ss-PCMs synthesized with the anionic surfactants sodium stearate (A) and sodium dodecyl benzenesulfonate (B).

It is also possible to synthesize monolithic ss-PCMs with different surfactants exhibiting high HLB values, such as sodium stearate (St) and sodium dodecyl benzenesulfonate (SDBS) with HLB values of 18 [6] and 11 [7], respectively (Fig. D1). The silica structure of the calcined ss-PCMs based on St consists of core-shell (cs) encapsulated PCM droplets, which are weakly-interconnected by covalent siloxane bonds and should be kept together mostly by physical interactions. The pore volume of these ss-PCMs is 2.1 cm³/g, the average pore diameter is 2378 nm and the pore distribution has two pore regions with modal pore diameters of 57 nm (pores on top of the cs-PCMs) and 10471 nm (cs-PCM diameter). The small pore volume compared to ss-PCMs synthesized with SDS as surfactant points to a leakage of PCM, which is supported by observing a liquid film on the outer surface of the ss-PCM. The ss-PCMs based on SDBS have silica structures formed by connected cs-PCMs, too. However, the cs-PCM particles are more connected and slightly deformed (Fig. D1 (B)). They have pore volumes of 2.0 cm³/g, average pore diameters of 5734 nm and similar pore distributions with two pore regions with modal pore diameters of 74 nm and 12903 nm. That is why the compressive strength of the ss-PCMs based on St and SDBS is quite low with 6 kPa at 30 °C (30 kPa at 10 °C) and 250 kPa at 30 °C (510 kPa at 10 °C). The shape-stability shows values of 95 % (St) and 100 % (SDBS) (100 °C, 7 days). Because of the low mechanical stability of these ss-PCMs, they were not analyzed further for the development of ss-PCMs, but their physicochemical properties are currently under investigation for the synthesis of cs-PCMs. No study is published so far about the synthesis of cs-PCMs by stabilized silica sol and, thus, further research is mandatory.

Cationic surfactants, such as cetyl trimethyl ammonium bromide (CTABr) (HLB: 21) [8], were also applied as surfactants in the sol-gel synthesis, but no ss-PCMs could be synthesized, maybe due to high attractive electrostatic forces between the negatively charged silica particles and the positively charged surfactant molecules under basic conditions.

Analyzing the influence of PVA as a porogen, it could have been shown that smaller amounts of PVA below 0.6 g seem to be unfeasible for a proper increase of the reaction mixture viscosity and, hence, to stop the macroscopic phase separation of the emulsion after stirring. Higher amounts of PVA above 0.6 g separate the emulsion in large hydrophilic and small hydrophobic regions. The structure of PVA in the ss-PCM samples before and after calcination cannot be imaged by SEM (Fig. 2.3). As a consequence, PVA should act as structure-directing agent and not as (hard) template during the sol-gel synthesis as also has been described for polymer-induced phase separations in sol-gel systems [9,10]. The PVA-induced phase separation process generates large aqueous microchannels between the PCM droplets covered with SDS during gelation. The larger microchannels should accelerate the water

evaporation process and shrink by the volume of water evaporated during the subcritical drying until all PCM/SDS droplets are covered by silica and an interconnected spherical silica structure is formed. Therefore, all pores are filled with PCM after drying and the water is completely removed from the ss-PCM. In this process, water should mainly evaporate by film diffusion processes and not as a gaseous phase because the rate of water evaporation decreases during the drying process due to the shrinking pore channels (Fig. D2).

It is reported that small amounts of PVA can order and stabilize secondary silica particles and silica aggregates during gelation by hydrogen bonding, which is named as sticker-effect (Fig. 15). Additionally, PVA can wrap around silica particles and aggregates in solution and hinder the formation of an interconnected silica phase in the ss-PCM during gelation, when the PVA concentration is too high. This effect is called bumper-effect. Because of the bumper-effect and the larger aqueous pore channels at higher PVA concentrations, the silica structures are shielded from each other and the dimension of the aqueous pore channels varies widely during gelation. Moreover, the silica structure of the ss-PCMs is fragmented and collapsed during drying, and the compressive strength of the ss-PCM is decreased from 1.24 MPa (0.68 MPa at 30 °C; 0.6 g PVA) to 0.58 MPa (0.34 MPa at 30 °C; 1.2 g PVA) at 10 °C.

The fragmented silica structures of the calcined ss-PCMs with high PVA concentrations (1.2 g) have an approximately eight times higher macropore width (8801 nm), a 17 % lower thermal conductivity at 10 °C (0.31 W/mK) and a marginal PCM leakage on the surface (2 %). The

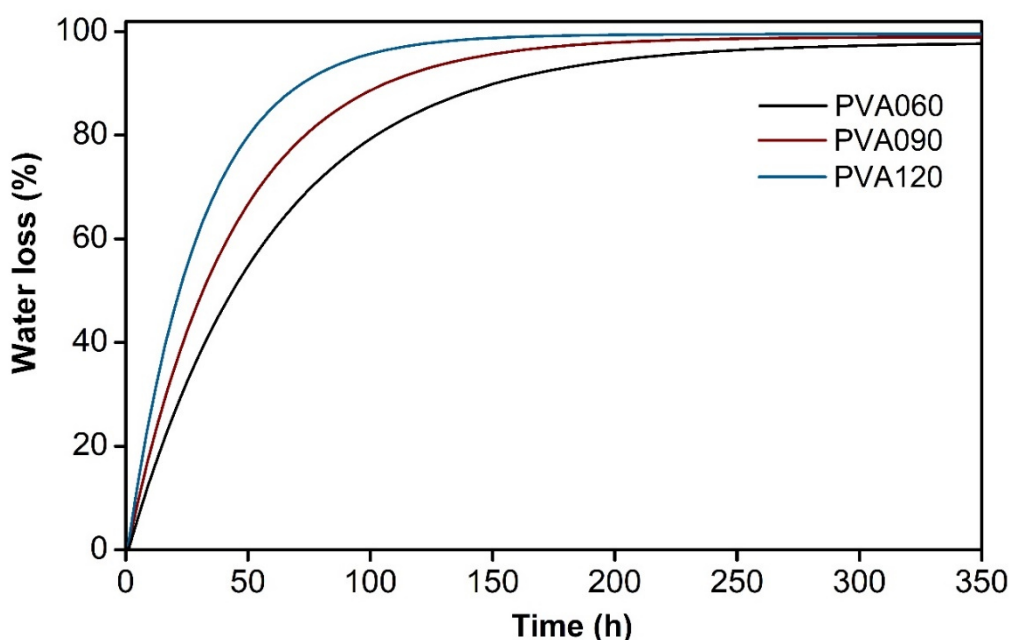


Fig. D2 Subcritical drying of ss-PCMs PVA060 (0.6 g PVA), PVA090 (0.9 g PVA) and PVA120 (1.2 g PVA), first at 40 °C for 168 h, then at 60 °C for 144 h and finally at 100 °C for 48 h. The water loss was recorded depending on the time (h). At a high PVA concentration, water evaporation of the ss-PCMs is faster due to larger pore channels.

concentration of PVA must be as low as possible for the formation of mechanically stable ss-PCMs. In summary, the sticker-effect, the increase of the emulsion viscosity and the accelerated water evaporation during drying underline the multiple functions of PVA and its beneficial role at a low concentration (0.6 g) in the sol-gel synthesis of ss-PCMs. In contrast to the surfactant, the PVA does not change the form of the spherical structure of the silica matrix completely and should play a supportive role in the sol-gel synthesis of mechanically stable ss-PCMs. Larger PVA polymers with molecular weights (M.W.) of more than 31.000 g/mol have performed not as good as PVA with M.W. of 13.000 - 23.000 g/mol in the sol-gel synthesis. For example, ss-PCMs synthesized with similar PVA concentrations (0.6 g PVA) but higher M.W. of 31.000 - 50.000 g/mol have low mechanical stabilities (125 kPa at 30 °C) and small shape-stabilities of 90 %. With even higher M.W. (88.000 - 97000 g/mol), no ss-PCMs could be synthesized at all, maybe due to an increased bumper-effect of longer PVA polymer chains. Because of the poor mechanical properties, these ss-PCMs were not further analyzed. However, the effect of the M.W. of PVA should be investigated in detail to gain mechanistical insights in the formation process of ss-PCMs in future studies.

The sol-gel synthesis of ss-PCMs highly depends on a basic pH value. If the pH value is decreased from 9.2 to 4.7 by addition of hydrochloric acid (3 M) to the synthesis of standard sample FS4, the ss-PCMs HCl3 are broken during subcritical drying, have shape-stabilities of 97 % and have low compressive strengths of 9 kPa at 30 °C (45 kPa at 10 °C) (Table D1).

Table D1 Physicochemical properties¹ of ss-PCMs HCl1 to HCl3 and NH1 to NH2 synthesized with 9 g Sol, 0.8 g SDS, 6.75 g H₂O, 20 g BS and 0.6 g PVA, and 0.2 ml HCl (HCl sample row) or 0.2 ml NaOH (NH sample row).

Sample	c (acid / base)	pH	σ at 10 °C (MPa)	σ at 30 °C (MPa)	$\Phi^{a,b}$ (%)	V_{total}^a (cm ³ /g)	V_{macro}^a (cm ³ /g)	D_{macro}^a (nm)	V_{meso}^b (cm ³ /g)
FS4	-	9.2	0.68	1.24	95	7.80	6.98	1007	0.82
HCl1	1M HCl	7.9	0.66	1.13	95	7.94	7.29	1762	0.65
HCl2	2M HCl	5.9	0.17	0.52	94	7.10	6.48	2082	0.62
HCl3	3M HCl	4.7	0.09	0.38	95	8.21	7.16	3692	1.08
NH1	1M NaOH	9.6	0.76	1.29	95	7.92	6.96	1155	0.96
NH2	2M NaOH	9.9	0.86	1.46	94	7.36	6.38	510	0.98

1: Molar concentration c of acid (HCl) or base (NaOH), pH value of the reaction mixture during gelation, compressive strength σ at 10 °C and 30 °C, porosity Φ , total pore volume V_{total} , macropore volume V_{macro} , mean macropore width/50% D_{macro} and mesopore volume V_{meso} of ss-PCMs. a: determined from mercury intrusion measurements after ss-PCM calcination. b: determined from nitrogen sorption measurements after ss-PCM calcination.

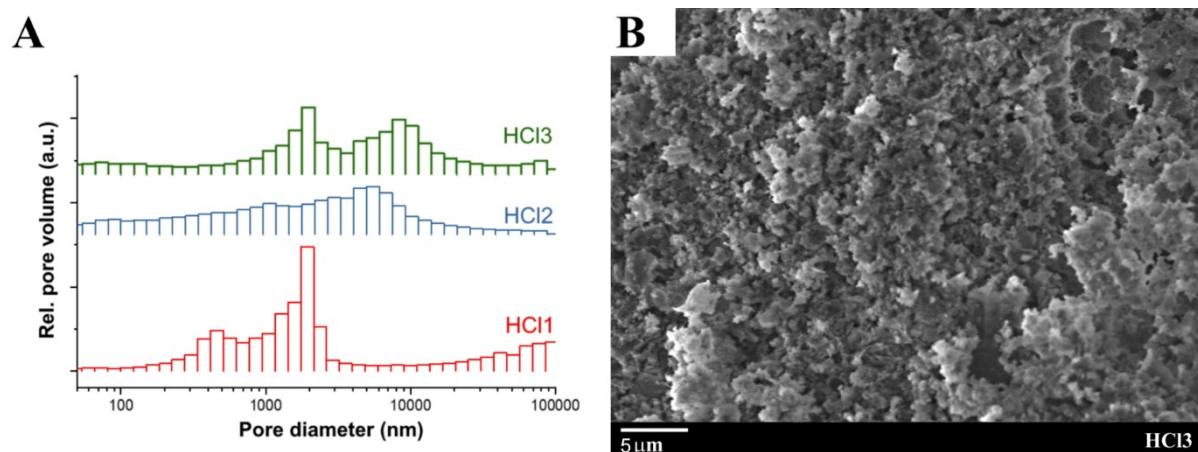


Fig. D3 Mercury intrusion measurements of calcined ss-PCMs HCl1, HCl2 and HCl3 (A). SEM image of the calcined ss-PCM HCl3 (B).

The silica structure of HCl3 is fragmented and has lost its spherical form nearly completely (Fig. D3). The Hg measurements detect interparticular space as silica pore volumes in calcined ss-PCM HCl3. Thus, the average macropore diameter of HCl3 is increased to 3692 nm. An acidic pH value decreases the rate of condensation and increase the rate of hydrolysis reactions during sol-gel syntheses. For this reason, the acidic pH conditions could slow down the silica particle growth and increase the agglomeration of silica particles of a specific size. Moreover, the critical micelle concentration (CMC) of SDS is decreased at a pH of 5 because of a decreased charge density at the surface of the SDS micelles by the pronounced appearance of hydrogen ions at low pH values [11]. The reduced charge density decreases the stability of the SDS micelle and therefore, could decrease the stability of the PCM droplets in the aqueous phase during gelation [11]. The decreased CMC of SDS and the higher hydrolysis rate could both hinder the formation of an interconnected spherical silica structure.

In contrast, the pH value of the reaction mixture of FS4 is increased from 9.2 to 9.9 by addition of NaOH (2 M) and the obtained ss-PCM is named as NH2 (Table D1, Fig. D4). No ss-PCMs with a pH value above 9.9 could be synthesized, possibly due to the increased dissolution rate of silica particles under strong basic conditions. In ss-PCM NH2 synthesized at a high pH value of 9.9, the average macropore width of FS4 is decreased from 1007 nm to 510 nm, the shape-stability is kept constant at 100 % and the compressive strength is increased from 0.68 MPa to 0.86 MPa at 30 °C (1.24 MPa to 1.46 MPa, 10 °C) (Fig. D4). Faster condensation reactions could be a reason for the positive influence of the more basic pH value for the mechanical properties of ss-PCMs.

The latent heats of the ss-PCMs synthesized at different pH values are summarized in Table D2. These values are not affected by varying the pH value. In contrast, an increase in pH from 4.7 to 9.9 leads to a decrease of the supercooling temperatures of BS in the silica structure of

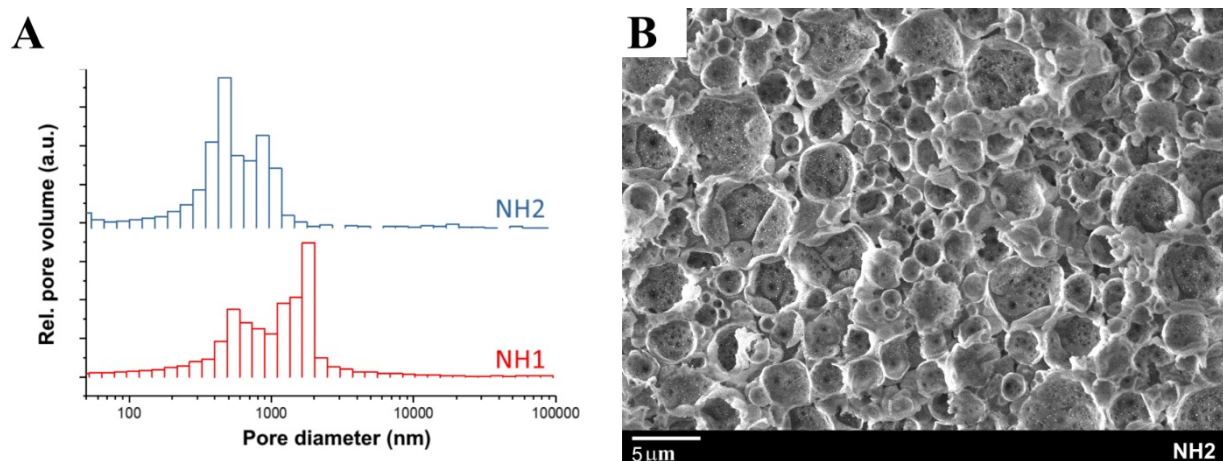


Fig. D4 Mercury intrusion measurements of calcined ss-PCMs NH1 and NH2 (A). SEM image of the calcined ss-PCM NH2 (B).

the ss-PCMs from 5.6 °C to 4.5 °C due to the higher interconnectivity of the silica structure. The thermal conductivity slightly increases with pH from 0.37 W/mK at 10 °C (0.22 W/mK, 30 °C) to 0.40 W/mK at 10 °C (0.24 W/mK, 30 °C). Therefore, the optimal pH value for the synthesis of ss-PCMs should be 9.9.

The amount and the chemical nature of the PCM affect the silica structure and the physicochemical properties of the ss-PCMs throughoutly. If low amounts of BS (69 wt%) are used for the ss-PCM synthesis, less SDS molecules are needed to cover the BS droplets in the emulsion and more SDS molecules can stabilize air inclusions as bubbles during gelation. This leads to an increased presence of silica pores filled with air and exhibiting pore sizes larger than 10000 nm and pore volumes of 0.6 cm³/g for ss-PCMs (69 wt% BS) (Fig. 1.9).

Table D2 Thermal properties¹ of FS4, samples HCl1 - HCl3 and samples NH1 and NH2 calculated by DSC and thermal conductivity measurements.

Sample	ΔH_{total} (J/g)	T_m (°C)	ΔT_s (°C)	$Ma(PCM)_{DSC}$ (wt%)	$Ma(PCM)_{max}$ (wt%)	E_{DSC} (%)	λ at 10 °C (mW/mK)	λ at 30 °C (mW/mK)
FS4	105	20.0	4.7	83.3	83.0	100.4	366	218
HCl1	106	19.8	4.9	84.0	83.0	101.2	355	209
HCl2	106	20.4	5.1	83.9	83.0	101.1	342	205
HCl3	105	20.2	5.6	83.5	83.0	100.6	334	196
NH1	107	19.6	4.8	84.7	83.0	102.1	384	235
NH2	107	19.5	4.4	85.0	83.0	102.4	398	237

1: Melting enthalpy of whole ss-PCM ΔH_{total} , melting point of BS signal T_m , supercooling ΔT_s , mean value for effective mass fraction of PCM, $Ma(PCM)_{DSC}$, highest value for effective mass fraction of PCM $Ma(PCM)_{max}$, PCM immobilization efficiencies E_{DSC} and thermal conductivity λ at 10 °C and 30 °C.

These air pores reduce the thermal conductivity and the compressive strength of the ss-PCMs (77 wt%) by 40 % and 75 % at 30 °C, respectively. The optimal ratio of BS to SDS was shown to be approximately 17:1 in this work.

If BS is substituted for paraffinic PCMs, the paraffins are emulsified as droplets in an aqueous phase in an analogous manner like BS. However, this macroemulsion is only stable for seconds from macroscopic phase separation due to the more hydrophobic nature of the paraffins. Therefore, the paraffins hexadecane (HD) or octadecane (OD) are mixed with the more polar BS in a ratio of 3:7 before they are emulsified (Fig. 3.4). After silica sol addition, the obtained macroemulsion is “frozen” during the gelation process and stopped from macroscopic phase separation. In general, the paraffinic ss-PCMs have similar physicochemical properties as the ss-PCMs based on BS, such as high shape stabilities (~100 %), spherical silica structures in the lower nano- to micrometer range (2 - 2000 nm), high compressive strengths up to 1.2 MPa at 5 °C (0.75 MPa at 40 °C), high long-term performances up to 3000 melting and freezing cycles and high chemical stabilities (Fig. 3.2, Fig. 3.3). Only the thermal properties of the paraffinic ss-PCMs vary from the ss-PCMs based solely on BS, such as the higher latent heats of 150 J/g (HD) and 160 J/g (OD), the melting points of 17 °C (HD) and 22 °C (OD) and the slightly decreased thermal stability of ~170 °C. If the PCM is hydrophobic and shape-stabilized during the sol-gel synthesis, the thermal properties of the ss-PCMs will mainly depend on the chemical nature of the PCM and the mechanical properties of the ss-PCMs synthesized from stabilized silica sol by sol-gel can be preserved. Consequentially, monolithic ss-PCMs with a broad range of different melting points and high heat storage capacities can be produced by the sol-gel synthesis. The need to increase the hydrophilicity of pure paraffins is, however, a disadvantage of the sol-gel synthesis because the high latent heats of pure HD (206 J/g) and OD (224 J/g) are decreased by the latent heat of BS (125 J/g). One possible solution is the increase of the reaction mixture viscosity during gelation. This can be achieved by either an acceleration of the gelation, for example by a more basic pH value, or by an increase in viscosity of the macroemulsion by a suitable additive, such as long-chain polymers. A second option is replacing BS in the paraffinic mixture by a hydrophobic PCM with a similar polarity. The company *Croda* sells fatty acid ester mixtures synthesized from plant-based feedstocks (product name: CrodaTherm™ bio-based PCMs) with a high purity and, thus, with a high latent heat [12]. For example, the bio-based PCM CrodaTherm™ 21 has a latent heat of 205 J/g and a melting point of 23 °C. After shape-stabilization of CrodaTherm™ 21, the obtained ss-PCM Cro consists of a similar interconnected spherical silica structure and has the same compressive strength (1.2 MPa, 5 °C; 0.73 MPa at 40 °C), but a higher latent heat of 167 J/g than the ss-PCMs synthesized with BS as technical product (Fig. D5). Even after

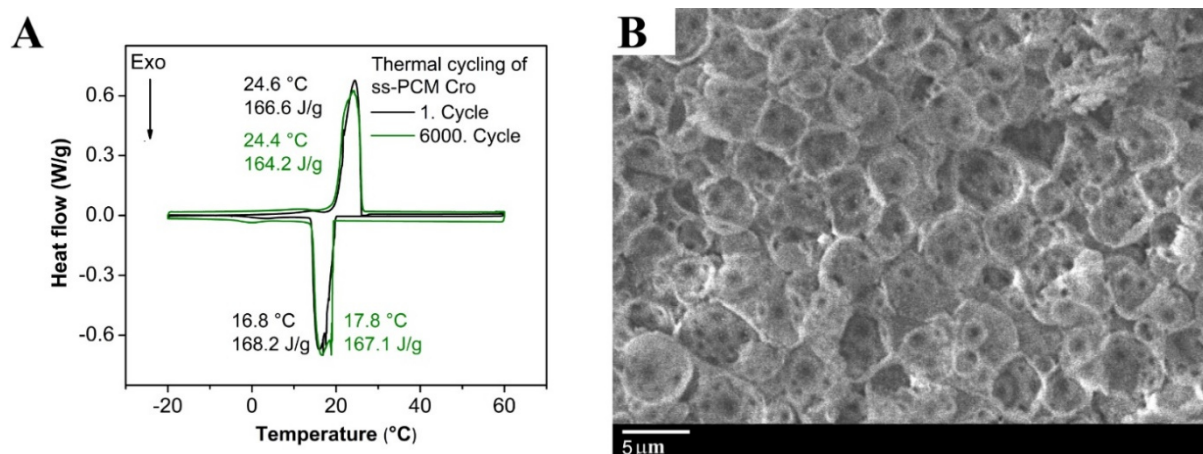


Fig. D5 DSC (A) of ss-PCM Cro and SEM image (B) of calcined ss-PCM Cro. Sample Cro is synthesized with PCM CrodaTherm™ 21 as substitute for BS in analogy to the synthesis of FS4.

6000 melting and freezing cycles, the ss-PCM Cro has nearly the same latent heat than before the cycling tests and a shape-stability of ~100 %, indicating a high long-term performance and durability.

The hydrophilic organic PCMs polyethylene glycol 600 (PEG600) and acetamide (Ac) with melting points of 23 °C and 73 °C and supercooling temperatures of 9 °C and 34 °C can be shape-stabilized as a substitute for BS during the sol-gel synthesis. They are soluble in the aqueous phase of the reaction mixture and, thus, do not act as hard/soft templates like BS/paraffin during the formation of the silica structure in the ss-PCMs. As a consequence, the silica pore geometries are different from those in hydrophobic ss-PCMs (Fig. 3.7). Both PCMs interact with the silica structure during sol-gel synthesis, resulting in an up to 70 wt% lower effective mass fraction of PCM after shape-stabilization (Table 3.1). PEG600 might form strong hydrogen bonds to the silica surface as a structure-directing agent, reducing the PEG fraction, which is able to undergo a phase transition from liquid to solid and *vice versa*. During the synthesis, PEG600 should shield silica particles and aggregates from each other by the bumper-effect due to hydrogen bonding between the PEG600 surface and the silanol-groups of the silica particles. In accordance, the structure-directing influence of polyethylene glycols is reported for the synthesis of xero- and aerogels by sol-gel [13]. The silica forms a structure out of weakly-connected aggregates with average macropore widths of 10000 nm (Table 3.1, Fig. 3.7). For this reason, the ss-PCMs have low compressive strength of 35 kPa at 5 °C (6 kPa at 40 °C) after drying (Table 3.1). The low compressive strength of the shape-stabilized PEG600 should be similar to the compressive strength of the ss-PCMs of Li *et al.* [14] because silica usually strongly interact with PEG600.

In comparison, the shape-stabilized Ac has a ~60 wt% lower weight after drying due to the formation and evaporation of acetic acid and ammonia under the basic reaction conditions of

the sol-gel synthesis (Fig. 3.3). Ac and its degradation products should weakly interact with the silica phase during the gelation and form translucent ss-PCMs, because the silica structure consists only of mesopores with average pore widths of 24 nm (Fig. 3.7). These silica structures should be formed by silica itself [15]. The average silica pore widths are smaller than for ss-PCMs based on hydrophobic PCMs showing values of approximately 14 nm (Ac) and 5 nm (PEG600), indicating a structure-directing influence of the hydrophilic PCMs on the silica phase (Table 3.1). The small interconnected silica structures increase the compressive strength of the ss-PCMs based on Ac to 9.6 MPa at 5 °C, which is the highest reported compressive strength for ss-PCMs with at least 10 wt% confined PCM. The low latent heat of the ss-PCMs based on Ac of 101 J/g and 80 J/g after 1 and 3000 thermal cycles prevents its widespread usage. If the hydrophilic PCM is chemically stable during and after shape-stabilization, the silica structures in ss-PCMs could have dimensions of some nanometers and, thus, could have similar high compressive strengths as the shape-stabilized Ac. Translucent ss-PCMs with high long-term performances are needed for glassy TES applications, such as for double-glazed windows or window shutters [16,17]. Therefore, appropriated hydrophilic PCMs have to be found for the sol-gel synthesis of ss-PCMs in the future.

4.2 Thermal conductivity enhancement of ss-PCMs

The thermal conductivity of the ss-PCMs based on BS (218 mW/mK at 30 °C, 366 mW/mK at 10 °C) is too low for some thermal energy storage applications, especially for the construction of ss-PCM battery cell holders to passively cool batteries and to enable fast charging processes in electrical vehicles. Different studies showed that hexagonal boron nitride platelets (BN) can increase the thermal conductivity of ss-PCMs to a higher extent compared to copper nanoparticles, expanded graphite, carbon nanotubes, aluminum nitride and hexagonal boron nitride sheets (Fig. 4.3). Therefore, BN with different platelet sizes from 3 μm to 45 μm and surface areas from 1 m^2/g to 20 m^2/g were added to the sol-gel synthesis of ss-PCMs as electrically insulating and thermally conductive additive.

Pure BN does not chemically react with the silica and the PCM and, thus, does not affect long-term performances, chemical stabilities and shape-stabilities of the ss-PCMs synthesized by the sol-gel process. This observation is in line with similar studies about PCMs thermally enhanced by applying BN [18,19] or expanded graphite (EG) [20,21].

The mass fraction of BN had the highest impact on the physicochemical properties of the ss-PCMs. Higher BN mass fractions increase the contact area between BN particles and the reaction mixture viscosity in the present work as well as in other studies [22,23]. The higher

viscosity increases the stability of the wet gel and, thus, accelerates the evaporation of water from the wet gel by film diffusion. Consequentially, the average compressive strength of the ss-PCMs is increased by 120 % at 10 °C for the ss-PCM sample row with 20 wt% confined BN (Fig. 4.9). The compressive strength of the ss-PCMs depends on the stability of the wet gel, the viscoelasticity of the confined liquid PCM and the interconnectivity and dimension of the silica structure in the ss-PCM. A higher amount of BN increases the viscosity, but disturbs the formation of an interconnected silica structure. For this reason, the relative increase of the compressive strength is higher for ss-PCMs containing 5 to 15 wt% than 20 wt% compared to ss-PCMs without BN, resulting in a non-linear increase of the compressive strength by adding BN to the reaction mixture.

The higher viscosity leads to a 50 % decreased average silica macropore width, a ~70 % shorter average gelation time and a 140 % increased average thermal conductivity (10 °C) of the ss-PCM sample row with 20 wt% confined BN with different particle sizes and specific surface areas (Fig. 4.2, Fig. 4.6, Table 4.4). Due to weak interactions to the silica surface, a higher mass fraction of BN decreases the porosity and the total pore volume of the calcined ss-PCMs to approximately the same values (Table 4.4), regardless of the specific surface area and size of the BN particles. If the BN was added after the PVA, SDS and water, some reaction mixtures foamed during stirring and gelation. Therefore, careful addition of BN in the first step of the synthesis is necessary to stop the fixation of air bubbles in the silica structure during gelation and, thus, to prevent lower thermal conductivities of ss-PCMs due to air inclusions. The major drawback of BN addition is, however, that the latent heat of the ss-PCM is decreased by the mass fraction of BN. Therefore, 10 wt% BN could be more appropriated for the synthesis of ss-PCMs for industrial applications. The thermal conductivity and the compressive strength of the sample row with 10 wt% BN are increased by 45 % and 28 % at 10 °C for the sample row containing 10 wt% BN compared to ss-PCMs synthesized without BN (366 mW/mK, 1.2 MPa, 10 °C), respectively (Fig. 4.2, Fig. 4.9).

Larger BN platelets with particle sizes up to 25 µm are best suited for the improvement of the thermal properties of ss-PCMs. For example, ss-PCMs synthesized with 20 wt% BN with a particle size of 25 µm have the highest thermal conductivity of 1.14 W/mK and the lowest supercooling temperature of PCM of ~3 °C, possibly due to a lower BN agglomeration (lower viscosity) and a higher exfoliation rate of BN particles during synthesis. It should be underlined that the small shear forces by magnetic stirring are sufficient to exfoliate BN particles in the sol-gel synthesis. The silica should stabilize BN nanosheets during gelation and, thus, play a supportive role in the exfoliation process of BN. These results are also observed by Bertolla *et al.* [24] for the exfoliation of BN by viscous water glass solutions. The supercooling

temperatures of PCM like the decomposition points of PCM are always lower for ss-PCMs with high thermal conductivities and heat transfer rates, when the samples consist of an interconnected silica structure. Additionally, the higher interconnected silica structure of the ss-PCMs synthesized with BN particle sizes of 25 μm should be the reason for the 187 % higher thermal conductivity compared to the ss-PCMs (blends) of Yang *et al.* [25] (BN sizes: 30 - 40 μm) (Fig. 4.3). The mechanical properties of ss-PCMs are improved for smaller BN particles, because large particles can hinder the formation of an interconnected, stable silica structure to a higher extent than small particles. Additionally, the emulsion viscosity is higher for smaller BN particles due to more dipole-dipole interactions of BN during gelation and the wet gel is more stabilized from cracking during drying. Compared to ss-PCMs without BN, BN particles with sizes of 3 μm and 25 μm increase the compressive strength of ss-PCMs by ~80 % and ~25 % (10 °C), respectively. The addition of larger BN particles above 25 μm (45 μm) lead to partially broken ss-PCMs with fragmented silica structures after drying because BN shielding of silica particles seems to be too high during gelation. In summary, the selection of the best suited BN for the synthesis of ss-PCMs depends on the type of application. For example, ss-PCMs need a higher compressive strength for building applications than for photovoltaic applications.

If the specific surface area of BN with particle sizes of 3 μm is increased from 12 m^2/g to 20 m^2/g , the reaction mixture becomes highly viscous and the stirring rate is decreased during gelation due to a higher interaction area of these BN particles with its surrounding. The high viscosity increases BN agglomeration effects (Fig. 4.7). Therefore, the compressive strength of the ss-PCMs (20 wt% BN) synthesized with BN with specific surface areas of 12 m^2/g and 20 m^2/g are increased by 100 % and 67 % at 10 °C, respectively, compared to ss-PCMs without BN. Additionally, the thermal conductivity (10 °C) is 32 % higher for the samples synthesized with BN with the specific surface area of 12 m^2/g compared to 20 m^2/g (Fig. 4.2). If the viscosity is, therefore, too high, the formation of a well-interconnected silica phase is disturbed, the shear forces during stirring are reduced, the exfoliation rate of BN is smaller and the thermal conductive additive starts to agglomerate. Hence, a low specific surface area of BN is best suited to increase the thermal conductivity as well as the compressive strength to the highest extent in this work or in syntheses similar to sol-gel, such as the synthesis of heat exchange polymer polyamide 66 in electronic devices [26,27] or poly(methyl methacrylate) in light emitting diodes [28]. High stirring rates realized by a KPG stirrer could help to minimize this negative side effect of the specific surface area of BN, if the inclusion of air is avoided and the structure of BN is not damaged.

The major drawback of BN is the high market price of 1912 €/kg (Merck) [29]. In contrast, hexagonal graphene platelets (EGP) are isoelectronic with BN and have the same 3D-structure as BN, but are available for lower market price of ~7 €/kg today [30]. If the ss-PCM based on EG is covered by an electrical insulating material, the ss-PCM is available as economical friendly battery cell holder in electrical vehicles. Therefore, 20 wt % graphene platelets (EGP) (trading name: GFG20; company: SGL Carbon SE [31]) with particle sizes of 20 μm and a particle thickness of 36 nm were added to the sol-gel synthesis to obtain the ss-PCM EGP_20 (20 wt% EGP) with similar physicochemical properties as the ss-PCMs based on 20 wt% BN with particle sizes of 25 μm . For a higher heat storage capacity, bio-based PCM (Crodatherm 21, 205 J/g) was used to substitute the BS (technical product) as PCM (Fig. D6).

In comparison to ss-PCMs based on BN (25 μm), the ss-PCM EGP_20 has the same shape-stability of 100 % after heating to 100 °C for 7 days, a latent heat of 136 J/g ($Ma(PCM)_{mass}$: 64.8 %; $Ma(PCM)_{DSC}$: 66.3 %; E_{DSC} : 100 %; E_{mass} : 97.6 %), a melting point of 24 °C and a supercooling temperature of confined PCM of 6.6 °C (measured by on- and end-set: 0.5 °C) (Fig. D6). After calcination, the form of the interconnected spherical silica structure and the pore volume of 2.34 cm^3/g (84 % porosity) of EGP_20 are similar to the BN-based ss-PCM, but the average macropore diameter of 516 nm is smaller (BN-based ss-PCM: 685 nm) (Fig. D7). Moreover, the sample EGP_20 has a 29 % higher compressive strength of 2.2 MPa at 5 °C (1.5 MPa at 40 °C) and a 163 % higher thermal conductivity of 3.0 W/mK at 5 °C (1.7 W/mK at 40 °C) than the shape-stabilized BS with particle sizes of 25 μm , indicating a better performance of EGP for the synthesis of thermally enhanced ss-PCMs. To understand the better performance, the thickness and the exfoliation of EGP before and after

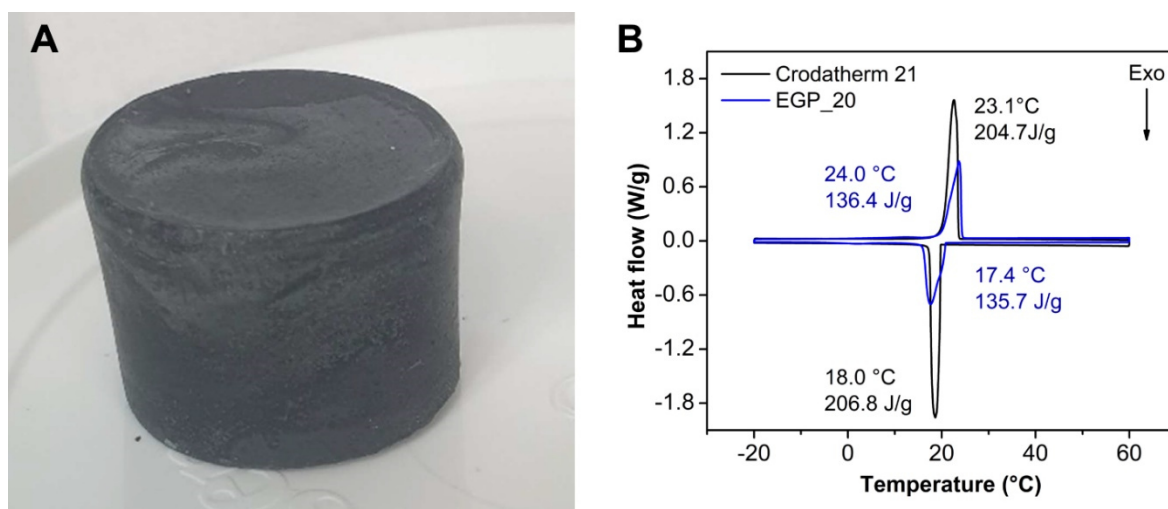


Fig. D6 Picture of ss-PCM EGP_20 (A) and DSC curves of pure PCM Crodatherm 21 and ss-PCM EGP_20 (B).

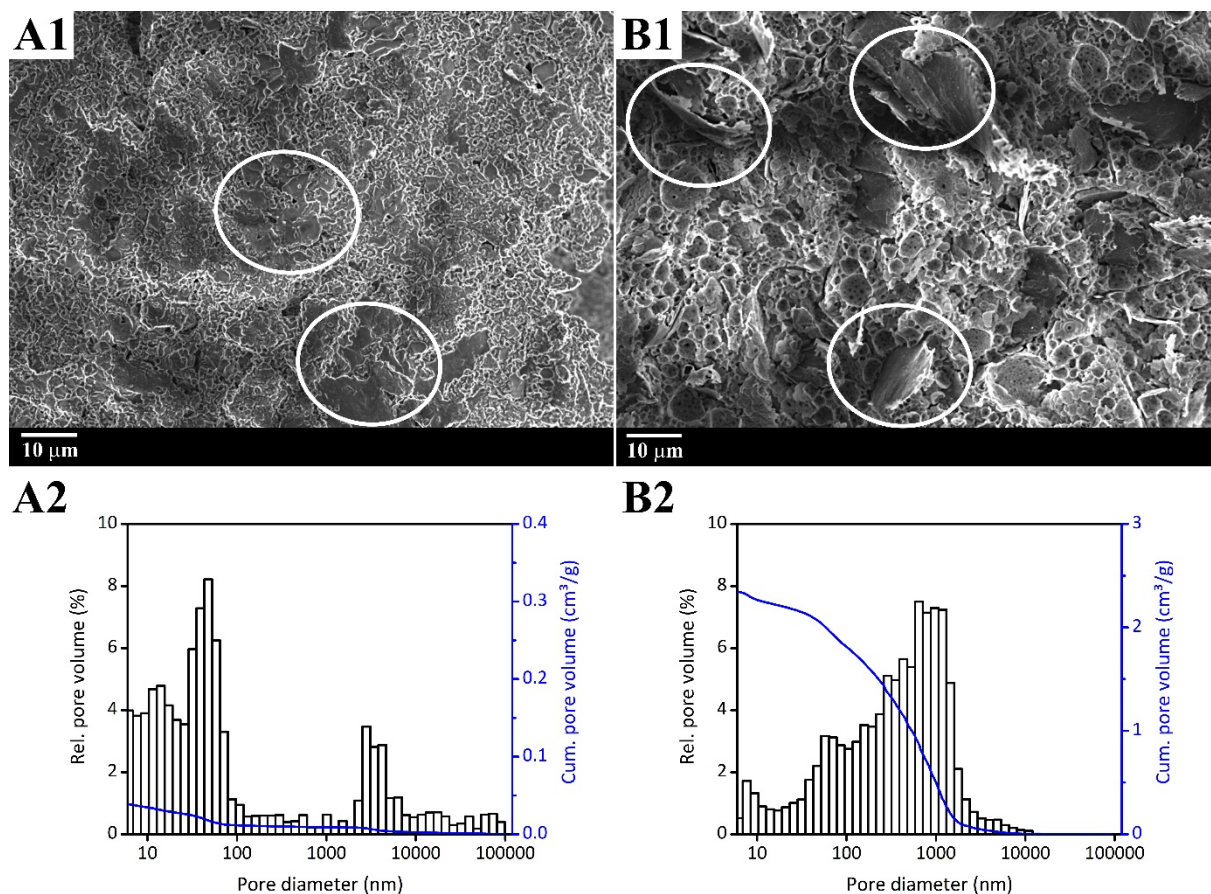


Fig. D7 SEM images (1) and mercury intrusion measurements (2) of ss-PCM EGP_20 before (A) and after (B) calcination at 600 °C for 6 h. The graphene platelets are marked by a white circle in the SEM images.

immobilization in the ss-PCM EGP_20 was analyzed by XRD (values for thickness not available by manufacturer).

The particle thickness of EGP for pure EGP and confined EGP in calcined ss-PCM EGP_20 is calculated according to Eq. 5.2 by using the diffraction peak with the highest intensity at 26.5° (002) (Fig. D8).

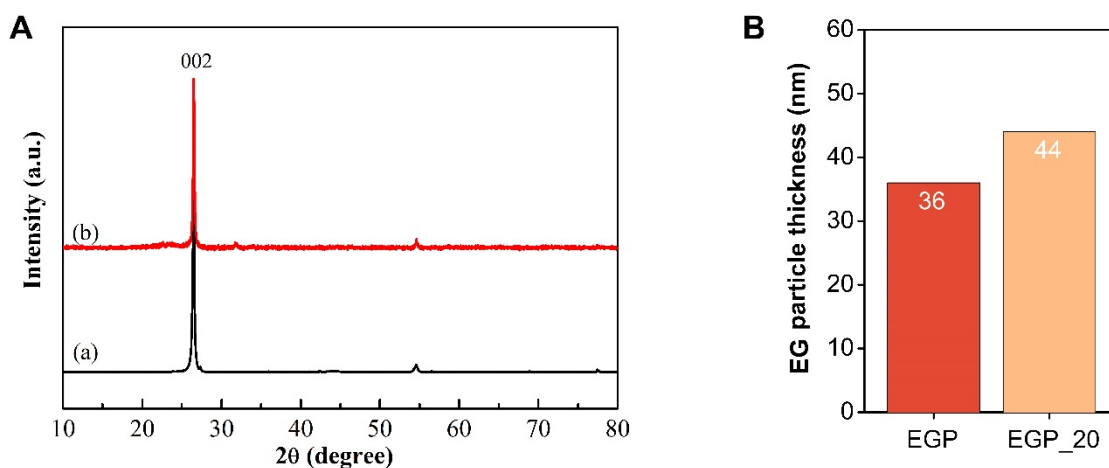


Fig. D8 (A) XRD patterns of pure graphite EGP (a) in comparison to ss-PCM EGP_20 after calcination (b). (B) Average particle thickness of pure graphite EGP (EG) and ss-PCM EGP_20 after calcination.

The particle thickness of EGP (EG) is 36 nm before and 44 nm after the synthesis of ss-PCM EGP_20, maybe due to aggregation and agglomeration effects during gelation. The particle thickness of EGP is ~60 % lower than for BN with particle sizes of 25 μm after immobilization in the ss-PCM structure, which should be a reason for the higher thermal conductivity and higher compressive strength of EGP_20. At the moment differently sized EG and EGP particles are under investigation for the synthesis of thermally enhanced ss-PCMs and to understand the better performance of the graphitic additives in ss-PCMs in detail.

4.3 Characterization of ss-PCMs

To date, the ss-PCMs are poorly characterized by only a small number of analytical methods in the current literature. Especially for ss-PCMs synthesized with silica precursor (mostly TEOS) and sol-gel techniques [14,32], the mechanical stability, the long-term performance over 1000 melting and freezing cycles and the interconnectivity and geometry of the silica pores are not analyzed. Therefore, novel analytical methods and equations are implemented as methodology for the characterization of the ss-PCMs in this work and are highly recommended for the proper characterization of all ss-PCMs in the future.

All results of this work suggest that smaller silica pores sizes with a higher degree of interconnectivity increase the thermal conductivity and mechanical stability of the ss-PCMs to the highest extent. For example, the ss-PCMs based on PEG600 had the lowest compressive strength of 6 kPa at 30 °C (35 kPa, 10 °C) of all ss-PCMs synthesized in this work due to the particulate and fragmented silica structure with a high average macropore width of 10000 nm (Fig. 3.5, Fig. 3.6). In contrast, the ss-PCMs based on butyl stearate (BS) or/and hexadecane (HD) and octadecane (OD) consist of a well-interconnected spherical silica structure with average macropore widths of 1000 - 2000 nm and compressive strengths of approximately 0.7 MPa at 30 °C (1.2 MPa, 10 °C), which is 117-times higher than the compressive strength of the ss-PCM based on PEG600 (Table 3.1). Moreover, the shape-stability test is the only method to evaluate, if the PCM is shape-stabilized and, thus, can be named as ss-PCM [33,34]. The ss-PCMs are generally tested by heating the ss-PCM above the melting point of the confined PCM for a certain time (here: 100°C for 7 days) [35]. After shape-stability tests, the ss-PCMs based on BS or paraffins showed no PCM leakage, whereas 5 wt% PCM leaked out of the structure of the ss-PCM based on PEG600. The leakage of PEG600 from the fragmented silica structure in the ss-PCM is quite low and in no relation to the huge difference in the mechanical stability of the different ss-PCMs in this work. Therefore, the characterization of the mechanical stability of ss-PCMs and the pore sizes, pore distributions and

interconnectivity of silica (or polymeric) structures in ss-PCMs are mandatory to prove the quality of ss-PCMs synthesized by sol-gel or by similar synthesis approaches.

Here, the mechanical stability of ss-PCMs was analyzed by a compressive strength test above and below the melting and freezing point of the respective PCM. The compressive strength of the ss-PCMs measured above the melting point showed the same trends than below the freezing point. Consequentially, ss-PCMs should be at least measured and compared with each other at one specific temperature to obtain and evaluate trends. For a detailed comparison of different studies published so far, both values for the compressive strength of one ss-PCM are necessary. The bending strength of the ss-PCMs was not measured, but could be interesting for the characterization of the mechanical properties of ss-PCMs in the future.

The X-ray imaging experiments (nanotomography (nano-CT)) is a useful analytical method to characterize the 3D silica structure and the orientation of additives, such as boron nitride, in ss-PCMs without further calcination steps, but it is limited to large pore sizes in the micrometer and higher nanometer range. The nano-CT images of the ss-PCMs were similar to the scanning electron microscopic (SEM) images of the calcined ss-PCMs (Fig. 1.10). As could have been shown, the calcination step maintained most of the structural properties of the silica phase in the ss-PCM and even enabled the characterization of the smaller nanopore structures (~24 nm) of the ss-PCM based on acetamide (Ac) by SEM, which could not be monitored by nano-CT (Fig. 3.7). The calcination step is more accurate for ss-PCM with higher mechanically stable silica phases. For example, large amounts of poly(vinyl alcohol) (PVA) (5 wt%) separated the emulsion in large hydrophilic and small hydrophobic regions during the gelation of ss-PCMs based on BS. These ss-PCMs have a compressive strength of just 0.34 MPa at 30 °C. The SEM images of the calcined ss-PCM (Fig. 2.3) show, however, a high degree of fractured silica structures, which may not only be fractured in the drying process at 100 °C but also in the calcination process at 600 °C.

By mercury intrusion (Hg) and nitrogen (N₂) sorption measurements of the ss-PCM before and after calcination, pores filled with PCM in the ss-PCMs could be distinguished from pores filled with air (Fig. 1.9). In comparison, the nano-CT imaging technique is not able to differentiate pores filled with air from pores filled with PCM. The low-pressure during N₂ sorption experiments should not damage the silica structure and, thus, should be an accurate method to characterize micro- and mesopore systems. The Hg measurements were used to analyze the macropore sizes, volumes and distributions. However, this method has some big disadvantages for the characterization of the ss-PCMs in this work. During Hg measurements,

liquid PCM in the ss-PCM should be compressed at high pressure. This high pressure is necessary to analyze pore structures below 100 nm. As a result, the Hg measurements detected porosities of 5 - 8% for the ss-PCMs (Table 1.2, Fig. S4.7), although N₂ sorption experiments did not detect any pores filled with air in the same detection range. Moreover, the pore width distributions obtained by Hg measurements of the calcined shape-stabilized BS detects only pore widths below 2000 nm. In contrast, SEM images of the same sample show many larger pores up to 10000 nm (Fig. S1.3). The spherical pores of the calcined ss-PCMs based on BS are covered by smaller pores below 500 nm. During mercury intrusion, mercury should be pushed in the bigger spherical pore volume via smaller pore channels. As a consequence, the pressure needed to fill a large pore with mercury should be significantly higher than expected and the average pore widths appears to be decreased. This drawback of mercury intrusion is called ink-bottle effect [36,37]. Thus, the combination of Hg measurements and SEM images is mandatory for the characterization of silica structures in ss-PCMs.

The characterization of the ss-PCM formation by standard *in situ* approaches was quite challenging. For example, the droplet size distribution in the macroemulsion could not be analyzed by dynamic light scattering (DLS, [38]) because of the fast macroscopic phase separation of the emulsion before the addition of stabilized silica sol and the high viscosity of the reaction mixture during gelation. Zeta-potential and conductivity measurements should be an appropriate method to indicate putative chemical and physical interactions on the surface of the PCM droplets in the emulsion [39,40]. However, the multi component system inhibited these types of measurements. Transmission electron microscopy could not be applied to image ss-PCM formation due to the fast phase separations and reactions during sol-gel synthesis. Freezing of the wet gel damaged the micellar structures and, thus, could not be used for additional analytical methods, such as cryogenic SEM. In contrast, imaging of the ss-PCM formation process by confocal fluorescence microscopy was successful and represents a quite new imaging technique for sol-gel syntheses. For imaging, different fluorescent dyes were used to mark the silica phase (FM-43, green-fluorescent), the aqueous phase (Alexa Fluor 488, green-fluorescent) and the hydrophobic PCM phase (perylene, blue-fluorescent) separately. When the aqueous phase is marked with Alexa Fluor 488 and the hydrophobic phase is marked with perylene, the silica structures appear as black circles in the images at early time points of gelation and aging (Fig. 2.1). The fluorescent microscopic images validated the type of emulsion (PCM droplets in an aqueous phase) and showed the rearrangement of core-shell like silica particles to a spherical interconnected silica phase during synthesis.

To determine the gelation times, five to ten samples of one ss-PCM were synthesized and turned upside down after a specific time in the reaction vessel during gelation. If the gelation was finished, the wet gel remained stationary and solid. The gelation time was always faster for higher viscous reaction mixtures, possibly due to the stabilizing effect of a higher viscosity during gelation. This method gives valuable information on the reaction rate of the sol-gel process but is very time-consuming.

The latent heat, effective mass fraction and supercooling of PCM are, up to date, solely analyzed by differential scanning calorimetry (DSC). However, the latent heat of ss-PCMs can have different values when looking at different spots of the sample (middle, top, bottom) due to an inhomogenous distribution of PCM, such as the ss-PCMs based on BS in this work (Fig. 1.6). Thus, multiple DSC measurements are mandatory to characterize the thermal properties of these ss-PCMs. Simply weighing the ss-PCM and calculating the effective mass fraction of PCM ($Ma(PCM)_{mass}$, Eq. 1.2) is a suitable method to quickly analyze how much PCM is immobilized during the shape-stabilization process. Setting $Ma(PCM)_{mass}$ in relation to $Ma(PCM)_{max}$ (Eq. 1.3), which is the highest possible mass fraction of PCM, the degree of PCM (%) immobilized in the ss-PCM structure based on weight measurements is calculated - named efficiency E_{mass} (Eq. 1.5). The effective mass fraction of PCM $Ma(PCM)_{DSC}$, derived from DSC measurements (Eq. 1.1), indicates, how much PCM performs the phase transition from solid to liquid and *vice versa*. $Ma(PCM)_{DSC}$ in relation to $Ma(PCM)_{max}$ describes the highest possible degree of PCM (efficiency E_{DSC}) performing the phase transition as pure substance or as ss-PCM (Eq. 1.4). In the case of ss-PCMs synthesized with Ac, 54 wt% PCM was immobilized by shape-stabilization ($Ma(PCM)_{mass}$) and 53 wt% of the ss-PCM is performing the phase transition ($Ma(PCM)_{DSC}$) (Table 3.2). Another measure to characterize the PCM fraction undergoing the phase transition is the constant a_t (Eq. D1).

$$a_t = \frac{Ma(PCM)_{DSC}}{Ma(PCM)_{mass}} \quad . \quad (Eq. D1)$$

This constant is used to calculate the amount of stored heat energy of PCMs Q in a certain temperature range (Eq. 3) and has values of 1 and 0.97 for ss-PCMs based on BS or Ac, respectively (100 % and 97 % of the PCM phase undergoes a phase transition in the ss-PCMs based on BS and Ac, respectively). After 3000 melting and freezing cycles, $Ma(PCM)_{DSC}$ and $Ma(PCM)_{mass}$ were decreased by 20 wt% for the shape-stabilized Ac samples. The reason for the decrease in these effective mass fractions of PCM is the chemical instability of Ac in the ss-PCM leading to partial chemical degradation and evaporation of the degradation products acetic acid and ammonia. As could have been shown, calculating the different effective PCM mass fractions enables a reliable and simple way to characterize the thermal properties of the

ss-PCMs. This methodology is similar to the calculation of covering rates and effective mass fractions of cs-PCMs (Eq. 5).

The supercooling temperature of PCM is not uniformly calculated and can be amongst others determined by the difference of the onset or the maximum/minimum temperature of the DSC peak. In this work, the maximum temperature of the DSC peak is generally taken as melting point and, thus, the values for the supercooling are slightly increased. In the future, both values should be noted for a better comparison of different ss-PCM studies. The thermal conductivity of PCMs and ss-PCMs are mostly measured below the freezing point of the PCM at room temperature [18,25,41–43]. However, the thermal conductivity of the liquid PCM in the solid ss-PCM structure is extremely important to evaluate the thermal performance of ss-PCMs. For the ss-PCMs based on paraffins or BS, the thermal conductivity is ~60% lower above the melting point than below the freezing point of PCM due to the high interfacial resistance of liquids in this work [44]. The thermogravimetric analysis is a useful method to determine the decomposition points and is already implemented as standard method for the characterization of ss-PCMs.

The ^{29}Si MAS NMR measurements are suitable to analyze the connectivity, the hydrolysis degree and the functionalization of the silica species. The ss-PCMs based on BS have similar peaks but different peak intensities compared to the pure stabilized silica sol, pointing to different hydrolyzed silica species (Fig. 1.4, Fig. 5.1). The peak with the highest intensity belongs to the $(\text{Si-O})_2\text{Si}(\text{O-Si})_2$ species (-111 ppm, Q^4). The peaks of the $(\text{Si-O})_2\text{Si}(\text{O-Si})(\text{OH})$ (Q^3) and $(\text{Si-O})_2\text{Si}(\text{OH})_2$ (Q^2) at -102 ppm and -92 ppm have lower intensities. All peaks are overlapped and no peaks for Si-O-C or Si-C can be seen in the NMR spectra (Fig. 1.4). Therefore, the silica surface is not functionalized, for example by SDS, and the silica shows a high degree of connectivity. The infrared (IR) spectroscopy is a standard method for the characterization of the chemical stability of ss-PCMs. For the ss-PCMs based on BS or paraffins, all absorption (or transmission) bands of the educts had the same position in the IR spectra before and after shape-stabilization, pointing to a high chemical stability of the ss-PCMs (Fig. S1.1, Fig. 5.2 to Fig. 5.5., Fig. 3.2). However, the ss-PCMs based on Ac showed also similar IR spectra for the educts and the product because the chemical degradation products of Ac, acetic acid and ammonia, are volatile and acetic acid has a similar IR spectrum to acetamide (Fig. 3.2). Therefore, IR measurements alone are not sufficient to characterize the chemical stability of ss-PCMs. The molar mass distribution for polymers was measured by ESI-MS, which can give insight in the chemical stability of ss-PCMs. For example, the molar mass distribution of PEG600 before and after shape-stabilization was exactly the same (Fig. S3.6, Fig. S.3.7) and, thus, the PEG600 was not chemically degraded though its 30 wt% lower

effective mass fraction of PCM. This result is in line to the studies of Li *et al.* [14] about ss-PCMs based on TEOS and PEG600.

Gas chromatography–mass spectrometry (GC/MS) with headspace technique is the method of choice to robustly analyze all volatile compounds evaporated from the ss-PCM during heating. In the mass spectrum of shape-stabilized Ac specific peaks at m/z 59 and m/z 60 for acetamide and acetic acid were observed indicating partial chemical hydrolysis of acetamide to acetic acid during synthesis (Fig. 3.3). Therefore, the combination of IR and GC/MS studies is a promising tool to characterize the degree of chemical stability of the ss-PCMs in this work and in future studies.

4.4 References

1. Ted Pella (2021) Safety Data Sheet of Colloidal Silica Suspension.
https://www.tedpella.com/SDS_html/815-110_sds.pdf. Accessed 15 Nov 2021
2. Merck (2020) Sicherheitsdatenblatt von LUDOX[®] HS-40 kolloidales Silica.
<https://www.sigmaaldrich.com/MSDS/MSDS/DisplayMSDSPage.do?country=DE&language=de&productNumber=420816&brand=ALDRICH&PageToGoToURL=https%3A%2F%2Fwww.sigmaaldrich.com%2Fcatalog%2Fproduct%2Faldrich%2F420816%3Flang%3Dde>. Accessed 2 Dec 2021
3. Marske F (2017) Synthese von Silika-Xerogelen als Wärmedämm- und speichermaterialien. Master Thesis, Leipzig
4. Hallak B (2016) Grundlagenuntersuchungen zur Herstellung von Silika-Xerogelen aus stabilisiertem Sol. Master Thesis, Leipzig
5. Sarı A, Biçer A, Karaipekli A (2009) Synthesis, characterization, thermal properties of a series of stearic acid esters as novel solid–liquid phase change materials. *Materials Letters*. Doi:10.1016/j.matlet.2009.02.045
6. Ong JT, Chowhan ZT, Samuels GJ (1993) Drug-exciipient interactions resulting from powder mixing. VI. Role of various surfactants. *International Journal of Pharmaceutics*. Doi:10.1016/0378-5173(93)90232-5
7. Xu C, Wang D, Wang H, Ma L, Zhu X, Zhu Y, Zhang Y, Liu F (2019) Experimental investigation of coal dust wetting ability of anionic surfactants with different structures. *Process Safety and Environmental Protection*. Doi:10.1016/j.psep.2018.10.010
8. Wen X, Lerch S, Wang Z, Aboudiab B, Tehrani-Bagha AR, Olsson E, Moth-Poulsen K (2020) Synthesis of Palladium Nanodendrites Using a Mixture of Cationic and Anionic Surfactants. *Langmuir*. Doi:10.1021/acs.langmuir.9b03804

9. Levy D, Zayat M (eds) (2015) *The Sol-Gel Handbook*. Wiley-VCH Verlag GmbH & Co. KGaA, Weinheim, Germany
10. Nakanishi K, Soga N (1991) Phase Separation in Gelling Silica-Organic Polymer Solution: Systems Containing Poly(sodium styrenesulfonate). *Journal of the American Ceramic Society*. Doi:10.1111/j.1151-2916.1991.tb06794.x
11. Rahman A, Brown CW (1983) Effect of pH on the critical micelle concentration of sodium dodecyl sulphate. *Journal of Applied Polymer Science*. Doi:10.1002/app.1983.070280407
12. Croda (2021) CrodaTherm™ 21. https://www.crodaenergytechnologies.com/en-gb/product-finder/product/979-CrodaTherm_1_21. Accessed 2 Dec 2021
13. Vong M, Bazin N, Sermon PA (1997) Chemical Modification of Silica Gels. *Journal of Sol-Gel Science and Technology*. Doi:10.1023/A:1018350227105
14. Li J, He L, Liu T, Cao X, Zhu H (2013) Preparation and characterization of PEG/SiO₂ composites as shape-stabilized phase change materials for thermal energy storage. *Solar Energy Materials and Solar Cells*. Doi:10.1016/j.solmat.2013.07.017
15. Feinle A, Elsaesser MS, Hüsing N (2016) Sol-gel synthesis of monolithic materials with hierarchical porosity. *Chemical Society Reviews*. Doi:10.1039/C5CS00710K
16. Silva T, Vicente R, Rodrigues F, Samagaio A, Cardoso C (2015) Performance of a window shutter with phase change material under summer Mediterranean climate conditions. *Applied Thermal Engineering*. Doi:10.1016/j.applthermaleng.2015.03.059
17. Khetib Y, Alotaibi AA, Alshahri AH, Rawa M, Cheraghian G, Sharifpur M (2021) Impact of phase change material on the amount of emission in the double-glazed window frame for different window angles. *Journal of Energy Storage*. Doi:10.1016/j.est.2021.103320
18. Jeong S-G, Lee J-H, Seo J, Kim S (2014) Thermal performance evaluation of Bio-based shape stabilized PCM with boron nitride for energy saving. *International Journal of Heat and Mass Transfer*. Doi:10.1016/j.ijheatmasstransfer.2013.12.017
19. Kang Y, Jeong S-G, Wi S, Kim S (2015) Energy efficient Bio-based PCM with silica fume composites to apply in concrete for energy saving in buildings. *Solar Energy Materials and Solar Cells*. Doi:10.1016/j.solmat.2015.07.026
20. Tan N, Xie T, Hu P, Feng Y, Li Q, Zhao S, Zhou H-N, Zeng W-B, Zeng J-L (2021) Preparation and characterization of capric-palmitic acids eutectics/silica xerogel/exfoliated graphite nanoplatelets form-stable phase change materials. *Journal of Energy Storage*. Doi:10.1016/j.est.2020.102016
21. Li M, Wu Z, Tan J (2012) Properties of form-stable paraffin/silicon dioxide/expanded graphite phase change composites prepared by sol-gel method. *Applied Energy*. Doi:10.1016/j.apenergy.2011.11.018

-
22. Yang J, Tang L-S, Bao R-Y, Bai L, Liu Z-Y, Yang W, Xie B-H, Yang M-B (2016) An ice-templated assembly strategy to construct graphene oxide/boron nitride hybrid porous scaffolds in phase change materials with enhanced thermal conductivity and shape stability for light–thermal–electric energy conversion. *Journal of Materials Chemistry A*. Doi:10.1039/C6TA08454K
 23. Yang J, Yu P, Tang L-S, Bao R-Y, Liu Z-Y, Yang M-B, Yang W (2017) Hierarchically interconnected porous scaffolds for phase change materials with improved thermal conductivity and efficient solar-to-electric energy conversion. *Nanoscale*. Doi:10.1039/C7NR05449A
 24. Bertolla L, Šulák I, Buršík J, Dlouhý I, Smilek J, Mácová P, Holas J (2021) Exfoliation of hexagonal boron nitride nanosheets in low-modulus concentrated alkali silicate pastes. *Materials Letters*. Doi:10.1016/j.matlet.2021.129551
 25. Yang J, Tang L-S, Bao R-Y, Bai L, Liu Z-Y, Yang W, Xie B-H, Yang M-B (2017) Largely enhanced thermal conductivity of poly (ethylene glycol)/boron nitride composite phase change materials for solar-thermal-electric energy conversion and storage with very low content of graphene nanoplatelets. *Chemical Engineering Journal*. Doi:10.1016/j.cej.2017.01.045
 26. Fu X, Yao C, Yang G (2015) Recent advances in graphene/polyamide 6 composites: a review. *RSC Advances*. Doi:10.1039/C5RA09312K
 27. Zhou S, Yu L, Song X, Chang J, Zou H, Liang M (2014) Preparation of highly thermally conducting polyamide 6/graphite composites via low-temperature in situ expansion. *Journal of Applied Polymer Science*. Doi:10.1002/app.39596
 28. Oh H, Kim J (2019) Fabrication of polymethyl methacrylate composites with silanized boron nitride by in-situ polymerization for high thermal conductivity. *Composites Science and Technology*. Doi:10.1016/j.compscitech.2019.01.021
 29. Merck (2021) Bornitrid. <https://www.sigmaaldrich.com/DE/de/product/aldrich/255475>. Accessed 2 Dec 2021
 30. GK Graphite (2021) Blähgraphit. <https://shop-graphite.com/collections/graphite/products/blahgraphit-es-100-c10?variant=36283064909986>
 31. SGL Carbon (2021) SIGRATHERM® hoch leitfähige expandierte Graphitpulver. <https://www.sglicarbon.com/loesungen/material/sigratherm-hoch-leitfaehige-expandierte-graphitpulver/>. Accessed 2 Dec 2021
 32. He L, Li J, Zhou C, Zhu H, Cao X, Tang B (2014) Phase change characteristics of shape-stabilized PEG/SiO₂ composites using calcium chloride-assisted and temperature-assisted sol gel methods. *Solar Energy*. Doi:10.1016/j.solener.2014.02.042

33. Rathore PKS, Shukla SK (2021) Enhanced thermophysical properties of organic PCM through shape stabilization for thermal energy storage in buildings: A state of the art review. *Energy and Buildings*. Doi:10.1016/j.enbuild.2021.110799
34. Umair MM, Zhang Y, Iqbal K, Zhang S, Tang B (2019) Novel strategies and supporting materials applied to shape-stabilize organic phase change materials for thermal energy storage—A review. *Applied Energy*. Doi:10.1016/j.apenergy.2018.11.017
35. Ye S, Zhang Q, Hu D, Feng J (2015) Core-shell-like structured graphene aerogel encapsulating paraffin: shape-stable phase change material for thermal energy storage. *Journal of Materials Chemistry A*. Doi:10.1039/C4TA05448B
36. Rootare HM, Prenzlow CF (1967) Surface areas from mercury porosimeter measurements. *The Journal of Physical Chemistry*. <https://doi.org/10.1021/j100867a057>
37. Moro F, Böhni H (2002) Ink-bottle effect in mercury intrusion porosimetry of cement-based materials. *Journal of colloid and interface science*. Doi:10.1006/jcis.2001.7962
38. Asua JM (2002) Miniemulsion polymerization. *Progress in Polymer Science*. Doi:10.1016/S0079-6700(02)00010-2
39. Acedo-Carrillo JI, Rosas-Durazo A, Herrera-Urbina R, Rinaudo M, Goycoolea FM, Valdez MA (2006) Zeta potential and drop growth of oil in water emulsions stabilized with mesquite gum. *Carbohydrate Polymers*. Doi:10.1016/j.carbpol.2006.01.016
40. Zhang W, Li MY, Lin MQ, Luo T, Yao C (2008) Electrical conductivity and stability of O/W emulsions. *Acta Petrolei Sinica (Petroleum Processing Section)*. <http://www.syxbsyhg.com/EN/Y2008/V24/I5/592>. Accessed 10 February 2021.
41. Wang W, Yang X, Fang Y, Ding J, Yan J (2009) Enhanced thermal conductivity and thermal performance of form-stable composite phase change materials by using β -Aluminum nitride. *Applied Energy*. Doi:10.1016/j.apenergy.2008.10.020
42. Zeng J-L, Zhu F-R, Yu S-B, Zhu L, Cao Z, Sun L-X, Deng G-R, Yan W-P, Zhang L (2012) Effects of copper nanowires on the properties of an organic phase change material. *Solar Energy Materials and Solar Cells*. Doi:10.1016/j.solmat.2012.06.013
43. Sarı A, Karaipekli A (2009) Preparation, thermal properties and thermal reliability of palmitic acid/expanded graphite composite as form-stable PCM for thermal energy storage. *Solar Energy Materials and Solar Cells*. Doi:10.1016/j.solmat.2008.11.057
44. Fang X, Fan L-W, Ding Q, Yao X-L, Wu Y-Y, Hou J-F, Wang X, Yu Z-T, Cheng G-H, Hu Y-C (2014) Thermal energy storage performance of paraffin-based composite phase change materials filled with hexagonal boron nitride nanosheets. *Energy Conversion and Management*. Doi:10.1016/j.enconman.2014.01.016

5 Conclusions

Organic shape-stabilized phase change materials (ss-PCMs) are a promising thermal energy storage (TES) material due to the high heat storage capacity, low supercooling effect, switchable heat dissipation, high nucleation rates and isothermal energy storage processes. However, the wide application of ss-PCMs is currently limited by several problems, such as the low mechanical stability, the leakage of liquid PCM during melting, the low thermal conductivity, the moderate flammability and the low latent heat of PCM after confinement. To obtain mechanically stable ss-PCMs with high latent heats, a novel sol-gel synthesis for ss-PCMs based on silica and different PCMs, such as fatty acid esters (butyl stearate (BS)), paraffins (hexadecane (HD), octadecane (OD)), polyethylene glycol (PEG600) and acetamide (Ac), is developed and analyzed in this work. Stabilized silica sol is taken as silica precursor in the sol-gel synthesis because of its high adsorption capacity, high mechanical stability, high fire resistance, non-toxicity and low market price. To alter the silica structures and increase the mechanical stability of ss-PCMs, the surfactant sodium dodecyl sulfate (SDS) and the structure-directing agent poly(vinyl alcohol) (PVA) are added to the reaction mixture during synthesis. The thermal conductivity of the ss-PCMs is further increased by the addition of hexagonal boron nitrides (BN) and the perfect particle size and surface area of BN for ss-PCMs is determined by using different BN particles in the sol-gel synthesis.

In this work, all ss-PCM samples are characterized above and below the melting point of the confined PCM to determine the different physicochemical properties of ss-PCMs immobilizing liquid and solid PCM, such as the mechanical stability and the thermal conductivity. The silica structure of the ss-PCMs is analyzed before and after calcination to distinguish silica pores filled with PCM from empty silica pores caused by air inclusion. The shape-stability and the leakage rate of PCM are tested by heating the ss-PCM above the melting point of PCM (100 °C) for at least 7 days and additional weighing of the ss-PCM afterwards. The durability of ss-PCMs is characterized by long-term performance tests. For these tests, the PCM in the ss-PCM is melted and frozen for 2000 - 6000-times and the loss of latent heat is recorded. It is assumed that one cycle of freezing and melting is equivalent for a one-day durability of ss-PCMs in buildings. Further physicochemical properties of the ss-PCMs are characterized by standard methods, such as fluorescence microscopy to image the silica formation, mercury intrusion, nitrogen adsorption, scanning electron microscopy (SEM) and nano tomography (nano-CT) for pore distributions, pore volumes and silica imaging, ²⁹Si MAS NMR, infrared spectroscopy (IR) and gas chromatography/mass spectrometry (GC/MS) for possible

interactions and irreversible reactions between the educts during synthesis, and differential scanning calorimetry (DSC), thermogravimetry (TG) and thermal conductivity measurements by the Hot Disk technique to analyze the thermal properties, PCM decomposition and heat storage capabilities of ss-PCMs.

By varying the amounts of silica sol, water, PVA and SDS, crack-free and monolithic ss-PCMs based on butyl stearate (technical product, latent heat of 125 J/g) as PCM are successfully synthesized by the sol-gel route under basic conditions (pH: ~9). These ss-PCM monoliths are the first reported ss-PCMs with high compressive strengths up to 1.2 MPa at 10 °C (0.7 MPa at 30 °C) as well as latent heats similar to pure PCM (86 wt% PCM). Moreover, the thermal conductivity of BS was increased by silica from 0.220 W/mK (0.117 W/mK, 30 °C) to 0.366 W/mK (0.218 W/mK, 30 °C) at 10 °C after shape-stabilization. The ss-PCMs keep its shape up to 94 wt% PCM, are hydrophobic (101 ° contact angle to water), thermally stable up to 320 °C and the latent heat of ~100 J/g is not reduced after 6000 melting and freezing cycles, pointing to a high durability of the ss-PCM (> 16 years in buildings). The melting (22 °C) and freezing point of BS (18 °C) are shifted by ~2 °C to lower temperatures after confinement in the ss-PCM, possibly due to weak interactions of BS with the silica surface and the accelerated heat transfer of BS in the silica structure. The weak interactions of BS to silica should prevent lower latent heats of BS after shape-stabilization, which could occur by irreversible PCM degradation reactions.

In the first synthesis step, hydrophobic BS is emulsified as droplets in an aqueous phase of water, PVA and SDS by magnetic stirring using low shear forces. By high shear force stirring, high amounts of air are distributed and stabilized in the viscous reaction mixture during gelation. The air bubbles act as templates for foam pore structures during gelation and should, therefore, be prevented in the ss-PCM synthesis. The BS droplets are covered and stabilized by SDS molecules in the macroemulsion and act as templates for the silica structure after silica sol addition, resulting in a spherical silica pore structure filled with liquid PCM in the range of 2 nm to 10000 nm. The hydrophilic regions are located between the PCM droplets covered by SDS and have a “worm”-like shape (indicated by confocal fluorescence microscopy). During the drying process of the ss-PCM, water should be evaporated by film diffusion through the worm-like pore channels and the ss-PCM shrinks by the volume of evaporated water.

The shape-stabilization of PCM as liquid reduces the risk of silica fractures by PCM volume expansions during melting of solid PCM and, thus, could be a reason for the high long-term performance of the ss-PCMs as well as the high shape-stability. A low BS amount of 69 wt% and 77 wt% lead to silica foam pores filled with air with average pore sizes above 10000 nm

and pore volumes of 0.6 cm³/g and 0.1 cm³/g in the ss-PCM, lowering the thermal conductivity and mechanical stability of the ss-PCM. Therefore, the formation of foam pores must be prevented by the usage of higher amounts of BS during sol-gel synthesis.

To stabilize the emulsion from macroscopic phase separation, at least 2.5 wt% SDS must be used in the synthesis of ss-PCMs. Higher SDS mass fractions up to 5 wt% increase the number of PCM droplets covered by SDS, the emulsion viscosity and stability of the wet gel, resulting in an eight times smaller silica pore width of 1332 nm (8070 nm at 2.5 wt% SDS). The higher emulsion viscosity prevents possible fractures of the silica structure during subcritical drying. As a consequence, the compressive strength and the thermal conductivity of the ss-PCMs (329 W/mK, 0.41 MPa, 10 °C) are increased by 149 % and 13 % at 10 °C, respectively. At very high SDS mass fractions above 5 wt%, the PCM phase should be fully covered by SDS molecules and the negatively charged SDS molecules should interact more intense with the silica phase and PVA. These interactions decrease the emulsion viscosity and seem to shield silica particles from each other during gelation. Therefore, the silica structure of the ss-PCM is fractured and the compressive strength and thermal conductivity of the ss-PCMs with SDS mass fractions of 7 wt% are decreased by 89 % and 24 % at 10 °C, respectively. These results suggest that SDS has two specific functions in the sol-gel synthesis. First, the amount of SDS has a structure-directing influence on the dimension and interconnectivity of the silica structure. Second, the SDS/PCM micelles act as typical templates for the silica structure during gelation because of the spherical form of the silica pores in the ss-PCMs.

The porogen PVA increases the viscosity and stability of the macroemulsion. Therefore, a certain amount of PVA (2.5 wt%) is used to stop macroscopic phase separations during sol-gel synthesis. Low PVA mass fractions in ss-PCMs can stabilize and order secondary silica particles by hydrogen bonding via a sticker-effect during gelation and increase the mechanical stability of wet gels (Fig. 15). Higher amounts of PVA up to 5 wt% increase the phase separation of the macroemulsion in a smaller hydrophobic and larger hydrophilic region due to hydrogen bonding between PVA and silica, resulting in larger, fractured silica structures with eight times higher average pore widths of 8801 nm after drying. Because of the fractured silica structures, these ss-PCMs (5 wt% PVA) have a 53 % and 17 % lower compressive strength and thermal conductivity at 10 °C than the ss-PCMs containing 2.5 wt% PVA, respectively. Additionally, if the PVA concentration is very high during gelation, the PVA shields more secondary silica particles from each other by the bumper-effect instead of connecting them by the sticker-effect (Fig. 15). For this reason, ss-PCMs with PVA mass fractions above 5 wt% could not be synthesized in this work.

The high shape stability (~100 %), the high chemical stability and high long-term performance of the ss-PCMs are not affected significantly by the variation of PVA and SDS mass fractions. In contrast, the thermal conductivity, decomposition points and compressive strength are higher for ss-PCM samples with smaller silica pore structures. Small silica pore structures seem to be superior for the confinement of PCM and are therefore highly recommended for the synthesis of ss-PCMs.

Fatty acid esters, such as BS, have high decomposition points, high chemical stabilities, good nucleation properties and are synthesized from plant stocks as technical products with different melting points. However, they have low latent heats as technical product compared to paraffins (200 - 240 J/g), limiting its application range. Therefore, hexadecane (206 J/g, 20 °C, HD) and octadecane (224 J/g, 32 °C, OD) are shape-stabilized as example for paraffinic PCMs by the sol-gel synthesis. The paraffin is emulsified as small droplets in a continuous aqueous phase. This macroemulsion separates in two macroscopic phases before the gelation is finished. To lower the high hydrophobicity of paraffins, 70 wt% paraffin (HD or OD) is mixed with 30 wt% BS. With these PCM mixtures, novel paraffinic ss-PCMs with high latent heats of 150 J/g (HD) and 160 J/g (OD), high thermal stabilities (~170 °C), high shape stabilities (~100 %) and melting points of 17 °C (HD) and 22 °C (OD) are synthesized. The paraffinic/BS droplets in the emulsion act as template structures for the spherical silica pores in the ss-PCM in the same way as pure BS during gelation. Due to the similar pore size distribution (2 - 2000 nm) and spherical form of the silica structures, the compressive strength of the paraffinic ss-PCMs is as high as of the ss-PCMs based on BS (1.2 MPa, 5 °C). Therefore, different hydrophobic PCMs can be shape-stabilized with high mechanical stabilities by the sol-gel route, when the emulsion is stopped from macroscopic phase separation during gelation. The thermal properties of the hydrophobic ss-PCMs depend mostly on the mass fraction and chemical nature of the PCM used in the synthesis, which is a great advantage to develop ss-PCMs for different application fields.

To analyze the effect of hydrophilic PCMs, pure PEG 600 and acetamide (Ac) with melting points of 23 °C and 73 °C and supercooling temperatures of 9 °C and 34 °C, respectively, are shape-stabilized by the sol-gel route. The effective mass fraction of PCM is 30 % lower for the shape-stabilized PEG600 and Ac than expected due to strong hydrogen bonding between silica and PEG600, and partial hydrolysis of Ac to acetic acid during the synthesis. Strong hydrogen bonding limits the amount of PEG600, which can perform a phase transition. In comparison, Ac is evaporated as acetic acid and ammonia during drying, decreasing the weight of the ss-PCM by ~60 %. During gelation, PEG600 shields the silica particles from each other by hydrogen bonding (bumper effect) and promotes the formation of a weakly connected

silica structure with an average macropore width of 10000 nm. Therefore, the ss-PCMs based on PEG600 have the lowest compressive strengths of 35 kPa at 5 °C (6 kPa at 40 °C) and latent heat of 81 J/g of all ss-PCMs. The ss-PCM based on Ac consists of a branched silica structure of mesopores with average pore widths of 24 nm. For this reason, the shape-stabilized Ac is translucent above the melting point of confined Ac and has a compressive strength of 9.6 MPa at 5 °C, which is the highest reported value for ss-PCMs with PCM mass fractions above 10 wt%. However, the hydrolysis of Ac in the sol-gel process decreases the expected latent heat of Ac after shape-stabilization from 160 J/g to 101 J/g after drying and to 80 J/g after 3000 melting and freezing cycles, pointing to a low to moderate durability of the ss-PCM. Thus, hydrophilic PCMs with strong interactions to silica, such as PEG600 and Ac, are not suitable for the sol-gel synthesis of mechanical stable ss-PCMs with high PCM loadings.

All hydrophobic ss-PCMs have mesopores with average pore widths of ~10 nm, regardless of the amount of porogen or the type of PCM used for the synthesis. In case of ss-PCMs based on PEG600 and Ac, the mesopore width of these pores is increased by 5 nm (PEG600) to 14 nm (Ac). These results suggest that silica itself acts as a structure-directing agent in the formation process of mesopores and that these types of mesopores are influenced by the strong interactions of PEG 600 or Ac with the silica surface.

For cooling of batteries in electric vehicles, the thermal conductivity of the silica phase in the ss-PCMs is too low and additional thermal conductive additives are needed. The graphite-like additive hexagonal boron nitride (BN) is one of the most promising materials for battery systems due to its high thermal conductivity and electrical insulating properties. To find the most appropriate type of BN for the synthesis of ss-PCMs, the influence of BN particles with different sizes from 3 μm to 45 μm and surface areas from 1 m^2/g to 20 m^2/g on the physicochemical properties of the monolithic ss-PCMs is investigated.

Higher BN mass fractions increase the emulsion and PCM viscosity, stabilize the wet gel during subcritical drying and, thus, increase the average compressive strength of the ss-PCM sample row containing 20 wt% BN by 120 % at 10 °C. Additionally, the average silica pore width of the ss-PCM sample row synthesized with 20 wt% BN is decreased by 50 % to 498 nm and the average thermal conductivity is increased by 140 % to 0.88 W/mK (10 °C). The latent heats of the ss-PCMs are reduced by the mass fraction of BN and not by chemical degradation reactions. The high long-term performances, the high chemical stabilities and high shape-stabilities of the ss-PCMs are not influenced by BN. The decomposition points are slightly decreased by higher BN mass fractions due to a higher heat transfer in the PCM phase

as shown by thermogravimetric measurements. These results underline the positive influence of the mass fraction of BN on the compressive strength as well as the thermal conductivity of the ss-PCMs.

When the BN particle size is increased up to 25 μm , the thermal conductivity is increased to the highest extent of 1.14 W/mK (10 $^{\circ}\text{C}$) and the supercooling is reduced by 2 $^{\circ}\text{C}$ due to less BN agglomeration effects and a higher amount of exfoliated BN particles. Compared to smaller BN particles (3 μm), the average pore width of the silica structure of these ss-PCMs is increased by $\sim 100\%$ and the compressive strength is decreased by up to 30 % at 10 $^{\circ}\text{C}$. Larger BN particles seem to shield silica particles from each other and disturb the formation of a mechanically stable silica structure in ss-PCMs, resulting in partially broken ss-PCMs with confined BN particles larger than 25 μm (45 μm).

A higher specific surface area of BN from 12 m^2/g to 20 m^2/g (particle size: 3 μm) lead to a highly viscous reaction mixture during sol-gel synthesis, which promotes the agglomeration of BN and hinders the homogenous distribution of BN in the ss-PCM. As a result, the average silica pore width in these ss-PCMs is increased by 58 % and the compressive strength is decreased by 17 % at 10 $^{\circ}\text{C}$. The higher interconnectivity of the silica phase in ss-PCMs containing BN with lower specific surface areas (20 m^2/g) results in a 32 % higher thermal conductivity at 10 $^{\circ}\text{C}$. Therefore, large BN particles (25 μm) with low specific surface areas (3 m^2/g) are best suited for the synthesis of ss-PCMs by sol-gel or similar syntheses of thermally enhanced polymers.

In summary, a novel class of monolithic ss-PCMs based on different PCMs with high mechanical stability, high heat storage capacity, high shape-stability, high durability, and adjustable thermal conductivity was obtained by a simple one pot synthesis. These ss-PCMs could be produced in different geometries suitable for a wide range of well-known as well as new application fields in the future.

6 Outlook and Perspective

The synthesized shape-stabilized phase change materials (ss-PCM) are a novel class of thermal energy storage (TES) materials with high mechanical stabilities as well as high heat storage capacities. The simple sol-gel synthesis by a one-step process makes these kind of ss-PCMs available for a low market price, too. Additionally, the ss-PCM can be produced using different organic PCMs, PCM mixtures and additives. As a consequence, the physicochemical properties of the ss-PCMs mainly depend on the properties of the PCM and additive used for the sol-gel synthesis, resulting in a wide range of possible applications with different temperature ranges and requirements for the mechanical stability and thermal conductivity.

To find the application fields most suited for the ss-PCMs presented in this work, a detailed analysis of the different applications and competing TES products is mandatory. Here, different TES products are compared to the ss-PCMs to investigate the perspectives and potentials of the ss-PCMs.

By varying and changing the sol-gel synthesis, novel ss-PCMs with high latent heats up to 190 J/g and high compressive strengths up to 2.9 MPa at 5 °C (2.0 Mpa at 40 °C) are obtained, which are named as Nanolope PCM and are currently registered for patent approval (registration date: 08/09/2021, reference number: 10 2021 123 240.6, *Deutsches Patent- und Markenamt* (DPMA)) (Fig. P1). In the following discussion, Nanolope PCM as successor product of the ss-PCMs based on paraffins and fatty acid esters is compared to possible competing products (Table P1).

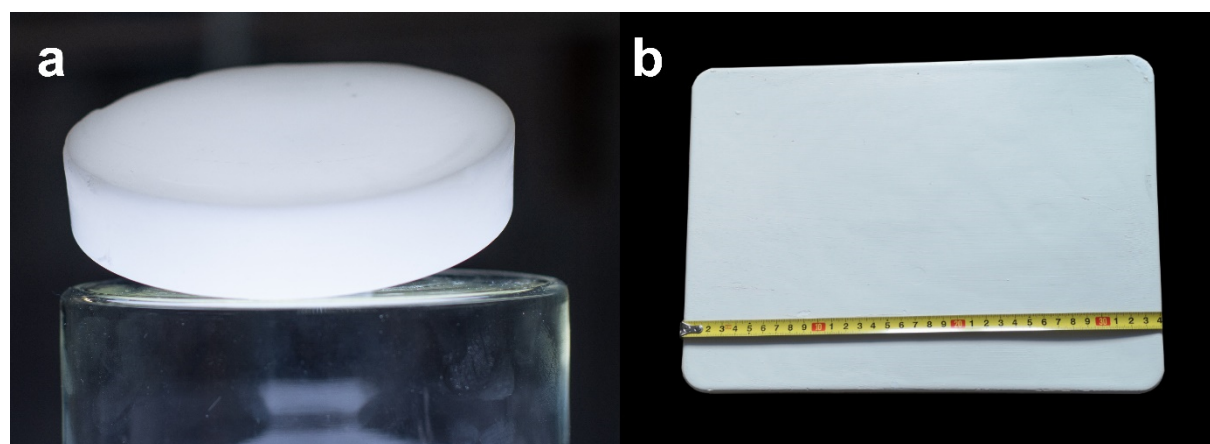


Fig. P1 Images of Nanolope PCM as monolithic board synthesized without (a) and with specific additives (b). Copyright to image (a): Marian Sorge. The utilization of image (a) is permitted.

Table P1 Properties of different monolithic ss-PCMs products compared to Nanolope PCM boards [1–4].

Company	Rubitherm	Microtek	Jekusol	Axiotherm	Nanolope
Product form	PCM-filled Alumina board	Micronal PCM concrete	PCM-filled Balls	PCM-filled HeatStixx	ss-PCM board
Temperature range	−50 to 90 °C	6 to 43 °C	−20 to 100 °C	−63 to 115 °C	−60 to 70 °C
Macroencapsulation	Yes	No	Yes	Yes	No
Heat storage	✓	✗✗	✓	✓	✓✓
Thermal conductivity	✗	✓✓	✗✗	✗	✓
Mechanical stability	✓	✓✓	✓	✓	✓✓
Congruent melting	✗	✓✓	✗	✗	✓✓
Market price	✗	✗✗	✓	✓	✓
Green product	✗	✗✗	✗	✗ ✓	✗ ✓
Recycling	✓	✗	✓	✓	✓

The price for pure paraffins and fatty acid esters is ~2 - 3 €/kg and ~7 - 10 €/kg, respectively [5]. After filling these PCMs in boxes, panels or sandwich structures (macroencapsulation), the market price is increased according to the containment material, such as metal boxes filled with paraffins by ~7 €/kg [6], and the latent heat is decreased by the mass of the containment material and the slow heat transfer in the PCM phase to 40 - 95 J/g during real conditions (latent heat of paraffins: 200 - 240 J/g) [6]. In contrast, Nanolope PCM needs no additional containment material, can be synthesized in different geometric forms and has a 90 % higher latent heat (190 J/g) than the macroencapsulated PCM with the highest possible latent heat available on the market. The total cost of the educts in the synthesis of Nanolope PCM is approximately 5 and 8% higher than of the pure PCMs fatty acid ester and paraffin, respectively. Therefore, Nanolope PCM could perfectly replace macroencapsulated PCM in the future.

Macroencapsulated PCM is available on the market for different TES applications. For example, the company va-Q-tec fills paraffinic PCM in plastic boxes to cool vaccines against SARS-Cov-2 without additional dry ice during transport [7]. Nanolope PCM based on octane (melting point: −57 °C) should have a suitable mechanical stability for transport applications and has a higher heat storage capacity than macroencapsulated PCMs, which could help to design smaller transport boxes for cooling applications in the future. The company Rubitherm fills PCMs in aluminium boxes to increase the heat transfer and uses these boxes for heat-water systems (hot boards) [8] or as climate-friendly ceilings in buildings (CSM products) [9]. The hot board series have dimensions of 520 × 200 × 18 mm, a melting point of 82 °C and a heat storage capacity of 65 J/g [8]. There are some attempts to improve the poor heat transfer in the PCM phase of the macroencapsulation technique. For example, the company Axiotherm

has improved the form and geometry of the plastic macrocapsules to increase the heat transfer in the PCM phase in a water-heating system for building applications [4]. However, the higher aspect ratio and smaller size of these capsules decrease the amount of the confined PCM. Nanolope PCM could be synthesized in similar geometries for a higher heat transfer without additional graphite or boron nitride addition and to increase the latent heat further.

Core-shell PCM (cs-PCM) consists of a PCM core covered by a polymeric shell, mostly polyacrylates, and is available for approximately 15 €/kg on the market [10]. The cs-PCM has 50 to 70 wt% PCM immobilized in one core-shell structure, resulting in latent heats of 100 J/g to 160 J/g regarding hexadecane (200 J/g) as core. Typical additives against flammability, leakage and for a higher thermal conductivity are immobilized in the core unit to broaden its application range, but decrease the latent heat, for example for Micronal DS 5008X (BASF) to ~100 J/g [11]. The high heat transfer, high durability, low PCM supercooling, high chemical and mechanical stability are the reasons for the great scientific interest in cs-PCMs for TES applications. In heat fluids, cs-PCMs can effectively increase the heat storage capacity and the thermal conductivity, when the suspension is stabilized. These kinds of cs-PCM suspensions are called nano-encapsulated PCMs (NEPCM) [12–14]. However, most applications must be monolithic. As a consequence, the cs-PCMs must be used as an additive in construction materials, such as concrete, plaster and wood, with mass fractions of 5 wt% (concrete) to 30 wt% cs-PCM to obtain monolithic TES materials. Higher mass fractions can lead to lower mechanical stabilities or even to a loss of shape-stability. Nanolope PCM consists of an interconnected silica structure with spherical silica pores similar to core-shell structures exhibiting a higher thermal conductivity due to silica but similar favorable physicochemical properties as pure cs-PCM. Therefore, Nanolope PCM can be used as a substitute for cs-PCM based construction materials, when it is not used as stabilizing and supportive element in buildings (e.g. as substitute for thermal insulation or gypsum boards).

The most promising application areas for Nanolope PCM are energy-saving materials for floor, ceilings, walls and roof tops in buildings, as replacement for fireclay heat storage materials in electrical heaters, as additive with specific shapes for water-heating systems, and as cooling medium for photovoltaic panels and batterie cells, especially as part in the battery thermal management system of electrical vehicles. For each application field, Nanolope PCM has to meet specific requirements, which are not fulfilled for every application mentioned above. A short impact-effort matrix is given in Fig. P2.

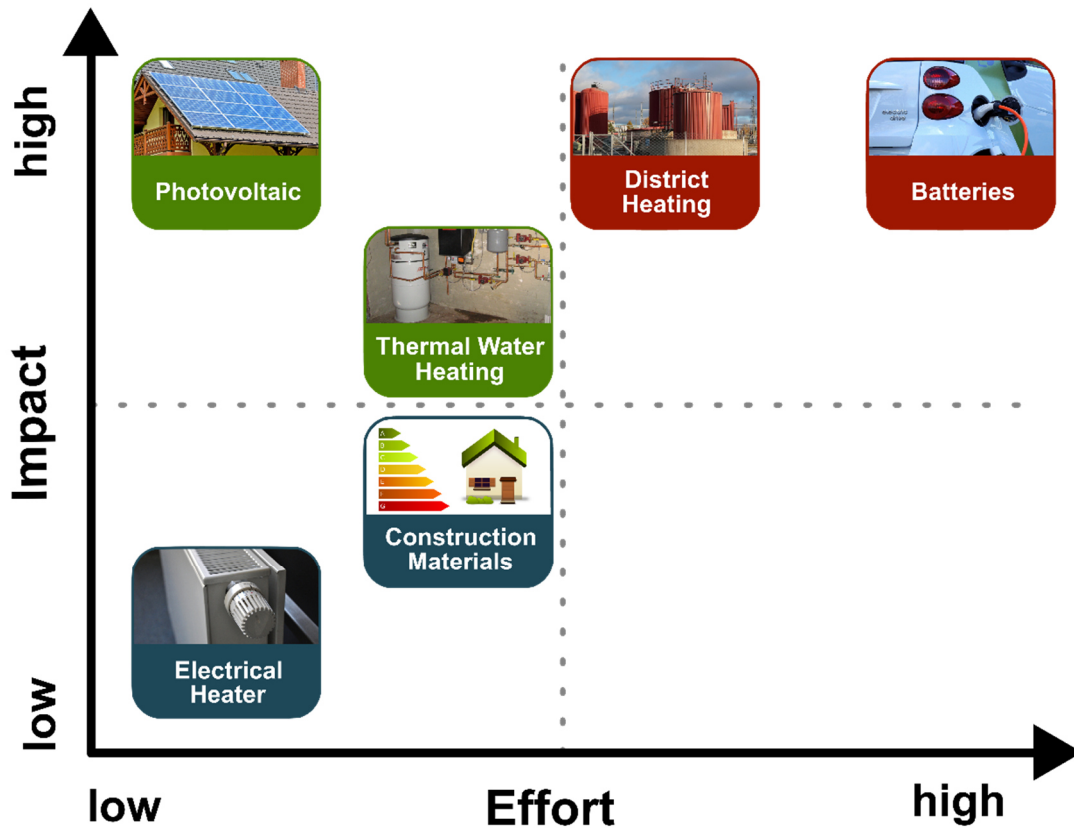


Fig. P2 Impact-effort matrix of Nanolope PCM for different applications.

To make use of off-peak electricity from solar- or wind energy, electrical and infrared heaters can be equipped with fireclay or soapstone to store large amounts of thermal energy. At a specific temperature, the stone material is heated via heating cycles to keep the room at a constant temperature [15]. The heat storage capacity of fireclay (sensible heat: 0.7 J/(g °C)) is 28 J/g in a temperature interval from 30 °C to 70 °C [16]. However, these electrical heaters have a high weight and are bulky. Nanolope PCM could help to reduce the dimension and weight of such electrical heaters by increasing the heat storage capacity to 270 J/g as substitute to fireclay in the same temperature interval (80 J/g sensible heat + 190 J/g latent heat). The effort of the installation of Nanolope PCM as boards is simple. The impact of electrical heaters equipped with Nanolope PCM is currently low, but could rise due to higher market prices for electricity (32 ct/kWh) and gas (6 ct/kWh) and due to political actions in the future [17].

PCM construction materials can help to reduce the high primary energy demand for heating and cooling in buildings. During hot day times, these PCM materials can store thermal energy by melting and keep the room on the same temperature level. During cold night times, the PCM materials release the stored thermal energy to the environment and passively heat the

room. The cs-PCM based concrete is currently used in different energy-saving buildings as construction material, such as at the Charles Sturt University in Australia [18]. The low overall PCM content in such composite concrete (~5 wt%) and gypsum is low (~15 wt%). A cs-PCM (Micronal) based gypsum board for a 67 m² ceiling area consists of 543 kg paraffinic PCM and has an amortization period of 5 years according to BASF [18]. Nanolope PCM has ~70 wt% more PCM immobilized as the PCM gypsum board by BASF, which should reduce the amortization period. It can be installed as a thermal energy storage board in front of concrete walls to store excess heat, such as gypsum boards. The effort of the installation is simple, but the moderate flammability of Nanolope PCM must be lowered by suitable additives in the future. The application of Nanolope PCM as energy-saving construction material is most interesting for countries with hot temperatures at day times and cold temperatures at night times, such as China, USA, Spain or Greece.

Solar-water heating systems are available in a wide range of applications. In smaller buildings, water-heating tanks are used as thermal energy storage medium to heat water by excess heat or electricity. These kinds of tanks are often combined with solar-thermal storage systems or with photovoltaic systems on roof tops, and are therefore of great interest to increase the efficiency of renewable energies [19,20]. For example, the water-heating system kraftBoxx based on macroencapsulated PCM (HeatStixx) by Axiotherm can store up to 2× to 3× more heat than water-based systems, underlining the relevance of PCMs for water-heating solutions [21]. The installation of Nanolope PCM in form of balls or HeatStixx is simple to moderate, and the impact is high. However, a suitable coating process has to be developed for Nanolope PCM for the use in hot-water systems. Additionally, holes and channels in the ss-PCM (product form: HeatStixx by Axiotherm) increase the heat transfer without further additives, but could lead to mechanical stress and breakage of the wet gel during drying. A faster drying process of Nanolope PCM with less cracking is one major problem compared to macroencapsulated PCMs that has to be solved, for example by the addition of suitable drying control chemical additives (DCCAs) or crosslinking polymers in future studies. For the application of Nanolope PCM in bigger district water heating systems, PCMs with higher melting points have to be shape-stabilized as Nanolope PCM, too.

Worldwide, around 90 % of the photovoltaic (PV) cells are based on monocrystalline silicon modules with an efficiency of 18 % (photon-to-electron conversion) [22,23]. A higher temperature of 1 °C of the PV module decreases the efficiency by 0.5 % [22,23]. Moreover, aging processes are accelerated by higher temperatures. Therefore, PV modules need an efficient cooling system. In general, PV modules are currently cooled by water (PV/T (Thermal)-systems). PV-PCM modules are passively cooled by a 3 cm PCM layer (PCM in a

steel box) installed behind the module. The market penetration is hindered by the various problems of macroencapsulated PCM, such as the incongruent melting, the low amount of PCM performing the melting and freezing process and the low thermal conductivities. Therefore, Ma *et al.* [23] suggested in 2019 to stop further studies about PV-PCM technique until novel ss-PCMs are synthesized and are available on the market. The requirements of such ss-PCMs described by Ma *et al.* [23] are fulfilled by Nanolope PCM, which is why the effort is low and the impact is high for this type of application (Fig. P2). An efficient PV-Nanolope PCM system could store more and faster heat during day time as macroencapsulated PCM and, thus, is a promising novel cooling technique for PV modules.

The overheating of batteries, especially in cars by fast charging, is a current problem of electric vehicles. In 2012, the Nissan Leaf lost over 50 % of its range due to the hot temperatures (> 50 °C) in Arizona [24]. The thermal battery management system (BTMS) of the Nissan Leaf was only cooled by forced air. Moreover, higher temperatures decrease the lifetime of a battery system and can lead to safety problems of batteries, such as burning and explosion risks. Today, water cooling systems are mainly used in the BTMS of electric vehicles. However, the cooling rate is not sufficient to charge electric vehicles in a short time period, for example electric power for 500 km in 10 minutes. Therefore, the development of novel cooling materials is desired for electric vehicles. In most studies [25,26] graphitic compounds are mixed with PCMs to increase the thermal conductivity and stabilize the PCM as blend. These blends are not shape-stable over multiple heating and cooling cycles and have low mechanical stabilities. Nanolope PCM enhanced by graphite or boron nitride addition seems to be a promising solution, if the flammability is reduced and the thermal conductivity is further increased. The vibrations occurring while a car is driving could lead to cracks of the monolithic Nanolope PCM boards. Moreover, battery cell holders with small dimensions of 1 - 3 mm layers of Nanolope PCM are complicated to realize by sol-gel and subcritical drying. Hence, the impact and the efforts of Nanolope PCM in BTMS are both higher than for the other Nanolope PCM applications (Fig. P2).

In summary, the ss-PCMs synthesized in this work and the successor product Nanolope PCM have superior properties to the PCMs available on the market and will help to reduce the primary energy demand in buildings by the integration in electrical heaters and solar-water heating systems. Additionally, ss-PCMs can be used as a passive cooling medium in photovoltaic panels and batteries to increase the efficiency of these systems. However, the upscaling, the flammability problems and the slow drying process have to be solved in future studies. The combination of the sol-gel process and the emulsion-templating is a useful approach to synthesize different ss-PCMs. With structure-directing agents and hard templates,

the structure of the silica phase is controlled and the physicochemical properties are adjusted. The basics of this concept could help future scientists to develop novel ss-PCMs with high mechanical stabilities and high latent heats based on graphite, boron nitride or alumina backbones, which should accelerate the heat transfer even more than silica in the PCM phase. Due to the low thermal conductivities of the monolithic Nanolope PCM after calcination (~ 37 mW/mK), the sol-gel synthesis by the emulsion strategy is interesting for the development of novel thermal insulation or catalyst carrier materials, too.

References

1. Rubitherm (2021) Produkte. <https://www.rubitherm.eu/produktkategorien.html>. Accessed 4 Nov 2021
2. Microtek Labs (2021) Micronal. <https://www.microteklabs.com/micronal>. Accessed 4 Nov 2021
3. Jekusol (2021) Jekusol Speicher-Ball. <https://www.jekusol.de/produkte/jekuhybrid/jekuhybrid-verkapslung/jekusol-speicher-ball/>. Accessed 4 Nov 2021
4. Axiotherm (2021) Axiotherm PCM. <https://www.axiotherm.de/de/produkte/axiotherm-pcm/>. Accessed 4 Nov 2021
5. Bland A, Khzouz M, Statheros T, Gkanas E (2017) PCMs for Residential Building Applications: A Short Review Focused on Disadvantages and Proposals for Future Development. *Buildings*. Doi:10.3390/buildings7030078
6. Pcmproducts (2021) Our standard range of Encapsulated PCM Products. https://www.pcmproducts.net/Encapsulated_PCMS.htm. Accessed 4 Nov 2021
7. Va-Q-tec (2021) Phase Change Material (PCM). <https://va-q-tec.com/technologie/phase-change-materials/>. Accessed 5 Nov 2021
8. Rubitherm (2021) Macroencapsulation – Heat storage elements - Hot boards. <https://www.rubitherm.eu/en/index.php/productcategory/makroverkapselung-warmhalteelemente>. Accessed 4 Nov 2021
9. Rubitherm (2021) CSM - Makroverkapselung - PCM in Aluminiumhülle. <https://www.rubitherm.eu/index.php/productkategorie/makroverkapselung-csm>. Accessed 4 Nov 2021
10. Bento A, Costa Neto R, Santos Silva C (2017) Modeling and validation of a thermal energy storage based on the utilization of Phase Change Materials (PCM) in an office room. *Mechanical Engineering*. DOI:10.13140/RG.2.2.13462.09281

11. Hunger M, Entrop AG, Mandilaras I, Brouwers H, Founti M (2009) The behavior of self-compacting concrete containing micro-encapsulated Phase Change Materials. *Cement and Concrete Composites*. Doi:10.1016/j.cemconcomp.2009.08.002
12. Huu-Quan D, Sheremet M, Kamel MS, Izadi M (2020) Investigation of thermal-hydro dynamical behavior on nano-encapsulated PCM suspension: Effect of fin position, fractioning and aspect ratio. *Chemical Engineering and Processing - Process Intensification*. Doi:10.1016/j.cep.2020.108122
13. Ghalambaz M, Mehryan S, Mozaffari M, Hashem Zadeh SM, Saffari Pour M (2020) Study of thermal and hydrodynamic characteristics of water-nano-encapsulated phase change particles suspension in an annulus of a porous eccentric horizontal cylinder. *International Journal of Heat and Mass Transfer*. Doi:10.1016/j.ijheatmasstransfer.2020.119792
14. Shehzad SA, Alshuraiaan B, Kamel MS, Izadi M, Ambreen T (2021) Influence of fin orientation on the natural convection of aqueous-based nano-encapsulated PCMs in a heat exchanger equipped with wing-like fins. *Chemical Engineering and Processing - Process Intensification*. Doi:10.1016/j.cep.2020.108287
15. Lupi S (2017) *Fundamentals of Electroheat: Electrical Technologies for Process Heating*. SpringerLink Bücher. Springer International Publishing, Cham
16. Amkpa JA, Badarulzaman NA (2016) Thermal Conductivity of Barkin-ladi Fireclay Brick as Refractory Material, 2016, Vol. 08.
https://www.researchgate.net/publication/311970140_Thermal_Conductivity_of_Aloji_Fire_clay_as_Refractory_Material. Accessed 15 July 2021.
17. BMWi (2021) *Energiepreise und Transparenz für Verbraucher*.
<https://www.bmwi.de/Redaktion/DE/Textsammlungen/Energie/strompreise.html>. Accessed 4 Nov 2021
18. BASF (2010) *Katalog für Architekten und Planer 2010*, 166.
<https://www.yumpu.com/en/document/view/53104608/micronal-pcm-katalog-fur-architekten-und-planer-2010>. Accessed 12 February 2021.
19. Duan J, Liu Y, Zeng L, Wang Y, Su Q, Wang J (2021) Experimental Investigation of a Novel Solar Energy Storage Heating Radiator with Phase Change Material. *ACS Omega*. Doi:10.1021/acsomega.1c00138
20. Javadi FS, Metselaar H, Ganesan P (2020) Performance improvement of solar thermal systems integrated with phase change materials (PCM), a review. *Solar Energy*. Doi:10.1016/j.solener.2020.05.106
21. KraftBoxx (2021) *Power to Heat Systemspeicher*. <https://heatstixx.de/produkt-kraftboxx/>. Accessed 4 Nov 2021

-
22. Ma T, Yang H, Zhang Y, Lu L, Wang X (2015) Using phase change materials in photovoltaic systems for thermal regulation and electrical efficiency improvement: A review and outlook. *Renewable and Sustainable Energy Reviews*. DOI:10.1016/j.rser.2014.12.003
 23. Ma T, Li Z, Zhao J (2019) Photovoltaic panel integrated with phase change materials (PV-PCM): technology overview and materials selection. *Renewable and Sustainable Energy Reviews*. Doi:10.1016/j.rser.2019.109406
 24. Jaguemont J, Omar N, van den Bossche P, Mierlo J (2018) Phase-change materials (PCM) for automotive applications: A review. *Applied Thermal Engineering*. Doi:10.1016/j.applthermaleng.2017.12.097
 25. Lin C, Xu S, Chang G, Liu J (2015) Experiment and simulation of a LiFePO₄ battery pack with a passive thermal management system using composite phase change material and graphite sheets. *Journal of Power Sources*. Doi:10.1016/j.jpowsour.2014.11.068
 26. Greco A, Jiang X, Cao D (2015) An investigation of lithium-ion battery thermal management using paraffin/porous-graphite-matrix composite. *Journal of Power Sources*. Doi:10.1016/j.jpowsour.2014.12.027

7 Appendix

7.1 Curriculum Vitae

Personal Data

Name: Felix Marske

Address: Martinstraße 25
06108 Halle (Saale)

Birthday: 16.05.1992

Birthplace: Wolfenbüttel

Nationality: German

E-mail: felix.marske@gmail.com

Education

Since 2017 **Ph.D. study in Chemistry**

- Martin-Luther-University Halle-Wittenberg, Halle (Saale).
- Doctoral Thesis: „Synthesis of monolithic shape-stabilized phase change materials via an *in situ* sol-gel process“

2014 - 2017 **Master of Science in Chemistry**

- University Leipzig, Leipzig.
- Master Thesis: „Synthese von Silika-Xerogelen als Wärmedämm- und speichermaterialien.“

2011 - 2014 **Bachelor of Science in Chemistry**

- University Leipzig, Leipzig.
- Bachelor Thesis: „Crossdehydrocoupling as a Central Method to Obtain Phosphine–Borane Polymers.“

2005 - 2011 **Allgemeine Hochschulreife (Abitur)**

- Gymnasium Große Schule, Wolfenbüttel.

7.2 List of publications

- [1] F. Marske, J. Martins de Souza e Silva, R. B. Wehrspohn, T. Hahn and D. Enke, Synthesis of monolithic shape-stabilized phase change materials with high mechanical stability via a porogen-assisted *in situ* sol-gel process, RSC Adv. 10 (2020), Gold Open Access, 3072–3083. <https://doi.org/10.1039/c9ra10631f>.
- [2] F. Marske, T. Lindenberg, J. Martins de Souza e Silva, R. B. Wehrspohn, A. W. Maijenburg, T. Hahn and D. Enke, Size and surface effects of hexagonal boron nitrides on the physicochemical properties of monolithic phase change materials synthesized via sol-gel route, Appl. Therm. Eng. 196 (2021), Copyright Elsevier, 117325. <https://doi.org/10.1016/j.applthermaleng.2021.117325>.
- [3] F. Marske, T. Lindenberg, J. Martins de Souza e Silva, R. B. Wehrspohn, A. W. Maijenburg, T. Hahn and D. Enke, Experimental data showing the influence of different boron nitride particles on the silica network, the butyl stearate and the porogens in shape-stabilized phase change materials, Data Br. 38 (2021), Open Access, 107428. <https://doi.org/10.1016/j.dib.2021.107428>.
- [4] F. Marske, J. Dasler, C. Haupt, K. Bacia, T. Hahn and D. Enke, Influence of surfactants and organic polymers on monolithic shape-stabilized phase change materials synthesized via sol-gel route, J. Energy Storage 49 (2022), Copyright Elsevier, 104127. <https://doi.org/10.1016/j.est.2022.104127>.
- [5] F. Marske, C. Haupt, C. Birkemeyer, K. Bacia, T. Hahn and D. Enke, Shape stabilization of organic phase change materials as mechanical stable silica boards with high latent heats via sol-gel route, J. Build. Eng. 60 (2022), Open Access, 105198. <https://doi.org/10.1016/j.jobbe.2022.105198>.

7.3 Project awards

12/2020

SCIDEA STAGE Pitch 2020, 1st Place

- Start-up Center University Halle, Halle (Saale).
- Winner of the SCIDEA STAGE Pitch 2020 for the best start up project and best presentation.

06/2020

IQ Innovation Award Central Germany 2020, 1st Place

- Metropolregion Mitteldeutschland Management GmbH.
- Winner of the IQ Innovation Award Central Germany 2020 in Automotive Cluster.
- Topic: "Form-stabilisierter Latentwärmespeicher ss-PCM zur Kühlung des Akkumulators im Elektroauto."

12/2019

Hugo Junkers Award 2019, 2nd Place

- Country Saxony-Anhalt.
- Winner of the Hugo Junkers Award 2019 in Basic Research.
- Topic: "Form-stabilisierte Latentwärmespeicherwände zur massiven Speicherung von Raumwärme."

11/2018

K.S.W. Sing Award 2018, 1st Place

- Porotec GmbH, Hofheim.
- Innovation Award Winner of the XIX. Porotec Conference.
- Topic: "Shape-stabilized phase change materials for thermal energy storage systems."

7.4 Statement of own contributions

I hereby declare, that I have written without any help of others the doctoral thesis "*Synthesis of monolithic shape-stabilized phase change materials by an in situ sol-gel process*" solely on my own and that I have marked all references correctly according to general standards in scientific publishing. All references used in this doctoral thesis are listed. The figures, tables and abbreviations are created by myself or marked with references, if they were changed or adopted. I assure that I have not published this doctoral thesis in any form or way at an internal or external university different from Martin-Luther University Halle-Wittenberg and that I have never written and published any other doctoral thesis than this one. Moreover, I declare that I have no financial, ethical or social conflicts of interest regarding this doctoral thesis.

Place, Date

Signature

7.5 Authorship contribution statement

The author of this doctoral thesis came up with the topic and the idea of silica-based ss-PCMs. To develop novel ss-PCMs with higher mechanical stabilities, he structured his idea, created a concept and synthesis plan according to a specific methodology, and investigated the ss-PCMs by different formal analyses. Moreover, he curated, visualized and validated the data of the analytical experiments and has written the original draft of the manuscripts himself.

The cooperation partners have developed and carried out specific analytical investigations for this doctoral thesis. Dr. Juliana Martins Souza e Silva of the research group of Prof. Dr. Ralf B. Wehrspohn investigated and imaged the silica structure by different X-ray imaging experiments, which were performed on a Carl Zeiss Xradia 810 Ultra. These imaging experiments helped to visualize the three-dimensional orientation and interconnectivity of the silica structure in ss-PCMs without a further calcination step. The three-dimensional orientation of boron nitride was investigated, too. During his final exam, Mr. Joe Dasler helped to synthesize and analyze the ss-PCMs with different porogen content by differential scanning calorimetry. Dr. Caroline Haupt of the research group of Prof. Dr. Kirsten Bacia developed strategies to image the ss-PCM formation *in situ* by confocal fluorescence microscopy. For this purpose, Dr. Caroline Haupt marked the silica phase, the aqueous phase and the PCM phase separately with different kinds of fluorescent dyes. Mr. Titus Lindenberg of the research group of Prof. Dr. A. Wouter Maijenburg improved and carried out the imaging of ss-PCMs before and after calcination by scanning electron microscopy to analyze the microstructure of the silica phase containing boron nitride. Dr. Claudia Birkemeyer analyzed the possible chemical degradation products of ss-PCMs based on paraffins, polyethylene glycols and acetamides by gas chromatography/mass spectrometry and electrospray ionization mass spectrometry to prove the durability and performance of the ss-PCMs. Prof. Dr. Ralf B. Wehrspohn, Prof. Dr. A. Wouter Maijenburg, Prof. Dr. Kirsten Bacia, Dr. Caroline Haupt, Dr. Claudia Birkemeyer, Mr. Titus Lindenberg and Dr. Juliana Martins Souza e Silva helped with the supply of resources and with the review and editing of the manuscripts. Prof. Dr. Dirk Enke helped with chemical questions regarding silica and sol-gel as a supervisor and with the review and editing of the manuscripts. Prof. Dr. Thomas Hahn was the supervisor for the project administration and funding acquisition. Moreover, he constructed and developed prototype applications for ss-PCMs. A summarized authorship contribution statement is included in every publication according to the contributor roles taxonomy (CRediT).